Guidance, Navigation, Control and Relative Dynamics for Spacecraft Proximity Maneuvers

Ankersen, Finn

Publication date:
2010

Document Version
Early version, also known as pre-print

Guidance, Navigation, Control and Relative Dynamics for Spacecraft Proximity Maneuvers

FINN ANKERSEN

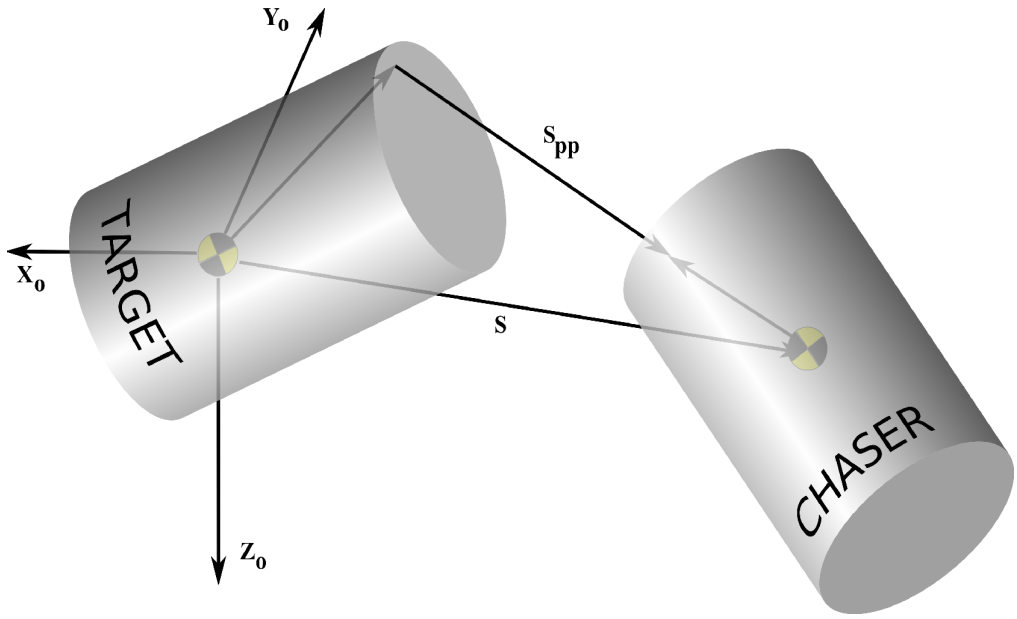

Automation & Control
Department of Electronic Systems
Aalborg University

Finn Ankersen

Ph.D. Thesis

Guidance, Navigation, Control and Relative Dynamics for Spacecraft Proximity Maneuvers

Guidance, Navigation, Control and Relative Dynamics for Spacecraft Proximity Maneuvers.

Ph.D. Thesis

First Edition
December 5, 2010

ISBN 978-87-92328-72-4

Typeset using LaTeX 2$_\varepsilon$ in book document class.
Design and simulation using MATLAB by The MathWorks Inc.
Design and simulation using MATRIX$_X$ by Integrated Systems Inc.
Integral verification using MATHEMATICA by Wolfram Research Inc.
Drawings produced in Xfig

Finn Ankersen, September 12, 2011

Preface and Acknowledgments

This thesis is submitted in fulfillment of the requirements for the degree of Doctor of Philosophy at the Department of Electronic Systems, Section for Automation and Control, Aalborg University, Denmark. The work has been carried out under the supervision of professor Jakob Stoustrup.

I would like to thank professor Jakob Stoustrup at Aalborg University for his dedication and continued support for the duration of the entire project. It has been a privilege to have been working autonomously, though under professional and focused guidance when needed.

Special thanks to my, since a long time, good friend Bo Andersen, director of the Norwegian Space Center, for discussions in the initial phases and his continued encouragement.

Also thanks to my colleague Samir Bennani and former colleague Bogdan Udrea at the European Space Agency for the occasional sparring when frustration mounted, as well as to staff at Aalborg University section for Automation and Control.

Finally, the greatest thanks go to Sisko Mäntylä for her love, support and immense patience, without which the success of this project would have been difficult. Special thanks for editing my few repetitive linguistic mistakes.

Aalborg, Denmark, September 12, 2011

Finn Ankersen

Abstract

The rendezvous and docking problem between spacecraft on elliptical orbits is dealt with in this doctoral thesis. The main contributions are on the relative dynamics solutions and the closed loop relative motion control.

The motivation is that such missions on non circular orbits have never been performed. As a study case for the development the European Automated Transfer Vehicle and the International Space Station is chosen.

First a linear dynamics model describing the relative position dynamics and kinematics between two spacecraft on any closed orbit will be developed. A compact closed form solution to this system of differential equations will be developed in the form of a minimum realization transition matrix. This will form the basis for developing the expressions for general ΔV maneuvers and the special properties of radial and tangential ones.

The differential equations for the relative position are combined with the developed attitude linear models. This will form a complete coupled linear model for 6 degree of freedom motion between any two arbitrary points on the two spacecraft.

Secondly control methods and designed Guidance, Navigation and Control for the 6 degree of freedom systems will be compared and traded off. The periodic time varying properties of the dynamic system are evaluated and domains with different design needs are established. The time varying parameters as well as uncertainties are treated fully in the robust control framework. Detailed Linear Fractional Transformation models are developed analytically for all relevant parameter variations, which leads to a unified design and analysis method for this type of systems.

Finally a comprehensive verification and validation of all the designs is performed. This is achieved using multi variable μ analysis in the linear domain. Further verification is performed by means of nonlinear simulations and statistical analysis.

Synopsis

Denne Ph.D. afhandling behandler Rendezvous og sammenkoblings problemerne mellem rumfartøjer i elliptiske baner. Afhandlingens hovedbidrag bliver løsninger af den relative dynamik og kinematik, samt reguleringsløsninger af de relative bevægelser.

Projektet er motiveret af, at sådanne missioner i elliptiske baner ikke tidligere har været opsendt. Det Europæiske rumfartøj Automated Transfer Vehicle og den Internationale Rumstation er i afhandlingen valgt som eksempel.

Først bliver udviklet en model for den relative dynamik og kinematik mellem to rumfartøjer i et vilkårlig kredsløb. En kompakt løsning til dette differentialligningssystem bliver udviklet i form af en overføringsmatrice på minimal realiserbar form. Dette danner grundlaget for udvikling af generelle udtryk for ΔV manøvrer og de specielle egenskaber for radiale og tangentiale manøvrer.

Differentialligningerne for den relative position bliver kombineret med den udledte lineære model for den relative attitude. Tilsammen giver de to modeller en komplet koblet model med 6 frihedsgrader for et vilkårligt punkt på de to rumfartøjer.

Dernæst sammenlignes design metoder og designs for Guidance, Navigation og Control systemer med 6 frihedsgrader og en strategi bliver valgt for det videre forløb. Det periodiske tidsvarierende systems egenskaber bliver evalueret og områder med forskellige kravspecifikationer identificeres. De tidsvarierende parametre, samt alle usikkerheder, bliver analyseret ved hjælp af metoder fra robust regulering. Detaljerede Linear Fractional Transformation modeller udvikles for alle relevante parameter variationer, hvilket fører frem til en samlet design og analyse metode for denne type systemer.

Til slut udføres en tilbundsgående verifikation og validering af alle udførte designs. Til dette anvendes multivariabel μ analyse i det lineære område. Dette verificeres yderligere ved hjælp af ulineære simuleringer og statistisk analyse.

Finn Ankersen, September 12, 2011

Contents

Abbreviations

AE	Approach Ellipsoid
AOCS	Attitude and Orbit Control System
ARP	ATV Rendezvous Predevelopment
ATV	Automated Transfer Vehicle
CW	Clohessy Wiltshire
CAE	Computer Aided Engineering
CAM	Collision Avoidance Maneuver
CCD	Charge Coupled Device
CMG	Control Moment Gyro
CNES	Centre National d'Etudes Spatiales
COM	Center of Mass
DCM	Direction Cosine Matrix
DM	Delay Margin
DOF	Degree of Freedom
EKF	Extended Kalman Filter
EPOS	European Proximity Operations Simulator
EPOSx	European Proximity Operations Simulator Extended
ESA	European Space Agency
ETS	Engineering Test Satellite
FCM	Flight Control Monitoring
FDIR	Failure Detection Isolation and Recovery
FEM	Finite Element Model
FF	Formation Flying
FOV	Field Of View
FTC	Fault Tolerant Control
GM	Gain Margin
GMS	General Measurement System
GNC	Guidance, Navigation and Control
GPS	Global Positioning System
HK	House Keeping

IAS	Institute of the Aerospace Sciences
IMU	Inertial Measurement Unit
IQC	Integral Quadratic Constraints
ISS	International Space Station
ITS	Integrated Truss Segment
KOZ	Keep Out Zone
LEO	Low Earth Orbit
LFT	Linear Fractional Transformation
LHP	Left Half Plane
LOS	Line Of Sight
LPV	Linear Parameter Varying
LQ	Linear Quadratic
LQG	Linear Quadratic Gaussian
LQR	Linear Quadratic Regulator
LTI	Linear Time Invariant
LTR	Loop Transfer Recovery
LTV	Linear Time Varying
LVLH	Local Vertical Local Horizontal
MC	Monte Carlo
MIB	Minimum Impulse Bit
MIL	Man In the Loop
MIMO	Multi Input Multi Output
MM	Mode Management
MPC	Model Predictive Control
MSIS	Mass Spectrometer Incoherent Scatter
MTFF	Man Tended Free Flyer
MVM	Mission and Vehicle Management
NP	Nominal Performance
NS	Nominal Stability
NTV	Nonlinear Time Varying
OMV	Orbital Maneuvering Vehicle
PID	Proportional Integral Differential
PM	Phase Margin
PWM	Pulse Width Modulation
PWPF	Pulse Width Pulse Frequency modulation
RAAN	Right Ascension of Ascending Node
RDOTS	Rendezvous and Docking Operation Test System
RGA	Relative Gain Array
RGPS	Relative GPS
RHP	Right Half Plane

RP	Robust Performance
RS	Robust Stability
RVD	RendezVous and Docking
RVS	RendezVous Sensor
SISO	Single Input Single Output
SK	Station Keeping
STR	Star Tracker
SVD	Singular Value Decomposition
TC	Tele Command
TEA	Torque Equilibrium Attitude
TM	Telemetry
UAV	Unmanned Aerial Vehicle
VCM	Vehicle Configuration Management
ZOH	Zero Order Hold

Chapter 1

Introduction and Background

Most missions in space involve only one spacecraft and they are the most common. This is nevertheless not sufficient to fulfill the objectives of certain missions. The RendezVous and Docking or Berthing (RVD) is a key technology, which is required for most missions involving more than one spacecraft. Missions of the following type will need this technology:

- In orbit assembly of space structures.
- Transportation of crew to and from space stations.
- Retrieval, capture and return to the Earth of a spacecraft. This can e.g. be rejoining a lander to an orbiting vehicle followed by a return.
- Supply to space stations or other spacecraft.
- Formation flying spacecraft constellations, excluding the docking part.

The first rendezvous and docking between two spacecraft took place on March 16, 1966, when Armstrong and Scott in a Gemini spacecraft performed manual RVD with the unmanned Agena target vehicle. The first automatic RVD took place on October 30, 1967, when the Soviet spacecraft Cosmos 186 and Cosmos 188 docked. Several RVD operations within and between the American(US) and Russian(Soviet) space programs have been there later, some automatic but most under manual control by astronauts and cosmonauts. Most of these operations have been in connection with the respective space programs like:

- Apollo (US, 1968-1972) and Skylab (1973-1974) programs.
- Salyute and Mir (Soviet and Russian) programs (1971-1999).
- Space Shuttle (US) service and retrieval missions to various satellites.

In western Europe RVD technology has been studied by the European Space Agency (ESA) since 1984 as technology studies and later in connection with the Columbus Man Tended Free Flyer (MTFF) and the Hermes space plane. The former intended to dock with space station Freedom and the latter to visit the MTFF (Cislaghi, Fehse, Paris & Ankersen 1999).

Under the influence of the political situation in Europe, both of those programs were canceled in the beginning of the nineties. After the merger of the Western and Eastern space station programs into the International Space Station (ISS), the unmanned Automated Transfer Vehicle (ATV), became part of the European contribution. The ATV will provide resupply and re-boost missions to the ISS. Part of the program is provided by other vehicles from the other international partners from the US, Russia and Japan.

RVD is a multi disciplinary technology which enables spacecraft to:

- Bring the two spacecraft co-orbiting on the same orbit.
- Perform maneuvers of the chaser spacecraft with respect to the target spacecraft. Maneuvers can be of many different types, which will be described in Chapter 2.
- Perform the actual docking/berthing between the two spacecraft to form a composite.
- Perform the attitude and orbit control of the composite.
- Facilitate the exchange of material, persons and signals between the two spacecraft.
- Perform the separation of the two spacecraft and the following separation maneuvers to bring them safely apart, both in the short and long term.

The first and second bullet in the previous list are the major and most complex ones in terms of both development and operations. The second bullet will be dealt with extensively in this work.

1.1 The RendezVous Process

The RVD process consists of a series of orbital maneuvers and controlled trajectories, which will bring the vehicles closer together and eventually into the close vicinity of each other. The last part of the approach will have to bring the chaser spacecraft close to the target spacecraft with increasingly narrow corridors for both the position, attitude and their respective time derivatives.

- In the case of *docking* the Guidance, Navigation and Control (GNC) system of the chaser spacecraft shall bring its state inside the envelope of the requirements for the docking system to enable the capture.

- In the case of *berthing* the GNC system of the chaser spacecraft shall place itself within a box with nominally zero relative velocity between the chaser and the target for grappling by a manipulator arm, which will then transfer the spacecraft to its position for the docking. See also (Strauch, Görlach & Ankersen 1996).

The complexity of the RVD process results in a multitude of different modes and constraints driven by different requirements to fulfill the mission. A high level overview will be provided here.

- **Launch and Phasing:** To arrive at the proximity of the target spacecraft the chaser spacecraft must be brought onto the orbital plane of the target with the same altitude and eccentricity. As the orbital planes drift with time, due to Earth gravity field irregularities, the difference in plane drifts must be taken into account for the choice of the chaser orbital plane at launch (Vinti 1998). The height of the chaser phasing orbit depends on the phasing angle which has to be caught up and the time available to do so. Delays due to a launch or a target readiness will have an impact on which orbit to launch into.

- **Proximity Operations:** Post launch changes of the target orbit, e.g. due to a debris avoidance maneuver, will have to be taken into account for the determination of the arrival point for starting the RVD maneuvers and the on board guidance will have to be updated.

  The illumination conditions during the final part of the RVD maneuvers have to be right in order to enable monitoring by the crew either directly or via cameras.

  During the RVD maneuvers there are requirements in terms of approach corridors to be followed and hold points to be waited at for monitoring. This has to be compatible with passively safe trajectories as far as possible, even in the case of lower or higher than nominal maneuver burns (Fehse & Ortega 1998). For the parts where this is physically not possible, due to the closeness and the associated velocity, an active Collision Avoidance Maneuver (CAM) shall be performed to bring the chaser to a passively safe location with respect to the target.

- **Attached Phase:** The part where there are no maneuvers but where the spacecraft is latched and locked to the other spacecraft. During this phase there is an exchange of material, liquids, electrical signals etc. This part will not be treated any further in this work.

- **Communication Constraints:** For the communication between the target and ground to the chaser there are many constraints which has an influence on the trajectory design. Even by utilizing relay satellites it is not possible to obtain a full coverage from ground for monitoring and intervention, which call for an autonomous on board design. Further the data rate is typically limited to a few kilobits per second, restricting the type of data that can be transmitted.

- **On Board System Constraints:** The attitude of the chaser will be imposed by sensors, communication constraints, possibly by the orientation of the solar panels, thermal radiators and the target attitude during the final approach. The thruster

layout of the chaser will also pose constraints on the maneuvers as well as those coming from the sensory equipment of the spacecraft. During the far away maneuvers the navigation is based on e.g. Global Positioning System (GPS) signals and during the close maneuvers on optical sensors which can provide both relative position and attitude measurements.

Chapter 2 will provide a more comprehensive description of the typically involved maneuvers.

1.2 A Panoramic Overview of the Field

This thesis will deal with the problem of bringing two spacecraft, each on their quasi coplanar orbit, together in space by means of either docking or berthing.

The motivation for the thesis is, that there has not earlier been performed any autonomous missions to a space station like the ISS, with its flexible structure, as well as the level of the ATV on board autonomy in elliptical orbits. There is also an increasing demand for GNC for proximity maneuvers for future missions with higher complexity than today.

1.2.1 Mission Concepts

Mission analysis leads to the main elements described in Chapter 1.1 and the requirements for the mission. They will not be detailed in this thesis, but different types of RVD missions have been addressed, with the planetary and comet type trajectory corrections planning and contingencies addressed in (McAdams 1997). Comet landing and relative trajectories for Rosetta is dealt with in (Hechler 1997). Mission design with concurrent engineering, minimization of mission life cost and the issue of the share between space and ground segments can be found in (Landshof, Harvey & Marshall 1994). Relative dynamics, safe trajectories and collision avoidance issues are covered by (Eckstein 1987) and general RVD mission planning for trajectories and navigation by (OMV 1985). Mission planning tools for the Shuttle and Apollo/Soyuz are described in (McGlathery 1973) and feasibility analysis, launch and operation windows and time line by the Flight Design System (Friedlander & Hare 1987). Autonomous on board mission planning using covariance techniques is developed in (Geller 2006) taking into account both the GNC system and the nonlinear dynamics in a linearized manner.

1.2.2 Relative Motion Circular Orbit

The relative dynamics between two spacecraft or bodies has been researched by several in the past. The first recognized work was by (Hill 1874) describing the perturbed Moon motion relative to its non perturbed orbit and later formulated linearly in (Hill 1878). Early ideas by (Clohessy & Wiltshire 1959) were presented at the Institute of the Aerospace Sciences (IAS) meeting and later published in (Clohessy & Wiltshire 1960). They have become the most well known and used relative motion

equations, though by modifying the results in (Hill 1878) by a constant term, the differential equations of (Clohessy & Wiltshire 1960) appear directly. Based on these results (Wheelon 1959) has worked on two pulse trajectories aiming at development of guidance strategies followed by work on optimal transfer time to minimize the ΔV by (Eggleston 1960). Fuel optimal ΔV expressions and guidance algorithms were developed by (Spradlin 1960) followed by equations of practical use for finite pulses and a closed form solution by (Tschauner & Hempel 1964). At the same time (London 1963) attempted to arrive at more accurate equations by means of second order approximations. Work on new circular orbits has been performed by (Anthony & Sasaki 1965) with approximate analytical solutions for ΔV terms and eccentric chaser orbits were addressed by (Berreen & Crisp 1976) with extensions of the domain of good approximation by a polar coordinate formulation followed by a nonlinear Taylor series formulation in configuration space of elliptic orbits with respect to circular ones by (Gurfil & Kasdin 2004). Fuel optimal maneuvers and simulation results are in (Carter 1984) with minimum fuel maneuvers in a quadratic programming formulation in (Neff & Fowler 1991). A Taylor series derivation with a closed form solution was performed in (Ankersen 1990*b*) leading to general analytical expressions for arbitrarily many finite pulse maneuvers as well as a traveling ellipse formulation of the closed solution and found in (Fehse 2003). Multi pulse phasing has been addressed in iterative algorithms for fuel saving in (Luo, Tang, Lei & Li 2007). Beyond the commonly used Clohessy Wiltshire (Schweighart & Sedwick 2002) has developed linear dynamics and closed solution taking into account the J_2 term in the equations and (Carter & Humi 2002) by including quadratic drag in the solution of the equations. A rather complex set of relative second order equations have been developed in polar coordinates by (Karlgaard & Lutze 2003), but with few applications in practice. The terminal rendezvous problem with minimum relative distance as performance index for genetic algorithms is dealt with in (Luo, Lei & Tang 2007).

1.2.3 Relative Motion Elliptic Orbit

Works on arbitrary elliptic orbits have been less addressed in the literature than circular ones and practical usable general closed form solutions are rare. One of the first to address the elliptic orbits was (Lawden 1954) in connection with two pulse coplanar transfers and minimal trajectories with and without the knowledge of time. This preceded the formulation of the well known circular orbit equations. A generalization of the results of (Clohessy & Wiltshire 1960) to a canonical form with the true anomaly as independent variable was done by (Tschauner & Hempel 1965) leading to a complex homogeneous solution in restricted cases. In (Tschauner 1965) the independent variable was changed to become the eccentric anomaly and by eliminating acceleration terms a full solution of guidance equations were found leading to a system with periodic coefficients reported in (Tschauner 1967). The Tschauner-Hempel system has also been addressed for small orbital elements' perturbations in (Sengupta & Vadali 2007) to solve the equations. (Shulman & Scott 1966) found analytical solutions using the true anomaly, but it suffered from strong limitations regarding initial conditions. Quadratic terms were considered by (Euler & Shulman 1967) and solved by a differential correc-

tion method without reaching a closed form solution. A matrix solution to the systems in (Tschauner 1965) were found by (Weiss 1981) using the eccentric anomaly leading to a rather complex solution for practical use. (Carter 1990) modified the integral used by (Lawden 1954) in order to remove singularities in the solution and make it valid for non circular orbits. In (Lawden 1993) optimal impulsive transfers were found based upon his earlier work. Further to the others' work (Humi 1993) attempts finding a solution having a time varying mass of the chaser spacecraft. A different approach than most other solutions is addressed in (Garrison, Gardner & Axelrad 1995) finding the differential dynamics by differences of the Keplerian elements directly leading to an analytical invertible transition matrix. A closed form solution using time and true anomaly is addressed in (Broucke 2002) and a global nonlinear motion is researched using energy matching conditions in (Gurfil 2005). Orbit transfers using the development and solutions in Chapter 4 and (Yamanaka & Ankersen 2002) is treated using a Linear Quadratic formulation as a Null Controllable with Vanishing Energy problem in (Shibata & Ichikawa 2007). Another polynomial approximation is proposed in (Guibout & Scheeres 2006), but formulated as a 2 point boundary value problem. Geometrical methods are used in (Gim & Alfriend 2003) to find a rather complicated state transition matrix including the J_2 gravitational term and a Δ-orbital element time explicit formulation in (Lane & Axelrad 2006) applied to Formation Flying (FF). μ control of such a system performed in (Xu, Fitz-Coy, Lind & Tatsch 2007). Manifolds for minimum, maximum and mean relative motion in orbital element form is found in (Gurfil & Kholshevnikov 2006) and RVD coordinates for a planar restricted 3 body problem is addressed by (Humi 2005).

1.2.4 GNC Architectures

This section will survey the on board GNC system architecture despite it is sparsely represented in the literature. In connection with the earlier Hermes and MTFF (Brondino & Legenne 1991) addresses the on board architecture seen from a system point of view, as well as mission and testing aspects. This took place at the same time as the Orbital Maneuvering Vehicle (OMV) , which on board architecture is addressed in (Parry, Golub & Southwood 1989) as well as Man In the Loop (MIL) issues in respect to the feedback loop architecture. An architecture for both RVD and planetary landing is proposed in (Jones 1992) using cruise missile technology. The ATV avionics architecture can be found described in (Fabrega, Godet, Pairot & Perarnaud 1998) together with analysis of the drivers for the avionics selection and its monitoring functions. The only, apart from Apollo 7 , technology demonstration satellite dedicated to RVD is the Engineering Test Satellite (ETS)-VII , where the architecture is in (Kawano, Mokuno, Kasai & Suzuki 2001) and it reports on the in flight performance of GPS based relative navigation. The general ETS-VII on board system is addressed by (Yamanaka 1997). Within the ATV Rendezvous Predevelopment (ARP) a RGPS flight experiment was performed between the Shuttle and the MIR space station described in (Moreau & Marcille 1998*a*) and its post flight analysis is addressed in (Moreau & Marcille 1998*b*). Within the same ARP program, the guidance and control tradeoffs are in (Gonnaud, Tsang &

Sommer 1997) together with a description of the integrated design approach leading to auto coded flight software. The GNC performance of ATV under thruster failures is addressed in (Ankersen 1990*c*). Further the influence of sensor and actuator failures on the robustness of the control system is addressed by (Peiman, Maghami, Sparks & Lim 1998) by means of measuring the poles distances to the imaginary axis. A convex optimization is applied in (Hechler & Fertig 1987) to control safe trajectories and relative motion for arbitrary perturbations and thrust is dealt with in (Ha & Mugellesi 1989) for the case of the Eureca spacecraft retrieval by the Shuttle manipulator arm. A guidance scheme for autonomous RVD using artificial potential functions is proposed in (Lopes & McInnes 1995) and later further developed for ARP. A distributed architecture for minimum time and fuel maneuvers with electrical propulsion in elliptic orbits is developed in (Campbell 2003). In summary has been addressed architectural issues dealing with on board implementation of GNC, MIL, guidance and distributed architectures. Parts of this information has flown into the development in Chapter 6.

Mission and Vehicle Management (MVM) and Failure Detection Isolation and Recovery (FDIR) are investigated in several areas. Development of a fault tolerant GNC system is in (Mokuno, Kawano, Horiguchi & Kibe 1995) together with safe mission profile trajectories and a 3 processor fault tolerant computer is developed in (Sund, Tailhades & Linden 1991) with FDIR directly on the chip. Fail safe computers are also addressed by (Vaissiere & Griseri 1990). A more extensive work on MVM and FDIR is reported by (Soppa, Sommer, Tobias, Panicucci & Olivier-Martin 1991) in terms of safe trajectories, voting concepts, parity mapping, consistency and coherence checks and $\mathcal{X}^2$ tests. RVD expert systems to improve operations are in (Goodwin & Bochsler 1987) and manual intervention in the navigation loop under failures based upon camera image information is developed by (Vankov, Alyoshin, Chliaev, Fehse & Ankersen 1996). The identification of the point of no return under thruster open failure is addressed by (Ankersen 1990*d*) and the accuracy for finite pulse transfers in (Ankersen 1991). How much on board autonomy is needed for ground control with minimum safe approach distance and communication delays is dealt with in (Geller 2007).

1.2.5 GNC Designs

Early guidance and navigation systems were not made for autonomy, but to off load part of the astronauts workload in steering the spacecraft. One such approach was the Minkey program, which would be estimating the position and velocity in a Kalman filter in (Copps & Goode 1971), performing ΔV computations and to be used for Apollo 15, 16, 17 and Skylab. The flight performance of Skylab using Apollo is reported in (Belew 1973) having a smooth RVD domain as it was using Control Moment Gyros (CMG) for the station control. The use of the Apollo radar and Inertial Measurement Unit (IMU) in the Shuttle during Station Keeping (SK) with vertical thrust leading to limit cycle motion is addressed by (Gustafson & Kriegsman 1973). They also devised a square root formulation of its covariance. To that, vision based discrete time navigation, is reported in (Ho & McClamroch 1993) with simulation results. A control design for berthing in a station assembly scenario is in (Hua, Kubiak, Lin & Kilby 1993)

together with results. A Multi Input Multi Output (MIMO) feedback design of the Shuttle manipulator arm is in (Scott, Gilbert & Demeo 1993) providing better damping using primarily tip mounted accelerometer measurements. A μ-synthesis MIMO design for arbitrary non cooperating targets for RVD is developed in (Mora, Ankersen & Serrano 1996). In (Ankersen 1993) Computer Aided Engineering (CAE) methods are described and advocated for RVD and general spacecraft design leading to an integrated design approach from concept and design to real time software in (Ankersen 1998). Further model reference control is addressed by (Ankersen 1990*a*). An Extended Kalman Filter (EKF) for homing position estimation and fly around as well as general control design is performed in (Philip & Malik 1993). A two Kalman filter design with relative and inertial data fusion is developed in (Carpenter & Bishop 1997), which includes a covariance propagation method. (Kunugi, Koyama, Okanuma, Nakamura, Mokuno, Kawano, Horiguchi & Kibe 1994) report on the on board GNC system level description. (Calhoun & Dabney 1995) address the determination of the relative position and attitude from measurements with a quadratic optimization for quaternions. Further data fusion is performed in (Hablani 2009) with an integrated sensor suite comprising an imaging sensor, a laser range finder, a GPS/IMU system and a star tracker. Non Gaussian range and Line Of Sight (LOS) navigation in elliptic orbits is proposed in (Karlgaard 2006), using a mixed l_1, l_2 maximum likelihood optimization in Kalman and Huber filters. An ATV pre development selection of Kalman structure and H_2 control is reported in (Fabrega, Frezet & Gonnaud 1997). A classical feedback design in polar coordinates to boundary conditions along a docking axis is performed in (Kluever 1999). Guidance for approach and fly around in an arbitrary plane with EKF based navigation is addressed by (Hablani, Tapper & Dana-Bashian 2002). Open loop station keeping control based upon a multiple revolution Lambert solution is reported in (Shen & Tsiotras 2003). An optimal two impulse station keeping control on periodic time varying dynamics is performed by (Wiesel 2003) and a minimum time and fuel planar guidance maneuvers for elliptic orbit Formation Flying is performed by (Zanon & Campbell 2006) as a Hamilton - Jacobi - Bellman formulation. A control law for stabilizing a class of unstable periodic orbits in the Hill restricted 3 body problem for proximity motion on halo orbits is reported in (Scheeres, Hsiao & Vinh 2003) followed by a control design for relative dynamics with respect to unstable trajectories in (Hsiao & Scheeres 2005). (Tong, Shijie & Songxia 2007) address the relative control problem using only line of sight and range measurements and iteratively only LOS to obtain the range. The experiences presented above form partly the basis for the present research and its furthering.

Several relevant papers on general control work and general spacecraft design have been used within the RVD field of which some are addressed in the following. Practical design of uncertain multi variable feedback is in (Doyle & Stein 1981) generalizing Single Input Single Output (SISO) to MIMO and minimum singular values of the return difference matrix is found in (Newsom & Mukhopadhyad 1985) providing expressions for the singular value gradient. Stability margins for simultaneous changes in phase and gain can be found in (Mukhopadhyad & Newsom 1984) extending the singular matrix value properties. Negative inverse describing function analysis of modulation for thruster controlled spacecraft is in (Anthony, Wie & Carroll 1989) and thruster modu-

lation techniques and stability analysis are reported by (Ankersen 1989) applied to the Eureca spacecraft. (Zimpfer, Shieh & Sunkel 1998) report on a control method for design of MIMO systems in the presence of thruster modulation including delays. LQG and H_∞ flexible spacecraft design and flight evaluation is in (Kida, Yamaguchi, Chida & Sekiguchi 1997) and robust control using block shifts to move sets of closed loop poles in (Seetharama-Bath, Sreenatha & Shrivastava 1991). Robust performance with time varying uncertainties in a general state space formulation is dealt with in (Zhou, Khargonekar, Stoustrup & Niemann 1995) and by means of Integral Quadratic Constraints (IQC) and exponential stability by (Jösson & Rantzer 1996) and (Megretski & Rantzer 1997). Adaptive output feedback control has been demonstrated in (Singla, Subbarao & Junkins 2006) to bound output errors driven by calibration errors, biases and bounded stochastic disturbances. Nonlinear parametric uncertainties for discrete time systems has been addressed in (Zhao & Stoustrup 1997) for the robust $\mathcal{H}_2$ type of control. A Linear Fractional Transformation (LFT) approach in robust μ-synthesized flight systems are applied to Unmanned Aerial Vehicles (UAV) in (Paw & Balas 2008).

1.2.6 Simulation and Verification Aspects

The complexity of on board autonomous GNC systems has increased significantly over the years as the operational demands grow. The implementation aspects and the methods for embedded testing of flight systems are addressed by (Sommer, Tobias, Ankersen & Pauvert 1992) and the aspects regarding automatic coding and flight software standards, life cycle, tests and verification are addressed by (Terraillon, Ankersen, Vardanega & Carranza 1999) leading to an ESA standard. The Shuttle flight software development process is analyzed by statistical principles and control of the process in (Florac, Carleton & Barnard 2000). A survey of the development of flight systems with a view from the Triad processor in 1972, which was the first general software system to fly, until today systems are given in (Malcom & Utterback 1999). Looking towards near future missions (Zetocha, Self, Wainwright, Burns & Surka 2000) addressed an agent based system for multiple satellite missions, like interferometer formation flying missions and their real time multiple processor testing. Simulation models for MIL are addressed by (Walls, Greene & Teoh 1987) for the OMV crew training purpose.

A verification process for RVD is outlined in (Pauvert, Ankersen & Soppa 1991) and in further details of simulation using a virtual operation system for portability of test platforms is in (Kruse & Ankersen 1992). Moving towards real time and hardware in the loop is described by (Soppa, Ankersen & Pauvert 1992). Computer vision in a mockup is used by (Mukundan & Ramakrishnan 1995) for attitude quaternion determination. Simulation and verification of a space station and the Shuttle connected via the manipulator arm is reported in (Montgomery & Wu 1993) for the composite attitude control. The European Proximity Operations Simulator (EPOS) , which is a $6 + 3$ Degree Of Freedom (DOF) gantry robot with hardware in the closed loop facility, is described in (Heimbold & Steward 1988) addressing the real time verification aspects. (Cruzen, Lomas & Dabney 2000) address a similar, but later, such facility with slightly longer range. A further but separate development of a 300 m range similar fa-

cility $EPOS_x$ is addressed in (Pery, Bouchery, Querrec, Maurel & Ruffino 2004) used for ATV testing. A Jaxa shorter range test facility Rendezvous and Docking Operation Test System (RDOTS) is described in (Yamamoto, Ishijima, Mitani, Oda, Ueda, Kase & Murata 2006).

1.3 Main Contributions of the Thesis

The main objectives and contributions of the thesis are in two areas; namely the generalized relative dynamics between two spacecraft on closed orbits and the automatic control domain finding time invariant GNC solutions for time varying relative dynamics. The focus will be on new findings, which are applicable to both the elliptical as well as the circular orbital rendezvous. The contributions will be founded solidly in their theoretical aspects and at the same time have a bearing towards practical applications. The latter will be achieved by using a specific mission as an example, where a few facts will be based on the experience of the author rather that citation.

A short description of the main contributions is detailed below and will be reflected via conclusions in the corresponding sections and chapters.

1. The general nonlinear relative motion dynamics between spacecraft will be derived. The equations of motion will be linearized to formulate a set of differential equations for relative motion in the time domain for general elliptical Keplerian orbits. These equations will form the basis for the development of a general solution to the problem of linear dynamics for the rendezvous problem.

2. A general closed form homogeneous and particular solution to the coupled in plane motion of the spacecraft will be developed as well as for the out of plane one. This solution will be generally valid for any closed Keplerian orbit and will in the special case of a circular orbit reduce to the well known Clohessy Wiltshire equations. The solution will have no singularities contrary to earlier partial solutions.

3. From the developed general state transition matrices there will be developed general expressions for impulsive maneuvers. They will be valid for general maneuvers in three dimensional space, focusing on the thrust being along the Velocity-bar and the Radial-bar.

4. A linear coupled model for the relative motion between two spacecraft for attitude and position is developed for use in GNC design, as well as a general linear attitude kinematics and dynamic model. This gives the complete framework of the plant for which the GNC system is developed.

5. An on board architecture is proposed for the GNC system and its avionics components, which is of general nature for this type of missions. It provides the main elements needed for such types of missions addressing the main issues of concern, seen from a system design point of view.

A general framework is proposed for the GNC design with focus on the closer phases of the mission, though equally applicable to but less critical for others. A worst case approach will be taken with uncertainties and time varying parameters represented and analyzed in the robust control framework.

6. The general GNC setup and control structure will be defined. The design plant parameter variations will be quantified and boundaries established. Properties of linear time varying systems will be established for RVD. A scaleable thruster management function will be designed. The full guidance design for rendezvous will be performed.

7. The absolute attitude control will be designed as a fully coupled system with a LQG controller. All main contributing uncertainties will be represented as Linear Fractional Transformations and the robust stability and performance will be established, particularly with respect to the eccentricity of the orbit.

8. The control of the translational relative motion in 3 DOF will be designed as a fully coupled $\mathcal{H}_\infty$ controller. The dynamics contain nonlinear time periodic parameters, which will be viewed as a bounded uncertainty and modeled as a LFT. Then a worst case analysis will be performed of the design by means of $\mu-$analysis to establish the robust stability and performance for a range of orbital eccentricities.

9. The full 6 DOF control will be based upon the earlier developed complete coupled model and worst case $\mathcal{H}_\infty$ control design. All relevant uncertainties and time varying plant parameters will be included as before. The robust performance and stability will be evaluated by means of the $\mu-$value for a range of orbital eccentricities.

1.4 Structure of the Thesis

The thesis is organized as follows:

- **Chapter 2** will describe what is involved in a typical RVD mission in LEO. The missions to the ISS are used as an example where all the maneuvers from the phasing orbit to the real proximity maneuvers are described.

- **Chapter 3** will provide a definition of all coordinate systems used in the thesis. The spacecraft data for the chaser and the target will be detailed and the models for the space environment of relevance to the subject matter.

- **Chapter 4** deals with the detailed development of the general mathematical models for the relative dynamics between two spacecraft on an arbitrary Keplerian elliptic orbit. A closed form solution for the state transition matrix and particular solution is found. The model is verified and expressions for impulsive maneuvers are developed for the general case and exemplified for verification.

- **Chapter 5** provides the general nonlinear and linear dynamics and kinematics models for attitude motion. The couplings between attitude and relative position will also be covered in this chapter with a development of a full coupled linear model.
- **Chapter 6** suggests an on board architecture for the GNC system and its implementation. This will deal with the avionics equipment which is relevant for proximity maneuvers of the nature covered by this thesis.
- **Chapter 7** will deal with the general GNC structure. Variations of the design models will be established and linear periodic time varying systems addressed. The guidance function for all modes will be designed.
- **Chapter 8** contains the absolute attitude and navigation coupled design. The robust control background and formulation is provided here together with the model uncertainty formulations.
- **Chapter 9** provides the relative position control design for the far away phases for both the out of and in plane control. All uncertainty models associated to relative position are developed.
- **Chapter 10** holds the 6 DOF coupled relative attitude and position control for the closer distances up to the docking point. The overall robustness and system performance are established.
- **Chapter 11** deals with the testing and verification of the overall design with respect to the specifications. A part of this will be based on a Monte Carlo simulation approach covering the full nonlinear uncertainty parameter space and all orbits considered.
- **Chapter 12** provides the conclusion of the thesis as well as it will give a methodology for the design of GNC systems for proximity in a general manner, which can be used for future designs. Further research and recommendations will be provided.

Chapter 2

Mission Description

This chapter will address all the different phases and maneuvers of a typical RVD mission from the launch until the docking to the target spacecraft. The description will be in synthesis and illustrative format with the objective to provide an overview of such type of missions, which differ from most space missions in many aspects. The ground segment of the mission will not be covered here but can be found in (Tobias, Ankersen, Fehse, Pauvert & Pairot 1992).

2.1 Launch and Orbital Injection

The orbital plane of a spacecraft is defined by the angle between the vernal equinox and the ascending node, the Right Ascension of Ascending Node (RAAN) (Wie 1998) and the inclination with respect to the equatorial plane. The RAAN will drift due to the deviation of the Earth shape from a sphere and a non spherical symmetric gravity field. The rate of this drift is a function of the altitude, which means that a spacecraft launched into a lower orbit than a target spacecraft will have a faster rotation of the orbital plane. For this reason a chaser spacecraft will be launched into an orbit with a RAAN such that at the end of the phasing maneuvers, see Section 2.2, this difference will be eliminated by the natural drift and the chaser will be coplanar with the target orbit with no additional use of fuel.

After the separation from the launcher the chaser spacecraft will be in its initial orbit and ready to start up all systems on board. Should the spacecraft erroneously be delivered by the launcher into a decaying orbit it is very important that all on board systems are operational so that it can perform a raising maneuver at apogee in order not to reenter.

2.2 Phasing Maneuvers

When two spacecraft are in two different elliptic orbits with one common focal point and co-aligned semi major axis , the angle between the two spacecraft measured at the common focal point is defined as the *Phasing Angle*, see also illustration in Figure 2.1.

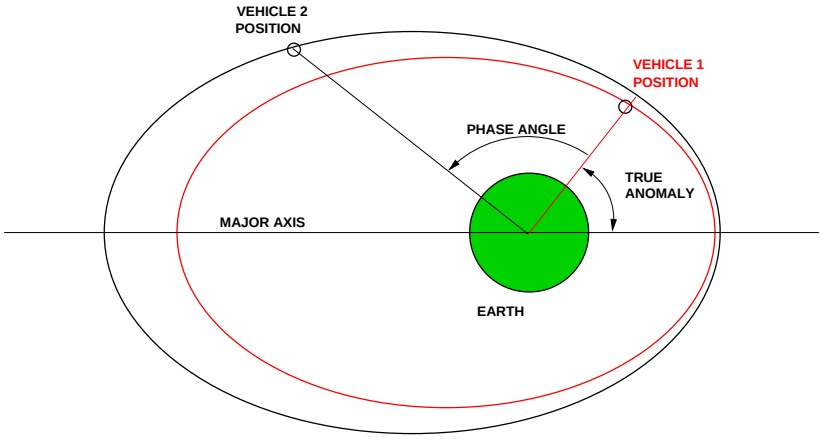

Figure 2.1: *Definition of the Phase Angle between two spacecraft moving on different or identical orbits. The perifocals are coinciding and the two orbits are quasi coplanar. The phase angle will be constant only for circular orbits of the same radius else it will increase or decrease. For same elliptical orbits it will vary periodically.*

There are a number of strategies, which can be utilized to reduce the magnitude of the phasing angle and bring the two spacecraft closer to each other.

- **Circular or Elliptic phasing:** A difference in orbital angular velocity will then make the chaser move forward or backward towards the target depending on a larger or smaller orbital angular velocity with respect to the target. This is sometimes referred to as a forward or a backward phasing. See also Figure 2.2.

- **Apogee and Perigee Changes:** These are used in two forms. One where the apogee is lifted to the level of the target orbit and the perigee is then later lifted progressively via intermediate orbits. This approach is used when no autonomous on board navigation is available and the maneuvers are performed from ground. It requires a propulsion system, which is capable of providing the large boosts needed, but on the other hand it provides the possibility to perform several fine tuning maneuvers for a precise adjustment.

  The other form involves lifting of both apogee and perigee via intermediate orbits towards the target orbit. This will slow down the approach rate and the correction points will be chosen such the chaser spacecraft will arrive at the aim point at the desired time. This is typically performed when an on board autonomous navigation system is available.

The selection of phasing strategy thus depends on the vehicles thrust capability and onboard navigation. The two approaches are schematically illustrated in Figure 2.3.

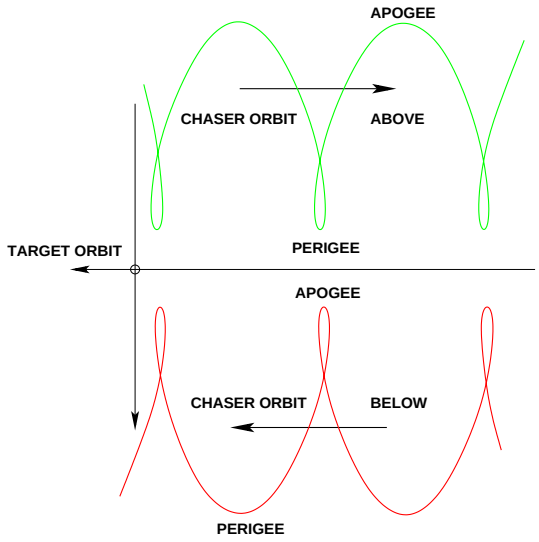

Figure 2.2: *Illustration of forward and backward phasing, below and above a target orbit, where the general motion is from right to left. The chaser orbital angular rate is larger respectively smaller below and above the target orbit.*

At the end of the phasing maneuvers the target spacecraft will be at its interface point to the start of the real proximity maneuvers. They are all performed with respect to the target local orbital frame. The location of this aim point can in principle be in all 4 quadrants of the target local orbital frame (behind, in front, below, above) but a convenient location is behind and below the target. In that case the natural drift between the two spacecraft will bring them closer together but still passively safe with respect to each other. During such a slow drift remaining errors in altitude, eccentricity and inclination can be corrected. This is the chosen strategy for the proximity operations of autonomous systems.

Another approach is to aim, not for a point, but for a so called entry gate. This means that the transition from phasing to proximity maneuvers is determined by a certain range in position, velocity and other possible operational constraints. This domain is reached by successive raises of the apogee and the perigee during the phasing. Such a strategy is mostly used during manual operations and the strategy implemented for the Space Shuttle.

All the maneuvers during phasing are performed in open loop and it might therefore be necessary to perform several small adjusting maneuvers at the end of the phasing to get the required accuracy. This is because the typical achievable accuracy from a Hohmann transfer maneuver is in the order of some hundred of meters in orbital radius and a few kilometers in the orbital direction. The most critical parameter is the accuracy of the orbital radius as it has a direct impact on the passive trajectory safety of the chaser

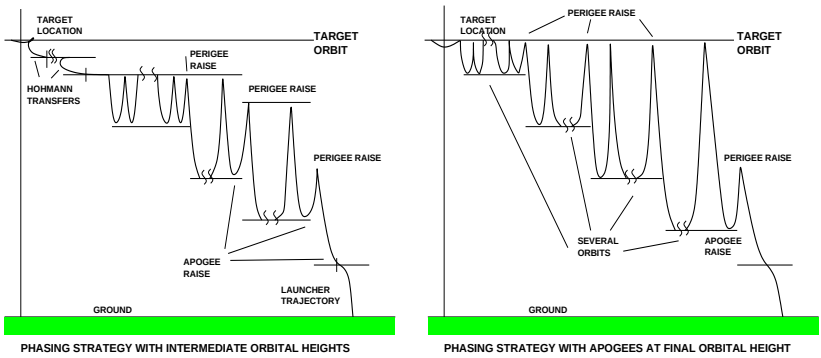

Figure 2.3: *Phasing strategies where time and motion are from right to left for common practice and historical reasons. It shall be recalled that apogee and perigee altitude changes are performed at perigee and apogee respectively (opposite).*

with respect to the target. A typical location at the end of the phasing is a few kilometers below the target orbit and some tens of kilometers behind.

2.3 Proximity Maneuvers

The maneuvers between the end of phasing and the contact between the chaser and target spacecraft will be described shortly here in order to give an overview of the complete mission. The close proximity maneuvers and the derivation of the dynamics models will take place in detail in Chapter 4.

During the phasing maneuvers the navigation is based on absolute GPS measurements for all orbital changes in Earth orbits. For non Earth missions the absolute navigation cannot use GPS but will have to rely on classical ground tracking or on board autonomous navigation techniques. The far away navigation is based upon relative GPS navigation and the close proximity navigation is based on optical sensors, contrary to the Kurs system used on Mir (Suslennikov 1992).

The curvilinear orbit direction is assumed a straight line and referred to as the V-bar; see also Section 3.1.

2.3.1 Far Proximity

The objectives are dispersion reduction after the phasing and the initialization of the first contact to the target in order to be able to perform relative navigation, contrary to the absolute navigation utilized during the phasing. The homing maneuver to bring the chaser in to the target orbit is typically performed as a Hohmann maneuver (tangential), which is fuel optimal. There may be other elements involved such as radial maneuvers to change the eccentricity, free drift trajectories and hold points. Time flexibility is included

by introducing a hold point on the target orbit, which has limited fuel consumption (ideally none). The final point location of this maneuver is partly driven by operational and passive safety constraints and partly by required accuracy constraints needed for subsequent maneuvers. Typically this point is a few kilometers behind the target on the negative V-bar, see Figure 2.4.

2.3.2 Closing

The objective of the closing maneuver is the acquisition of the nominal conditions of the docking corridor towards the target. The closing maneuver is typically a two pulse maneuver, which brings the chaser from one point in the target orbit to another one closer to the target. The maneuver can be performed either in open loop or in closed loop for better endpoint performance. At the end of the maneuver the distance to the target is around 500 m. The end conditions of the closing phase are that the chaser spacecraft will be inside the position, attitude and rates required to start the final approach maneuver within the safety corridor boundaries. A typical accuracy used is about 1 % of the range, which in this case gives a required navigation accuracy to be less than 5 m (Fehse 2003). This is the accuracy that the optical sensor used for the final approach has to be able to handle. In most cases the docking axis is along the V-bar otherwise a fly around maneuver is needed. There is also a possibility to perform a closing maneuver directly to the starting point on the docking axis, which is off the V-bar. It shall be noted that the latter is a less passively safe approach.

Trajectory strategies must be performed in such a manner that the trajectories are robust to the incapacity to execute a thrust maneuver, whether partly or in full. For such reasons, the closing maneuver is performed primarily by means of radial thrusts, rather than tangential ones, the latter being cheaper in fuel. The radial two pulse maneuver ensures that the spacecraft will return towards or to its initial position in case of a fully missed second thrust in one orbit; see also (Fehse 2003) and (Hartje 1997). For eccentric orbits a collision avoidance must be ensured for several orbits in order to provide time for contingency, as elliptic orbits do not provide the same safety criteria as circular orbits do. Straight line approaches from far distances are prohibitive in terms of fuel consumption.

2.3.3 Final Approach

The objectives of the final approach maneuver are to achieve the contact conditions for docking or the entry conditions for berthing, in terms of position, velocity, relative attitude and relative attitude rates.

In the case of a docking mechanism, there must be a certain axial speed of the chaser spacecraft to trigger it. In the case of soft docking, not performed in space yet, the impact speed is very low and the capture latches are actuated by individual motors.

The trajectory utilized for this maneuver is a straight line approach in the target docking frame, irrespective of the orientation of the docking axis. The maneuver is performed in closed loop with respect to the target in both the position and the attitude.

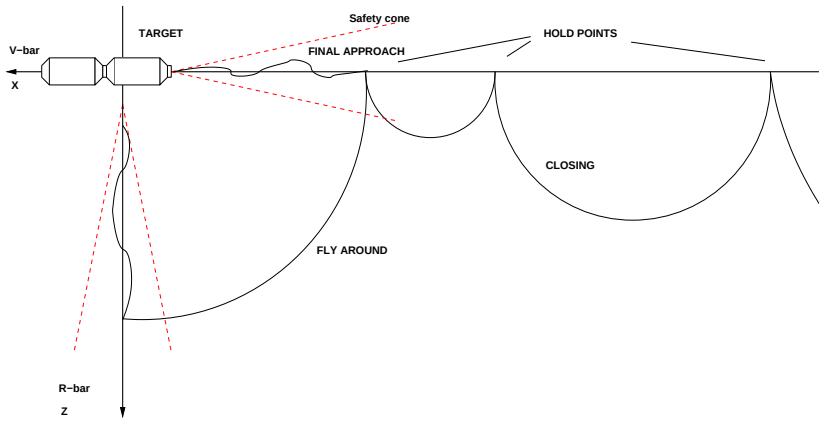

Figure 2.4: *Different types of proximity maneuvers in the LVLH frame (except departure). Maneuver pulses are typically performed at the hold points with either free drift, mid course correction or closed loop control along the trajectory. V-bar is along the x-axes in the LVLH frame and R-bar points to the planetary center.*

Relative attitude is only used for the last $20 - 30$ m. For berthing the relative attitude is not critical, but the relative velocity is normally about 5 times lower than for docking and must remain there for about 60 s which makes berthing a harder problem than docking seen from a GNC point of view.

The straight line of the docking axis is not fixed in space due to the attitude motion of the target docking port, and the navigation is therefore based on the relative position and attitude measurements from an optical sensor, the RVS.

For safety and observability reasons one normally defines an approach cone, which has its top at the center of the target docking port and is symmetric about the docking axis with a typical half cone angle of $10 - 15$ deg. This facilitates monitoring by both crew and autonomous system. In case of violations a CAM is performed.

Another issue which is important during a final approach is the plume impingement on the target spacecraft by the chaser. The concerns are forces, contamination and heat load. The criticality comes from the fact that in order to reduce the approach velocity, it is necessary to thrust in the direction of the target spacecraft, in addition to attitude control thrusts which are in all directions, though smaller. To reduce such an impact, the chaser performs the major braking thrust at some distance from the target and maintains the contact velocity for the last few meters. This nevertheless means that the disturbance will have a larger impact during the last critical meters.

2.3.4 Fly Around

The objectives of the fly around maneuver are to bring the chaser spacecraft from a location on the V-bar to a location on the docking axis within the safety approach cone, followed by the final approach, previously described. The fly around maneuver can be performed either as a trajectory closed loop controlled maneuver typically with a constant radius circumventing the target or as a two pulse maneuver with an open or a closed loop trajectory control. The former has the advantage of larger flexibility in terms of duration and interruptions but also carries a higher fuel consumption with it. The RVS sensor can only be used when the docking axis is reached.

The aim point at the end of the fly around maneuver is not a stable equilibrium like the hold points on the V-bar. It is necessary to have active closed loop control to maintain the position, as the chaser spacecraft is actually on a different orbit than the target. Obviously a minimum amount of time shall be spent in such a location to lower the fuel consumption. The passive safety is also lower than for hold points on the V-bar due to the natural drift of the hold point.

2.3.5 Departure

The objectives of the departure maneuver are to separate the attached spacecraft from the target spacecraft and send it on a non returning trajectory. When the chaser spacecraft is at a sufficiently safe distance, a large thrust maneuver is performed to initiate the deorbitation and reentry. Depending on the critical distance between the two spacecraft the departure maneuver can be performed as a reverse final approach or the chaser can make directly use of the impulse provided by the push off mechanism and depart with an open loop strategy. Clearly the controlled one is safer, but also requires all equipment operational as well as the plume impingement problem exists at such a close proximity. Normally a safety departure cone is defined, within which the vehicle must remain until a distance of a few hundred meters from the target is obtained.

The impulse provided by the mechanism must be large enough to enable the departing spacecraft to reach the safe departure velocity, although it shall be remarked that at very close proximity such trajectories are inherently unsafe, and a collision might occur should some of the thrusts go wrong.

For a departure along the minus V-bar several radial thrusts are performed to remain inside the departure cone and at a larger distance supplemented by a tangential thrust, which is more efficient. The departure from a docking on the R-bar is similar, but tangential thrusts are used. This departure is also safer due to the fact that the departing spacecraft Center Of Mass (COM) is below the V-bar, and the natural motion will carry it ahead and below the target.

2.4 Reference Mission Scenario

The past sections have described what is involved in a full mission for a typical type in a low Earth orbit. The present thesis will not contain all the elements of a full mission,

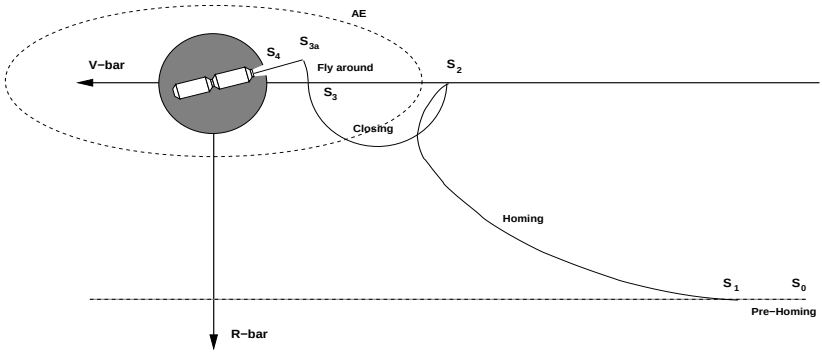

Figure 2.5: *This figure shows the RVD phases considered in the design work. The labels are the nomenclature used for all hold and intermediate way points. The shaded area is the Keep Out Zone, which is defined for safety reasons.*

but it will be restricted in size and number of phases included.

As reference mission target spacecraft the International Space Station will be used, while the chaser spacecraft is assumed to be a vehicle alike the unmanned European Automated Transfer Vehicle.

The phases included will consider what is described in Section 2.3.2 for homing and closing as well as the final approach in Section 2.3.3.

The design will concentrate on addressing all the GNC related aspects for the final approach, as illustrated in Figure 2.4, and will address the critical issues for the fly around, closing and homing. The attitude control will be designed for absolute and relative attitude. The final approach of the reference mission will contain a full detailed GNC design, whereas the previous phases will rely partly on previous results.

To remain within the subject of this thesis the overall mission analysis will be taken from the general ATV one. The launch and phasing parts of the mission will not be considered directly, as the GNC parts needed there will be similar to the ones for the closer phases. For the homing and closing phases the navigation is GPS based. Contact dynamics, equipment and redundancy mode switching as such will not be considered in the design, as it does not influence the GNC design proper, but more the mode management. Failure Detection Isolation and Recovery and the software implementation are subjects of their own.

2.4.1 Reference Mission Description

The reference mission will be described briefly here, it being the limitations of the work, where the actual numerical requirements will be listed in Section 2.4.2.

The orbit will be a slightly eccentric low Earth orbit with eccentricity $\varepsilon = 0.1$ in order to deal with the general case. A lowest perigee of 450 km is assumed.

Point	$[x, y, z]^{\mathrm{T}}$ m
s_1	$[-29000, 0, 5000]^{\mathrm{T}}$
s_2	$[-3500, 0, 0]^{\mathrm{T}}$
s_3	$[-500, 0, 0]^{\mathrm{T}}$
s_{3a}	$[-500\cos(15\text{ deg}), 0, 500\sin(15\text{ deg})]^{\mathrm{T}}$
s_4	20 m along docking axis from target port

Table 2.1: *Location of intermediate points for the reference mission defined in Figure 2.5.*

To finalize the definition of the reference mission, we will detail the nominal location of the points shown in Figure 2.5 and listed in Table 2.1 for the LVLH frame. The numbers in Table 2.1 will be used as reference locations for the guidance part of the GNC system.

2.4.2 Requirements Specification

This section will detail the mission level GNC requirements for the reference mission considered in this work and illustrated in Figure 2.5 and Table 2.1. The requirements of the attitude and the position will be stated, based upon detailed analysis elsewhere. All requirements for the GNC system performance with respect to the nominal reference points are to be understood as 99 % confidence interval values, 3σ if Gaussian distributed. To give an example with a nominal reference point of 1000 m on the V-bar and a GNC performance specification of 100 m at 3σ. It then means that about 99 % of the samples shall be in the range $[900; 1100]$ m.

The requirements are based on mission analysis, the spacecraft design and the available performances of the avionics equipment.

Attitude: The attitude requirements are split into the ones during Earth pointing attitude between the chaser body frame and the LVLH frame and those, which are valid for the relative attitude between the chaser and the target docking ports. The requirement is tighter during the ΔV burns than in the drift modes but to keep the number of requirements low, we select the one for the boosts.

Mode	Attitude	Attitude rate
Earth pointing	3 deg	0.2 deg/s
Relative pointing	5 deg	0.15 deg/s

Table 2.2: *Attitude requirements for all 3 axes and all encountered modes.*

Position: The position requirement for the trajectory part between 2 points takes the requirement of the preceding point when closed loop trajectory control is performed. In the case with no trajectory control, but an open loop boost, the requirement shall be understood for the departing point and the dispersion will clearly be larger at the arriving

point. In both cases the station keeping control of the arriving point will have to bring the GNC performance to the level of that point. The arriving point typically has a tighter requirement than the departing point for a nominal approach.

The initial point of the rendezvous part of the mission is s_1, see Figure 2.5, but we do not have a requirement for this location as it is in a drift orbit at lower altitude and the chaser is not at rest in s_1. The guaranteed proximity link with the station is at a radial distance of 30 km. Relative GPS based navigation is then available. The s_1 point is specified in terms of navigation knowledge at that location and is given in Table 2.3.

	Relative Position	Relative Velocity
x-axis	≤ 30 m	≤ 0.1 m/s
y-axis	≤ 30 m	≤ 0.2 m/s
z-axis	≤ 50 m	≤ 0.2 m/s

Table 2.3: *Required chaser navigation accuracy at location s_1. Note: this is not the GNC specification for the point.*

The values for s_2 are the GNC requirement to be fulfilled at that location and listed in Table 2.4. The GNC requirements for the location s_3 are listed in Table 2.5 and they

	Position	Velocity
x-axis	≤ 50 m	≤ 0.3 m/s
y-axis	≤ 30 m	≤ 0.15 m/s
z-axis	≤ 50 m	≤ 0.3 m/s

Table 2.4: *GNC position and velocity requirements at location s_2.*

are retained for the location after the fly around maneuver to acquire the docking axis at s_{3a}. The values in Table 2.5 are not valid after s_{3a} during the final approach. The values

	Position	Velocity
x-axis	≤ 20 m	≤ 0.1 m/s
y-axis	≤ 20 m	≤ 0.1 m/s
z-axis	≤ 20 m	≤ 0.1 m/s

Table 2.5: *GNC position and velocity requirements at location s_3 and s_{3a}.*

are now given between the 2 docking ports. The approach velocity between s_3 or s_{3a} and s_4 is $[0.05; 0.35]$ m/s and the hold point is in Table 2.6.

During the last part of the final approach, where we use the relative attitude, the requirements are in Table 2.7. The requirements between the point s_4 and docking is a

	Position	Velocity
x-axis	≤ 1 m	≤ 0.02 m/s
y-axis	≤ 1 m	≤ 0.1 m/s
z-axis	≤ 1 m	≤ 0.1 m/s

Table 2.6: *GNC position and velocity requirements at location s_4.*

	Position	Velocity
x-axis		$[0.05; 0.10]$ m/s
y-axis	≤ 0.1 m	≤ 0.02 m/s
z-axis	≤ 0.1 m	≤ 0.02 m/s

Table 2.7: *GNC position and velocity requirements at docking.*

linear interpolation between the two points whose values are listed in Tables 2.6 and 2.7 respectively. In practice the latter requirements are often used a bit prior to docking.

Chapter 3

Frames, Equipment, Spacecraft Data and Environment Models

This chapter will contain definitions of all the coordinate systems needed for the general orbital descriptions as well as for those related to the spacecraft. This will be followed by definitions of the avionics equipment and equivalent models for some equipment, not modeled in details, like the GPS system. The spacecraft properties in terms of mass, inertia, flexible modes, sloshing and physical dimensions will be provided for the actual hardware. Finally this chapter will provide the mathematical models needed for the space environment of the reference mission defined in Chapter 2.4.1.

3.1 Coordinate Systems Definition

All coordinate systems needed are defined in this chapter. They are logically separated into 3 sections for general mission related frames and those specific to the target and chaser spacecraft themselves.

3.1.1 General Coordinate Systems

In the following there will be defined the coordinate frames used for the orbital parts.

Inertial Frame $\mathcal{F}_i$: Has its origin at the center of the Earth, the axes defined as and illustrated in Figure 3.1:

- X_i-axis: from the Earth center along the line of vernal equinox in the equatorial plane.
- Y_i-axis: in the Earth equatorial plane $Y_i = Z_i \times X_i$ completing the triad.
- Z_i-axis: to the north along the angular momentum vector of the Earth.

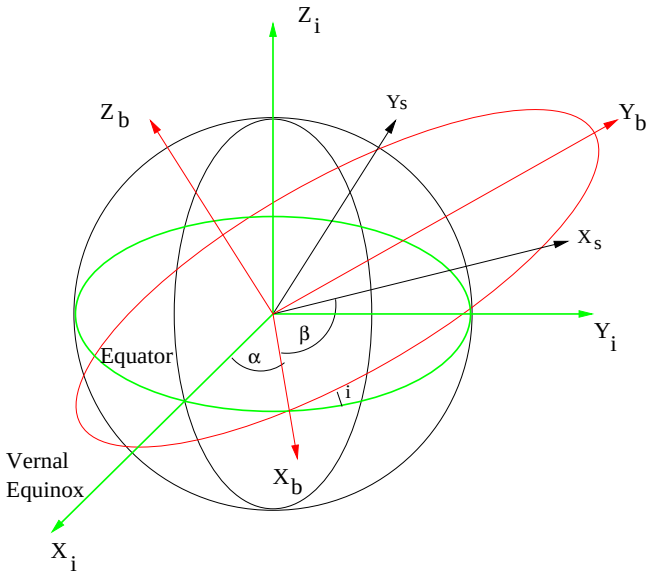

Figure 3.1: *Definition of Earth centered frames and the precise definition is in Section 3.1.1.*

Intermediate Frame $\mathcal{F}_b$: Has its origin at the center of the Earth, the axes defined as and illustrated in Figure 3.1:

- X_b-axis: from the Earth center along the line of ascending node in the equatorial plane, rotated the angle α around Z_i.
- Y_b-axis: in the orbital plane $Y_b = Z_b \times X_b$ completing the triad.
- Z_b-axis: normal to the plane inclined an angle i around the X_b axis and parallel to the orbital angular momentum.

Orbit Frame $\mathcal{F}_s$: Has its origin at the center of the Earth, the axes defined as and illustrated in Figure 3.1:

- X_s-axis: from the Earth center in the orbital plane to the orbital location of the spacecraft and at an angle β from the ascending node.
- Y_s-axis: in the orbital plane $Y_s = Z_s \times X_s$ completing the triad.
- Z_s-axis: identical to the Z_b in the frame $\mathcal{F}_b$ and parallel to the orbital angular momentum.

Local Orbital Frame $\mathcal{F}_o$: Has its origin at the center of mass of the spacecraft and the axes defined as and illustrated in Figure 3.2. This frame is also often referred to as the Local Vertical Local Horizontal (LVLH) frame. For the target spacecraft this frame will be referred to as $\mathcal{F}_t$ and for the chaser spacecraft as $\mathcal{F}_c$.

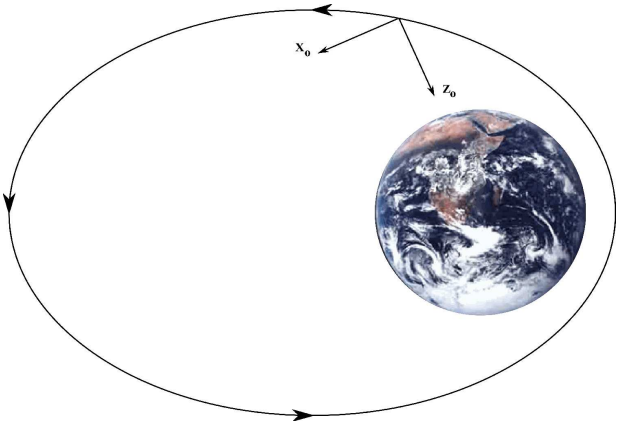

Figure 3.2: *Definition of the local orbital frame.*

- X_o-axis: $X_o = Y_o \times Z_o$ which is in the direction of the velocity vector of the spacecraft. In the RendezVous literature it is often referred to as the **V-bar**.
- Y_o-axis: normal to the orbital plane and in the opposite direction and parallel to the orbital angular momentum vector. In the RendezVous literature it is often referred to as the **H-bar**.
- Z_o-axis: in the orbital plane from the spacecraft COM towards the Earth center. In the RendezVous literature it is often referred to as the **R-bar**.

3.1.2 Target Coordinate Systems

The target, which here is modeled on the ISS, will have 4 frames defined, namely the geometrical reference frame, the body reference frame, the docking port frame and the auxiliary docking port frame.

ISS Geometrical Reference Frame $\mathcal{F}_{gt}$: Has its origin at the geometric center of the Integrated Truss Segment (ITS) and illustrated in Figure 3.3.

- X_{gt}-axis: parallel to the longitudinal axis of the module clusters with positive direction forward.
- Y_{gt}-axis: along the ITS axis with positive in the starboard direction.
- Z_{gt}-axis: $Z_{gt} = X_{gt} \times Y_{gt}$ with positive in Nadir direction.

ISS Body Reference Frame $\mathcal{F}_{bt}$: Has its origin at the ISS center of mass and is illustrated in Figure 3.3. The origin is located at $\mathbf{r}_{bt} = [-4.94, -0.21, 4.40]^{\mathrm{T}}$ m in $\mathcal{F}_{gt}$ for the 16A configuration.

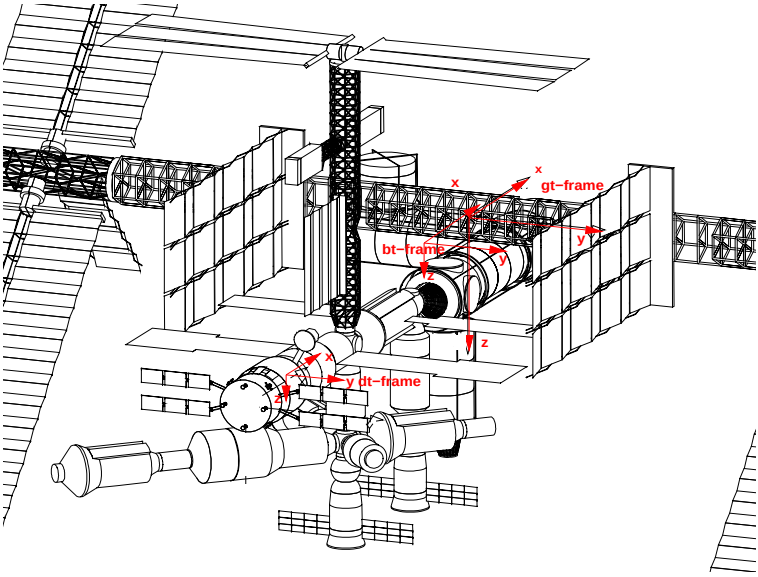

Figure 3.3: *International Space Station coordinate frames.*

- X_{bt}-axis: aligned with X_{gt}.
- Y_{bt}-axis: aligned with Y_{gt}.
- Z_{bt}-axis: aligned with Z_{gt}.

ISS Docking Reference Frame $\mathcal{F}_{dt}$: Has its origin at the interface plane of the Russian docking port and is illustrated in Figure 3.3. The origin is located at $\mathbf{r}_{gdt} = [-35.84, 0, 4.14]^{\mathrm{T}}$ m in $\mathcal{F}_{gt}$, when no structural flexibility is considered. The frame is attached to the docking port structure.

- X_{dt}-axis: aligned with X_{gt} when no flexible modes are considered.
- Y_{dt}-axis: aligned with Y_{gt} when no flexible modes are considered.
- Z_{dt}-axis: aligned with Z_{gt} when no flexible modes are considered.

ISS Auxiliary Docking Reference Frame $\mathcal{F}_{dt0}$: It is identical to $\mathcal{F}_{dt}$ when no structural flexibility is considered.

When structural flexibility is considered, this frame $\mathcal{F}_{dt0}$ will represent the port motion due to the ISS rigid attitude motion only. In this situation it becomes a fictitious frame not attached to a physical structure.

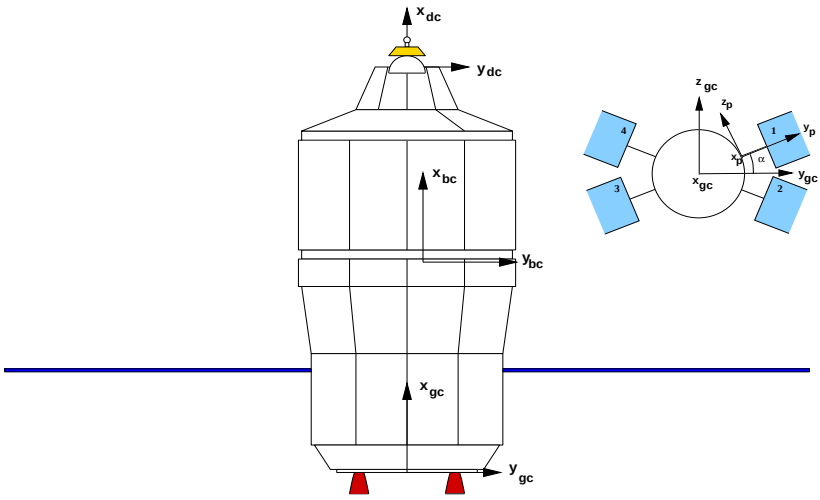

Figure 3.4: *Chaser coordinate frames for both the rigid spacecraft and the flexible solar panels.*

3.1.3 Chaser Coordinate Systems

The chaser will have 5 different frames defined, namely the geometrical reference frame, the body reference frame and the docking reference frame.

Chaser Geometrical Reference Frame $\mathcal{F}_{gc}$: Has its origin at the launcher interface ring level A0 at geometric center of the ring and is illustrated in Figure 3.4.

- X_{gc}-axis: longitudinal towards the docking port and normal to the A0 plane.
- Y_{gc}-axis: along the geometrical center line of the solar panels in the A0 plane, as illustrated in Figure 3.4.
- Z_{gc}-axis: $Z_{gc} = X_{gc} \times Y_{gc}$ in the A0 plane.

Chaser Body Reference Frame $\mathcal{F}_{bc}$: Has its origin at the chaser center of mass and is illustrated in Figure 3.4. The origin is located at $\mathbf{r}_{bc}$ in $\mathcal{F}_{gc}$, which varies during the mission phases.

- X_{bc}-axis: aligned with X_{gc}.
- Y_{bc}-axis: aligned with Y_{gc}.
- Z_{bc}-axis: aligned with Z_{gc}.

Chaser Docking Reference Frame $\mathcal{F}_{dc}$: Has its origin at the intersection of the X_{gc}-axis and the docking port interface plane A4 as illustrated in Figure 3.4. The origin is located at $\mathbf{r}_{gdc} = [8.5, 0, 0]^{\mathrm{T}}$ m in $\mathcal{F}_{gc}$.

- X_{dc}-axis: aligned with X_{gc}.
- Y_{dc}-axis: aligned with Y_{gc}.
- Z_{dc}-axis: aligned with Z_{gc}.

Chaser Rendezvous Sensor Reference Frame $\mathcal{F}_{rc}$: The frame is the sensor frame in which the range and LOS angles are measured. The origin is located at $\mathbf{r}_{rc} = [7.6, 1.5, 0]^{\mathrm{T}}$ m in $\mathcal{F}_{gc}$.

- X_{rc}-axis: aligned with X_{gc}.
- Y_{rc}-axis: aligned with Y_{gc}.
- Z_{rc}-axis: aligned with Z_{gc}.

Chaser Solar Panel Frames $\mathcal{F}_p$: The frame is used to specify the flexible modal data for the solar panel. The Y_p and Z_p axes are in plane of the panel. The origins of the 4 panels frames are located as in Table 3.1 and expressed in $\mathcal{F}_{gc}$. The nominal non rotated panel is shown in Figure 3.4, where the rotation about the x-axis is $\alpha = 25\,\mathrm{deg}$ and symmetric for the other panels with respect to Y_{gc}.

- X_p-axis: aligned with X_{gc}.
- Y_p-axis: aligned with the solar panel longitudinal axis pointing away from the spacecraft for each panel and $\perp$ to X_p.
- Z_p-axis: $Z_p = X_p \times Y_p$.

Panel #	x m	y m	z m
1	1.8	1.9	0.6
2	1.8	1.9	-0.6
3	1.8	-1.9	-0.6
4	1.8	-1.9	0.6

Table 3.1: *Location of solar panel attachment points in $\mathcal{F}_{gc}$.*

3.2 Spacecraft Data

The specific data for the chaser and target spacecraft will be presented in this section. The data concerns the mechanical data needed for the kinematics and dynamics models later.

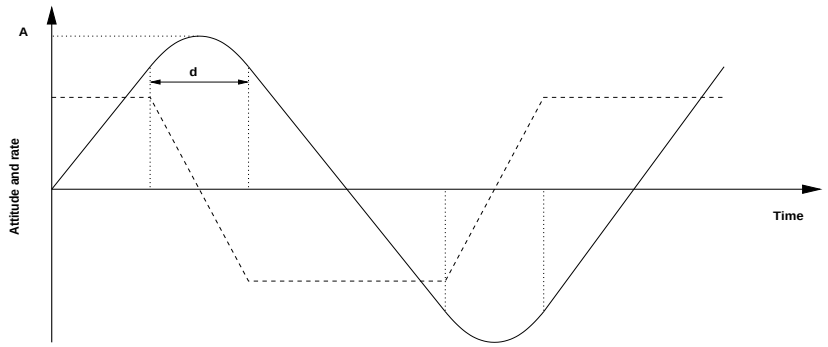

Figure 3.5: *Definition of ISS attitude β (full line) motion for one axis of its rigid body frame, and velocity (dashed line). It consist of straight lines with parabola segments as the control is pulsed with pulse width of d.*

3.2.1 Target Data

The data for the ISS is valid for the configuration 16A, which is close to the final version of the station (ISS 2006). The mass m_t and the inertia $\mathbf{I}_t$ is specified numerically in Section C.1.

When docking to the Russian port, the ISS is attitude controlled using a two sided limit cycle controller. The attitude then becomes a sawtooth as illustrated in Figure 3.5 with the data in Table 3.2. The 3 axes are not necessarily in phase with each other and the phase angle between the axes is uniformly distributed.

In addition to the rigid body attitude motion described in Figure 3.5 and Table 3.2 there is a contribution from the structural flexibility to the motion of the docking port and the two are super positioned. Both motions contribute to a translation of the docking port frame $\mathcal{F}_{dt}$ as neither $\mathcal{F}_{dt}$ nor $\mathcal{F}_{dt0}$ are located at the COM. The data for the first three modes are in Table C.1, which is based upon structural analysis including 175 flex modes performed by Energia.

	Range	Distribution
Amplitude A	$[0.55; 0.7]$ deg	uniform
Reversal time d	$[8; 40]$ s	uniform
Angular rate v_t	0.02 deg/s	
Maximum bias	$3.4 - A$ deg	
Period	$\frac{4A}{v_t} + d$	

Table 3.2: *ISS attitude motion data. The distribution is provided for simulation initialization purposes.*

The flexible modes, as in Table C.1, of the ISS for the attitude of $\mathcal{F}_{dt}$ with respect to $\mathcal{F}_{dt0}$ shall be used as follows:

- Either the attitude amplitude α_i is used and the rate $\dot{\alpha}_i$ is found by differentiation, i being the axis
- Or the attitude rate $\dot{\alpha}_i$ is used and the attitude α_i is found by integration.

The linear motion of the $\mathcal{F}_{dt}$ frame with respect to the $\mathcal{F}_{dt0}$ frame expressed in $\mathcal{F}_{dt0}$ is presented in Table C.1 and illustrated in Figure 3.6. All flexible modes are super positioned sinusoids. The requirements stated in Section 2.4.2 regarding docking port performances are valid in the $\mathcal{F}_{dt0}$ frame.

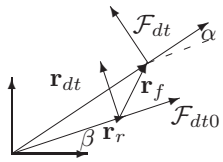

Figure 3.6: *Illustration of the ISS flexible modes, where $\mathbf{r}_r$ is the rigid location of the docking port and $\mathbf{r}_f$ is the flexible part.*

With respect to the geometrical frame $\mathcal{F}_{gt}$ the COM is located at $\mathbf{r}_{bt}$ and the center of the docking port is located at $\mathbf{r}_{gdt}$. With respect to the COM the docking port is located at $\mathbf{r}_{dt} = \mathbf{r}_r = \mathbf{r}_{gdt} - \mathbf{r}_{bt}$ for $\mathbf{r}_f = 0$. The cross sectional profile of the spacecraft is specified in Section C.1.

3.2.2 Chaser Data

The chaser data provided here will be the mass, inertia and their uncertainties. The data for the spacecraft flexible modes and the fuel sloshing will be provided together with the respective models in Section 3.4.

The chaser spacecraft has lower and upper values for different configurations . The mass m_c and the inertia matrix $\mathbf{I}_c$ are specified in Section C.2 with the respective uncertainties. All uncertainties are uniformly distributed and are 3σ values.

The COM location $\mathbf{r}_{bc}$ is for the x component $[2.4; 4.3]$ m and the lateral location is $[0; 0.075]$ m given as a radius and an angle of $360\,\text{deg}$. The uncertainty is ± 0.045 m, uniform at 3σ. With respect to the COM the docking port is located at $\mathbf{r}_{dc} = \mathbf{r}_{gdc} - \mathbf{r}_{bc}$. The cross sectional profile of the spacecraft along the x,y,z body axes is 51, 40 and 40 m^2 respectively.

3.3 Avionics Equipment

The avionic components of sensors and actuators will be defined in this section for the purpose of GNC design. It will include all needed data and characteristics for the sensors and actuators as well as for the equivalent models used, where the equipment proper is not included.

3.3.1 Propulsion

The only propulsion system on the chaser spacecraft is a thruster assembly consisting of 28 thrusters, which provides the needed forces and torques. The location and orientation of the thrusters are listed in Table C.6.

The force vector $\mathbf{F}_p$ from the propulsion is computed as the sum of the individual thruster forces, see Equation (3.1)

$$\mathbf{F}_p = \sum_{i=1}^{n} \mathbf{F}_{th_i} \tag{3.1}$$

The torque vector $\mathbf{N}_p$ is computed in Equation (3.2) with respect to the COM,

$$\mathbf{N}_p = \sum_{i=1}^{n} \mathbf{N}_i = \sum_{i=1}^{n} (\mathbf{r}_{bc} - \mathbf{r}_{th_i}) \times \mathbf{F}_{th_i} \tag{3.2}$$

where $\mathbf{r}_{bc}$ is the COM location and $\mathbf{r}_{th_i}$ is the location of the i^{th} thruster. The uncertainties for the thrusters can be found in Table C.5.

To ensure that no saturation occurs a spherical envelope is applied, and according to analysis in (Silva, Martel & Delpy 2005) this leads to a maximum force and torque of 220 N and 250 Nm respectively. This will be available at any time in any direction without saturation.

3.3.2 Gyros

The gyro assembly consists of 4 two axes sensitive gyros of type DTG T100 mounted in a tetrahedron configuration for redundancy reasons. They are all mounted on a stiff common baseplate to minimize misalignments. The performances along the spacecraft axes are shown in Table C.2. The measured angular rate vector is expressed in Equation (3.3) as (Iwens & Farrenkopf 1971)

$$\boldsymbol{\omega}_g(t) = (1 + k_g)\boldsymbol{\omega}(t - \tau) + \mathbf{d}_g(t - \tau) + \mathbf{n}_g(t - \tau) \tag{3.3}$$

where k_g is the scale factor, $\boldsymbol{\omega}$ is the true angular rate vector, $\mathbf{d}_g$ is the vector of drift and $\mathbf{n}_g$ is the vector of white noise. The sensor has a delay of 0.1 s and a sampling frequency of 10 Hz.

3.3.3 Star Sensor

The chaser will have 2 star sensors which are mounted orthogonal in order to get 3 axes high resolution coverage, though not always used simultaneously. The output of the sensors will be in the inertial frame $\mathcal{F}_i$. The specification in Table C.3 is for one sensor unit.

The sensor output can be a quaternion or Euler(3,2,1) angles. The measured angles are computed as

$$\boldsymbol{\theta}_{str}(t) = \boldsymbol{\theta}(t - \tau) + \boldsymbol{\theta}_{str_b}(t - \tau) + \boldsymbol{\theta}_{str_n}(t - \tau) \tag{3.4}$$

where $\boldsymbol{\theta}$ is the true attitude and the two last terms are bias and noise terms respectively. The sensor has a delay τ of 1 s and a sampling frequency of 5 Hz.

	POSITION			
	Range m		LOS deg	
R in meters	Bias	Noise	Bias	Noise
$0-1$	$0.01(1+R)$	$0.005+0.01R$	0.5	<0.2
$1-2$		$0.01(1+0.5R)$		
$2-10$	$0.01(1.12+0.94R)$	$0.01R$		
$10-20$			0.3	
$20-100$	$0.01R$	$0.0225R-0.25$		
$100-150$		$0.11R-9$		
$150-500$		$0.05R$		
	ATTITUDE (deg)			
	x-axis(axial)		y,z-axes(lateral)	
R in meters	Bias	Noise	Bias	Noise
$0-20$	<0.8	0.1	$0.55+0.0125R$	$0.05+0.0475R$
$20-30$	$-0.6+0.07R$		$-0.6+0.07R$	

Table 3.3: *GNC relevant specifications for the Rendezvous sensor. Noise is 3σ Gaussian values. The data in this table has been obtained from measurements on a real sensor. Many values in different ranges are driven by internal modes of the sensor.*

3.3.4 Rendezvous Sensor

This is a Charge Coupled Device (CCD) based type of camera sensor, which is the primary sensor for the proximity maneuvers of the RVD phase. It has a circular Field Of View (FOV) of 5 deg below 200 m and 8 deg above. The operational range of the sensor is up to about 500 m. The sensor delivers the following measurements.

- **Range**: The range R is measured between the sensor frame $\mathcal{F}_{rc}$ and a target pattern, which is mounted on the Russian service module of the ISS. The target pattern location in the target docking frame $\mathcal{F}_{dt}$ is $\mathbf{r}_{rt} = [0, 1.5, 0]^{\mathrm{T}}$ m.
- **LOS**: The LOS azimuth β_{rvs} and elevation α_{rvs} angles, which are rotations around the z-axis and the minus y-axis respectively. The x-axis is along the bore sight.
- **Relative Attitude**: The Euler(3,2,1) angles are between the sensor frame and the target docking frame. This measurement can also be provided in quaternion notation. The relative attitude is only available for a range smaller than 30 m.

The noise and bias in Table 3.3 shall be applied to the primary measurements and the Cartesian measurement in the sensor frame $\mathcal{F}_{rc}$ is then found as

$$\mathbf{x}_{rvs} = R \begin{bmatrix} \cos(\alpha_{rvs})\cos(\beta_{rvs}) \\ \cos(\alpha_{rvs})\sin(\beta_{rvs}) \\ \sin(\alpha_{rvs}) \end{bmatrix} \tag{3.5}$$

The application of bias and noise is of the same form as expressed in Equation (3.4) for both position and relative attitude when applicable. The sensor has a delay of 0.3 s and a sampling frequency of 1 Hz.

Noise (3σ)	Position	Velocity
x_{LVLH}	5 m	0.015 m/s
y_{LVLH}	3 m	0.005 m/s
z_{LVLH}	5 m	0.015 m/s

Table 3.4: *GNC relevant specifications for the RGPS based navigation. Noise is Gaussian.*

3.3.5 Relative GPS

The relative GPS based navigation will not be designed in detail and therefore it will be necessary with an equivalent performance model of the RGPS navigation. The output of the model is obtained by adding Gaussian white noise to the true state vector, which is then filtered through a second order filter with stationary gain of one, a bandwidth of 0.0165 rad/s and a damping of 0.6 as typical values.

3.4 Disturbance Models

This section will describe the relevant disturbance models from the environment respectively from the spacecraft itself. Only the disturbances which are of any significant value have been taken into account.

3.4.1 Gravity Gradient

The gravity field is producing a torque on a body, which is not in the equilibrium attitude due to the different force acting on different particles of the body. If the gravity field had been uniform, contrary to inverse square as in Equation (4.1), no gravity gradient torque would be present (Hughes 1986).

The gravity gradient torque $\mathbf{N}_g$ is found from integrating over the body solid to calculate the torque. If the geometric center of iteration is chosen to be at the COM then $\mathbf{N}_g$ can be expressed as

$$\mathbf{N}_g = 3\frac{\mu}{r^3}\hat{\mathbf{r}} \times \mathbf{I}\hat{\mathbf{r}} \tag{3.6}$$

where r is the distance from gravity field center to the COM and $\hat{\mathbf{r}}$ is a unit vector from the COM to the gravity field center. The gravity field is expressed in Equation (4.1) and the detailed derivation of Equation (3.6) can be seen in (Hughes 1986).

We observe that $\hat{\mathbf{r}}$ is always along the local vertical axis of the orbital frame $\mathcal{F}_o$, so we have that $\hat{\mathbf{r}} = \mathbf{k}_o = [0, 0, 1]^{\mathrm{T}}$ in $\mathcal{F}_o$. We also see that there is no torque produced around the z-axis as expected.

We need $\mathbf{N}_g$ in the body frame $\mathcal{F}_{bc}$, where $\mathbf{I}$ is time invariant, and we therefore need to represent $\mathbf{k}_o$ in the body frame, which becomes the last column of the rotation matrix in Equation (B.4). Finally we will linearize Equation (3.6) around the nominal attitude of $\boldsymbol{\theta}_0 = [0, \theta_0, 0]^{\mathrm{T}}$ using a general Taylor expansion as in Equation (4.8). The detailed

calculations finding the partial derivatives can be found in Section B.5. The linear model for the gravity gradient in the chaser body frame yield

$$\mathbf{N}_{glin} = 3\frac{\mu}{r^3}\begin{bmatrix} I_{21}s_y c_y - I_{23}c_y^2 \\ (I_{33}-I_{11})s_y c_y + I_{13}c_y^2 - I_{31}s_y^2 \\ I_{21}s_y^2 - I_{23}s_y c_y \end{bmatrix} + 3\frac{\mu}{r^3}\begin{bmatrix} (I_{33}-I_{22})c_y^2 - I_{31}s_y c_y & I_{21}(c_y^2 - s_y^2) - 2I_{23}s_y c_y & 0 \\ I_{12}c_y^2 + I_{32}s_y c_y & (I_{33}-I_{11})c_y^2 + I_{11}s_y^2 - 2(I_{13}+I_{31})s_y c_y & 0 \\ (I_{11}-I_{22})s_y c_y - I_{13}c_y^2 & 2I_{21}s_y c_y - I_{23}(c_y^2 - s_y^2) & 0 \end{bmatrix}\begin{bmatrix} \theta_x \\ \theta_y \\ \theta_z \end{bmatrix} \tag{3.7}$$

where s_y, c_y are $\sin(\theta_0), \cos(\theta_0)$ respectively.

The linear model in Equation (3.7) can either be used as it is to find the disturbance torques or it can be in included in a linear design model of the attitude dynamics. The latter should be done if the disturbance torque is large in respect to the nominally needed torque to fulfill control performance. The former is sufficient when the disturbance torque is small and leaves sufficient available torque for the primary tracking task of the controller, which is the case here.

3.4.2 Differential Air Drag

The residual atmosphere, which exist for most Earth orbits, causes a force on the spacecraft when molecules impact the spacecraft surface. We can write the well known equation for the drag force as (Larson & Wertz 1991)

$$\mathbf{F}_d = -\frac{1}{2}\rho C_d |\mathbf{v}| \mathbf{A}\mathbf{v} \tag{3.8}$$

where ρ is the atmospheric density, C_d is the drag coefficient, $\mathbf{A}$ is the cross sectional spacecraft area for each axis along the diagonal of the matrix and $\mathbf{v}$ is the velocity vector relative to the atmosphere. For typical spacecraft $C_d = 2.2$.

For relative proximity maneuvers only the relative drag is of real interest and we can find the differential drag acceleration as the difference between the chaser and target drag accelerations found from Equation (3.8) dividing by the respective masses. As the drag almost entirely acts along the x-axis we will consider the scalar formulation only.

$$\frac{F_{dd}}{m_c} = -\frac{1}{2}\rho C_d v^2 \left(\frac{A_c}{m_c} - \frac{A_t}{m_t}\right) \tag{3.9}$$

The velocities for the two spacecraft can be considered the same for this purpose, as well as the drag coefficients. The differential drag force acting on the chaser yield

$$F_{dd} = -\frac{1}{2}\rho C_d v^2 \left(A_c - A_t\frac{m_c}{m_t}\right) \tag{3.10}$$

where A_c is the cross section of the chaser and A_t is the cross section of the target spacecraft, which is the form used here. For completeness it shall be said that the equation

is often expressed as an acceleration using the ballistic coefficient C_B instead, where $C_B = \frac{m}{C_d A}$ in general.

The most uncertain part of Equation (3.10) is the atmospheric density ρ, which varies with the sun rotation, the Earth seasons and the 11 year cycle of the sun, the latter being dominant. Within the time scale of a RVD mission it can therefore be considered non stochastic. ρ is modeled empirically by one of the two well known models; JACCHIA (Jacchia 1977) and MSIS (Hedin 1986).

The atmosphere density is modeled by data in JACCHIA and the sub model Harris-Priestler is used (Vallado 2004). Above 1000 km altitude the density is considered to be zero.

For the relatively symmetric chaser spacecraft in this work, the air drag induced torques are small and therefore neglected as well as the shadowing effect between the spacecraft.

3.4.3 Chaser Flexible Modes Model

Here will be established a new general form of model for multiple flexible appendices of a rigid body spacecraft. The flexible modes are expressed in terms of eigen frequencies, damping and the modal coupling factors. These data are typically obtained from Finite Element Models (FEM), like e.g. the NASTRAN program. The modal data for one flexible solar panel is provided in Table C.4 and is valid for all four panels used. We will not deal with the modal analysis here, but some basic background information can be found in e.g. (Wie 1998). The modal analysis is performed for a free-free body with the modal data expressed at the attachment to the rigid body spacecraft in frame $\mathcal{F}_p$.

The general form of the model is (Fle 1994)

$$\mathbf{M}_T \begin{bmatrix} \ddot{\mathbf{x}} \\ \dot{\boldsymbol{\omega}} \end{bmatrix} = \begin{bmatrix} \mathbf{F} \\ \mathbf{N} \end{bmatrix} - \mathbf{L}\ddot{\boldsymbol{\eta}} \tag{3.11}$$

$$\ddot{\eta}_k + 2\zeta_k\omega_k\dot{\eta}_k + \omega_k^2\eta_k = -\frac{1}{m_k}\mathbf{L}^{\mathrm{T}} \begin{bmatrix} \ddot{\mathbf{x}} \\ \dot{\boldsymbol{\omega}} \end{bmatrix} \tag{3.12}$$

where

$\mathbf{M}_T$	:	mass/inertia matrix of the rigid body inclusive the flexible panels
$\ddot{\mathbf{x}}, \dot{\boldsymbol{\omega}}$	:	linear and angular acceleration of the rigid body
$\mathbf{F}, \mathbf{N}$	:	forces and torques acting on the spacecraft
η_k	:	the k^{th} flexible state
ζ_k	:	the k^{th} flexible damping factor
ω_k	:	the k^{th} flexible eigen frequency
m_k	:	modal mass for the k^{th} mode (normalized to 1)
$\mathbf{L}$	:	modal participation matrix of the k^{th} flexible mode at the COM

Before setting up the general structure for Equations (3.11) and (3.12), we will consider an example for one axis with one flexible mode for illustrative purpose. Taking the

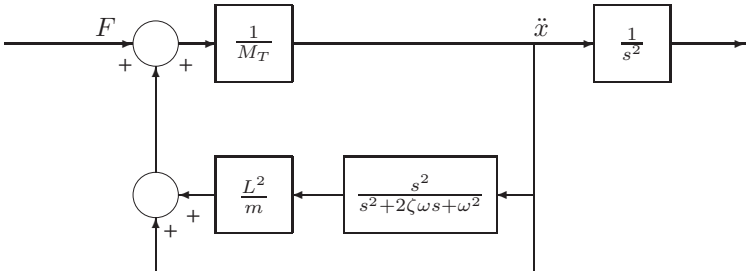

Figure 3.7: *Illustration of the principle structure of the flexible modes modeling, here shown for one mode and one axis. Further modes add along the lower lines. It consists of second order systems with coupling factors.*

Laplace transform of both sides of Equation (3.12) we get

$$\frac{\eta}{x} = -\frac{L}{m}\frac{s^2}{s^2 + 2\zeta\omega s + \omega^2} \tag{3.13}$$

Combining Equation (3.13) with Equation (3.11) in the Laplace domain, we can draw a principal block diagram in Figure 3.7.

We will now go through the steps of forming the matrix $\mathbf{L}$ starting from the modal data in Table C.4. The index j will indicate the panel number and we consider we have m modes and p panels. Recall that the modal data is for one panel given in the panel attached frame $\mathcal{F}_p$.

$$\mathbf{l}_{kjp} = \begin{bmatrix} \mathbf{l}_{kjpm} \\ \mathbf{l}_{kjpi} \end{bmatrix} = [L_{kmx} L_{kmy} L_{kmz} L_{kix} L_{kiy} L_{kiz}]^{\mathrm{T}} \tag{3.14}$$

The panels can rotate around their longitudinal axis Y_p by an angle $\boldsymbol{\beta} = [0, \beta, 0]^{\mathrm{T}}$. The rotation from the nominal panel frame to the actual frame is $\mathbf{R}_p(\boldsymbol{\beta})$ and we need to represent $\mathbf{l}_{kjp}$ in the nominal frame

$$\mathbf{l}_{kjp_n} = \begin{bmatrix} \mathbf{l}_{kjp_n m} \\ \mathbf{l}_{kjp_n i} \end{bmatrix} = \begin{bmatrix} \mathbf{R}_p^{\mathrm{T}} \mathbf{l}_{kjpm} \\ \mathbf{R}_p^{\mathrm{T}} \mathbf{l}_{kjpi} \end{bmatrix} \tag{3.15}$$

Further we rotate the vector $\mathbf{l}_{kjp_n}$ from the nominal panel frame into the spacecraft body frame. The rotation is $\mathbf{R}_{pbc}(\boldsymbol{\alpha})$ by an angle $\boldsymbol{\alpha} = [\alpha, 0, 0]^{\mathrm{T}}$.

$$\mathbf{l}_{kjb1} = \begin{bmatrix} \mathbf{l}_{kjb1m} \\ \mathbf{l}_{kjb1i} \end{bmatrix} = \begin{bmatrix} \mathbf{R}_{pbc}^{\mathrm{T}} \mathbf{l}_{kjp_n m} \\ \mathbf{R}_{pbc}^{\mathrm{T}} \mathbf{l}_{kjp_n i} \end{bmatrix} \tag{3.16}$$

We must now include the term from the modal mass, which is still located at the attachment point, to the modal inertia accounting for the lever arm.

$$\mathbf{l}_{kjb} = \begin{bmatrix} \mathbf{l}_{kjbm} \\ \mathbf{l}_{kjbi} \end{bmatrix} = \begin{bmatrix} \mathbf{l}_{kjb1m} \\ \mathbf{l}_{kjb1i} + \mathbf{l}_{kjb1m} \times \mathbf{r}_j \end{bmatrix} \tag{3.17}$$

where $\mathbf{r}_j$ is the vector from the COM to the attachment point j. For one flexible mode k, we will now stack the modal participation vectors as follows

$$\mathbf{L}_k = \begin{bmatrix} \mathbf{l}_{k1bm} & \mathbf{l}_{k2bm} & \cdots & \mathbf{l}_{kpbm} \\ \mathbf{l}_{k1bi} & \mathbf{l}_{k2bi} & \cdots & \mathbf{l}_{kpbi} \end{bmatrix}_{6\times p} \tag{3.18}$$

Finally we can form the matrix $\mathbf{L}$ by stacking blocks for each flexible mode

$$\mathbf{L} = \begin{bmatrix} \mathbf{L}_1 & \mathbf{L}_2 & \cdots & \mathbf{L}_m \end{bmatrix}_{6\times mp} \tag{3.19}$$

Equation (3.19) gives the general modal participation matrix for any number of panels with any possible orientation in the spacecraft body frame.

The dynamical equations for the flexible modes are expressed most conveniently in state space form. For one mode and one panel we define the state vector as $\mathbf{x}_{fk} = [\eta, \dot{\eta}]^{\mathrm{T}}$ and $\dot{\mathbf{x}}_{fk} = [\dot{\eta}, \ddot{\eta}]^{\mathrm{T}}$ and from Equation (3.12) we find

$$\ddot{\eta}_k = -2\zeta_k\omega_k\dot{\eta}_k - \omega_k^2\eta_k - \frac{1}{m_k}\mathbf{l}_k^{\mathrm{T}}\begin{bmatrix} \ddot{\mathbf{x}} \\ \dot{\boldsymbol{\omega}} \end{bmatrix} \tag{3.20}$$

which will be the output of the state space model. We can write

$$\dot{\mathbf{x}}_{fk} = \mathbf{A}_{fk}\mathbf{x}_{fk} + \mathbf{B}_{fk}\mathbf{u} = \begin{bmatrix} 0 & 1 \\ -\omega_k^2 & -2\zeta_k\omega_k \end{bmatrix}\mathbf{x}_{fk} + \begin{bmatrix} 0 \\ -\frac{1}{m_k}\mathbf{l}_k^{\mathrm{T}} \end{bmatrix}\mathbf{u} \tag{3.21}$$

where $\mathbf{u} = [\ddot{\mathbf{x}}, \dot{\boldsymbol{\omega}}]^{\mathrm{T}}$ and the output becomes from Equations (3.20) and (3.11)

$$\mathbf{y}_{fk} = -\mathbf{l}_k[\mathbf{C}_k\mathbf{x}_{fk} + \mathbf{D}_{fk}\mathbf{u}] = -\mathbf{l}_k\begin{bmatrix} -\omega_k^2 & -2\zeta_k\omega_k \end{bmatrix}\mathbf{x}_{fk} - \mathbf{l}_k[-\frac{1}{m_k}\mathbf{l}_k^{\mathrm{T}}]\mathbf{u} \tag{3.22}$$

Finally we will combine the state space system for each panel and each flexible mode into one complete model following the organization of Equations (3.18) and (3.19). We define the general state vector as $\mathbf{x}_f = [\eta_{11}, \dot{\eta}_{11}, \cdots, \eta_{1p}, \dot{\eta}_{1p}, \cdots, \eta_{mp}, \dot{\eta}_{mp}]^{\mathrm{T}}$

$$\dot{\mathbf{x}}_f = \mathbf{A}_f\mathbf{x}_f + \mathbf{B}_f\mathbf{u} \tag{3.23}$$

$$\mathbf{y}_f = -\mathbf{L}\mathbf{C}_f\mathbf{x}_f - \mathbf{L}\mathbf{D}_f\mathbf{u} \tag{3.24}$$

where

$$\mathbf{A}_f = \begin{bmatrix} \begin{bmatrix} \mathbf{A}_{11} & & \\ & \ddots & \\ & & \mathbf{A}_{1p} \end{bmatrix}_{2p\times 2p} & & & \\ & \ddots & & \\ & & \begin{bmatrix} \mathbf{A}_{m1} & & \\ & \ddots & \\ & & \mathbf{A}_{mp} \end{bmatrix}_{2p\times 2p} & \end{bmatrix}_{2(mp\times mp)} \tag{3.25}$$

$$\mathbf{B}_f = \begin{bmatrix} & \begin{bmatrix} \mathbf{0} \\ \mathbf{L}_{1,1..6} \\ \mathbf{0} \\ \mathbf{L}_{2,1..6} \\ \vdots \\ \mathbf{0} \\ \mathbf{L}_{p,1..6} \end{bmatrix}_1 \\ -\frac{1}{m_1} & \\ & \vdots \\ & \begin{bmatrix} \mathbf{0} \\ \mathbf{L}_{1,1..6} \\ \mathbf{0} \\ \mathbf{L}_{2,1..6} \\ \vdots \\ \mathbf{0} \\ \mathbf{L}_{p,1..6} \end{bmatrix}_m \\ -\frac{1}{m_m} & \end{bmatrix}_{2mp\times 6} \tag{3.26}$$

$$\mathbf{C}_f = \begin{bmatrix} \begin{bmatrix} \mathbf{C}_{11} & & \\ & \ddots & \\ & & \mathbf{C}_{1p} \end{bmatrix}_{p\times 2p} & & \\ & \ddots & \\ & & \begin{bmatrix} \mathbf{C}_{m1} & & \\ & \ddots & \\ & & \mathbf{C}_{mp} \end{bmatrix}_{p\times 2p} \end{bmatrix}_{mp\times 2mp} \tag{3.27}$$

$$\mathbf{D}_f = \begin{bmatrix} & \begin{bmatrix} \mathbf{L}_{1,1..6} \\ \mathbf{L}_{2,1..6} \\ \vdots \\ \mathbf{L}_{p,1..6} \end{bmatrix}_1 \\ -\frac{1}{m_1} & \\ & \vdots \\ & \begin{bmatrix} \mathbf{L}_{1,1..6} \\ \mathbf{L}_{2,1..6} \\ \vdots \\ \mathbf{L}_{p,1..6} \end{bmatrix}_m \\ -\frac{1}{m_m} & \end{bmatrix}_{mp\times 6} \tag{3.28}$$

It shall be noted that the minus on the last term in Equation (3.11) is included in the output of Equation (3.23).

3.4.4 Chaser Fuel Sloshing Model

The perturbation from fuel sloshing is caused by partially filled tanks with some free motion of the fuel. The best approach to minimize this is by designing anti sloshing baffles in the tanks, though it will not be able to eliminate the effect totally. Therefore we need models of the effect, though it is very difficult to model accurately fluid motion in a zero gravity environment.

Fluid behaves differently as a function of the acceleration on it, for which reason it is not simple to find a model which covers a larger range. We can consider two models.

The first being based on a pendulum equivalent model being adequate during the orbital boost modes and a second being based on a spring, mass and damper equivalent for the other RVD modes. We will consider the latter here. Both models have been verified with the FLOW3D software.

We will divide the liquid into a sloshing part m_1 and a solid part m_0 as

$$m_1 = (1 - \lambda(\tau))m_L \tag{3.29}$$

$$m_0 = \lambda(\tau)m_L \tag{3.30}$$

where m_L is the total fuel mass in the tank, τ is the filling ratio and

$$\lambda = \tau(4\alpha_s - 1) + \tau^2(2 - 4\alpha_s) \tag{3.31}$$

where $\alpha_s = \lambda(0.5) = 0.62$ and Equation (3.31) is found empirically from FLOW3D analysis and valid for spherical tanks with conic baffles used here . The perturbation force $\mathbf{F}_P$ from the slosh can be written as a liquid minus a solid part

$$\mathbf{F}_P = \mathbf{F}_L - \mathbf{F}_S \tag{3.32}$$

which we will separate into parts for m_1 and m_0 respectively.

$$\mathbf{F}_L = \mathbf{F}_{L_1} + \mathbf{F}_{L_0} \quad \text{and} \quad \mathbf{F}_S = \mathbf{F}_{S_1} + \mathbf{F}_{S_0} \tag{3.33}$$

As $\mathbf{F}_{L_0} = \mathbf{F}_{S_0}$ Equation (3.32) yield

$$\mathbf{F}_P = \mathbf{F}_{L_1} - \mathbf{F}_{S_1} \tag{3.34}$$

and

$$\mathbf{F}_{L_1} = k_s\mathbf{x}_1 + c_s\dot{\mathbf{x}}_1 \tag{3.35}$$

$$\mathbf{F}_{S_1} = m_1\boldsymbol{\gamma}_{tank} \tag{3.36}$$

where $\mathbf{x}_1$ is the displacement of m_1 in a tank centered coordinate system, k_s is the spring stiffness, c_s is the damping and $\boldsymbol{\gamma}_{tank}$ is the acceleration of the tank. $\mathbf{F}_{S_1}$ is accounted for by the normal rigid body motion, so we only need to deal with Equation (3.35).

We will now calculate the general acceleration $\boldsymbol{\gamma}_1$ acting on the mass m_1

$$\boldsymbol{\gamma}_1 = \boldsymbol{\gamma}_c - \boldsymbol{\omega} \times (\boldsymbol{\omega} \times \mathbf{r}_1) - 2\boldsymbol{\omega} \times \dot{\mathbf{r}}_1 - \dot{\boldsymbol{\omega}} \times \mathbf{r}_1 \tag{3.37}$$

where

$\boldsymbol{\gamma}_1$	:	acceleration of m_1 with respect to the spacecraft reference frame
$\boldsymbol{\gamma}_c$	:	acceleration of the rigid spacecraft
$\boldsymbol{\omega}$	:	angular velocity of the spacecraft
$\mathbf{r}_1$	:	m_1 location with respect to the COM with $\mathbf{r}_1 = \mathbf{r}_{tank} + \mathbf{x}_1$ where $\mathbf{r}_{tank}$ is the tank center with respect to the COM

We can write the spring, mass and damper model for one axis as

$$m_1\ddot{x}_1 = -k_s x_1 - c_s\dot{x}_1 + m_1\gamma_1 \tag{3.38}$$

which gives the displacement x_1 of the mass m_1. Combining Equation (3.38) with Equation (3.35) to eliminate the displacement, we can write the transfer function from the forcing function γ_1 to the perturbation force F_L in the scalar case as

$$\frac{F_L(s)}{\gamma_1(s)} = \frac{c_s s + k_s}{s^2 + \frac{c_s}{m_1}s + \frac{k_s}{m_1}} \tag{3.39}$$

This model has a very similar structure as illustrated in Figure 3.7 , except the transfer function is different. The torque produced on the spacecraft is $\mathbf{N}_L = \mathbf{r}_1 \times \mathbf{F}_L$ and in practice the term $\mathbf{x}_1$ can be neglected as small.

We will now express Equation (3.39) in a state space form for all 3 axes for one single tank, where $\mathbf{x}_s = [x_x, \dot{x}_x, x_y, \dot{x}_y, x_z, \dot{x}_z]^{\mathrm{T}}$ and for simplicity reasons, we write the matrices for the x-axis only, as the full model is block diagonal

$$\dot{\mathbf{x}}_s = \mathbf{A}_s\mathbf{x}_s + \mathbf{B}_s\mathbf{u} \tag{3.40}$$

$$\mathbf{y}_s = \mathbf{C}_s\mathbf{x}_s \tag{3.41}$$

where $\mathbf{u} = \boldsymbol{\gamma}_1$ and

$$\mathbf{A}_{s_x} = \begin{bmatrix} 0 & 1 \\ -\frac{k_s}{m_1} & -\frac{c_s}{m_1} \end{bmatrix} \tag{3.42}$$

$$\mathbf{B}_{s_x} = \begin{bmatrix} 0 \\ 1 \end{bmatrix} \tag{3.43}$$

$$\mathbf{c}_{s_x} = \begin{bmatrix} k_s & c_s \end{bmatrix} \tag{3.44}$$

The total perturbation is the sum from each individual tank and can be constructed in a similar manner as for the flexible modes in Section 3.4.3. From analysis elsewhere, we know that the natural frequency range is $[0.01; 0.04]$ Hz for $\tau = 0.5$ and the damping $c_s \in [0.16; 0.5]$ s^{-1}. Typical mass to consider is $m_L = 600$ kg. The location of the four tanks are as in Table 3.5 in the geometrical frame $\mathcal{F}_{gc}$.

Tank #	x m	y m	z m
1	1.4	0.85	0.85
2	1.4	-0.85	0.85
3	1.4	-0.85	-0.85
4	1.4	0.85	-0.85

Table 3.5: *Location of tanks.*

3.5 Conclusion

All the needed coordinate frames have been rigorously defined together with their inter relationships. The data for both chaser and target spacecraft has been provided. Linear multivariable models have been developed for gravity gradient torques, differential drag forces and dynamical state space models for both flexible modes and sloshing phenomena.

Chapter 4

Relative Position Dynamics and Kinematics

The relative position dynamics between 2 spacecraft moving in arbitrary elliptical orbits will be developed in this chapter. Until today all space missions involving close proximity maneuvers has been for RVD missions on circular orbits. This is going to change for future planned missions of landing, sample and return type and proximity encounters with small celestial bodies typically in elliptical orbits. Other emerging missions are Formation Flying ones also utilizing elliptical orbits (Inalhan, Tillerson & How 2002). Earlier work has been performed in this field but it has mostly been concentrated on the theoretical aspects leading to restricted solutions which are of less importance for the practicing designer; see e.g. (Berreen & Sved 1979), (Garrison et al. 1995), (Kechichian 1992), (Lancaster 1970), (Melton 2000), (Weiss 1981), (Tschauner & Hempel 1965) and later (Humi & Carter 2002). The linear solution will be found with respect to the target spacecraft for any elliptical orbit. The special case for the circular orbits will be found in the Clohessy Wiltshire equations (Clohessy & Wiltshire 1960).

The general solution will finally be tested and verified with respect to a complete nonlinear numerical solution and error functions developed to determine error boundaries.

4.1 General Differential Equation System

The only assumption for this derivation is that the motion is under the action of a central gravity field and forces from thruster actuation or disturbances. The spacecraft are considered as point masses for this work.

The position vectors in inertial space are defined as in Figure 4.1 for the chaser $\mathbf{r}_c$ and target $\mathbf{r}_t$. Their relative position is denoted $\mathbf{s}$. The equations of motion will be derived conveniently in the target local orbital frame, illustrated in Figure 3.2.

In the following scalars will be in normal types and vectors and matrices will be in

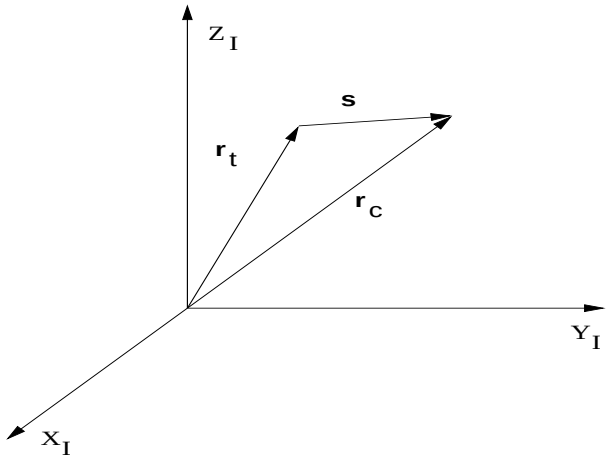

Figure 4.1: *Definition of the position vectors to the chaser* $\mathbf{r}_c$ *and target* $\mathbf{r}_t$ *as well as the relative vector* $\mathbf{s}$ *in the inertial frame* $\mathcal{F}_i$.

bold, and it will be clear from the context what is what. Vectors are defined as column vectors.

The general equation for motion under the influence of a central force is as follows (Newton 1713).

$$\mathbf{F}_g(\mathbf{r}) = -G\frac{Mm}{r^2}\frac{\mathbf{r}}{r} = -\mu\frac{m}{r^3}\mathbf{r} \tag{4.1}$$

and

G	:	universal gravitational constant	Nm^2/kg^2
M	:	mass of the Earth	kg
m	:	mass of the spacecraft (second mass)	kg
$\mathbf{r}$	:	the radius vector $r = \lvert\mathbf{r}\rvert$	m
μ	:	$\mu = GM$	Nm^2/kg

Dividing by the mass on both sides of Equation (4.1) to normalize one obtains for the general motion as follows

$$\mathbf{f}_g(\mathbf{r}) = -\mu\frac{\mathbf{r}}{r^3} \tag{4.2}$$

Target motion from Equation (4.1):

$$\mathbf{F}_g(\mathbf{r}_t) = m_t\ddot{\mathbf{r}}_t = -\mu\frac{m_t}{r_t^3}\mathbf{r}_t$$

$$\mathbf{f}_g(\mathbf{r}_t) = \ddot{\mathbf{r}}_t = -\mu\frac{\mathbf{r}_t}{r_t^3} \tag{4.3}$$

Chaser motion from Equation (4.1) and non gravitational force:

$$m_c\ddot{\mathbf{r}}_c = \mathbf{F}_g(\mathbf{r}_c) + \mathbf{F} = -\mu\frac{m_c}{r_c^3}\mathbf{r}_c + \mathbf{F}$$

and inserting Equation (4.2) yield

$$\ddot{\mathbf{r}}_c = \mathbf{f}_g(\mathbf{r}_c) + \frac{\mathbf{F}}{m_c} \tag{4.4}$$

The relative motion $\mathbf{s}$ is defined as follows and the relative accelerations become directly the derivatives in inertial space

$$\mathbf{r}_t + \mathbf{s} = \mathbf{r}_c \tag{4.5}$$

$$\ddot{\mathbf{s}} = \ddot{\mathbf{r}}_c - \ddot{\mathbf{r}}_t \tag{4.6}$$

Inserting Equations (4.3) and (4.4) into Equation (4.6) one obtains

$$\ddot{\mathbf{s}} = \mathbf{f}_g(\mathbf{r}_c) - \mathbf{f}_g(\mathbf{r}_t) + \frac{\mathbf{F}}{m_c} \tag{4.7}$$

We will now linearize $\mathbf{f}_g(\mathbf{r}_c)$ around the vector $\mathbf{r}_t$ by means of a Taylor expansion to first order.

$$\mathbf{f}_g(\mathbf{r}_c) = \mathbf{f}_g(\mathbf{r}_t) + \left.\frac{\partial \mathbf{f}_g(\mathbf{r})}{\partial \mathbf{r}}\right|_{\mathbf{r}=\mathbf{r}_t}(\mathbf{r}_c - \mathbf{r}_t) \tag{4.8}$$

The elements of the Jacobian matrix (Wie 1998) in Equation (4.8) are derived in details in Section A.1.1 for the partial derivatives. We define $\mathbf{r} = [r_x, r_y, r_z]^{\mathrm{T}}$ and $r = |\mathbf{r}| = (r_x^2 + r_y^2 + r_z^2)^{\frac{1}{2}}$.
We will now rewrite Equation (4.8) and insert Equation (4.6), $\mathbf{M}$ and that $\mathbf{r} = \mathbf{r}_t$.

$$\mathbf{f}_g(\mathbf{r}_c) - \mathbf{f}_g(\mathbf{r}_t) = -\frac{\mu}{r_t^3}\mathbf{M}\mathbf{s}$$

where

$$\mathbf{M} = \begin{bmatrix} 1 - 3\frac{r_x^2}{r_t^2} & 3\frac{r_x r_y}{r_t^2} & 3\frac{r_x r_z}{r_t^2} \\ 3\frac{r_y r_x}{r_t^2} & 1 - 3\frac{r_y^2}{r_t^2} & 3\frac{r_y r_z}{r_t^2} \\ 3\frac{r_z r_x}{r_t^2} & 3\frac{r_z r_y}{r_t^2} & 1 - 3\frac{r_z^2}{r_t^2} \end{bmatrix} \tag{4.9}$$

after inserting from Section A.1.1 and Equation (4.7) becomes

$$\ddot{\mathbf{s}} = -\frac{\mu}{r_t^3}\mathbf{M}\mathbf{s} + \frac{\mathbf{F}}{m_c} \tag{4.10}$$

The interest is to represent the chaser motion in the rotating target local orbital frame, see Section 3.1. From a general kinematic equation for translation and rotating systems, we can obtain the chaser acceleration in the rotating target frame. The translation is trivial and part of the equations (Symon 1979). Generally one obtains the following, where the starred $(*)$ system is rotating with the angular velocity vector $\boldsymbol{\omega}$.

$$\frac{d^2\mathbf{x}}{dt^2} = \frac{d^{*2}\mathbf{x}^*}{dt^2} + \boldsymbol{\omega} \times (\boldsymbol{\omega} \times \mathbf{x}^*) + 2\boldsymbol{\omega} \times \frac{d^*\mathbf{x}^*}{dt} + \frac{d\boldsymbol{\omega}}{dt} \times \mathbf{x}^* \tag{4.11}$$

We now define $\mathbf{s} = \mathbf{x}$ and $\mathbf{s}^* = [x, y, z]^{\mathrm{T}}$ in the rotating starred system and inserting Equation (4.10) yield

$$\frac{d^{*2}\mathbf{s}^*}{dt^2} + \boldsymbol{\omega} \times (\boldsymbol{\omega} \times \mathbf{s}^*) + 2\boldsymbol{\omega} \times \frac{d^*\mathbf{s}^*}{dt} + \frac{d\boldsymbol{\omega}}{dt} \times \mathbf{s}^* + \frac{\mu}{r_t^3}\mathbf{M}\mathbf{s}^* = \frac{\mathbf{F}}{m_c} \tag{4.12}$$

Expressed in the target frame we get for $\mathbf{r}_t$ and $\boldsymbol{\omega}$ directly from the frame definition

$$\mathbf{r}_t = \begin{bmatrix} 0 \\ 0 \\ -r \end{bmatrix} \text{ and } \boldsymbol{\omega} = \begin{bmatrix} 0 \\ -\omega \\ 0 \end{bmatrix}$$

The terms of Equation (4.12) can be found by inserting $\mathbf{r}_t$ and $\boldsymbol{\omega}$ and carrying out all the cross products as well as finding the elements of the Jacobian $\mathbf{M}$ in Equation (4.9). See also Section A.1.2.

We will now find a more convenient expression for the term $\frac{\mu}{r_t^3}$ in Equation (4.12) as a function of the orbital angular velocity. To do that we observe that the angular momentum $\mathbf{L}$ is constant for fixed elliptic orbits and we can express its magnitude as follows:

$$\begin{array}{rcccccc} mr_t^2\omega = L & \Rightarrow & r_t^2\omega & = & \frac{L}{m} & = & h \\ & \Downarrow & r_t & = & \sqrt{\frac{L}{m\omega}} & = & \sqrt{\frac{h}{\omega}} \end{array} \tag{4.13}$$

We will now reformulate as follows, for extensive use in the subsequent solutions, using the result in Equation (4.13):

$$\frac{\mu}{r_t^3} = \mu\left(\frac{\omega}{h}\right)^{\frac{3}{2}} = \underbrace{\mu\left(\frac{1}{h}\right)^{\frac{3}{2}}}_{k}\omega^{\frac{3}{2}} = k\omega^{\frac{3}{2}} \tag{4.14}$$

We now insert Equations (4.13) and (4.14) into Equation (4.12) together with the elements of Equation (4.12) yielding:

$$\begin{aligned} \ddot{x} - \omega^2 x - 2\omega\dot{z} - \dot{\omega}z + k\omega^{\frac{3}{2}}x &= \frac{1}{m_c}F_x \\ \ddot{y} + k\omega^{\frac{3}{2}}y &= \frac{1}{m_c}F_y \\ \ddot{z} - \omega^2 z + 2\omega\dot{x} + \dot{\omega}x - 2k\omega^{\frac{3}{2}}z &= \frac{1}{m_c}F_z \end{aligned} \tag{4.15}$$

It shall be noted that the system of linear time varying differential equations in Equation (4.15) is the general system valid for an arbitrary relative trajectory between a chaser

spacecraft and a target spacecraft, where the latter moves under the influence of a central gravity field only. Hence the validity of Equation (4.15) for the target spacecraft. The reduction of this system restricted to circular or near circular orbits can be found in Section 4.3. The system can now be formulated conveniently in state space form as follows.

In plane: With state vector $\mathbf{x}_{pi} = [x, z, \dot{x}, \dot{z}]^{\mathrm{T}}$ and $\mathbf{F}_i = [F_x, F_z]^{\mathrm{T}}$

$$\dot{\mathbf{x}}_{pi} = \begin{bmatrix} 0 & 0 & 1 & 0 \\ 0 & 0 & 0 & 1 \\ \omega^2 - k\omega^{\frac{3}{2}} & \dot{\omega} & 0 & 2\omega \\ -\dot{\omega} & \omega^2 + 2k\omega^{\frac{3}{2}} & -2\omega & 0 \end{bmatrix} \mathbf{x}_{pi} + \begin{bmatrix} 0 & 0 \\ 0 & 0 \\ \frac{1}{m_c} & 0 \\ 0 & \frac{1}{m_c} \end{bmatrix} \mathbf{F}_i \tag{4.16}$$

$$\boxed{\dot{\mathbf{x}}_{pi} = \mathbf{A}_{pi}\mathbf{x}_{pi} + \mathbf{B}_{pi}\mathbf{F}_i} \tag{4.17}$$

Out of plane: With state vector $\mathbf{x}_{po} = [y, \dot{y}]^{\mathrm{T}}$ and $\mathbf{F}_o = [F_y]^{\mathrm{T}}$

$$\dot{\mathbf{x}}_{po} = \begin{bmatrix} 0 & 1 \\ -k\omega^{\frac{3}{2}} & 0 \end{bmatrix} \mathbf{x}_{po} + \begin{bmatrix} 0 \\ \frac{1}{m_c} \end{bmatrix} \mathbf{F}_o \tag{4.18}$$

$$\boxed{\dot{\mathbf{x}}_{po} = \mathbf{A}_{po}\mathbf{x}_{po} + \mathbf{B}_{po}\mathbf{F}_o} \tag{4.19}$$

Defining a state vector $\mathbf{x}_p = [x, y, z, \dot{x}, \dot{y}, \dot{z}]^{\mathrm{T}}$ and $\mathbf{F} = [F_x, F_y, F_z]^{\mathrm{T}}$, and system matrices $\mathbf{A}_p$ and $\mathbf{B}_p$ the in and out of plane state space systems can be combined into one model, which is detailed in Section A.5.

4.2 General Homogeneous Solution

We will now prepare to find the generic closed form homogeneous solution to Equation (4.15), which will give the transition matrix of the system. Equation (4.15) is not solvable in its present form, so the first step will be to reformulate it by performing a nonlinear transformation of its variables and intermediate computations can be found in A.3.1. The idea is to make use of the fact that elliptical orbits governed by the Equation (4.1) hold many of the properties of conic sections, see also Section A.2.

The strategy is now to replace the independent variable t with the true anomaly θ, see illustration in Figure 2.1. Defining a function

$$\varrho(\theta) \triangleq 1 + \varepsilon\cos(\theta) \quad \text{and} \quad \varrho(\theta) \in]0; 2[\tag{4.20}$$

we can then rearrange Equation (A.12), the expression for a general conic section, to obtain another expression for ω in Equation (4.15), the objective being to simplify Equation (4.15).

$$r = \frac{p}{1 + \varepsilon\cos(\theta)} = \frac{p}{\varrho} \tag{4.21}$$

where ε is the orbit eccentricity, $p = h^2\mu^{-1}$ and h is the specific orbital angular momentum as defined in Equation (4.13). Rearranging Equation (4.21) and inserting we obtain

$$\varrho = \frac{p}{r} = \frac{h^2}{\mu r}$$

and inserting Equation (4.13)

$$\varrho = \frac{h^2}{\mu}\left(\frac{h}{\omega}\right)^{-\frac{1}{2}} = \frac{h^{\frac{3}{2}}}{\mu}\omega^{\frac{1}{2}}$$

and from Equation (4.14) we get the inverse of k and combining we obtain for ω, where the argument θ is omitted for simplicity.

$$\varrho = k^{-1}\omega^{\frac{1}{2}}$$

$$\omega = k^2\varrho^2 \tag{4.22}$$

We will now derive the intermediate differentials needed in Equation (4.15) with respect to θ and define $\frac{da}{d\theta} = a'$ where a is an arbitrary variable,

$$\frac{da}{dt} = \frac{da}{d\theta}\frac{d\theta}{dt} = \omega\frac{da}{d\theta} = \omega a' \tag{4.23}$$

and after some manipulations we obtain for the second derivative

$$\begin{aligned}\frac{d^2a}{dt^2} &= \frac{d^2a}{d\theta^2}\left(\frac{d\theta}{dt}\right)^2 + \frac{da}{d\theta}\frac{d^2\theta}{dt^2} \\ &= \omega^2 a'' + \omega\omega' a'\end{aligned} \tag{4.24}$$

The derivative of Equation (4.22) becomes

$$\begin{aligned}\frac{d\omega}{d\theta} &= \omega' \\ &= \frac{d}{d\theta}\left(k^2(1+\varepsilon\cos(\theta))^2\right) \\ &= -2\varepsilon k^2\varrho\sin(\theta)\end{aligned} \tag{4.25}$$

Details of Equations (4.24) and (4.25) are in Section A.3.1.

We now have all the intermediate equations needed Equations (4.22) to (4.25) to insert into Equation (4.15). We will consider the homogeneous part of the equation and the right hand side becomes zero (the initial value problem). The particular solution cannot be general per definition to be of practical interest. We will rewrite Equation (4.15) row by row, see Section A.3.1 for details, commencing with the second row of Equation (4.15), which is the simplest, and inserting Equation (4.24) for y we obtain

$$\omega^2 y'' + \omega\omega' y' + k\omega^{\frac{3}{2}} y = 0$$

We now insert Equations (4.22) and (4.25) and after some algebraic manipulations we obtain

$$\varrho y'' - 2\varepsilon \sin(\theta) y' + y = 0 \tag{4.26}$$

Inserting Equation (4.24) for x and z into the first row of Equation (4.15) we obtain

$$\omega^2 x'' + \omega\omega' x' - \omega^2 x - 2\omega^2 z' - \omega\omega' z + k\omega^{\frac{3}{2}} x = 0$$

We can now regroup the terms with respect to ω and inserting Equations (4.22) and (4.25). After rearranging and simplifying terms we arrive at

$$\varrho x'' - 2\varepsilon \sin(\theta) x' + 2\varepsilon \sin(\theta) z - \varepsilon \cos(\theta) x - 2\varrho z' = 0 \tag{4.27}$$

Inserting Equation (4.24) for x and z into the third row of Equation (4.15) we obtain

$$\omega^2 z'' + \omega\omega' z' - \omega^2 z + 2\omega^2 x' + \omega\omega' x - 2k\omega^{\frac{3}{2}} z = 0$$

We can now regroup the terms with respect to ω and inserting Equations (4.22) and (4.25), dividing both sides with $(k^2\varrho^2)$ and then by $(k^2\varrho)$, expanding terms and simplifying we obtain

$$\varrho z'' - 2\varepsilon \sin(\theta) z' - 2\varepsilon \sin(\theta) x + 2\varrho x' - (3 + \varepsilon \cos(\theta)) z = 0 \tag{4.28}$$

To get a better overview of the system of Equations (4.26), (4.27) and (4.28), we will write the system together in Equation (4.29).

$$\begin{aligned} \varrho x'' &= 2\varepsilon \sin(\theta) x' - 2\varepsilon \sin(\theta) z + \varepsilon \cos(\theta) x + 2\varrho z' \\ \varrho y'' &= 2\varepsilon \sin(\theta) y' - y \\ \varrho z'' &= 2\varepsilon \sin(\theta) z' + 2\varepsilon \sin(\theta) x - 2\varrho x' + (3 + \varepsilon \cos(\theta)) z \end{aligned} \tag{4.29}$$

We will now define a transformation to be applied to Equation (4.29) to simplify the equation system further. Proposed the first time by (Lawden 1954).

$$\begin{bmatrix} \alpha \\ \beta \\ \gamma \end{bmatrix} \triangleq \varrho \begin{bmatrix} x \\ y \\ z \end{bmatrix} = (1 + \varepsilon \cos(\theta)) \begin{bmatrix} x \\ y \\ z \end{bmatrix} \tag{4.30}$$

To apply the transformation in Equation (4.30) to the system in Equation (4.29) we will compute the derivative terms for the α component in Equation (4.30), which will then be used for β and γ as well. From Equation (4.20) it follows that

$$\begin{aligned} \varrho &= 1 + \varepsilon \cos(\theta) \\ \varrho' &= -\varepsilon \sin(\theta) \\ \varrho'' &= -\varepsilon \cos(\theta) \end{aligned} \tag{4.31}$$

The general transformation for one component of Equation (4.30), e.g. α has the first derivative,

$$\alpha' = \varrho' x + \varrho x'$$

and inserting x from Equation (4.30) and solving for x' we obtain

$$x' = \frac{1}{\varrho}\left(\alpha' - \frac{\varrho'}{\varrho}\alpha\right) \tag{4.32}$$

see also Equation (A.25). The second derivative of α becomes

$$\alpha'' = \varrho''x + \varrho'x' + \varrho'x' + \varrho x''$$

and inserting x from Equation (4.30) and x' from Equation (4.32) we obtain

$$\varrho x'' = \alpha'' - \frac{\varrho''}{\varrho}\alpha - 2\frac{\varrho'}{\varrho}\left(\alpha' - \frac{\varrho'}{\varrho}\alpha\right) \tag{4.33}$$

see also Equation (A.26). We will now rewrite Equation (4.29) by writing the coefficients in terms of ϱ and its derivatives from Equation (4.31).

$$\begin{aligned} \varrho x'' &= -2\varrho'x' + 2\varrho'z - \varrho''x + 2\varrho z' \\ \varrho y'' &= -2\varrho'y' - y \\ \varrho z'' &= -2\varrho'z' - 2\varrho'x - 2\varrho x' + (2+\varrho)z \end{aligned} \tag{4.34}$$

We will now rewrite Equation (4.34) by using the transformation Equation (4.30) and by inserting Equations (4.32) and (4.33). Starting with the second row of Equation (4.34) we get

$$\varrho y'' = -2\varrho'y' - y$$

$$\beta'' - \frac{\varrho''}{\varrho}\beta - 2\frac{\varrho'}{\varrho}\left(\beta' - \frac{\varrho'}{\varrho}\beta\right) = -2\frac{\varrho'}{\varrho}\left(\beta' - \frac{\varrho'}{\varrho}\beta\right) - \frac{\beta}{\varrho}$$

and by recognizing that $\frac{1-\varrho''}{\varrho} = 1$ and by rearranging the terms, we get

$$\beta'' = -\beta \tag{4.35}$$

For the first row of Equation (4.34) we obtain

$$\varrho x'' = -2\varrho'x' + 2\varrho'z - \varrho''x + 2\varrho z'$$

and substituting and rearranging terms as before we obtain

$$\alpha'' - \frac{\varrho''}{\varrho}\alpha - 2\frac{\varrho'}{\varrho}\left(\alpha' - \frac{\varrho'}{\varrho}\alpha\right) = -2\frac{\varrho'}{\varrho}\left(\alpha' - \frac{\varrho'}{\varrho}\alpha\right) + 2\frac{\varrho'}{\varrho}\gamma - \frac{\varrho''}{\varrho}\alpha + \frac{2\varrho}{\varrho}\left(\gamma' - \frac{\varrho'}{\varrho}\gamma\right)$$

$$\alpha'' = 2\gamma' \tag{4.36}$$

For the third row of Equation (4.34) we obtain, see also Equation (A.27),

$$\varrho z'' = -2\varrho'z' - 2\varrho'x - 2\varrho x' + (2+\varrho)z$$

and substituting and rearranging terms as before we obtain

$$\gamma''-\frac{\varrho''}{\varrho}\gamma-2\frac{\varrho'}{\varrho}\left(\gamma'-\frac{\varrho'}{\varrho}\gamma\right)=-2\frac{\varrho'}{\varrho}\left(\gamma'-\frac{\varrho'}{\varrho}\gamma\right)-2\frac{\varrho'}{\varrho}\alpha-\frac{2\varrho}{\varrho}\left(\alpha'-\frac{\varrho'}{\varrho}\alpha\right)+(2+\varrho)\frac{\gamma}{\varrho}$$

$$\gamma''=\frac{3}{\varrho}\gamma-2\alpha' \tag{4.37}$$

We will now write Equations (4.35) to (4.37) together having obtained a simple set of differential equations as a function of the true anomaly θ.

$$\begin{aligned}\alpha'' &= 2\gamma' \\ \beta'' &= -\beta \\ \gamma'' &= \frac{3}{\varrho}\gamma-2\alpha'\end{aligned} \tag{4.38}$$

The system in Equation (4.38) is rather simple in its appearance and the out of plane motion is just a harmonic oscillator as in the circular ($\varepsilon = 0$) case. Again, we will begin to find the full solution for the out of plane equation. This will be performed in Section 4.2.1 and the two other coupled equations for the in plane motion will be solved in Section 4.2.2.

4.2.1 General Solution for the Out of Plane Motion

It shall be recalled that the variables of the system in Equation (4.38) are all functions of θ. The solution for the harmonic oscillator becomes in the θ domain

$$\beta(\theta)=c_1\sin(\theta)+c_2\cos(\theta)$$

and using Equation (4.30) to obtain the solution in the time domain

$$y(t)=\frac{1}{\varrho(\theta(t))}\Big(\,c_1\sin(\theta(t))+c_2\cos(\theta(t))\Big) \tag{4.39}$$

We will determine the constants c_1 and c_2 from the initial conditions in the θ domain, β_0 and β_0', where the derivative is

$$\beta'(\theta)=c_1\cos(\theta)-c_2\sin(\theta)$$

and to find c_1 and c_2 we will write the β equation in matrix notation

$$\begin{bmatrix}\beta(\theta)\\ \beta'(\theta)\end{bmatrix}=\begin{bmatrix}c_1\sin(\theta)+c_2\cos(\theta)\\ c_1\cos(\theta)-c_2\sin(\theta)\end{bmatrix}=\begin{bmatrix}\sin(\theta) & \cos(\theta)\\ \cos(\theta) & -\sin(\theta)\end{bmatrix}\begin{bmatrix}c_1\\ c_2\end{bmatrix}=\mathbf{A}(\theta)\begin{bmatrix}c_1\\ c_2\end{bmatrix}$$

and as c_1 and c_2 holds all the information of the initial conditions, this is the solution, but we will eliminate the 2 constants.

$$\begin{bmatrix}\beta_0\\ \beta_0'\end{bmatrix}=\mathbf{A}_0(\theta_0)\begin{bmatrix}c_1\\ c_2\end{bmatrix}$$

and the inverse becomes

$$\begin{bmatrix} c_1 \\ c_2 \end{bmatrix} = \mathbf{A}_0(\theta_0)^{-1} \begin{bmatrix} \beta_0 \\ \beta_0' \end{bmatrix}$$

We see from the matrix $\mathbf{A}$ that the system is orthonormal and that the inverse matrix is the transpose of it. Nevertheless we will find the inverse by utilizing cofactors to confirm this statement. The determinant of $\mathbf{A}$ is $\det \mathbf{A} = -\sin^2 - \cos^2 = -1$ and with the cofactors we get

$$\mathbf{A}(\theta)^{-1} = \frac{1}{-1} \begin{bmatrix} -\sin(\theta) & -\cos(\theta) \\ -\cos(\theta) & \sin(\theta) \end{bmatrix} = \begin{bmatrix} \sin(\theta) & \cos(\theta) \\ \cos(\theta) & -\sin(\theta) \end{bmatrix}$$

The solution in the θ domain becomes

$$\begin{bmatrix} \beta \\ \beta' \end{bmatrix} = \mathbf{A}(\theta)\mathbf{A}_0(\theta_0)^{-1} \begin{bmatrix} \beta_0 \\ \beta_0' \end{bmatrix} = \mathbf{B}(\theta, \theta_0) \begin{bmatrix} \beta_0 \\ \beta_0' \end{bmatrix} \tag{4.40}$$

where $\mathbf{B}(\theta, \theta_0)$ can easily be expressed as

$$\mathbf{B}(\theta, \theta_0) = \begin{bmatrix} \cos(\theta - \theta_0) & \sin(\theta - \theta_0) \\ -\sin(\theta - \theta_0) & \cos(\theta - \theta_0) \end{bmatrix}$$

We will now find the general matrix formulated transformation between the θ domain and the time domain, which we will need heavily in the future for all utilization of this work. We will derive it for the y out of plane component, but it is general and applicable to the other two components x and z. From Equation (4.23) we have that

$$\dot{y} = \omega y'$$

$$y' = \omega^{-1}\dot{y}$$

and from Equation (4.22) we find

$$\omega^{-1} = k^{-2}\varrho^{-2}$$

From the transformation in Equation (4.30) we find the derivative of β to

$$\beta = \varrho y$$

$$\beta' = \varrho' y + \varrho y'$$

and by inserting y' and ω^{-1} one obtains

$$\beta' = -\varepsilon \sin y + \frac{1}{k^2 \varrho}\dot{y}$$

By writing this in matrix form we obtain the relation from the time domain to the θ domain

$$\begin{bmatrix} \beta(\theta) \\ \beta'(\theta) \end{bmatrix} = \begin{bmatrix} \varrho(\theta) & 0 \\ -\varepsilon \sin(\theta) & \frac{1}{k^2 \varrho(\theta)} \end{bmatrix} \begin{bmatrix} y(t) \\ \dot{y}(t) \end{bmatrix} = \mathbf{\Lambda}(\theta) \begin{bmatrix} y(t) \\ \dot{y}(t) \end{bmatrix} \tag{4.41}$$

The reverse relationship is also needed and it becomes

$$\begin{bmatrix} y(t) \\ \dot{y}(t) \end{bmatrix} = \begin{bmatrix} \varrho(\theta) & 0 \\ -\varepsilon \sin(\theta) & \frac{1}{k^2 \varrho(\theta)} \end{bmatrix}^{-1} \begin{bmatrix} \beta(\theta) \\ \beta'(\theta) \end{bmatrix}$$

We find the determinant of $\mathbf{\Lambda}$ to be

$$\det \mathbf{\Lambda} = \frac{1}{k^2}$$

and from finding the cofactors and dividing by the determinant we obtain

$$\begin{bmatrix} y(t) \\ \dot{y}(t) \end{bmatrix} = \begin{bmatrix} \frac{1}{\varrho(\theta)} & 0 \\ \varepsilon k^2 \sin(\theta) & k^2 \varrho(\theta) \end{bmatrix} \begin{bmatrix} \beta(\theta) \\ \beta'(\theta) \end{bmatrix} = \mathbf{\Lambda}^{-1}(\theta) \begin{bmatrix} \beta(\theta) \\ \beta'(\theta) \end{bmatrix} \tag{4.42}$$

Equations (4.40), (4.41) and (4.42) constitute the complete solution to the out of plane motion with the two way transformation between the time and the θ domain. The true anomaly θ is obviously needed, but it is found routinely for elliptic orbits, and as such not considered part of this solution.

4.2.2 General Solution for the In Plane Motion

We will now seek the solution for the coupled in plane motion, which is significantly more complex than the out of plane solution, which we have just established. From the equation system in Equation (4.38) we recall the two coupled equations for the in plane motion as the first and the third equation. We integrate the first equation of Equation (4.38) once and obtain

$$\alpha' = 2\gamma + k_{\alpha_1} \tag{4.43}$$

By inserting Equation (4.43) into the third equation of Equation (4.38) it yields

$$\gamma'' = \frac{3}{\varrho}\gamma - 2(2\gamma + k_{\alpha_1})$$

and by rearranging in terms of coefficients of γ, we obtain

$$\gamma'' + \left(4 - \frac{3}{\varrho}\right)\gamma = -2k_{\alpha_1} \tag{4.44}$$

As we will see soon, Equation (4.44) is central to the finding of the complete solution. Equation (4.44) has non constant coefficients and cannot be solved by elementary methods directly (Bronstein 1999). It has no singular points with ϱ as defined in Equation (4.20), which makes it analytical in the domain of the argument. The complete solution of Equation (4.44) consists of the homogeneous and the particular solution, as $\gamma = \gamma_h + \gamma_p$ respectively. First we will look at the homogeneous solution of Equation (4.44).

$$\gamma_h = k_{\gamma_1}\varphi_1 + k_{\gamma_2}\varphi_2$$

where k_{γ_1} and k_{γ_2} are the constants of integration, which we will consider later in this section. One solution could be of the following form

$$\varphi_1(\theta) = \varrho(\theta)\sin(\theta) \tag{4.45}$$

That Equation (4.45) is a solution can be verified by differentiating Equation (4.45) twice to find φ_1'' and substitute back into Equation (4.44) for the homogeneous part. It turns out to fulfill the equation and it is a solution.

For the second solution φ_2 there has been proposed several solutions in the past. One solution proposed by (Lawden 1954) is the following using an integral $I(\theta)$

$$\varphi_2(\theta) = \varphi_1(\theta)I(\theta) = \varphi_1(\theta)\int_{\theta_0}^{\theta} \frac{1}{\sin^2(\tau)\varrho^2(\tau)}d\tau$$

but this solution is singular for $\theta = \pm\pi$. The integral $I(\theta)$ appears consistently in his work since then (Lawden 1993).

This singularity problem was removed by (Carter 1990), who proposed a new formulation of the integral of the form

$$I(\theta) = \int_{\theta_0}^{\theta} \frac{\cos(\tau)}{\varrho^3(\tau)}d\tau$$

$$\varphi_2(\theta) = 2\varepsilon\varphi_1(\theta)I(\theta) - \frac{\cos(\theta)}{\varrho(\theta)}$$

but it has the restriction that the resulting transition matrix is not valid for $\varepsilon = 0$, hence not usable for circular orbits. To improve this constraint in terms of generality, (Carter 1998) proposed yet another integral of the form

$$I(\theta) = \frac{\sin(\theta)}{\varrho^3(\theta)} - 3\varepsilon\int_{\theta_0}^{\theta} \frac{\sin^2(\tau)}{\varrho^4(\tau)}d\tau$$

but the solution becomes rather complex, and it distances itself from more practical applications and use.

We will now propose a simpler integral and look for a solution along the same lines as referenced above. The motivation is to get rid of the high power terms of the integral in the denominator of the past solutions and combine it with the relations of elliptical orbits.

Lemma 4.1
Let an integral function be defined as follows

$$J(\theta) \triangleq \int_{\theta_0}^{\theta} \frac{d\tau}{\varrho^2(\tau)} \tag{4.46}$$

which can be reformulated as and shown in the proof Equations (4.48) to (4.51)

$$J(\theta) = k^2(t - t_0)$$

Then the solution to the differential Equation (4.44) can be formulated as

$$\gamma(\theta) = k_{\gamma_1}\varrho(\theta)\sin(\theta) + k_{\gamma_2}(3\varepsilon^2\varrho(\theta)\sin(\theta)J(\theta) + \varrho(\theta)\cos(\theta) - 2\varepsilon) - \frac{k_{\alpha_1}}{\varepsilon}\varrho(\theta)\cos(\theta) \tag{4.47}$$

where k_{γ_1}, k_{γ_2} and k_{α_1} are integration constants.

Proof: Before proceeding with a solution $\varphi_2(\theta)$, we will try to find a solution of the new integral in Equation (4.46). From the intermediate calculations Equations (4.20) to (4.22) and using Equation (4.13) we obtain

$$r = \frac{p}{\varrho} \ \wedge \ r^2 = \frac{h}{\omega}$$

$$\left(\frac{p}{\varrho}\right)^2 \omega = h \tag{4.48}$$

where h is a constant. We can now express Equation (4.46) in a simpler manner by combining it with Equation (4.48), integrating and recalling that $\frac{d\theta}{dt} = \omega$.

$$h = \left(\frac{p}{\varrho}\right)^2 \omega = \left(\frac{p}{\varrho}\right)^2 \frac{d\theta}{dt}$$

$$hdt = \frac{p^2}{\varrho^2}d\theta$$

and by definite integration

$$h\int_{t_0}^{t} dt = p^2 \int_{\theta_0}^{\theta} \frac{d\tau}{\varrho^2(\tau)}$$

$$J(\theta) = \frac{h}{p^2}(t - t_0) \tag{4.49}$$

From Equation (4.14) and the general properties of conic sections, see also Equation (A.12) or (Symon 1979), we obtain

$$p = \frac{h^2}{\mu} \ \wedge \ k = \mu h^{-\frac{3}{2}}$$

$$p^2 = \frac{h^4}{k^2h^3} = hk^{-2} \tag{4.50}$$

Inserting Equation (4.50) into Equation (4.49) we obtain

$$\boxed{J(\theta) = k^2(t - t_0)} \tag{4.51}$$

The expression in Equation (4.51) is indeed a very simple expression only based upon the transfer time in the orbit and has no complex integrals to solve as seen in earlier solutions.

As Equation (4.44) looks a bit alike the harmonic oscillator, we propose a solution in the direction of

$$\varphi_2(\theta) = k_1 \varrho(\theta)\sin(\theta)J(\theta) + k_2\varrho(\theta)\cos(\theta) + k_3 \tag{4.52}$$

We must now differentiate Equation (4.52) and insert it into Equation (4.44) to try finding the constants (those in Equation (4.52) are not the normal arbitrary constants).

We will now rewrite Equation (4.52) in preparation of finding a solution, and we divide it through by k_3, which just gives a scaled solution, but only 2 constants to find. We will still call the function φ_2 and keep the constants for convenience and clarity. Let us define the following 2 functions

$$\phi(\theta) \triangleq \varrho(\theta)\sin(\theta)$$

$$\lambda(\theta) \triangleq \varrho(\theta)\cos(\theta)$$

By rewriting Equation (4.52) and leaving out the θ argument we get

$$\varphi_2 = k_1\phi J + k_2\lambda + 1 \tag{4.53}$$

$$\varphi_2' = k_1(\phi' J + \phi J') + k_2\lambda' \tag{4.54}$$

$$\varphi_2'' = k_1(\phi'' J + 2\phi' J' + \phi J'') + k_2\lambda'' \tag{4.55}$$

We now insert Equations (4.53) and (4.55) into the original Equation (4.44) for the homogeneous part and obtain

$$\varphi_2'' + (4 - \frac{3}{\varrho})\varphi_2 = 0$$

$$k_1(\phi'' J + 2\phi' J' + \phi J'') + k_2\lambda'' + (4 - \frac{3}{\varrho})(k_1\phi J + k_2\lambda + 1) = 0$$

and after some manipulations

$$k_1(\underbrace{(\phi'' + (4 - \frac{3}{\varrho})\phi)}_{=0}J + 2\phi' J' + \phi J'') + k_2(\underbrace{\lambda'' + (4 - \frac{3}{\varrho})\lambda)}_{=2\varepsilon} + (4 - \frac{3}{\varrho}) = 0 \tag{4.56}$$

We know that in Equation (4.56) $\phi = \varphi_1$ from Equation (4.45) and that it is a solution and the first under braced equation equals zero. λ is not a solution to Equation (4.44) , but we can find what it gives by backward substitution. We will find λ'' and insert into the form of the homogeneous part of Equation (4.44) to find the value of the second under brace in Equation (4.56), which is detailed in Equation (A.28).

$$\lambda'' = \varrho''\cos - \varrho'\sin - \varrho'\sin - \varrho\cos$$

and by inserting as defined in Equation (4.31) we get as follows, writing the θ argument only when double angle

$$\lambda'' = -2\varepsilon\cos(2\theta) - \cos$$

By back substituting we obtain

$$\begin{aligned}\lambda'' + (4 - \tfrac{3}{\varrho})\lambda &= -2\varepsilon\cos(2\theta) - \cos + 4\varrho\cos - 3\cos \\ &= 2\varepsilon\end{aligned}$$

Equation (4.56) is now simplified significantly and becomes

$$k_1(2\phi' J' + \phi J'') + k_2 2\varepsilon + (4 - \frac{3}{\varrho}) = 0 \tag{4.57}$$

The next stage is to replace the integral term J' and J'' in Equation (4.57). Differentiating Equation (4.46) we obtain

$$J' = \varrho^{-2}$$

$$J'' = -2\varrho^{-3}\varrho'$$

and

$$\phi' = \varrho'\sin + \varrho\cos$$

Inserting into Equation (4.57) using also Equation (4.31) we get

$$k_1(2(\varrho\cos - \varepsilon\sin^2)\varrho^{-2} + 2\varrho\sin^2\varrho^{-3}\varepsilon) + k_2 2\varepsilon + 4 - \frac{3}{\varrho} = 0$$

and after rearranging we obtain, with details in Equation (A.29)

$$(2k_1 + 4\varepsilon + 2k_2\varepsilon^2)\cos + 2\varepsilon k_2 + 1 = 0 \tag{4.58}$$

To make the left side of Equation (4.58) equal zero, the two constant terms must both be zero, which leads to the following for k_1 and k_2.

$$k_2 = -\frac{1}{2\varepsilon}$$

and

$$k_1 = -\frac{3}{2}\varepsilon$$

Finally we can write Equation (4.52) as

$$\varphi_2 = -\frac{3}{2}\varepsilon\varrho\sin J - \frac{1}{2\varepsilon}\varrho\cos + 1$$

By multiplying through with -2ε and inserting the argument θ we get for the second solution

$$\varphi_2(\theta) = 3\varepsilon^2\varrho(\theta)\sin(\theta)J(\theta) + \varrho(\theta)\cos(\theta) - 2\varepsilon \tag{4.59}$$

We will now have to check that φ_1 and φ_2 are linearly independent. We will find the Wronskian of the solutions φ_1 and φ_2 (Rabenstein 1975). If the Wronskian is different from zero at just one point in the space, the solutions are linearly independent. The Wronskian is defined as the determinant of

$$W = \begin{vmatrix} \varphi_1 & \varphi_2 \\ \varphi_1' & \varphi_2' \end{vmatrix}$$

From Equation (4.45) one gets

$$\varphi_1' = \varepsilon(\cos^2 - \sin^2) + \cos$$

From Equation (4.59) one gets

$$\varphi_2' = 3\varepsilon^2(\varrho' \sin J + \varrho \cos J + \varrho \sin J') + \varrho' \cos - \varrho \sin$$

The Wronskian now becomes after inserting φ_1' and φ_2' and reducing all the trigonometric terms, see also Section A.3.3

$$\begin{aligned} W &= \varphi_1\varphi_2' - \varphi_1'\varphi_2 \\ &= \varepsilon^2 - 1 \end{aligned} \tag{4.60}$$

For elliptic orbits $\varepsilon \in [0; 1[$ and W in Equation (4.60) is always different from zero and φ_1 and φ_2 are linearly independent.

The particular solution will be found by using the method of *variation of parameters* (Kreyszig 1979), which only require that the homogeneous solution is known. We attempt to find the solution of

$$a_0(x)y^{(n)} + a_1(x)y^{(n-1)} + \cdots + a_{n-1}(x)y^{(1)} + a_n(x)y = F(x)$$

which is of the form

$$y_p(x) = C_1(x)u_1(x) + C_2(x)u_2(x) + \cdots + C_n(x)u_n(x) \tag{4.61}$$

where $u_1 \cdots u_n$ are the linear independent solutions to the homogeneous equation and the coefficients need to be determined. For a second order system the conditions to fulfill are (Rabenstein 1975)

$$\begin{aligned} C_1'u_1 + C_2'u_2 &= 0 \\ C_1'u_1' + C_2'u_2' &= \frac{F(x)}{a_0(x)} \end{aligned}$$

which we recognize as the Wronskian

$$\begin{bmatrix} u_1 & u_2 \\ u_1' & u_2' \end{bmatrix} \begin{bmatrix} C_1' \\ C_2' \end{bmatrix} = \begin{bmatrix} 0 \\ \frac{F(x)}{a_0(x)} \end{bmatrix}$$

We solve for the constants and then find the particular solution by integration. The $C_{1,2}$ shall not be confused with the $c_{1,2}$ in Section 4.2.1. For the actual system we get

$$\begin{bmatrix} \varphi_1 & \varphi_2 \\ \varphi_1' & \varphi_2' \end{bmatrix} \begin{bmatrix} C_1' \\ C_2' \end{bmatrix} = \begin{bmatrix} 0 \\ -2k_{\alpha_1} \end{bmatrix}$$

From using Cramers rule (Ogata 1970) we obtain

$$C_1' = \frac{\begin{vmatrix} 0 & \varphi_2 \\ -2k_{\alpha_1} & \varphi_2' \end{vmatrix}}{W}$$

$$C_2' = \frac{\begin{vmatrix} \varphi_1 & 0 \\ \varphi_1' & -2k_{\alpha_1} \end{vmatrix}}{W}$$

where W is the Wronskian and $W = \varepsilon^2 - 1$.

$$C_1' = \frac{2k_{\alpha_1}}{\varepsilon^2 - 1}\varphi_2 \tag{4.62}$$

$$C_2' = -\frac{2k_{\alpha_1}}{\varepsilon^2 - 1}\varphi_1 \tag{4.63}$$

and according to Equation (4.61), we can now formulate the particular solution

$$\varphi_p = \varphi_1 \int C_1' + \varphi_2 \int C_2' \tag{4.64}$$

By inserting Equations (4.62) and (4.63) into Equation (4.64), we obtain

$$\varphi_p = \frac{2k_{\alpha_1}}{\varepsilon^2 - 1}\left(\varphi_1 \int \varphi_2(\tau)d\tau - \varphi_2 \int \varphi_1(\tau)d\tau\right) \tag{4.65}$$

We will now find the two integrals in Equation (4.65). From Equation (4.45) we have

$$\varphi_1 = \varrho \sin = -\frac{1}{\varepsilon}\varrho\varrho'$$

and by inserting

$$\int \varphi_1(\theta)d\theta = \int -\frac{1}{\varepsilon}\varrho(\theta)\varrho'(\theta)d\theta = -\frac{1}{2\varepsilon}\varrho^2(\theta) \tag{4.66}$$

We will now find the integral of φ_2 and will integrate Equation (4.59) by using partial integration . We will take the first term separately. All the intermediate calculations are to be found in Section A.3.4.

$$\int 3\varepsilon^2\varrho(\theta)\sin(\theta)J(\theta)d\theta = 3\varepsilon^2 \int \varrho(\theta)\sin(\theta)J(\theta)d\theta = -3\varepsilon \int \varrho(\theta)\varrho'(\theta)J(\theta)d\theta \tag{4.67}$$

We will now substitute $g = \frac{1}{2}\varrho^2$ and $g' = \varrho\varrho'$ and rewrite Equation (4.67) as follows leaving out the θ argument, see details in Equation (A.31)

$$\begin{aligned} -3\varepsilon \int Jg'd\theta &= -3\varepsilon \left[Jg - \int J'g \right] \\ &= -\frac{3}{2}\varepsilon\varrho^2 J + \frac{3}{2}\varepsilon\theta \end{aligned} \tag{4.68}$$

The last terms of Equation (4.59) give with details in Equation (A.32)

$$\begin{aligned} \int (\varrho\cos -2\varepsilon)d\theta &= \int ((1+\varepsilon\cos)\cos -2\varepsilon)\, d\theta \\ &= \sin -\frac{3}{2}\varepsilon\theta + \frac{1}{2}\varepsilon\sin\cos \end{aligned} \tag{4.69}$$

We now add Equations (4.68) and (4.69) to get the integral yielding, see also Equation (A.33)

$$\begin{aligned} \int \varphi_2 d\theta &= -\frac{3}{2}\varepsilon\varrho^2 J + \frac{3}{2}\varepsilon\theta + \sin -\frac{3}{2}\varepsilon\theta + \frac{1}{2}\varepsilon\sin\cos \\ &= -\frac{3}{2}\varepsilon\varrho^2 J + \frac{1}{2}(1+\varrho)\sin \end{aligned} \tag{4.70}$$

To find the particular solution φ_p we insert Equations (4.45), (4.59), (4.66) and (4.70) into Equation (4.65) and obtain as follows, which is detailed in Equation (A.34)

$$\begin{aligned} \varphi_p &= \frac{2k_{\alpha_1}}{\varepsilon^2 - 1}\left[\varrho\sin\left(-\frac{3}{2}\varepsilon\varrho^2 J + \frac{1}{2}(1+\varrho)\sin\right)\right] \\ &\quad -\frac{2k_{\alpha_1}}{\varepsilon^2 - 1}\left[(3\varepsilon^2\varrho\sin J + \varrho\cos -2\varepsilon)\left(-\frac{1}{2\varepsilon}\varrho^2\right)\right] \\ &= -\frac{k_{\alpha_1}}{\varepsilon}\varrho\cos \end{aligned} \tag{4.71}$$

The complete solution of Equation (4.44) now becomes by adding Equations (4.45), (4.59) and (4.71) giving

$$\gamma(\theta) = k_{\gamma_1}\varphi_1(\theta) + k_{\gamma_2}\varphi_2(\theta) + \varphi_p(\theta) \tag{4.72}$$

where k_{γ_1} and k_{γ_2} are the integration constants.

$$\begin{aligned} &\gamma(\theta) = \\ &k_{\gamma_1}\varrho(\theta)\sin(\theta) + k_{\gamma_2}(3\varepsilon^2\varrho(\theta)\sin(\theta)J(\theta) + \varrho(\theta)\cos(\theta) - 2\varepsilon) - \frac{k_{\alpha_1}}{\varepsilon}\varrho(\theta)\cos(\theta) \end{aligned} \tag{4.73}$$

This completes the proof of Lemma 4.1, which is a key element in finding the overall solution. ■

We will now rearrange Equation (4.73) as follows for a convenient matrix notation later

$$\gamma(\theta) = k_{\gamma_1}\varrho(\theta)\sin(\theta) + \left(k_{\gamma_2} - \frac{k_{\alpha_1}}{\varepsilon}\right)\varrho(\theta)\cos(\theta) - k_{\gamma_2}\varepsilon(2 - 3\varepsilon\varrho(\theta)\sin(\theta)J(\theta)) \tag{4.74}$$

We note that k_{α_1} is also an integration constant from Equation (4.43). We will now find the other component $\alpha(\theta)$ from Equation (4.43), which can be done by inserting Equation (4.74) followed by integration.

$$\alpha' = 2\gamma + k_{\alpha_1}$$

$$\alpha' = 2k_{\gamma_1}\varrho\sin + 2\left(k_{\gamma_2} - \frac{k_{\alpha_1}}{\varepsilon}\right)\varrho\cos - 2k_{\gamma_2}\varepsilon(2 - 3\varepsilon\varrho\sin J) + k_{\alpha_1}$$

We now expand the last parenthesis and aim to get eliminated the single term k_{α_1}, yielding after some manipulations in Equation (A.35)

$$\alpha' = 2k_{\gamma_1}\varrho\sin + \left(k_{\gamma_2} - \frac{k_{\alpha_1}}{\varepsilon}\right)(2\varrho\cos - \varepsilon) - 3k_{\gamma_2}\varepsilon(1 - 2\varepsilon\varrho\sin J) \tag{4.75}$$

We can now integrate the terms of Equation (4.75) term by term as follows by leaving out the constants, where the details are in Section A.3.5

$$\begin{aligned}\int \varrho\sin d\theta &= \int (1+\varepsilon\cos)\sin d\theta \\ &= -\frac{1}{2}(\varrho+1)\cos \end{aligned} \tag{4.76}$$

and

$$\begin{aligned}\int (2\varrho\cos - \varepsilon)d\theta &= \int (2(1+\varepsilon\cos)\cos - \varepsilon)d\theta \\ &= (\varrho+1)\sin \end{aligned} \tag{4.77}$$

and finally using the substitutions between Equation (4.67) and Equation (4.68)

$$\begin{aligned}\int (1 - 2\varepsilon\varrho\sin J)d\theta &= \int d\theta - 2\int \varepsilon\varrho\sin J d\theta \\ &= \theta + 2\int \varrho\varrho' J d\theta \\ &= \varrho^2 J \end{aligned} \tag{4.78}$$

We will now back substitute Equations (4.76), (4.77) and (4.78) into Equation (4.75) to obtain the integrated solution.

$$\begin{aligned}&\alpha(\theta) = \\ &- k_{\gamma_1}\cos(\theta)(\varrho(\theta)+1) + \left(k_{\gamma_2} - \frac{k_{\alpha_1}}{\varepsilon}\right)\sin(\theta)(\varrho(\theta)+1) - 3k_{\gamma_2}\varepsilon\varrho^2(\theta)J(\theta) + k_{\alpha_2}\end{aligned} \tag{4.79}$$

We will redefine the constants for the sake of simplicity and insert into Equations (4.74) and (4.79) for $\gamma(\theta)$ and $\alpha(\theta)$ respectively. Defining coefficients as follows

$$\begin{aligned} k_1 &= k_{\alpha_2} \\ k_2 &= k_{\gamma_1} \\ k_3 &= k_{\gamma_2} - \frac{1}{\varepsilon} k_{\alpha_1} \\ k_4 &= -k_{\gamma_2}\varepsilon \end{aligned} \tag{4.80}$$

and insertion gives

$$\alpha(\theta) = k_1 - k_2\cos(\theta)(\varrho(\theta)+1) + k_3\sin(\theta)(\varrho(\theta)+1) + 3k_4\varrho^2(\theta)J(\theta) \tag{4.81}$$

$$\gamma(\theta) = k_2\varrho(\theta)\sin(\theta) + k_3\varrho(\theta)\cos(\theta) + k_4(2 - 3\varepsilon\varrho(\theta)\sin(\theta)J(\theta)) \tag{4.82}$$

The velocities of Equations (4.81) and (4.82) can be obtained by differentiating or by using the original differential equations. For $\alpha(\theta)$ we get directly from Equation (4.75)

$$\alpha'(\theta) = 2k_2\varrho(\theta)\sin(\theta) + k_3(2\varrho(\theta)\cos(\theta) - \varepsilon) + 3k_4(1 - 2\varepsilon\varrho(\theta)\sin(\theta)J(\theta)) \tag{4.83}$$

For $\gamma'(\theta)$ it is easier to differentiate Equation (4.82)

$$\begin{aligned} \gamma'(\theta) &= k_2[\cos(\theta) + \varepsilon\cos(2\theta)] - k_3[\sin(\theta) + \varepsilon\sin(2\theta)] \\ &\quad -3k_4\varepsilon\left[(\cos(\theta) + \varepsilon\cos(2\theta))J(\theta) + \frac{1}{\varrho(\theta)}\sin(\theta)\right] \end{aligned} \tag{4.84}$$

We can now write the in plane Equations (4.81), (4.82), (4.83) and (4.84) in a matrix form to obtain the transition matrix.

$$\begin{bmatrix} \alpha(\theta) \\ \gamma(\theta) \\ \alpha'(\theta) \\ \gamma'(\theta) \end{bmatrix} = \mathbf{\Phi} \begin{bmatrix} k_1 \\ k_2 \\ k_3 \\ k_4 \end{bmatrix} \tag{4.85}$$

and

$$\mathbf{\Phi} = \begin{bmatrix} 1 & -(\varrho(\theta)+1)\cos(\theta) & (\varrho(\theta)+1)\sin(\theta) & 3\varrho^2(\theta)J(\theta) \\ 0 & \varrho(\theta)\sin(\theta) & \varrho(\theta)\cos(\theta) & 2 - 3\varepsilon\varrho(\theta)\sin(\theta)J(\theta) \\ 0 & 2\varrho(\theta)\sin(\theta) & 2\varrho(\theta)\cos(\theta) - \varepsilon & 3(1 - 2\varepsilon\varrho(\theta)\sin(\theta)J(\theta)) \\ 0 & \cos(\theta) + \varepsilon\cos(2\theta) & -(\sin(\theta) + \varepsilon\sin(2\theta)) & -3\varepsilon\left[(\cos(\theta) + \varepsilon\cos(2\theta))J(\theta) + \frac{\sin(\theta)}{\varrho(\theta)}\right] \end{bmatrix}$$

We will now find the transition matrix and eliminate the integration constants, like what was done for the out of plane motion in Equation (4.40).

$$\begin{bmatrix} \alpha_0(\theta) \\ \gamma_0(\theta) \\ \alpha_0'(\theta) \\ \gamma_0'(\theta) \end{bmatrix} = \mathbf{\Phi}_0 \begin{bmatrix} k_1 \\ k_2 \\ k_3 \\ k_4 \end{bmatrix} \Rightarrow \begin{bmatrix} k_1 \\ k_2 \\ k_3 \\ k_4 \end{bmatrix} = \mathbf{\Phi}_0^{-1} \begin{bmatrix} \alpha_0(\theta) \\ \gamma_0(\theta) \\ \alpha_0'(\theta) \\ \gamma_0'(\theta) \end{bmatrix} \tag{4.86}$$

We now have to obtain the inverse matrix of $\mathbf{\Phi}_0$. For the initial conditions , where $t = t_0$ and $\theta = \theta_0$ we obtain from Equation (4.46) or Equation (4.51) that

$$J(\theta_0) = 0 \tag{4.87}$$

which simplifies $\mathbf{\Phi}_0$ slightly

$$\mathbf{\Phi}_0 = \begin{bmatrix} 1 & -(\varrho(\theta_0)+1)\cos(\theta_0) & (\varrho(\theta_0)+1)\sin(\theta_0) & 0 \\ 0 & \varrho(\theta_0)\sin(\theta_0) & \varrho(\theta_0)\cos(\theta_0) & 2 \\ 0 & 2\varrho(\theta_0)\sin(\theta_0) & 2\varrho(\theta_0)\cos(\theta_0)-\varepsilon & 3 \\ 0 & \cos(\theta_0)+\varepsilon\cos(2\theta_0) & -(\sin(\theta_0)+\varepsilon\sin(2\theta_0)) & -3\varepsilon\frac{\sin(\theta_0)}{\varrho(\theta_0)} \end{bmatrix} \tag{4.88}$$

We will find the determinant of Equation (4.88) by using the first row for elimination, see also Section A.3.7

$$\det \mathbf{\Phi}_0 = \varepsilon^2 - 1 \tag{4.89}$$

We observe that the result in Equation (4.89) gives the same result as the Wronskian in Equation (4.60). It is clear that $\mathbf{\Phi}_0^{-1}$ exists for all closed orbits as the determinant never becomes zero. Elliptic orbits open up to parabolic trajectories as $\varepsilon \to 1$.

The inverse matrix of $\mathbf{\Phi}_0$ we will find by utilizing cofactors and the transpose of the adjoint matrix (Ogata 1970). The detailed calculations can be found in Section A.3.8, where $\varrho(\theta_0) = \varrho_0$. The inverse of Equation (4.88) becomes

$$\mathbf{\Phi}_0^{-1} = \frac{1}{1-\varepsilon^2}\begin{bmatrix} 1-\varepsilon^2 & 3\varepsilon\frac{\varrho_0+1}{\varrho_0}\sin(\theta_0) & -(\varrho_0+1)\varepsilon\sin(\theta_0) & 2-\varrho_0\varepsilon\cos(\theta_0) \\ 0 & -3\left(\frac{\varepsilon^2}{\varrho_0}+1\right)\sin(\theta_0) & (\varrho_0+1)\sin(\theta_0) & \varrho_0\cos(\theta_0)-2\varepsilon \\ 0 & -3(\varepsilon+\cos(\theta_0)) & \varepsilon+(\varrho_0+1)\cos(\theta_0) & -\varrho_0\sin(\theta_0) \\ 0 & \varepsilon^2+3\varrho_0-1 & -\varrho_0^2 & \varepsilon\varrho_0\sin(\theta_0) \end{bmatrix} \tag{4.90}$$

4.2.3 Summary of General Solution

This section contains in summary the resulting equations for the in plane and out of plane motions as well as the transformation between the θ and the time domain.

In plane:

$$\begin{bmatrix} \alpha(\theta) \\ \gamma(\theta) \\ \alpha'(\theta) \\ \gamma'(\theta) \end{bmatrix} = \mathbf{\Phi}(\theta)\mathbf{\Phi}_0^{-1}(\theta_0)\begin{bmatrix} \alpha(\theta_0) \\ \gamma(\theta_0) \\ \alpha'(\theta_0) \\ \gamma'(\theta_0) \end{bmatrix} \tag{4.91}$$

where $\mathbf{\Phi}(\theta)$ and $\mathbf{\Phi}_0^{-1}(\theta_0)$ are defined in Equations (4.85) and (4.90) respectively.

Out of plane:

$$\begin{bmatrix} \beta(\theta) \\ \beta'(\theta) \end{bmatrix} = \mathbf{A}(\theta)\mathbf{A}_0^{-1}(\theta_0)\begin{bmatrix} \beta(\theta_0) \\ \beta'(\theta_0) \end{bmatrix} = \mathbf{B}(\theta,\theta_0)\begin{bmatrix} \beta(\theta_0) \\ \beta'(\theta_0) \end{bmatrix} \tag{4.92}$$

where $\mathbf{A}(\theta)$, $\mathbf{A}_0^{-1}(\theta_0)$ and $\mathbf{B}(\theta,\theta_0)$ are defined in Equation (4.40) .

To transform from the time domain to the θ domain and reverse can generally be formulated according to Equation (4.41) and Equation (4.42), here exemplified for the β component.

$$\begin{bmatrix} \beta(\theta) \\ \beta'(\theta) \end{bmatrix} = \mathbf{\Lambda} \begin{bmatrix} y(t) \\ \dot{y}(t) \end{bmatrix} \qquad \begin{bmatrix} y(t) \\ \dot{y}(t) \end{bmatrix} = \mathbf{\Lambda}^{-1} \begin{bmatrix} \beta(\theta) \\ \beta'(\theta) \end{bmatrix} \tag{4.93}$$

and

$$\mathbf{\Lambda} = \begin{bmatrix} \varrho(\theta) & 0 \\ -\varepsilon \sin(\theta) & \frac{1}{k^2 \varrho(\theta)} \end{bmatrix} \qquad \mathbf{\Lambda}^{-1} = \begin{bmatrix} \frac{1}{\varrho(\theta)} & 0 \\ \varepsilon k^2 \sin(\theta) & k^2 \varrho(\theta) \end{bmatrix} \tag{4.94}$$

where we obtain from Equation (4.20) that

$$\varrho(\theta) = 1 + \varepsilon \cos(\theta) \tag{4.95}$$

and from Equation (4.14)

$$k^2 = \frac{\mu^2}{h^3} \qquad h = |\mathbf{r} \times \dot{\mathbf{r}}| \tag{4.96}$$

and from Equation (4.51)

$$J(\theta) = k^2(t - t_0) \tag{4.97}$$

This is all what is needed to calculate the complete relative motion. Larger parts of these results are also published in (Yamanaka & Ankersen 2002) and their correctness and precision independently evaluated by (Melton 2003). To predict the relative motion in an elliptic orbit performs the following steps:

1. From the initial time t_0 to the final time t compute the true anomaly $\theta(t)$, which is well known from solving Kepler's equation. h, μ and ε are known from the target orbit, which is time invariant.

2. Compute Equations (4.96), (4.97), (4.95) and (4.94) which give the domain transformations.

3. Use Equation (4.93) to obtain the initial state vector in the θ domain. Compute the out of plane transition matrices from Equation (4.40). Compute the in plane transition matrices from Equations (4.90) and (4.85) respectively.

4. Compute Equations (4.91) and (4.92) to get the propagated state vector. Then use Equation (4.93) to return to the time domain.

4.3 Circular Orbits Restricted Solution

In the following the special case will be derived, and most commonly used so far, valid for near circular and circular orbits only. This means that the orbital angular rate is constant, $\dot{\omega} = 0$. Inserting into Equation (4.15) one obtains:

$$\begin{aligned} \ddot{x} - \omega^2 x - 2\omega\dot{z} + k\omega^{\frac{3}{2}} x &= \frac{1}{m_c} F_x \\ \ddot{y} + k\omega^{\frac{3}{2}} y &= \frac{1}{m_c} F_y \\ \ddot{z} - \omega^2 z + 2\omega\dot{x} - 2k\omega^{\frac{3}{2}} z &= \frac{1}{m_c} F_z \end{aligned} \tag{4.98}$$

By combining the following two expressions (Renner 1983) one can find an expression for k, where T is the orbital time.

$$T = 2\pi\sqrt{\frac{r^3}{\mu}} \quad \wedge \quad T = \frac{2\pi}{\omega} \Rightarrow \omega = \sqrt{\frac{\mu}{r^3}}$$

and inserting into Equation (4.14)

$$k = \sqrt{\omega}$$

which gives

$$\begin{aligned} \ddot{x} - 2\omega\dot{z} &= \frac{1}{m_c} F_x \\ \ddot{y} + \omega^2 y &= \frac{1}{m_c} F_y \\ \ddot{z} - 3\omega^2 z + 2\omega\dot{x} &= \frac{1}{m_c} F_z \end{aligned} \tag{4.99}$$

The formulation in Equation (4.99) was found by (Hill 1878) and the solution to the system was obtained by Clohessy and Wiltshire (Clohessy & Wiltshire 1960), but are commonly referred to as the Clohessy Wiltshire equations. An alternative method of derivation is documented in (Ankersen 1990*b*). From Equation (4.51) we find the integral function J to become by inserting k

$$J = k^2(t - t_0) = \omega(t - t_0)$$

In plane: From Equation (4.91) we find the in plane transition matrix.

$$\mathbf{\Phi} = \begin{bmatrix} 1 & -2\cos(\theta) & 2\sin(\theta) & 3\omega(t - t_0) \\ 0 & \sin(\theta) & \cos(\theta) & 2 \\ 0 & 2\sin(\theta) & 2\cos(\theta) & 3 \\ 0 & \cos(\theta) & -\sin(\theta) & 0 \end{bmatrix} \tag{4.100}$$

We now find the inverse matrix of Equation (4.100) and insert the initial conditions

$$\mathbf{\Phi}_0^{-1} = \begin{bmatrix} 1 & 0 & 0 & 2 \\ 0 & -3\sin(\theta_0) & 2\sin(\theta_0) & \cos(\theta_0) \\ 0 & -3\cos(\theta_0) & 2\cos(\theta_0) & -\sin(\theta_0) \\ 0 & 2 & -1 & 0 \end{bmatrix} \tag{4.101}$$

By multiplying Equations (4.100) and (4.101) we obtain

$$\mathbf{\Phi}\mathbf{\Phi}_0^{-1} = \begin{bmatrix} 1 & 6(\omega(t-t_0) - \sin(\theta-\theta_0)) & 4\sin(\theta-\theta_0) - 3\omega(t-t_0) & 2(1-\cos(\theta-\theta_0)) \\ 0 & 4 - 3\cos(\theta-\theta_0) & 2(\cos(\theta-\theta_0) - 1) & \sin(\theta-\theta_0) \\ 0 & 6(1-\cos(\theta-\theta_0)) & 4\cos(\theta-\theta_0) - 3 & 2\sin(\theta-\theta_0) \\ 0 & 3\sin(\theta-\theta_0) & -2\sin(\theta-\theta_0) & \cos(\theta-\theta_0) \end{bmatrix} \tag{4.102}$$

We recall that Equation (4.102) is in the θ domain. We will formulate it directly in the time domain by inserting the transformations from Equations (4.93) and (4.94).

$$\mathbf{\Lambda}_{circular} = \begin{bmatrix} 1 & 0 \\ 0 & \omega^{-1} \end{bmatrix} \qquad \mathbf{\Lambda}_{circular}^{-1} = \begin{bmatrix} 1 & 0 \\ 0 & \omega \end{bmatrix} \tag{4.103}$$

We pre- and post-multiply Equation (4.102) with Equation (4.103) for both in plane axes and obtain

$$\mathbf{\Phi}_{CW}(t,\theta) = \begin{bmatrix} 1 & 0 & 0 & 0 \\ 0 & 1 & 0 & 0 \\ 0 & 0 & \omega & 0 \\ 0 & 0 & 0 & \omega \end{bmatrix} \mathbf{\Phi}\mathbf{\Phi}_0^{-1} \begin{bmatrix} 1 & 0 & 0 & 0 \\ 0 & 1 & 0 & 0 \\ 0 & 0 & \omega^{-1} & 0 \\ 0 & 0 & 0 & \omega^{-1} \end{bmatrix}$$

We now introduce the following relative changes

$$\tau = t - t_0 \qquad\qquad \theta - \theta_0 = \omega\tau \tag{4.104}$$

and inserting into Equation (4.102) gives

$$\mathbf{\Phi}_{CW}(\tau) = \begin{bmatrix} 1 & 6(\omega\tau - \sin(\omega\tau)) & \frac{4}{\omega}\sin(\omega\tau) - 3\tau & \frac{2}{\omega}(1-\cos(\omega\tau)) \\ 0 & 4 - 3\cos(\omega\tau) & \frac{2}{\omega}(\cos(\omega\tau) - 1) & \frac{1}{\omega}\sin(\omega\tau) \\ 0 & 6\omega(1-\cos(\omega\tau)) & 4\cos(\omega\tau) - 3 & 2\sin(\omega\tau) \\ 0 & 3\omega\sin(\omega\tau) & -2\sin(\omega\tau) & \cos(\omega\tau) \end{bmatrix} \tag{4.105}$$

Equation (4.105) is the Clohessy Wiltshire solution to Hill's equation for the in plane and can be written directly as in Equation (4.106) using the initial values to obtain the final state.

$$\begin{bmatrix} x(\tau) \\ z(\tau) \\ \dot{x}(\tau) \\ \dot{z}(\tau) \end{bmatrix} = \mathbf{\Phi}_{CW}(\tau) \begin{bmatrix} x(0) \\ z(0) \\ \dot{x}(0) \\ \dot{z}(0) \end{bmatrix} \tag{4.106}$$

Out of plane: We will now perform the similar reduction for the out of plane motion, where we get from Equation (4.40)

$$\mathbf{A}\mathbf{A}_0^{-1} = \begin{bmatrix} \cos(\theta-\theta_0) & \sin(\theta-\theta_0) \\ -\sin(\theta-\theta_0) & \cos(\theta-\theta_0) \end{bmatrix} \tag{4.107}$$

We will pre- and post-multiply Equation (4.107) with Equation (4.94) to obtain

$$\mathbf{A}_{CW}(\tau) = \begin{bmatrix} 1 & 0 \\ 0 & \omega \end{bmatrix} \mathbf{A}\mathbf{A}_0^{-1} \begin{bmatrix} 1 & 0 \\ 0 & \omega^{-1} \end{bmatrix} \tag{4.108}$$

and inserting Equation (4.104) we finally get

$$\mathbf{A}_{CW}(\tau) = \begin{bmatrix} \cos(\omega\tau) & \frac{1}{\omega}\sin(\omega\tau) \\ -\omega\sin(\omega\tau) & \cos(\omega\tau) \end{bmatrix} \tag{4.109}$$

The solution of the Clohessy Wiltshire equation for the out of plane can now be written as in Equation (4.110) using the initial values to obtain the final state.

$$\begin{bmatrix} y(\tau) \\ \dot{y}(\tau) \end{bmatrix} = \mathbf{A}_{CW}(\tau) \begin{bmatrix} y(0) \\ \dot{y}(0) \end{bmatrix} \tag{4.110}$$

The development and formulation presented here, is coauthored and published in detail in the only dedicated book on RVD (Fehse 2003).

4.4 Verification of General Solution

The general solution summarized in Section 4.2.3 will now be verified together with the Clohessy Wiltshire equations and a numerical integration of the nonlinear Keplerian equations.

The verification methodology is based upon a comparison with a numerical obtained result (Roy 1976), which is considered as the *reference model*. The reference results are based on the solution of Kepler's equations in a spherical gravitational field. A target reference orbit is found providing the positions, velocities and the true anomaly. The initial relative position and velocity between chaser and target, specified in the LVLH rotating frame, is transformed into inertial coordinates and added to the target vectors to obtain the chaser inertial initial position and velocity, see also Equation (4.5).

From the initial chaser position and velocity, all the orbital parameters are identified. Then the chaser orbit is propagated during the same time span as the target orbit. The relative motion is then found again according to Equation (4.5), after which the relative position and velocity is transformed into the target rotating frame $\mathcal{F}_o$.

The accuracy of the reference positions are better than 10^{-7} m comparing repetitive orbits. This is considered sufficiently stable orbital propagation and the accuracy is actually better than what is needed in this context.

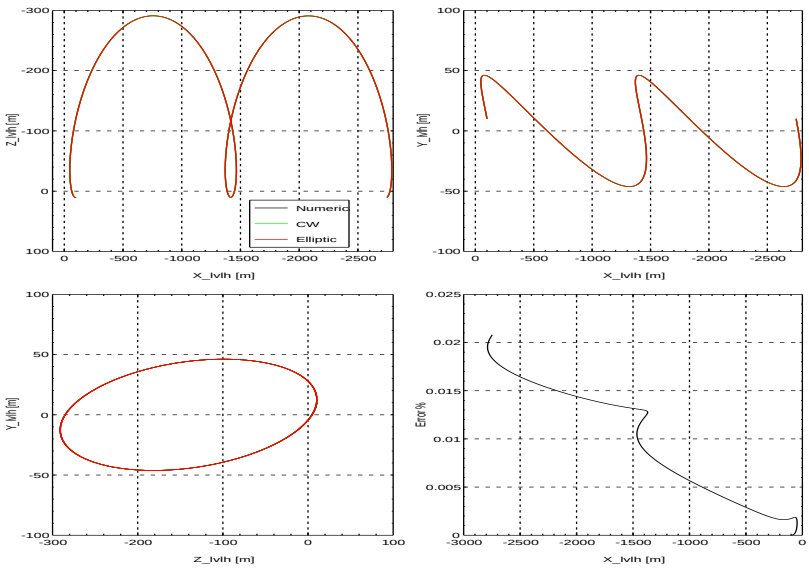

Figure 4.2: *Circular orbit, $\varepsilon = 0$. The relative motion of the numerical solution, the Clohessy Wiltshire equations and the elliptic solution. The first 3 plots show the relation positions in the 3 planes of the target LVLH frame. The 4th plot shows the position error in percentage of the x-axis distance. The legend is valid for the 3 first plots. Note that the 3 curves are on top of each other.*

The relative position and velocity from the Clohessy Wiltshire equations are computed from Equations (4.106) and (4.110). The output of the Clohessy Wiltshire equations are directly available in the target rotating frame $\mathcal{F}_o$ and can be compared to the numerically obtained results.

The relative position and velocity from the general solution equations are computed from Equations (4.91) and (4.92). The output is also directly available in the target rotating frame $\mathcal{F}_o$, but in the θ domain. It is therefore required to perform the transformations to and from this domain using the known true anomaly values from the knowledge of the target orbit propagation.

The error between the numerical result $\mathbf{s}_{num}$ and the CW solution and the general solution, respectively $\mathbf{s}_{cw}$ and $\mathbf{s}_{gen}$, is computed directly as the difference of the vectors after which the modulus is taken. This gives the error in size, but without any direction. This absolute error is not directly interesting, as the acceptable errors relate to the distance between the two spacecraft. For that reason we will compute the error relative to the true curvilinear result in the direction of the x-axis in the LVLH frame. The expression for this is in Equation (4.111).

$$\mathbf{s}_{error} = \frac{|\mathbf{s}_{num} - \mathbf{s}_{cw}|}{|s_{num_x}|} 100 \tag{4.111}$$

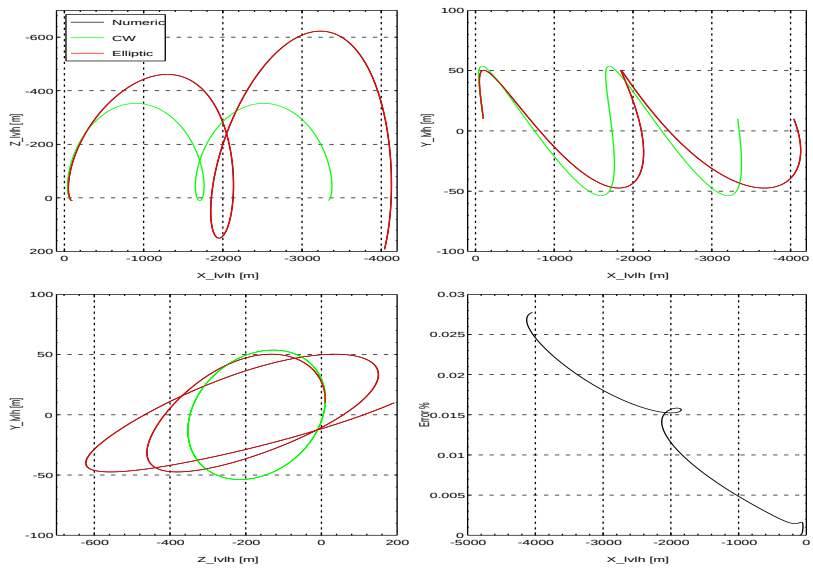

Figure 4.3: *Eccentric orbit, $\varepsilon = 0.1$. The relative motion of the numerical solution, the Clohessy Wiltshire equations and the elliptic solution. The first 3 plots show the relation positions in the 3 planes of the target LVLH frame. The 4th plot shows the position error in percentage of the x-axis distance. The legend is valid for the 3 first plots. Note that the red curve is on top of the black one.*

The same equation is used for the general solution. The result is expressed in percentage. It should be noted that Equation (4.111) is not valid for $s_{num_x} = 0$.

We will consider 3 different test cases, which have the same initial conditions, except for the orbital eccentricity. All initial values are selected such that all are different from zero in order to have full test coverage of all terms in the equations. The data is defined in Table 4.1.

In Figure 4.2 there is the special case for circular orbits. We have displayed only the positions, but the velocities are clearly matching as well. The first plot showing the so called in plane motion is the most interesting, as it is the plane for the most common maneuvers for proximity operations. It should be noted that the axes are plotted reverse, which is the traditional manner to view this plane. The plots contain the results from the numerical, CW and the general solution, and they are plotted on top of each other indicating an extremely small error. The plots 2 and 3 show the same, but in the two other planes with the same good accuracy. In plot 4 there is displayed an error of the CW or the general solution according to Equation (4.111). We see that there is an error of only 0.02 % at the distance of 3 km. This error comes from the actual linearization as we compare to the true curvilinear results accounting for the orbital curvature.

In the circular case it is actually possible to account for this error in the z-axis direc-

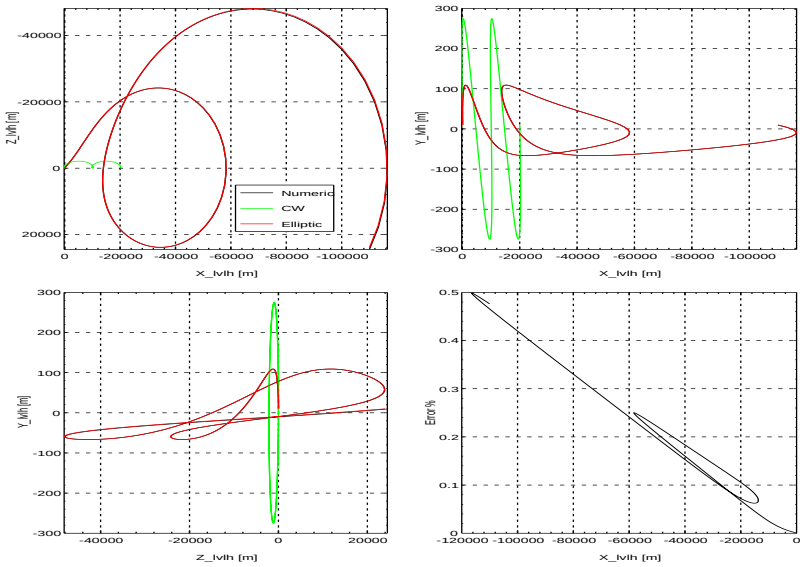

Figure 4.4: *Eccentric orbit, $\varepsilon = 0.7$. The relative motion of the numerical solution, the Clohessy Wiltshire equations and the elliptic solution. The first 3 plots show the relation positions in the 3 planes of the target LVLH frame. The 4th plot shows the position error in percentage of the x-axis distance. The legend is valid for the 3 first plots. Note that the red curve is on top of the black one.*

tion in a very simple manner, recalling that the x-axis is always tangent to the orbit at any location. We can find an analytical expression for the distance between the tangent and the intersection of the orbit and a line from the orbital center to the spacecraft location along the tangent. The expression is as follows

$$c_{comp} = r(1 - \cos(\arctan(\frac{|s_{cw_x}|}{r}))) \tag{4.112}$$

where r is the orbital radius and s_{cw_x} is the chaser spacecraft location along the x-axis. The term c_{comp} is then added to the s_{cw_z} to account for the orbital curvature. This simple nonlinear correction is recommended for distances beyond $1 - 2$ km.

In Figure 4.3 we see the same kind of plots as just discussed for Figure 4.2. We now deal with an eccentric orbit, which is not accounted for by the CW equations, but well by the general solution. It is clear that the CW trajectories are soon diverging from the real result. There is very quickly an error of about 20 %, though in this test case the shape of the trajectories are similar. The trajectories of the general solution behave very well and are in practice equivalent to the true ones, remaining at errors of about 0.025 % at distances of about 4 km.

The last test case, displayed in Figure 4.4, is highly eccentric and therefore it is expected to visualize the nonlinear effects more pronounced. It is clear from the plot

Case	ε	θ_0 deg	Position m			Velocity m/s		
1	0.0	void	-100	10	10	0.1	0.05	0.01
2	0.1	30	-100	10	10	0.1	0.05	0.01
3	0.7	30	-100	10	10	0.1	0.05	0.01

Table 4.1: *Definition of the initial position and velocities in the $\mathcal{F}_o$ frame, the eccentricity and the initial true anomaly for the 3 test cases in Figure 4.2, 4.3 and 4.4 respectively.*

that the CW trajectories are meaningless for such types of orbits. The general solution shows its full power for such orbits. It remains within the same small error as before, despite the higher complexity of the trajectories between the spacecraft. We see that we have errors of about 0.5 % but at distances of around 120 km and it seems to scale fairly linearly.

In conclusion it has been demonstrated that the new general solution derived in this work functions very well for all types of orbits, with easily predictable errors and possesses robustness and generality.

Finally we will address the point when to use one set of description or the other. In the in plane plot of Figure 4.3 we see that the error between the CW solution and the numerical or general solution is roughly 20 %. After running several simulations it can be shown that this error scales fairly linearly in this low end of the eccentricity domain. If we do not want larger deviations than some $6-7$ %, it means that the largest eccentricity where the CW solution should be used without compensation is about $\varepsilon = 0.04$. This matches well with the values, which are known from operational experience, in particular from the Russian space program (Duboshin 1963).

4.5 Impulsive and Station Keeping Maneuvers for Circular Orbits

This section will contain the development of the equations for performing station keeping at an arbitrary position as well as the expressions for the impulsive maneuvers. The latter is split into the general expressions and expressions for impulses along the V-bar and the R-bar respectively.

4.5.1 Station Keeping

The objective of station keeping is to stay in one and the same location. If the spacecraft is exactly in the V-bar no forces are needed, but this will never be the case in practice where there are always disturbances.

We are interested in the forces needed to be applied in order not to move. From Equation (4.99) we can obtain expressions for station keeping forces by setting all the

derivatives to zero, yielding:

$$\begin{aligned} F_x &= 0 \\ F_y &= m\omega^2 y_0 \\ F_z &= -3m\omega^2 z_0 \end{aligned} \tag{4.113}$$

where the index 0 means the station keeping location.

4.5.2 General ΔV Maneuver

The general expressions for ΔV for out of and in plane maneuvers will be derived, commencing with the former. For practical purposes transfer maneuvers of longer duration than one orbital period have no interest, and the development will be according to that.

Out of plane: Equation (4.110) expresses the motion for the out of plane. The left side is the final position y_f and velocity $\dot{y}_f$ and the right hand side the corresponding initial values y_0 and $\dot{y}_0$, where the latter is the unknown variable we are seeking. By calculating the first row of Equation (4.110) we have one equation with one unknown. By solving this and inserting the elements of the matrix $\mathbf{A}_{CW}(\tau)$, we obtain

$$\dot{y}_0 = \omega \frac{y_f - \cos(\omega\tau) y_0}{\sin(\omega\tau)} \tag{4.114}$$

It shall be recalled that Equation (4.114) expresses the change in initial velocity, so the total initial velocity is this added to whatever velocity might exist already giving y_0^+. The velocity at the final point we can obtain from the second row of Equations (4.110) and (4.114). Rearranging terms it yields

$$\dot{y}_f = \frac{\omega}{\tan(\omega\tau)} y_f - \frac{\omega}{\sin(\omega\tau)} y_0^+ \tag{4.115}$$

To stop the motion at the final point y_f an impulse opposite to $\dot{y}_f$ needs to be applied.

It shall be noted that Equation (4.114) is singular for $\omega\tau = 0, \pi, 2\pi, 3\pi, ...$ For $\tau = \frac{\pi}{\omega}$ we get that $\tau = \frac{T}{2}$, which is half the orbital time. For this time we must find the expressions directly for the elements of Equation (4.110), which leads to $y_f = -y_0$. As this is independent of the initial speed, and governed by the natural motion, it is not possible to perform maneuvers where the transfer time is half the orbital time or multiples there off.

In plane: We follow now the same procedure as for the out of plane maneuver but using Equation (4.106) instead. From the 2 first rows of Equation (4.106), we can find the 2 unknowns $\dot{x}_0$ and $\dot{z}_0$ respectively. After some algebraic manipulations and expanding all elements of the matrix $\mathbf{\Phi}_{CW}(\tau)$ we obtain

$$\dot{x}_0 = \frac{\sin(\omega\tau)(x_f - x_0) - 2(1 - \cos(\omega\tau)) z_f + (14(1 - \cos(\omega\tau)) - 6\omega\tau \sin(\omega\tau)) z_0}{\frac{8}{\omega}(1 - \cos(\omega\tau)) - 3\tau \sin(\omega\tau)} \tag{4.116}$$

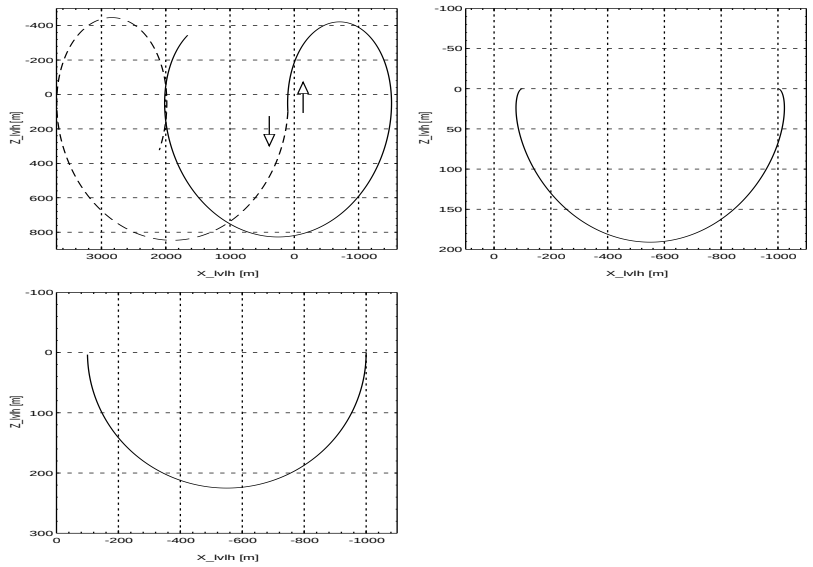

Figure 4.5: *Impulsive maneuvers. Top left for* $x_0 = [100, 0, 100]^T$ *m,* $x_f = [2000, 0, -50]^T$ *m and transfer times* 4 *% longer (full line) and* 4 *% less (dotted line) than an orbit. The trajectory is shown for longer time for illustrative purpose. Second graph is a V-bar transfer with* $x_0 = [-1000, 0, 0]^T$ *m and* $x_f = [-100, 0, 0]^T$ *m. Third graph is the same as second but for R-bar pulses.*

$$\dot{z}_0 = \frac{2(1-\cos(\omega\tau))(x_f - x_0) + (4\sin(\omega\tau) - 3\omega\tau)z_f + (3\omega\tau\cos(\omega\tau) - 4\sin(\omega\tau))z_0}{\frac{8}{\omega}(1-\cos(\omega\tau)) - 3\tau\sin(\omega\tau)} \tag{4.117}$$

The final velocities are found as for the out of plane but by using the last 2 rows of Equations (4.106), (4.116) and (4.117).

The Equations (4.116) and (4.117) are both singular at the same points in time. Inserting $\omega = \frac{2\pi}{T}$ the denominator becomes zero, and one singularity is identified. For times larger than the orbital time T, there are singularities at multiples of T as well as in between but they are not considered, as beyond one orbit. We now have to check for singularities for $\tau \in]0; T[$. Due to the transcendent nature of the denominator in Equation (4.116), we cannot find an easy explicit solution. Instead we can rewrite the denominator as

$$\frac{8}{\omega}(1-\cos(\omega\tau)) - 3\tau\sin(\omega\tau) = 0$$

$$\cos(\omega\tau) = 1 - \frac{3}{8}\omega\tau\sin(\omega\tau) \tag{4.118}$$

Considering the properties of the equality in Equation (4.118) for the area close to zero and consider the derivatives on both sides, it is clear that the equality is only fulfilled

for $\tau = 0$ and $\tau = T$. For all other points the right hand side is larger than the left. Hence we have no singularities for the interval $\tau \in]0;T[$. In Figure 4.5 there is a plot where the transfer time is close to the singularity point of time T. For the example given the trajectory moves in the minus z-axis direction leaving the initial point for times slightly larger than T, and the opposite for slightly smaller than T values. The transition between the two trajectories goes via infinity as the cycloid radius approaches infinity as time approaches T.

For the special case of singularity for $\tau = T$, the expressions can be found directly from Equation (4.106). The first two rows give the following equations

$$x_f = x_0 + 6\omega T z_0 - 3T\dot{x}_0 \tag{4.119}$$

$$z_f = z_0 \tag{4.120}$$

We see that it is not possible to select freely both the transfer time and the final z_f. This is because the trajectories are periodic cycloids and an infinite change in velocity would be needed. From Equation (4.119) we can now compute the change in velocity, by finding the limit for $\tau \to T$. For $\dot{x}_0$ in Equation (4.116) we get zero divided by zero and will need to apply L'Hospitals rule of differentiating the numerator and the denominator separately, which gives:

$$\lim_{\tau \to T} \dot{x}_0 = \frac{\omega\cos(\omega\tau)(x_f - x_0) - 2\omega\sin(\omega\tau)z_f + (14\omega\sin(\omega\tau) - 6\omega(\sin(\omega\tau) + \omega\tau\cos(\omega\tau)))z_0}{5\sin(\omega\tau) - 3\omega\tau\cos(\omega\tau)} \tag{4.121}$$

For $\dot{z}_0$ in Equation (4.117) we obtain as follows for $\tau = T$

$$\lim_{\tau \to T} \dot{z}_0 = \frac{3\omega T(z_0 - z_f)}{0} \tag{4.122}$$

which gives infinite for $z_0 \neq z_f$, but according to Equation (4.120) that is not possible for $\tau = T$ and then we get zero in the numerator of Equation (4.122) and need to differentiate it to find the limit applying L'Hospitals rule

$$\lim_{\tau \to T} \dot{z}_0 = \frac{\omega(z_f - z_0)}{5\sin(\omega\tau) - 3\omega\tau\cos(\omega\tau)} = \frac{0}{3T} \tag{4.123}$$

for $z_0 = z_f$ according to Equation (4.120). We can now write the equations for ΔV for $\tau = T$, where $\dot{x}_0$ could also have been found directly from Equation (4.119).

$$\dot{x}_0 = \frac{x_0 + 6\omega T z_0 - x_f}{3T} \tag{4.124}$$

$$\dot{z}_0 = 0 \tag{4.125}$$

Equations (4.124) and (4.125) express that we can only provide pulses in the V-bar direction and we will end up at the same height as where we started.

4.5.3 Tangential and Radial ΔV Maneuver

The objectives in this section will be to find some special restricted but very useful maneuvers. This relates to maneuvers with ΔV along either the V-bar or the R-bar.

V-bar: The initial and final z location is on the V-bar, meaning $z_0 = z_f = 0$. The initial state vector is as follows $[x_0, 0, \dot{x}_0, 0]^{\mathrm{T}}$. The transfer time for such a maneuver can be found from the second row of Equation (4.106), recalling $z_f = 0$. The transfer time becomes one orbital period T.

This leads us to use the solution provided by Equation (4.124) and inserting that $T = \frac{2\pi}{\omega}$ we obtain

$$\dot{x}_0 = \frac{\omega}{6\pi}(x_0 - x_f) \tag{4.126}$$

By rearranging Equation (4.126), we can see that the distance between the initial and final point on the V-bar, is a constant times the initial change in velocity.

$$x_0 - x_f = \frac{6\pi}{\omega}\dot{x}_0 \tag{4.127}$$

This difference is illustrated in Figure 4.5, which also represents a typical shape of the trajectory. We see that $\dot{x}_f = \dot{x}_0$, so to stop at the final point the total ΔV needed is $\Delta \mathrm{V}_x = 2\dot{x}_0$. The curve in Figure 4.5 is the highest for $\frac{T}{2}$ and can be found from the second row of Equation (4.106) to be

$$z\left(\frac{T}{2}\right) = -\frac{4}{6\pi}(x_0 - x_f) \tag{4.128}$$

It shall be stressed that this maneuver is also useful for either a fly around maneuver or a transfer to another orbital height. This is achieved by halting the transfer at half its duration after half an orbit.

R-bar: The initial and final z location is on the V-bar, meaning $z_0 = z_f = 0$. The initial state vector is as follows $[x_0, 0, 0, \dot{z}_0]^{\mathrm{T}}$. The transfer time for such a maneuver can be found from the second row of Equation (4.106), recalling $z_f = 0$. The transfer time becomes half an orbital period $\frac{T}{2}$.

As no singularities are involved for the R-bar, Equation (4.117) can be used directly leading to

$$\dot{z}_0 = \frac{\omega}{4}(x_f - x_0) \tag{4.129}$$

By rearranging Equation (4.129) we can see that the distance between the initial and final point on the V-bar is a constant times the initial change in velocity.

$$x_0 - x_f = -\frac{4}{\omega}\dot{z}_0 \tag{4.130}$$

This difference is illustrated in Figure 4.5, which also represents a typical shape of the trajectory. We have that $\dot{z}_f = -\dot{z}_0$, so to stop at the final point the total ΔV needed is $\Delta \mathrm{V}_z = 2|\dot{z}_0|$. The curve in Figure 4.5 is the highest for $\frac{T}{4}$ and can be found from the second row of Equation (4.106) to be

$$z\left(\frac{T}{4}\right) = \frac{1}{\omega}\dot{z}_0 \tag{4.131}$$

The ΔV expense for moving on the V-bar is not the same for the two maneuvers. The ratio can be found dividing Equation (4.129) with Equation (4.126) yielding

$$\frac{\dot{z}_0}{\dot{x}_0} = \frac{3}{2}\omega \tag{4.132}$$

which shows that it is significantly more expensive in fuel to perform R-bar maneuvers. Despite this fact, some distinctive advantages make it attractive:

- The same displacement on the V-bar takes half the time.
- There is no propagation along the V-bar as a function of time.
- In case of failure to perform the second pulse at x_f, the spacecraft will return to its original position at x_0.

The last point is particularly attractive seen from an operational safety point of view.

4.6 Impulsive and Station Keeping Maneuvers for Elliptic Orbits

This section will contain the development of the equations for performing station keeping at an arbitrary position as well as the expressions for the impulsive maneuvers. The latter is split into the general expressions and expressions for impulses along the V-bar and the R-bar respectively.

4.6.1 Station Keeping

The objective of station keeping is to stay in one and the same location. If the spacecraft is exactly in the V-bar no forces are needed, but this will never be the case in practice as there are always disturbances.

We are interested in the forces needed to be applied in order not to move. From Equation (4.15) we can obtain expressions for station keeping forces by setting all the derivatives to zero, yielding:

$$\begin{aligned} F_x &= m(k\omega^{\frac{3}{2}}x_0 - \dot{\omega}z_0 - \omega^2 x_0) \\ F_y &= mk\omega^{\frac{3}{2}}y_0 \\ F_z &= m(\dot{\omega}x_0 - \omega^2 z_0 - 2k\omega^{\frac{3}{2}}z_0) \end{aligned} \tag{4.133}$$

where the index 0 means the location of station keeping.

4.6.2 General ΔV Maneuver

The general expressions for ΔV for out of and in plane maneuvers will be derived commencing with the former. For practical purposes transfer maneuvers of longer duration than one orbital period have no interest, and the development will be accordingly. It shall be noted that for the general elliptic orbit the expressions will be significantly more complex than seen in Section 4.5.

Out of plane: Equations (4.92) and (4.93) express together the out of plane motion in the time domain. In order to illustrate the principle, the two equations will be combined here in Equation (4.134)

$$\begin{bmatrix} y_f \\ \dot{y}_f \end{bmatrix} = \mathbf{\Lambda}^{-1}(\theta_f)\mathbf{B}(\theta_f,\theta_0)\mathbf{\Lambda}(\theta_0) \begin{bmatrix} y_0 \\ \dot{y}_0 \end{bmatrix} \tag{4.134}$$

where $\dot{y}_0$ is unknown. By multiplying the 3 matrices in Equation (4.134) and expanding and rearranging all the terms in the first row one obtains the general expression for the ΔV

$$\dot{y}_0 = \frac{k^2\varrho(\theta_0)}{\sin(\theta_f-\theta_0)}\left[\varrho(\theta_f)y_f - (\cos(\theta_f-\theta_0)+\varepsilon\cos(\theta_f))y_0\right] \tag{4.135}$$

The final speed $\dot{y}_f$ can be calculated directly from the second row of Equation (4.134), and nothing is gained by expanding this row into all terms explicitly. To stop the motion at y_f one needs

$$\Delta \mathrm{V}_{stop} = -\dot{y}_f \tag{4.136}$$

under the assumption of no initial residual speed.

Equation (4.135) is singular for $\sin(\theta_f-\theta_0)=0$ leading to $\theta_f-\theta_0 = n\pi$ and $n = 0,1,2,\cdots$, but $n=0$ is of no interest in practice. Inserting directly into Equation (4.134) for the argument equal to π or 2π the $\mathbf{B}$ matrix becomes $-\mathbf{I}$ or $\mathbf{I}$, being the identity matrix. By finding now the complete transition in Equation (4.134) it turns out that y_f becomes only a scaled value of y_0 and not any longer a function of $\dot{y}_0$. Hence it is not possible to perform a maneuver of this duration, as is the case for circular orbits.

In plane: The approach for the in plane follows the same principles as for the out of plane maneuvers, but with a higher complexity in the solutions.

Equation (4.91) provides the transition in the θ domain and utilizing the transforms in Equation (4.94) one obtains the complete transition in the time domain as

$$\begin{bmatrix} x_f \\ z_f \\ \dot{x}_f \\ \dot{z}_f \end{bmatrix} = \mathbf{\Lambda}_i^{-1}(\theta_f)\mathbf{\Phi}(\theta_f)\mathbf{\Phi}_0^{-1}(\theta_0)\mathbf{\Lambda}_i(\theta_0) \begin{bmatrix} x_0 \\ z_0 \\ \dot{x}_0 \\ \dot{z}_0 \end{bmatrix} \tag{4.137}$$

The first column of the product $\mathbf{\Phi}(\theta_f)\mathbf{\Phi}_0^{-1}(\theta_0)$ is $[1,0,0,0]^{\mathrm{T}}$, but when pre- and post-multiplied by $\mathbf{\Lambda}_i$ the complete transition matrix is a full matrix. We denote it D and its

elements d_{ij}. To find the initial velocities we need only to solve for the first 2 rows of Equation (4.137), becoming

$$\begin{bmatrix} x_f \\ z_f \end{bmatrix} = \begin{bmatrix} d_{11} & d_{12} & d_{13} & d_{14} \\ d_{21} & d_{22} & d_{23} & d_{24} \end{bmatrix} \begin{bmatrix} x_0 \\ z_0 \\ \dot{x}_0 \\ \dot{z}_0 \end{bmatrix} \tag{4.138}$$

where the unknowns are $\dot{x}_0$ and $\dot{z}_0$. After some algebraic manipulation this gives the 2 general expressions as follows

$$\dot{x}_0 = \frac{d_{14}z_f + (d_{24}d_{11} - d_{21}d_{14})x_0 + (d_{24}d_{12} - d_{22}d_{14})z_0 - d_{24}x_f}{d_{23}d_{14} - d_{24}d_{13}} \tag{4.139}$$

$$\dot{z}_0 = \frac{d_{23}x_f - d_{13}z_f + (d_{13}d_{21} - d_{11}d_{23})x_0 + (d_{13}d_{22} - d_{12}d_{23})z_0}{d_{23}d_{14} - d_{24}d_{13}} \tag{4.140}$$

The final velocities are found by inserting directly into Equation (4.137). The Equations (4.139) and (4.140) are functions of time t, eccentricity ε and the initial true anomaly θ_0. The equations have singularities for the denominator $d_{23}d_{14} - d_{24}d_{13} = 0$, which is a function of the same 3 variables. Due to Kepler's equation it is not possible to determine analytically possible singularities of the denominator. Nevertheless it has been investigated numerically over the range of the 3 variables that there are no singularities, except for a complete orbit of transfer.

It can be shown analytically that there is a singularity for $t = T$, which might be a special case, as for the circular case. In this case $\theta(T) = 2\pi + \theta_0$, which means that we are at the same orbital location. To find the transition in Equation (4.137) we will calculate the elements for $t = T$. Recalling that $J(\theta_0) = 0$ in $\mathbf{\Phi}_0^{-1}$ in Equation (4.90) and that it is the only missing term preventing the center product in Equation (4.137) to become the identity matrix. By using that knowledge it is clear that the product of the two matrices, will only have elements containing the $J(\theta)$ term from Equation (4.85) except for the pre- and post-multiplications. Those elements are derived in detail in Section A.4. By inserting Equations (A.52), (A.53), (A.54) and (A.55) into the denominator of Equation (4.139) and multiplying through with $1 - \varepsilon^2$ we get

$$(3\varepsilon\varrho_0 \sin(\theta_0)T)(3\varepsilon\varrho_0 \sin(\theta_0)T) - (-3\varepsilon^2 \sin(\theta_0)^2 T)(-3\varrho_0^2 T) = 0$$

which is identically zero. It is proven that for any value of the variables there is a singularity for $t = T$.

By inserting all the coefficients into Equation (4.138) it turns out not to be possible to avoid the same set of singularities. It can therefore be concluded that for elliptic orbits, it is not possible to perform impulsive maneuvers of the duration of the orbit.

4.6.3 Tangential and Radial ΔV Maneuver

The objective in this section is to find some special restricted, but very useful maneuvers. This relates to maneuvers with ΔV along either the V-bar or the R-bar.

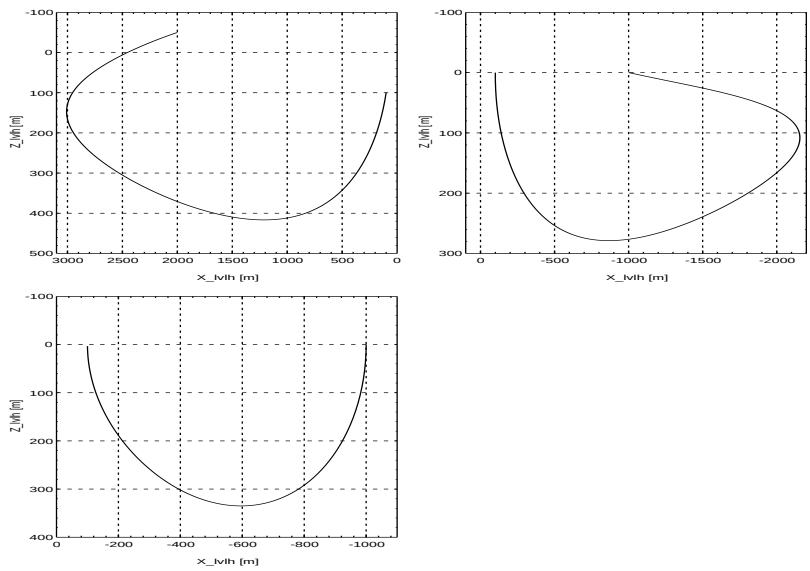

Figure 4.6: *Impulsive maneuvers,* $\varepsilon = 0.4$*. The first graph is for* $x_0 = [100, 0, 100]^T$ *m,* $x_f = [2000, 0, -50]^T$ *m and the transfer time is* 90 *% of an orbit. The second graph is a V-bar transfer with* $x_0 = [-1000, 0, 0]^T$ *m and* $x_f = [-100, 0, 0]^T$ *m. The third graph is the same as second but for R-bar pulses.*

V-bar: The initial and final z location is on the V-bar, meaning $z_0 = z_f = 0$. The initial state vector is as follows $[x_0, 0, \dot{x}_0, 0]^{\mathrm{T}}$. We can now write 2 equations from Equation (4.138) as

$$x_f = d_{11}x_0 + d_{13}\dot{x}_0 \qquad \text{and} \qquad 0 = d_{21}x_0 + d_{23}\dot{x}_0 \tag{4.141}$$

We cannot solve for the two unknowns in Equation (4.141), the transfer time and $\dot{x}_0$, as they are functions of the Kepler equation. Instead a qualified guess is a solution at a transfer time of one orbital revolution T, based upon the nature of orbital mechanics. The expression for the ΔV then becomes using the left equation

$$\dot{x}_0 = \frac{x_f - d_{11}x_0}{d_{13}} \tag{4.142}$$

This solution is confirmed by back substitution into Equation (4.138) and is then a solution. An illustration of a maneuver with pulses along the x-axis of $\mathcal{F}_o$ only can be seen in Figure 4.6. Due to the nature of the motion, this restricted maneuver, is valid for $\theta_0 = 0$, transfer time of one orbit $t = T$ and transfer angle $\theta = 2\pi$.

R-bar: The initial and final z location is on the V-bar, meaning $z_0 = z_f = 0$. The initial state vector is as follows $[x_0, 0, 0, \dot{z}_0]^{\mathrm{T}}$. We can now write 2 equations from

Equation (4.138) as

$$x_f = d_{11}x_0 + d_{14}\dot{z}_0 \qquad \text{and} \qquad 0 = d_{21}x_0 + d_{24}\dot{z}_0 \tag{4.143}$$

It is the same problem as before with respect to solve for the transfer time. The expression for the ΔV then becomes

$$\dot{z}_0 = \frac{x_f - d_{11}x_0}{d_{14}} \tag{4.144}$$

A transfer time of $t = \frac{T}{2}$ for Equation (4.144) is valid for the radial maneuver. The initial true anomaly $\theta_0 = 0$ or π and the transfer angle is $\theta = \pi$. An illustration of a maneuver with pulses along the z-axis of $\mathcal{F}_o$ only can be seen in Figure 4.6. A property of the radial transfer is that if the second pulse is not executed, the trajectory returns to the initial position, and does not propagate along the V-bar.

From what has been derived and analyzed it can be stated that the maneuvers in the general elliptic case preserve all the convenient properties described for the circular case, though it is more complex to compute the parameters. The ratio between radial and tangential pulses is similar to the circular case, though no exact expression for it can be found.

4.7 Particular Solution for Circular Orbits

In the previous sections we have developed all solutions needed for all practical applications of initial condition based relative maneuvers. In this section we will complete the solutions also to include relevant particular solutions, which will improve the accuracy of maneuvers under influence of the particular disturbances. In the sequel we will focus on present disturbances like relative drag and solar radiation pressure. This will be generalized to find solutions for arbitrary constant forces in the local orbital frame $\mathcal{F}_o$ and in the inertial frame $\mathcal{F}_i$.

4.7.1 Constant Force in the Local Orbital Frame $\mathcal{F}_o$

We will seek a solution for the differential equation system in Equation (4.99) for an arbitrary but constant force $\mathbf{F} = [F_x, F_y, F_z]^{\mathrm{T}}$. As the system is LTI and all matrices of the homogeneous solution are known, we will use Laplace transformations to obtain the particular solutions.

The general time domain solution to a state space system can be written from the Laplace domain as (Fehse 2003)

$$\mathbf{x}(t) = \underbrace{\mathcal{L}^{-1}\left[\mathbf{\Phi}(s)\mathbf{x}(0_+)\right]}_{\text{zero input component}} + \underbrace{\mathcal{L}^{-1}\left[\mathbf{\Phi}(s)\mathbf{B}\mathbf{u}(s)\right]}_{\text{zero state component}} \tag{4.145}$$

where the zero state component is the particular solution we seek. A general constant signal can be formulated as

$$f(t) \triangleq k \cdot u_{t_0}(t) \;\text{ and }\; u_a(t) = \begin{cases} 1 & \text{for} \quad t \geq a \\ 0 & \text{for} \quad t < a \end{cases} \tag{4.146}$$

which provides a constant step at time t_0 and its Laplace transform is

$$\mathcal{L}[f(t)] = F(s) = \frac{k}{s} e^{-t_0 s} \tag{4.147}$$

Equations (4.145) and (4.147) will be used for all elements to derive the solution.

In Equation (4.145) we have that $\mathbf{u}(s) = \mathbf{F}(s)$. We will first compute the out of plane solution, where $\mathbf{B} = [0, \frac{1}{m}]^{\mathrm{T}}$ and $\mathbf{\Phi}(s)$ are obtained by transforming Equation (4.109) and it is observed that only the right column is used due to $\mathbf{B}$. The argument of Equation (4.145) now becomes

$$\mathbf{\Phi}(s)\mathbf{B}\mathbf{u}(s) = \frac{1}{m} \begin{bmatrix} \frac{1}{s^2+\omega^2} \\ \frac{s}{s^2+\omega^2} \end{bmatrix} \frac{F_y}{s} e^{-t_0 s} = \frac{F_y}{m} \begin{bmatrix} \frac{1}{s(s^2+\omega^2)} \\ \frac{1}{s^2+\omega^2} \end{bmatrix} e^{-t_0 s} \tag{4.148}$$

and the out of plane particular solution yields

$$\mathbf{x}_{p_o}(\tau) = \mathcal{L}^{-1}(\mathbf{\Phi}(s)\mathbf{B}\mathbf{u}(s)) = \frac{F_y}{m} \begin{bmatrix} \frac{1}{\omega^2}(1-\cos(\omega(t-t_0))) \\ \frac{1}{\omega}\sin(\omega(t-t_0)) \end{bmatrix} = \frac{F_y}{m} \begin{bmatrix} \frac{1}{\omega^2}(1-\cos(\omega\tau)) \\ \frac{1}{\omega}\sin(\omega\tau) \end{bmatrix} \tag{4.149}$$

using from Equation (4.104) that $\tau = t - t_0$.
The in plane solution follows the exact same method, where the input matrix is

$$\mathbf{B} = \begin{bmatrix} 0 & 0 \\ 0 & 0 \\ \frac{1}{m} & 0 \\ 0 & \frac{1}{m} \end{bmatrix} \tag{4.150}$$

and only the two right most columns of the transition matrix in Equation (4.105) are used. We obtain

$$\mathbf{\Phi}(s)\mathbf{B}\mathbf{u}(s) = \frac{1}{m} \begin{bmatrix} \frac{4}{s^2+\omega^2} - \frac{3}{s^2} & \frac{2\omega}{s(s^2+\omega^2)} \\ \frac{-2\omega}{s(s^2+\omega^2)} & \frac{1}{s^2+\omega^2} \\ \frac{4s}{s^2+\omega^2} - \frac{3}{s} & \frac{2\omega}{s^2+\omega^2} \\ \frac{-2\omega}{s^2+\omega^2} & \frac{s}{s^2+\omega^2} \end{bmatrix} \frac{1}{s} \begin{bmatrix} F_x \\ F_z \end{bmatrix} e^{-t_0 s} \tag{4.151}$$

We multiply the Laplace terms together in Equation (4.151) and find the inverse Laplace transform of each element of the matrix and obtain the following solution with $\tau = t - t_0$

$$\mathbf{x}_{p_i}(\tau) = \mathcal{L}^{-1}(\mathbf{\Phi}(s)\mathbf{B}\mathbf{u}(s)) = \frac{1}{m} \begin{bmatrix} \frac{4}{\omega^2}(1-\cos(\omega\tau)) - \frac{3}{2}\tau^2 & \frac{2}{\omega^2}(\omega\tau - \sin(\omega\tau)) \\ \frac{2}{\omega^2}(\sin(\omega\tau) - \omega\tau) & \frac{1}{\omega^2}(1-\cos(\omega\tau)) \\ \frac{4}{\omega}\sin(\omega\tau) - 3\tau & \frac{2}{\omega}(1-\cos(\omega\tau)) \\ \frac{2}{\omega}(\cos(\omega\tau)-1) & \frac{1}{\omega}\sin(\omega\tau) \end{bmatrix} \begin{bmatrix} F_x \\ F_z \end{bmatrix} \tag{4.152}$$

The effect of accounting for the particular solution is illustrated in Figure 4.7 compared with the classical homogeneous one. The result is also compared with a numerical result of the differential equation system and seen to compare very well. The error in Figure 4.7 is computed according to the definition in Equation (4.111). In summary we

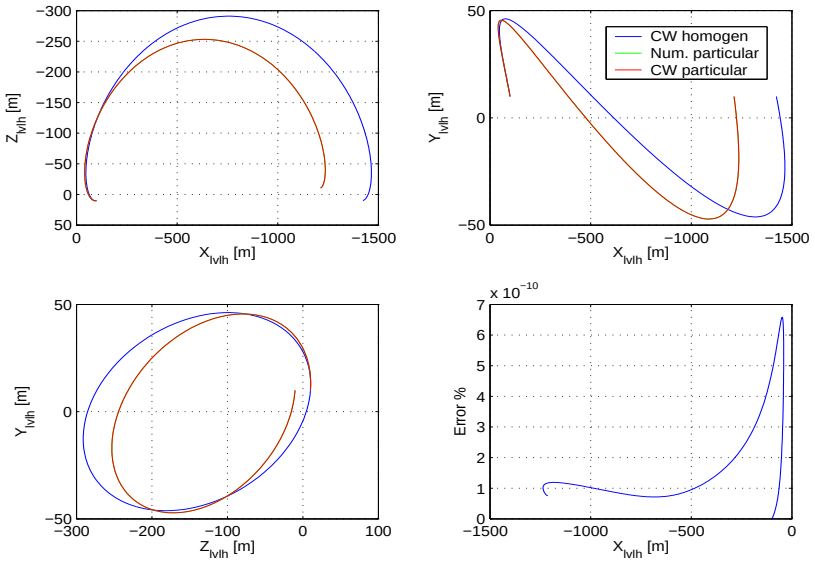

Figure 4.7: *A two pulse maneuver in circular orbit under the influence of a constant force in the $\mathcal{F}_o$ frame, where* $\mathbf{F} = [0.02, -0.01, 0.3]^T$ *N. The initial conditions are* $\mathbf{x}(0) = [-100, 10, 10]^T$ *m and* $\dot{\mathbf{x}}(0) = [0.1, 0.05, 0.01]^T$ *m/s, where the duration is one orbit and* $\varepsilon = 0$*. Note that the red curve is on top of the green curve.*

list the two particular solutions for the in and out of plane.

Out of plane:

$$\mathbf{x}_{p_o}(\tau) = \frac{1}{m}\begin{bmatrix} \frac{1}{\omega^2}(1-\cos(\omega\tau)) \\ \frac{1}{\omega}\sin(\omega\tau) \end{bmatrix} F_y \tag{4.153}$$

In plane:

$$\mathbf{x}_{p_i}(\tau) = \frac{1}{m}\begin{bmatrix} \frac{4}{\omega^2}(1-\cos(\omega\tau)) - \frac{3}{2}\tau^2 & \frac{2}{\omega^2}(\omega\tau - \sin(\omega\tau)) \\ \frac{2}{\omega^2}(\sin(\omega\tau) - \omega\tau) & \frac{1}{\omega^2}(1-\cos(\omega\tau)) \\ \frac{4}{\omega}\sin(\omega\tau) - 3\tau & \frac{2}{\omega^2}(1-\cos(\omega\tau)) \\ \frac{2}{\omega}(\cos(\omega\tau) - 1) & \frac{1}{\omega}\sin(\omega\tau) \end{bmatrix} \begin{bmatrix} F_x \\ F_z \end{bmatrix} \tag{4.154}$$

4.7.2 Constant Force in the Inertial Frame $\mathcal{F}_i$

We will now consider the perturbation of solar radiation pressure, which we will approximate to be constant in the Earth centered inertial frame $\mathcal{F}_i$. This is an insignificant approximation, as it affects the modulus of the force vector by less than 0.02 % per day and practical relative maneuvers are of shorter duration. The development will therefore be generalized for an arbitrary constant force represented in the $\mathcal{F}_i$ frame.

This constant force needs to be represented in the orbital frame $\mathcal{F}_o$ as in Section 4.7.1. From Figure 3.1 there are 3 angles involved. The angle α and the inclination i both constant for the duration of maneuvers and the angle β. $\beta = \theta + \gamma$ where θ is the true anomaly and γ is the argument of perigee. The latter is undefined for circular orbits and we can set $\gamma = 0$ without loss of generality. We now transform a vector $\mathbf{v}_i$ in $\mathcal{F}_i$ into $\mathcal{F}_o$ as

$$\mathbf{v}_o = \mathbf{R}_{os}\mathbf{R}_{sb}\mathbf{R}_{bi}\mathbf{v}_i \tag{4.155}$$

where

$$\mathbf{R}_{bi} = \begin{bmatrix} 1 & 0 & 0 \\ 0 & \cos(i) & \sin(i) \\ 0 & -\sin(i) & \cos(i) \end{bmatrix} \begin{bmatrix} \cos(\alpha) & \sin(\alpha) & 0 \\ -\sin(\alpha) & \cos(\alpha) & 0 \\ 0 & 0 & 1 \end{bmatrix} \tag{4.156}$$

and

$$\mathbf{R}_{sb} = \begin{bmatrix} \cos(\beta) & \sin(\beta) & 0 \\ -\sin(\beta) & \cos(\beta) & 0 \\ 0 & 0 & 1 \end{bmatrix} \quad \text{and} \quad \mathbf{R}_{os} = \begin{bmatrix} 0 & 1 & 0 \\ 0 & 0 & -1 \\ -1 & 0 & 0 \end{bmatrix} \tag{4.157}$$

We define $\mathbf{v}_b = \mathbf{R}_{bi}\mathbf{v}_i = \mathbf{R}_{bi}\mathbf{F}_i$, where the force vector $\mathbf{F}_i$ is now just another constant vector $\mathbf{v}_b$ in the $\mathcal{F}_b$ frame. Let us define $\mathbf{v}_b = [k_x, k_y, k_z]^{\mathrm{T}}$ and combining with Equation (4.157) we obtain

$$\mathbf{v}_o = \begin{bmatrix} -\sin(\beta) & \cos(\beta) & 0 \\ 0 & 0 & -1 \\ -\cos(\beta) & -\sin(\beta) & 0 \end{bmatrix} \mathbf{v}_b \tag{4.158}$$

It is observed that the out of plane component is minus the solution in Equation (4.153), so we can proceed directly to solve the in plane part recalling that $\beta = \omega t$.

The same method and matrices apply as used in Section 4.7.1 except the input vector is now time varying. The input can be formulated as

$$\mathbf{u}(t) = \begin{bmatrix} -\sin(\omega t) & \cos(\omega t) \\ -\cos(\omega t) & -\sin(\omega t) \end{bmatrix} \begin{bmatrix} k_x \\ k_y \end{bmatrix} \mathbf{u}_{t_0}(t) \tag{4.159}$$

and taking the Laplace transform and multiplying onto the $\mathbf{B}$ matrix we obtain

$$\mathbf{B}\mathbf{u}(s) = \frac{1}{m} \begin{bmatrix} 0 & 0 \\ 0 & 0 \\ -\frac{\omega}{s^2+\omega^2} & \frac{s}{s^2+\omega^2} \\ -\frac{s}{s^2+\omega^2} & -\frac{\omega}{s^2+\omega^2} \end{bmatrix} \begin{bmatrix} k_x \\ k_y \end{bmatrix} e^{-t_0 s} \tag{4.160}$$

From Equation (4.160) we see that only the two right most columns of the transition matrix in Equation (4.105) are used. Multiplying matrices and combining terms we

obtain

$$\mathbf{\Phi}(s)\mathbf{B}\mathbf{u}(s)=\frac{1}{m}\begin{bmatrix} \frac{3\omega}{s^2(s^2+\omega^2)}-\frac{6\omega}{(s^2+\omega^2)^2} & \frac{4s}{(s^2+\omega^2)^2}-\frac{3}{s(s^2+\omega^2)}-\frac{2\omega^2}{s(s^2+\omega^2)^2} \\ \frac{2\omega^2}{s(s^2+\omega^2)^2}-\frac{s}{(s^2+\omega^2)^2} & -\frac{3\omega}{(s^2+\omega^2)^2} \\ \frac{3\omega}{s(s^2+\omega^2)}-\frac{6\omega s}{(s^2+\omega^2)^2} & \frac{4s^2}{(s^2+\omega^2)^2}-\frac{3}{s^2+\omega^2}-\frac{2\omega^2}{(s^2+\omega^2)^2} \\ \frac{2\omega^2}{(s^2+\omega^2)^2}-\frac{s^2}{(s^2+\omega^2)^2} & -\frac{3\omega s}{(s^2+\omega^2)^2} \end{bmatrix}\begin{bmatrix} k_x \\ k_y \end{bmatrix}e^{-t_0 s} \tag{4.161}$$

The inverse transformations are found from Laplace tables, but the first term of element $(2,1)$ has not been found. We will therefore use the following identity to solve it. Proof can be found in (Kreyszig 1979).

$$\mathcal{L}\left\{\int_0^t f(\tau)d\tau\right\}=\frac{1}{s}\mathcal{L}\left(f(t)\right)\Leftrightarrow\mathcal{L}^{-1}\left\{\frac{1}{s}F(s)\right\}=\int_0^t f(\tau)d\tau \tag{4.162}$$

We obtain

$$\begin{aligned}\mathcal{L}^{-1}\left\{\frac{1}{s}\frac{1}{(s^2+\omega^2)^2}\right\} &= \frac{1}{2\omega^3}\int_0^t(\sin(\omega\tau)-\omega\tau\cos(\omega\tau))d\tau \\ &= \frac{1}{2\omega^4}\left[2-2\cos(\omega t)-\omega t\sin(\omega t)\right]\end{aligned} \tag{4.163}$$

Using the results of Equation (4.163) we can compute the results of Equation (4.161) and summarize as follows for both the in and out of plane, where $\tau=t-t_0$.

Out of plane:

$$\mathbf{x}_{p_o}(\tau)=\frac{1}{m}\begin{bmatrix} -\frac{1}{\omega^2}(1-\cos(\omega\tau)) \\ -\frac{1}{\omega}\sin(\omega\tau) \end{bmatrix}k_z \tag{4.164}$$

In plane:

$$\mathbf{x}_{p_i}(\tau)=\frac{1}{m}\begin{bmatrix} \frac{3}{\omega}\tau(\cos(\omega\tau)+1)-\frac{6}{\omega^2}\sin(\omega\tau) & \frac{5}{\omega^2}(\cos(\omega\tau)-1)+\frac{3}{\omega}\tau\sin(\omega\tau) \\ \frac{2}{\omega^2}(1-\cos(\omega\tau))-\frac{3}{2\omega}\tau\sin(\omega\tau) & \frac{3}{2\omega^2}(\omega\tau\cos(\omega\tau)-\sin(\omega\tau)) \\ 3(\frac{1}{\omega}(1-\cos(\omega\tau))-\tau\sin(\omega\tau)) & 3\tau\cos(\omega\tau)-\frac{2}{\omega}\sin(\omega\tau) \\ \frac{1}{2\omega}\sin(\omega\tau)-\frac{3}{2}\tau\cos(\omega\tau) & -\frac{3}{2}\tau\sin(\omega\tau) \end{bmatrix}\begin{bmatrix} k_x \\ k_y \end{bmatrix} \tag{4.165}$$

In Figure 4.8 we see the comparison between the homogeneous solution and the complete solution under the influence of a constant disturbance in the inertial frame, which is non constant in the LVLH frame. The result is also compared with a time varying numerical solution showing identical results.

4.8 Particular Solution for Elliptical Orbits

The elliptical equivalent particular solution of Section 4.7 will be developed in this section for elliptical orbits. As for the homogeneous solution the development will be performed with the true anomaly θ as the independent variable in the θ domain.

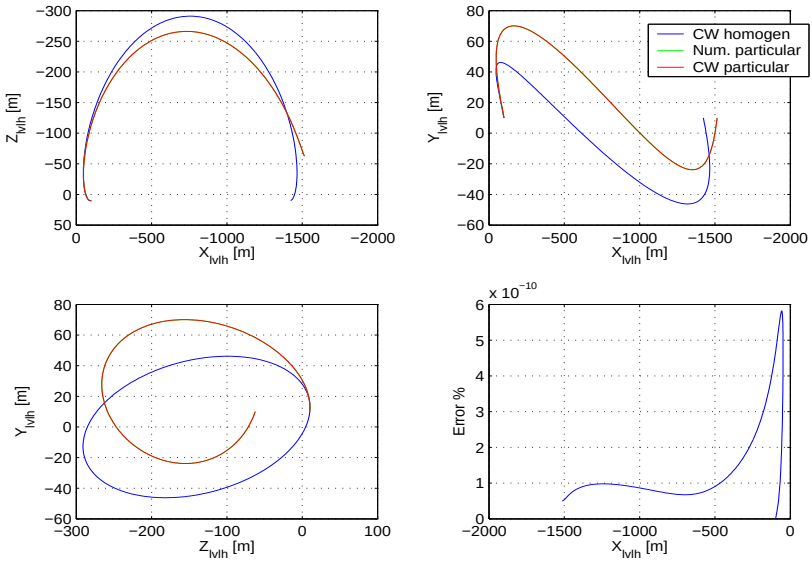

Figure 4.8: *A two pulse maneuver in circular orbit under the influence of a constant inertial force in the $\mathcal{F}_i$ frame, where* $\mathbf{F} = [0.02, 0.01, -0.3]^T$ *N. The initial conditions are* $\mathbf{x}(0) = [-100, 10, 10]^T$ *m and* $\dot{\mathbf{x}}(0) = [0.1, 0.05, 0.01]^T$ *m/s, where the duration is one orbit and* $\varepsilon = 0$*. Note that the red curve is on top of the green curve.*

It is recalled that the fundamental set of differential equations we need to solve is the time domain system in Equation (4.15). This was transformed into the system in Equation (4.38) for the homogeneous solution taking advantage of the simplification that the input to Equation (4.15) was set to zero. Now the input functions are needed and it is necessary to perform the transformations with the right hand side present. The algebraic computations from Equation (4.20) to (4.38) will not be repeated here, but the resulting equation system yields

$$\begin{aligned} \alpha'' - 2\gamma' &= \frac{F_x}{mk^4\varrho^3} \\ \beta'' + \beta &= \frac{F_y}{mk^4\varrho^3} \\ \gamma'' - \frac{3}{\varrho}\gamma + 2\alpha' &= \frac{F_z}{mk^4\varrho^3} \end{aligned} \tag{4.166}$$

and it is observed that all the inputs of Equation (4.15) are transformed with $\frac{1}{k^4\varrho^3}$, where ϱ is defined in Equation (4.20). Equation (4.166) is the non homogeneous system for which particular solutions are sought. Notation and definitions of Section 4.7 are used.

4.8.1 Constant Force in the Local Orbital Frame $\mathcal{F}_o$

As the angular rate for elliptical orbits is nonlinear time varying, we cannot use the approach of Section 4.7, but we will use the general method of *variation of parameters* as briefly described in Equation (4.61), though we will vectorize the formulation here.

To a general non homogeneous system of the form $\mathbf{x}' = \mathbf{A}\mathbf{x} + \mathbf{B}$ the particular solution $\mathbf{u}_p(t)$ can be written as (Rabenstein 1975)

$$\mathbf{u}_p(t) = \mathbf{U}(t)\mathbf{c}(t) = \mathbf{U}(t)\int_{t_0}^{t} \mathbf{U}(s)^{-1}\mathbf{B}(s)ds \tag{4.167}$$

where $\mathbf{U}(t)$ is the fundamental or transition matrix for $\mathbf{x}' = \mathbf{A}\mathbf{x}$ and consists of the set of solutions $\mathbf{u}_1 \cdots \mathbf{u}_n$ in Equation (4.61). The constants in Equation (4.61) are vectorized and become the integral in Equation (4.167). It can be verified by back substitution into the original equation.

We will commence with the out of plane in Equation (4.166) and use the transition matrix from Equation (4.40) such that $\mathbf{U}(\theta) = \mathbf{A}(\theta)\mathbf{A}_0(\theta_0)^{-1}$ and inserting into Equation (4.167) we obtain using[1]

$$\mathbf{x}_{p_o}(\theta) = \mathbf{A}(\theta)\mathbf{A}_0(\theta_0)^{-1}\int_{\theta_0}^{\theta} \mathbf{A}_0(\theta_0)\mathbf{A}(s)^{-1}\mathbf{B}(s)ds \tag{4.168}$$

and moving the constant outside we have

$$\mathbf{x}_{p_o}(\theta) = \mathbf{A}(\theta)\underbrace{\mathbf{A}_0(\theta_0)^{-1}\mathbf{A}_0(\theta_0)}_{\mathbf{I}}\int_{\theta_0}^{\theta} \mathbf{A}(s)^{-1}\mathbf{B}(s)ds \tag{4.169}$$

From Equation (4.169) it is observed that the transition matrix of the initial conditions in general will reduce to identity matrix, so we need only operate with the transition matrix such that $\mathbf{U} = \mathbf{A}$. In the following the argument θ will mostly be omitted for simplicity of the notation.

The input matrix for the out of plane becomes from Equation (4.166) in state space form $\mathbf{B} = \left[0, \frac{F_y}{mk^4\varrho^3}\right]^{\mathrm{T}}$ and the inverse of the transition matrix in Equation (4.40) is itself and we obtain

$$\mathbf{U}(s)^{-1}\mathbf{B}(s) = \mathbf{A}(s)^{-1}\mathbf{B}(s) = \mathbf{A}(s)\mathbf{B}(s) = \frac{F_y}{mk^4}\begin{bmatrix} \sin(s) & \cos(s) \\ \cos(s) & -\sin(s) \end{bmatrix}\begin{bmatrix} 0 \\ \frac{1}{\varrho(s)^3} \end{bmatrix} \tag{4.170}$$

We can now write the integral of Equation (4.167) as

$$\int_{\theta_0}^{\theta} \mathbf{U}(s)^{-1}\mathbf{B}(s)ds = \frac{F_y}{mk^4}\int_{\theta_0}^{\theta}\begin{bmatrix} \frac{\cos(s)}{\varrho(s)^3} \\ -\frac{\sin(s)}{\varrho(s)^3} \end{bmatrix} ds \tag{4.171}$$

[1]When the inverse exists the following holds $(\mathbf{AB})^{-1} = \mathbf{B}^{-1}\mathbf{A}^{-1}$.

This leads to solving two integrals to find the particular solution.

$$I_{s_3} = \int_{\theta_0}^{\theta} \frac{\sin(\theta)}{(1+\varepsilon\cos(\theta))^3} d\theta = \frac{1}{2\varepsilon}\left[\frac{1}{(1+\varepsilon\cos(\theta))^2}\right]_{\theta_0}^{\theta} = \frac{1}{2\varepsilon}\left[\frac{1}{\varrho^2} - \frac{1}{\varrho_0^2}\right] \quad (4.172)$$

The other integral is nontrivial in its present form for which reason we will perform a substitution of variable from the true anomaly θ to the eccentric anomaly E as below (Vinti 1998)

$$\cos(\theta) = \frac{\cos(E)-\varepsilon}{1-\varepsilon\cos(E)} \quad \text{and} \quad \sin(\theta) = \frac{\sqrt{1-\varepsilon^2}\sin(E)}{1-\varepsilon\cos(E)} \quad (4.173)$$

and the inverse relations are

$$\cos(E) = \frac{\varepsilon+\cos(\theta)}{1+\varepsilon\cos(\theta)} \quad \text{and} \quad \sin(E) = \frac{\sqrt{1-\varepsilon^2}\sin(\theta)}{1+\varepsilon\cos(\theta)} \quad (4.174)$$

We can now write

$$I_{c_3} = \int_{\theta_0}^{\theta} \frac{\cos(\theta)}{(1+\varepsilon\cos(\theta))^3} d\theta = \int_{E_0}^{E} f(E)dE \quad (4.175)$$

Then inserting $\cos(\theta)$

$$f(E) = \frac{\frac{\cos(E)-\varepsilon}{1-\varepsilon\cos(E)}}{\left(1+\varepsilon\frac{\cos(E)-\varepsilon}{1-\varepsilon\cos(E)}\right)^3} =$$

$$\frac{\cos(E)-\varepsilon}{1-\varepsilon\cos(E)}\frac{(1-\varepsilon\cos(E))^3}{(1-\varepsilon^2)^3} = (1-\varepsilon^2)^{-3}(\cos(E)-\varepsilon)(1-\varepsilon\cos(E))^2 \quad (4.176)$$

We now need to find $d\theta$ and using the chain rule and Equation (4.173) we get

$$\frac{d(\cos(\theta))}{dE} = \frac{d(\cos(\theta))}{d\theta}\frac{d\theta}{dE} = -\sin(\theta)\frac{d\theta}{dE}$$

$$\frac{d}{dE}\left((\cos(E)-\varepsilon)(1-\varepsilon\cos(E))^{-1}\right) = -\sin(\theta)\frac{d\theta}{dE}$$

$$\left(-1-\varepsilon\cos(E)(1-\varepsilon\cos(E))^{-1} + \varepsilon^2(1-\varepsilon\cos(E))^{-1}\right)\sin(E)(1-\varepsilon\cos(E))^{-1} =$$

$$-\sqrt{1-\varepsilon^2}\sin(E)(1-\varepsilon\cos(E))^{-1}\frac{d\theta}{dE}$$

$$1 + \frac{\varepsilon\cos(E)-\varepsilon^2}{1-\varepsilon\cos(E)} = \sqrt{1-\varepsilon^2}\frac{d\theta}{dE}$$

$$\frac{1-\varepsilon^2}{\sqrt{1-\varepsilon^2}}(1-\varepsilon\cos(E))^{-1} = \frac{d\theta}{dE}$$

$$d\theta = \sqrt{1-\varepsilon^2}(1-\varepsilon\cos(E))^{-1}dE \quad (4.177)$$

We can now insert Equations (4.176) and (4.177) into the integral in Equation (4.175) as

$$I_{c_3} = \int_{E_0}^{E} (1-\varepsilon^2)^{-3}(\cos(E)-\varepsilon)(1-\varepsilon\cos(E))^2(1-\varepsilon^2)^{\frac{1}{2}}(1-\varepsilon\cos(E))^{-1}dE \quad (4.178)$$

$$\begin{aligned} I_{c_3} &= (1-\varepsilon^2)^{-\frac{5}{2}} \int_{E_0}^{E} (\cos(E)-\varepsilon)(1-\varepsilon\cos(E))dE \\ &= (1-\varepsilon^2)^{-\frac{5}{2}} \int_{E_0}^{E} \left[(1+\varepsilon^2)\cos(E) - \varepsilon\cos(E)^2 - \varepsilon\right] dE \end{aligned} \quad (4.179)$$

and after some further manipulations and substitutions we obtain

$$\begin{aligned} I_{c_3} &= (1-\varepsilon^2)^{-\frac{5}{2}} \left[(1+\varepsilon^2)(\sin(E)-\sin(E_0)) \right. \\ &\quad \left. -\frac{\varepsilon}{2}\left(\sin(E)\cos(E) - \sin(E_0)\cos(E_0) + 3(E-E_0)\right)\right] \end{aligned} \quad (4.180)$$

By inserting the solved integrals in Equations (4.172) and (4.180) into Equation (4.171) and then into Equation (4.167) the out of plane particular solution can be written as

$$\mathbf{u}_{p_o}(\theta) = \frac{1}{mk^4} \begin{bmatrix} \sin(\theta) & \cos(\theta) \\ \cos(\theta) & -\sin(\theta) \end{bmatrix} \begin{bmatrix} I_{c_3}(E) \\ -I_{s_3}(\theta) \end{bmatrix} F_y \quad (4.181)$$

This expression is then added to the homogeneous solution found earlier and their sum transformed back into the time domain provides the complete solution.

For the in plane solution we need the transition matrix $\mathbf{\Phi}$ from Equation (4.85). From Equation (4.169) it is clear we do not need $\mathbf{\Phi}_0$ from Equation (4.88). We need to find $\mathbf{\Phi}^{-1}$ and we cannot use the results in Equation (4.90) as it was performed after simplifying conditions were applied.

The determinant of $\mathbf{\Phi}$ is the same as earlier in Equation (4.89) as the additional terms in the last column of $\mathbf{\Phi}$ in Equation (4.85) holding J cancel out to zero. A proof is provided in Section A.3.9.

Due to the structure of the $\mathbf{B}$ matrix we only need to find the lower two rows of the minor, which is needed to find the inverse. Only the terms containing J are different than those found earlier in Section A.3.7 and a careful inspection of Equation (4.85) reveals that elements of the last column, of the minor, are identical to earlier as no terms with J. This leads to the need of finding 6 new elements of the minor. The detailed computations can be found in Section A.3.10.

Using the elements of the minor in Section A.3.10, the cofactors and multiplying through by (-1) $\mathbf{\Phi}^{-1}$ yields, where $\star$ replaces arbitrary elements and we leave out the argument

$$\mathbf{\Phi}^{-1} = \frac{1}{1-\varepsilon^2} \begin{bmatrix} \star & \star & -(\varrho+1)\varepsilon\sin + 3\varrho^2 J & 2-\varepsilon\varrho\cos - 3\varepsilon\varrho\sin J \\ \star & \star & (\varrho+1)\sin - 3\varepsilon\varrho^2 J & \varrho\cos - 2\varepsilon + 3\varepsilon^2\varrho\sin J \\ \star & \star & (\varrho+1)\cos + \varepsilon & -\varrho\sin \\ \star & \star & -\varrho^2 & \varepsilon\varrho\sin \end{bmatrix} \quad (4.182)$$

The input matrix for the system in Equation (4.166) is of the form in the state space of Equation (4.16) and becomes including the input

$$\mathbf{B} = \frac{1}{mk^4}\begin{bmatrix} 0 & 0 \\ 0 & 0 \\ \frac{1}{\varrho^3} & 0 \\ 0 & \frac{1}{\varrho^3} \end{bmatrix}\begin{bmatrix} F_x \\ F_z \end{bmatrix} \tag{4.183}$$

and we can now compute the integrand of Equation (4.167) where $\mathbf{U} = \mathbf{\Phi}$ as earlier

$$\mathbf{U}(s)^{-1}\mathbf{B}(s) = \frac{1}{m(1-\varepsilon^2)k^4}\begin{bmatrix} -\frac{\varrho+1}{\varrho^3}\varepsilon\sin + \frac{3}{\varrho}J & \frac{2}{\varrho^3} - \varepsilon\frac{\cos}{\varrho^2} - 3\varepsilon\frac{\sin}{\varrho^2}J \\ \frac{\varrho+1}{\varrho^3}\sin - \frac{3\varepsilon}{\varrho}J & \frac{\cos}{\varrho^2} - \frac{2\varepsilon}{\varrho^3} + 3\varepsilon^2\frac{\sin}{\varrho^2}J \\ \frac{\varrho+1}{\varrho^3}\cos + \frac{\varepsilon}{\varrho^3} & -\frac{\sin}{\varrho^2} \\ -\frac{1}{\varrho} & \varepsilon\frac{\sin}{\varrho^2} \end{bmatrix}\begin{bmatrix} F_x \\ F_z \end{bmatrix} \tag{4.184}$$

By inspection of Equation (4.184) it is observed that 8 distinct integrals need to be solved to find the particular solution. Two of those are known from Equations (4.172) and (4.180). We will make use of splitting as follows $\frac{\varrho+1}{\varrho^3} = \frac{1}{\varrho^3} + \frac{1}{\varrho^2}$. The unknown integrals are

$$\int\frac{\sin}{\varrho^2},\ \int\frac{\cos}{\varrho^2},\ \int\frac{1}{\varrho^3},\ \int\frac{1}{\varrho},\ \int\frac{1}{\varrho}J,\ \int\frac{\sin}{\varrho^2}J \tag{4.185}$$

which will be found in the following leaving out the trivial intermediate algebraic manipulations and some of the obvious arguments.

We need the integral of J, which is defined in Equation (4.46) in Lemma 4.1 and solved for the time domain to a very simple form. A solution in terms of angle is more convenient here and needed in the many terms, so we solve it by substituting Equations (4.173) and (4.177) as

$$\begin{aligned} J(\theta) &= \int_{\theta_0}^{\theta}\frac{d\tau}{\varrho^2(\tau)} = (1-\varepsilon^2)^{-\frac{3}{2}}\int_{E_0}^{E}(1-\cos(E))dE \\ J(E) &= (1-\varepsilon^2)^{-\frac{3}{2}}\left[E-\varepsilon\sin(E)\right]_{E_0}^{E} = (1-\varepsilon^2)^{-\frac{3}{2}}\left[E-\varepsilon\sin(E)-E_0+\varepsilon\sin(E_0)\right] \\ J(E) &= (1-\varepsilon^2)^{-\frac{3}{2}}\left[E-\varepsilon\sin(E)+C_1\right] \quad \text{and} \quad C_1 = \varepsilon\sin(E_0) - E_0 \end{aligned} \tag{4.186}$$

We now proceed to solve the integrals listed in Equation (4.185).
Integral I_{s_2} becomes

$$I_{s_2}(\theta) = \int_{\theta_0}^{\theta}\frac{\sin(\theta)}{\varrho(\theta)^2}d\theta = \frac{1}{\varepsilon}\left[\frac{1}{\varrho} - \frac{1}{\varrho_0}\right] \tag{4.187}$$

Integral I_{c_2} becomes inserting Equations (4.173) and (4.177)

$$\begin{aligned} I_{c_2}(\theta) &= \int_{\theta_0}^{\theta}\frac{\cos(\theta)}{\varrho(\theta)^2}d\theta = \int_{E_0}^{E}f(E)dE = (1-\varepsilon^2)^{-\frac{3}{2}}\int_{E_0}^{E}(\cos(E)-\varepsilon)dE \\ I_{c_2}(E) &= (1-\varepsilon^2)^{-\frac{3}{2}}\left[\sin(E) - \sin(E_0) - \varepsilon(E-E_0)\right] \end{aligned} \tag{4.188}$$

Integral I_3 becomes, where the details for the solution can be found in Equation (A.58)

$$\begin{aligned} I_3(\theta) &= \int_{\theta_0}^{\theta} \frac{1}{\varrho(\theta)^3} d\theta = \int_{E_0}^{E} f(E)dE = (1-\varepsilon^2)^{-\frac{5}{2}} \int_{E_0}^{E} (1-\varepsilon\cos(E))^2 dE \\ I_3(E) &= (1-\varepsilon^2)^{-\frac{5}{2}} \left[(\frac{1}{2}\varepsilon^2+1)(E-E_0) + \frac{1}{2}\varepsilon^2(\sin(E)\cos(E) - \sin(E_0)\cos(E_0)) \right. \\ &\quad \left. -2\varepsilon(\sin(E)-\sin(E_0)) \right] \end{aligned} \tag{4.189}$$

Integral I_1 becomes

$$\begin{aligned} I_1(\theta) &= \int_{\theta_0}^{\theta} \frac{1}{\varrho(\theta)} d\theta = \int_{E_0}^{E} f(E)dE = (1-\varepsilon^2)^{-\frac{1}{2}} \int_{E_0}^{E} dE \\ I_1(E) &= (1-\varepsilon^2)^{-\frac{1}{2}} [E-E_0] \end{aligned} \tag{4.190}$$

Integral I_{1J} becomes, where the inner integral is solved in Equation (4.186)

$$I_{1J}(\theta) = \int_{\theta_0}^{\theta} \frac{J(\theta)}{\varrho(\theta)} d\theta = \int_{\theta_0}^{\theta} \frac{1}{\varrho(\theta)} \left(\int_{\theta_0}^{\theta} \frac{1}{\varrho(\tau)^2} d\tau \right) d\theta$$

We now insert Equation (4.186) and use the result of Equation (4.190)

$$\begin{aligned} I_{1J}(\theta) &= (1-\varepsilon^2)^{-\frac{1}{2}} (1-\varepsilon^2)^{-\frac{3}{2}} \int_{E_0}^{E} 1 \cdot (E - \varepsilon\sin(E) + C_1) dE \\ I_{1J}(E) &= (1-\varepsilon^2)^{-2} \left[\frac{1}{2}E^2 + \varepsilon\cos(E) + C_1 E \right]_{E_0}^{E} \\ I_{1J}(E) &= (1-\varepsilon^2)^{-2} \left[\frac{1}{2}(E^2-E_0^2) + \varepsilon(\cos(E)-\cos(E_0)) + C_1(E-E_0) \right] \end{aligned} \tag{4.191}$$

Integral $I_{s_{2J}}$ becomes, where the details for the solution can be found in Equation (A.59)

$$I_{s_{2J}}(\theta) = \int_{\theta_0}^{\theta} \frac{\sin(\theta)}{\varrho(\theta)^2} J(\theta) d\theta = \int_{\theta_0}^{\theta} \frac{\sin(\theta)}{\varrho(\theta)^2} \left(\int_{\theta_0}^{\theta} \frac{1}{\varrho(\tau)^2} d\tau \right) d\theta$$

$$\begin{aligned} I_{s_{2J}}(E) = (1-\varepsilon^2)^{-\frac{5}{2}} \Big[&\sin(E)(1+\frac{\varepsilon}{2}\cos(E)) - E(\frac{\varepsilon}{2}+\cos(E)) \\ &- \sin(E_0)(1+\frac{\varepsilon}{2}\cos(E_0)) + E_0(\frac{\varepsilon}{2}+\cos(E_0)) - C_1(\cos(E)-\cos(E_0)) \Big] \end{aligned} \tag{4.192}$$

We are now able to write the particular solution from Equation (4.167) in terms of the solved integrals as follows

$$\mathbf{u}_{p_i}(\theta) = \mathbf{U}(\theta) \frac{1}{mk^4(1-\varepsilon^2)} \begin{bmatrix} 3I_{1J} - \varepsilon(I_{s3}+I_{s2}) & 2I_3 - \varepsilon(I_{c2}+3I_{s_{2J}}) \\ I_{s3}+I_{s2} - 3\varepsilon I_{1J} & I_{c2} - \varepsilon(2I_3 - 3\varepsilon I_{s_{2J}}) \\ I_{c3}+I_{c2}+\varepsilon I_3 & -I_{s2} \\ -I_1 & \varepsilon I_{s2} \end{bmatrix} \begin{bmatrix} F_x \\ F_z \end{bmatrix} \tag{4.193}$$

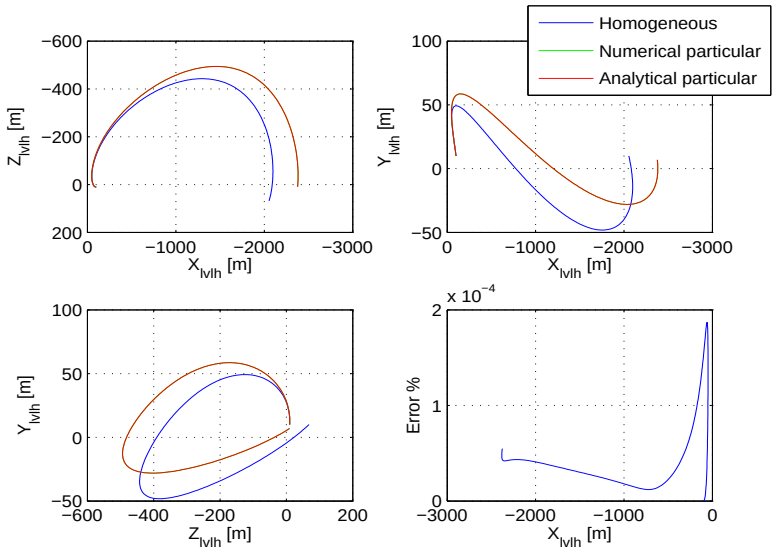

Figure 4.9: *A two pulse maneuver in elliptical orbit under the influence of a constant force in the $\mathcal{F}_o$ frame where $\mathbf{F} = [0.05, 0.1, 0.02]^T$ N and the initial conditions are $\mathbf{x}(0) = [-100, 10, 10]^T$ m and $\dot{\mathbf{x}}(0) = [0.1, 0.05, 0.01]^T$ m/s. The duration is one orbit and $\varepsilon = 0.1$ and $\theta_0 = 20$ deg. Note that the red curve is on top of the green curve.*

where Equation (4.193) depends directly on Equations (4.172), (4.180), (4.187), (4.188), (4.189), (4.190), (4.191) and (4.192) which need to be inserted.

In Figure 4.9 we see the comparison between using the homogeneous solution and the complete solution under the influence of a constant disturbance in the LVLH frame. The result is also compared to a numerical solution showing identical results. We observe that the error in Figure 4.9 is larger than in Figure 4.7. This is caused by the interpolation used between orbital points used for the numerical solution and a slightly less accurate orbital propagator. In summary the particular solution for the in and out of plane is

Out of plane:

$$\mathbf{u}_{p_o}(\theta) = \frac{1}{mk^4} \begin{bmatrix} \sin(\theta) & \cos(\theta) \\ \cos(\theta) & -\sin(\theta) \end{bmatrix} \begin{bmatrix} I_{c_3}(E) \\ -I_{s_3}(\theta) \end{bmatrix} F_y \tag{4.194}$$

In plane:

$$\mathbf{u}_{p_i}(\theta) = \mathbf{U}(\theta)\frac{1}{mk^4(1-\varepsilon^2)}\begin{bmatrix} 3I_{1J} - \varepsilon(I_{s3} + I_{s2}) & 2I_3 - \varepsilon(I_{c2} + 3I_{s_{2J}}) \\ I_{s3} + I_{s2} - 3\varepsilon I_{1J} & I_{c2} - \varepsilon(2I_3 - 3\varepsilon I_{s_{2J}}) \\ I_{c3} + I_{c2} + \varepsilon I_3 & -I_{s2} \\ -I_1 & \varepsilon I_{s2} \end{bmatrix}\begin{bmatrix} F_x \\ F_z \end{bmatrix} \tag{4.195}$$

The particular solution for the elliptical orbit will not reduce to the circular solution for $\varepsilon \to 0$ as it was the case for the homogeneous solution. This is caused by the term $\frac{1}{2\varepsilon}$ in e.g. Equation (4.172), which will approach ∞ and no form of $\frac{0}{0}$ or $\frac{\infty}{\infty}$ can be obtained to apply L'Hospitals reduction rules.

4.8.2 Constant Force in the Inertial Frame $\mathcal{F}_i$

As for the circular orbit in Section 4.7.2 we consider a constant force in the inertial frame $\mathcal{F}_i$ valid under the assumptions provided in Section 4.7.2.

Contrary to the circular case the argument of perigee γ does have an importance for elliptical orbits. We can nevertheless base the development on the true anomaly alone without loss of generality as γ is merely an offset angle.

The transformation in Equation (4.158) is equally valid for elliptical orbits and we will use that as a starting point.

As for the circular case the out of plane solution is minus the solution found in Equation (4.194) and we can proceed directly with the in plane solution.
The input matrix in Equation (4.183) together with the transformation of Equation (4.158) yield

$$\mathbf{B} = \frac{1}{mk^4}\begin{bmatrix} 0 & 0 \\ 0 & 0 \\ \frac{1}{\varrho^3} & 0 \\ 0 & \frac{1}{\varrho^3} \end{bmatrix}\begin{bmatrix} -\sin(\theta) & \cos(\theta) \\ -\cos(\theta) & -\sin(\theta) \end{bmatrix}\begin{bmatrix} k_x \\ k_y \end{bmatrix}$$

$$\mathbf{B} = \frac{1}{mk^4}\begin{bmatrix} 0 & 0 \\ 0 & 0 \\ -\frac{\sin(\theta)}{\varrho^3} & \frac{\cos(\theta)}{\varrho^3} \\ -\frac{\cos(\theta)}{\varrho^3} & -\frac{\sin(\theta)}{\varrho^3} \end{bmatrix}\begin{bmatrix} k_x \\ k_y \end{bmatrix} \tag{4.196}$$

Compared to earlier we now have couplings in the input matrix leading to higher complexity of the integrand $\mathbf{U}(s)^{-1}\mathbf{B}(s)$ in Equation (4.167) recalling that $\mathbf{U}(s)$ is the transition matrix , which we compute multiplying Equation (4.182) with Equation (4.196) leaving out the argument θ for convenience and expanding the term $\frac{\varrho+1}{\varrho^3}$ to simplify

$$\mathbf{U}(s)^{-1}\mathbf{B}(s) = \frac{1}{mk^4(1-\varepsilon^2)}\begin{bmatrix} \mathbf{B}_{41} & \mathbf{B}_{42} \end{bmatrix}\begin{bmatrix} k_x \\ k_y \end{bmatrix} \tag{4.197}$$

where

$$\mathbf{B}_{41} = \begin{bmatrix} \varepsilon\frac{\sin^2}{\varrho^3} + \varepsilon\frac{1}{\varrho^2} - 3\frac{\sin}{\varrho}J - 2\frac{\cos}{\varrho^3} + 3\varepsilon\frac{\sin\cos}{\varrho^2}J \\ -\frac{\sin^2}{\varrho^3} - \frac{1}{\varrho^2} + 3\varepsilon\frac{\sin}{\varrho}J + 2\varepsilon\frac{\cos}{\varrho^3} - 3\varepsilon^2\frac{\sin\cos}{\varrho^2}J \\ -\frac{\sin\cos}{\varrho^3} - \varepsilon\frac{\sin}{\varrho^3} \\ \frac{\sin}{\varrho} - \varepsilon\frac{\sin\cos}{\varrho^2} \end{bmatrix} \tag{4.198}$$

and

$$\mathbf{B}_{42} = \begin{bmatrix} -\varepsilon\frac{\sin\cos}{\varrho^3} + 3\frac{\cos}{\varrho}J - 2\frac{\sin}{\varrho^3} + 3\varepsilon\frac{\sin^2}{\varrho^2}J \\ \frac{\sin\cos}{\varrho^3} - 3\varepsilon\frac{\cos}{\varrho}J + 2\varepsilon\frac{\sin}{\varrho^3} - 3\varepsilon^2\frac{\sin^2}{\varrho^2}J \\ \frac{\cos^2}{\varrho^3} + \frac{1}{\varrho^2} + \varepsilon\frac{\cos}{\varrho^3} \\ -\frac{\cos}{\varrho} - \varepsilon\frac{\sin^2}{\varrho^2} \end{bmatrix} \tag{4.199}$$

It is observed that Equation (4.197) contains 14 distinct integrals of which 2 are known from the LVLH solution in Section 4.8.1. The additional unknown integrals are

$$\int\frac{\sin^2}{\varrho^3},\ \int\frac{\sin}{\varrho},\ \int\frac{\sin\cos}{\varrho^3},\ \int\frac{\sin^2}{\varrho^2},\ \int\frac{1}{\varrho^2},\ \int\frac{\sin\cos}{\varrho^2},\ \int\frac{\cos^2}{\varrho^3},\ \int\frac{\cos}{\varrho} \tag{4.200}$$

$$\int\frac{\sin}{\varrho}J,\ \int\frac{\sin\cos}{\varrho^2}J,\ \int\frac{\cos}{\varrho}J,\ \int\frac{\sin^2}{\varrho^2}J \tag{4.201}$$

which will be solved in the following leaving out most intermediate manipulations. Integral $I_{s_{32}}$ becomes using the substitutions of Equations (4.173) and (4.177) to obtain an integrand $f(E)$, which is a function of the eccentric anomaly, where the detailed computations can be found in Equation (A.60)

$$\begin{aligned} I_{s_{32}}(\theta) &= \int_{\theta_0}^{\theta}\frac{\sin(\theta)^2}{\varrho(\theta)^3}d\theta = \int_{E_0}^{E} f(E)dE \\ I_{s_{32}}(E) &= \frac{1}{2}(1-\varepsilon^2)^{-\frac{3}{2}}\left[E - E_0 - (\sin(E)\cos(E) - \sin(E_0)\cos(E_0))\right] \end{aligned} \tag{4.202}$$

Integral I_{s_1} becomes

$$\begin{aligned} I_{s_1}(\theta) &= \int_{\theta_0}^{\theta}\frac{\sin(\theta)}{\varrho(\theta)}d\theta = \left[-\frac{1}{\varepsilon}\ln(1+\varepsilon\cos)\right]_{\theta_0}^{\theta} \\ I_{s_1}(\theta) &= \frac{1}{\varepsilon}\left[\ln(1+\varepsilon\cos(\theta_0) - \ln(1+\varepsilon\cos(\theta))\right] \end{aligned} \tag{4.203}$$

Integral I_{sc_3} becomes, where the detailed computations can be found in Equation (A.61)

$$\begin{aligned} I_{sc_3}(\theta) &= \int_{\theta_0}^{\theta}\frac{\sin(\theta)\cos(\theta)}{\varrho(\theta)^3}d\theta = \int_{E_0}^{E} f(E)dE \\ I_{sc_3}(E) &= (1-\varepsilon^2)^{-2}\left[\frac{1}{2}(\sin(E)^2 - \sin(E_0)^2) + \varepsilon(\cos(E) - \cos(E_0))\right] \end{aligned} \tag{4.204}$$

Integral $I_{s_{22}}$ becomes, where integral tables are used to obtain the solution

$$\begin{aligned}
I_{s_{22}}(\theta) &= \int_{\theta_0}^{\theta} \frac{\sin(\theta)^2}{\varrho(\theta)^2} d\theta \\
I_{s_{22}}(\theta) &= \frac{1}{\varepsilon^2}\left[\varepsilon\frac{\sin}{\varrho} - \theta + 2\frac{1}{\sqrt{1-\varepsilon^2}}\arctan\left(\frac{1-\varepsilon}{\sqrt{1-\varepsilon^2}}\tan\left(\frac{\theta}{2}\right)\right)\right]_{\theta_0}^{\theta} \\
I_{s_{22}}(\theta) &= \frac{1}{\varepsilon^2}\left[\varepsilon\left(\frac{\sin(\theta)}{\varrho} - \frac{\sin(\theta_0)}{\varrho_0}\right) - (\theta-\theta_0)\right. \\
&\quad +2\frac{1}{\sqrt{1-\varepsilon^2}}\left\{\arctan\left(\frac{1-\varepsilon}{\sqrt{1-\varepsilon^2}}\tan\left(\frac{\theta}{2}\right)\right)\right. \\
&\quad \left.\left. -\arctan\left(\frac{1-\varepsilon}{\sqrt{1-\varepsilon^2}}\tan\left(\frac{\theta_0}{2}\right)\right)\right\}\right]
\end{aligned} \tag{4.205}$$

Integral I_{sc_2} becomes, where the detailed computations can be found in Equation (A.62)

$$\begin{aligned}
I_{sc_2}(\theta) &= \int_{\theta_0}^{\theta} \frac{\sin(\theta)\cos(\theta)}{\varrho(\theta)^2} d\theta \\
I_{sc_2}(\theta) &= -\frac{1}{\varepsilon^2}\left[\frac{1}{\varrho} + \ln(\varrho) - \left(\frac{1}{\varrho_0} + \ln(\varrho_0)\right)\right]
\end{aligned} \tag{4.206}$$

Integral $I_{c_{32}}$ becomes, where the detailed computations can be found in Equation (A.63)

$$\begin{aligned}
I_{c_{32}}(\theta) &= \int_{\theta_0}^{\theta} \frac{\cos(\theta)^2}{\varrho(\theta)^3} d\theta = \int_{E_0}^{E} f(E)dE \\
I_{c_{32}}(E) &= (1-\varepsilon^2)^{-\frac{5}{2}}\left[\left(\frac{1}{2}+\varepsilon^2\right)(E-E_0) - 2\varepsilon(\sin(E)-\sin(E_0))\right. \\
&\quad \left. +\frac{1}{4}(\sin(2E)-\sin(2E_0))\right]
\end{aligned} \tag{4.207}$$

Integral I_{c_1} becomes, where the detailed computations can be found in Equation (A.64)

$$\begin{aligned}
I_{c_1}(\theta) &= \int_{\theta_0}^{\theta} \frac{\cos(\theta)}{\varrho(\theta)} d\theta \\
I_{c_1}(\theta) &= \frac{1}{\varepsilon}\left[\theta - \theta_0 - \frac{2}{\sqrt{1-\varepsilon^2}}\left\{\arctan\left(\frac{1-\varepsilon}{\sqrt{1-\varepsilon^2}}\tan\left(\frac{\theta}{2}\right)\right)\right.\right. \\
&\quad \left.\left. -\arctan\left(\frac{1-\varepsilon}{\sqrt{1-\varepsilon^2}}\tan\left(\frac{\theta_0}{2}\right)\right)\right\}\right]
\end{aligned} \tag{4.208}$$

The above provides the analytical solutions to all the integrals in Equation (4.200). The remaining ones in Equation (4.201) are significantly more difficult and as an illustration the first one from the four in Equation (4.201) will be considered. We perform the change of variable to the eccentric anomaly as earlier using Equations (4.173)

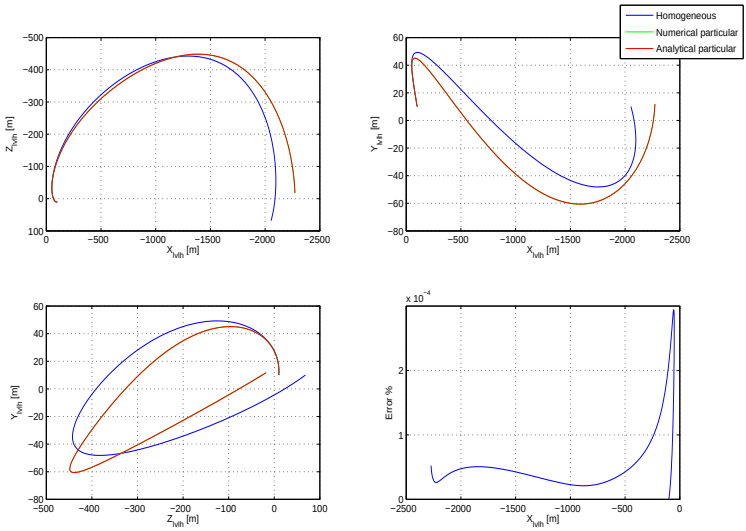

Figure 4.10: *A two pulse maneuver in elliptical orbit under the influence of a constant inertial force in the $\mathcal{F}_i$ frame where $\mathbf{F} = [0.05, -0.1, 0.02]^T$ N and the initial conditions are $\mathbf{x}(0) = [-100, 10, 10]^T$ m and $\dot{\mathbf{x}}(0) = [0.1, 0.05, 0.01]^T$ m/s. The duration is one orbit and $\varepsilon = 0.1$ and $\theta_0 = 20$ deg. Note that the red curve is on top of the green curve.*

and (4.177) and obtain

$$
\begin{aligned}
I_{s_{1J}}(\theta) &= \int_{\theta_0}^{\theta} \frac{\sin(\theta)}{\varrho(\theta)} J(\theta) d\theta = \int_{\theta_0}^{\theta} \frac{\sin(\theta)}{\varrho(\theta)} \left(\int_{\theta_0}^{\theta} \frac{1}{\varrho(\tau)^2} d\tau \right) d\theta = \int_{E_0}^{E} f(E) dE \\
I_{s_{1J}}(E) &= (1-\varepsilon^2)^{-\frac{3}{2}} \int_{E_0}^{E} \frac{\sin(E)(E - \varepsilon \sin(E) + C_1)}{1 - \varepsilon \cos(E)} dE \\
I_{s_{1J}}(E) &= (1-\varepsilon^2)^{-\frac{3}{2}} \left[\int_{E_0}^{E} \frac{E \sin(E)}{1 - \varepsilon \cos(E)} dE - \varepsilon \int_{E_0}^{E} \frac{\sin(E)^2}{1 - \varepsilon \cos(E)} dE \right. \\
&\quad \left. + C_1 \int_{E_0}^{E} \frac{\sin(E)}{1 - \varepsilon \cos(E)} dE \right] \qquad (4.209)
\end{aligned}
$$

It is observed that the first term of Equation (4.209) has a numerator with trigonometric functions multiplied by their own argument and the integral is only tractable in the form of hypergeometric polylogarithmic functions (Wolfram 1999). Such functions are complex infinite power series (Gradshteyn & Ryzhik 2007) and prohibit a closed form analytical solution.

The other integrals in Equation (4.201) contain integrals of the same form, all with

the same denominator as in Equation (4.209). The distinct intractable ones have numerators N_i of the form

$$N_1 = E,\ N_2 = E\sin(E),\ N_3 = E\sin(E)\cos(E),\ N_4 = E\cos(E) \text{ and } N_5 = E\sin(E)^2 \tag{4.210}$$

whereas the remaining integrals, not expanded here, are tractable.

An attempt to solve Equation (4.201) directly in the θ domain has been performed. This leads to integrals with integrands of the form of Equation (4.208), which turn out to be intractable (Wolfram 1999). This leaves a mathematically intractable problem to which either analytical approximations need to be developed or numerical solutions applied. In order to demonstrate that the approach taken here leads to a correct and complete solution, the few intractable integrals will be found numerically and applied to the final solution.

We are now able to write the particular solution from Equations (4.197) and (4.167) in terms of the solved integrals as follows

$$\mathbf{u}_{p_i}(\theta) = \mathbf{U}(\theta)\frac{1}{mk^4(1-\varepsilon^2)}\mathbf{F}(\theta, E)\begin{bmatrix} k_x \\ k_y \end{bmatrix} \tag{4.211}$$

and

$$\mathbf{F}(\theta, E) = \begin{bmatrix} \varepsilon(I_{s_{32}}+J+3I_{sc_{2J}})-3I_{s_{1J}}-2I_{c_3} & \varepsilon(3I_{s_{22J}}-I_{sc_3})+3I_{c_{1J}}-2I_{s_3} \\ \varepsilon(3I_{s_{1J}}+2I_{c_3}-3\varepsilon I_{sc_{2J}})-I_{s_{32}}-J & \varepsilon(2I_{s_3}-3I_{c_{1J}}-3\varepsilon I_{s_{22J}})+I_{sc_3} \\ -I_{sc_3}-\varepsilon I_{s_3} & I_{c_{32}}+J+\varepsilon I_{c_3} \\ I_{s_1}-\varepsilon I_{sc_2} & -I_{c_1}-\varepsilon I_{s_{22}} \end{bmatrix} \tag{4.212}$$

where Equation (4.212) depends directly on Equations (4.172), (4.180), (4.186),(4.202), (4.203), (4.204), (4.205), (4.206), (4.207), (4.208) and solutions of Equation (4.201).

In Figure 4.10 we see a comparison using the homogeneous solution and the complete solution under the influence of a constant force in the inertial frame, which is typically the solar radiation pressure. The result is also compared to a numerical solution showing identical results. The errors shown are very similar to the elliptical LVLH solution in Figure 4.9. In summary the particular solution for the in and out of plane is

Out of plane:

$$\mathbf{u}_{p_o}(\theta) = \frac{1}{mk^4}\begin{bmatrix} \sin(\theta) & \cos(\theta) \\ \cos(\theta) & -\sin(\theta) \end{bmatrix}\begin{bmatrix} -I_{c_3}(E) \\ I_{s_3}(\theta) \end{bmatrix} k_z \tag{4.213}$$

In plane:

$$\mathbf{u}_{p_i}(\theta) = \mathbf{U}(\theta)\frac{1}{mk^4(1-\varepsilon^2)}$$

$$\begin{bmatrix} \varepsilon(I_{s_{32}}+J+3I_{sc_{2J}})-3I_{s_{1J}}-2I_{c_3} & \varepsilon(3I_{s_{22J}}-I_{sc_3})+3I_{c_{1J}}-2I_{s_3} \\ \varepsilon(3I_{s_{1J}}+2I_{c_3}-3\varepsilon I_{sc_{2J}})-I_{s_{32}}-J & \varepsilon(2I_{s_3}-3I_{c_{1J}}-3\varepsilon I_{s_{22J}})+I_{sc_3} \\ -I_{sc_3}-\varepsilon I_{s_3} & I_{c_{32}}+J+\varepsilon I_{c_3} \\ I_{s_1}-\varepsilon I_{sc_2} & -I_{c_1}-\varepsilon I_{s_{22}} \end{bmatrix}\begin{bmatrix} k_x \\ k_y \end{bmatrix} \tag{4.214}$$

4.9 Conclusion

The general nonlinear dynamics relative motion equations for any Keplerian orbit are formulated in a rotating LVLH coordinate frame. These are linearized around the target passive motion and linear differential equations result for the coupled in plane motion and the out of plane one. This reflects the part formulated in point 1 of Section 1.3.

This set of differential equations is solved for the homogeneous solution to form the general state transition matrix. The key to the non trivial solution of the in plane coupled equations is formulated in Lemma 4.1 followed by the proof. This solution is valid for any closed Keplerian orbit, is free of any singularities and reduces to the well known Clohessy Wiltshire equations for circular orbits.

Particular solutions are found for arbitrary constant forces in both the LVLH frame as in the inertial frame. This provides solutions for relative drag and solar radiation pressure disturbances. Contribution 2 from Section 1.3 is hereby reflected.

Based upon the general state transition matrix, general expressions for two pulse impulsive maneuvers are derived for both the elliptical as well as the circular case in Section 4.6 and 4.5 respectively. They are available for both R-bar and V-bar maneuvers and reflect point 3 in Section 1.3.

These solutions have recently been successfully demonstrated with in flight experiments by the French National Space Agency (CNES) on the Swedish RendezVous and Formation Flying technology demonstration mission *Prisma*.

Chapter 5

Attitude and Coupled Model Dynamics and Kinematics

This chapter contains the development of the nonlinear attitude models for simulation and their linear counterparts for design purposes mainly. In addition to the pure attitude models, the coupled attitude and position linear model will be included as well. It should be noted that the notation for small and large signal variables often will be the same to keep the number low, but will be clear from the context.

5.1 Nonlinear Dynamics

The torque vector $\mathbf{N}$ can be expressed in a rotating frame as (Symon 1979)

$$\mathbf{N} = \frac{d^*(\mathbf{I}\boldsymbol{\omega}^*)}{dt} + \boldsymbol{\omega} \times \mathbf{I}\boldsymbol{\omega}^* \tag{5.1}$$

where $\mathbf{I}$ is the inertia matrix and $\boldsymbol{\omega}$ the inertial angular velocity vector. As $\boldsymbol{\omega}$ is also the angular velocity of the rotating frame $\boldsymbol{\omega}^* = \boldsymbol{\omega}$. If we also consider the rotating frame fixed to the body, the inertia matrix is constant and we can express Equation (5.1) in the body frame as

$$\boxed{\mathbf{I}\dot{\boldsymbol{\omega}} + \boldsymbol{\omega} \times \mathbf{I}\boldsymbol{\omega} = \mathbf{N}} \tag{5.2}$$

In the special case of the body axes being along the principal axes of inertia, the inertia matrix $\mathbf{I}$ is diagonal and Equation (5.2) becomes

$$\begin{aligned} I_x\dot{\omega}_x + (I_z - I_y)\omega_z\omega_y &= N_x \\ I_y\dot{\omega}_y + (I_x - I_z)\omega_x\omega_z &= N_y \\ I_z\dot{\omega}_z + (I_y - I_x)\omega_y\omega_x &= N_z \end{aligned} \tag{5.3}$$

From Equation (5.3) we see that a body cannot spin with constant angular velocity $\boldsymbol{\omega}$, except about a principal axis, unless external torques are applied. If $\dot{\boldsymbol{\omega}} = \mathbf{0}$ Equa-

tion (5.2) becomes $\boldsymbol{\omega} \times \mathbf{I}\boldsymbol{\omega} = \mathbf{N}$ and the left member is zero only if $\mathbf{I}\boldsymbol{\omega}$ is parallel to $\boldsymbol{\omega}$, that is, if $\boldsymbol{\omega}$ is along a principal axis of the body.

5.2 Linear Dynamics

We now derive a linear model of Equation (5.2) around a general operating point, $\boldsymbol{\omega}_{oi} = [\omega_x, \omega_y, \omega_z]^{\mathrm{T}}$ being the angular rate of the orbital frame. As angular velocity vectors are cumulative we can write the inertial angular velocity as

$$\boldsymbol{\omega} = \boldsymbol{\omega}_{bci} = \boldsymbol{\omega}_{bco} + \boldsymbol{\omega}_{oi} \tag{5.4}$$

We will perform a Taylor series expansion of Equation (5.2) around the operating point, noting that Equation (5.2) is a function of two variables, namely $\boldsymbol{\omega}$ and $\mathbf{N}$. The form of the Taylor series is as in Equation (4.8). Inserting Equation (5.2) into the two variables of Equation (4.8) we can write it as

$$\mathbf{I}\dot{\boldsymbol{\omega}} = \mathbf{N}_0 - \boldsymbol{\omega}_0 \times \mathbf{I}\boldsymbol{\omega}_0 + \left.\frac{\partial \mathbf{I}\dot{\boldsymbol{\omega}}}{\partial \boldsymbol{\omega}}\right|_{\boldsymbol{\omega}_0, \mathbf{N}_0} (\boldsymbol{\omega} - \boldsymbol{\omega}_0) + \left.\frac{\partial \mathbf{I}\dot{\boldsymbol{\omega}}}{\partial \mathbf{N}}\right|_{\boldsymbol{\omega}_0, \mathbf{N}_0} (\mathbf{N} - \mathbf{N}_0) \tag{5.5}$$

where $\mathbf{N}_0 = \mathbf{0}$, $\boldsymbol{\omega} - \boldsymbol{\omega}_0 = \boldsymbol{\omega}_{bco}$ and $\mathbf{N}_0 - \boldsymbol{\omega}_0 \times \mathbf{I}\boldsymbol{\omega}_0 = \mathbf{I}\dot{\boldsymbol{\omega}}_0$. The second Jacobian obviously becomes the identity matrix and the first Jacobian is derived in detail in Chapter B.2.

Inserting the operating point $\boldsymbol{\omega}_{oi} = [0, -\omega_0, 0]^{\mathrm{T}}$ into the general Equation (B.7) and the result from Equation (B.8) into Equation (5.5) and multiplying through with the inverse inertia matrix we obtain

$$\dot{\boldsymbol{\omega}}_{bco} = \omega_0 \mathbf{I}^{-1} \begin{bmatrix} I_{31} & 2I_{32} & I_{33} - I_{22} \\ -I_{32} & 0 & I_{12} \\ I_{22} - I_{11} & -2I_{12} & -I_{13} \end{bmatrix} \boldsymbol{\omega}_{bco} + \mathbf{I}^{-1}\mathbf{N} \tag{5.6}$$

$$\boxed{\dot{\boldsymbol{\omega}}_{bco} = \mathbf{A}_d \boldsymbol{\omega}_{bco} + \mathbf{B}_d \mathbf{N}} \tag{5.7}$$

If we are close to the principal axes of the body, the inertia matrix becomes diagonal, and Equation (5.6) will then reduce to the following simpler uncoupled equation

$$\dot{\boldsymbol{\omega}}_{bco} = \begin{bmatrix} 0 & 0 & \omega_0 \frac{I_{33} - I_{22}}{I_{11}} \\ 0 & 0 & 0 \\ \omega_0 \frac{I_{22} - I_{11}}{I_{33}} & 0 & 0 \end{bmatrix} \boldsymbol{\omega}_{bco} + \begin{bmatrix} \frac{1}{I_{11}} & 0 & 0 \\ 0 & \frac{1}{I_{22}} & 0 \\ 0 & 0 & \frac{1}{I_{33}} \end{bmatrix} \mathbf{N} \tag{5.8}$$

5.3 Nonlinear Kinematics based on Euler Angles

For the kinematics we seek the differential equations of the motion of the body frame with respect to the reference frame, relating the Euler(3,2,1) angles with the angular velocity vector $\boldsymbol{\omega}_{bco}$.

The $\boldsymbol{\omega}_{bco}$ between the frames is the sum of the individual rotation rates, referred and added in the final frame. Using the individual rotation matrices from the Euler(3,2,1) rotation in Equation (B.2) we can write $\boldsymbol{\omega}_{bco}$ as a function of the rate of the Euler angles. The inverse relationship becomes (Wie 1998)

$$\boxed{\begin{bmatrix} \dot{\theta}_x \\ \dot{\theta}_y \\ \dot{\theta}_z \end{bmatrix} = \frac{1}{\cos(\theta_y)} \begin{bmatrix} \cos(\theta_y) & \sin(\theta_x)\sin(\theta_y) & \cos(\theta_x)\sin(\theta_y) \\ 0 & \cos(\theta_x)\cos(\theta_y) & -\sin(\theta_x)\cos(\theta_y) \\ 0 & \sin(\theta_x) & \cos(\theta_x) \end{bmatrix} \boldsymbol{\omega}_{bco}} \quad (5.9)$$

5.4 Nonlinear Kinematics based on Quaternions

The kinematic motion can also be described by means of quaternions or Euler parameters as they are also called. The advantage is that there are no singularities in the formalism of describing a rotation of one coordinate system into another one. We will use the following definition, which is the most utilized in European space programs.

$$\mathbf{q} = \begin{bmatrix} \cos(\frac{\theta}{2}) \\ e_1 \sin(\frac{\theta}{2}) \\ e_2 \sin(\frac{\theta}{2}) \\ e_3 \sin(\frac{\theta}{2}) \end{bmatrix} \quad (5.10)$$

where $\mathbf{e} = [e_1, e_2, e_3]^{\mathrm{T}}$ is the Euler rotational eigen axis, which is indifferent in the two coordinate systems and θ is the angle rotated around the eigenvector $\mathbf{e}$. The eigenvector $\mathbf{e}$ can be found from differencing the symmetric off diagonal elements of the DCM, see also (Junkins & Turner 1986).

In Equation (5.11) we find the general relationship between the angular rate vector and the derivative of the quaternion

$$\dot{\mathbf{q}} = \frac{1}{2} \begin{bmatrix} 0 & -\omega_x & -\omega_y & -\omega_z \\ \omega_x & 0 & \omega_z & -\omega_y \\ \omega_y & -\omega_z & 0 & \omega_x \\ \omega_z & \omega_y & -\omega_x & 0 \end{bmatrix} \mathbf{q} \quad (5.11)$$

which is the general quaternion differential equation, see also (Junkins & Turner 1986). For the present application we have that $\boldsymbol{\omega} = \boldsymbol{\omega}_{bco}$ and $\mathbf{q} = \mathbf{q}_{bco}$. This formulation will be used for simulation purposes.

In Section B.4 can be found the basic equations for the needed quaternion algebra and transformations to and from DCM and Euler angles as well as a short derivation leading to Equation (5.11).

5.5 Linear Kinematics

It will be advantageous to obtain a model, which supports an in plane rotational offset, for which reason it shall be parameterized with an operating point on the y-axis different

from the more common zero. In Equation (5.9) we have the input output relation we need for the kinematics. $\boldsymbol{\omega}_{bco}$ in Equation (5.9) is already expressed in the body frame, as it also is in Equation (5.7), with which we later combine it.

As Equation (5.9) describes the kinematics between any two arbitrary frames, we are not constrained by absolute inertial relationships as for the dynamics. This means we will linearize the kinematics around the orbital frame as before, but the operating point is not with respect to inertial space, but the orbital frame.

Using the form of Equation (4.8) we can linearize Equation (5.9) as

$$\dot{\boldsymbol{\theta}} = \dot{\boldsymbol{\theta}}_0 + \left.\frac{\partial \dot{\boldsymbol{\theta}}}{\partial \boldsymbol{\theta}}\right|_{\boldsymbol{\omega}_0, \boldsymbol{\theta}_0} (\boldsymbol{\theta} - \boldsymbol{\theta}_0) + \left.\frac{\partial \dot{\boldsymbol{\theta}}}{\partial \boldsymbol{\omega}}\right|_{\boldsymbol{\omega}_0, \boldsymbol{\theta}_0} (\boldsymbol{\omega} - \boldsymbol{\omega}_0) \tag{5.12}$$

and the operating point is then $\boldsymbol{\theta}_0 = [0, \theta_0, 0]^{\mathrm{T}}$ and $\boldsymbol{\omega}_0 = \mathbf{0}$. As the angular rate multiplies all in Equation (5.9), the first Jacobian will always be zero for this operating point. The second Jacobian in Equation (5.12) becomes the identity matrix and the first term in Equation (5.12) is zero. We can now formulate the linear kinematics in state space form as

$$\dot{\boldsymbol{\theta}} = \mathbf{0}\boldsymbol{\theta} + \mathbf{I}\boldsymbol{\omega}_{bco} \tag{5.13}$$

$$\boxed{\dot{\boldsymbol{\theta}} = \mathbf{A}_k\boldsymbol{\theta} + \mathbf{B}_k\boldsymbol{\omega}_{bco}} \tag{5.14}$$

5.6 Linear Attitude Model

Let us define a state vector for the attitude motion $\mathbf{x}_c = [\theta_x, \theta_y, \theta_z, \omega_{bco_x}, \omega_{bco_y}, \omega_{bco_z}]^{\mathrm{T}}$ which enables us to combine Equations (5.7) and (5.14) into a complete linear attitude model yielding

$$\dot{\mathbf{x}}_c = \begin{bmatrix} \mathbf{A}_k & \mathbf{B}_k \\ \mathbf{0}_{3\times3} & \mathbf{A}_d \end{bmatrix} \mathbf{x}_c + \begin{bmatrix} \mathbf{0}_{3\times3} \\ \mathbf{B}_d \end{bmatrix} \mathbf{N} \tag{5.15}$$

$$\boxed{\dot{\mathbf{x}}_c = \mathbf{A}_c\mathbf{x}_c + \mathbf{B}_c\mathbf{N}} \tag{5.16}$$

It shall be observed that the linear model in the operating point is unstable by nature for non spherical bodies with inertia diagonal elements monotonously increasing or decreasing, as the matrix $\mathbf{A}_d$ typically contributes a real pole in the right half plane. This appears in the region of 10^{-4}.

5.7 Coupled Attitude and Position Model

For close proximity maneuvers are not only the relative COM position of interest, but also the position and velocity between two docking ports, which are located elsewhere on the spacecraft.

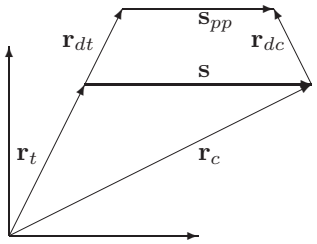

Figure 5.1: *Illustration of the vectors involved to determine the COM to COM location and the port to port location in the general vector space.*

Consequently there is an interest and need for a linear model of the port to port dynamics and kinematics, which includes all the possible couplings in the system. Such a model will be developed in this section grouping together elementary models and couplings, keeping in mind that there is only control authority on the chaser spacecraft in the form of forces and torques, not on the target.

Strictly speaking one should perform a nonlinear formulation of $\mathbf{s}_{pp}$ referencing inertial, but an insignificant approximation will be made using the already linear and known vector $\mathbf{s}$. The port to port distance can be expressed as

$$\mathbf{s}_{pp} = \mathbf{s} + \mathbf{r}_{dc} - \mathbf{r}_{dt} \tag{5.17}$$

We will have to linearize $\mathbf{s}_{pp}$ around the various operating points noting that $\mathbf{s}$ is already known from Equation (4.15). Therefore, only the last two terms need to be linearized and it shall be noticed that the large signal will be needed to calculate a physical meaningful $\mathbf{s}_{pp}$ and not only the variations around nominal.

5.7.1 Target Attitude

Seen from a control point of view the target is uncontrollable, but as the attitude motion of the target influences the docking port motion, the attitude modes need to be modeled.

The attitude motion of the target is described in Section 3.2.1 as a saw tooth type of motion resulting from a two sided thrust reversal type of controller on the Russian segments of the ISS. This is nonlinear, but can be well approximated with a sinus motion. This can be modeled by a harmonic oscillator for the i^{th} axis, with θ_{t_i} being the small signal motion off the operating point

$$\ddot{\theta}_{t_i} + k_i^2 \theta_{t_i} = 0 \tag{5.18}$$

for which we chose the motion to be a sinusoid, leading to the initial conditions of $\theta_{t_i}(0) = A\cos(\varphi)$ and $\dot{\theta}_{t_i}(0) = -A\omega\sin(\varphi)$, where A being the amplitude, $\varphi = -2\pi\frac{t_{start}+0.5d}{T_t}$ and t_{start} is the time of the first amplitude of the nonlinear motion in Section 3.2.1. The period of the motion is known from Section 3.2.1 Table 3.2 to be $T_t = \frac{4A}{v_t} + d$ and the eigen frequency in Equation (5.18) can be computed as

$$k = \frac{2\pi}{T_t} = \frac{2\pi v_t}{4A + dv_t} \tag{5.19}$$

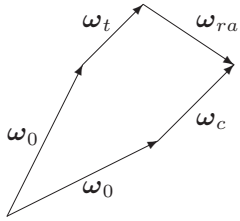

Figure 5.2: *All angular rate vectors from inertial frame to chaser docking port.*

In state space form for the 3 axes the model becomes with $\mathbf{x}_t = [\boldsymbol{\theta}_t, \boldsymbol{\omega}_t]^{\mathrm{T}}$

$$\dot{\mathbf{x}}_t = \begin{bmatrix} 0 & 0 & 0 & 1 & 0 & 0 \\ 0 & 0 & 0 & 0 & 1 & 0 \\ 0 & 0 & 0 & 0 & 0 & 1 \\ -k_x^2 & 0 & 0 & 0 & 0 & 0 \\ 0 & -k_y^2 & 0 & 0 & 0 & 0 \\ 0 & 0 & -k_z^2 & 0 & 0 & 0 \end{bmatrix} \mathbf{x}_t \tag{5.20}$$

$$\boxed{\dot{\mathbf{x}}_t = \mathbf{A}_t \mathbf{x}_t} \tag{5.21}$$

5.7.2 Relative Attitude

The relative attitude between the two spacecraft need to be based on the angular rate vectors, as the Euler angles are not cumulative. This is illustrated in Figure 5.2, where we have that $\boldsymbol{\omega}_0 + \boldsymbol{\omega}_t + \boldsymbol{\omega}_{ra} = \boldsymbol{\omega}_0 + \boldsymbol{\omega}_c$ and we get directly

$$\boldsymbol{\omega}_{ra} = \boldsymbol{\omega}_c - \boldsymbol{\omega}_t \tag{5.22}$$

where $\boldsymbol{\omega}_{ra}$ is the relative angular rate. $\boldsymbol{\omega}_t$ is known in the orbital frame and needs to be transformed into the chaser body frame, where $\boldsymbol{\omega}_c$ is known and where we will represent the relative rate $\boldsymbol{\omega}_{ra}$. Equation (5.22) in the chaser body frame becomes

$$\boldsymbol{\omega}_{ra} = \boldsymbol{\omega}_c - \mathbf{R}_{bco}\boldsymbol{\omega}_t \tag{5.23}$$

Equation (5.9) can be used to express the rate of the relative Euler angles as $\dot{\boldsymbol{\theta}}_{ra} = f(\boldsymbol{\theta}_{ra}, \boldsymbol{\omega}_{ra})$ and inserting Equation (5.23) it becomes a function of 4 variables $\dot{\boldsymbol{\theta}}_{ra} = f(\boldsymbol{\theta}_{ra}, \boldsymbol{\theta}_c, \boldsymbol{\omega}_c, \boldsymbol{\omega}_t)$. All operating points are zero except for $\boldsymbol{\theta}_{c_0} = [0, \theta_0, 0]^{\mathrm{T}}$ as earlier. Inserting Equation (5.23) into Equation (5.9) we obtain using the notation that $s_i = \sin(\theta_i)$, $c_i = \cos(\theta_i)$ and $i = x, y, z$

$$\dot{\boldsymbol{\theta}}_{ra} = \frac{1}{c_y} \underbrace{\begin{bmatrix} c_y & s_x s_y & c_x s_y \\ 0 & c_x c_y & -s_x c_y \\ 0 & s_x & c_x \end{bmatrix}}_{g(\boldsymbol{\theta}_{ra})} \boldsymbol{\omega}_c$$

$$-\frac{1}{c_y} \underbrace{\begin{bmatrix} c_y & s_x s_y & c_x s_y \\ 0 & c_x c_y & -s_x c_y \\ 0 & s_x & c_x \end{bmatrix}}_{g(\boldsymbol{\theta}_{ra})} \underbrace{\begin{bmatrix} c_z c_y & c_y s_z & -s_y \\ s_x s_y c_z - c_x s_z & s_x s_y s_z + c_x c_z & s_x c_y \\ c_x s_y c_z + s_x s_z & c_x s_y s_z - s_x c_z & c_x c_y \end{bmatrix}}_{g(\boldsymbol{\theta}_c)} \boldsymbol{\omega}_t \quad (5.24)$$

We will now perform a linearization of Equation (5.24) as

$$\begin{aligned} \dot{\boldsymbol{\theta}}_{ra} &= \dot{\boldsymbol{\theta}}_{ra_0} + \left.\frac{\partial \dot{\boldsymbol{\theta}}_{ra}}{\partial \boldsymbol{\theta}_{ra}}\right|_{op} (\boldsymbol{\theta}_{ra} - \boldsymbol{\theta}_{ra_0}) + \left.\frac{\partial \dot{\boldsymbol{\theta}}_{ra}}{\partial \boldsymbol{\theta}_c}\right|_{op} (\boldsymbol{\theta}_c - \boldsymbol{\theta}_{c_0}) \\ &\quad + \left.\frac{\partial \dot{\boldsymbol{\theta}}_{ra}}{\partial \boldsymbol{\omega}_c}\right|_{op} (\boldsymbol{\omega}_c - \boldsymbol{\omega}_{c_0}) + \left.\frac{\partial \dot{\boldsymbol{\theta}}_{ra}}{\partial \boldsymbol{\omega}_t}\right|_{op} (\boldsymbol{\omega}_t - \boldsymbol{\omega}_{t_0}) \end{aligned} \quad (5.25)$$

From Equation (5.24) we see that $\dot{\boldsymbol{\theta}}_{ra_0} = \mathbf{0}$ and that the two first Jacobians in Equation (5.25) give the zero matrix, when the operating points are inserted. The third Jacobian becomes the identity matrix. The state space formulation for the angular part is expressed in Equation (5.26) with the last Jacobian

$$\dot{\boldsymbol{\theta}}_{ra} = \mathbf{0}\boldsymbol{\theta}_{ra} + \mathbf{I}\boldsymbol{\omega}_c - \begin{bmatrix} c_y & 0 & -s_y \\ 0 & 1 & 0 \\ s_y & 0 & c_y \end{bmatrix} \boldsymbol{\omega}_t \quad (5.26)$$

$$\boxed{\dot{\boldsymbol{\theta}}_{ra} = \mathbf{A}_{ra}\boldsymbol{\theta}_{ra} + \mathbf{B}_{ra_1}\boldsymbol{\omega}_c - \mathbf{B}_{ra_2}\boldsymbol{\omega}_t} \quad (5.27)$$

Equation (5.27) does not hold the full state vector for the relative attitude as $\dot{\boldsymbol{\omega}}_{ra}$ is not explicitly known. Instead the full state can be expressed in the output equation rather than the state equation defining $\mathbf{y}_{ra} = [\boldsymbol{\theta}_{ra}, \boldsymbol{\omega}_{ra}]^{\mathrm{T}}$ and building the matrix as

$$\boxed{\mathbf{y}_{ra} = \begin{bmatrix} \mathbf{I} & \mathbf{0} & \mathbf{0} \\ \mathbf{0} & \mathbf{B}_{ra_1} & -\mathbf{B}_{ra_2} \end{bmatrix} \begin{bmatrix} \boldsymbol{\theta}_{ra} \\ \boldsymbol{\omega}_c \\ \boldsymbol{\omega}_t \end{bmatrix}} \quad (5.28)$$

5.7.3 Target Docking Port Motion

As one step to derive the coupled model, the target docking port needs to be presented in the orbital reference frame $\mathcal{F}_o$. This is the simple transformation $\tilde{\mathbf{r}}_{dt} = \mathbf{R}_{bto}^{\mathrm{T}} \mathbf{r}_{dt}$ which will be linearized as

$$\tilde{\mathbf{r}}_{dt} = \tilde{\mathbf{r}}_{dt_0} + \left.\frac{\partial \tilde{\mathbf{r}}_{dt}}{\partial \boldsymbol{\theta}_t}\right|_{\boldsymbol{\theta}_{t_0}} (\boldsymbol{\theta}_t - \boldsymbol{\theta}_{t_0}) \quad (5.29)$$

and $\boldsymbol{\theta}_{t_0} = [0, \theta_0, 0]^{\mathrm{T}}$. The Jacobian matrix will be derived in Section B.3 in detail and yields from Equation (B.9)

$$\frac{\partial \tilde{\mathbf{r}}_{dt}}{\partial \boldsymbol{\theta}_t} = \begin{bmatrix} s_y r_{dt_y} & c_y r_{dt_z} - s_y r_{dt_x} & -r_{dt_y} \\ -r_{dt_z} & 0 & c_y r_{dt_x} + s_y r_{dt_z} \\ c_y r_{dt_y} & -(c_y r_{dt_x} + s_y r_{dt_z}) & 0 \end{bmatrix} = \mathbf{B}_{dt_1} \tag{5.30}$$

and the operating point vector is computed as

$$\tilde{\mathbf{r}}_{dt_0} = \begin{bmatrix} c_y r_{dt_x} + s_y r_{dt_z} \\ r_{dt_y} \\ c_y r_{dt_z} - s_y r_{dt_x} \end{bmatrix} \tag{5.31}$$

The velocity can be expressed as in Equation (5.1), where the first right hand term is zero as the vector is fixed in the target body frame and only the cross product remains. This needs transformation to the orbital reference frame as for the positions and can be written as $\dot{\tilde{\mathbf{r}}}_{dt} = \mathbf{R}_{bto}^{\mathrm{T}}(\boldsymbol{\omega}_t \times \mathbf{r}_{dt})$, where $\boldsymbol{\omega}_{t_0} = \mathbf{0}$. The Taylor expansion becomes

$$\dot{\tilde{\mathbf{r}}}_{dt} = \dot{\tilde{\mathbf{r}}}_{dt_0} + \left.\frac{\partial \dot{\tilde{\mathbf{r}}}_{dt}}{\partial \boldsymbol{\theta}_t}\right|_{op} (\boldsymbol{\theta}_t - \boldsymbol{\theta}_{t_0}) + \left.\frac{\partial \dot{\tilde{\mathbf{r}}}_{dt}}{\partial \boldsymbol{\omega}_t}\right|_{op} (\boldsymbol{\omega}_t - \boldsymbol{\omega}_{t_0}) \tag{5.32}$$

where $\frac{\partial \dot{\tilde{\mathbf{r}}}_{dt}}{\partial \boldsymbol{\theta}_t} = \mathbf{0}$ as $\boldsymbol{\omega}_t = \mathbf{0}$ in the operating point. The Jacobian matrix will be derived in Section B.3 in detail and yields from Equation (B.11)

$$\frac{\partial \dot{\tilde{\mathbf{r}}}_{dt}}{\partial \boldsymbol{\omega}_t} = \begin{bmatrix} s_y r_{dt_y} & c_y r_{dt_z} - s_y r_{dt_x} & -c_y r_{dt_y} \\ -r_{dt_z} & 0 & r_{dt_x} \\ c_y r_{dt_y} & -(s_y r_{dt_z} + c_y r_{dt_x}) & s_y r_{dt_y} \end{bmatrix} = \mathbf{B}_{dt_2} \tag{5.33}$$

and the operating point vector is $\dot{\tilde{\mathbf{r}}}_{dt_0} = \mathbf{0}$.

It is not possible to write a state equation as there is no dynamics involved, but only the kinematics part which is computed based on other state variables of the attitude system. Only the output equation is possible to formulate as

$$\boxed{\mathbf{y}_{dt} = \begin{bmatrix} \tilde{\mathbf{r}}_{dt} - \tilde{\mathbf{r}}_{dt_0} \\ \dot{\tilde{\mathbf{r}}}_{dt} \end{bmatrix} = \begin{bmatrix} \mathbf{B}_{dt_1} & \mathbf{0} \\ \mathbf{0} & \mathbf{B}_{dt_2} \end{bmatrix} \begin{bmatrix} \boldsymbol{\theta}_t \\ \boldsymbol{\omega}_t \end{bmatrix}} \tag{5.34}$$

5.7.4 Chaser Docking Port Motion

Contrary to the target port motion, based upon the kinematic target attitude motion, the chaser port motion can be fully controlled by forces and torques. It is therefore intriguing to base the model upon the dynamics equations, as in Equation (4.11) having torque as input to the model. As the attitude dynamics has the torque as input and drives completely the port motion for rotation, this would lead to the introduction of redundant modes resulting in a non minimal realization.

A closer look reveals, that the problem is the same as for the target and that model can be reused with different parameters, but otherwise identical. This kinematic model and the more complex dynamic model give the exact same result. From Equation (5.34) the chaser port model then becomes

$$\boxed{\mathbf{y}_{dc} = \begin{bmatrix} \tilde{\mathbf{r}}_{dc} - \tilde{\mathbf{r}}_{dc_0} \\ \dot{\tilde{\mathbf{r}}}_{dc} \end{bmatrix} = \begin{bmatrix} \mathbf{B}_{dc_1} & \mathbf{0} \\ \mathbf{0} & \mathbf{B}_{dc_2} \end{bmatrix} \begin{bmatrix} \boldsymbol{\theta}_c \\ \boldsymbol{\omega}_c \end{bmatrix}} \tag{5.35}$$

5.7.5 Coupled Linear State Space Model

All the individual sub models so far are small signal models, which are adequate for synthesis work. Some large signals are needed for analysis, in particular the port to port values.

This can be achieved in a combined, but yet segregated model, by extending the input vector to hold also the operating points and can therefore be easily included or excluded.

The state vector consists of relative COM position, the chaser attitude, the target attitude, their rates and the relative attitude and defined as $\mathbf{x} = [\mathbf{x}_p, \dot{\mathbf{x}}_p, \boldsymbol{\theta}_c, \boldsymbol{\omega}_c, \boldsymbol{\theta}_t, \dot{\boldsymbol{\theta}}_t, \boldsymbol{\theta}_{ra}]^{\mathrm{T}}$, where $\mathbf{x}_p$ is in the orbital reference frame and the rest in the body frames.

The input vector holds the force, torque (in chaser body frame) and the operating point vectors for the chaser and target attitude and chaser and target ports respectively as $\mathbf{u} = [\mathbf{F}, \mathbf{N}, \boldsymbol{\theta}_{c_0}, \boldsymbol{\theta}_{t_0}, \tilde{\mathbf{r}}_{dt_0}, \tilde{\mathbf{r}}_{dc_0}]^{\mathrm{T}}$. The last four vectors in $\mathbf{u}$ are constant and the model provides large output signal values for those states. If they are assigned to zero the model gives all small signal values with respect to the operating point. *It shall be noted, that if the input vector is reduced to hold only force and torque and the* $\mathbf{B}$ *and* $\mathbf{D}$ *matrix dimensions are reduced correspondingly, a true small signal model is obtained.*

Finally the output vector contains relative COM position, chaser and target attitude, the port to port position, relative attitude and their respective derivatives as $\mathbf{y} = [\mathbf{x}_p, \dot{\mathbf{x}}_p, \boldsymbol{\theta}_c, \boldsymbol{\omega}_c, \boldsymbol{\theta}_t, \dot{\boldsymbol{\theta}}_t, \mathbf{x}_{pp}, \dot{\mathbf{x}}_{pp}, \boldsymbol{\theta}_{ra}, \boldsymbol{\omega}_{ra}]^{\mathrm{T}}$. The model is verified for two separate attitudes and illustrated in Figure 5.3.

The state space model is of standard form, though to get the operating points included conveniently the $\mathbf{D}$ matrix is used.

$$\boxed{\begin{aligned} \dot{\mathbf{x}} &= \mathbf{A}\mathbf{x} + \mathbf{B}\mathbf{u} \\ \mathbf{y} &= \mathbf{C}\mathbf{x} + \mathbf{D}\mathbf{u} \end{aligned}} \tag{5.36}$$

The matrices are defined as follows using the sub matrices derived in the preceding sections in this chapter and $\mathbf{A}_p$ from Equation (A.57).

$$\mathbf{A} = \begin{bmatrix} \mathbf{A}_p & \mathbf{0}_{6\times6} & \mathbf{0}_{6\times6} & \mathbf{0}_{6\times3} \\ \mathbf{0}_{6\times6} & \mathbf{A}_c & \mathbf{0}_{6\times6} & \mathbf{0}_{6\times3} \\ \mathbf{0}_{6\times6} & \mathbf{0}_{6\times6} & \mathbf{A}_t & \mathbf{0}_{6\times3} \\ \mathbf{0}_{3\times6} & [\mathbf{0}_{3\times3} \quad \mathbf{B}_{ra_1}] & [\mathbf{0}_{3\times3} \quad -\mathbf{B}_{ra_2}] & \mathbf{A}_{ra} \end{bmatrix} \tag{5.37}$$

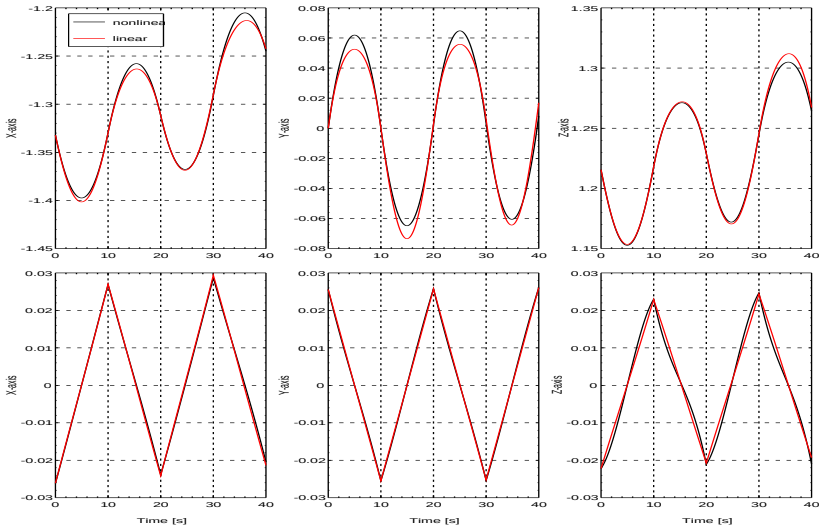

Figure 5.3: *Example of a linear model for port to port computation for two ports located at* $[4, 1, 1]$ *m and* $[3, 1, 1]$ *m in the respective body frames with a diagonal inertia matrix with elements* $[100, 90, 110]$ *kgm*^{2}*, for testing the derived model. The torque inputs are adjusted to give amplitudes of about* 5 *deg with operating points of* 10 *deg and* -10 *deg on the y-axis.*

$$\mathbf{B} = \begin{bmatrix} \mathbf{B}_p & \mathbf{0}_{6\times3} & \mathbf{0}_{6\times12} \\ \mathbf{0}_{6\times3} & \mathbf{B}_c & \mathbf{0}_{6\times12} \\ \mathbf{0}_{6\times3} & \mathbf{0}_{6\times3} & \mathbf{0}_{6\times12} \\ \mathbf{0}_{3\times3} & \mathbf{0}_{3\times3} & \mathbf{0}_{3\times12} \end{bmatrix} \tag{5.38}$$

In the definition of the $\mathbf{C}$ and $\mathbf{D}$ matrices all sub matrices are of dimension 3×3 for notational clarity reasons.

$$\mathbf{C} = \begin{bmatrix} \mathbf{I} & \mathbf{0} & \mathbf{0} & \mathbf{0} & \mathbf{0} & \mathbf{0} & \mathbf{0} \\ \mathbf{0} & \mathbf{I} & \mathbf{0} & \mathbf{0} & \mathbf{0} & \mathbf{0} & \mathbf{0} \\ \mathbf{0} & \mathbf{0} & \mathbf{I} & \mathbf{0} & \mathbf{0} & \mathbf{0} & \mathbf{0} \\ \mathbf{0} & \mathbf{0} & \mathbf{0} & \mathbf{I} & \mathbf{0} & \mathbf{0} & \mathbf{0} \\ \mathbf{0} & \mathbf{0} & \mathbf{0} & \mathbf{0} & \mathbf{I} & \mathbf{0} & \mathbf{0} \\ \mathbf{0} & \mathbf{0} & \mathbf{0} & \mathbf{0} & \mathbf{0} & \mathbf{I} & \mathbf{0} \\ \mathbf{I} & \mathbf{0} & \mathbf{B}_{dc_1} & \mathbf{0} & -\mathbf{B}_{dt_1} & \mathbf{0} & \mathbf{0} \\ \mathbf{0} & \mathbf{I} & \mathbf{0} & \mathbf{B}_{dc_2} & \mathbf{0} & -\mathbf{B}_{dt_2} & \mathbf{0} \\ \mathbf{0} & \mathbf{0} & \mathbf{0} & \mathbf{0} & \mathbf{0} & \mathbf{0} & \mathbf{I} \\ \mathbf{0} & \mathbf{0} & \mathbf{0} & \mathbf{B}_{ra_1} & \mathbf{0} & -\mathbf{B}_{ra_2} & \mathbf{0} \end{bmatrix} \tag{5.39}$$

$$\mathbf{D} = \begin{bmatrix} \mathbf{0} & \mathbf{0} & \mathbf{0} & \mathbf{0} & \mathbf{0} & \mathbf{0} \\ \mathbf{0} & \mathbf{0} & \mathbf{0} & \mathbf{0} & \mathbf{0} & \mathbf{0} \\ \mathbf{0} & \mathbf{0} & \mathbf{I} & \mathbf{0} & \mathbf{0} & \mathbf{0} \\ \mathbf{0} & \mathbf{0} & \mathbf{0} & \mathbf{0} & \mathbf{0} & \mathbf{0} \\ \mathbf{0} & \mathbf{0} & \mathbf{0} & \mathbf{I} & \mathbf{0} & \mathbf{0} \\ \mathbf{0} & \mathbf{0} & \mathbf{0} & \mathbf{0} & \mathbf{0} & \mathbf{0} \\ \mathbf{0} & \mathbf{0} & \mathbf{0} & \mathbf{0} & -\mathbf{I} & \mathbf{I} \\ \mathbf{0} & \mathbf{0} & \mathbf{0} & \mathbf{0} & \mathbf{0} & \mathbf{0} \\ \mathbf{0} & \mathbf{0} & \mathbf{0} & \mathbf{0} & \mathbf{0} & \mathbf{0} \\ \mathbf{0} & \mathbf{0} & \mathbf{0} & \mathbf{0} & \mathbf{0} & \mathbf{0} \end{bmatrix} \tag{5.40}$$

5.8 Conclusion

The nonlinear attitude dynamics and kinematics are formulated in the LVLH frame and linearized analytically by means of a Taylor expansion. From this is derived the relative attitude motion between the two spacecraft.

There is then developed a complete 6 DOF coupled state space model describing the general port to port motion combining the development of Chapter 4 and 5 together with the port locations with respect to the COM. This answers the objective in point 4 in Section 1.3.

Chapter 6

Control System Architecture

This short chapter will provide a high level overview of the mission involved avionics seen from a hardware point of view and how that architecture is at high functional level. Then it will be continued for the architecture of the flight software, which is a combination of general services, mission management and the GNC software. Finally the general architecture of the GNC feedback loop will be explained functionally.

6.1 System Functionality

The objectives are to control the spacecraft by means of an optimized, both technically and financially, organization of hardware and software, which together constitute the on board system.

The GNC software containing all the algorithms and mode management runs on a central computer, which for high reliability systems, as e.g. fail operational fail operational fail safe systems, are duplicate/triplicate and voting can take place.

The propulsion system, in this case 28 reaction hot gas thrusters, will produce the required control forces and torques.

The attitude sensors will measure the absolute attitude and attitude rate as well as the relative attitude between chaser and target. The relative position between both center of mass and the direct port to port distance needs to be measured.

6.2 Avionics Main Components

This section will provide an overview of the needed avionics equipment together with a short description of the items.

- **Computer:** The chip and peripherals shall preferably be of a failure tolerant design for reasons of system reliability. It shall provide full floating point capabilities preferably in 32-bit double precision, which far from all space qualified radiation

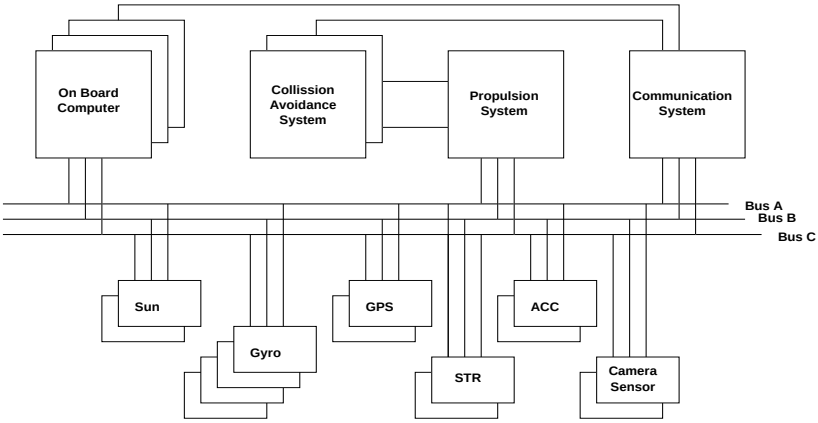

Figure 6.1: *A structure for the hardware units and avionics equipment for a typical spacecraft for RVD missions. As Earth bound RVD missions are mostly to manned spacecraft there is triple redundancy compared to less on ordinary spacecraft.*

hardened processors do. Obviously it shall have enough computing capability to execute the real time GNC and mode management software, together with all the house keeping, with sufficient margin for the sampling time as well as handling the real time interface to the data bus.

- **Thrusters:** They shall be able to produce the thrust required for the maneuvers to be performed for the specific mission. This shall be achieved with as small rise time as possible and the MIB must not be too large as this corresponds to a delay seen from the controller view point. The mechanical layout shall be such as to ensure coverage of the required envelope for the needed force and torque. There are in reality couplings between force and torque generation but shall be sought minimized mechanically, which is not always possible due to thermal, accommodation and manufacturing constraints.

- **GPS:** This navigation system can primarily be used in Low Earth Orbit (LEO), where all past and present automatic RVD missions are. It measures the absolute position and velocity in inertial coordinates from which the relative position and velocity is estimated after receiving GPS data from the target spacecraft. It is therefore only possible for a cooperative target as well as they both shall have the receiver antennae located such that 4 or more common GPS satellites are in the FOV. The estimator provides the values between COMs. The GPS is not used at closer proximity than a couple of hundred meters, due the the increased multi path effect and shadowing from the ISS.

- **Camera:** This sensor takes over when the GPS is not used and when a higher precision on the measurements is needed. The camera is used during the final

approach to docking as well as departure. It provides the position along all 3 axes between the camera and a target pattern. The relative attitude becomes available from a distance of less than about 30 meters. The rates are not measured directly.

- **Gyro:** The sensor system provides the angular rate around the two axes of the gyro mounting frame directly. Typically there are 4 gyros mounted in a tetrahedron configuration, such that 3 axis information can still be provided with one malfunctioning gyro. The complete assembly provides as output the angular rate around the axis of the body frame.

- **STR:** This sensor provides the inertial attitude of the spacecraft with high accuracy around all 3 spacecraft axes. It will autonomously find the inertial orientation at initialization. Two such units are used for redundancy.

- **Sun Sensor:** These sensors provide a course measurement of the direction to the sun in the spacecraft frame. They need to be mounted on the spacecraft such that the effective FOV is 4π steradian, as they are not used in the closed loop control system, but for contingency modes to orient the spacecraft to ensure electrical power generation.

- **Accelerometers:** They provide the acceleration along the 3 spacecraft axes, but are typically not used in the control loop due to their noisy behavior. They are mainly used to measure the main boosts for orbital maneuvers and to better determine the shut off time for the main engines.

An architecture of how the hardware units and equipments are organized and communicating together is illustrated in Figure 6.1 for a typical spacecraft of the type addressed here.

6.3 Software Structure

An overview of the high level structure will be given without any attempt of software design or addressing detailed software implementation aspects. A derived functional diagram of generic parts is shown in Figure 6.2. The software is structured such that the high level supervisor is not part of the GNC system flight software proper, but is shared between the GNC and other functionalities of the spacecraft, which need to be managed in real time like data management and telemetry. This part of the on board system also contains the high level FDIR functionality, which is handling the recovery from malfunctions at other places leading to change in phases of the mission like e.g. triggering a collision avoidance maneuver or retreat to a predefined hold point other than the nominal ones.

The other part, which is more directly GNC related, consists of the General Measurement System (GMS) for obtaining the measurements from the sensors via the on board data bus and performs plausibility checks and provides them for the control system. There is a local Mode Management (MM) which schedules the various controllers

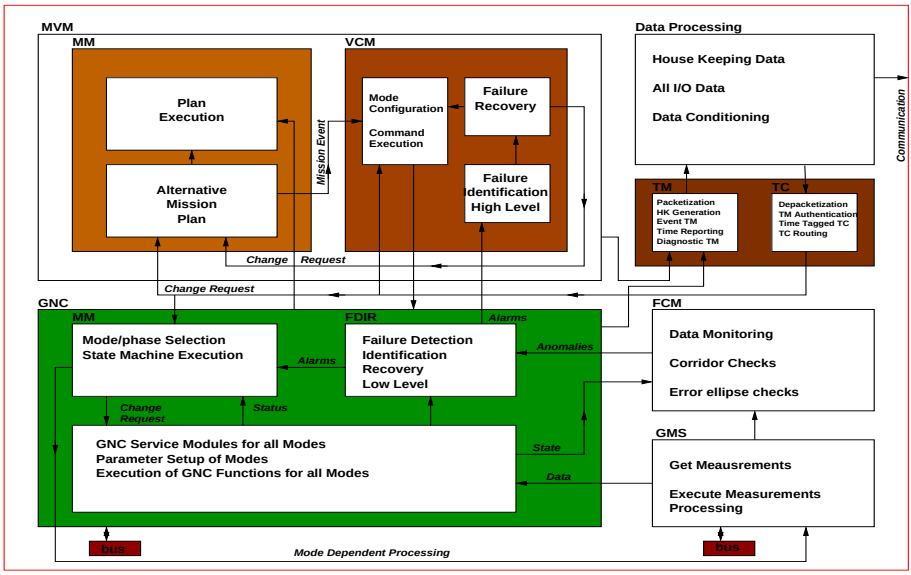

Figure 6.2: *A general structure for the on board software system for a typical spacecraft for RVD missions. It implements all the main functions except certain independent safety functions.*

and filters for the different parts of the mission. This is performed autonomously, but in coordination with the higher level mode management in the supervisor function. The low level FDIR deals with the low level management and requests of e.g. switching to redundant sensors, check of measurement data and status of equipment. This is clearly managed in the manner of informing the higher level functions, which need to be updated for the Vehicle Configuration Management (VCM) which manages the lower modes and failures. The Flight Control Monitoring (FCM) is an independent function which oversees the performance of the vehicle and uses partly independent sensors.

The GNC software part proper is clearly separated into the G, N and C parts with clear interfaces for all the blocks. Each element contains dedicated modules for the various filters and controllers, where the structure is typically service routines used in several modes but initialized with mode dependent parameters. These are then scheduled in such a manner and order as to form the feedback loops and the feed forward control from the guidance part.

6.4 Conclusion

The general set of avionics equipment needed for RVD missions is described briefly followed by a proposed architecture for an on board software system implementing the needed functionalities. This is of general nature and reflects on the objective 5 in Section 1.3.

Chapter 7

General GNC Structure and Guidance Design

This is the main chapter dealing with the design of a Guidance, Navigation and Control system to perform RVD in elliptical orbits.

The principal structure of the control feedback loop for the various modes will be explained, followed by the different ways of approach between chaser and target for the final approach to docking.

The domain of plant variation and sensitivity will be investigated first to obtain insight into which parts of an elliptical orbit will be driving the design, despite the reference orbit eccentricity will be fixed at $\varepsilon = 0.1$.

The theory of periodic time varying systems will be addressed for the periodic nature of the models. A flexible thruster selection method based on optimization for implementation will be designed.

Then the guidance profiles and feed forward control will be designed for the separate attitude and position control. This will be followed by the design of the various feedback loops in the system leading to the design for the final approach to docking. Finally the stability and performance of the complete system will be evaluated.

7.1 Loop Structure

The general structure of the principal feedback GNC system used in all modes for both position and attitude control is illustrated in Figure 7.1.

The guidance block handles the computation of all reference signals for all the states for both trajectory and station keeping points for both position and attitude. It is designed to be in compliance with the propulsive capabilities of the spacecraft. It also provides the feed forward control for phases where accelerations are required, which will ensure a more responsive and less oscillatory system characteristics. As illustrated in Figure 7.1

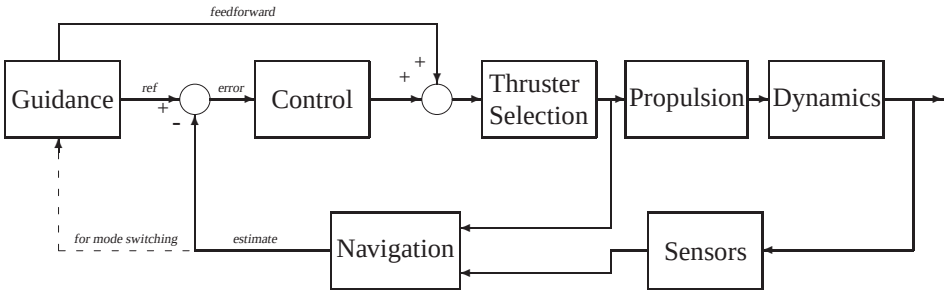

Figure 7.1: *Principal GNC organization for both attitude and position in all modes.*

there is a connection from the navigation to the guidance, which is used to inform the guidance such that the different modes for different locations can be initiated.

The navigation block receives inputs from the measurement system as well as the commanded forces and torques from the thruster selection block. The output is the estimated state vector for the next sampling time relevant to the respective phases of the RVD mission.

The control block has the task of driving the error signal to zero as well as ensuring a good system response and guarantee the stability margins of the feedback system.

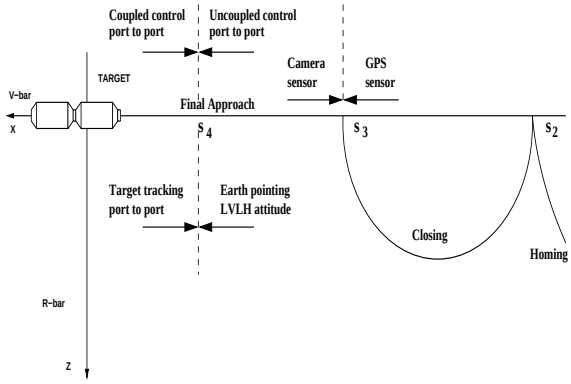

Figure 7.2: *This figure illustrates in different segments of the Rendezvous approach the different types of control and sensors used in the feedback loop.*

The thruster management function has as input the requested forces and torques from the controller and its task is to select the optimum set of thrusters to activate for the next sampling time to fulfill the demand from the controller. This has to be done as close as possible within the propulsive envelope available. The available propulsive capability is not necessarily constant, as failures of a single thruster or a cluster can occur. In that case they are declared not available for the thruster selection function.

Figure 7.2 shows the approach to the target and the different principal segments. The

attitude is plain LVLH oriented up to point s_4 after which the relative attitude between chaser and target is used. The navigation is based on GPS sensors until point s_3 after which the camera sensor is used. The control between the spacecraft is between COM and COM until point s_3 and then for the final part it is between docking port to docking port for position after s_3 and attitude after s_4.

7.2 Control Strategy

The strategy for most of the phases for the RVD is of fairly straight forward servo or regulator types. The last few meters before docking requires a bit of additional attention.

For the control problem of the last phase prior to contact, three concepts of approach are illustrated in Figure 7.3.

1 The first concept is the simplest as the relative position and attitude of the docking ports are not controlled. Only the relative COM position and the attitude with respect to LVLH is controlled. The aim point is the nominal target port center, not the actual one. The alignment error between the two docking ports becomes the sum of the target attitude error and the lateral contribution from the fact that there is a distance from the COM to the port.

   This option is too inaccurate seen in the light of realistic reception ranges of docking mechanisms. It is also impractical as there is not sufficiently accurate sensing capability available for measuring the relative COM position.

2 The second concept features a relative lateral position control between the actual target docking port and the chaser COM. This requires at least a line of sight measurement between the two ports. The individual attitudes remain individually controlled with respect to LVLH. The alignment error is now reduced to only the relative attitude.

   This option has been applied in some early scenarios with manual relative position control and automatic LVLH attitude control of both spacecraft. It still requires a fairly large angular reception range of the docking mechanisms as in the first option.

3 The third concept is the only one where both the relative position and the relative attitude are simultaneously controlled. This achieves full alignment in translation as well as in rotation. This requires on board estimation of the relative orientation of the docking port. A result of this scheme is that the translational and rotational motions are now coupled and typically calls for a more complex feedback design.

   This option is the one applied on almost all docking scenarios, manual, automatic or semi automatic. It requires measurements such that the relative position and attitude can be estimated in the navigation function for all 6 DOF. This option is the one adopted further in this work.

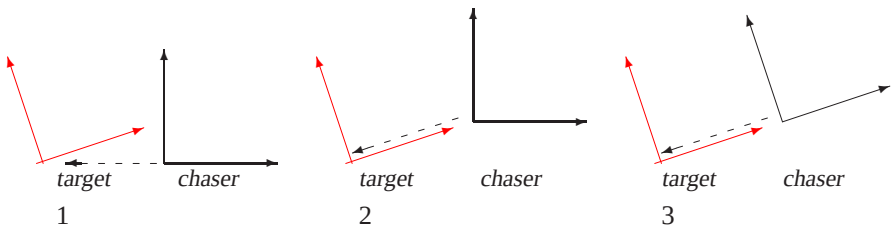

Figure 7.3: *Illustration of 3 different concepts of maneuvers of docking ports with respect to each other. The dashed arrows illustrate the direction of motion of the chaser COM. The first is COM to COM with no attitude regarded. The second follows the target docking axis but not the relative attitude. The third follows the target docking axis and accounts for the relative attitude.*

A further aspect to consider in the third concept, is whether the chaser control is performed around the COM or the docking port, though forces and torques always act with respect to the COM on a free body. If the bandwidth of the position control is faster than the attitude, the translation will align the ports and the attitude align later. The opposite is similarly valid, but if the two bandwidths are similar the spacecraft will appear to rotate around the docking port through a coupled motion, though this is giving a slower settling. Other requirements will determine which is the better solution in a particular case.

The overall control strategy is such that for the part between s_3 to s_4 the attitude control is Earth pointing and separate from the relative position control. This simplify the overall complexity, where accuracy and couplings are less demanding. For the last part from s_4 until docking the relative attitude and the relative position will be designed as one coupled 6 DOF system as this is the critical part with the highest precision needed.

7.3 Design Domain

This section will investigate the variations which exist in the orbital domain leading to variations and changing characteristics of models. In the end a justification leading to the selection of a sampling time will be presented.

7.3.1 Orbital Variations

The variation of the altitude and the orbital angular velocity will be evaluated, as those parameters appear in all the linear design models. From Section 2.4.1 the perigee is at an altitude of 450 km and the orbital eccentricity is $\varepsilon = 0.1$.

To get an overview of the domain, we will investigate the true anomaly, its rate and the velocity for 3 different locations in the orbit. The equations describing the 3 quantities are derived in Section A.2.1, and the general results for the special cases can be found in Table 7.1.

	θ	$r = \frac{p}{1+\varepsilon\cos(\theta)}$	$\dot{\theta} = \sqrt{\frac{\mu}{p^3}}(1+\varepsilon\cos(\theta))^2$	$v = \sqrt{\mu\left(\frac{2}{r} - \frac{1}{a}\right)}$
perigee	$0\,\mathrm{deg}$	$\frac{p}{1+\varepsilon}$	$\sqrt{\frac{\mu}{p^3}}(1+\varepsilon)^2$	$\sqrt{\mu\left(\frac{2(1+\varepsilon)}{p} - \frac{1}{a}\right)}$
	$90\,\mathrm{deg}$	p	$\sqrt{\frac{\mu}{p^3}}$	$\sqrt{\mu\left(\frac{2}{p} - \frac{1}{a}\right)}$
apogee	$180\,\mathrm{deg}$	$\frac{p}{1-\varepsilon}$	$\sqrt{\frac{\mu}{p^3}}(1-\varepsilon)^2$	$\sqrt{\mu\left(\frac{2(1-\varepsilon)}{p} - \frac{1}{a}\right)}$

Table 7.1: *General expressions for the orbital radius, the true anomaly rate and the orbital angular velocity at* 3 *different orbital locations.*

The orbital radius is smallest at perigee, where the gravitational and atmospheric disturbances are larger than elsewhere in the orbit. The orbital angular rate is largest at perigee leading to a faster dynamics environment in that region. The orbital velocity is largest at perigee leading to more drag disturbance than elsewhere.

From the above observations it is clear that the perigee region is a driver for the design and parameters from there should be used as design values for the whole orbit.

As the true anomaly and its rate has no closed form solution, it would be convenient to approximate the rate for design purposes. Figure 7.4 illustrates the true anomaly and its rate for different eccentricities. For low eccentricities the rate can be well approximated by a cosine function and a constant as shown for the reference orbit. For higher eccentricities it could be approximated by extended cycloidal functions.

Another approach, which is applicable to higher eccentricities, is to use approximate data for the parameters. Orbital parameters are very well known from the ground tracking by mission control and can be used on board. If varying between orbital passes, the parameters vary very slowly over the lifetime of the mission, and approximate interpolated values can be used for the GNC. Such parameters are known with less than 1 % error in practice.

7.3.2 Variation of Parameters

The orbital variations identified in Section 7.3.1 cause some minimum and maximum values for the reference orbit. The variations become as in Table 7.2 using the formulae from Table 7.1. The orbit has a period of 6566 s duration.

The angular rate and acceleration affect directly the plant models and will be investigated in Section 7.3.3, whereas the influence on disturbances will be addressed here.

The change in attitude affects directly the gravity gradient torque , see Equation (3.6). We will evaluate the variation of the torque for an attitude with respect to the LVLH of $15\,\mathrm{deg}$ corresponding to a possible TEA mode for the ISS. The maximum values for the inertia matrix in Equation (C.6) are used. The torque is directly proportional to the inertia.

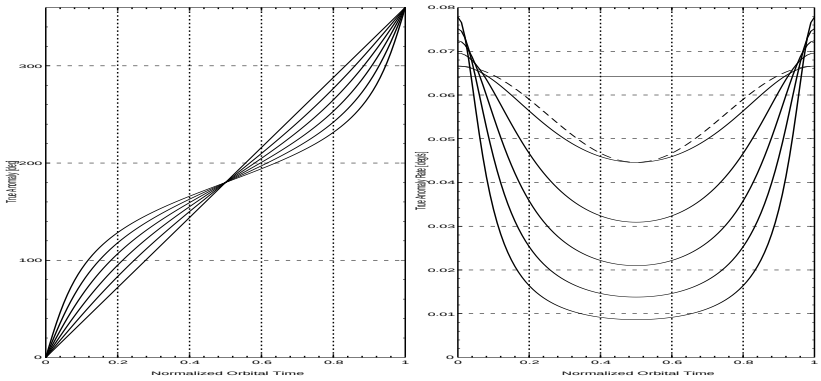

Figure 7.4: *The true anomaly and its rate as a function of the normalized orbital time. It is shown for eccentricities from zero to* 0.5 *in steps of* 0.1*. On the left half of the graphs the eccentricity is increasing for the non straight line curves. The dotted curve on the right graph is an approximation of the rate which only works well for low eccentricities.*

It is recalled from Equation (3.10), that the differential drag force is a function of the velocity to the power of two. It shall be taken into account that the atmospheric density also changes drastically with altitude and is a rather uncertain parameter (Larson & Wertz 1991). The differential drag force is very small, even at perigee and negligible. The reason being the ballistic coefficients of the two spacecraft are very similar, see definition in Section 3.4.2.

7.3.3 Variation of Design Plants

This section will analyze the plant dynamics of all the linear models developed in Chapter 4 and 5 to get an overview of their domain and properties.

The relative position from Equations (4.17) and (4.19) is illustrated in Figure 7.5

	Perigee	Apogee	%
r	6821.0 km	8336.8 km	22 %
$\dot{\theta}$	$1.175 \cdot 10^{-3}$ rad/s	$7.869 \cdot 10^{-4}$ rad/s	-33 %
v	$8.018 \cdot 10^{3}$ m/s	$6.560 \cdot 10^{3}$ m/s	-18 %
	$\theta = 1.29$ rad	$\theta = 4.98$ rad	
$\ddot{\theta}$	$-1.968 \cdot 10^{-7}$ rad/s^2	$1.968 \cdot 10^{-7}$ rad/s^2	-200 %

Table 7.2: *Variations for the reference orbit of the essential parameters. The last two lines give the two values of the true anomaly where it has its largest accelerations. It is found from further differentiation of the formula in Table 7.1.*

Attitude	Perigee	Apogee	%
$\boldsymbol{\theta}_0 = [0, 0, 0]\,\text{deg}$	$7.1095 \cdot 10^{-3}$ Nm	$3.8939 \cdot 10^{-3}$ Nm	-45 %
$\boldsymbol{\theta}_0 = [0, 15, 0]\,\text{deg}$	$8.1550 \cdot 10^{-2}$ Nm	$4.4666 \cdot 10^{-2}$ Nm	-45 %

Table 7.3: *Variations of the gravity gradient torque on the chaser.*

	Perigee	Apogee
ρ	$1.6 \cdot 10^{-12}$ kg/m^3	$< 10^{-16}$ kg/m^3
drag	$8.7 \cdot 10^{-4}$ N	$3.7 \cdot 10^{-8}$ N

Table 7.4: *Variations of the differential drag force and the atmospheric density.*

in plot 1 and 2. For circular orbits there are, as well known from Equation (4.99), a double integrator and 4 complex poles on the $j\omega$ axis. For elliptical orbits it is somewhat different, though the out of plane remains with two poles on the $j\omega$ axis. The in plane changes characteristic over the orbit. At perigee all poles are on the $j\omega$ axis and at apogee two poles remain oscillatory on the $j\omega$ axis and two become symmetric around zero with one Right Half Plane (RHP) pole and one Left Half Plane (LHP) pole. In between perigee and apogee, the system has two $j\omega$ poles and two RHP real poles.

The attitude from Equation (5.15) is found in Figure 7.5 in plot 3. It turns out that the poles are independent from the operating point $\boldsymbol{\theta}_0$ though it introduces couplings. It can be seen by finding the determinant analytically of $\mathbf{A}_c$ in Equation (5.16). The non diagonal elements of $\mathbf{B}_k$ disappear and the elements of $\mathbf{A}_k$ reduce to a zero and a one in the characteristic equation. The dynamics part $\mathbf{A}_d$ contributes with a real RHP pole for monotonously increasing or decreasing diagonal elements of the inertia matrix, which is the present situation. For other combinations the poles are complex in the LHP.

The port to port dynamics is in Figure 7.5 in plot 4. In a similar manner as for the attitude, it turns out that the poles are independent of the matrices $\mathbf{B}_{ra_1}$ and $\mathbf{B}_{ra_2}$ in Equation (5.27). Consequently all poles are contributed directly by the individual models. The six fast complex poles on the $j\omega$ axis stems from the relatively fast target attitude motion.

Finally we will establish the boundaries of the orbital angular rate as a function of the eccentricity ε. This will be needed later for the robust control analysis of the time varying plant. In Figure 7.6 is shown the lower and upper bounds of the orbital angular rate at apogee and perigee respectively. The frequency of the orbit is also illustrated and seen to follow the lower bound direction. It is observed that for the circular case $\varepsilon = 0$, the values are all identical.

7.3.4 Sampling Frequency

The implementation will be performed directly in the discrete time domain, rather than a continuous design, approximating to the discrete time via some transformation intro-

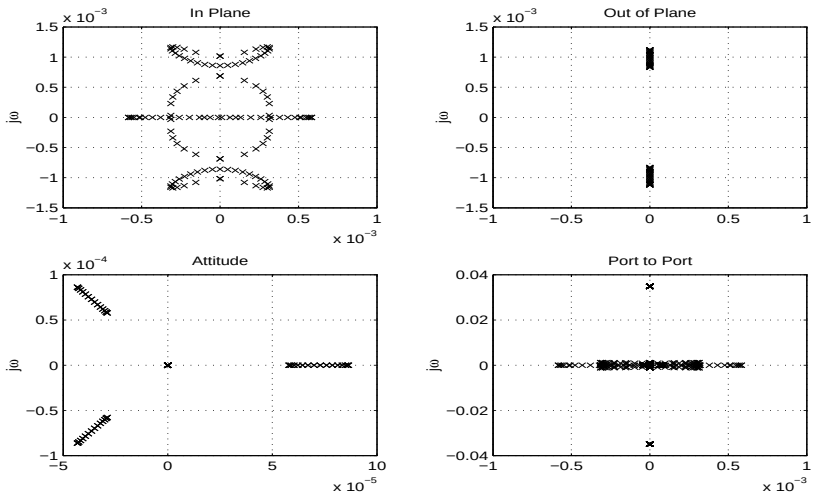

Figure 7.5: *Root locus of the linear plants in the Laplace plane. They are generated for one full orbit with* $\varepsilon = 0.1$.

ducing small unnecessary inaccuracies. This means an appropriate sampling frequency needs to be selected in advance and perhaps adjusted during the design.

The Nyquist criterion obviously needs to be fulfilled to avoid aliasing, but that is insufficient to obtain a well performing system. To have that, a sampling frequency of $7 - 10$ times the fastest mode that needs to be controlled in the closed loop system is needed. (Åström 1997).

The modes of the sloshing and the flexible modes shall not be controlled, but rather attenuated and can be omitted for consideration here. The ISS attitude motion, see Section 3.2.1, needs to be tracked and will be one driver for the closed loop bandwidth selection. External disturbances are of orbital frequencies and therefore very slow and insignificant. Past experiences have shown a need for a closed loop bandwidth in the area of $0.08 - 0.1$ Hz.

Based upon the above described considerations and the data delivery frequency of some of the main avionics equipment, described in Section 3.3, a sampling frequency of 1 Hz is selected.

7.4 Properties of Linear Time Varying Systems

The linear systems developed in Chapter 5.2 are time varying in the strict sense . The stability issues of such systems will be addressed in this section. A general linear time varying system can be expressed as

$$\dot{\mathbf{x}}(t) = \mathbf{A}(t)\mathbf{x}(t) \tag{7.1}$$

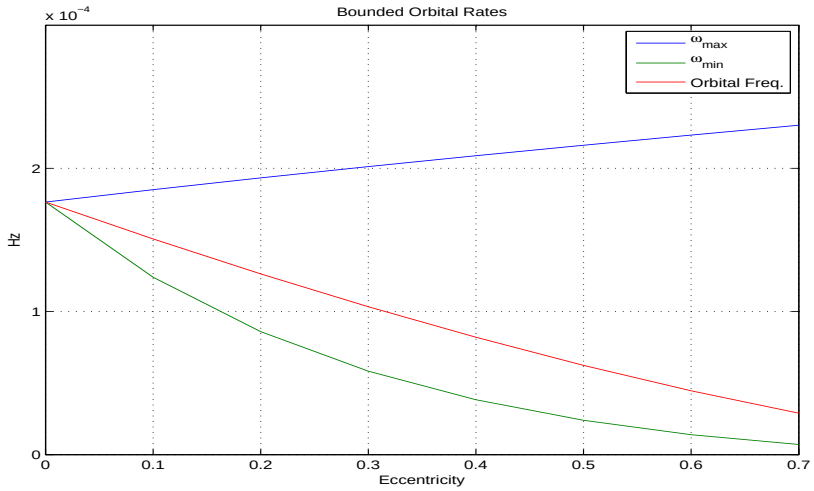

Figure 7.6: *The orbital angular rates at apogee(min) and perigee(max) are illustrated together with the orbital angular rate.*

and the stability behavior of the origin as an equilibrium point can be characterized completely in terms of the state transition matrix of the system. The solution to Equation (7.1) is known from linear systems theory (Lathi 1974) to be given by

$$\mathbf{x}(t) = \mathbf{\Phi}(t, t_0)\mathbf{x}(t_0) \tag{7.2}$$

where $\mathbf{\Phi}(t, t_0)$ is the state transition matrix. The stability of equilibrium point $\mathbf{x} = \mathbf{0}$ of Equation (7.1) is globally uniformly asymptotically stable if and only if the state transition satisfies the inequality[1]

$$\|\mathbf{\Phi}(t, t_0)\| \leq ke^{-\gamma(t-t_0)}, \quad \forall t \geq t_0 \geq 0 \tag{7.3}$$

for some positive constants k and γ. A detailed proof of Equation (7.3) can be found in (Khalil 1996).

This is just the general entry point as the following will be restricted to periodic linear time varying systems reflecting the systems for elliptical periodic orbits.

7.4.1 Continuous Periodic Linear Time Varying Systems

We now consider the class of systems as in Equation (7.1), where $\mathbf{A}(t) = \mathbf{A}(t + T)$ for some $T > 0$ and all t. The stability theory developed below is part of Floquet theory.

[1] $\|\mathbf{A}\|$is the induced 2-norm defined as $\|\mathbf{A}\|_2 = \sqrt{\lambda_{max}\mathbf{A}^{\mathrm{T}}\mathbf{A}}$, where $\lambda_{max}\mathbf{A}^{\mathrm{T}}\mathbf{A}$ is the maximum eigenvalue of $\mathbf{A}^{\mathrm{T}}\mathbf{A}$ (Zhou, Doyle & Glover 1995)

Equation (7.2) is equally valid for periodic systems. We now find the differential equation for the state transition matrix by differentiating Equation (7.2) and inserting Equation (7.1) giving

$$\dot{\mathbf{x}}(t) = \dot{\mathbf{\Phi}}(t, t_0)\mathbf{x}(t_0) = \mathbf{A}(t)\mathbf{x}(t) = \mathbf{A}(t)\mathbf{\Phi}(t, t_0)\mathbf{x}(t_0)$$

leading to

$$\dot{\mathbf{\Phi}}(t, t_0) = \mathbf{A}(t)\mathbf{\Phi}(t, t_0) \tag{7.4}$$

We will now define the following function

$$\mathbf{\Phi}(t + T, t_0) \triangleq \mathbf{\Phi}(t, t_0)\mathbf{M} \tag{7.5}$$

where $\mathbf{M}$ is some constant matrix. It is easy to verify that Equation (7.5) is valid by differentiating and inserting Equation (7.4)

$$\dot{\mathbf{\Phi}}(t + T, t_0) = \dot{\mathbf{\Phi}}(t, t_0)\mathbf{M} = \mathbf{A}(t)\mathbf{\Phi}(t, t_0)\mathbf{M}$$

and $\mathbf{M}$ drops off and we have verified by Equation (7.4). From (Khalil 1996) and (Mohler 1991) we now define $\mathbf{M}$ as

$$\mathbf{M} \triangleq e^{\mathbf{R}T} \tag{7.6}$$

which is a constant matrix and named the monodromy matrix in the literature. Recalling that $\mathbf{\Phi}(t, t) = \mathbf{I}$ we can evaluate Equation (7.5) at t_0 and without the loss of generality we consider $t_0 = 0$ and we get

$$\boxed{\mathbf{\Phi}(T, 0) = e^{\mathbf{R}T}} \tag{7.7}$$

The solution to Equation (7.1) therefore consists of a periodically modulated exponential matrix function.

Stability of the system in Equation (7.1) can now be evaluated in analogy to Equation (7.3) using Equation (7.7). Therefore Equation (7.7) is asymptotically stable if the eigenvalues of $\mathbf{R}$ all have negative real parts. We recognize that $e^{\mathbf{R}T}$ is exactly the mapping of the left half plane in the Laplace domain onto the open unit circle by means of the proper Z-transform. Alternatively we can evaluate $e^{\mathbf{R}T}$ directly giving

$$\det[\lambda\mathbf{I} - e^{\mathbf{R}T}] = 0 \tag{7.8}$$

and asymptotic stability implies

$$|\lambda_i| < 1 \tag{7.9}$$

where λ_i is the i^{th} characteristic multiplier of $\mathbf{A}(t)$ or the roots of $e^{\mathbf{R}T}$. This holds assuming knowledge of either the transition matrix $\mathbf{\Phi}$ or $\mathbf{R}$. A comprehensive proof of Equations (7.6) and (7.7) can be found in (Rugh 1996).

To use the theory above, the monodromy matrix $\mathbf{M}$ or $\mathbf{R}$ need to be found. This turns out to be the main problem, as to find $\mathbf{\Phi}$ often is difficult or even impossible (Rugh 1996), except in simple cases. [2]

[2] It shall be recalled that $\mathbf{\Phi}(t, t_0) = \exp\left(\int_{t_0}^{t} \mathbf{A}(\alpha)d\alpha\right)$ only is valid for $\mathbf{A}(t_1)\mathbf{A}(t_2) = \mathbf{A}(t_2)\mathbf{A}(t_1),\ \forall\ t_1, t_2 > 0$ and the latter condition is rarely fulfilled.

Using Picard's method of successive approximation the state transition matrix is proposed computed to first order in (Wisniewski 1996) as

$$\mathbf{\Phi}(t,t_0) \approx \mathbf{\Phi}(t_0,t_0) + \int_{t_0}^{t} \mathbf{A}(\alpha)d\alpha$$

$$\mathbf{\Phi}(t,t_0) \approx \mathbf{I} + \int_{t_0}^{t} \mathbf{A}(\alpha)d\alpha \tag{7.10}$$

and the $\mathbf{A}$ matrix is averaged to become invariant as

$$\mathbf{A} = \frac{1}{T}\int_{t_0}^{t_0+T} \mathbf{A}(\alpha)d\alpha \tag{7.11}$$

This approach still has its shortcomings in terms of accuracy and for higher order systems.

Numerical methods can be applied to find the monodromy matrix. The state transition matrix in Equation (7.2) for $t = T$ can be found by successively building it from initial state vectors of the form $\mathbf{x}_1 = [1\,0\,0\,0\,\ldots]^{\mathrm{T}}$, $\mathbf{x}_2 = [0\,1\,0\,0\,\ldots]^{\mathrm{T}}$ up to $\mathbf{x}_n = [0\,0\,0\,0\,\ldots\,0\,1]^{\mathrm{T}}$ for a n^{th} order system. It is accurate, but computationally it is not interesting.

Finally when the periodic time varying elements of the matrix $\mathbf{A}(t)$ are smooth and bounded functions, the eigenvalues will be likewise. Therefore the domain and bounds of the eigenvalues over one period can be computed, and if all have real negative values the system is stable. This property of the system will be utilized later in the design.

7.4.2 Discrete Periodic Linear Time Varying Systems

The discrete counterpart of the periodic system in Section (7.4.1) will be treated here. We consider systems of the type

$$\mathbf{x}(k+1) = \mathbf{F}(k)\mathbf{x}(k) \tag{7.12}$$

where k is a discrete time index. The system is periodic

$$\mathbf{F}(k) = \mathbf{F}(k+T) \tag{7.13}$$

with T being the discrete period of the system. The stability theory developed below is part of the discrete Floquet theory.

The discrete form of the zero input solution to the Equation (7.12) in terms of a transition matrix looks exactly as Equation (7.2). The difference equation for the state transition matrix is found from Equations (7.2) and (7.12) as

$$\mathbf{x}(k+1) = \mathbf{\Phi}(k+1,k_0)\mathbf{x}(k_0) = \mathbf{F}(k)\mathbf{x}(k) = \mathbf{F}(k)\mathbf{\Phi}(k,k_0)\mathbf{x}(k_0)$$

$$\mathbf{\Phi}(k+1,k_0) = \mathbf{F}(k)\mathbf{\Phi}(k,k_0) \tag{7.14}$$

We make the same definition in discrete time as done in Equation (7.5). It is easy to prove the validity by shifting forward one step Equation (7.5) and inserting Equation (7.14) as

$$\mathbf{\Phi}(k+1+T,k_0) = \mathbf{\Phi}(k+1,k_0)\mathbf{M} = \mathbf{F}(k)\mathbf{\Phi}(k,k_0)\mathbf{M} \tag{7.15}$$

From (Rugh 1996) we define $\mathbf{M}$ as

$$\mathbf{M} \triangleq \mathbf{R}^T \tag{7.16}$$

and with no loss of generality we can set $k_0 = 0$ and evaluating Equation (7.15) it gives

$$\mathbf{\Phi}(T,0) = \mathbf{R}^T \tag{7.17}$$

We see that the system is asymptotically stable if the roots of $\mathbf{R}^T < 1$ meaning inside the unit circle in the discrete domain. A detailed proof is provided in (Rugh 1996) and outside the scope here.

The problem of finding the matrix $\mathbf{R}$ in practice remains the same as for the continuous case in Section (7.4.1). The same type of approximations and arguments holds for the discrete case and are not repeated here. One additional difficulty nevertheless is the problem of finding the discrete time domain state space model of an arbitrary periodic time varying system.

7.5 Actuators

Various types of actuators exist for spacecraft maneuvers depending on the mission and if the spacecraft has only to perform attitude maneuvers, as is the case with most, or if it also has to perform simultaneous translational maneuvers.

Actuators, like reaction wheels, control momentum gyros and magnetic torquers, all produce pure torques. If the same spacecraft has to control attitude with thrusters, the layout is often such that almost pure torques can be generated, but not always.

So far, it is only spacecraft performing RVD which needs both attitude and position control capabilities simultaneously, though upcoming formation flying missions will have the same needs. The space Shuttle e.g. has a very complex thruster layout and it is used such that certain engines are preassigned for certain modes, often in a non fuel efficient manner. The Soyuz and Progress spacecraft on the contrary have a thruster layout, which is very much engineered from the physics point of view and has very few attitude and position couplings. It is operated via a pre computed lookup table in connection with nonlinear controllers and is fairly fuel efficient.

Based on the works and methods in (Voloshinov & Levitin 1999) and (Ankersen, Wu, Aleshin, Vankov & Volochinov 2004), an approach is under research, based on convex closeness of non convex nonlinear continuous and integer problems, aiming at a set of feasible pre computed solutions for thruster selection (Ankersen, Wu, Aleshin, Vankov & Volochinov 2005). This is targeted to be used efficiently on board in real time.

There are often many constraints leading to a non optimal thruster layout, seen from a GNC point of view. It ranges from lack of optimization at system design level, to

physical constraints on the spacecraft, manufacturing limitations, plume impingement constraints etc. The thruster layout used here and listed in Table C.6 suffers from several such constraints. It is therefore necessary to find a way to optimize the selection of the thruster to use efficiently and in real time.

7.5.1 Thruster Management

In this section we will develop a method for reliable thruster selection, which is robust and flexible towards failures of some of the thrusters. It will optimize the selection under certain constraints and under simultaneous request for arbitrary (within capability) force and torque vectors. We will base it on linear programming solved by a simplex algorithm, detailed in Section D.1.

The actual thruster optimization selection problem will now be formulated within this framework. From Table C.6 we define $\mathbf{n}_n$ being the direction unit vector of the n^{th} thruster, F_{th_n} its thrust size and $\mathbf{r}_{th_n}$ its location in the geometrical frame $\mathcal{F}_{gc}$. We can write the force from one thruster as

$$F_n = x_n F_{th_n} \tag{7.18}$$

where $x_n \in [0;1]$ and $F_{th_n} \geq 0$ and x_n is one of the variables in Equation (D.1) for which we seek a solution. It shall be noticed that the thrust F_n is considered variable here though in reality it is fixed, but it is based on the duality between duration and module of the thrust. The n^{th} thrust vector becomes

$$\mathbf{F}_n = F_n \mathbf{n}_n = x_n F_{th_n} \mathbf{n}_n \tag{7.19}$$

The n^{th} torque vector can be formulated as follows from Equations (3.2) and (7.19)

$$\mathbf{N}_n = x_n F_{th_n} (\mathbf{b}_n \times \mathbf{n}_n) \tag{7.20}$$

where $\mathbf{b}_n = \mathbf{r}_{bc} - \mathbf{r}_{th_n}$ is the lever arm for the n^{th} thruster. The total force and torque now become the sum over all N thrusters

$$\mathbf{F} = \sum_{n=1}^{N} \mathbf{F}_n = \sum_{n=1}^{N} x_n F_{th_n} \mathbf{n}_n \tag{7.21}$$

$$\mathbf{N} = \sum_{n=1}^{N} \mathbf{N}_n = \sum_{n=1}^{N} x_n F_{th_n} (\mathbf{b}_n \times \mathbf{n}_n) \tag{7.22}$$

where $\mathbf{F}$ and $\mathbf{N}$ are the commanded force and torque, which should be realized as close as possible.

The performance index, which will be maximized, will naturally be formulated such as to minimize the fuel consumption, which is almost always the main concern. As the fuel consumption is practically proportional to the thruster opening duration time, we can formulate the performance index as

$$z_{th} = \min \sum_{n=1}^{N} F_n = \min \sum_{n=1}^{N} x_n F_{th_n} = \max \left(- \sum_{n=1}^{N} x_n F_{th_n} \right) \tag{7.23}$$

where we multiply with minus to maximize in compliance with Equation (D.1), where $a_{0n} = -F_{th_n}$ relates to Equation (7.23). The other constraints can now be summarized within the framework as follows:

- In Equation (D.3) we have $m_1 = N$ leading to N inequalities of the form $x_n \leq 1$ with all the coefficients equal 1 and $b_n = 1$.
- There are no constraints of the form in Equation (D.4) so $m_2 = 0$.
- The final constraint comes from Equations (7.21) and (7.22) which give 6 equalities as in Equation (D.5) with $m_3 = 6$. The a coefficients in Equation (D.5) are clearly computed from Equations (7.21) and (7.22). The b right coefficients in Equation (D.5) become the components of the left vectors of Equations (7.21) and (7.22), but one has to ensure that b is positive, which is not ensured by Equations (7.21) and (7.22). To ensure this we multiply both sides of Equations (7.21) and (7.22) with the sign function $sgn(\cdot)$ and it becomes finally

$$sgn(\mathbf{F})\mathbf{F} = sgn(\mathbf{F}) \sum_{n=1}^{N} x_n F_{th_n} \mathbf{n}_n \tag{7.24}$$

$$sgn(\mathbf{N})\mathbf{N} = sgn(\mathbf{N}) \sum_{n=1}^{N} x_n F_{th_n} (\mathbf{b}_n \times \mathbf{n}_n) \tag{7.25}$$

When activating the thruster the MIB time T_{MIB} must be taken into account. This can be done directly on the x_n variables, where rounding will be used rather than truncation in the implementation.

$$F_{n_{min}} = \frac{T_{MIB}}{T} F_{th_n} = x_{n_{min}} F_{th_n}$$

$$x_{n_{min}} = \frac{T_{MIB}}{T} \tag{7.26}$$

The constraint placed on x_n becomes as follows and applied after the simplex optimization has been performed

$$x_n = \begin{cases} x_n & \text{for} \quad x_n \geq x_{n_{min}} \\ x_{n_{min}} & \text{for} \quad x_{n_{min}} > x_n \geq 0.5 x_{n_{min}} \\ 0 & \text{for} \quad x_n < 0.5 x_{n_{min}} \end{cases} \tag{7.27}$$

An illustration of its function and performance is shown in Figure 7.7 where a set of arbitrary but realistic force and torque signals are shown together with the realized signals and which thrusters were selected at any point in time.

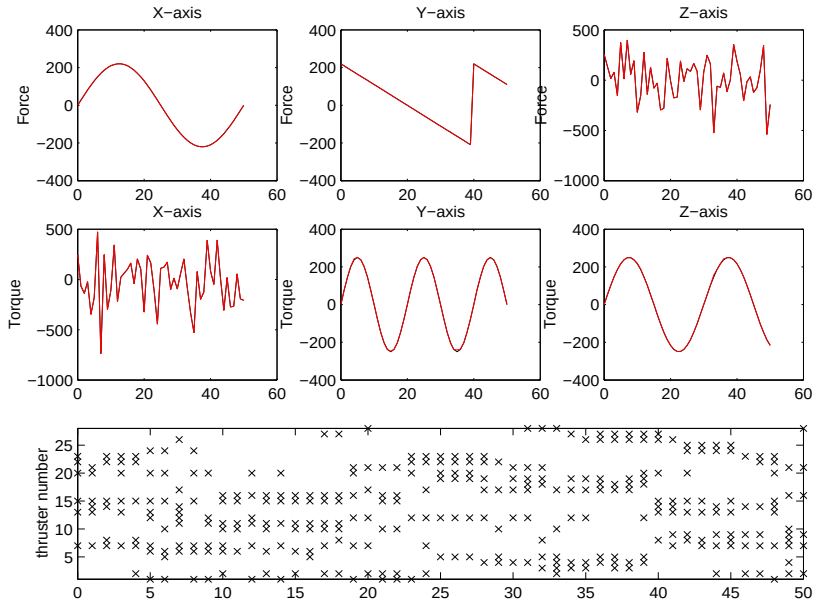

Figure 7.7: *The black line is the commanded forces and torques and the red line the result of the thruster selection. They are almost completely the same. If saturation occur then there can be larger differences between commanded and actuated. The last plot shows the engine number active. It illustrates that the optimization works well as little difference between the curves.*

7.6 Discrete Time Domain Models

The implementation of any spacecraft GNC system is done in software running on an on board computer. It is therefore logical to perform the designs directly in the discrete domain or Z-plane.

The control output is in principle kept constant between samples. A step invariant Z-transformation with a Zero Order Hold (ZOH) shall be applied. It is exact to the continuous system at the sampling times and maps the continuous poles λ to the discrete poles $\lambda_d = e^{\lambda T}$ where T is the sampling time (Ljung 1981).

A design in Laplace domain and then a discretization using a bilinear or Euler approximate transformation, as often seen in practice, is discouraged. It leads to less robustness and performance of the system. To recover that, a smaller sampling time is needed, which places unnecessary requirements on the computer and actuator hardware. Nevertheless it shall be noted that the $\mathcal{H}_\infty$ norm is preserved by the bilinear transformation, hence it is applicable for the $\mathcal{H}_\infty$ controller design (Green & Limebeer 1995).

7.6.1 Pulse Width Modulation of Actuators

The actuators are thrusters as described in Section 3.3.1, which operates in an on/off mode. The output from the controller will use a ZOH as explained in Section 7.6, which will have values between zero and some maximum value.

After the thruster selection has taken place the normalized required thrust is computed as in Equation (7.18) over one sampling period T. As the possible thrust is larger, it will have to be applied over a shorter time t_{on} such the following is fulfilled

$$F_{th}t_{on} = FT \tag{7.28}$$

which provides the same impulse to the system and $t_{on} \leq T$.

The PWM is essentially a discrete time device. Contrary to a Pulse Width Pulse Frequency (PWPF) modulator, which alters the bandwidth and phase, the PWM is practically only introducing more damping to the system. See also (Wie 1998) and (Ankersen 1989).

In order to illustrate the functioning of a PWM, a simple but representative state feedback loop is designed for a mass. This results in a 2^{nd} order closed loop system. The selected mass is 10^4 kg to be representative.

In Figure 7.8 is seen the step response for the system with and without PWM. It is clear that the bandwidth is virtually unchanged, but slightly more damping is introduced. This means the PWM does not affect stability margins in a negative manner. The system output raises marginally faster as expected because more energy is inserted into the system during a shorter time. Therefore we also note a slight difference in the controller output compared to the system without PWM.

Using the equivalent area in Equation (7.28) the straight forward and common implementation is to let the pulses start at the beginning of the sampling period. (Ieko, Ochi & Kanai 1997) consider the optimum time delay of the pulse, expressed as the error between the states of the output without and with PWM. The first order of the residual suggests the pulse to be centered in the sampling period. (Bernelli-Zazzera, Mantegazza & Nurzia 1998) propose beyond centering to split the pulse into several smaller pulses, evenly distributed over a sampling period. This only gives a marginal improvement, but will require thrusters with much longer lifetime. Such marginal improvements do not justify thruster qualified for many more duty cycles. The PWM is recommended to have a $50 - 100$ times higher resolution than the sampling time. One centered pulse is therefore recommended and will be used further on.

Finally we see that the output of the PWM can contain rather narrow pulses leading to a high frequency content. This is nevertheless completely filtered by the low pass nature of the system itself and is not present in the output.

From this analysis we conclude that the PWM needs not be included in the synthesis, but it will be used during the overall verification in line with (Wie 1998) and (Bernelli-Zazzera et al. 1998).

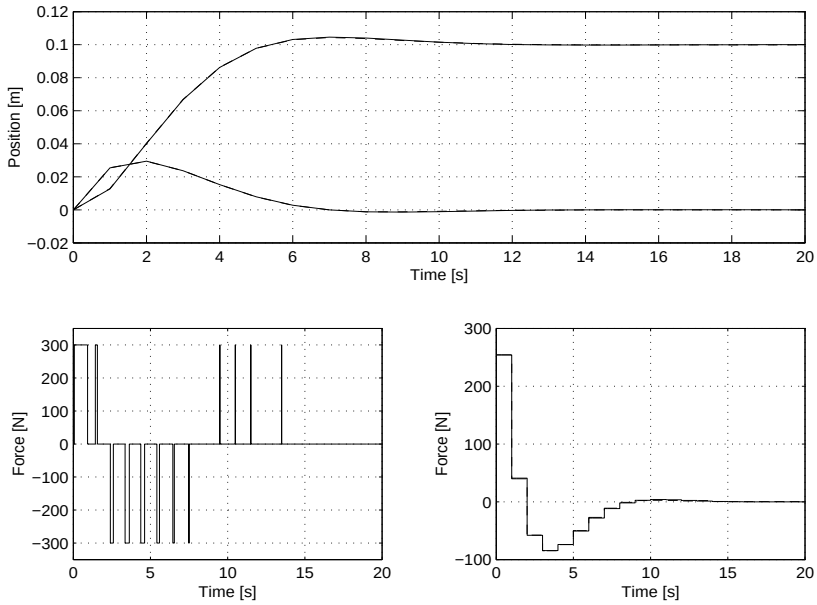

Figure 7.8: *Step response for double integrator full discrete state feedback. The full line is for the response without PWM and the dotted with. The bottom left graph shows the modulated input signal to the system, which is centered on the sampling period. It illustrates that it is possible to have very small impact from the modulation.*

7.7 Guidance

The guidance function is needed for both the position and the attitude loops. Its function is to provide the reference state vectors as well as to compute and provide any feed forward control signals.

As illustrated in Figure 7.1 the guidance function has as input the estimated state vector. It is used to determine when to change to another mode together with stored information of the mission plan and time line.

The following sections will cover the impulsive and the continuous trajectory maneuvers for the position, the required attitude reference and the station keeping references for both. The GNC design will be performed having the ISS in LVLH hold rather than TEA as explained before. This case is a worse one with more disturbances.

7.7.1 Impulsive Maneuvers

We recall the maneuvers to be considered as explained in Section 2.4 and illustrated in Figure 2.5. The guidance considered here will be a closing maneuver to reach point s_3 on the V-bar. The commonly used type is a tangential 2 pulse maneuver for which all

equations have already been derived in Section 4.6. Instead of repeating all the equations here, references to earlier ones will be used.

The principle is that the natural trajectory of a 2 pulse maneuver is used as the reference signal for position and velocity. The closed loop controller shall then follow the reference under the disturbance of differential drag. This method keeps a small error ellipse along and at the end of the trajectory. This is contrary to an open loop maneuver with a possible mid-term correction, which has much larger final uncertainty and no less fuel consumption.

Trajectory: All equations needed are in Section 4.2.3 for the in plane motion. The out of plane reference is zero. The state transition matrix with associated transformations are implemented in the guidance and provides position and velocity as a function of time.

Δ-V: The initial Δ-V is implemented as a feed forward control and computed as in Equation (4.142). The final pulse at the end of the maneuver is computed according to Equation (4.136), but using 3^{rd} row of Equation (4.137).

An example of the guidance reference trajectory is given as the 2^{nd} graph in Figure 4.6.

7.7.2 Station Keeping

This reference signal will keep the spacecraft at a chosen location and the position reference is then the coordinates of that point. The velocity reference is zero.

The feed forward force for the station keeping is calculated according to Equation (4.133). It shall be noticed that feed forward is not constant due to the orbital eccentricity.

7.7.3 Velocity Profile

The guidance for the final approach consists of an acceleration part followed by a constant velocity part. Then a deceleration to reach the final docking velocity. Past research has focused on various acceleration profiles to have smooth velocity profiles with indifferent results. The profile here will be based on having constant accelerations leading to simple and fast profiles.

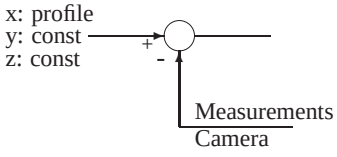

Figure 7.9: *Summation of measurements, directly creating the control error port to port.*

The sensor is the camera measuring the port to port distance. The value in Table 2.1 for s_3 is 500 m in LVLH leading to a shorter distance between ports. The lateral references y and z are zero. This means the camera measures directly the deviation, see also Figure 7.9. As mentioned earlier the final approach will be along the V-bar with the ISS in LVLH hold rather than TEA.

The phase plane profile for the final approach is illustrated in Figure 7.10. The guidance profile needs to be generated for the separate segments as illustrated. It is necessary to find the location and the time at the shift points. This is

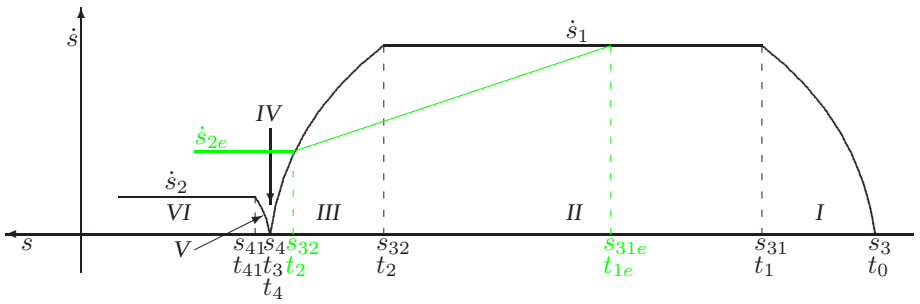

Figure 7.10: *Principal illustration of a final approach profile in the phase plane. The times are all with respect to a real time, at the beginning of the maneuver. The profile is general along any vector, here needed for the x-axis. The green trajectories are for exponential braking.*

all done based on the standard kinematic equation $s = s_0 + v_0 t + \frac{1}{2}at^2$ where s is the distance and v_0 initial speed and a the applied acceleration. The intermediate calculation of this well known equation is omitted, but all final results are shown in Table 7.5.

The initial values needed are the start location s_3 and switch location to final speed s_4. Also the two constant speeds $\dot{s}_1$ and $\dot{s}_2$ must be specified as well as a possible SK duration t_{sk} at s_4. If $\dot{s}_2 = 0$ then the transfer stops at s_4. It can then also be used for a general transfer between two locations with constant cruising speed.

For the equations in Table 7.5 it is mandatory that the cruising speed is first reached before braking occur or $s_{32} - s_{31} > 0, \forall \dot{s}_1 > 0$.

For the case where the constant speed $\dot{s}_1$ is not reached, we have that $t_1 = t_2$ and that $s_{31} = s_{32}$. Phase II disappear. The results from these constraints are listed in Table 7.6. For the case of $t_{sk} = 0$ the tables can be found in Section D.2, noting that $s_{41} = s_4$ and $t_3 = t_4 = t_{41}$.

For safety reasons it is not always desirable to arrive at s_4 too fast. Instead of a constant deceleration an exponential braking can be applied, which is the sloping trajectory in Figure 7.10. The equation for the trajectory in the phase plane is $\dot{s} = \nu s + b$, where $\nu = \frac{\dot{s}_{2e} - \dot{s}_1}{s_{32} - s_{31e}}$ and $b = \dot{s}_1 - \nu s_{31e}$.

As there is no time information in the phase plane, it is less straight forward to find the explicit equations. In general we have $\dot{s} = \frac{ds}{dt} \Rightarrow dt = \frac{ds}{\dot{s}}$ and integrating

$$\int_{t_0}^{t} dt = \int_{s_{31e}}^{s} \frac{ds}{\dot{s}} = \int_{s_{31e}}^{s} \frac{ds}{\nu s + b} = \left[\frac{1}{\nu}\ln(\nu s + b)\right]_{s_{31e}}^{s} = \frac{1}{\nu}(\ln(\nu s + b) - k) \quad (7.29)$$

where $k = \ln(\nu s_{31e} + b) = \ln(\dot{s}_1)$ by inserting b. Rearranging terms in Equation 7.29 and taking the exponential on both sides the position function becomes, where t_0 is an arbitrary initial time

$$s(t) = \frac{1}{\nu}\left(e^k e^{\nu(t-t_0)} - b\right) \quad (7.30)$$

	Time	Location	Position	Speed
I	t_0	s_3	$s = s_3 + \frac{1}{2}at^2$	$\dot{s} = at$
II	$t_1 = \frac{\dot{s}_1}{a}$	$s_{31} = s_3 + \frac{1}{2}at_1^2$	$s = s_{31} + \dot{s}_1(t - t_1)$	$\dot{s} = \dot{s}_1$
II	$t_{1e} = t_1 + \frac{s_{31e} - s_{31}}{\dot{s}_1}$	s_{31e}	$s = s_{31} + \dot{s}_1(t - t_1)$	$\dot{s} = \dot{s}_1$
III	$\delta t = t_3 - t_2 = \frac{\dot{s}_2 - \dot{s}_1}{d}$ $t_2 = t_1 + \frac{s_{32} - s_{31}}{\dot{s}_1}$	$s_{32} = s_4 - \dot{s}_1\delta t - \frac{d}{2}\delta t^2$	$x = t - t_2$ $s = s_{32} + \dot{s}_1 x + \frac{1}{2}dx^2$	$\dot{s} = \dot{s}_1 + dx$
III	$\delta t = \frac{-\dot{s}_{2e}}{d}$ $t_2 = t_{1e} + \frac{1}{\nu}\ln\frac{\dot{s}_{2e}}{\dot{s}_1}$	$s_{32} = s_4 - \dot{s}_{2e}\delta t - \frac{d}{2}\delta t^2$	$x = t - t_{1e}$ $s = \frac{\dot{s}_1}{\nu}\left(e^{\nu x} - 1\right) + s_{31e}$	$\dot{s} = \dot{s}_1 e^{\nu x}$
IV	$t_3 = t_2 - \frac{\dot{s}_1}{d}$	s_4	$s = s_4$	$\dot{s} = 0$
V	$t_4 = t_3 + t_{sk}$	s_4	$s = s_4 + \frac{1}{2}a(t - t_4)^2$	$\dot{s} = a(t - t_4)$
VI	$t_{41} = t_4 + \frac{\dot{s}_2}{a}$	$s_{41} = s_4 + \frac{1}{2}a(t_{41} - t_4)^2$	$s = s_{41} + \dot{s}_2(t - t_{41})$	$\dot{s} = \dot{s}_2$

Table 7.5: *Lists all equations needed to calculate the profile illustrated in Figure 7.10. Observe in III that d is a deceleration and $d < 0$. Typically $d = -a$. The green fields all refer to the exponential braking illustrated in Figure 7.10*

For $t = t_0$ we can find $e^k = \dot{s}_1$, and inserting b we obtain

$$s(t) = \frac{\dot{s}_1}{\nu}\left(e^{\nu(t-t_0)} - 1\right) + s_{31e} \tag{7.31}$$

and by differentiation

$$\dot{s}(t) = \dot{s}_1 e^{\nu(t-t_0)} \tag{7.32}$$

The transfer time for exponential braking we find setting $t_0 = 0$ without loss of generality and $s(t) = s$

$$t_e = \frac{1}{\nu}\ln\left(\frac{\dot{s}_{2e}}{\dot{s}_1}\right) \quad \text{and} \quad \lim_{\dot{s}_{2e}\to 0} t_e = \infty \tag{7.33}$$

It is observed from Equation 7.33 that the final speed cannot become zero.

Implementing all the equations and switching thresholds from Table 7.5 and 7.6 one has a general guidance function for a profile as in Figure 7.10.

	Time	Location	Position	Speed
III	$\delta t = t_3 - t_2 = \frac{\dot{s}_2 - \dot{s}_{31}}{d}$ $t_1 = \sqrt{\frac{1}{d}(s_4 - s_3 + \frac{\dot{s}_2^2}{2d})}$	$s_{31} = \frac{s_3 + s_4}{2} + \frac{\dot{s}_2^2}{4d}$	$x = t - t_1$ $s = s_{31} + \dot{s}_{31}x + \frac{1}{2}dx^2$	$\dot{s} = \dot{s}_{31} + dx$
IV	$t_3 = t_1 - \frac{\dot{s}_{31}}{d}$	s_4	$s = s_4$	$\dot{s} = 0$

Table 7.6: *Lists all equations, different from Table 7.5, needed to calculate the profile in Figure 7.10, when $\dot{s}_1$ is not reached. This means phase II is omitted and $t_1 = t_2$, $s_{31} = s_{32}$ and $\dot{s}_{31} = at_1$ from I.*

7.7.4 Attitude Slew

Slew maneuvers can be viewed in two categories. The first one being a non constrained maneuver from a present quaternion to a target quaternion. This is a minimum time maneuver performing the rotation around an axis normal to the plane spanned by the vector components of two quaternions. This is typically used for observatory type of spacecraft.

The second one being a constrained maneuver from one Euler angle to a target Euler angle. This is often driven by sensor FOV and physical constraints on or around the spacecraft. Such is typical for proximity maneuvers for RVD. For those reasons and safety issues one typically rotates one axis at the time. Often there is no need for general rotations.

In this work there is only a need for slew for a fly around maneuver as described in Section 2.3.4 to reach the docking axis with ISS in TEA mode.

The profile for a slew maneuver, here around the spacecraft y-axis, is similar to the one in Figure 7.10, with $\dot{s}_2 = 0$. Therefore one can reuse all equations from Table 7.5 and 7.6 for the slew. We simply replace the position variable with the angular variable and it is all applicable.

7.8 Conclusion

A control structure and GNC design approach have been defined. A GNC design domain has been defined in terms of variation of parameters and design plants. Relevant properties of linear periodic time varying systems have been evaluated. A general thruster management function has been designed. A general guidance profile has been designed. This answers well to objective 6 of Section 1.3.

Chapter 8

Robust and Attitude Control

The functions for the navigation and control will be dealt with in this chapter, organized along the functionality of general attitude control, relative position control between COM and finally the full control between docking ports.

The structure will be such, that theory will be developed and used as the need will arise. A choice of designs will be selected in a justified manner in order to reflect the requirements laid down in Section 2.4.2. The theoretical parts will then later be used for other functionalities, than for what it was developed, by reference. The order of development is based upon increased system complexity.

All analysis and synthesis will be performed on linear models. Nonlinear models will be used for verification by simulation.

8.1 Earth Pointing

The general attitude control is needed in all phases of the mission, except where relative attitude is required, as explained in Section 2.4 and illustrated at high level in Figure 2.5.

The general requirements are not very demanding for this kind of missions compared to e.g. Earth observation ones. The requirements are listed for all parts in Table 2.2 and we recall them here as 3 deg and 0.2 deg/s for pointing and rate for each axis.

8.2 Plant Description and Variation

The model for the attitude kinematics and dynamics was developed in Section 5.6 and we will use the Linear Time Varying (LTV) model given in Equation (5.16). We recall that the matrix $\mathbf{A}_d$ in Equation (5.15) is a function of the orbital angular rate and therefore, we have a periodic plant.

We will now characterize the plant inputs and the plant variations. It is clear from the thruster layout in Table C.5, that the 3 dimensional force and torque envelope will form a multifaceted polytope. It is impractical to be used for design for which reason

$\varepsilon = 0$	$\mathbf{I}_{min}$	$\mathbf{I}_{max}$	$\%\Delta$
	$[0,0,0]$	$[0,0,0]$	
	$8.2 \cdot 10^{-5}$	$6.3 \cdot 10^{-5}$	$-23\,\%$
	$(-4.1 \pm j8.2)10^{-5}$	$(-3.2 \pm j6)10^{-5}$	$-26\,\%$

$\varepsilon = 0.1$	$\theta = 0$ deg	$\theta = 180$ deg	$\%\Delta$
$\mathbf{I}_{min}$	$[0,0,0]$	$[0,0,0]$	
	$8.6 \cdot 10^{-5}$	$5.8 \cdot 10^{-5}$	$-33\,\%$
	$(-4.3 \pm j8.6)10^{-5*}$	$(-2.9 \pm j5.8)10^{-5}$	$-33\,\%$

Table 8.1: *Examples of main variations of plant poles for variations in inertia and orbit.* $*$*(Become real for some inertia)*

we will use a spherical shaped envelope all being inside the polytope. From analysis in (Silva et al. 2005), it can be ensured with one failure the following is always available simultaneously.

$$\left.\begin{array}{rcl} \mathbf{F}_{max} & = & 150 \text{ N} \\ \mathbf{N}_{max} & = & 190 \text{ Nm} \end{array}\right\} \text{in any direction} \tag{8.1}$$

The pole variations of the rigid plant are already dealt with and shown in Figure 7.5 Here we will also consider the flex and slosh modes as well as inertia variations and listed in Table 8.1

The poles coming from the flexible modes and the sloshing are as in Table 8.2. The couplings of the slosh is weaker than for the panels and is hardly noticeable. We therefore include only the flex modes in the plants for design.

The typical frequency response, for one of the main channels, is illustrated in Figure 8.4, where one clearly observes the difference in the two contributors.

There are no transmission zeros in the plant minimal realization. The strategy further in the design is to design controllers for the rigid part without considering the flex modes. The rationale for this decision is that the modes cannot be actively controlled but only filtered. This might be considered with notch filters if deemed necessary later looking at stability and performance. More in depth work on control of flexible modes can be found in (Bodineau, Boulade, Frapard, Chen, Salehi & Ankersen 2005).

4 panels 1^{st} mode	Lumped tanks
$-1.4 \cdot 10^{-3} \pm j1.38$	$-6.7 \cdot 10^{-4} \pm j0.13$

Table 8.2: *Poles for flexible first mode with* 4 *panels and lumped sloshing tanks.*

8.3 Control Design LQR

The attitude control design is very often performed on a per axis basis employing classical manner, first developed in (Ziegler & Nichols 1942).

As the plant is of multi variable nature we will embark directly on a MIMO design approach. As we do not take the flex modes into account for the synthesis there is no need for loop shaping techniques using notch filters or $\mathcal{H}_\infty$ techniques. A natural approach is to use Linear Quadratic (LQ) techniques, which are well proved and multi variable. They have been particularly successful, where the plant models are well known as in the case in aerospace applications. Based upon the well known separation theorem (Kwakernaak & Sivan 1972), we will first consider the Linear Quadratic Regulator (LQR) part and design the estimation filter after.

We will target the following control requirements of a rise time $t_r < 100\,\mathrm{s}$, an overshoot of $M_P < 30\%$ and a steady state error of $e_{max} < 2\,\mathrm{deg}$.

The plant is LTV as shown in Section 8.2 and we need to select an operating point to get a LTI plant. We select the plant valid at the perigee of the orbit, which is where the fastest dynamics exist. The rational being that a faster control can later follow a slower dynamics, but not necessarily the opposite. For a state space plant of the form

$$\dot{\mathbf{x}}(t) = \mathbf{A}\mathbf{x}(t) + \mathbf{B}\mathbf{u}(t) \tag{8.2}$$

we will seek an input signal $\mathbf{u}(t)$ which will bring a non-zero initial state $\mathbf{x}(0)$ to a zero state. This we will do by minimizing a quadratic deterministic cost function as stated in theorem 8.1.

Theorem 8.1
The stationary optimal linear controller $\boldsymbol{L}$, which minimizes the quadratic cost function.

$$J = \int_0^\infty (\boldsymbol{x}(t)^T \boldsymbol{Q}\boldsymbol{x}(t) + \boldsymbol{u}(t)^T \boldsymbol{R}\boldsymbol{u}(t))dt \tag{8.3}$$

under the constraint of input behavior

$$\boldsymbol{u}(t) = -\boldsymbol{L}\boldsymbol{x}(t) \tag{8.4}$$

is given by

$$\boldsymbol{L} = \boldsymbol{R}^{-1}\boldsymbol{B}^T\boldsymbol{X} \tag{8.5}$$

where $\boldsymbol{X} = \boldsymbol{X}^T$ is the positive (semi)definite solution of the Algebraic Riccati Equation (ARE)

$$\boldsymbol{A}^T\boldsymbol{X} + \boldsymbol{X}\boldsymbol{A} - \boldsymbol{X}\boldsymbol{B}\boldsymbol{R}^{-1}\boldsymbol{B}^T\boldsymbol{X} + \boldsymbol{Q} = 0 \tag{8.6}$$

and $\boldsymbol{Q} = \boldsymbol{Q}^T$ is a positive (semi)definite matrix and $\boldsymbol{R} = \boldsymbol{R}^T$ is a positive definite matrix.

The proof of Theorem 8.1 can be found in (Ogata 1970) and is briefly outlined by inserting Equation (8.4) into Equation (8.3), assigning to a Lyapunov type function, replacing $\mathbf{R}$ with a matrix product and finding the minimum. General algorithms for solving AREs are beyond the scope of this work, but found in (Arnold & Laub 1984).

The weighting matrices in the performance index in Equation (8.3) are selected as

$$\mathbf{Q} = \begin{bmatrix} \frac{1}{x_{1_{max}}^2} & & \\ & \ddots & \\ & & \frac{1}{x_{m_{max}}^2} \end{bmatrix}, \quad \mathbf{R} = \begin{bmatrix} \frac{1}{u_{1_{max}}^2} & & \\ & \ddots & \\ & & \frac{1}{u_{n_{max}}^2} \end{bmatrix} \tag{8.7}$$

where in this case $m = 6$ and $n = 3$. By selecting the weights with respect to the square of the expected maximum values the performance index integrand is normalized to a value of about 1. This is a starting point for the iterative process of the control design.

The rigid body plant has been chosen for the synthesis contrary to include the flexible and sloshing modes during design.The difference is an insignificant very small ripple on the output with $\mathbf{L} \in \mathcal{R}^{3\times 6}$. This ripple can be removed including all modes leading to a larger $\mathbf{L} \in \mathcal{R}^{3\times 18}$ and keeping in mind that those modes are not measurable in practice.

After several iterations and simulations the following values are selected

$$x_{1\to 3_{max}} = 1 \text{ deg}, \qquad x_{4\to 6_{max}} = 0.05 \text{ deg/s} \quad \text{and} \quad u_{max} = 190 \text{ Nm} \tag{8.8}$$

This leads to closed loop bandwidths of about 0.01 Hz, which is just below the frequency of the flexible modes (the sloshing was shown to have little influence). This gives very acceptable response times of about 100 s to steps.

The design of LQR is recalled to exhibit guaranteed stability margins in the feedback channels for Gain Margin (GM) and Phase Margin (PM) of

$$GM = \infty \qquad \text{and} \qquad PM \geq 60 \text{ deg} \tag{8.9}$$

The steady state error should be close or equal to zero. The y-axis of the system is type 1 (one pure integrator), hence one is having a steady state error of zero without any integral terms in the controller. The other axes have real poles very close to the imaginary axis, thus exhibiting integral type of behavior. This leads to very small steady state errors of a few percent. We therefore conclude, that there is no need to extend the design with explicit integrator and their anti windup logic. This is seen clearly in the plot in Figure 8.2.

The design domain chosen is the continuous one. The justification for that choice is that the later robust control analysis has its theory and available tools primarily in the continuous domain. This means that the designed controllers need to be transformed into the discrete domain. With the control bandwidth to sampling frequency ratio used, the errors introduced are negligible in the practical implementation. To do this, cost equivalents has been used as in Theorem 8.2.

Theorem 8.2
The discrete equivalent optimal controllers minimizing the continuous cost function

$$J = \int_0^\infty (\boldsymbol{x}(t)^T \boldsymbol{Q}\boldsymbol{x}(t) + \boldsymbol{u}(t)^T \boldsymbol{R}\boldsymbol{u}(t))dt \tag{8.10}$$

can be found by minimizing the following discrete equivalent cost function using a step invariant discretized plant

$$J_d = \sum_{k=0}^{\infty} [\boldsymbol{x}^T(k)\boldsymbol{u}^T(k)] \begin{bmatrix} \boldsymbol{M}_{11} & \boldsymbol{M}_{12} \\ \boldsymbol{M}_{21} & \boldsymbol{M}_{22} \end{bmatrix} \begin{bmatrix} \boldsymbol{x}(k) \\ \boldsymbol{u}(k) \end{bmatrix} \tag{8.11}$$

where

$$\begin{bmatrix} \boldsymbol{M}_{11} & \boldsymbol{M}_{12} \\ \boldsymbol{M}_{21} & \boldsymbol{M}_{22} \end{bmatrix} = \int_0^T \begin{bmatrix} \boldsymbol{F}^T(\tau) & \boldsymbol{0} \\ \boldsymbol{G}^T(\tau) & \boldsymbol{I} \end{bmatrix} \begin{bmatrix} \boldsymbol{Q} & \boldsymbol{0} \\ \boldsymbol{0} & \boldsymbol{R} \end{bmatrix} \begin{bmatrix} \boldsymbol{F}(\tau) & \boldsymbol{G}(\tau) \\ \boldsymbol{0} & \boldsymbol{I} \end{bmatrix} d\tau \tag{8.12}$$

*and **F**, **G** are part of the discretized system.*

The proof and derivations in more details can be found in (Franklin, Powell & Workman 1998).

The continuous and discrete designs have been implemented, compared and found to give rather precisely similar closed loop responses. Before presenting the closed loop results, we will proceed with the design of a state estimator in order to filter the measurement noise from the sensors.

8.4 Control Design LQG

As stated in Section 8.3 one can separate the controller and estimator design retaining optimality upon final combination to form the LQG compensator.
We will base the filtering on a stationary Kalman filter of the following stochastic system

$$\begin{array}{rcl} \dot{\mathbf{x}}(t) & = & \mathbf{A}\mathbf{x}(t) + \mathbf{B}\mathbf{u}(t) + \mathbf{v} \\ \mathbf{y}(t) & = & \mathbf{C}\mathbf{x}(t) + \mathbf{D}\mathbf{u}(t) + \mathbf{e} \end{array} \tag{8.13}$$

where the state noise $\mathbf{v}$ and output noise $\mathbf{e}$ are white weak stationary stochastic processes with the covariance matrices,

$$E\{\mathbf{v}(t)\mathbf{v}(s)^{\mathrm{T}}\} = \begin{cases} \mathbf{R}_1 & s = t \\ \mathbf{0} & s \neq t \end{cases} \tag{8.14}$$

$$E\{\mathbf{e}(t)\mathbf{e}(s)^{\mathrm{T}}\} = \begin{cases} \mathbf{R}_2 & s = t \\ \mathbf{0} & s \neq t \end{cases} \tag{8.15}$$

$E\{\cdot\}$ being the expectation.

The state noise $\mathbf{v}$ is not really known, hence it will be treated as a free design parameter in the tuning of the filter.
The output covariance can be defined by the sensor noise as a diagonal matrix.

$$\mathbf{R}_2 = \begin{bmatrix} \mathbf{R}_{STR} & \mathbf{0} \\ \mathbf{0} & \mathbf{R}_{gyro} \end{bmatrix} \tag{8.16}$$

For the STR we use the largest noise value from Table C.3 of $3\sigma = 5.28 \cdot 10^{-2}$ deg for all axes. The gyro is used in fine mode with an angular rate noise from Table C.2 of $3\sigma = 6$ deg/hour.

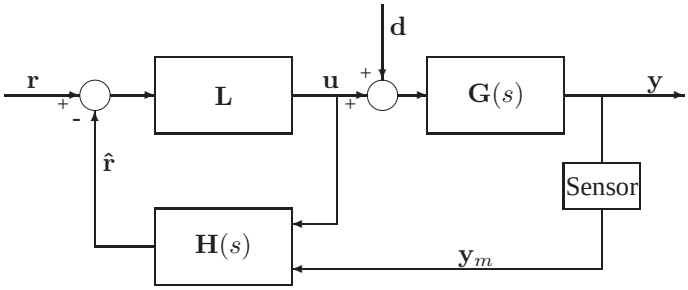

Figure 8.1: *Illustration of the LQG interconnections with the load disturbances* $\mathbf{d}$*, plant* $\mathbf{G}(s)$*, sensors and reference* $\mathbf{r}$*.*

Theorem 8.3
The Kalman filter has the structure of an ordinary state estimator

$$\dot{\hat{\boldsymbol{x}}}(t) = \boldsymbol{A}\hat{\boldsymbol{x}}(t) + \boldsymbol{B}\boldsymbol{u}(t) + \boldsymbol{K}_f(\boldsymbol{y}_m(t) - \boldsymbol{C}\hat{\boldsymbol{x}}(t)) \tag{8.17}$$

The optimal gain matrix $\boldsymbol{K}_f$*, which minimizes the expectation of the estimation error* $E\{[\boldsymbol{x} - \hat{\boldsymbol{x}}]^T[\boldsymbol{x} - \hat{\boldsymbol{x}}]\}$*, is given by*

$$\boldsymbol{K}_f = \boldsymbol{Y}\boldsymbol{C}^T\boldsymbol{R}_2^{-1} \tag{8.18}$$

where $\boldsymbol{Y} = \boldsymbol{Y}^T$ *is the positive semidefinite solution of the algebraic Riccati equation*

$$\boldsymbol{Y}\boldsymbol{A}^T + \boldsymbol{A}\boldsymbol{Y} - \boldsymbol{Y}\boldsymbol{C}^T\boldsymbol{R}_2^{-1}\boldsymbol{C}\boldsymbol{Y} + \boldsymbol{R}_1 = 0 \tag{8.19}$$

Derivations and proofs of Theorem 8.3 can be found e.g. in (Kwakernaak & Sivan 1972). The structure of the LQG controller is shown in Figure 8.1

With the same reason as for the controller in Section 8.3, the filter will be designed in continuous time and the discrete version found by equivalence of the optimization as in Theorem 8.4.

Theorem 8.4
When the sampling time T *is small with respect to the plant time constant, the following relation is valid between the covariance matrices*

$$\boldsymbol{R}_1 = \frac{1}{T}\boldsymbol{R}_{1d} \quad \textit{and} \quad \boldsymbol{R}_2 = \frac{1}{T}\boldsymbol{R}_{2d} \tag{8.20}$$

index d *being the discrete equivalence.*

The proof of Theorem 8.4 is provided in (Franklin et al. 1998).

The filter gain $\mathbf{K}$ is found after several iterations and simulations, and has a bandwidth an order of magnitude faster than the LQR to ensure proper tracking response. In

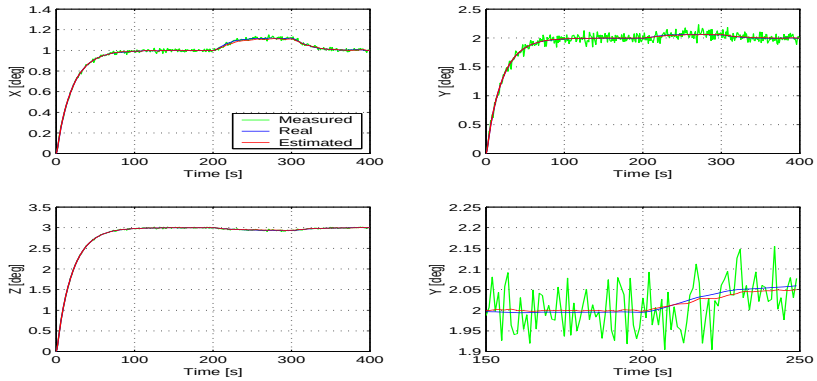

Figure 8.2: *Step response of the LQG with a short pulse of load disturbance between* 200 *and* 300 *seconds.*

Figure 8.2 we see a step response for the LQG shown in Figure 8.1. The design exhibits a critically dampened response with very good stationary behavior. The steady state error is negligible small clearly underlining no need for explicit integral terms in the loops. It is also seen that the measurement noise is well filtered. The lower right plot shows a zoom of the area where the load disturbance is applied.

The closed loop poles are the union of the controller and the estimator poles. By combining Equations (8.17), (8.4), (8.2) and forming the estimation error the closed loop poles can be determined by

$$\det(\lambda \mathbf{I} - (\mathbf{A} - \mathbf{BL}))\det(\lambda \mathbf{I} - (\mathbf{A} - \mathbf{K}_f \mathbf{C})) \tag{8.21}$$

which also confirms the separation theorem. The closed loop poles for the LQG are listed in Table 8.3.

We see they are well placed away from the imaginary axis and the frequency separation between the controller and the estimator.

We will now define from Figure 8.1 the sensitivity $\mathbf{S}$ and the complementary sensitivity $\mathbf{T}$ functions and we combine estimator and controller into a general compensator

Controller	Estimator
$-5.3259 \cdot 10^{-1}$	$-8.1071 \cdot 10^{-2} \pm j9.9071 \cdot 10^{-6}$
$-5.0002 \cdot 10^{-2}$	$-3.2105 \cdot 10^{-1} \pm j3.0054 \cdot 10^{-4}$
$-2.6875 \cdot 10^{-1}$	$-1.5123 \cdot 10^{-2}$
$-5.0009 \cdot 10^{-2}$	$-3.2596 \cdot 10^{-1}$

Table 8.3: *Closed loop poles for the attitude control loops.*

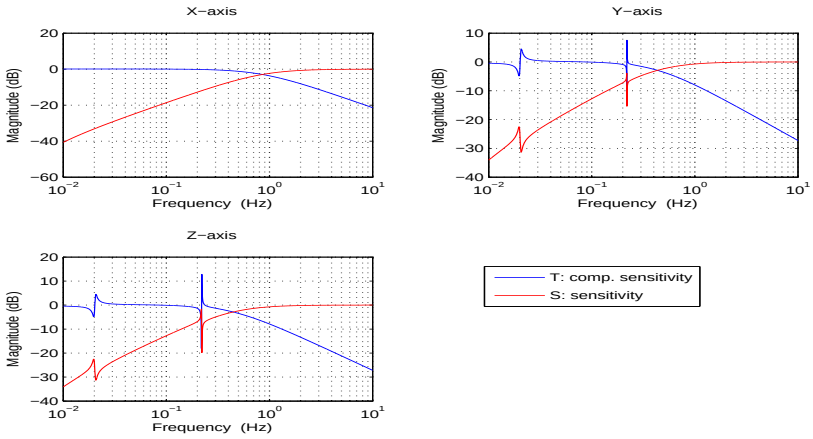

Figure 8.3: *The sensitivity function* $\mathbf{S}$ *and the complementary sensitivity function* $\mathbf{T}$ *for the attitude LQG design. The resonance peaks are from the flexible modes. They do not appear on the x-axis due to their edge on orientation.*

$\mathbf{K}$ in the forward path (Åström & Wittenmark 1989)

$$\mathbf{S} = (\mathbf{I} + \mathbf{GK})^{-1} \tag{8.22}$$

$$\mathbf{T} = (\mathbf{I} + \mathbf{GK})^{-1}\mathbf{GK} \tag{8.23}$$

$$\mathbf{S} + \mathbf{T} = \mathbf{I} \tag{8.24}$$

$\mathbf{S}$ gives the closed loop transfer from the disturbance $\mathbf{d}$ to the output $\mathbf{y}$ (scaled by $\mathbf{G}$ if at input or output), while $\mathbf{T}$ gives the closed loop from the reference $\mathbf{r}$.

It is therefore desirable to keep $\mathbf{S}$ small at frequencies where disturbance suppression is needed, typically at low frequencies. Contrary $\mathbf{T}$ should be unity at low frequencies. As for physical systems $\mathbf{G}(s)\mathbf{K}(s)$ is proper and in practice strictly proper we have that

$$\lim_{s\to\infty} \mathbf{G}(s)\mathbf{K}(s) = 0 \tag{8.25}$$

which implies that

$$\lim_{s\to\infty} \mathbf{S}(s) = 1 \tag{8.26}$$

and

$$\lim_{s\to\infty} \mathbf{T}(s) = 0 \tag{8.27}$$

In Figure 8.3 we see the $\mathbf{S}$ and $\mathbf{T}$ functions for the LQG design. They are very well behaved and the 2 functions are rather symmetric about the cross over frequency with no real overshoot indicating reasonable stability properties. This is consistent with

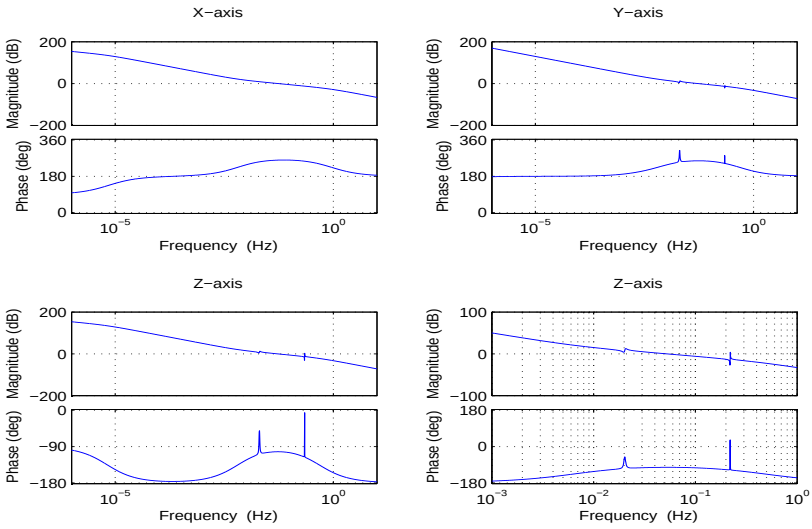

Figure 8.4: *Attitude open loop transfer frequency response one loop at the time, with rigid, flexible and sloshing modes. Shows response for the x and y-axes in the upper row and z-axis below, with z-axis zoom in graph(2,2).*

observed step responses for the system. The flexible modes are clearly visible, around the bandwidth and not a concern for reference tracking and of moderate size.

The LQG has, contrary to the Equation (8.9), not the guaranteed stability margins of the LQR. This was first demonstrated by (Doyle 1978) by an example and an adjustment procedure to recover most of the properties was presented in (Doyle & Stein 1979) later matures into the Loop Transfer Recovery (LTR) procedure. We will in the next section analyze the closed loop LQG stability margins with that in mind as well as recalling that we are applying linear methods on nonlinear models, which in the final stage will be evaluated by simulation.

8.5 Classical Stability Analysis and Nonlinear Performance Simulation

As mentioned earlier the tradition is SISO design for such systems and SISO analysis. Therefore we will first perform a classical analysis of the LQG MIMO design. It will be performed by opening one loop at the time for the angles on the 3 axes. This will ensure that the couplings to the other loops are accounted for as far as possible. The frequency response for that is shown in Figure 8.4.

Before proceeding we will calculate the Relative Gain Array (RGA) of the system, which will be able to indicate how diagonal (coupled) the system is in relative measures.

	x	y	z
GM[db, Hz]	∞(at ∞)	∞(at ∞)	∞(at ∞)
PM[deg, Hz]	80.2(at 0.054)	76(at 0.054)	77(at 0.052)
Delay Margin [s]	4.1	4.0	4.1

Table 8.4: *Summary of the closed loop SISO stability margins for the LQG design extracted from the plots in Figure 8.4. Delay Margin (DM) is $DM = PM(\omega_c) \cdot \omega_c$.*

It will help determine how representative the margins are.

The RGA of a complex non singular $m \times m$ matrix $\mathbf{A}$ is a complex $m \times m$ matrix defined by

$$RGA(\mathbf{A}) \triangleq \mathbf{A} \times (\mathbf{A}^{-1})^{\mathrm{T}} \tag{8.28}$$

where $\times$ denotes the element by element multiplication and was introduced by (Bristol 1966). The many properties of the RGA are well proven and derived in (Skogestad & Postlethwaite 1996) and will not be repeated here. For a non square matrix $\mathbf{A}$ of dimensions $l \times m$ the pseudo inverse can be used instead, (Chang & Yu 1990). One property we need is that it indicates the relative size of the elements with respect to each other.

For the system $\mathbf{G}(s)$ in Figure 8.1 of size 6×3 and $\mathbf{G}_{fr}$ being the complex frequency response, we complete the RGA and take the absolute value of each element

$$|RGA(\mathbf{G}_{fr})|_{ij} = \begin{bmatrix} 0.995 & \cdot & < 10^{-3} \\ & 0.995 & \cdot \\ & & 0.995 \\ \hline 6 \cdot 10^{-3} & \cdot & < 4 \cdot 10^{-6} \\ & 6 \cdot 10^{-3} & \cdot \\ & & 6 \cdot 10^{-3} \end{bmatrix} \tag{8.29}$$

We see that the diagonal elements are about a factor 10^3 larger than the corresponding off diagonal. This clearly indicates that the plant is weakly coupled.

The plots in Figure 8.4 are displayed for no rotation of the solar panels, as in Figure 3.4 with $\beta = 0$, and that is why the modes are not visible for the x-axis. Other angles have been analyzed with similar results.

For the x and y-axes we see an increasing phase, which is caused by the LHP zeros appearing when the two other loops are closed via the controller and estimator and manifest themselves in the loop transfer.

The concern of the flex modes we can investigate from the zoom in plot $2,2$ in Figure 8.4. If the damping of the close modes increases or decreases the gain zero db cross over will change frequency in a jump.This will only affect the GM and we see that we actually will get an increase in PM as the gain will cross at a lower frequency where the phase is lower. For this design they will therefore not have a destabilizing effect and we need not be too concerned in the nominal situation. The actual SISO margins for all axis and loops are summarized in Table 8.4.

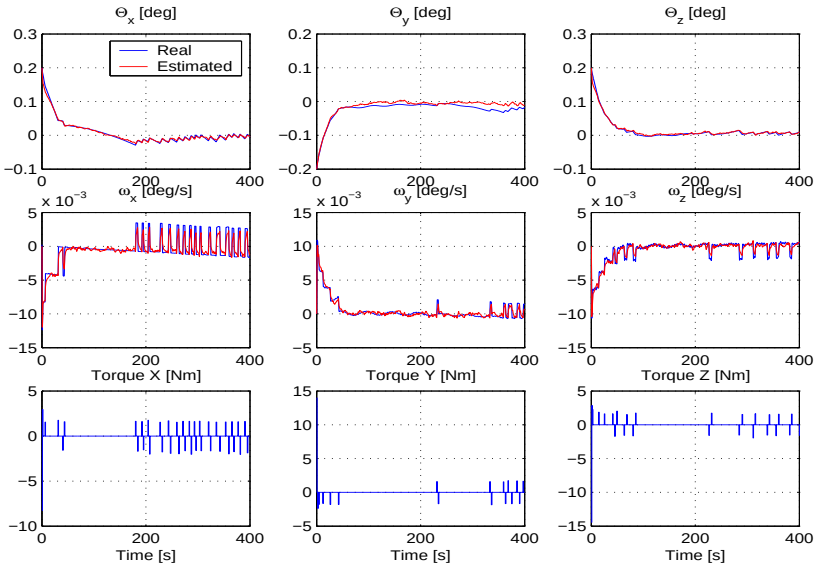

Figure 8.5: *The full nonlinear simulation showing the attitude, the rates and the input torques.* $\boldsymbol{\theta}(0) = [0.2, -0.2, 0.2]^T$ *deg and* $\omega(0) = \mathbf{0}$*. The larger torque around the y-axis is caused by the gravity gradient disturbance torque.*

We will now consider the LQG design discretely implemented in a full nonlinear simulation, which includes all details documented in this thesis concerning dynamics, disturbances, noises in avionics equipment. We choose a stationary attitude keeping with nonzero initial conditions. The results are displayed in Figure 8.5.

We see clearly the nonlinear effects, but all values are very well inside specifications. It has been chosen to display the torques per axis, rather than per engine, as much more illustrative and the latter well documented in Figure 7.7. The pulsed torque behavior is caused by the dead band in the PWM. It can be concluded that the design well fulfills all performance specifications.

Finally the system is tested for tracking capabilities combining a set of different types of reference signals into one continuous reference Figure 8.6. Also here it is seen that the design performs very satisfactory.

8.6 Floquet Stability Analysis

The asymptotic stability of the periodic LTV system will be assessed using the theory derived in Section 7.4.1. For simplicity the analysis will be illustrated for the LQR design, though the computations are for the complete LQG.

We will consider the closed loop system of the form of Equation (7.1) and we obtain

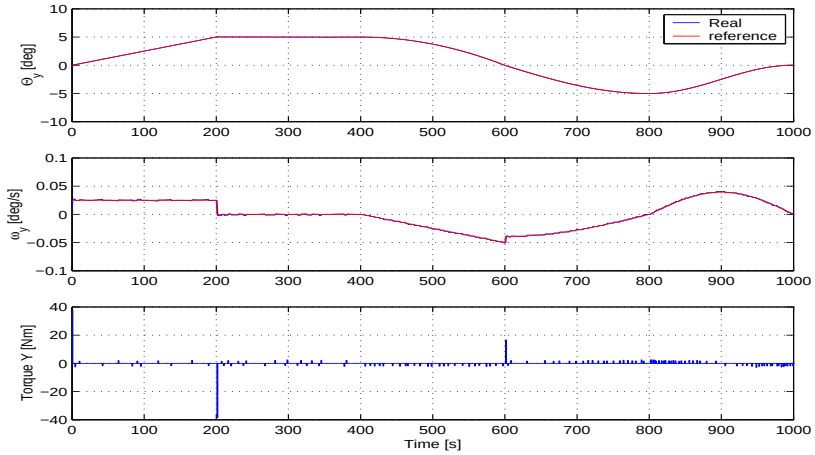

Figure 8.6: *Nonlinear simulation result following a more complex reference signal for the attitude and rates. The reference is a ramp, a constant, a parabola and two different sinusoidal signals.*

combining Equations (8.2) and (8.4)

$$\dot{\mathbf{x}}(t) = (\mathbf{A}(t) - \mathbf{BL})\mathbf{x}(t) \tag{8.30}$$

where the only time varying periodic part is one quarter of $\mathbf{A}(t)$, see also Equations (5.15) and (5.7).

To find the monodromy matrix $\mathbf{M}$ in Equation (7.6) we use Picard's approximation from Equations (7.10) and (7.11). It turns out, that for this type of very slow dynamics, the approximations are inadequate and lead of eigenvalue relocations. The method is discarded and we turn to numerical computations to find the monodromy matrix, as described in Section 7.4.1.

Successive simulations are performed to find each final value $\mathbf{x}_i(T)$ for each initial state element $\mathbf{x}_i(t_0)$. The reference state for the closed loop is zero, hence a pure initial value problem. The monodromy $\mathbf{M}$ or state transition matrix $\mathbf{\Phi}(T, 0)$ is formed successively by the $\mathbf{x}_i(T)$ column vectors.

The result becomes $\mathbf{\Phi}(T, 0) = \mathbf{0}$ (apart from numerical noise) leading to eigenvalues at the origin. Thus the periodic closed loop system is asymptotically stable from Equation (7.3). It is expected that $\mathbf{\Phi}(T, 0) = \mathbf{0}$ as we have a closed loop system with a settling time of about 100 s and the period of $\mathbf{A}(t)$ is about 8000 s. Therefore any initial nonzero value will be driven to the origin long time before one period is reached.

These results confirm the expected behavior, when the closed loop dynamic is so much faster than the periodicity. The reliable computation of the monodromy matrix in the Floquet theory is not practical as well as it only provides information about the asymptotic stability. Stability margin indicators can be developed by shifting the imaginary axis, but this is an iterative process and not so attractive in practice.

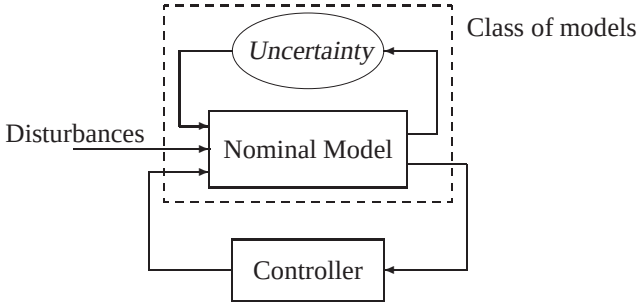

Figure 8.7: *Illustration of the concept of combination of a nominal model with some sort of uncertainty modeling resulting in a class of models describing better the real physical behavior.*

The Floquet method will therefore not be utilized further in this project, but the periodic variations will be treated instead as uncertainties in the framework of worst case analysis.

8.7 Principal Uncertainty Description

During control design we make use of linear mathematical models, which are to represent the real physical world. Such models are approximations such that:

- Nominal models are not considering any possible uncertainties.
- Worst case models are typically a combination of nominal models and some form of modeling of known uncertainties. There can still be unknown uncertainties unaccounted for.

The grouping of models can also be illustrated graphically in Figure 8.7. The use of the way of modeling in Figure 8.7 can be done in different ways.

- The nominal model can be used for both synthesis and analysis. This is a classical approach.
- The nominal model is used for synthesis and the uncertainties are accounted for in analysis.
- The full uncertainty model is used for both synthesis and analysis, which is the most complex and numerically demanding situation.

The approach selected here is the second one; which leads to the need for deriving the non nominal models for the analysis part.

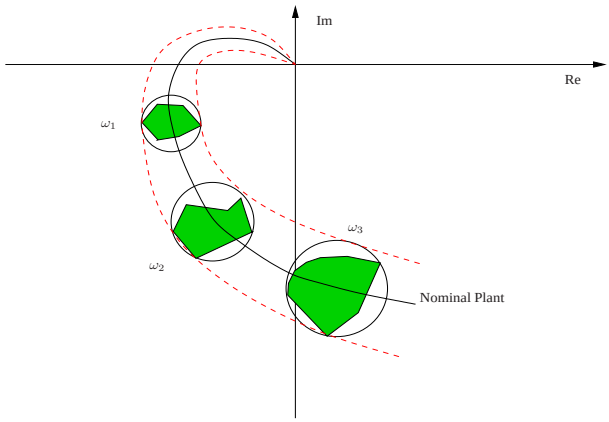

Figure 8.8: *Uncertainty regions in the Nyquist plot at given frequencies ω_1, ω_2 and ω_3. The green polyhedron are the real uncertainties approximated by the circumscribed circles.*

As the robust control framework is frequency domain based, it is beneficial to illustrate how uncertainties can be interpreted and approximated in the frequency domain. Let us consider an uncertain plant $\mathbf{G}_p(s)$ with some form of uncertainty description in the Nyquist plot in Figure 8.8.

The full line in Figure 8.8 is the curve for the nominal plant and the 2 dashed lines give bounds for the class of uncertain models outlined in Figure 8.7. The irregular shaped regions are the parametric uncertainties of the model varying certain parameters in a specified region. The disc shaped regions are used to represent the uncertainties, but are more conservative as non existing plants are allowed. They can e.g. be modeled as multiplicative uncertainties of the form

$$\mathbf{G}_p(s) = \mathbf{G}(s)(1 + \mathbf{w}_I(s)\mathbf{\Delta}_I(s)), \quad |\mathbf{\Delta}_I(j\omega)| \leq 1, \quad \forall\omega \tag{8.31}$$

where the radius of the disc in Figure 8.8 becomes $|\mathbf{G}(j\omega)\mathbf{w}_I(j\omega)|$. See e.g. (Doyle & Stein 1981).

One can view $\mathbf{w}_I(s)$ as a weight introduced to normalize the perturbation to be less than 1 in magnitude at each frequency. In most cases $\mathbf{w}_I(s)$ is a rational transfer function and we will always choose weights to be stable minimum phase further on.

Care should be taken, that the uncertainty is not larger than 100 % meaning $|\mathbf{w}_I(s)| > 1$, in which case the disc at that particular frequency includes the origin. We loose the phase information and plant zeros cross from the left to the right half plane. There exists then a $|\mathbf{\Delta}_I(j\omega_i)| < 1$ such that $\mathbf{G}_p(j\omega_i) = 0$ in Equation (8.31), which means possible plant zeros at ω_i. This means the input has no effect on the output at that frequency, so no control.

When dealing with systems having several multi variable uncertainties which influence several input and output channels the complete system becomes increasingly

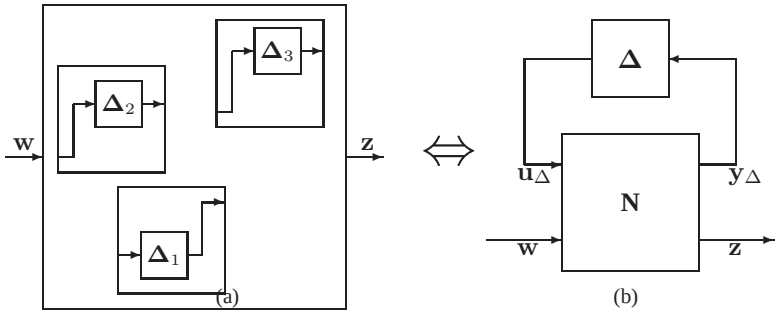

Figure 8.9: *How to pull out the uncertainties and form the general* 2×2 *port form, where the individual* Δ *are collected into one.*

difficult to analyze. It is convenient to reformulate the problem in the general 2×2 representation illustrated in Figure 8.9. There the principle of how to isolate each $\mathbf{\Delta}_i$ is shown and how to structure it into a larger block diagonal $\mathbf{\Delta}$ matrix external to the original inner structure. This is a description of structured uncertainty, contrary to unstructured uncertainty where $\mathbf{\Delta}$ is a full complex matrix.

The resulting $\mathbf{N\Delta}$ can conveniently be manipulated by means of Linear Fractional Transformations. This will be explained in detail in Section 8.8 and LFTs are detailed in Section D.3.

8.8 Uncertainty Description in General Form

This section will cover derivation of all relevant uncertainty descriptions and bring them into the general form of Figure 8.9.

The viewpoint adopted to deal with the periodic LTV system, is to consider the time varying parameters as ordinary uncertainties. We will consider the bounds on variations and neglect any knowledge of how they vary over time. This is a novel contribution to the field treated here and a core part of this project in the GNC part of it. Therefore special attention is paid to its detailed treatment together with the robustness analysis of the feedback loops and more detailed justification is provided in Section 8.13.

The reason for formulating the problem in the general form is to make it modular and to fit with the framework of the robust control field. The latter being treated in detail in Section 8.13.

The main objective of this section is to define the uncertainties and pull them out into one common $\mathbf{\Delta}$ block. The ones considered are

- Uncertainties in the LTV model in Equation (5.15) for the inertia matrix and the orbital angular rate.

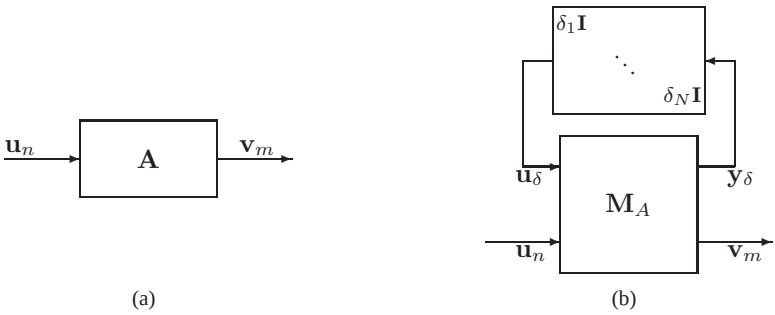

Figure 8.10: *LFT representation of a matrix parametric uncertainty.*

- The damping of the flexible modes in Equation (3.21).
- Uncertainty in the torque level caused by thruster uncertainty and COM location.
- Delay uncertainty caused primarily by the sensors.

All of these are bounded variations of real parameters at various locations in the individual models. This leads to more complicated uncertainty modeling than a lumped complex one but also more representative towards the real world.

As we will be dealing with real parameter variations mostly for state space formulations a general partition of the matrices will be convenient. A matrix $\mathbf{A}$ can be written as

$$\mathbf{A} = \mathbf{A}_0 + \sum_{i=1}^{N} \delta_i \mathbf{A}_i \quad \in \mathcal{C}^{m\times n}, \quad \|\delta_i\| \leq 1 \tag{8.32}$$

Then the expression $\mathbf{v}_m = \mathbf{A}\mathbf{u}_n$ can be formulated as a LFT in Figure 8.10. The partitioning can be performed in at least 3 different manners giving different size of possible repeated uncertainty δ_i. This is illustrated in Figure 8.11, from which we see that the dimension of the repeated δ_i is either the input or output dimensions m, n for the first two ways. The right diagram in Figure 8.11 represents a decomposition using the Singular Value Decomposition (SVD), where a matrix can be written as (Green & Limebeer 1995)

Lemma 8.1
A complex $m \times n$ matrix $\boldsymbol{A}$ can be factorized into a Singular Value Decomposition

$$\boldsymbol{A} = \boldsymbol{U}\boldsymbol{\Sigma}\boldsymbol{V}^H \tag{8.33}$$

where the $m \times m$ matrix $\boldsymbol{U}$ and the $n \times n$ matrix $\boldsymbol{V}$ are unitary [1] *and the $m \times n$ matrix $\boldsymbol{\Sigma}$ contains the diagonal matrix $\boldsymbol{\Sigma}_0$ of real, non negative singular values σ_i arranged in*

[1] A complex matrix $\mathbf{U}$ is unitary if $\mathbf{U}^{\mathrm{H}} = \mathbf{U}^{-1}$ (Skogestad & Postlethwaite 1996).

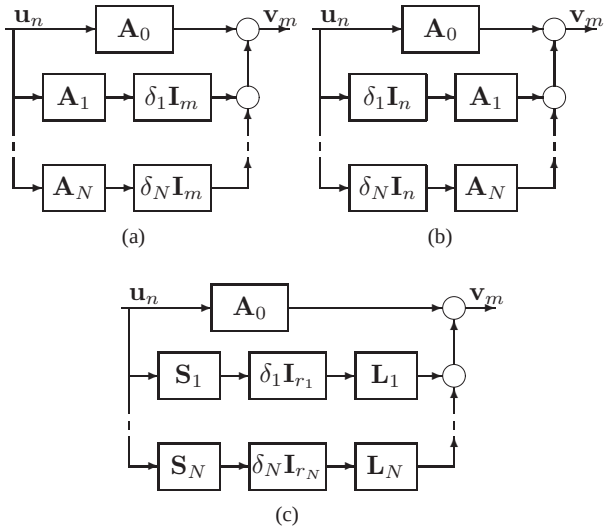

Figure 8.11: *Different ways to partition the* $\mathbf{A}$ *matrix leading to different dimensions of the delta.*

descending order as in

$$\mathbf{\Sigma} = \begin{bmatrix} \mathbf{\Sigma}_0 \\ \boldsymbol{0} \end{bmatrix} \quad \textit{for} \quad m \geq n \tag{8.34}$$

or

$$\mathbf{\Sigma} = [\mathbf{\Sigma}_0 \;\; \boldsymbol{0}] \quad \textit{for} \quad m \leq n \tag{8.35}$$

where

$$\mathbf{\Sigma}_0 = diag\{\sigma_1, \sigma_2, \cdots, \sigma_k\}, \quad k = \min(m, n) \tag{8.36}$$

and

$$\bar{\sigma} \triangleq \sigma_1 \geq \sigma_2 \geq \cdots \geq \sigma_k \triangleq \underline{\sigma} \tag{8.37}$$

and

$$\sigma_i(\boldsymbol{A}) = \sqrt{\lambda_i(\boldsymbol{A}^H\boldsymbol{A})} = \sqrt{\lambda_i(\boldsymbol{A}\boldsymbol{A}^H)} \tag{8.38}$$

where λ_i *is the eigenvalue*

We now use Lemma 8.1 to find the minimum formulation in Figure 8.11. The rank $r_i = \text{rank}(\mathbf{A})$ is defined as the minimum number of non zero singular values in Equation (8.36) (Zhou, Doyle & Glover 1995). We can write for $\mathbf{A}_i$ in Equation (8.32)

$$r_i = \text{rank}(\mathbf{A}_i) \leq \min(m, n) \tag{8.39}$$

and we will now strip the non needed columns in $\mathbf{U}$ and $\mathbf{V}$ in Equation (8.33) such that

$$\mathbf{U}_i = \mathbf{U}(:, 1 : r_i), \;\; \mathbf{\Sigma}_i = \mathbf{\Sigma}(1 : r_i, 1 : r_i), \;\; \mathbf{V}_i = \mathbf{V}(:, 1 : r_i) \tag{8.40}$$

and define

$$\mathbf{L}_i = \mathbf{U}_i \quad \text{and} \quad \mathbf{S}_i = \mathbf{\Sigma}_i \mathbf{V}_i^{\mathrm{H}} \tag{8.41}$$

such that

$$\delta_i \mathbf{A}_i = \mathbf{L}_i \delta_i \mathbf{I}_{r_i} \mathbf{S}_i, \quad \|\delta_i\| \leq 1 \tag{8.42}$$

Extracting the δ_i in Equation (8.42) and structuring as in Figure 8.10, the matrix $\mathbf{M}_A$ is of the form

$$\mathbf{M}_A = \begin{bmatrix} \mathbf{0} & \cdots & & \mathbf{S}_1 \\ \vdots & & & \vdots \\ & & & \mathbf{S}_N \\ \mathbf{L}_1 & \cdots & \mathbf{L}_N & \mathbf{A}_0 \end{bmatrix} \tag{8.43}$$

and formulated as an upper LFT the expression in Figure 8.10 becomes

$$\mathbf{v}_m = F_u(\mathbf{M}_A, \mathbf{\Delta}) \cdot \mathbf{u}_n \tag{8.44}$$

This is a general form for parametric uncertainty which guarantee the minimum size of $\mathbf{\Delta}$. (Manceaux-Cumer & Chretien 2001) This is important to be as little conservative as possible and improves the well-posedness with respect to the algorithms used for computing the robustness measures. This can all be summarized as Lemma 8.2.

Lemma 8.2
Let a perturbed state space system be described as

$$\dot{\boldsymbol{x}}(t) = (\boldsymbol{A} + \sum_i \delta_i \boldsymbol{A}_i)\boldsymbol{x}(t) + (\boldsymbol{B} + \sum_i \delta_i \boldsymbol{B}_i)\boldsymbol{u}(t) \tag{8.45}$$

$$\boldsymbol{y}(t) = (\boldsymbol{C} + \sum_i \delta_i \boldsymbol{C}_i)\boldsymbol{x}(t) + (\boldsymbol{D} + \sum_i \delta_i \boldsymbol{D}_i)\boldsymbol{u}(t) \tag{8.46}$$

Then the minimum number of repetitions δ_i in the $\mathbf{\Delta}$ matrix is equal to the rank of

$$\begin{bmatrix} \boldsymbol{A}_i & \boldsymbol{B}_i \\ \boldsymbol{C}_i & \boldsymbol{D}_i \end{bmatrix}$$

8.9 Attitude Model Uncertainty Description

The uncertain parameters in Equation (5.15) are the diagonal elements of the inertia matrix and the orbital angular rate. We reformulate $\mathbf{B}_c$ as

$$\mathbf{B}_c = \begin{bmatrix} \mathbf{0} \\ \mathbf{B}_d \end{bmatrix} = \begin{bmatrix} \mathbf{0} \\ \mathbf{I}_c^{-1} \end{bmatrix} = \begin{bmatrix} \mathbf{0} \\ \mathbf{I} \end{bmatrix} \mathbf{I}_c^{-1} \tag{8.47}$$

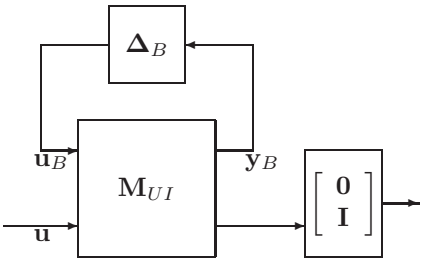

Figure 8.12: *Illustration of the LFT implementation of the input matrix* $\mathbf{B}_c$.

The inertia matrix $\mathbf{I}_c$ can be written as

$$\begin{aligned} \mathbf{I}_c &= \mathbf{I}_{c_0} + \begin{bmatrix} \delta_1 & & \\ & \delta_2 & \\ & & \delta_3 \end{bmatrix} \begin{bmatrix} k_1 & & \\ & k_2 & \\ & & k_3 \end{bmatrix} \\ &= \mathbf{I}_{c_0} + \underbrace{\begin{bmatrix} \mathbf{I} \end{bmatrix}}_{\mathbf{L}} \underbrace{\begin{bmatrix} \delta_1 & & \\ & \delta_2 & \\ & & \delta_3 \end{bmatrix}}_{\mathbf{\Delta}_B} \underbrace{\begin{bmatrix} k_1 & & \\ & k_2 & \\ & & k_3 \end{bmatrix}}_{\mathbf{S}} \end{aligned} \tag{8.48}$$

where $\delta_i k_i = [-\mathbf{I}_{\delta_i}; \mathbf{I}_{\delta_i}] \;\; i = 1..3$ and the numerical values are in Section C.2. The last term in Equation (8.48) has rank $= 3$ and no repeated uncertainty. $\mathbf{I}_c$ can be written as an upper LFT $\mathbf{I}_c = F_u(\mathbf{M}, \mathbf{\Delta}_B)$ where

$$\mathbf{M} = \begin{bmatrix} \mathbf{0} & \mathbf{S} \\ \mathbf{L} & \mathbf{I}_{c_0} \end{bmatrix} \tag{8.49}$$

according to Equations (8.43) and (8.48). From Section D.3.3.2 we obtain

$$\mathbf{I}_c^{-1} = F_u(\mathbf{M}, \mathbf{\Delta}_B)^{-1} = F_u(\mathbf{M}_{UI}, \mathbf{\Delta}_B) \tag{8.50}$$

and

$$\mathbf{M}_{UI} = \begin{bmatrix} \mathbf{M}_{11} - \mathbf{M}_{12}\mathbf{M}_{22}^{-1}\mathbf{M}_{21} & \mathbf{M}_{12}\mathbf{M}_{22}^{-1} \\ -\mathbf{M}_{22}^{-1}\mathbf{M}_{21} & \mathbf{M}_{22}^{-1} \end{bmatrix} \tag{8.51}$$

Graphically Equation (8.47) is then implemented as illustrated in Figure 8.12.

We will now partition the $\mathbf{A}$ matrix of the dynamical model. $\mathbf{A}_c$ of Equation (5.16) can be formulated as

$$\mathbf{A}_c = \mathbf{A}_0 + \mathbf{A}_1 \;\; \wedge \;\; \mathbf{A}_1 = \begin{bmatrix} \mathbf{0} & \mathbf{0} \\ \mathbf{0} & \mathbf{X} \end{bmatrix} = \begin{bmatrix} \mathbf{0} \\ \mathbf{I} \end{bmatrix} \mathbf{X} \begin{bmatrix} \mathbf{0} & \mathbf{I} \end{bmatrix} \tag{8.52}$$

and $\mathbf{X}$ will be formulated in the form of a LFT. From Equation (5.6) we get that

$$\mathbf{X} = \omega_0 \mathbf{I}_c^{-1} \mathbf{M} \tag{8.53}$$

and from Equation (B.8)

$$\mathbf{M} = \begin{bmatrix} I_{31} & 2I_{32} & I_{33} - I_{22} \\ -I_{32} & 0 & I_{12} \\ I_{22} - I_{11} & -2I_{12} & -I_{13} \end{bmatrix} \tag{8.54}$$

There are 4 independent uncertainties namely ω_0 and the diagonal of $\mathbf{I}_c$.

LFT 1: ω_0 can be written as

$$\omega_0 = \bar{\omega}_0 + \delta k_p \wedge \|\delta\| \leq 1, \quad \forall \delta \in \mathcal{R} \tag{8.55}$$

where $\omega_0 \in [\omega_l; \omega_u]$ and ω_l and ω_u are the lower and the upper bounds respectively. Then

$$\bar{\omega}_0 = \frac{1}{2}(\omega_l + \omega_u) \quad \text{and} \quad k_p = \frac{1}{2}(\omega_u - \omega_l) \tag{8.56}$$

which expanded to all 3 axis becomes

$$\omega_0 \mathbf{I} = \bar{\omega}_0 \mathbf{I} + \delta \mathbf{I} \cdot k_p = F_u(\mathbf{M}_\omega, \mathbf{\Delta}_\omega) \tag{8.57}$$

and the upper LFT is shown in Figure 8.13. It shall be noted that despite ω_0 is a scalar, due to the fact it is multiplied by a matrix and influencing all 3 vector elements, it leads to 3 repeated uncertainties.

LFT 2: This is already calculated and the result is in Equation (8.50).

LFT 3: Using Equation (8.32) we can formulate Equation (8.54) as

$$\mathbf{M} = \mathbf{M}_0 + \sum_{i=1}^{3} \mathbf{M}_i = \mathbf{M}_0 + \delta_1 \mathbf{M}_{11}(k_1) + \delta_2 \mathbf{M}_{22}(k_2) + \delta_3 \mathbf{M}_{33}(k_3) = F_u(\mathbf{M}_M, \mathbf{\Delta}_M) \tag{8.58}$$

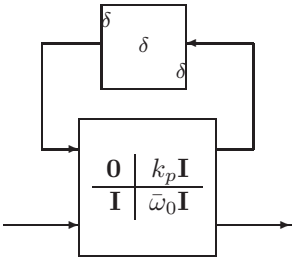

Figure 8.13: *The LFT for uncertainty on* ω_0.

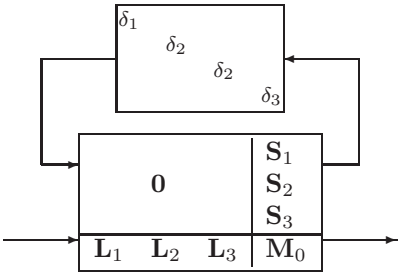

Figure 8.14: *The LFT for uncertainty of the* $\mathbf{M}$ *matrix in Equation (8.58).*

where k_i is defined and used in Equation (8.48) already. The nominal matrix, as the uncertainty is symmetric, is $\mathbf{M}_0 = \mathbf{M}(\mathbf{I}_c)$. The 3 factorizations become

$$\delta_1 \mathbf{M}_{11}(k_1) = \delta_1 \begin{bmatrix} 0 & 0 & 0 \\ 0 & 0 & 0 \\ -k_1 & 0 & 0 \end{bmatrix} = \underbrace{\begin{bmatrix} 0 \\ 0 \\ 1 \end{bmatrix}}_{\mathbf{L}_1} \delta_1 \underbrace{\begin{bmatrix} -k_1 & 0 & 0 \end{bmatrix}}_{\mathbf{S}_1}, \quad \text{rank} = 1 \tag{8.59}$$

$$\delta_2 \mathbf{M}_{22}(k_2) = \delta_2 \begin{bmatrix} 0 & 0 & -k_2 \\ 0 & 0 & 0 \\ k_2 & 0 & 0 \end{bmatrix} =$$

$$\underbrace{\begin{bmatrix} 0 & 1 \\ 0 & 0 \\ 1 & 0 \end{bmatrix}}_{\mathbf{L}_2} \begin{bmatrix} \delta_2 & 0 \\ 0 & \delta_2 \end{bmatrix} \underbrace{\begin{bmatrix} k_2 & 0 & 0 \\ 0 & 0 & -k_2 \end{bmatrix}}_{\mathbf{S}_2}, \quad \text{rank} = 2 \tag{8.60}$$

$$\delta_3 \mathbf{M}_{33}(k_3) = \delta_3 \begin{bmatrix} 0 & 0 & k_3 \\ 0 & 0 & 0 \\ 0 & 0 & 0 \end{bmatrix} = \underbrace{\begin{bmatrix} 1 \\ 0 \\ 0 \end{bmatrix}}_{\mathbf{L}_3} \delta_3 \underbrace{\begin{bmatrix} 0 & 0 & k_3 \end{bmatrix}}_{\mathbf{S}_3}, \quad \text{rank} = 1 \tag{8.61}$$

and combining Equations (8.58) to (8.61) the LFT $F_u(\mathbf{M}_M, \boldsymbol{\Delta}_M)$ is illustrated in Figure 8.14.

The 3 LFTs for the $\mathbf{A}_c$ matrix will be concatenated into one using Equation (D.25) and $\mathbf{X}$ in Equation (8.53) becomes

$$\mathbf{X} = F_u(\mathbf{M}_X, \boldsymbol{\Delta}_A) = F_u(\mathbf{M}_\omega, \boldsymbol{\Delta}_\omega) F_u(\mathbf{M}_{UI}, \boldsymbol{\Delta}_B) F_u(\mathbf{M}_M, \boldsymbol{\Delta}_M) \tag{8.62}$$

where

$$\boldsymbol{\Delta}_A = diag([\underbrace{\delta\ \delta\ \delta}_{\omega_0}\ \delta_{1_I}\delta_{1_M}\delta_{2_I}\delta_{2_M}\delta_{2_M}\delta_{3_I}\delta_{3_M}]) \tag{8.63}$$

where the second index refers to the δ_i origin. The δ_i will be combined with the one from the $\mathbf{B}_c$ LFT. It is recalled that there are only 4 independent δ_i. For $\mu-$analysis all the $\boldsymbol{\Delta}_i$ uncertainties need be collected into one $\boldsymbol{\Delta}$ following the canonical formulation in (Balas, Packard, Safonov & Chiang 2004) and (Balas, Doyle, Glover, Packard & Smith 1998). This formulation requires that repeated δ_i are grouped together such that $\boldsymbol{\Delta}$ becomes block diagonal. In this case we find the same δ_i in both $\boldsymbol{\Delta}_A$ and $\boldsymbol{\Delta}_B$ and they need be merged such that the repeated δ_i are grouped together. The uncertainties are then combined as

$$\boldsymbol{\Delta} = diag([\underbrace{\delta\ \delta\ \delta}_{\omega_0}\ \delta_{1_I}\delta_{1_M}\delta_{1_B}^{\downarrow}\delta_{2_I}\delta_{2_M}\delta_{2_M}\delta_{2_B}^{\downarrow}\delta_{3_I}\delta_{3_M}\delta_{3_B}^{\downarrow}]) \tag{8.64}$$

and the $\delta_i^{\downarrow}$ are the repeated δ_i from the $\boldsymbol{\Delta}_B$ matrix common with the same ones from the $\boldsymbol{\Delta}_A$ matrix. This is obviously not convenient, as the LFT input-output structure is not preserved. Therefore a general scheme for combining several LFTs with repeated uncertainties will be developed.

We can now formulate the $\boldsymbol{\Delta}$ structure as

$$\begin{bmatrix} \mathbf{u_A} \\ \mathbf{u_B} \end{bmatrix} = \begin{bmatrix} \boldsymbol{\Delta_A} & \\ & \boldsymbol{\Delta_B} \end{bmatrix} \begin{bmatrix} \mathbf{y_A} \\ \mathbf{y_B} \end{bmatrix} = \mathbf{L}_{if}\boldsymbol{\Delta}\mathbf{S}_{if} \begin{bmatrix} \mathbf{y_A} \\ \mathbf{y_B} \end{bmatrix} \tag{8.65}$$

where the $\boldsymbol{\Delta}$ is of the structure in Equation (8.64). The general structure of $\mathbf{S}_{if}$ exemplified by the need of Equation (8.64) yields

$$\mathbf{S}_{if} = \begin{bmatrix} \mathbf{I}_5 & & & & & \vdots & & & \\ \dots & \mathbf{0}_m & & \dots\dots\dots & & \vdots & \mathbf{I}_m & \dots & \\ & \Downarrow & & & & \vdots & & & \\ & \ddots & \mathbf{I}_3 & & & \vdots & & & \\ & \dots\dots & & \mathbf{0}_n & \dots & \vdots & \dots & \mathbf{I}_n & \dots \\ & & & \Downarrow & & \vdots & & & \\ & & & \ddots & \mathbf{I}_2 & \vdots & & & \\ & \dots\dots\dots & & & \mathbf{0}_m & \vdots & \dots & \mathbf{I}_m & \end{bmatrix} \tag{8.66}$$

Where in this case $m = n = 1$, all matrices are square and $\mathbf{L}_{if} = \mathbf{S}_{if}^{\mathrm{T}}$. The complete structure for the uncertain dynamics is illustrated in Figure 8.15.

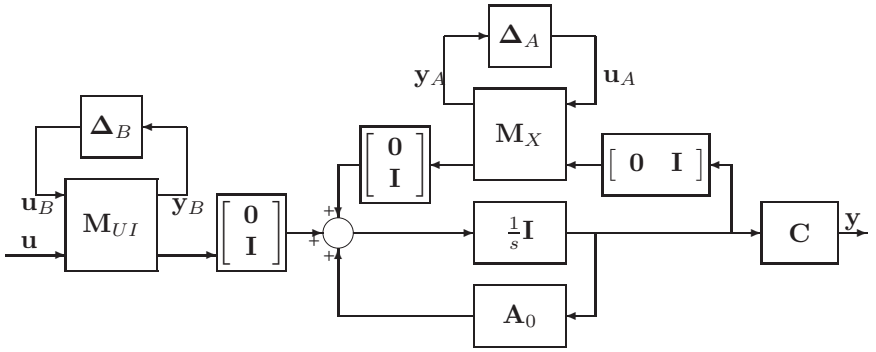

Figure 8.15: *The complete parametric uncertain state space system. The $\mathbf{\Delta}_A$, $\mathbf{\Delta}_B$ are pulled out using the factorization in Equations (8.65) and (8.66) without interfering with this structure (not illustrated).*

8.10 Flexible Modes Uncertainty Description

The uncertainty of the four flexible panels described in Section 3.4.3, will be lumped into one model with equivalent stronger coupling. We define one system matrix

$$\mathbf{G}_f(s) = \begin{bmatrix} \mathbf{A}_f & \mathbf{B}_f \\ \mathbf{C}_f & \mathbf{D}_f \end{bmatrix} \tag{8.67}$$

and the uncertainty model will be a stand alone state space system. The critical uncertainty for such systems is the damping ζ and much less the eigen frequency. The panel rotation angle β has been analyzed and found to influence results negligible. Emphasis will be on the former in order to focus on the essentials. We can formulate the uncertainty range as

$$\zeta \in [\zeta_l; \zeta_u] = [1; 5] \cdot 10^{-3} \tag{8.68}$$

where ζ_l and ζ_u are the lower and upper bounds respectively and

$$\bar{\zeta} = \frac{1}{2}(\zeta_l + \zeta_u) \quad \text{and} \quad k_f = \frac{1}{2}(\zeta_u - \zeta_l) \tag{8.69}$$

such that we reformulate Equation (8.68) as

$$\zeta = \bar{\zeta} + \delta \cdot k_f \wedge \|\delta\| \leq 1, \quad \forall \delta \in \mathcal{R} \tag{8.70}$$

In Equation (8.67) the two uncertain matrices are $\mathbf{A}_f$ and $\mathbf{C}_f$, and we reformulate Equation (3.21) as

$$\mathbf{A}_{f_p}(\zeta) = \mathbf{A}_{f_0}(\bar{\zeta}) + \delta \cdot \mathbf{A}_{f_1}(k_f) \tag{8.71}$$

where

$$\mathbf{A}_{f_0} = \begin{bmatrix} 0 & 1 \\ -\omega^2 & -2\bar{\zeta}\omega \end{bmatrix} \quad \text{and} \quad \mathbf{A}_{f_1} = \begin{bmatrix} 0 & 0 \\ 0 & -2\omega k_f \end{bmatrix} \tag{8.72}$$

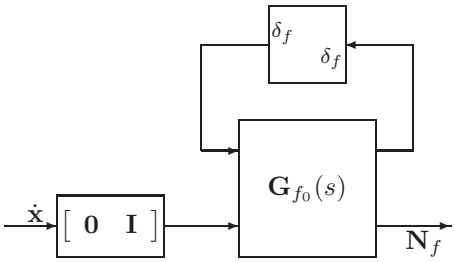

Figure 8.16: *The flexible modes LFT model of lumped solar panels into one model. Its connection to the dynamics is in principle as in Figure 3.7.*

Factorizing $\mathbf{A}_{f_1}$ in line with Equation (8.42) we get one δ and trivial $\mathbf{L}$ and $\mathbf{S}$ matrices as the rank $= 1$. In the exact same manner we can formulate $\mathbf{C}_f$ such

$$\mathbf{C}_{f_0} = \begin{bmatrix} \omega^2\mathbf{l}_1 & 2\bar{\zeta}\omega\mathbf{l}_1 \end{bmatrix} \quad \text{and} \quad \mathbf{C}_{f_1} = \begin{bmatrix} \mathbf{0} & 2\omega k_f\mathbf{l}_1 \end{bmatrix} \tag{8.73}$$

where $\mathbf{l}_1 = [l_1\ l_2\ l_3]^{\mathrm{T}}$ from Equation (3.22). $\mathbf{C}_{f_1}$ also has rank $= 1$. We can now finalize the model as an LFT illustrated in Figure 8.16.

8.11 Input Gain Uncertainty Description

The input uncertainty is a non nominal change in the torque. There are 3 main contributors to that:

- The thrust variation and bias of the individual engines as listed in Table C.5. Both are about 3 %.
- The uncertainty in the thrust vector direction, see Table C.5. Less than 1 deg half cone angle.
- The uncertainty of the COM location is about 0.045 m as listed in Section 3.2.2. This is 2.25 % on the shortest lever arm of about 2 m.

It is considered that the bias can be calibrated away, so this leaves about 5.25 % torque uncertainty. The uncertainties on the 3 axes are considered independent. Based on the previous development we can write this LFT directly in Figure 8.17, where $k_t \in [0; 0.06]$. This uncertainty is a direct change in the loop gain and therefore prominent.

8.12 Time Delay Uncertainty Description

Both sensors and actuators contribute with delays of varying size, the former the largest. We will consider delays of up to 1 s as specified for the sensors in Section C. As a sensor

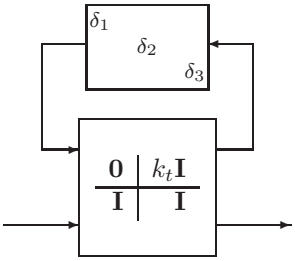

Figure 8.17: *LFT model of the torque input uncertainty. Inter axis independent.*

delay is not a random parameter, but linked to the internal operation of the equipment, it is typically the same for all outputs of the unit. We therefore consider to have the same delay on all channels. The delays will be considered all present at the plant input as invariant for linear systems.

A delay τ expressed in the Laplace domain can be approximated to a 1^{st} order Padé form as (Skogestad & Postlethwaite 1996)

$$e^{-\tau s} \approx \frac{1-\frac{\tau}{2}s}{1+\frac{\tau}{2}s} = \frac{-\tau s+2}{\tau s+2} = \frac{4}{\tau s+2} - 1 \tag{8.74}$$

Equation (8.74) can be transformed into a multi variable state space description as

$$\mathbf{G}_d(s) = \left[\begin{array}{c|c} -\frac{2}{\tau}\mathbf{I} & \frac{4}{\tau}\mathbf{I} \\ \hline \mathbf{I} & -\mathbf{I} \end{array}\right] = \left[\begin{array}{cc} \mathbf{A}_\tau & \mathbf{B}_\tau \\ \mathbf{C}_\tau & \mathbf{D}_\tau \end{array}\right] \tag{8.75}$$

and it shall be observed that this form, needed for the LFT, introduces a singularity for $\tau = 0$ which is not present in the transfer function form. The delay time is

$$\tau = \bar{\tau} + \delta \cdot k_d \quad \wedge \quad \|\delta\| \leq 1, \quad \forall \delta \in \mathcal{R} \tag{8.76}$$

where

$$\bar{\tau} = \frac{1}{2}(\tau_{max} + \tau_{min}) \quad \text{and} \quad k_d = \frac{1}{2}(\tau_{max} - \tau_{min}) \tag{8.77}$$

and $\tau_{min} > 0$.

We first consider the LFT for the matrix $\mathbf{A}_\tau$ observing that the uncertain parameter is in the denominator and thus nonlinear. Therefore let

$$\mathbf{A}_\tau^{-1} = -\frac{1}{2}\tau \cdot \mathbf{I} = -\frac{1}{2}\mathbf{I}(\bar{\tau} + \delta k_d) = F_u(\mathbf{M}_A, \mathbf{\Delta}_\tau) \tag{8.78}$$

where

$$\mathbf{M}_A = \left[\begin{array}{c|c} \mathbf{0} & -\frac{1}{2}k_d\mathbf{I} \\ \hline \mathbf{I} & -\frac{1}{2}\bar{\tau}\mathbf{I} \end{array}\right] \tag{8.79}$$

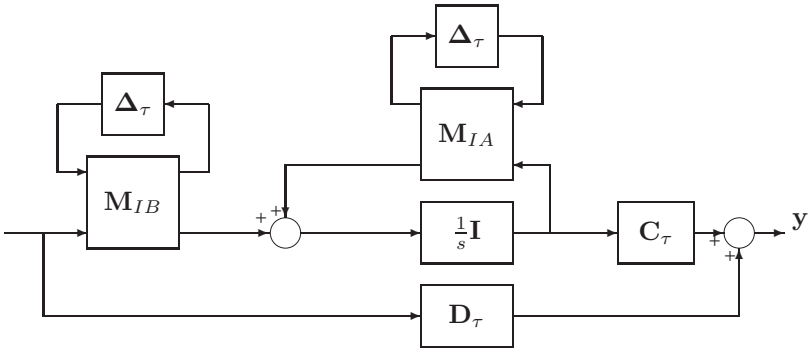

Figure 8.18: *Illustration of the uncertain time delay model with the two LFTs.*

Using the properties of inverse LFTs in Equation (D.18) the following holds

$$\mathbf{A}_\tau = F_u(\mathbf{M}_A, \mathbf{\Delta}_\tau)^{-1} = F_u(\mathbf{M}_{IA}, \mathbf{\Delta}_\tau) \tag{8.80}$$

where according to Equation (D.19)

$$\mathbf{M}_{IA} = \left[\begin{array}{c|c} -\frac{k_d}{\bar{\tau}}\mathbf{I} & \frac{k_d}{\bar{\tau}}\mathbf{I} \\ \hline \frac{2}{\bar{\tau}}\mathbf{I} & -\frac{2}{\bar{\tau}}\mathbf{I} \end{array}\right] \tag{8.81}$$

We observe that $\mathbf{B}_\tau = -2\mathbf{A}_\tau$ and we can write $\mathbf{B}_\tau = F_u(\mathbf{M}_{IB}, \mathbf{\Delta}_\tau)$ and

$$\mathbf{M}_{IB} = \left[\begin{array}{c|c} -\frac{k_d}{\bar{\tau}}\mathbf{I} & \frac{k_d}{\bar{\tau}}\mathbf{I} \\ \hline -\frac{4}{\bar{\tau}}\mathbf{I} & \frac{4}{\bar{\tau}}\mathbf{I} \end{array}\right] \tag{8.82}$$

The complete multi variable time delay model is illustrated in Figure 8.18.

8.13 Robust Stability

In the previous sections we have developed a way of how to represent an uncertain set of plants in terms of the $\mathbf{N\Delta}$ structure in Figure 8.9. The next step forward is to investigate if we have stability for all plants in the set.

> **Robust Stability (RS) analysis:** to ensure that with a given controller $\mathbf{K}$, we determine whether the system remains stable for all plants in the defined uncertainty set.

Further to the uncertainty regions illustrated in Figure 8.8, we will, in terms of SISO, illustrate the principal of RS in Figure 8.19, based upon the multiplicative uncertainty in Equation (8.31). For RS to be fulfilled the uncertainty circles must not include the -1 point, which can also be written as $|\mathbf{w}_I\mathbf{GK}| < |1 + \mathbf{GK}|$.

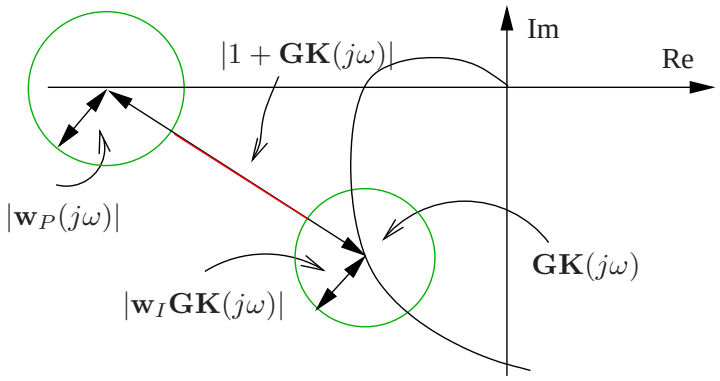

Figure 8.19: *Illustration of Robust Stability and Robust Performance for a SISO case. See the text for detailed definitions.*

The general control configuration is shown in Figure 8.20 (Dahleh & Kammash 1993), where the $\mathbf{N\Delta}$ structure on the right hand side is formed by closing the lower LFT such as

$$\mathbf{N} = F_l(\mathbf{P}, \mathbf{K}) = \mathbf{P}_{11} + \mathbf{P}_{12}\mathbf{K}(\mathbf{I} - \mathbf{P}_{22}\mathbf{K})^{-1}\mathbf{P}_{21} \tag{8.83}$$

Closing the upper LFT for the $\mathbf{N\Delta}$ structure gives

$$F_u(\mathbf{N}, \mathbf{\Delta}) = \mathbf{N}_{22} + \mathbf{N}_{21}\mathbf{\Delta}(\mathbf{I} - \mathbf{N}_{11}\mathbf{\Delta})^{-1}\mathbf{N}_{12} \tag{8.84}$$

for which system we want to ensure RS. The requirements for stability are summarized as follows

NS: $\mathbf{N}$ is internally stable with all poles in the LHP.

RS: $F_u(\mathbf{N}, \mathbf{\Delta})$ is stable $\forall \mathbf{\Delta}$, $\|\mathbf{\Delta}\|_\infty \leq 1$ and NS.

We suppose that the system in Equation (8.84) is nominally stable, with $\mathbf{\Delta} = \mathbf{0}$, which means that $\mathbf{N}$ is stable (not only $\mathbf{N}_{22}$). Following that we see directly from Equation (8.84) that the feedback term $(\mathbf{I}-\mathbf{N}_{11}\mathbf{\Delta})^{-1}$ is the only possible source of instability. The stability of Equation (8.84) is therefore equivalent to the stability of the $\mathbf{M\Delta}$ structure, when $\mathbf{M} = \mathbf{N}_{11}$. It can also be seen in Figure 8.21. Stability can be based upon the Generalized Nyquist theorem, see (Skogestad & Postlethwaite 1996), such that we have RS if and only if

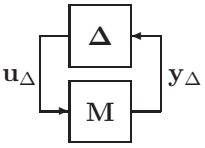

Figure 8.21: $\mathbf{M\Delta}$ *structure for robust stability analysis.*

$$\det(\mathbf{I} - \mathbf{M\Delta}(j\omega)) \neq 0 \quad , \quad \forall\omega \quad , \quad \forall\mathbf{\Delta} \tag{8.85}$$

but this criteria is unstructured and therefore conservative.

As we are only dealing with structured uncertainty, as developed in the past sections, we will utilize the structured singular value μ, which is defined as (Zhou, Doyle & Glover 1995).

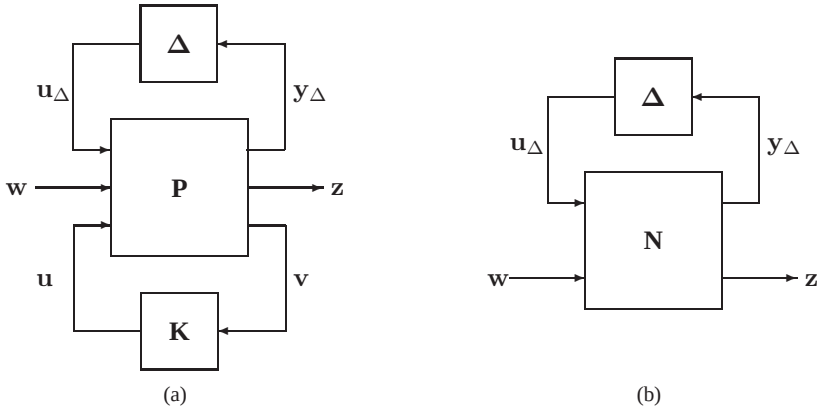

Figure 8.20: *General control configuration (left) and the* $\mathbf{N\Delta}$ *structure (right) for robustness analysis.*

Definition 8.1
Structured Singular Value: *Let* $\boldsymbol{M}$ *be a complex matrix and let* $\boldsymbol{\Delta} = diag\{\boldsymbol{\Delta}_i\}$ *be a set of complex matrices with* $\bar{\sigma}(\boldsymbol{\Delta}) \leq 1$ *and with a given block diagonal structure, where some blocks may be real and some may be repeated. The real non negative function* $\mu(\boldsymbol{M})$ *is defined by*

$$\mu(\boldsymbol{M}) \triangleq \frac{1}{\min\{\bar{\sigma}(\boldsymbol{\Delta}) | \textit{ for structured } \boldsymbol{\Delta}, \det(\boldsymbol{I} - \boldsymbol{M\Delta}) = 0\}} \tag{8.86}$$

If no such structured $\boldsymbol{\Delta}$ *exists then* $\mu(\boldsymbol{M}) = 0$.

Then μ can be implemented as the reciprocal of the smallest $\bar{\sigma}$ of a structured $\boldsymbol{\Delta}$ which makes the system singular. One problem with μ is that it cannot be calculated directly as it has local extrema (Skogestad & Postlethwaite 1996). Instead upper and lower bounds for μ can be computed (Packard & Doyle 1993) such that

$$\rho(\mathbf{M}) \leq \mu(\mathbf{M}) \leq \bar{\sigma}(\mathbf{M}) \tag{8.87}$$

where ρ is the spectral radius [2]. The lower bound is reached for $\boldsymbol{\Delta}$ being scalar diagonal and the upper bound for a full $\boldsymbol{\Delta}$ matrix. Proofs of this can be found in (Zhou, Doyle & Glover 1995). The bounds in Equation (8.87) are not sufficient to determine μ as they can be arbitrarily large apart.

This problem can be solved by scaling, as stability does not depend on that. We introduce block diagonal scaling as

$$\mathbf{D} = diag\{d_i \mathbf{I}_i\} \tag{8.88}$$

[2]The spectral radius $\rho(\mathbf{A})$ is the magnitude of the largest eigenvalue of a matrix $\mathbf{A}$, $\rho(\mathbf{A}) = \max_i |\lambda_i(\mathbf{A})|$

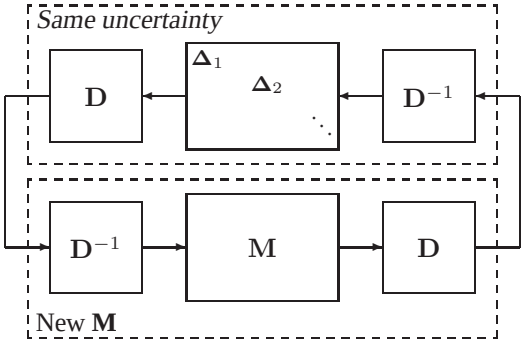

Figure 8.22: *Block diagonal scaling, where* $\mathbf{\Delta D} = \mathbf{D\Delta}$.

where d_i is a scalar and $\mathbf{I}_i$ is the identity matrix of the same dimension as the corresponding perturbation block $\mathbf{\Delta}_i$. This is illustrated in Figure 8.22, where it is clear that nothing has actually changed. As $\mathbf{D}$ commutes with $\mathbf{\Delta}$ we have that $\mathbf{\Delta D} = \mathbf{D\Delta}$, which means that $\mathbf{\Delta} = \mathbf{D\Delta D}^{-1}$. We can therefore replace $\mathbf{M}$ with $\mathbf{DMD}^{-1}$ in all the computations for the RS. This means that the $\mathbf{D}$ scaling does not affect $\mu(\mathbf{M}) = \mu(\mathbf{DMD}^{-1})$, but it does affect $\rho(\mathbf{M})$ and $\bar{\sigma}(\mathbf{M})$ (Zhou, Doyle & Glover 1995). This fact is used in the solvers to get the bounds as close as possible to μ at each frequency. The actual algorithm to compute the upper and lower bounds is explained in (Skogestad & Postlethwaite 1996).

We will finally express the condition to be used for establishing a criteria for robust stability with structured uncertainty in Theorem 8.5

Theorem 8.5
RS for block diagonal real or complex perturbations: *Assume that the nominal system* $\boldsymbol{M}$ *and the perturbations* $\mathbf{\Delta}$ *are stable. Then the* $\boldsymbol{M\Delta}$ *system in Figure 8.21 is stable for all perturbations with* $\bar{\sigma}(\mathbf{\Delta}) \leq 1, \ \ \forall\omega$ *if and only if*

$$\mu(\boldsymbol{M}(j\omega)) < 1, \ \ \forall\omega \tag{8.89}$$

The proof of Theorem 8.5 is presented in (Skogestad & Postlethwaite 1996). If μ in Equation (8.89) should be larger than 1 at some frequencies by a factor of k_m, it means that the perturbations must be scaled by a factor of $\frac{1}{k_m}$ for the system to remain stable.

It remains to bridge the gap between a constant $\mathbf{\Delta}$ as presented so far and the uncertain LTV plant we have at hand, where $\mathbf{\Delta}$ is a time varying uncertainty. This problem has been addressed in (Zhou, Khargonekar, Stoustrup & Niemann 1995) for state space systems with time varying uncertain parameters. They demonstrated that the problem can be cast as a convex optimization problem providing a less conservative solution for robustness than the small gain approach for a certain class of systems. The generalization to any LFT formulated uncertain system remained open. A similar problem has been considered by (Shamma 1994) with time varying structured uncertainty and he showed

that robust stability only holds, if there exist scalings of $\mathbf{DMD}^{-1}$, which lead to a small gain condition. This has been furthered by (Poolla & Tikku 1995) considering robust performance. They show the existence of frequency dependent scales being necessary and sufficient for robust performance against arbitrarily slowly varying structured linear perturbations of norm less than one.

The present situation is shown in Figure 7.6 to have slowly varying parameters with the largest frequency of about $1.8 \cdot 10^{-4}$ Hz. Closed loop bandwidths are expected faster than 10^{-2} Hz. In addition it is noticed that at the highest frequency, there is no time varying uncertainty and in addition as the distance between the bounds increase the frequency decrease favorably. This leaves almost two orders of magnitude difference at worst and it is considered justifiable to consider the time varying uncertainty as a standard bounded uncertainty as stated in Section 8.8.

We have now established the background needed to evaluate the RS of the LQG controller designed in Section 8.4 under the presence of all the uncertainties developed in Sections 8.9 to 8.12. We have to bring all the elements into the general form in Figure 8.20. This is being done by interconnecting the elements numerically as it is not feasible to collect it all together analytically into one model. For the RS analysis we let the exogenous input $\mathbf{w}$ be the reference signal $\mathbf{r}$ from Figure 8.1. The exogenous output $\mathbf{z}$ is the system output $\mathbf{y}$ in Figure 8.1.

To form the controller $\mathbf{K}$ in Figure 8.20 we consider it to include the controller gain matrix, the estimator and the summation point. Then we can define the input to $\mathbf{K}$ as $\mathbf{v} = [\mathbf{r}, \ \mathbf{y}]^T$, and $\mathbf{u}$ remains unchanged.

The overall plant $\mathbf{P}$ in Figure 8.20 is formed by extracting in an orderly manner all the $\mathbf{\Delta}$ blocks following the principle illustrated in Figure 8.9. Then the individual plants are interconnected using the program `sysic` described in (Balas et al. 1998). Then the lower LFT in Equation (8.83) is computed to form the system $\mathbf{N}$ in Figure 8.20.

Due to the tools interface in (Balas et al. 1998), the repeated individual uncertainties need to be defined consecutively as explained in Equation (8.64). This is easier for the other uncertainties as they appear naturally after each other. Combining all the uncertainties we obtain the following $\mathbf{\Delta}$-block of dimension 24.

$$\mathbf{\Delta} = diag([\mathbf{\Delta}_{dyn}(13), \ \ \mathbf{\Delta}_{flex}(2), \ \ \mathbf{\Delta}_{input}(3), \ \ \mathbf{\Delta}_{\tau}(6)]) \tag{8.90}$$

where the $\mathbf{\Delta}(\cdot)$ specifies the dimension of the diagonal real uncertainty.

The fact that all uncertainties are of parametric real type is causing problems for the solutions to find the lower bound in Equation (8.87) in line with Definition 8.1, where $\mathbf{\Delta}$ is assumed some complex parts. To circumvent that problem a small complex part will be added to the $\mathbf{\Delta}$-block so it is not pure real. This is done in the way of modifying the $\mathbf{M\Delta}$ structure to the one illustrated in Figure 8.23.

This means that we add a bit of conservatism into the system as we add uncertainty not physically present. The added complex part needed is about 2.5 % to get reliable lower bounds. One can debate if it is sufficient to add only complex on one channel. In this case it has proved to give the best results to add the same complexity to all channels.

It is recalled that the core part of the research is to investigate the use of LTI control for time varying elliptical orbital environment. For that reason the prime uncertainty is

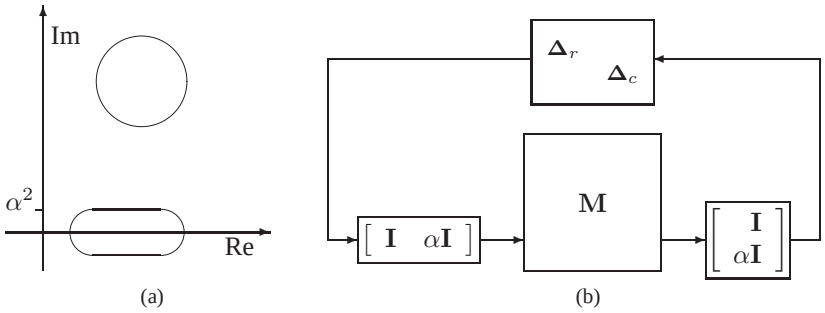

Figure 8.23: *Illustration of artificially added complex uncertainty component α^2 and the modified interconnections in graph (b).The graph (a) illustrates, in the complex plane, a pure complex uncertainty as the circle in line with Figure 8.8, and a real uncertainty with a small complex component. The pure real uncertainty is the horizontal line in the oval area in graph (a).*

the variation of the orbital environment simultaneously with the other known ones. The objectives are for eccentricities of $\varepsilon = 0.1$ and the RS found is shown in Figure 8.24.

In Figure 8.24 we see the upper and lower bounds for $\varepsilon = 0.1$ are very close, which is particularly important for the frequency range of maximum μ. It is clear that the driver for the RS is the damping of the flexible modes and less for RP as shown in Section 8.14. The gradient of the μ-plot has been investigated to find it changes sign of its derivative, which indicates that we are capturing the peak value. It shall be recalled that no notch filters have been used in the LQG design to actually reduce the peak, but that would be feasible should it be deemed necessary. Just in order to try explore the boundaries of the design a very high eccentricity orbit has been analyzed. This leads only to slightly elevated μ value at lower frequencies with ample margin. It shall be said that the same controller is used for both analyses.

In conclusion it can be said that a successful and very robustly stable design has been achieved. This clearly demonstrates that for such plants and requirements, it is feasible to employ LTI designs to this type of Nonlinear Time Varying (NTV) system with success. This is worth to keep in mind before embarking directly on LTV designs like e.g. Linear Parameter Varying (LPV) control only because it is an elliptical slowly time varying orbit, as it brings with it increased design complexity and today open verification issues.

8.14 Robust Performance

We have discussed the presentation of uncertainty sets and have analyzed the RS. The next step is to check that we also have Robust Performance (RP) for all plants in the set.

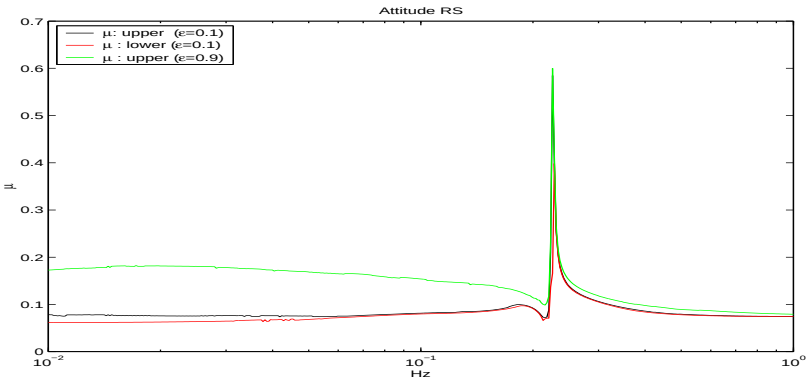

Figure 8.24: *Robust Stability structured singular value plots for orbital eccentricity $\varepsilon = 0.1$ and the large value $\varepsilon = 0.9$. For the latter the lower bound is omitted only not to clutter the graph.*

When RS is satisfied, we will determine how large the transfer function from the exogenous inputs $\mathbf{w}$ to the outputs $\mathbf{z}$ can be for all plants in the uncertainty set.

In terms of the $\mathbf{N\Delta}$ structure in Figure 8.20 the requirements for RP can be formulated as follows (Skogestad & Postlethwaite 1996)

NP: $\|\mathbf{N}_{22}\|_\infty < 1$ and NS

RP: $\|\mathbf{F}\|_\infty < 1, \forall \mathbf{\Delta}, \|\mathbf{\Delta}\|_\infty \leq 1$ and NS

where $\mathbf{F} = F_u(\mathbf{N}, \mathbf{\Delta})$. Illustrated by a SISO situation we return to the Nyquist diagram in Figure 8.19. We have RP when the two circles do not intersect. The circle centered in $(-1, 0)$ can be viewed as an extended critical point.

To test for RP as stated above the $\mathcal{H}_\infty$ norm of the transfer function $\mathbf{F} = F_u(\mathbf{N}, \mathbf{\Delta})$ must remain less than 1 for all allowed perturbations. This can be viewed as the equivalent to the $\mathbf{M\Delta}$ structure in Figure 8.20, but now having closed the upper LFT such it becomes an $\mathbf{F\Delta}_p$ structure, where $\mathbf{\Delta}_p$ is a fictitious full complex uncertainty representing the $\mathcal{H}_\infty$ performance specification. It is a full complex block as there is no structure closing the loop on the exogenous signals. This can be stated in the following theorem.

Theorem 8.6

Robust Performance: *Formulate the system into the $\boldsymbol{N\Delta}$ -structure in Figure 8.20 and assume we have nominal stability such that $\boldsymbol{N}$ is internally stable. Then*

$$\mu(\boldsymbol{N}(j\omega)) < 1, \quad \forall \omega \tag{8.91}$$

where μ is computed with respect to the structure

$$\begin{bmatrix} \mathbf{\Delta} & \\ & \mathbf{\Delta}_p \end{bmatrix} \tag{8.92}$$

and $\mathbf{\Delta}_p$ is a full complex perturbation with the same dimensions as $\boldsymbol{F}^T$

The proof of Theorem 8.6 starts with the definition of RP, namely that $\|\mathbf{F}\|_\infty < 1$. We recall from Equation (8.85) that it is RS when $\|\mathbf{M}\|_\infty < 1$ for $\mathbf{\Delta}$ being a full unstructured matrix. From this we get that RP of $\|\mathbf{F}\|_\infty < 1$ is equivalent to RS for the $\mathbf{F}\mathbf{\Delta}_p$ structure. Replacing $\mathbf{F}$ with $F_u(\mathbf{N}, \mathbf{\Delta})$ we obtain the block diagonal matrix in Equation (8.92). ■

We now have established the framework and criteria needed to evaluate RP of MIMO systems. It shall be recalled that all criteria used are normalized to one. Contrary to the RS problem, it is important that all the exogenous inputs and outputs are scaled correctly and normalized to one.

Signals which have the same units and are comparable will have the same scale factors, like e.g. reference, output and control error signals. As an example for the reference we define

$$\mathbf{r} = \mathbf{D}_e \mathbf{r}' \tag{8.93}$$

where $\mathbf{D}_e$ is a diagonal scaling matrix and the primed variable $|\mathbf{r}'| \leq 1$ is normalized. The scaling is based upon the expected maximum signal value e.g. r_{max}. Therefore it becomes for the attitude

$$\mathbf{D}_e = diag([r_{max},\ \ r_{max},\ \ r_{max}]) \tag{8.94}$$

and we define $r_{max} = 20\,\text{deg}$. This is the maximum expected attitude in the linear domain. We also need to scale the disturbance input $\mathbf{d}$ in the same manner, where we obtain the maximum disturbance torque from Table 7.4 giving $d_{max} = 8.2 \cdot 10^{-2}$ Nm and

$$\mathbf{d} = \mathbf{D}_d \mathbf{d}' \tag{8.95}$$

We will insert these scalings into Figure 8.1, which is then repeated in Figure 8.25 including the weighting functions, where $\mathbf{W}_d$ is the weight representing the characteristics of the disturbance.

To define the performance weights we face the problem of translating time domain requirements into the equivalent and meaningful frequency domain ones. For real engineering type of problems requirements are more often in the time domain than not.

The mapping is performed based on the following second order system for SISO loop transfer as an example

$$L = \frac{\omega^2}{s(s + 2\zeta\omega)} \tag{8.96}$$

with the following classical parameters

$$t_r \approx \frac{0.6 + 2.16\zeta}{\omega_n}, \quad t_s \approx \frac{4}{\zeta\omega}, \quad M_P = e^{\frac{-\pi\zeta}{\sqrt{1-\zeta^2}}} \tag{8.97}$$

where t_r is the rise time $10 - 90\,\%$, t_s the setting time $2\,\%$ and M_P the percentage overshoot $100 \cdot M_P$ (Zhou & Doyle 1998).We also define

$$M_S = \|\mathbf{S}\|_\infty \quad \text{and} \quad M_T = \|\mathbf{T}\|_\infty \tag{8.98}$$

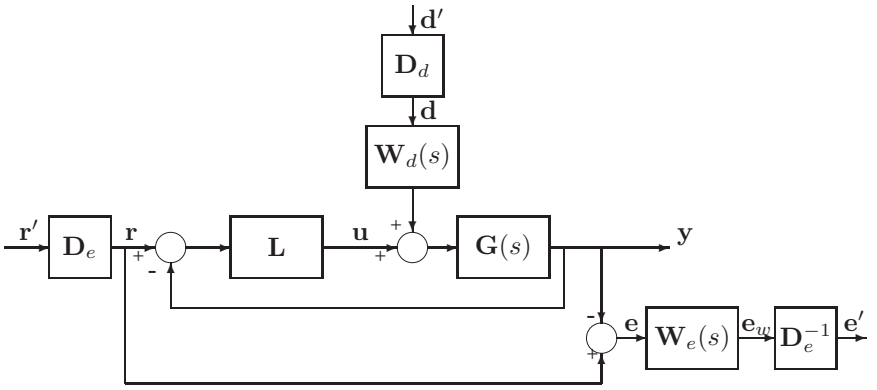

Figure 8.25: *The normalized system from Figure 8.1 including the performance weighting functions* $\mathbf{W}_d$ *and* $\mathbf{W}_e$.

and the relationship between M_S, M_T and M_P is tabulated in (Skogestad & Postlethwaite 1996), but could also be easily computed formulating the functions directly. A typical choice for performance is $\mathbf{F} = \mathbf{W}_e\mathbf{S}$, the weighted sensitivity function, where $\mathbf{W}_e$ is the performance weight and $\mathbf{S}$ is the set of perturbed sensitivity functions. We have that

$$|\mathbf{W}_e\mathbf{S}| < 1 \Rightarrow |\mathbf{S}| < |\mathbf{W}_e^{-1}| \tag{8.99}$$

and we select a general weight of the form

$$w_e = \frac{\frac{1}{M}s + \omega}{s + \omega \cdot A} \tag{8.100}$$

and the weighting matrix $\mathbf{W}_e$ in Figure 8.25 as a diagonal matrix of size k containing $w_{e_1} \cdots w_{e_k}$. Equations (8.99) and (8.100) are illustrated in Figure 8.26.

The weight $\mathbf{W}_e$ in Figure 8.25 is naturally placed such that $\mathbf{e} = \mathbf{r} - \mathbf{y} = \mathbf{r} - \mathbf{Tr} = (\mathbf{I} - \mathbf{T})\mathbf{r} = \mathbf{Sr}$ and the transfer from $\mathbf{r}$ to $\mathbf{e}_w$ becomes $\mathbf{e}_w = \mathbf{W}_e\mathbf{Sr}$. We demonstrate the equivalence of placing the weight right after $\mathbf{D}_e$ at the input. This gives $\mathbf{e}_w = \mathbf{r}_w - \mathbf{y} = \mathbf{r}_w - \mathbf{Tr}_w = (\mathbf{I} - \mathbf{T})\mathbf{r}_w = \mathbf{Sr}_w$ and as $\mathbf{r}_w = \mathbf{W}_e\mathbf{r}$ we get $\mathbf{e}_w = \mathbf{W}_e\mathbf{Sr}$ which is identical.

For the weight specification we consider the following values as acceptable

$$\begin{array}{rcl} r_{max} & = & 20 \text{ deg} \\ \theta_{max}(error) & = & 2 \text{ deg} \\ M_P & < & 30\ \% \\ t_s & \approx & 100 \text{ s} \end{array} \tag{8.101}$$

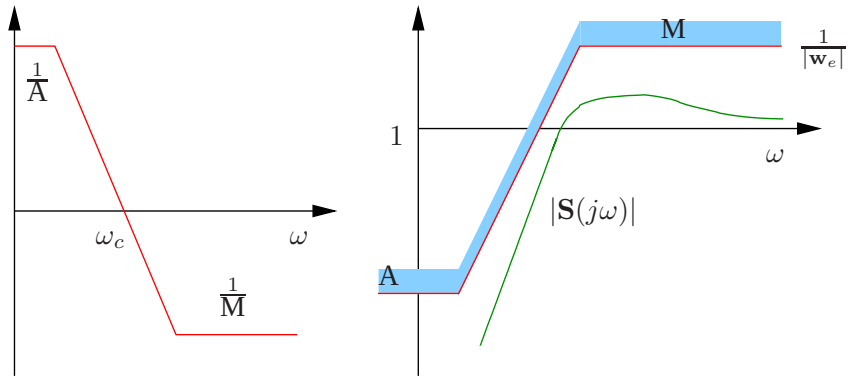

Figure 8.26: *The left graph shows the weight w_e and the right one illustrates the bounding of the sensitivity to obtain RP.*

For the low frequency part we need a suppression from $r = 20$ deg $\curvearrowright e = 2$ deg and to fulfill Sw_e we need to amplify so $e_w = r = 20$ deg leading to

$$w_e(0) = \frac{20}{2} = 10 \tag{8.102}$$

from Equation (8.100) and $A = 0.1$. For the high frequency part we use the peak overshoot criteria. From Equation (8.101) we get $M_P = 1.3$ which from (Skogestad & Postlethwaite 1996) leads to $M_S = 1.8$ so we set $M = 2$ in Equation (8.100). The filter frequency we find from the closed loop step response in Figure 8.5. From Equation (8.97) we get $\omega = \frac{4}{\zeta t_s} = \frac{4}{100} \approx 0.04 s^{-1}$ or 6.4 mHz.

$$w_e = \frac{0.5 \text{ s} + 0.04}{s + 0.004} \tag{8.103}$$

$\mathbf{W}_e$ will then be of dimension 3 containing Equation (8.103) on the diagonal.

When looking at robustness it is very important only to consider the driving performance variables, which in this case is the attitude $\boldsymbol{\theta}$. Only parts of the state vector shall therefore be used in $\mathbf{z}$ in Figure 8.20 and connected to $\mathbf{w}$ via $\boldsymbol{\Delta}_p$, which is a full complex matrix. This ensures that we are not introducing non-existing cross couplings between the exogenous signals which would be meaningless.

When computing the μ value for the RP analysis $\boldsymbol{\Delta}_p$ provides sufficient complexity for good convergence of both upper and lower bound and the extra $\boldsymbol{\Delta}_c$ in Figure 8.23 can be omitted.

Figure 8.27 displays the RP plots for the main eccentricity of $\varepsilon = 0.1$ and a large increase to check possible limitations. As for the RS μ plot the flexible modes are clearly visible, but are not causing any problems. The largest μ value is within the closed loop bandwidth and provides sufficient performance margin indeed. As the μ value is not very

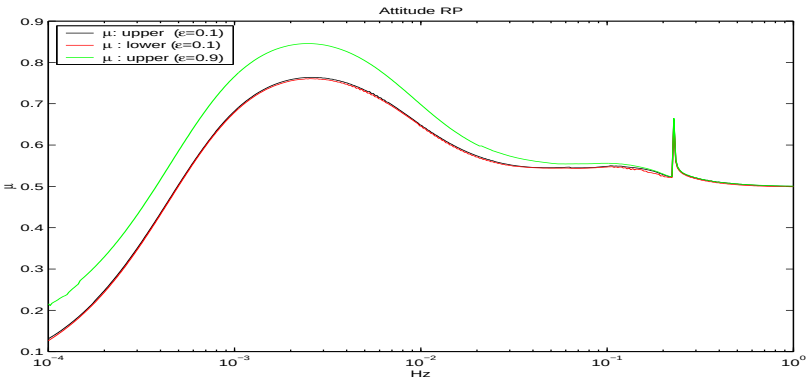

Figure 8.27: *Robust Performance structured singular value plots for orbital eccentricity* $\varepsilon = 0.1$ *and the large value* $\varepsilon = 0.9$.

small but with ample margin it indicates a design which is using the system capabilities to be responsive and well performing and simultaneously keeping some margin. For the high eccentricity we see a reduced margin, but it remains comfortably below 1.

In conclusion it can be said that a successful and robustly performing LTI design has been designed to remain both RS and RP over a very large LTV domain.

Finally the worst case $\mathbf{\Delta}$ has been unwrapped in the analysis. The information is then being used as a part of the Monte Carlo (MC) validation campaign, which is performed in Chapter 11. This ensures a logical link between the worst case analysis performed here and the classical MC.

8.15 Conclusion

A fully coupled LQG attitude control design has been performed. All relevant parametric uncertainties have been analytically derived and formulated as LFTs. In particular the periodic time varying plant is analytically formulated as a bounded uncertainty eliminating the LTV and periodic nature.

Based upon this development the robust stability and the robust performance of the MIMO design have been analyzed by means of the μ-value. The design is demonstrated robust to orbital eccentricities larger than 0.9 and the LTI controller successfully obtains robustness of the time varying plant. This answers well to objective 7 of Section 1.3.

Chapter 9

Relative Position Control

Having finalized the LVLH attitude control in Chapter 8, we now proceed with the synthesis and analysis of the final approach position control. The trajectory profile for the different phases of the mission is recalled from Figure 2.4 and Figure 2.5. The final approach is from point s_3 to s_4 and further on until docking. The hand over from GPS to RVS sensors takes place at s_3, as well as a change from COM to COM control to port to port control.

The research here will focus on the latter part after change over to the final approach as this is the more critical and demanding part.

The position control is 3 DOF and the attitude control of the chaser remains with respect to the LVLH frame. This is the second situation illustrated in Figure 7.3. The lateral control objective along the y and z-axis is to keep the center of the docking ports aligned, but at this large distance it is not desirable to track the target port oscillatory motion. Instead we will design a controller which will track the mean motion of the target docking port and thereby conserve fuel without any loss of performance. This means controlling the relative differences to zero along the y and z-axes. The control objective along the x-axis of the LVLH frame is to follow the guidance profile developed in Section 7.7 and detailed in Figure 7.10 and tables 7.5 and 7.6. Further to this servo type problem the control system shall also handle disturbance rejection, which is mostly the presence of differential drag, which is described in Section 3.4.2.

9.1 Control Requirement Detailing

The location of s_3 and s_4 is recalled from Table 2.1 to be $s_3 = [-500, 0, 0]^{\mathrm{T}}$ m COM to COM and $s_4 = [-20, 0, 0]^{\mathrm{T}}$ m port to port respectively. It shall be recalled that s_4 is along the target docking port x-axis in the $\mathcal{F}_{dt0}$ frame.

From Table 2.5 it is evident that at s_3 the chaser docking port shall stay inside a cube of 20 m with corresponding rates smaller than 0.1 m/s. This box is parallel to LVLH and will move around as the target docking port is moving with respect to LVLH due to the

ISS attitude motion.

At s_4 there are two sets of requirements namely the arrival and departure ones as listed in Tables 2.6 and 2.7 respectively. This location is used for changing control structure from 3 DOF to 6 DOF and some transients are anticipated before reaching the departure requirements. The arrival box is 1 m and rates less than 0.1 m/s for y and z-axes and 0.02 m/s for the x-axis. The departure requirements are not applicable for 3 DOF controller. The approach velocity shall be in the range of $[0.05; 0.35]$ m/s.

From Figure 2.5 we see that the approach corridor in the AE and into the KOZ is conical, but there are no formal requirements between s_3 and s_4 except the definition of the KOZ.

For practical reasons we will consider the requirement linearly connected between s_3 and s_4 and we will try to aim directly for s_4 departure requirements, as defined in Table 2.7, with the 3 DOF controller.

9.2 Target and Sensor Characteristic

The target docking port motion is described in detail in Section 3.2.1 and from that we will derive the needs for propulsion and control bandwidth in order to be able to track the motion.

The worst case of fastest reverse time $d = 8$ s and largest amplitude $0.7\,\mathrm{deg}$ is used as a basis. From the data in Section 3.1.2 for $\mathbf{r}_{bt}$ and $\mathbf{r}_{gdt}$ we can compute the lever arm as the first component of $\mathbf{r}_{dt}$ to be about 31 m. From the angular rate v_t in Table 3.2 we can find the largest acceleration needed to be $a \cong \frac{2v_t|\mathbf{r}_{dt}|}{d} = 2.7 \cdot 10^{-3}$ m/s^2. For the largest chaser mass from Equation (C.5) we then need a force of at least $F_{min} = 55$ N. This is well covered by the $\mathbf{F}_{max}$ specified in Equation (8.1) of 150 N.

A good estimate of the minimum bandwidth required can be obtained by considering the acceleration of a sinusoidal $A\omega^2 = a$ giving $\omega = 0.014$ Hz.

The only sensor used is the RVS which measures only distance and angles. There are no measurements of rates or accelerations or other sensors to measure such. The RVS is described in Section 3.3.4 and Table 3.3 which reveals a complex internal functioning with many modes. We will not use all those details for controller synthesis, but extract the essential worst case characteristics.

We will use the range values R directly for the x-axis direction and the lateral values we approximate with $R\sin(LOS)$. The simplified data is presented in Table 9.1

	x-axis	y,z-axis
Bias [m]	$[0.01; 5]$	$[0; 2.6]$
Noise 3σ[m]	$[0.005; 25]$	$[0; 1.75]$

Table 9.1: *Simplified sensor data extracted from Table 3.3. The lower and upper values correspond to a range of* $[0; 500]$ *m.*

The data in Table 9.1 is considered to vary linearly between the two boundary values, though it is not exactly so.

This can also be expressed such that the range has 5 % noise of the range and the lateral noise is 8.75 %. This formulation will be convenient in the following control design.

If we compare the requirements at s_4, but use the docking requirements departing s_4, as is often done, the sensor bias does not fit departing s_4 initially. The bias is 0.2 m and the requirement is half of that. One could estimate the bias with a filter like $H(s) = \frac{s}{s-p}$ and subtract it from the measurements. The problem with that approach is the filter time constant, as in (Ignagni 1990), needs to be comparable to the travel time from s_3 to s_4. The filter then needs to be initialized fairly close to the real values, which might then be used directly.

The latter approach will be used and the sensor calibration values for the bias will be subtracted before used for control.

9.3 Plant Description and Variation

The model for the relative dynamics was developed in Section 4.1 and we will use the LTV models in Equations (4.16) and (4.18) for the controller designs.

We see that the spacecraft mass does not affect the plant dynamics, but only the orbital parameter variations.

Out of plane: The pole variations for the rigid plant are all on the $j\omega$ axis and are symmetric over half an orbit. The variation is listed in Table 9.2.

$\varepsilon = 0.1$	$\theta = 0$ deg	$\theta = 180$ deg	$\%\Delta$
	$0 \pm 1.12 \cdot 10^{-3}$	$0 \pm 8.29 \cdot 10^{-4}$	-26 %

Table 9.2: *Pole variation for the out of plane plant for the true anomaly $\theta \in [0; 180]$ deg.*

In plane: The pole variation is more complex than for the out of plane and is better illustrated by the graphs in Figure 9.1.

The root locus in Figure 9.1 is for half an orbit only. The locus for the complete orbit is symmetric around the $j\omega$ axis. This is caused by the fact that the derivative of the orbital rate $\dot{\omega}$ in Equation (4.16) changes sign on each side of the semi major axis. The locus for the full orbit is available in Figure 7.5.

We observe in Figure 9.1 that 2 poles remain with an imaginary component in the LHP. The 2 other poles move in the RHP, then become real and one of them relocate to the LHP. This transition from RHP to LHP happens when the true anomaly is of such value that the spacecraft in the orbit intersects the minor axis of the elliptical orbit. This is exactly one quarter and three quarters around the orbit measured from perigee and where one can say the orbit is the widest.

Figure 9.1 illustrates the locus for 3 different orbital eccentricities ε and one observes that they are not all that different, mostly a faster dynamics for higher ε around perigee.

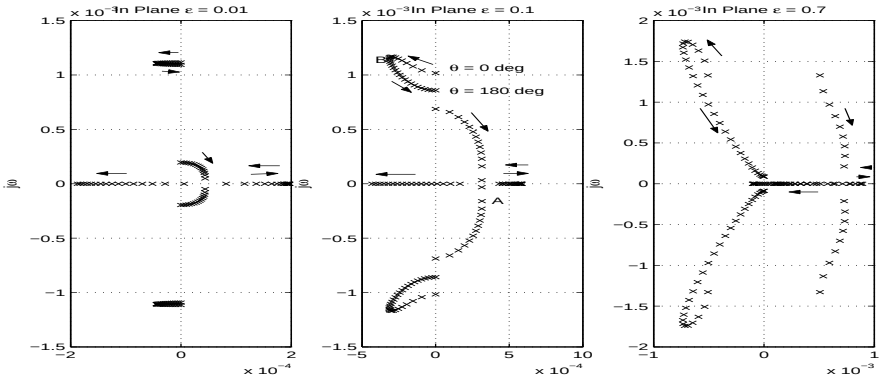

Figure 9.1: *Pole variation for the in plane plant for the true anomaly* $\theta \in [0; 180]$ *deg and for* 3 *different eccentricities* $\varepsilon \in [0.01, 0.1, 0.7]$. *The point marked as A are where two complex conjugate poles become real and point B is the smallest value for the other complex poles.*

In Figure 9.1 the point A indicates where one set of complex poles becomes real. The point B indicates the smallest real value for the other set of poles. Both these phenomena happen exactly at the points of maximum acceleration of the true anomaly.

For $\varepsilon = 0.1$, the eccentricity for this research work, the poles are bounded by $[-4.3; 5.5] \cdot 10^{-4}$ for the real parts and $\pm 1.2 \cdot 10^{-3}$ for the imaginary parts.

The poles originating from the flexible modes and sloshing are as listed in Table 8.2, though the couplings to the rigid dynamics are different than they were for the attitude dynamics. Those modes will not be considered for the control design, though loop shaping might be applied if deemed necessary by stability and performance analysis.

9.4 Position $\mathcal{H}_\infty$ Control Design

For the complete range of the relative position control we will perform the synthesis by means of $\mathcal{H}_\infty$ control. This is a worst case design method and suits well for the critical uncertainties and variations present in the system. Further this is a novel approach applied to all the phases of the relative motion in a multi variable manner, where a single axis design for final mode is presented in (Bourdon, Delpy, Ganet, Quinquis & Ankersen 2003).

For completeness and insight the theory and assumptions for the $\mathcal{H}_\infty$ design will be explained followed by general scaling of the plants. Then the simpler out of plane control will be performed followed by the coupled in plane control.

The control problem can be formulated as a 2×2 system illustrated in Figure 9.2 The system in Figure 9.2 is formulated by

$$\begin{bmatrix} \mathbf{z} \\ \mathbf{v} \end{bmatrix} = \mathbf{P}(s) \begin{bmatrix} \mathbf{w} \\ \mathbf{u} \end{bmatrix} = \begin{bmatrix} \mathbf{P}_{11}(s) & \mathbf{P}_{12}(s) \\ \mathbf{P}_{21}(s) & \mathbf{P}_{22}(s) \end{bmatrix} \begin{bmatrix} \mathbf{w} \\ \mathbf{u} \end{bmatrix} \tag{9.1}$$

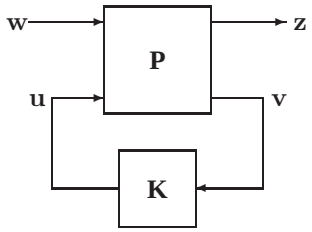

Figure 9.2: *General control configuration with exogenous signals.*

$$\mathbf{u} = \mathbf{K}(s)\mathbf{v} \tag{9.2}$$

and the plant $\mathbf{P}(s)$ becomes in state space form

$$\mathbf{P} = \left[\begin{array}{c|cc} \mathbf{A} & \mathbf{B}_1 & \mathbf{B}_2 \\ \hline \mathbf{C}_1 & \mathbf{D}_{11} & \mathbf{D}_{12} \\ \mathbf{C}_2 & \mathbf{D}_{21} & \mathbf{D}_{22} \end{array}\right] \tag{9.3}$$

The closed loop transfer function becomes

$$\mathbf{z} = F_l(\mathbf{P}, \mathbf{K})\mathbf{w} \tag{9.4}$$

where the lower LFT is defined in Equation (D.9). The $\mathcal{H}_\infty$ control design involves the minimization of the $\mathcal{H}_\infty$ norm of Equation (9.4). A certain set of assumptions are typically needed in order to solve the problem (Skogestad & Postlethwaite 1996) as follows

A1: $(\mathbf{A}, \mathbf{B}_2, \mathbf{C}_2)$ is controllable and observable.
$(\mathbf{A}, \mathbf{B}_2)$ is controllable if and only if $\mathbf{F}$ exists such that $\mathbf{A} + \mathbf{B}_2\mathbf{F}$ is stable and $\mathbf{u} = \mathbf{F}\mathbf{x}$.
$(\mathbf{A}, \mathbf{C}_2)$ is observable if and only if $\mathbf{A} + \mathbf{L}\mathbf{C}_2$ is stable and $\mathbf{L}$ exists.

A2: $\mathbf{D}_{12}$ and $\mathbf{D}_{21}$ have full rank.

A3: $\left[\begin{array}{cc} \mathbf{A} - j\omega\mathbf{I} & \mathbf{B}_2 \\ \mathbf{C}_1 & \mathbf{D}_{12} \end{array}\right]$ has full column rank $\forall\omega$. Ensure no pole/zero cancellation on the $j\omega$ axis.

A4: $\left[\begin{array}{cc} \mathbf{A} - j\omega\mathbf{I} & \mathbf{B}_1 \\ \mathbf{C}_2 & \mathbf{D}_{21} \end{array}\right]$ has full row rank $\forall\omega$.

A5: $\mathbf{D}_{11} = \mathbf{D}_{22} = \mathbf{0}$ $\mathbf{D}_{11} = \mathbf{0}$ makes $\mathbf{P}$ strictly proper.

Insight into the general $\mathcal{H}_\infty$ algorithm from (Doyle, Glover, Khargonekar & Francis 1989) is provided in Theorem 9.1

Theorem 9.1

(i) $\boldsymbol{X}_\infty \geq 0$ *is a solution to the Riccati equation*

$$\boldsymbol{A}^T\boldsymbol{X}_\infty + \boldsymbol{X}_\infty\boldsymbol{A} + \boldsymbol{C}_1^T\boldsymbol{C} + \boldsymbol{X}_\infty(\gamma^{-2}\boldsymbol{B}_1\boldsymbol{B}_1^T - \boldsymbol{B}_2\boldsymbol{B}_2^T)\boldsymbol{X}_\infty = 0 \tag{9.5}$$

such that

$$Re\ \ \lambda_i[\boldsymbol{A} + (\gamma^{-2}\boldsymbol{B}_1\boldsymbol{B}_1^T - \boldsymbol{B}_2\boldsymbol{B}_2^T)\boldsymbol{X}_\infty)] < 0, \ \ \forall_i \ \ \textit{and} \tag{9.6}$$

(ii) $\boldsymbol{Y}_\infty \geq 0$ *is a solution to the Riccati equation*

$$\boldsymbol{A}\boldsymbol{Y}_\infty + \boldsymbol{Y}_\infty\boldsymbol{A}^T + \boldsymbol{B}_1\boldsymbol{B}_1^T + \boldsymbol{Y}_\infty(\gamma^{-2}\boldsymbol{C}_1^T\boldsymbol{C}_1 - \boldsymbol{C}_2^T\boldsymbol{C}_2)\boldsymbol{Y}_\infty = 0 \tag{9.7}$$

such that

$$Re\ \ \lambda_i[\boldsymbol{A} + \boldsymbol{Y}_\infty(\gamma^{-2}\boldsymbol{C}_1^T\boldsymbol{C}_1 - \boldsymbol{C}_2^T\boldsymbol{C}_2)] < 0, \ \ \forall_i \ \ \textit{and} \tag{9.8}$$

(iii) $\rho(\boldsymbol{X}_\infty\boldsymbol{Y}_\infty) < \gamma^2$ *and* ρ *is the spectral radius. All controllers are by* $\boldsymbol{K} = F_l(\boldsymbol{K}_c, \boldsymbol{Q})$ *where*

$$\boldsymbol{K}_c(s) = \left[\begin{array}{c|cc} \boldsymbol{A}_\infty & -\boldsymbol{Z}_\infty\boldsymbol{L}_\infty & \boldsymbol{Z}_\infty\boldsymbol{B}_2 \\ \hline \boldsymbol{F}_\infty & 0 & \boldsymbol{I} \\ -\boldsymbol{C}_2 & \boldsymbol{I} & 0 \end{array}\right] \tag{9.9}$$

and

$$\boldsymbol{F}_\infty = -\boldsymbol{B}_2^T\boldsymbol{X}_\infty, \ \ \boldsymbol{L}_\infty = -\boldsymbol{Y}_\infty\boldsymbol{C}_2^T, \ \ \boldsymbol{Z}_\infty = (\boldsymbol{I} - \gamma^{-2}\boldsymbol{Y}_\infty\boldsymbol{X}_\infty)^{-1} \tag{9.10}$$

$$\boldsymbol{A}_\infty = \boldsymbol{A} + \gamma^{-2}\boldsymbol{B}_1\boldsymbol{B}_1^T\boldsymbol{X}_\infty + \boldsymbol{B}_2\boldsymbol{F}_\infty + \boldsymbol{Z}_\infty\boldsymbol{L}_\infty\boldsymbol{C}_2 \tag{9.11}$$

and $\boldsymbol{Q}(s)$ *is stable proper function such* $||\boldsymbol{Q}||_\infty < \gamma$. *For* $\boldsymbol{Q}(s) = 0$ *we get*

$$\boldsymbol{K}(s) = \boldsymbol{K}_{c_{11}}(s) = -\boldsymbol{Z}_\infty\boldsymbol{L}_\infty(s\boldsymbol{I} - \boldsymbol{A}_\infty)^{-1}\boldsymbol{F}_\infty \tag{9.12}$$

This is the central controller with the same number of states as the plant $\boldsymbol{P}(s)$. *Equation (9.12) can be separated into a state estimator of the form*

$$\dot{\hat{\boldsymbol{x}}} = \boldsymbol{A}\hat{\boldsymbol{x}} + \boldsymbol{B}_1\underbrace{\gamma^{-2}\boldsymbol{B}_1^T\boldsymbol{X}_\infty\hat{\boldsymbol{x}}}_{\hat{w}_{worst}} + \boldsymbol{B}_2\boldsymbol{u} + \boldsymbol{Z}_\infty\boldsymbol{L}_\infty(\boldsymbol{C}_2\hat{\boldsymbol{x}} - \boldsymbol{y}) \tag{9.13}$$

and

$$\boldsymbol{u} = \boldsymbol{F}_\infty\hat{\boldsymbol{x}} \tag{9.14}$$

The proof of Theorem 9.1 is presented in (Zhou, Doyle & Glover 1995). We see in Theorem 9.1 that there is a separation similar to the LQG build in between observer and controller. The term $\hat{w}_{\text{worst}}$ can be interpreted as a worst case estimate of the exogenous disturbances. The typical implementation of the algorithm in Theorem 9.1 is described in (Glover & Doyle 1988) for the iterations to achieve a minimum value of γ.

Before performing a design it is important to scale the plant as comparisons are based on normalized norms. Let's consider a plant $\mathbf{G}$ such that the output is $\mathbf{y} = \mathbf{G}\mathbf{u}$ unscaled. We now define the scaled variables as

$$\mathbf{u}' = \frac{\mathbf{u}}{\mathbf{u}_{max}} \quad \text{and} \quad \mathbf{y}' = \frac{\mathbf{y}}{\mathbf{y}_{max}} \tag{9.15}$$

where the denominator is the maximum expected signal. We can now write the input output relations as

$$\mathbf{y}'\mathbf{y}_{max} = \mathbf{G}\mathbf{u}_{max}\mathbf{u}' \tag{9.16}$$

$$\mathbf{y}' = \underbrace{\frac{1}{\mathbf{y}_{max}}\mathbf{G}\mathbf{u}_{max}}_{\mathbf{G}'}\mathbf{u}' \tag{9.17}$$

For design we need the control error $\mathbf{e}$, which has the same units as the plant output so we scale it as

$$\mathbf{e}' = \frac{\mathbf{e}}{\mathbf{y}_{max}} \tag{9.18}$$

and when $\mathbf{u}' = \mathbf{K}\mathbf{e}'$ we get for the real controller that

$$\mathbf{u} = \mathbf{u}_{max}\mathbf{K}\frac{1}{\mathbf{y}_{max}}\mathbf{e} \tag{9.19}$$

For the MIMO case we define the maximum values as

$$\mathbf{U}_m = diag(\mathbf{u}_{1_{max}} \cdots \mathbf{u}_{n_{max}}), \mathbf{Y}_m = diag(\mathbf{y}_{1_{max}} \cdots \mathbf{y}_{n_{max}}) \tag{9.20}$$

and the general MIMO scaling is illustrated in Figure 9.3 for the scaled design and the real controller implementation.

9.5 Out of Plane Position Control

The simpler out of plane control will be dealt with first and all the control setup will be performed in that context and reused later.

From the assumptions A3 and A4 one observes that the $\mathcal{H}_\infty$ algorithm cannot handle pure imaginary poles, which is in the out of plane dynamics. This is nevertheless not a problem as the design plant **P** in Equation (9.3) is augmented by the weights and no precautions need be taken.

The requirement for the control will be derived from the available force in Equation (8.1) and the maximum cruise speed of 0.35 m/s specified in Section 2.4.2. The maximum chaser mass from Equation (C.5) is used $m_c \approx 2 \cdot 10^4$ kg. Considering the

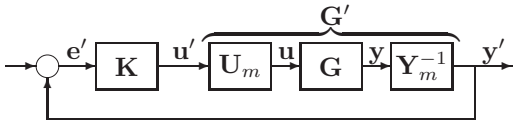

(a) Synthesis(scaled)

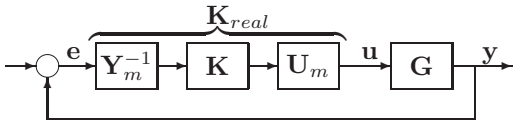

(b) Implementation(unscaled)

Figure 9.3: *On the left the scaled plant for controller analysis and synthesis is illustrated, and on the right the unscaled implementation of the controller on the real plant.*

maximum acceleration in the guidance a distance of $s = \frac{1}{2}\frac{v^2 \cdot m_c}{F_{max}} = 8.2$ m is reached. We consider this as the amplitude of a sinusoid $A\sin(\omega t)$ and its derivative gives the speed from which we find the frequency as $v = A\omega$ giving $\omega \approx 0.01$ Hz. This is about the same range as to track the target motion in Table 3.2. We therefore select a closed loop bandwidth of

$$\omega_{cl} = 0.01 \text{ Hz} \tag{9.21}$$

with some margin. We will aim at a steady state control error below 1 %.

The controller shown in Figure 9.2 will now be found by minimizing the transfer function in Equation (9.4). This will be done by shaping the transfer function by means of weighting functions on the exogenous inputs and outputs. This is often referred to as the mixed sensitivity problem (Stoustrup & Niemann 1997), in which the sensitivity function $\mathbf{S}$ is shaped along with one or more other closed loop transfer functions such as the complementary sensitivity function $\mathbf{T}$ and $\mathbf{KS}$.

In the present case we have more a regulation and less a tracking problem. As $\mathbf{S}$ is the transfer function from disturbances to the output it shall be small at low frequencies. $\mathbf{KS}$ limits the size and bandwidth of the controller, as it is the transfer from disturbance to the control signals as well as it is important to the robust stability. The shaping of the $\mathbf{T}$ transfer function influences the tracking capabilities and the noise attenuation as well as it influences on the robust stability. The mixed sensitivity setup used is illustrated in Figure 9.4. The generalized plant $\mathbf{P}$ in Figure 9.4 becomes

$$\mathbf{P} = \left[\begin{array}{ccc|c} -\mathbf{W}_1\mathbf{G}'\mathbf{W}_0 & \mathbf{W}_1\mathbf{W}_r & -\mathbf{W}_1\mathbf{W}_n & -\mathbf{W}_1\mathbf{G}' \\ \mathbf{W}_2\mathbf{G}'\mathbf{W}_0 & \mathbf{0} & \mathbf{0} & \mathbf{W}_2\mathbf{G}' \\ \mathbf{0} & \mathbf{0} & \mathbf{0} & \mathbf{W}_3 \\ \hline -\mathbf{G}'\mathbf{W}_0 & \mathbf{W}_r & -\mathbf{W}_n & -\mathbf{G}' \end{array}\right] \tag{9.22}$$

where $\mathbf{G}'$ is the scaled version of the plant in Equation (4.17), $\mathbf{W}_1$, $\mathbf{W}_2$, $\mathbf{W}_3$ are the

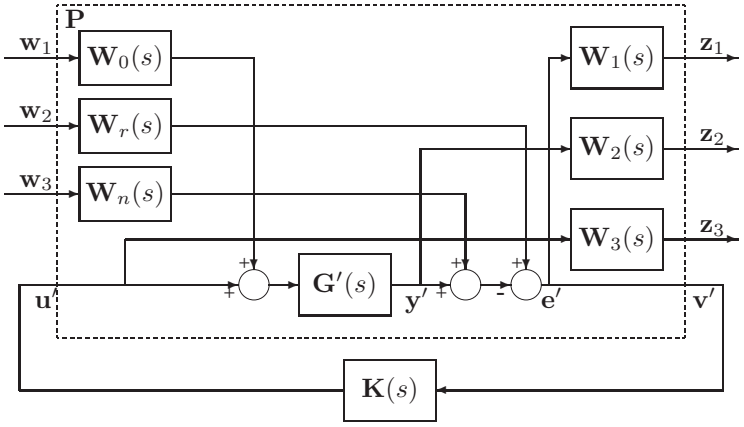

Figure 9.4: $\mathbf{S/KS/T}$ *mixed sensitivity configuration used for the* $\mathcal{H}_\infty$ *design.*

weights on the outputs for $\mathbf{S}$, $\mathbf{T}$ and $\mathbf{KS}$ respectively. $\mathbf{W}_0$ is the weighted disturbance on the control signal. $\mathbf{W}_r$ is the weight on the reference signal and $\mathbf{W}_n$ is the weight on the measurement noise and a practical approach to their selection is addressed in (Hu, Unbehauen & Bohn 1996). $\mathbf{W}_0$ and $\mathbf{W}_n$ are selected as constant values as there is no knowledge of the frequency characteristic. It is chosen to shape the sensitivity function $\mathbf{S}$ by means of only $\mathbf{W}_1$ as the complexity increases by also tuning on the reference weight $\mathbf{W}_r$, which is therefore kept at a constant value of one. The added complexity in Figure 9.4 on the input side by having 3 inputs is driven by the desire to be able to specify separately the weights. The classical formulation would be the right column in Equation 9.23.

After some manipulations $F_l(\mathbf{P}, \mathbf{K})$ in Equation (9.4) becomes

$$F_l(\mathbf{P}, \mathbf{K}) = \begin{bmatrix} -\mathbf{W}_1\mathbf{S}\mathbf{G}'\mathbf{W}_0 & \mathbf{W}_1\mathbf{S}\mathbf{W}_r & -\mathbf{W}_1\mathbf{S}\mathbf{W}_n \\ \mathbf{W}_2\mathbf{S}\mathbf{G}'\mathbf{W}_0 & \mathbf{W}_2\mathbf{T}\mathbf{W}_r & -\mathbf{W}_2\mathbf{T}\mathbf{W}_n \\ -\mathbf{W}_3\mathbf{K}\mathbf{S}\mathbf{G}'\mathbf{W}_0 & \mathbf{W}_3\mathbf{K}\mathbf{S}\mathbf{W}_r & -\mathbf{W}_3\mathbf{K}\mathbf{S}\mathbf{W}_n \end{bmatrix} = \mathbf{M} \qquad (9.23)$$

and to find $\mathbf{K}$ we need to minimize

$$||F_l(\mathbf{P}, \mathbf{K})||_\infty < \gamma \qquad (9.24)$$

It is observed that the left column is scaled by the disturbance or noise on the control signal and it is zero if noise free. The right column is the standard mixed sensitivity often found in the literature and it is scaled by the measurement noise and $\mathbf{W}_n = \mathbf{I}$ if no noise is present.

In order to help define the weights it is interesting to evaluate the low (LF) and high

frequency (HF) boundaries of Equation (9.23)

$$\mathbf{M}_{LF} = \begin{bmatrix} -\mathbf{W}_1\mathbf{K}^{-1}\mathbf{W}_0 & \mathbf{W}_1(\mathbf{G}'\mathbf{K})^{-1}\mathbf{W}_r & \mathbf{W}_1(\mathbf{G}'\mathbf{K})^{-1}\mathbf{W}_n \\ \mathbf{W}_2\mathbf{K}^{-1}\mathbf{W}_0 & \mathbf{W}_2\mathbf{W}_r & \mathbf{W}_2\mathbf{W}_n \\ -\mathbf{W}_3\mathbf{W}_0 & \mathbf{W}_1\mathbf{G}'\mathbf{W}_r & \mathbf{W}_1\mathbf{G}'\mathbf{W}_n \end{bmatrix} \tag{9.25}$$

$$\mathbf{M}_{HF} = \begin{bmatrix} -\mathbf{W}_1\mathbf{G}'\mathbf{W}_0 & \mathbf{W}_1\mathbf{W}_r & \mathbf{W}_1\mathbf{W}_n \\ \mathbf{W}_2\mathbf{G}'\mathbf{W}_0 & \mathbf{W}_2\mathbf{G}'\mathbf{K}\mathbf{W}_r & \mathbf{W}_2\mathbf{G}'\mathbf{K}\mathbf{W}_n \\ \mathbf{W}_3\mathbf{K}\mathbf{G}'\mathbf{W}_0 & \mathbf{W}_3\mathbf{K}\mathbf{W}_r & \mathbf{W}_3\mathbf{K}\mathbf{W}_n \end{bmatrix} \tag{9.26}$$

It is a well known fact that the $\mathcal{H}_\infty$ design framework can suffer from pole/zero cancellations and that RHP open loop poles can reappear in the closed loop mirrored around the $j\omega$ axis (Tsai, Geddes & Postlethwaite 1990*a*) and (Tsai, Geddes & Postlethwaite 1992). This is addressed for a scalar case in (Tsai, Postlethwaite & Geddes 1990) and a multi variable case in (Tsai, Geddes & Postlethwaite 1990*b*). This phenomenon has been experienced for $\mathbf{W}_0 = \mathbf{0}$, but for $\mathbf{W}_0 \neq \mathbf{0}$ the closed loop poles can be well placed avoiding robustness problems for parametric uncertainties (Cao 1997). It is therefore important to proceed the design with well described disturbance on the control signals.

The next step in the design process is to define the weighting functions, but first we shall identify some fundamental constraints on their selection. The constraint $\mathbf{S} + \mathbf{T} = \mathbf{I}$ is recalled and this leads to the fact that the weights $\mathbf{W}_1$ and $\mathbf{W}_2$ in particular must be smaller than 1 in the cross over region and therefore be well separated in cross over frequency. This is illustrated in Figure 9.5, where the weight on $\mathbf{T}$ crosses at a larger frequency than the weight on $\mathbf{S}$.

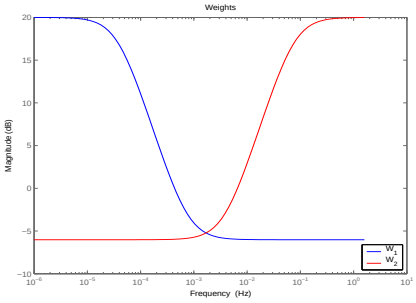

Figure 9.5: *Illustration of the* $\mathbf{W}_1$ *and* $\mathbf{W}_2$ *cross over frequencies and magnitudes to illustrate a frequency range both being below one.*

For the weight definition we consider it desirable to aim at a closed loop characteristics of 2^{nd} order type. We therefore consider a system of unity feedback with a loop transfer as in Equation (8.96), which exactly gives a closed loop 2^{nd} order system. From Figure 9.4 we see that the transfer from the reference to z_1 is $\frac{z_1}{r} = SW_1$ in the scalar case and ignoring measurement noise. The weight is of the same form as used earlier in Equation (8.100) and illustrated in Figure 8.26.

$$\begin{array}{rcl} r_{max} & = & 6 \text{ m} \\ e_{max} & = & 0.6 \text{ m} \\ M_P & < & 30 \text{ \%} \\ t_r & \approx & 50 \text{ s} \end{array} \tag{9.27}$$

Assuming a 10 % control error we get $W_1(0) = \frac{1}{0.1} = 10$ and from Equation (8.100) $A = 0.1$, but to improve the integral action of the controller A can be reduced if needed.

Similar as in Section 8.14 we find from the peak criteria $M \cong 2$. The filter cross over frequency ω_1 is found from the rise time t_r and the natural frequency

$$\omega_n = \frac{1}{t_r\sqrt{1-\zeta^2}}\left[\arctan(\frac{-\sqrt{1-\zeta^2}}{\zeta}) + \pi\right] \tag{9.28}$$

and $\omega_1 \cong \frac{\omega_n}{\sqrt{2}}$ (Ogata 1970), giving $\omega_1 = 2.4 \cdot 10^{-2}$. At the distances we operate from the target, we do not want to track the docking port motion, but only its mean motion. To obtain that we select ω_1 one decade lower than computed above, namely at $\omega_1 = 2.4 \cdot 10^{-3}$.

The weight for the complementary sensitivity $\mathbf{T}$ is basically found from a peak criteria keeping $||\mathbf{T}||_\infty < 2$ and of the following form

$$W_2 = \frac{s + \omega_2 A}{\frac{1}{M}s + \omega_2} \tag{9.29}$$

That leads to $A = 0.5$ and we select $M \geq 10$ and the frequency to be $\omega_2 = 20\omega_1$, which gives good results.

The weight W_3 which affects the control signal is of the same form as in Equation (9.29). At low frequencies we will bound the control signal to a bit less than the maximum from Equation (8.1) such $u = 100 \curvearrowright z_3 = 1$ and $A = 100$. At high frequencies we need penalize the control so as not to track the noise and select $M = 0.01$ and $\omega_3 = 20\omega_1$.

From Table C.5 we select $W_0 = 0.03$ as representing the thruster noise and for the measurement noise from Section 9.2 $W_n = 0.08$. With the low bandwidth used it has shown to be of no benefit to model it as a filter, while a constant weight suffice and makes the controller of lower order. It has been an iterative process to find the good weights for the $\mathcal{H}_\infty$ design and they are summarized in Table 9.3.

	A	M	ω
$W_0 = 0.03$			
$W_1 = \frac{\frac{1}{M}s+\omega}{s+A\omega}$	0.1	2	0.0024
$W_2 = \frac{s+A\omega}{\frac{1}{M}s+\omega}$	0.5	10	0.048
$W_3 = \frac{\frac{1}{M}s+\omega}{s+A\omega}$	100	0.01	0.048
$W_n = 0.08$			
$W_r = 1.0$			

Table 9.3: *Summary of all weights used for $\mathcal{H}_\infty$ design.*

It is now possible to solve Equation (9.24) using optimization software implementing the algorithm in Theorem 9.1. This is the suboptimal $\mathcal{H}_\infty$ controller achieving

$$\gamma_{min} = 0.84 \tag{9.30}$$

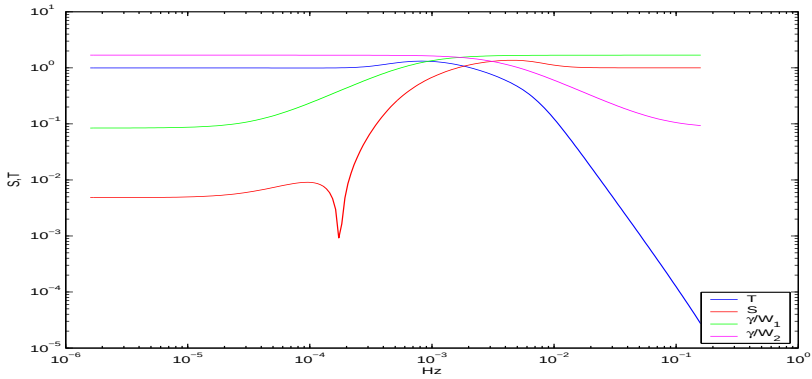

Figure 9.6: *Plots of the* $\mathbf{S}$ *and* $\mathbf{T}$ *functions for the out of plane controller design. The inverse of the weights* W_1 *and* W_2 *multiplied by* γ_{min} *are also shown.*

The interpretation of γ is such that nominally we have $||\mathbf{W}_1\mathbf{S}|| < 1$, but suboptimally the inequality becomes $||\mathbf{W}_1\mathbf{S}|| < \gamma$ which means we need to keep $||\mathbf{S}|| < ||\frac{\gamma}{\mathbf{W}_1}||$ rather than just the inverse weight. This means for $\gamma < 1$ disturbances are suppressed more than designed for by the weights and for $\gamma > 1$ less suppression takes place.

The results obtained for the tuning of the controller are displayed in Figure 9.6, where we see that $\mathbf{S}$ is enveloped by the inverse weight and that $\mathbf{S}$ and $\mathbf{T}$ are well separated in the cross over region. The steep dip on $\mathbf{S}$ at low frequencies has its origin in the plant imaginary poles. In Figure 9.7 we see that the rise time is about 110 s and an overshoot of some 22 % is observed. The control error at steady state is less than 1 % which is fully acceptable. We obtain very good stability margins with a gain and phase

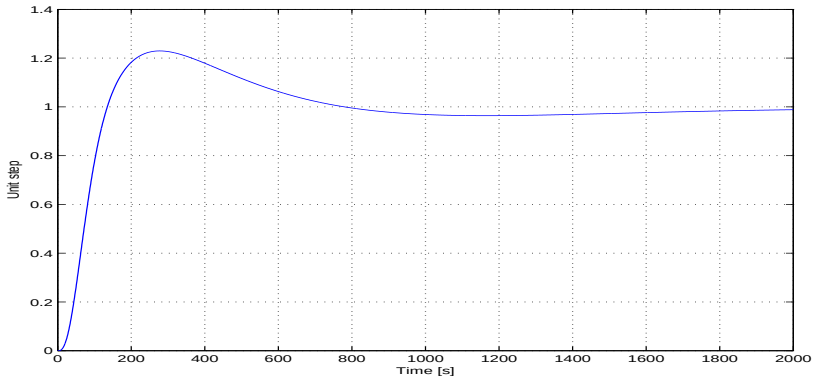

Figure 9.7: *Unit step response.*

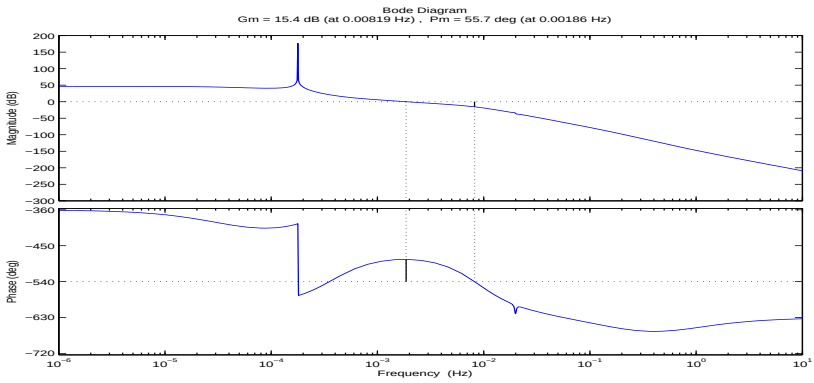

Figure 9.8: *Bode plot of the loop transfer function exhibiting very good margins in the presence of sloshing and flexible modes.*

margin of

$$GM = 15.4 \text{ db (at } 0.008 \text{ Hz)} \quad \text{and} \quad PM = 56 \deg \text{ (at } 0.002 \text{ Hz)} \tag{9.31}$$

which can be seen on the Bode plot in Figure 9.8. The phase and gain jumps have the origin in the plant poles. It shall be pointed out that all spikes in the open loop are completely absent in the closed loop response (not displayed).

The designed controller $\mathbf{K}$ is of order 5 with a pole at -840 being significantly faster than the rest. For both implementation and simulation reasons it is desirable to eliminate it by means of model reduction techniques.

There are basically two methods used in practice, namely truncation and singular perturbation, the latter also known as residualization. We select the residualization as it preserves the steady state gain of the system which is important in this case. The basic approach is to set the desired state derivative equal to zero, solve for it and back substitute to eliminate the state. We will not go into depth here on the subject of model reduction techniques but refer to (Skogestad & Postlethwaite 1996) and (Zhou, Doyle & Glover 1995) amongst some in the literature. Usually the system will have to be put into a Jordan form and the state order rearranged. This has been performed and the resulting 4^{th} order reduced controller characteristic is shown in Figure 9.9, where the non reduced would look identical within the shown frequency range.

The controller needs to be discretized for the real implementation and we chose a bilinear transformation as the $\mathcal{H}_\infty$ norm is then preserved (Green & Limebeer 1995). The sampling time $T_s = 1$ s as earlier. The discretized controller is plotted together with the continuous one in Figure 9.9 and it is seen that there is only a small visible difference at the highest frequency. It is therefore judged to be well representing the originally designed $\mathcal{H}_\infty$ controller.

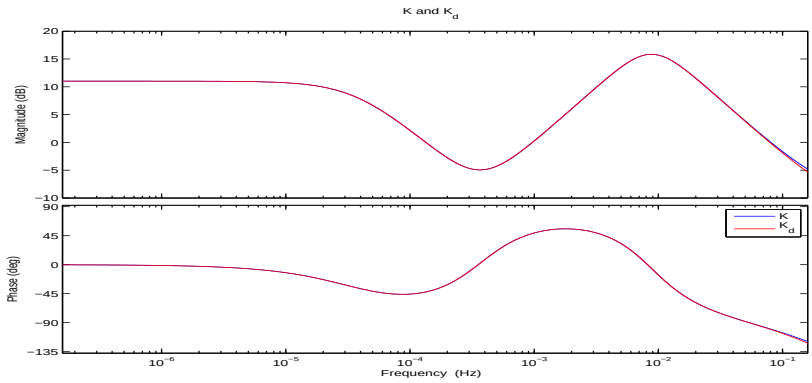

Figure 9.9: *Reduced order controller Bode plot as well as discretized reduced controller sampled at* 1 *Hz.*

9.6 In Plane Position Control

The $\mathcal{H}_\infty$ design for the in plane relative motion is a 2 axes coupled design. It will follow the same approach as in Section 9.5 and the mixed sensitivity used is illustrated in Figure 9.4. The plant pole variation as a function of the orbital position is recalled from Figure 9.1. Also for this design the perigee plant is selected as design plant as it has the fastest dynamics. We select it slightly after perigee to ensure we have RHP poles for the design case.

Before proceeding with the design the plant will be analyzed by computing the RGA as defined in Equation (8.28). We find the frequency response $\mathbf{G}_{fr}$ of the 2×2 plant and observe that the RGA varies significantly over frequency.

At low frequency the RGA has diagonal values of 1.1 and the off diagonal 0.1 and at high frequency the off diagonal becomes 10^{-4}. At a frequency around the orbital one all RGA elements are the same. This indicates that the plant exhibits strong cross axial couplings at the orbital frequency. This has been verified by removing the 2ω terms in the $\mathbf{A}_{pi}$ matrix in Equation (4.17) after which the RGA is dominantly diagonal over all frequencies.

The same coupled behavior can be observed by computing the condition [1] number which reaches 10^3 around the orbital frequency.

Despite the couplings in the plant we will proceed with the control design without assigning any specific weights for that. The weighting functions needed for the setup in Figure 9.4 will be defined as two dimensional diagonal transfer matrices. The individual weights will be similar to those used for the out of plane design in Section 9.5 but with different parameters. The same criteria are used as described in Equation (9.27). The

[1] The condition number $\gamma = \frac{\bar{\sigma}}{\underline{\sigma}}$ is the ratio between the maximum and the minimum singular values of a matrix.

	A_x	A_z	M_x	M_z	ω
$\mathbf{W}_{0_{x,z}} = [0.03, 0.03]$					
$\mathbf{W}_{1_{x,z}} = \frac{\frac{1}{M}s+\omega}{s+A\omega}$	0.1	0.1	2	2	0.0024
$\mathbf{W}_{2_{x,z}} = \frac{s+A\omega}{\frac{1}{M}s+\omega}$	0.6	0.6	10	10	0.048
$\mathbf{W}_{3_{x,z}} = \frac{\frac{1}{M}s+\omega}{s+A\omega}$	100	100	0.01	0.01	0.048
$\mathbf{W}_{n_{x,z}} = [0.05, 0.08]$					
$\mathbf{W}_{r_{x,z}} = [1.0, 1.0]$					

Table 9.4: *Summary of all weights used for the x,z axes $\mathcal{H}_\infty$ design.*

frequency separation for $\mathbf{W}_1$ and $\mathbf{W}_2$ in the cross over region is illustrated in Figure 9.5.

Following the design iterations aiming to fulfill the requirements the design results in the weights listed in Table 9.4

It is now possible to solve Equation (9.23) using optimization software implementing the algorithm in Theorem 9.1. This suboptimal $\mathcal{H}_\infty$ controller gives

$$\gamma_{min} = 0.93 \tag{9.32}$$

The results obtained for the tuning of the controller are displayed in Figure 9.10, where we see that $\mathbf{S}$ is enveloped by the inverse weights and that $\mathbf{S}$ and $\mathbf{T}$ are well separated in the cross over region.

The individual axes are plotted in Figure 9.10 and it is observed that the low frequency levels of $\mathbf{S}$ for each axis are different. This is the best compromise as it appears not possible to lower both further at the same time. The limiting factor appears to be

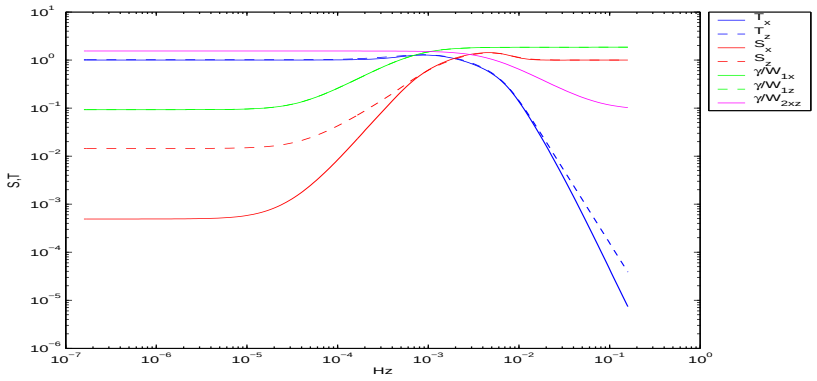

Figure 9.10: *Plots of $\mathbf{S}$ and $\mathbf{T}$ functions for the in plane controller. The inverse of the weights $\mathbf{W}_1$ and $\mathbf{W}_2$ multiplied by γ_{min} are also shown.*

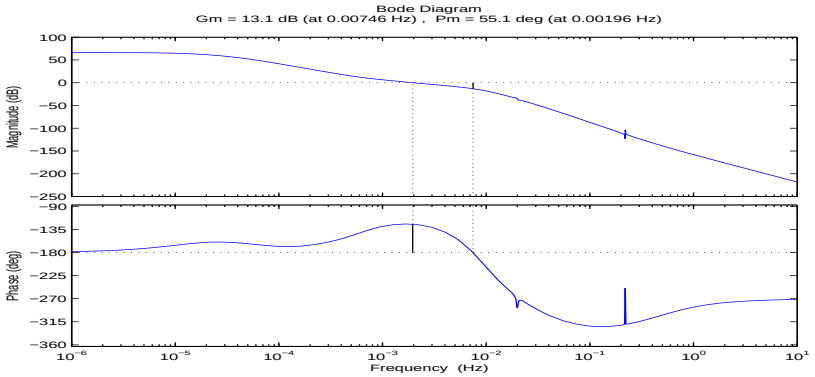

Figure 9.11: *Bode plot for the x-axis open loop in the presence of sloshing and flexible modes.*

$\mathbf{W}_3$ on the actuation. If that constant is relaxed both become smaller as well as γ_{min}, but at the price of a fast noise sensitive system, which is undesirable.

The step response for the x and z-axis is very similar to the one illustrated in Figure 9.7. The x-axis has an overshoot of 28 % and the z-axis has 15 % and also here it has not been possible to reach the same values.

The classical stability margins are evaluated in one open loop at the time as was performed for the attitude LQG controller in Section 8.5. We obtain the following results

$$\begin{aligned} GM_x &= 13.1 \text{ db (at } 0.008 \text{ Hz)} \quad \text{and} \quad PM_x = 55 \deg \text{ (at } 0.002 \text{ Hz)} \\ GM_z &= 14.8 \text{ db (at } 0.008 \text{ Hz)} \quad \text{and} \quad PM_z = 55 \deg \text{ (at } 0.002 \text{ Hz)} \end{aligned} \tag{9.33}$$

which are illustrated in Figures 9.11 and 9.12 respectively including the flexible and

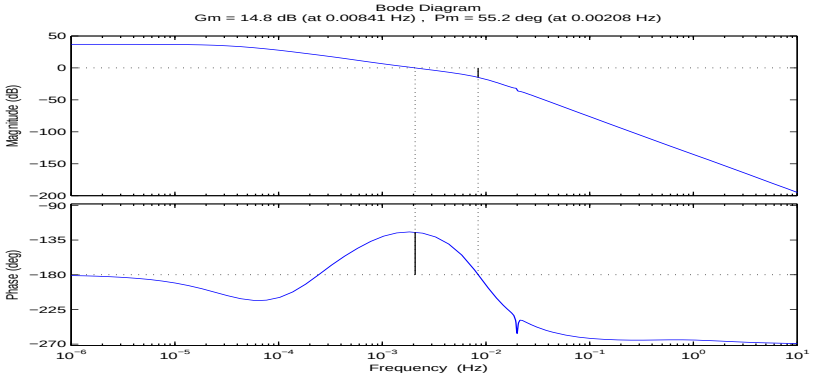

Figure 9.12: *Bode plot for the z-axis open loop in the presence of sloshing and flexible modes.*

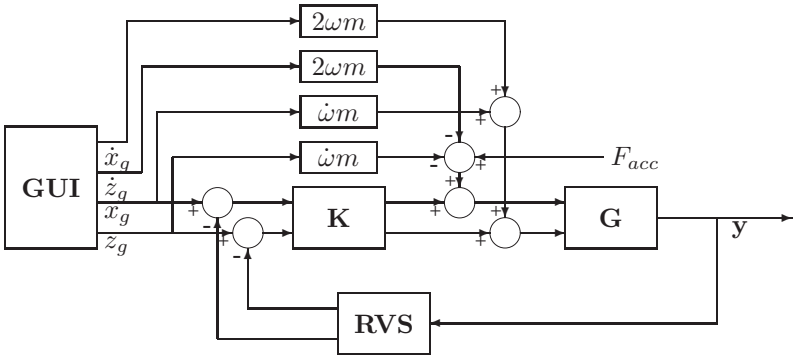

Figure 9.13: *Illustration of the feed forward compensation scheme interconnections. The parameters ω and $\dot{\omega}$ are the time varying cross coupling terms in Equation (4.16).*

sloshing modes.

The controller has been reduced in order to remove 2 very fast modes. It has a similar shape as the out of plane controller in Figure 9.9 and the discretization has been performed similarly.

Due to the cross couplings present in the plant especially around the orbital frequency, it is important to implement a decoupling to avoid cross effects between the axes. From Equation (4.16) we see that we need to compensate as follows

$$F_{x_{ff}} = -m(2\omega(t)\dot{z}_g + \dot{\omega}(t)z_g) \tag{9.34}$$

$$F_{z_{ff}} = m(2\omega(t)\dot{x}_g + \dot{\omega}(t)x_g) \tag{9.35}$$

where $F_{x_{ff}}$ and $F_{z_{ff}}$ are the feed forward signals. The last term containing $\dot{\omega}(t)$ appears small, but it is very important to compensate it for larger distances in either x or z direction. For a distance in x direction of -500 m the contribution from the two terms is the same order of magnitude. If not accounted for it clearly introduces undesired oscillations on the other axis.

It is chosen to compensate using the guidance signals rather than estimating the states and compensate from them. The advantage is that it is decoupled from the feedback loops and will not affect the robust stability and performance. For a well tuned controller the control error will be small and the approach of guidance feedforward gives good results. The connection structure is illustrated in Figures 9.13 and 7.1.

The term F_{acc} in Figure 9.13 is the computed force needed to provide the guidance profile acceleration. For constant acceleration F_{acc} is a pulse and for exponential braking a certain profile. The computations are found in Table 7.5 and illustrated in Figure 7.10 in Section 7.7.

We will now consider the $\mathcal{H}_\infty$ position control design discretely implemented in a

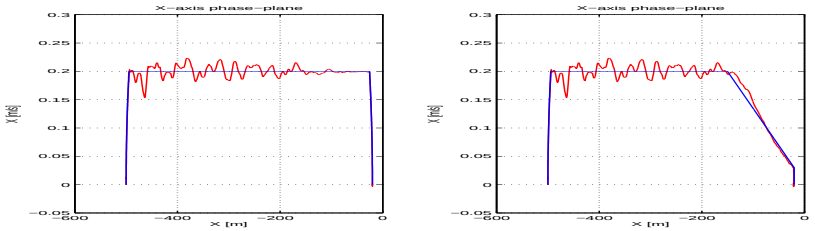

Figure 9.14: *Phase plane plot for s_3 to s_4 approach following the constant and exponential braking profiles.*

full nonlinear simulation, which implements all details documented in this thesis. It will simulate the complete GNC from s_3 to s_4 with an approach velocity of 0.2 m/s. The guidance profile selected is the constant acceleration and constant braking as more demanding for the GNC. For comparison also exponential braking has been tried and the result is illustrated in Figure 9.14. Both perform very well and are comfortably inside specifications.

It is recalled that the target docking port can oscillate due to the ISS attitude motion described in Figure 3.5. This will cause a motion of $\mathbf{r}_{dt}$ in the LVLH frame. At the larger distances the controller tries to track the mean motion of $\mathbf{r}_{dt}$ as it is meaningless to follow tightly the docking port, although this is what is measured. The control is port to port.

In Figure 9.15 is shown the results of a full nonlinear simulation providing relative port to port positions, velocities and the forces on the chaser spacecraft. The plots provide the port to port relative values $\mathbf{s}_{pp}$, which is the control error and the COM motion of the chaser. The oscillations are due to the motion of the target docking port.

For the x-axis we observe the offset between the COM and port locations and that the motion moves smooth from -500 m to -20 m. The approach speed reaches well the 0.2 m/s and starts after 50 s at the s_3 point. The acceleration and braking pulses are clearly visible on the force plot.

For the y and z-axes we see clearly on the motion of the COM that the controller is not tracking all the target oscillations. As the chaser attitude motions is very small, see Figure 8.5, the $\mathbf{s}_{pp}$ motion is mostly due to the target motion. For the force on the z-axis we clearly see the feed forward compensation due to the approach velocity along the x-axis.

In Figure 9.16 we see the lateral positions for the target and chaser ports in absolute terms in the LVLH frame. The oscillation on the z-axis is caused by the cross coupling due to the acceleration pulse. The two right most plots show the lateral relative motion in the y-z plane which gives a good idea of the motion observed from one of the ports. The box shaped lateral velocities of $\dot{\mathbf{s}}_{pp}$ is caused by the constant parts of the velocity shown in Figure 3.5. We see that the design performs well inside specifications. The same plots are shown including target flexible motion in Section D.4 showing little impact.

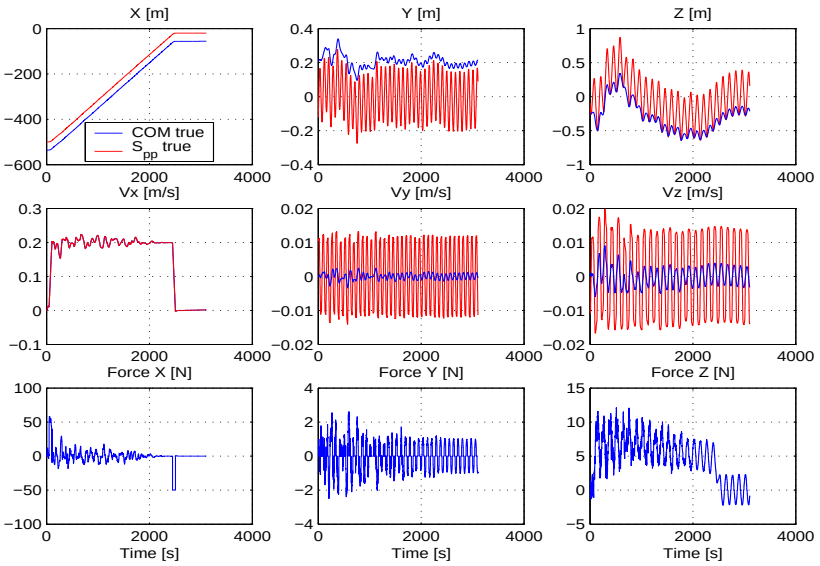

Figure 9.15: *The full nonlinear simulation showing the port to port $\mathbf{s}_{pp}$ motion, the chaser COM motion, the associated velocities and the forces. $\mathbf{s}_{pp}(0) = [-500, 0, 0]^T$ m and $\dot{\mathbf{s}}_{pp}(0) = \mathbf{0}$ m/s.*

9.7 Out of Plane Model Uncertainty

The uncertain parameters in the out of plane model in Equation (4.18) are the mass m_c and the orbital angular rate ω. The former we will treat later, when in and out of plane models are combined.

The variation of ω is shown in Table 7.2 and we notice from Equation (4.18) that it appears in the model as $\omega^{\frac{3}{2}}$. We see from the development in Section D.3.4 that it is possible to represent any matrix $\mathbf{X} \in \mathcal{C}^{m\times n}$ to the power N such that $\mathbf{X}^N \forall N \in Z$ is an exact LFT. This is not the case for $N \in R$ and therefore we need to approximate $\omega^{\frac{3}{2}}$. For $\varepsilon = 0.1$ it is not so far from a straight line, but for larger eccentricities it clearly has a convex curvature, with more curvature for lower ω.

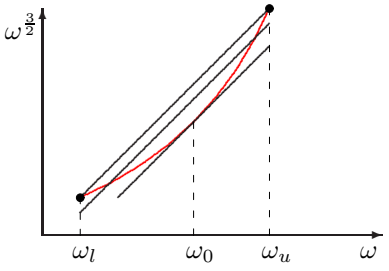

Figure 9.17: *Taylor, chord and area matching approximations for the orbital rate $\omega^{\frac{3}{2}}$.*

As illustrated in Figure 9.17 there are various ways to approximate the function of the orbital rate. We consider a chord, a shifted chord with a least squared error and Taylor approximations up to order 3.

The performance of the approximations is evaluated by computing the true and ap-

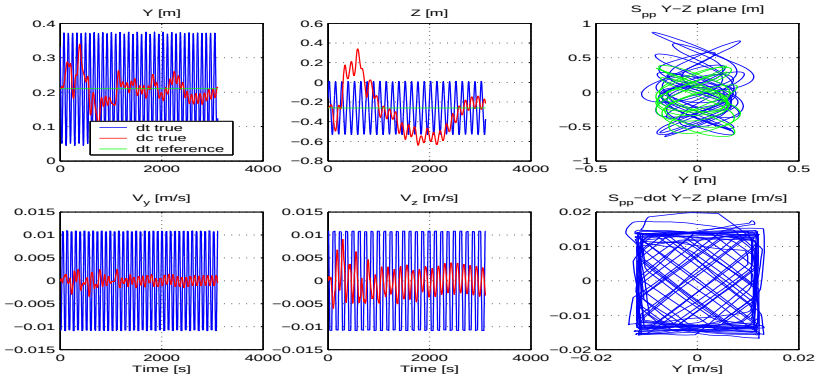

Figure 9.16: *The full nonlinear simulation showing the true LVLH lateral port motions as well as the relative motion in the cross section y-z plane. The green part of the curve is for relative distance smaller than* 100 *m.*

proximated eigenvalues of Equation (4.18). Then the error is found using the same principle as in Equation (4.111). This gives the radius in percentage of an error disc centered at the true eigenvalues. We consider the eigenvalue approximation rather than only the matrix parameters alone as it is the important characteristics for stability and performance. The result of the various methods investigated is listed in Table 9.5. It is seen that only the second and third order Taylor expansions have very small errors. As the eccentricity increases the error grows close to 10 % for $\varepsilon = 0.7$ beyond which a third order approximation is recommended. We select a second order Taylor as it has small errors as well as it fits well with the natural presence of second order parameters of the in plane dynamics.

Type	Error in %
Chord	$[0; 0.8]$
Area matching	$[-0.7; 0.2]$
Taylor 1^{st} order	$[-1; 0]$
Taylor 2^{nd} order	$[-0.04; 0.02]$
Taylor 3^{rd} order	$[-0.003; 0]$

Table 9.5: *Out of plane eigenvalue errors as a function of approximation of the* $\omega^{\frac{3}{2}}$ *parameter in the transition matrix in Equation (4.18). The eccentricity is* $\varepsilon = 0.1$.

We find $\omega_0 = \frac{1}{2}(\omega_{max} + \omega_{min})$ and let us define $z(\omega) \approx \omega^{\frac{3}{2}}$. Then we can find the 2^{nd} order Taylor approximation as

$$z(\omega) = \frac{3}{8}\omega_0^{-\frac{1}{2}}\omega^2 + \frac{3}{4}\omega_0^{\frac{1}{2}}\omega - \frac{1}{8}\omega_0^{\frac{3}{2}} = a\omega^2 + b\omega + c \tag{9.36}$$

which will be used further in the robustness analysis.

The $\mathbf{A}_{po}$ matrix of Equation (4.19) can now be partitioned as follows inserting Equation (9.36)

$$\mathbf{A}_{po} = \begin{bmatrix} 0 & 1 \\ -kz(\omega) & 0 \end{bmatrix} = \mathbf{A}_0 + \mathbf{A}_1 \tag{9.37}$$

where

$$\mathbf{A}_0 = \begin{bmatrix} 0 & 1 \\ -kc & 0 \end{bmatrix} \quad \text{and} \quad \mathbf{A}_1 = \begin{bmatrix} 0 & 0 \\ -k(a\omega^2 + b\omega) & 0 \end{bmatrix} = \begin{bmatrix} 0 \\ 1 \end{bmatrix} X \begin{bmatrix} 1 & 0 \end{bmatrix} \tag{9.38}$$

and

$$X = -ka\omega^2 - kb\omega = \underbrace{-ka\omega}_{1} \underbrace{\omega}_{2} \underbrace{-kb\omega}_{3} \tag{9.39}$$

The LFT formulation of ω is recalled from Equation (8.55) as $\omega = \bar{\omega} + \delta k_p$. In Equation (9.39) we observe 3 LFTs consisting of a product of 1 and 2 followed by the addition of 3.

The LFT for ω in Equation (9.39) is the scalar version of what is shown in Figure 8.13 and is denoted as $F_{u2}(\mathbf{M}_2, \delta)$. The first one is a constant times $F_{u2}(\mathbf{M}_2, \delta)$ and is $F_{u1}(\mathbf{M}_1, \delta)$ where

$$\mathbf{M}_1 = \left[\begin{array}{c|c} 0 & -kak_p \\ \hline 1 & -ka\bar{\omega} \end{array}\right] \tag{9.40}$$

$F_{u3}(\mathbf{M}_3, \delta)$ is found similar as in Equation (9.40). We can now write Equation (9.39) as

$$X = F_u(\mathbf{M}, \delta\mathbf{I}_3) = F_{u2}(\mathbf{M}_2, \delta)F_{u1}(\mathbf{M}_1, \delta) + F_{u3}(\mathbf{M}_3, \delta) \tag{9.41}$$

Using Lemma D.4 for concatenating LFTs $\mathbf{M}$ is found to be

$$\mathbf{M} = \left[\begin{array}{ccc|c} 0 & 0 & 0 & -kak_p \\ k_p & 0 & 0 & -kak_p\bar{\omega} \\ 0 & 0 & 0 & -kbk_p \\ \hline \bar{\omega} & 1 & 1 & -ka\bar{\omega}^2 - kb\bar{\omega} \end{array}\right] \tag{9.42}$$

The final uncertainty model for the out of plane dynamics, excluding the $\mathbf{B}_{po}$ matrix, is illustrated in Figure 9.18.

9.8 In Plane Position Model Uncertainty

The uncertain parameter of the in plane model in Equation (4.16) are the mass m_c and the orbital angular rate ω.

We see that the orbital angular acceleration is present and we can write $\dot{\omega} = f(\omega)$, where $f(\omega)$ is some function. This means that its uncertainty should vary with the same repeated δ as for the rate in order to be as little conservative as possible. Some points should be observed for $\dot{\omega}$

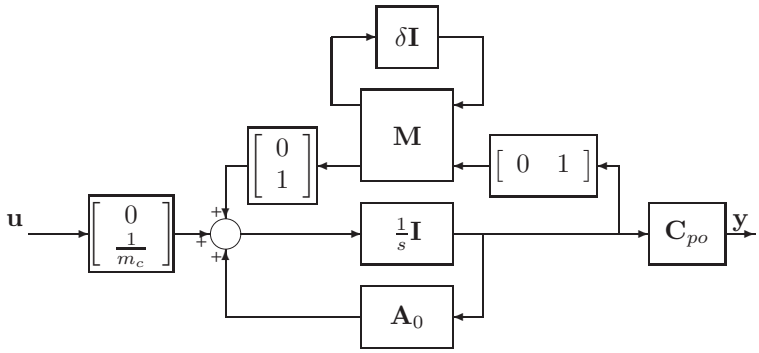

Figure 9.18: *Uncertainty model for the out of plane dynamics. It shall be noted that the mass m_c uncertainty will be handled when combined with the in plane model.*

- From Table 7.2, where $\dot{\theta} = \omega$ and $\ddot{\theta} = \dot{\omega}$, we see that its value is about 3 to 4 orders of magnitude smaller than the orbital rate at any point in time.
- Despite its sign change over the orbit, its influence on the eigenvalues of the dynamics is rather small.
- $f(\omega)$ has no analytical closed form and its characteristics change drastically as a function of the eccentricity as well as it is mathematically not a function (2 values of $\dot{\omega}$ for the same ω).

The phase plane trajectories of $\dot{\omega}$ vary from a point at zero ($\varepsilon = 0$) over ellipses (ε in midrange) to an onion shaped trajectory (ε higher). We can represent it as an ellipse such

$$\frac{\dot{\omega}^2}{a^2} + \frac{\omega^2}{b^2} = 1 \qquad \Longrightarrow \qquad \dot{\omega} = \pm a\sqrt{1 - \frac{\omega^2}{b^2}} \tag{9.43}$$

The square root could then be approximated by a Taylor series together with a resolution of the sign ambiguity. The added complexity should be considered with respect to its very small influence.

Based upon these considerations it is decided to take a worst case approach and consider the $\dot{\omega}$ uncertainty independent of ω.

The $\mathbf{A}_{pi}$ matrix of Equation (4.17) can now be approximated as for the out of plane using Equation (9.36) for the $\omega^{\frac{3}{2}}$ terms and become

$$\mathbf{A}_{pi} \approx \begin{bmatrix} 0 & 0 & 1 & 0 \\ 0 & 0 & 0 & 1 \\ \omega^2 - ka\omega^2 - kb\omega - kc & \dot{\omega} & 0 & 2\omega \\ -\dot{\omega} & \omega^2 + 2ka\omega^2 + 2kb\omega + 2kc & -2\omega & 0 \end{bmatrix} \tag{9.44}$$

$$\approx \mathbf{A}_0 + \mathbf{A}_1(\omega^2) + \mathbf{A}_2(\omega) + \mathbf{A}_3(\dot{\omega}) \tag{9.45}$$

We will first deal with a general formulation of the terms containing ω^2. For a scalar case of the LFT in Figure 8.13 for ω we can multiply two of those using Equation (D.21) to obtain the LFT of ω^2 as $\omega^2 = F_u(\mathbf{M}, \mathbf{\Delta})$ where

$$\mathbf{M} = \left[\begin{array}{cc|c} 0 & 0 & k_p \\ k_p & 0 & k_p\bar{\omega} \\ \hline \bar{\omega} & 1 & \bar{\omega}^2 \end{array}\right] \quad \text{and} \quad \mathbf{\Delta} = \begin{bmatrix} \delta & 0 \\ 0 & \delta \end{bmatrix} \tag{9.46}$$

It is useful to formulate a general solution to matrices of the form at hand, which is found in Theorem 9.2

Theorem 9.2
For a matrix $\boldsymbol{A} \in \mathcal{C}^{m\times n}$ with all nonzero elements of the form $A_{ij} = a_{ij}x^2 + b_{ij}$ and $x = \bar{x} + \delta k_p$ with $\|\delta\| \leqslant 1$, $\bar{x} = \frac{1}{2}(x_{max} + x_{min})$ and $k_p = \frac{1}{2}(x_{max} - x_{min})$ the general LFT can be expressed as

$$\boldsymbol{A} = \boldsymbol{A}_1(x^2) + \boldsymbol{A}_0 = F_u(\boldsymbol{R}, \delta\boldsymbol{I}_{2r}) \tag{9.47}$$

where

$$\boldsymbol{R} = \left[\begin{array}{c|c} \boldsymbol{I}_r(\boldsymbol{M}_{11}) & \boldsymbol{I}_r(\boldsymbol{M}_{12})\boldsymbol{S} \\ \hline \boldsymbol{L}\boldsymbol{I}_r(\boldsymbol{M}_{21}) & \boldsymbol{A}_0 + \boldsymbol{L}\boldsymbol{I}_r(\bar{x}^2)\boldsymbol{S} \end{array}\right] \tag{9.48}$$

In Equation (9.47) $\boldsymbol{A}_0$ holds all constant b_{ij} terms and $\boldsymbol{A}_1$ all terms of $a_{ij}x^2$. $\boldsymbol{M}_{ij}$ are the partitioned elements of the fundamental LFT in Equation (9.46) and $r = rank(\boldsymbol{A}_1)$. The terms $\boldsymbol{L}$ and $\boldsymbol{S}$ come from the SVD of $\boldsymbol{A}_1$ as

$$\boldsymbol{A}_1 = \boldsymbol{L}\boldsymbol{I}_r(x^2)\boldsymbol{S} \tag{9.49}$$

where $\boldsymbol{I}_r(\cdot)$ is block diagonal of the argument of dimension $r \times r$ in block terms.

Proof: We split $\mathbf{A} = \mathbf{A}_0 + \mathbf{A}_1$ where $\mathbf{A}_0$ contains all constant terms b_{ij} and $\mathbf{A}_1$ all terms of the form $a_{ij}x^2$. We can now place x^2 outside the matrix and write

$$\mathbf{A}_1 = \begin{bmatrix} a_{11}x^2 & \cdots & \\ \vdots & \ddots & \\ & & a_{ij}x^2 \end{bmatrix} = \begin{bmatrix} a_{11} & \cdots & \\ \vdots & \ddots & \\ & & a_{ij} \end{bmatrix} x^2 = \mathbf{L}(x^2\mathbf{I}_r)\mathbf{S} \tag{9.50}$$

Using Equations (8.32), (8.42) and (8.43) we can write

$$\mathbf{A} = F_u(\mathbf{P}, x^2\mathbf{I}_r) \quad \text{and} \quad \mathbf{P} = \left[\begin{array}{c|c} \mathbf{0} & \mathbf{S} \\ \hline \mathbf{L} & \mathbf{A}_0 \end{array}\right] \tag{9.51}$$

The upper block of the LFT in Equation (9.51) we can conveniently express as another LFT

$$x^2\mathbf{I}_r = \begin{bmatrix} x_1^2 & & \\ & \ddots & \\ & & x_r^2 \end{bmatrix} = \sum_{i=1}^{r} \begin{bmatrix} 0 & & & \\ & \ddots & & \\ & & x_i^2 & \\ & & & \ddots \\ & & & & 0 \end{bmatrix} \tag{9.52}$$

where $\mathbf{I}_r$ has rank $= r$ and each matrix in the sum has rank 1. The i^{th} matrix can then be decomposed as

$$\begin{bmatrix} 0 & & & & \\ & \ddots & & & \\ & & x_i^2 & & \\ & & & \ddots & \\ & & & & 0 \end{bmatrix} = \begin{bmatrix} 0 \\ \vdots \\ 1 \\ \vdots \\ 0 \end{bmatrix}_{r\times 1} x^2 \begin{bmatrix} 0 & \cdots & 1 & \cdots & 0 \end{bmatrix}_{1\times r} = \mathbf{L}_i x^2 \mathbf{S}_i \quad (9.53)$$

We now use Equation (9.46) to represent x^2 as a LFT and Equation (9.53) becomes

$$\begin{aligned} \mathbf{L}_i x^2 \mathbf{S}_i &= \mathbf{L}_i(\mathbf{M}_{22} + \mathbf{M}_{21}\boldsymbol{\Delta}(\mathbf{I} - \mathbf{M}_{11}\boldsymbol{\Delta})^{-1}\mathbf{M}_{12})\mathbf{S}_i \\ &= \underbrace{\mathbf{L}_i\mathbf{M}_{22}\mathbf{S}_i}_{\mathbf{N}_{22\,i}} + \underbrace{\mathbf{L}_i\mathbf{M}_{21}}_{\mathbf{N}_{21\,i}}\boldsymbol{\Delta}(\mathbf{I} - \underbrace{\mathbf{M}_{11}}_{\mathbf{N}_{11_i}}\boldsymbol{\Delta})^{-1}\underbrace{\mathbf{M}_{12}\mathbf{S}_i}_{\mathbf{N}_{12_i}} \\ &= F_u(\mathbf{N}_i, \boldsymbol{\Delta}) \end{aligned} \quad (9.54)$$

Completing the sum in Equation (9.52) we get

$$x^2\mathbf{I}_r = \sum_{i=1}^{r} F_u(\mathbf{N}_i, \boldsymbol{\Delta}) = F_u(\mathbf{Q}, \delta\mathbf{I}_{2r}) \quad (9.55)$$

where

$$\mathbf{Q} = \left[\begin{array}{ccc|c} \mathbf{N}_{11_1} & & & \mathbf{N}_{12_1} \\ & \ddots & & \vdots \\ & & \mathbf{N}_{11_r} & \mathbf{N}_{12_r} \\ \hline \mathbf{N}_{21_1} & \cdots & \mathbf{N}_{21_r} & \sum_{i=1}^{r}\mathbf{N}_{22_i} \end{array}\right] \quad (9.56)$$

for coupling LFTs in parallel and pulling out all upper blocks. We now express $\mathbf{Q}$ in terms of the primary parameters from Equation (9.46) and using the structural information of Equations (9.52) and (9.53) it gives the following block diagonal matrices

$$\mathbf{Q}_{11} = \mathbf{M}_{11}\mathbf{I}_r, \qquad \dim = 2r \times 2r \quad (9.57)$$

$$\mathbf{Q}_{12} = \begin{bmatrix} \mathbf{M}_{12_1} & & \\ & \ddots & \\ & & \mathbf{M}_{12_r} \end{bmatrix}, \qquad \dim = 2r \times r \quad (9.58)$$

$$\mathbf{Q}_{21} = \begin{bmatrix} \mathbf{M}_{21_1} & & \\ & \ddots & \\ & & \mathbf{M}_{21_r} \end{bmatrix}, \qquad \dim = r \times 2r \quad (9.59)$$

$$\mathbf{Q}_{22} = \mathbf{M}_{22}\mathbf{I}_r, \qquad \dim = r \times r \quad (9.60)$$

Combining Equation (9.55) with Equation (9.51) we get the generalized star product

$$\mathbf{A} = F_u(\mathbf{P}, x^2\mathbf{I}_r) = F_u(\mathbf{P}, F_u(\mathbf{Q}, \delta\mathbf{I}_{2r})) = F_u(\mathcal{S}(\mathbf{Q}, \mathbf{P}), \delta\mathbf{I}_{2r}) \quad (9.61)$$

which is easily seen from Figure D.3. We finally need to compute $\mathcal{S}(\mathbf{Q},\mathbf{P})$ from Equation (D.29) observing from Equation (9.51) that $\mathbf{P}_{11}=\mathbf{0}$

$$F_l(\mathbf{Q},\mathbf{P}_{11})=\mathbf{Q}_{11} \tag{9.62}$$

$$F_u(\mathbf{P},\mathbf{Q}_{22})=\mathbf{P}_{22}+\mathbf{P}_{21}\mathbf{Q}_{22}\mathbf{P}_{12}=\mathbf{A}_0+\mathbf{L}(\bar{x}^2\mathbf{I}_r)\mathbf{S} \tag{9.63}$$

$$\mathbf{Q}_{12}\mathbf{P}_{12}=(\mathbf{M}_{12}\mathbf{I}_r)\mathbf{S} \tag{9.64}$$

$$\mathbf{P}_{21}\mathbf{Q}_{21}=\mathbf{L}(\mathbf{K}_{21}\mathbf{I}_r) \tag{9.65}$$

From Equation (9.62) to Equation (9.65) we see that $\mathbf{R}=\mathcal{S}(\mathbf{Q},\mathbf{P})$ which completes the proof. ■

We can now use Theorem 9.2 to find the first two terms of Equation (9.45) and from Equation (9.44)

$$\mathbf{A}_0=\begin{bmatrix}0&0&1&0\\0&0&0&1\\-kc&0&0&0\\0&2kc&0&0\end{bmatrix}\quad\text{and}\quad\mathbf{A}_1=\begin{bmatrix}0&0&0&0\\0&0&0&0\\(1-ka)\omega^2&0&0&0\\0&(1+2ka)\omega^2&0&0\end{bmatrix} \tag{9.66}$$

From SVD in Lemma 8.1 of $\mathbf{A}_1$ we get

$$\mathbf{L}=\begin{bmatrix}0&0\\0&0\\1&0\\0&1\end{bmatrix}\quad\text{and}\quad\mathbf{S}=\begin{bmatrix}1-ka&0&0&0\\0&1+2ka&0&0\end{bmatrix},\qquad\text{rank}=2 \tag{9.67}$$

and using Theorem 9.2 and Equations (9.48) and (9.46) we can write the LFT for $\mathbf{A}_0+\mathbf{A}_1$ in Equation (9.45) as $F_u(\mathbf{M}_1,\boldsymbol{\Delta}_1)$ where

$$\mathbf{M}_1=\left[\begin{array}{c|c}\begin{bmatrix}\mathbf{M}_{11}&\\&\mathbf{M}_{11}\end{bmatrix}&\begin{bmatrix}\mathbf{M}_{12}&\\&\mathbf{M}_{12}\end{bmatrix}\mathbf{S}\\\hline\mathbf{L}\begin{bmatrix}\mathbf{M}_{21}&\\&\mathbf{M}_{21}\end{bmatrix}&\mathbf{A}_0+\mathbf{L}\begin{bmatrix}\bar{\omega}^2&\\&\bar{\omega}^2\end{bmatrix}\mathbf{S}\end{array}\right]\quad\text{and}\quad\boldsymbol{\Delta}_1=\begin{bmatrix}\delta&&&\\&\delta&&\\&&\delta&\\&&&\delta\end{bmatrix} \tag{9.68}$$

For $\mathbf{A}_2$ in Equation (9.45) it can be decomposed using Lemma 8.2 and Equations (8.42) and (8.43) as

$$\mathbf{A}_2=\mathbf{Y}_0+\delta\mathbf{Y}_1\qquad\text{and}\qquad\mathbf{Y}_0=\begin{bmatrix}0&0&0&0\\0&0&0&0\\-kb\bar{\omega}&0&0&2\bar{\omega}\\0&2kb\bar{\omega}&-2\bar{\omega}&0\end{bmatrix} \tag{9.69}$$

and

$$\delta\mathbf{Y}_1=\underbrace{\begin{bmatrix}0&0\\0&0\\0&1\\1&0\end{bmatrix}}_{\mathbf{L}_2}\begin{bmatrix}\delta&\\&\delta\end{bmatrix}\underbrace{\begin{bmatrix}0&2kbk_p&-2k_p&0\\-kbk_p&0&0&2k_p\end{bmatrix}}_{\mathbf{S}_2},\qquad\text{rank}=2 \tag{9.70}$$

We then obtain

$$\mathbf{A}_2 = F_u(\mathbf{M}_2, \mathbf{\Delta}_2) \tag{9.71}$$

where

$$\mathbf{M}_2 = \left[\begin{array}{c|c} \mathbf{0} & \mathbf{S}_2 \\ \hline \mathbf{L}_2 & \mathbf{Y}_0 \end{array}\right] \quad \text{and} \quad \mathbf{\Delta}_2 = \begin{bmatrix} \delta & \\ & \delta \end{bmatrix} \tag{9.72}$$

For the last term $\mathbf{A}_3$ in Equation (9.45) a worst case will be applied, as explained earlier, and $\dot{\omega}$ is considered independent from ω. We have

$$\dot{\omega} = \bar{\dot{\omega}} + \delta_{\dot{\omega}} k_{\dot{\omega}} \wedge \|\delta_{\dot{\omega}}\| \leq 1, \quad \forall \delta_{\dot{\omega}} \in \mathcal{R} \tag{9.73}$$

but as $\dot{\omega}_{min} = -\dot{\omega}_{max}$ we get

$$\bar{\dot{\omega}} = 0 \quad \text{and} \quad k_{\dot{\omega}} = \dot{\omega}_{max} \tag{9.74}$$

We then get directly

$$\mathbf{A}_3 = \underbrace{\begin{bmatrix} 0 & 0 \\ 0 & 0 \\ 0 & -1 \\ 1 & 0 \end{bmatrix}}_{\mathbf{L}_3} \begin{bmatrix} \delta_{\dot{\omega}} & \\ & \delta_{\dot{\omega}} \end{bmatrix} \underbrace{\begin{bmatrix} -k_{\dot{\omega}} & 0 & 0 & 0 \\ 0 & -k_{\dot{\omega}} & 0 & 0 \end{bmatrix}}_{\mathbf{S}_3}, \qquad \text{rank} = 2 \tag{9.75}$$

obtaining

$$\mathbf{A}_3 = F_u(\mathbf{M}_3, \mathbf{\Delta}_3) \tag{9.76}$$

where

$$\mathbf{M}_3 = \left[\begin{array}{c|c} \mathbf{0} & \mathbf{S}_3 \\ \hline \mathbf{L}_3 & \mathbf{0} \end{array}\right] \quad \text{and} \quad \mathbf{\Delta}_3 = \begin{bmatrix} \delta_{\dot{\omega}} & \\ & \delta_{\dot{\omega}} \end{bmatrix} \tag{9.77}$$

The final uncertainty model for the in plane dynamics, excluding the $\mathbf{B}_{pi}$ matrix, is illustrated in Figure 9.19.

9.9 Chaser Mass Uncertainty Description

The input matrices for the out of and in plane models in Figures 9.18 and 9.19 we combine into one as

$$\mathbf{B} = \begin{bmatrix} \mathbf{0} \\ \frac{1}{m_c}\mathbf{I} \end{bmatrix} = \begin{bmatrix} \mathbf{0} \\ \mathbf{I}_m^{-1} \end{bmatrix} = \begin{bmatrix} \mathbf{0} \\ \mathbf{I} \end{bmatrix} \mathbf{I}_m^{-1} \tag{9.78}$$

The uncertainty on the mass m_c is

$$m_c = \bar{m}_c + \delta_m k_m \wedge \|\delta_m\| \leq 1, \quad \forall \delta_m \in \mathcal{R} \tag{9.79}$$

where $\bar{m}_c$ and k_m are completed in a similar manner as in Equation (8.69). We select the worst case, which is when the chaser is the lightest, from Equation (C.5) with $m_{c_{min}} =$

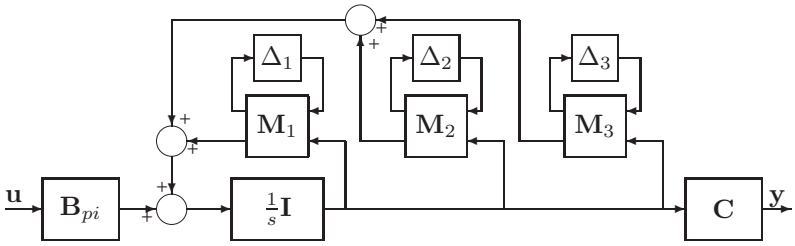

Figure 9.19: *Uncertainty model for the in plane dynamics. It shall be noted that the mass m_c uncertainty will be handled when combined with the out of plane model.*

14000 kg and $m_{c_{max}} = 15000$ kg. This gives a variation of about ± 3.5 % and larger than specified in Section C.2.

The formulation in Equation (9.78) is equivalent to the one in Equations (8.47) and (8.48). $\mathbf{I}_m$ then becomes

$$\mathbf{I}_m = \mathbf{I}_{m_0} + \underbrace{\begin{bmatrix} \mathbf{I} \end{bmatrix}}_{\mathbf{L}} \underbrace{\begin{bmatrix} \delta_m & & \\ & \delta_m & \\ & & \delta_m \end{bmatrix}}_{\mathbf{\Delta}_m} \underbrace{\begin{bmatrix} k_m & & \\ & k_m & \\ & & k_m \end{bmatrix}}_{\mathbf{S}}, \quad \text{rank} = 3 \tag{9.80}$$

and

$$\mathbf{M}_m = \begin{bmatrix} \mathbf{0} & \mathbf{S} \\ \mathbf{L} & \mathbf{I}_{m_0} \end{bmatrix} \tag{9.81}$$

We can now write

$$\mathbf{I}_m^{-1} = F_u(\mathbf{M}_m, \mathbf{\Delta}_m)^{-1} = F_u(\mathbf{M}_{Um}, \mathbf{\Delta}_m) \tag{9.82}$$

where $\mathbf{M}_{Um}$ is equivalent to Equation (8.51) for the inverse of a LFT as defined in Section D.3.3.2. $\mathbf{I}_{m_0}$ is the diagonal of $\bar{m}_c$ from Equation (9.79).

9.10 Sloshing Model Uncertainty Description

The sloshing model used for the worst case analysis will lump the 4 tanks into 1 tank with the equivalent mass. It is retained for all axes and the damping is the major uncertainty in the model. The uncertainty of the damping $c_s \in [0.16; 0.5]$ defined in Section 3.4.4 is

$$c_s = \bar{c}_s + \delta_s \kappa \wedge \|\delta_s\| \leq 1, \quad \forall \delta_s \in \mathcal{R} \tag{9.83}$$

where $\bar{c}_s$ and κ_s are computed in a similar manner as in Equation (8.69). The uncertainty is present in both the transition and output matrices and from Equations (3.40) and (3.42) we can perform the partitioning as follows for one axis

$$\mathbf{A}_{s_x} = \mathbf{A}_{0_x} + \mathbf{A}_{1_x} = \begin{bmatrix} 0 & 1 \\ -\frac{k_s}{m_1} & -\frac{\bar{c}_s}{m_1} \end{bmatrix} + \delta_s \begin{bmatrix} 0 & 0 \\ 0 & -\frac{\kappa}{m_1} \end{bmatrix} \tag{9.84}$$

and

$$\mathbf{C}_{s_x} = \mathbf{C}_{0_x} + \mathbf{C}_{1_x} = \begin{bmatrix} k_s & \bar{c}_s \end{bmatrix} + \delta_s \begin{bmatrix} 0 & \kappa \end{bmatrix} \tag{9.85}$$

As in Equations (3.40) and (3.42) it is block diagonal and Equation (9.84) for all axes becomes

$$\mathbf{A}_s = \mathbf{A}_0 + \mathbf{A}_1 = \begin{bmatrix} \mathbf{A}_{0_x} & & \\ & \mathbf{A}_{0_x} & \\ & & \mathbf{A}_{0_x} \end{bmatrix} + \begin{bmatrix} \mathbf{A}_{1_x} & & \\ & \mathbf{A}_{1_x} & \\ & & \mathbf{A}_{1_x} \end{bmatrix} \tag{9.86}$$

As earlier we perform a SVD of $\mathbf{A}_1$ in Equation (9.86)

$$\mathbf{A}_1 = \underbrace{\begin{bmatrix} 0 & 0 & 0 \\ 0 & 1 & 0 \\ 0 & 0 & 0 \\ 1 & 0 & 0 \\ 0 & 0 & 0 \\ 0 & 0 & 1 \end{bmatrix}}_{\mathbf{L}} \underbrace{\begin{bmatrix} \delta_s & & \\ & \delta_s & \\ & & \delta_s \end{bmatrix}}_{\mathbf{\Delta}_{A_s}} \underbrace{\begin{bmatrix} 0 & 0 & 0 & 1 & 0 & 0 \\ 0 & 1 & 0 & 0 & 0 & 0 \\ 0 & 0 & 0 & 0 & 0 & 1 \end{bmatrix}}_{\mathbf{S}} \left(-\frac{\kappa}{m_1}\right), \text{ rank} = 3 \tag{9.87}$$

and

$$\mathbf{A}_s = F_u(\mathbf{M}_{A_s}, \mathbf{\Delta}_{A_s}) \tag{9.88}$$

where

$$\mathbf{M}_{A_s} = \begin{bmatrix} \mathbf{0} & \mathbf{S} \\ \mathbf{L} & \mathbf{A}_0 \end{bmatrix} \tag{9.89}$$

The output matrix $\mathbf{C}_s$ in Equation (3.42) takes the same form as in Equation (9.86) and it is not written out here. The SVD of $\mathbf{C}_1$ becomes

$$\mathbf{C}_1 = \underbrace{\begin{bmatrix} 1 & & \\ & 1 & \\ & & 1 \end{bmatrix}}_{\mathbf{L}} \underbrace{\begin{bmatrix} \delta_s & & \\ & \delta_s & \\ & & \delta_s \end{bmatrix}}_{\mathbf{\Delta}_{C_s}} \underbrace{\begin{bmatrix} 0 & 1 & & & & \\ & & 0 & 1 & & \\ & & & & 0 & 1 \end{bmatrix}}_{\mathbf{S}} \kappa, \quad \text{rank} = 3 \tag{9.90}$$

and

$$\mathbf{C}_s = F_u(\mathbf{M}_{C_s}, \mathbf{\Delta}_{C_s}) \tag{9.91}$$

where $\mathbf{M}_{C_s}$ is having the same partitioning as in Equation (9.89) replacing the elements. The complete uncertainty model is illustrated in Figure 9.20.

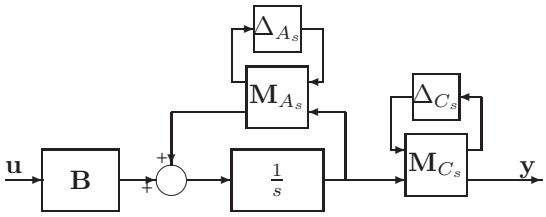

Figure 9.20: *Sloshing uncertainty model.*

9.11 Combined Relative Position Model Uncertainty

The uncertainty models for the out of plane dynamics in Section 9.7 an in plane in Section 9.8 will now be combined into one model.

The LFTs in Figure 9.18 and 9.19 are combined into one leading to a size of the $\mathbf{\Delta} = diag([\delta \mathbf{I}_9, \delta_\omega \mathbf{I}_2])$ with 11 elements in the diagonal.

The uncertainty of the mass m_c of the input matrix of Equations (4.16) and (4.18) is performed in Section 9.9. This is simply concatenated to the above LFT and it has a $\mathbf{\Delta}_m$ of dimension 3.

The thruster uncertainty will be lumped into an uncertainty directly on the input of the plant on the 3 axes. The structure is equivalent to the one developed in Section 8.11, which will be used directly. The structure of the LFT is the same as illustrated in Figure 8.17. From Table C.5 we have a 3σ thrust uncertainty of 3.1 %. Lumping it together and accounting for orientation uncertainty, we will apply an uncertainty of 5 % independent on all axes giving a $\mathbf{\Delta}_{th}$ of dimension 3.

The delay in the feedback loop is reused directly from the development in Section 8.12 adding a repeated uncertainty block $\mathbf{\Delta}_\tau$ of dimension 6.

The uncertainty model of the flexible modes used is identical to the one developed in Section 8.10 and can be used directly, only keeping in mind that a different part of the modal coupling matrix in Equation (3.18) is used for the translational motion than for the rotational motion. This adds a $\mathbf{\Delta}_f$ of dimension 2.

The uncertainty model for the fuel sloshing is developed in Section 9.10 and is connected to the rest like the flexible model, as they have the same inputs and their outputs are summed. See also principal illustration in Figure 3.7. This contributes a $\mathbf{\Delta}_s$ of dimension 6.

In total this leads to an uncertainty dimension of 31 of which all are real parametric and many repeated.

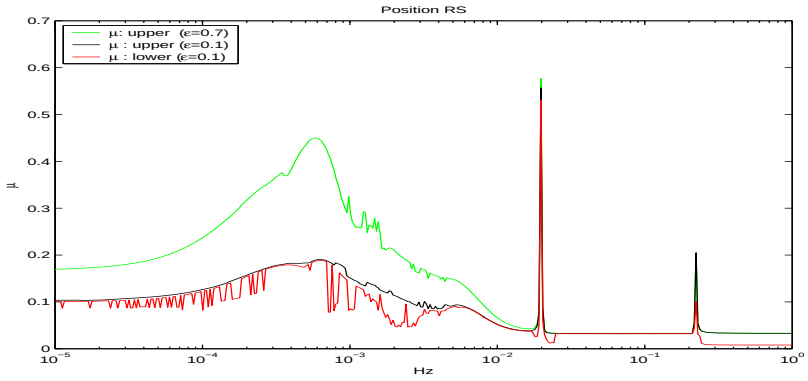

Figure 9.21: *Robust Stability structured singular value plots for orbital eccentricity $\varepsilon = 0.1$ and the large value $\varepsilon = 0.7$. For the latter the lower bound is omitted for increased readability but follows closely the upper bound. The first large peak is due to the sloshing uncertainty and the smaller peak the flexible modes. The bounds are close together even for the largest value at the peak.*

9.12 Robust Stability

The theory for RS is explained in detail in Section 8.13 and is all used as it is for the present problem.

As evident from the past sections there are only real parametric uncertainties, which means we need to add some complex uncertainty in order to reliably find the lower bound of the structured singular value μ. The procedure and structure are the same as illustrated in Figure 8.23. In order to reliably find the lower bound and to have it close to the upper bound, we need to add about $15 - 20$ % complex uncertainty.

It is recalled that the prime research is for the use of LTI controllers for the time varying elliptical orbital environment. The objectives are for eccentricities of $\varepsilon = 0.1$ and the RS found is shown in Figure 9.21.

In Figure 9.21 we see that the upper and lower bounds for $\varepsilon = 0.1$ are very close, which is particular important for the frequency of maximum μ. Is is clear, that the driver for the RS is the damping of the sloshing, which is more dominant than the flexible modes. This is contrary to the RS for the attitude, where we omitted the sloshing, as it appeared to be insignificant. It has been ensured by gradient investigations that the peak has been captured.

To explore the boundaries of the design a high eccentricity of $\varepsilon = 0.7$ has been investigated. This leads to a slightly elevated μ value but with ample margin. It shall be observed that the higher eccentricity is lower than for the attitude. This is due to keep consistency with the approximation used for the $\omega^{\frac{3}{2}}$ uncertainty, which was recommended as a Taylor series of third order for $\varepsilon > 0.7$ and second order has been used.

In conclusion it can be seen that a very robust controller design has been achieved,

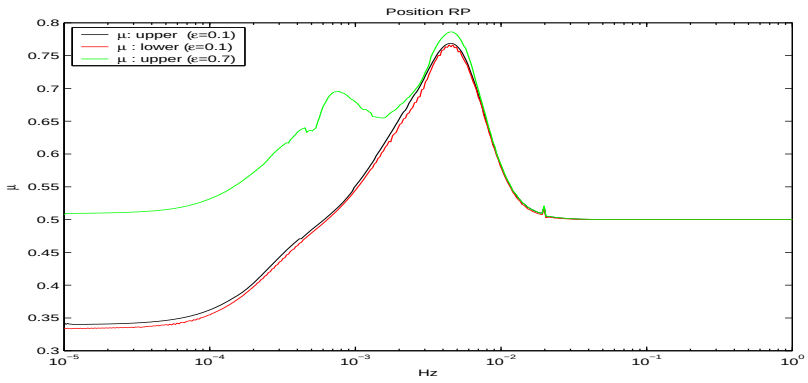

Figure 9.22: *Robust Performance structured singular value plots for orbital eccentricity* $\varepsilon = 0.1$ *and the large value* $\varepsilon = 0.7$.

which is covering a wide range of uncertainties with a very comfortable margin.

9.13 Robust Performance

The theory of RP is explained in detail in Section 8.14 and is used directly for the position $\mathcal{H}_\infty$ controller performance evaluation.

As for the attitude control the overall feedback system needs to be normalized by scaling of the input and output. How this is done as well as the setup for the RP evaluation is identical to earlier and is illustrated in Figure 8.25 and Equations (8.93) and (8.95).

For the scaling of the input output we use the maximum value from Equation (9.27) for the calculation of the $\mathbf{D}_e$ matrix in Equation (8.94). For the scaling of the disturbance we use the maximum value for the differential drag listed in Table 7.4.

As the $\mathcal{H}_\infty$ control design is a worst case one, we shall use the same performance weight for $\mathbf{W}_e$ in Figure 8.25 as we specified for the design in Figure 9.4 and listed in Table 9.3. This means that $\mathbf{W}_e = \mathbf{W}_1$ for the RP analysis.

When looking at the robustness it is important to only consider the driving performance variables, which are the relative position. $\mathbf{\Delta}_p$ in Equation (8.92) is a full complex matrix connecting the relevant part of $\mathbf{z}$ to $\mathbf{w}$ in Figure 8.20 for the RP analysis.

Figure 9.22 displays the RP for the main eccentricity and a large eccentricity to analyze wider performance. As for the RS the sloshing is visible in Figure 9.22, but the flexible modes hardly. The largest μ value is within the closed loop bandwidth and provides sufficient performance margin. With a maximum μ of about 0.8 it indicates a design with some performance margin, but still responsive and well performing. For $\varepsilon = 0.7$ a slightly reduced margin is observed, but it remains comfortably below 1.

In conclusion a successful and robustly performing LTI $\mathcal{H}_\infty$ design has been performed and exhibits good RS and RP behavior over a large LTV domain.

The worst case $\boldsymbol{\Delta}$ has been unwrapped from the analysis and used as input for the MC validation to be performed in Section 11.3.

9.14 Conclusion

A 3 DOF relative position control has been developed for the docking port to port control. It is based on the $\mathcal{H}_\infty$ worst case approach and has resulted in a well performing closed loop design exhibiting excellent RS and RP properties. The worst case $\boldsymbol{\Delta}$ has been successfully used in the time simulations in Chapter 11.

Further uncertainty LFT models have been developed for the relative position dynamics from Chapter 4. As an outcome of that, Theorem 9.2 has been developed with associated proof providing a general LFT formulation of a matrix with an arbitrary number of uncertain square terms. Finally LFTs for the inverse mass input matrix and the fuel sloshing are developed.

This development and results correspond to the objectives of bullet 8 in Section 1.3.

Chapter 10

Coupled Relative Attitude and Position Control

After the finalized LVLH attitude and control in Chapter 8 and the relative port to port position control in Chapter 9, we proceed with the final part where both are coupled. The final approach is recalled from Figure 2.5 and goes from point s_4 until contact.

The switching from the previous controller type and structure to the present one is not considered as a research topic in this context. It is considered that wait in the hold point s_4 until specifications are achieved in order to proceed.

The control is 6 DOF and both position and attitude is with respect to the target docking port. This is the third situation illustrated in Figure 7.3. The lateral control objective along the y and z-axis is to keep the centers of the docking ports aligned. This means controlling the relative difference to zero along the y and z-axis. The control objective along the x-axis of the target port frame $\mathcal{F}_{dt}$ is to follow the guidance profile developed in Section 7.7 and Tables 7.5 and 7.6. The relative attitude shall be controlled to zero around all 3 axes.

10.1 Control Requirements Detailing

The location of s_4 is recalled from Table 2.1 to be $s_4 = [-20, 0, 0]^{\mathrm{T}}$ port to port. From Table 2.2 the attitude shall be less than $5\,\mathrm{deg}$ on all axes and the relative position requirements are in Table 2.7. It means that the relative position on the lateral y and z-axis shall be between ± 0.1 m. As the port is circular, we will consider this bound as the maximum radius in the y-z plane. The approach velocity we select to 0.05 m/s, as we are then exposed to disturbances and time varying parameters for longer time and range creating a worst case situation.

	POS [m]		ATT [deg]	
	x-axis	y,z-axis	x-axis	y,z-axis
Bias	$[0.01; 0.2]$	$[0; 0.1]$	0.8	$[0.55; 0.8]$
Noise 3σ	$[0.005; 0.2]$	$[0; 0.07]$	0.1	$[0.05; 1.0]$

Table 10.1: *Simplified sensor data extracted from Table 3.3. The lower and upper values correspond to a range of* $[0; 20]$ *m.*

10.2 Target and Sensor Characteristic

The target docking port motion is described in detail in Section 3.2.1 and the bandwidth derivation is performed in Section 9.2. The specific values for the 6 DOF will be identified here by extracting the characteristic values from Table 3.3.

This can also be expressed such that the range has 1.0% noise of the range and the lateral noise is 0.35%. The attitude noise is constant 2% of the requirement around the x-axis and about 5% as a function of the range around the y and z-axis.

10.3 Plant Description and Variation

The plant variations are all described in Section 8.2 for the attitude and in Section 9.3 for the relative position.

The fully coupled 6 DOF model is derived in Chapter 5 and the coupled linear state space model in Section 5.7.5. We will use the model in Equation (5.36) for the synthesis and analysis.

For the sake of clarity we recall the state vector to be $\mathbf{x} = [\mathbf{x}_p, \dot{\mathbf{x}}_p, \boldsymbol{\theta}_c, \boldsymbol{\omega}_c, \boldsymbol{\theta}_t, \dot{\boldsymbol{\theta}}_t, \boldsymbol{\theta}_{ra}]^{\mathrm{T}}$ and the output vector to be $\mathbf{y} = [\mathbf{x}_p, \dot{\mathbf{x}}_p, \boldsymbol{\theta}_c, \boldsymbol{\omega}_c, \boldsymbol{\theta}_t, \dot{\boldsymbol{\theta}}_t, \underbrace{\mathbf{x}_{pp}, \dot{\mathbf{x}}_{pp}, \boldsymbol{\theta}_{ra}, \boldsymbol{\omega}_{ra}}]^{\mathrm{T}}$. The under braced elements of $\mathbf{y}$ is what need to be controlled.

We recall that the model includes the target motion as a harmonic oscillator, which is not reachable from the control inputs. We therefore need to evaluate the model and adapt such that it is both controllable and observable. When both are fulfilled we also have a minimal realization. The input signal is as before

$$\mathbf{u} = [\ \underbrace{\mathbf{F}, \mathbf{N}}_{small\ signal}\ , \boldsymbol{\theta}_{c_0}, \boldsymbol{\theta}_{t_0}, \tilde{\mathbf{r}}_{dt_0}, \tilde{\mathbf{r}}_{dc_0}]^{\mathrm{T}} \tag{10.1}$$

which is for the large signal model. The small signal model input in Equation (10.1) are $\mathbf{F}$ and $\mathbf{N}$.

Controllability: As the target states are not controllable, we will remove them $[\boldsymbol{\theta}_t, \dot{\boldsymbol{\theta}}_t]^{\mathrm{T}}$ from the state space model. This is nevertheless not fully solving the problem as $\boldsymbol{\theta}_t$ is used to compute the relative attitude $\boldsymbol{\theta}_{ra}$. Computing the controllability matrix $\mathcal{C}$ (Glad. & Ljung 1981)

$$\mathcal{C} \triangleq \left[\mathbf{B}\ \mathbf{AB}\ \mathbf{A}^2\mathbf{B} \cdots \mathbf{A}^{n-1}\mathbf{B}\right] \tag{10.2}$$

for the pair $(\mathbf{A}, \mathbf{B})$ it should have full row rank n, where n is the number of states. As expected it is rank deficient with 3, which is exactly the 3 states of $\boldsymbol{\theta}_{ra}$. To fulfill condition A1 in Section 9.4 for the $\mathcal{H}_\infty$ algorithm, we need to reduce the model further by removing $\boldsymbol{\theta}_{ra}$ from the state vector. This means the state vector is now $\mathbf{x} = [\mathbf{x}_p, \dot{\mathbf{x}}_p, \boldsymbol{\theta}_c, \boldsymbol{\omega}_c]^{\mathrm{T}}$ and the input vector $\mathbf{u} = [\mathbf{F}, \mathbf{N}]^{\mathrm{T}}$. The matrices in Equations (5.37) and (5.38) are reduced correspondingly.

This has two consequences. One is that the target motion will have to be modeled as a disturbance to the plant with a weight describing its characteristic behavior. The other is that the variable to control $\boldsymbol{\theta}_{ra}$ is no longer in the model. This does not pose a problem as the synthesis can equivalently be performed for the chaser attitude $\boldsymbol{\theta}_c$, as known from Section 5.7.2, as the target cannot be influenced. Therefore $\boldsymbol{\theta}_{ra}$ is anyhow controlled by controlling physically $\boldsymbol{\theta}_c$ only.

Observability: From Equation (5.39) of the $\mathbf{C}$ matrix, we see all states are observable, which can also be found analytically from the full column rank n of

$$\mathcal{O} \triangleq \begin{bmatrix} \mathbf{C} \\ \mathbf{CA} \\ \vdots \\ \mathbf{CA}^{n-1} \end{bmatrix} \tag{10.3}$$

the pair $(\mathbf{A}, \mathbf{C})$. (Glad. & Ljung 1981)

The output vector we then define as $\mathbf{y} = [\mathbf{x}_{pp}, \dot{\mathbf{x}}_{pp}, \boldsymbol{\theta}_c, \boldsymbol{\omega}_c]^{\mathrm{T}}$. It means we will control $\boldsymbol{\theta}_c$ to another reference than $\boldsymbol{\theta}_t$, but that is equivalent as long as we include the characteristics of $\boldsymbol{\theta}_t$. This will ensure equivalence, when we replace with $\boldsymbol{\theta}_{ra}$ in the actual implementation.

The matrices for the reduced order design model modifying Equations (5.37) to (5.40) become

$$\mathbf{A} = \begin{bmatrix} \mathbf{A}_p & \mathbf{0} \\ \mathbf{0} & \mathbf{A}_c \end{bmatrix}, \ \mathbf{B} = \begin{bmatrix} \mathbf{B}_p & \mathbf{0} \\ \mathbf{0} & \mathbf{B}_c \end{bmatrix}, \ \mathbf{C} = \begin{bmatrix} \mathbf{I} & \mathbf{0} & \mathbf{B}_{dc_1} & \mathbf{0} \\ \mathbf{0} & \mathbf{I} & \mathbf{0} & \mathbf{B}_{dc_2} \\ \mathbf{0} & \mathbf{0} & \mathbf{I} & \mathbf{0} \\ \mathbf{0} & \mathbf{0} & \mathbf{0} & \mathbf{I} \end{bmatrix}, \ \mathbf{D} = \mathbf{0} \tag{10.4}$$

Finally we will investigate the RGA to evaluate the couplings in the 12×6 plant. There are weak couplings between attitude and relative position. There are stronger interactions between the axes of the position and the attitude is mostly diagonal. As earlier the plant exhibits strong axial couplings at the orbital frequency as detailed in Section 9.6.

In Equation (10.4) we see that the only linear cross couplings are from the kinematics in the $\mathbf{C}$ matrix. This can conveniently be decoupled for the controller synthesis. It is observed that the couplings are

- From the attitude to the position due to the port lever arms
- There are no couplings from the position to the attitude

We will find a matrix $\mathbf{V}_d$ such that we get only the original diagonal of the $\mathbf{C}$ matrix. We write the $\mathbf{C}$ matrix of Equation (10.4) as a partitioned matrix as follows

$$\mathbf{C} = \begin{bmatrix} \mathbf{I} & \mathbf{0} & \mathbf{B}_{dc_1} & \mathbf{0} \\ \mathbf{0} & \mathbf{I} & \mathbf{0} & \mathbf{B}_{dc_2} \\ \mathbf{0} & \mathbf{0} & \mathbf{I} & \mathbf{0} \\ \mathbf{0} & \mathbf{0} & \mathbf{0} & \mathbf{I} \end{bmatrix} = \begin{bmatrix} \mathbf{I} & \mathbf{B}_1 \\ \mathbf{0} & \mathbf{I} \end{bmatrix} \tag{10.5}$$

and

$$\mathbf{V}_d\mathbf{C} = \mathbf{I} \tag{10.6}$$

$$\mathbf{V}_d = \mathbf{C}^{-1} \tag{10.7}$$

By the inversion theorem of a partitioned matrix (Bernstein 2005) and inserting the partitioned $\mathbf{C}$ matrix we obtain

$$\mathbf{V}_d = \begin{bmatrix} \mathbf{I} & -\mathbf{B}_1 \\ \mathbf{0} & \mathbf{I} \end{bmatrix} = \begin{bmatrix} \mathbf{I} & \mathbf{0} & -\mathbf{B}_{dc_1} & \mathbf{0} \\ \mathbf{0} & \mathbf{I} & \mathbf{0} & -\mathbf{B}_{dc_2} \\ \mathbf{0} & \mathbf{0} & \mathbf{I} & \mathbf{0} \\ \mathbf{0} & \mathbf{0} & \mathbf{0} & \mathbf{I} \end{bmatrix} \tag{10.8}$$

The new plant is now completely decoupled and the controllers for position and attitude can be designed independently. For the implementation of the controllers one only needs to pre multiply the controller input by $\mathbf{V}_d^{-1}$.

10.4 Out of Plane Position Control and Controller Type Selection

The objective of the design here is to obtain a well tracking controller from s_4 until docking. This is contrary to the slow average motion tracking design in Chapter 9 and might require a different problem formulation, which will be addressed here.

A signal based $\mathcal{H}_\infty$ controller design will be addressed, which is very general and is appropriate for multi variable problems in which several objectives must be taken into account simultaneously. The focus of attention is on the minimization of the size of the defined error signals contrary to the earlier design, where the focus was on shaping certain transfer functions over frequency (Skogestad & Postlethwaite 2005). Before embarking on this approach, we will first see how well we perform by redesigning the earlier controllers.

For performing the designs and tradeoffs the out of plane control will be used, as it can be seen as representative for the other ones to a large degree.

10.4.1 Mixed sensitivity

The formulation of the control problem is the same as illustrated in Figure 9.4 but with different weights. The weight $\mathbf{W}_r$ is selected as a low pass filter in order to lower the γ

	A	M	ω
$W_0 = 0.03$			
$W_1 = \frac{\frac{1}{M}s+\omega}{s+A\omega}$	0.01	2	0.63
$W_2 = \frac{s+A\omega}{\frac{1}{M}s+\omega}$	0.5	10	12.6
$W_3 = \frac{\frac{1}{M}s+\omega}{s+A\omega}$	100	0.01	12.6
$W_n = 0.1$			
$W_r = \frac{\omega}{s+\omega}$			1.89

Table 10.2: *Summary of all weights used for the mixed sensitivity $\mathcal{H}_\infty$ design.*

value. This is now needed as all the other weights have higher cross over frequencies. The following values in Table 10.2 are obtained after some iterations

The shape of all functions are not much different from those in Section 9.5, except shifted in frequency, and will not be repeated here. For this suboptimal controller we obtain

$$\gamma_{min} = 0.99 \tag{10.9}$$

and stability margins of

$$GM = 25 \text{ db (at } 0.79 \text{ Hz)} \text{ and } PM = 59 \deg \text{ (at } 0.13 \text{ Hz)} \tag{10.10}$$

The performance is well fulfilled at both the s_4 point and at docking. This is illustrated in Figure 10.6. It was experienced non trivial to obtain a good balance between the weights to fulfill the requirements. At s_4 where measurement noise dominates the control signal is relatively large.

10.4.2 Signal Based

In the signal based approach weighting functions are applied to the signals of concern in the design process. We will formulate the problem as a model reference one, where the controller shall try to make the closed loop behave as a reference model $\mathbf{W}_{ref}$.

The objective of $\mathbf{W}_{ref}$ is to represent a transfer function, which will be able to track the worst case target port motion. This is of the triangular shape shown in Figure 3.5 and the worst case is for the shortest reversal time $d = 8$ s and amplitude $A = 0.7 \deg$ as listed in Table 3.2. We need to follow the ramp part of the signal as well as the critical part and not to have too large overshoot at the peaks. We define a reference model as

$$\mathbf{W}_{ref} = \frac{\omega^2}{s^2 + 2\zeta\omega s + \omega^2} \frac{s+\omega_1}{\omega_1} \tag{10.11}$$

The 2^{nd} order part in Equation (10.11) follows well the slope, but overshoots too much at the corners. The first step is to lower the damping to $\zeta = 0.5$ in order to keep the phase close to zero for higher frequency and reduce the lag. To further keep the phase at zero

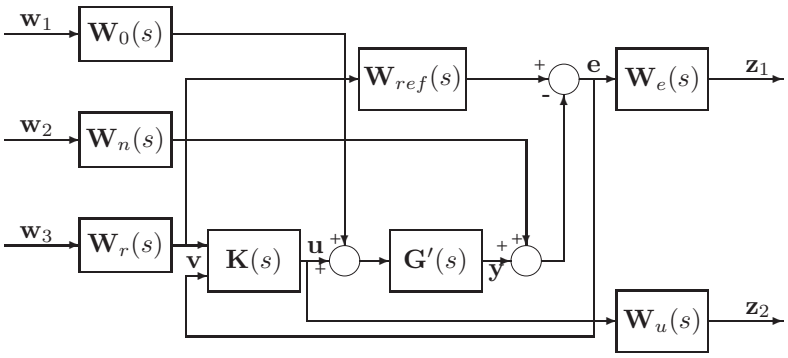

Figure 10.1: *Signal based model reference configuration for the $\mathcal{H}_\infty$ design of the two degree of freedom controller.*

we add a lead component in Equation (10.11). This enables us to keep the phase very flat before it drops and provides sufficient tracking. The parameters of Equation (10.11) are

$$\omega = \omega_1 = 0.05\,\text{Hz} \;\text{ and }\; \zeta = 0.5 \tag{10.12}$$

Having identified $\mathbf{W}_{ref}$ we now proceed to formulate the design structure, which is illustrated in Figure 10.1. The generalized plant $\mathbf{P}$ in Figure 10.1 becomes as follows with $\mathbf{K}$ pulled out in a lower LFT

$$\mathbf{P} = \left[\begin{array}{ccc|c} -\mathbf{W}_e\mathbf{G}'\mathbf{W}_0 & -\mathbf{W}_e\mathbf{W}_n & \mathbf{W}_e\mathbf{W}_{ref}\mathbf{W}_r & -\mathbf{W}_e\mathbf{G}' \\ \mathbf{0} & \mathbf{0} & \mathbf{0} & \mathbf{W}_u \\ \hline \mathbf{0} & \mathbf{0} & \mathbf{W}_r & \mathbf{0} \\ -\mathbf{G}'\mathbf{W}_0 & -\mathbf{W}_n & \mathbf{W}_{ref}\mathbf{W}_r & -\mathbf{G}' \end{array}\right] \tag{10.13}$$

and the closed loop transfer function is computed as in Equation (9.4).

It is chosen to consider a two degree of freedom controller, as shown in Figure 10.1. This is driven by the more demanding docking conditions and that feed forward control generally contributes well to the control performance. Therefore the controller is of the form (Limebeer, Kasenally & Perkins 1993)

$$\mathbf{K} = [\mathbf{K}_1 \; \mathbf{K}_2] \tag{10.14}$$

where $\mathbf{K}_1$ is the feed forward part and $\mathbf{K}_2$ is the stabilizing feedback controller. The drawbacks are increased controller complexity and that the target attitude needs to be measurable. The latter is assumed to be available, though on ISS it is not for non technical reasons, and we will later consider the Fault Tolerant Control (FTC) of the design should it drop out.

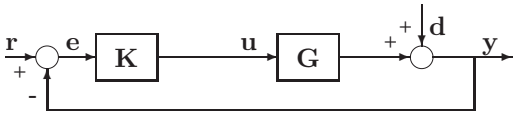

(a) 1 degree of freedom controller

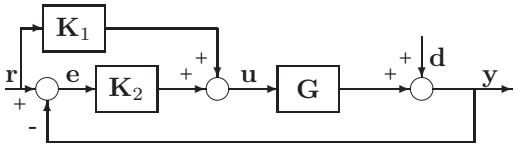

(b) 2 degree of freedom controller

Figure 10.2: *Principal structure of the standard 1 degree of freedom controller and the used 2 degree of freedom controller.*

Before we proceed, some differences between the two controller architectures in Figure 10.2 need to be highlighted. The properties of $\mathbf{S}$ and $\mathbf{T}$ in Equations (8.22) to (8.24) are clear from Figure 10.2 and valid for one degree of freedom controllers

$$\mathbf{y} = \underbrace{(\mathbf{I}+\mathbf{GK})^{-1}\mathbf{GK}}_{\mathbf{T}}\mathbf{r} + \underbrace{(\mathbf{I}+\mathbf{GK})^{-1}}_{\mathbf{S}}\mathbf{d} \tag{10.15}$$

For the two degree of freedom controller we can formulate the functionally equivalent transfer functions from Figure 10.2 as

$$\mathbf{y} = \underbrace{(\mathbf{I}+\mathbf{GK}_2)^{-1}\mathbf{G}(\mathbf{K}_1+\mathbf{K}_2)}_{\mathbf{T}_2}\mathbf{r} + \underbrace{(\mathbf{I}+\mathbf{GK}_2)^{-1}}_{\mathbf{S}_2}\mathbf{d} \tag{10.16}$$

and the index 2 is used to distinguish from the classical ones. It is observed that $\mathbf{S}_2 = \mathbf{S}$ in Equation (10.16), but that $\mathbf{T}_2 \neq \mathbf{T}$. The sum becomes

$$\mathbf{S}_2 + \mathbf{T}_2 = \mathbf{I} + (\mathbf{I}+\mathbf{GK}_2)^{-1}\mathbf{GK}_1 = \mathbf{I} + \mathbf{S}_2\mathbf{GK}_1 \tag{10.17}$$

and it is highlighted that the property of Equation (8.24) does not hold for two degree of freedom controllers.

We can now compute the closed loop transfer function from Equations (9.4) and (10.13), which after some algebraic manipulations becomes

$$F_l(\mathbf{P},\mathbf{K}) = \begin{bmatrix} \mathbf{W}_e\mathbf{G}'(\mathbf{K}_2\mathbf{S}_2-\mathbf{I})\mathbf{W}_0 & -\mathbf{W}_e\mathbf{S}_2\mathbf{W}_n & \mathbf{W}_e(\mathbf{W}_{ref}\mathbf{S}_2-\mathbf{G}'\mathbf{K}_1)\mathbf{W}_r \\ -\mathbf{W}_u\mathbf{K}_2\mathbf{S}_2\mathbf{G}'\mathbf{W}_0 & -\mathbf{W}_u\mathbf{K}_2\mathbf{S}_2\mathbf{W}_n & \mathbf{W}_u(\mathbf{K}_1+\mathbf{K}_2\mathbf{S}_2\mathbf{W}_{ref})\mathbf{W}_r \end{bmatrix} \tag{10.18}$$

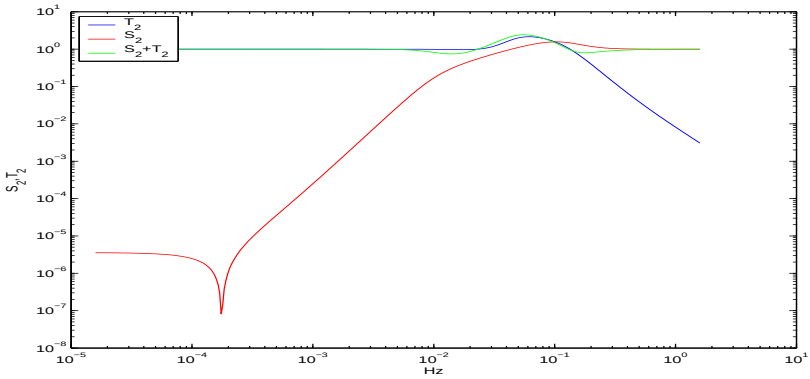

Figure 10.3: *Plots of the* $\mathbf{S}_2$ *and* $\mathbf{T}_2$ *functions for the out of plane controller for the model reference design in Equation (10.13).*

The selection of the weights is driven by the requirements, but also to achieve a balance between feed forward and stabilization. If allowed the algorithm in Theorem 9.1 will try to perform a plant inversion, which is obviously not desirable (and not possible if RHP zeros are contained in the plant). This is achieved with $\mathbf{W}_0$ and $\mathbf{W}_n$. The requirements for the design can mostly be formulated as

$$\begin{array}{rcl} r_{max} & = & 0.4 \text{ m} \\ e_{max} & = & 5\,\% \\ M_P & < & 30 - 40\,\% \\ t_r & \approx & 4 - 5 \text{ s} \end{array} \tag{10.19}$$

The form of the weights are similar to those used earlier and after design iterations the weights become as in Table 10.3

The weight $\mathbf{W}_0$ on the control signal is kept at the same value as earlier. $\mathbf{W}_n$

	A	M	ω
$W_0 = 0.03$			
$W_n = 0.5$			
$W_r = \frac{\frac{1}{M}s+\omega}{s+A\omega}$	1	100	0.63
$W_e = \frac{\frac{1}{M}s+\omega}{s+A\omega}$	0.01	2	0.31
$W_u = \frac{\frac{1}{M}s+\omega}{s+A\omega}$	100	0.01	6.28

Table 10.3: *Summary of all weights used for the two degree of freedom* $\mathcal{H}_\infty$ *design.* $\mathbf{W}_{ref}$ *is defined in Equations (10.11) and (10.12).*

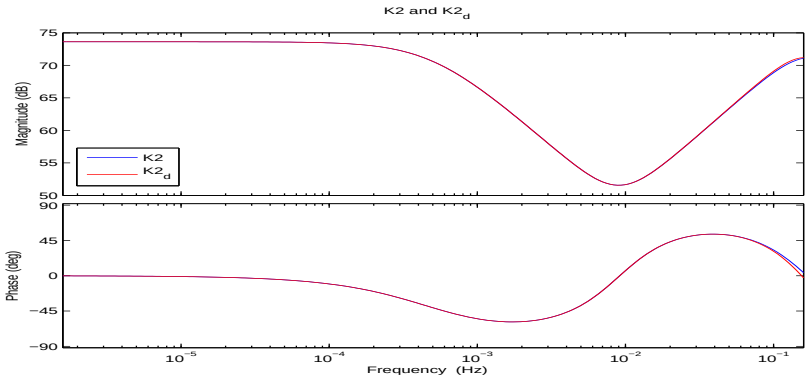

Figure 10.4: *Reduced order $\mathbf{K}_2$ controller Bode plot as well as the discretized reduced controller sampled at 1 Hz.*

represents both measurement noise and load disturbance on the output and is used as a free design parameter. For $\mathbf{W}_e$ we select ω around the frequency of the parabolic part of the target motion in Figure 3.5, which is approximately $\frac{1}{2d_{min}}$. The low frequency value corresponds to about 1% error. For $\mathbf{W}_u$ we penalize the control at higher frequencies as well as we need a cross over frequency separation to the other weights to obtain a lower γ. One needs to limit the control signal in order to handle the target port vibrations from the ISS flexibility as described in Section 3.2.1. This is more sizing in the worst case than measurement noise to ensure the relative velocity specification is fulfilled.

With $\mathbf{W}_r$ one can adjust the amount of the feed forward by its gain. It turns out that the gain adjustment is advantageously done by lowering the bandwidth as γ can then be lowered simultaneously. Using the weights in Table 10.3 and solving Equation (9.4) the suboptimal $\mathcal{H}_\infty$ controller achieves

$$\gamma_{min} = 0.65 \tag{10.20}$$

In Figure 10.3 the $\mathbf{S}_2$ and $\mathbf{T}_2$ functions, as well as their sum, are illustrated. The cross over frequency is slightly higher than specified and $\mathbf{S}_2$ exhibits well a low value at low frequencies as desired.

The step response of the closed loop has a rise time of about 4 s, a settling time of 30 s and a 53 % first peak overshoot. The last is driven by the lower damping in $\mathbf{W}_{ref}$ to avoid lag.

The open loop Bode plot is rather similar in shape to Figure 9.8, though shifted in frequency and shows good stability margins

$$GM = 12.7 \text{ db (at } 0.17 \text{ Hz)} \quad \text{and} \quad PM = 51.1 \deg \text{ (at } 0.05 \text{ Hz)} \tag{10.21}$$

The shape of the feedback part of the controller $\mathbf{K}_2$ is illustrated in Figure 10.4 with a shape not too different from earlier ones, but significantly larger gain. The feed forward

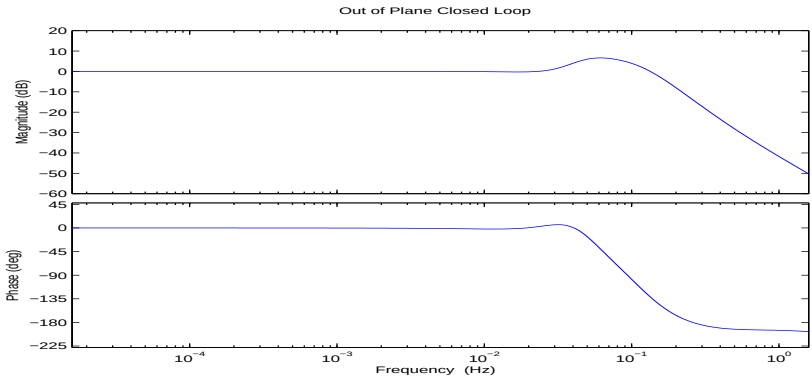

Figure 10.5: *Closed loop characteristic for the two degree of freedom controller* $\mathbf{K} = [\mathbf{K}_1 \ \mathbf{K}_2]$.

controller $\mathbf{K}_1$ has a low frequency gain of about 10 and it increases steeply towards the closed loop bandwidth with a phase advance in the same region. In Figure 10.5 the closed loop response is illustrated, which shows a small gain increase at the desired frequency to track the peaks of the reference signal. Further is it noted that a very flat invariant phase has been achieved ensuring little lag resulting in very good tracking performance.

10.4.3 One degree of freedom model reference

Further to the two previous designs a combination of the two has been tested. It is a reduced mixed sensitivity type using $\mathbf{W}_{ref}$, feedback from the error, but without weighting the complementary sensitivity function. The design setup and the selected weights are reported in Section D.5. Its performance is shown in Figure 10.6. The stability margins are lower than the others and yield

$$GM = 11 \text{ db (at } 0.21 \text{ Hz)} \quad \text{and} \quad PM = 43 \deg \text{ (at } 0.09 \text{ Hz)} \tag{10.22}$$

and

$$\gamma_{min} = 0.77 \tag{10.23}$$

10.4.4 Design Trade Off

Three different designs have been performed and a trade off will be performed to select one for the complete coupled design.

We will consider the worst case target port motion with and without measurement noise to compare the controllers directly. This is evaluated at s_4 and at docking, with the plots for the former illustrated in Figure D.7 in Section D.5. The results at docking are shown in Figure 10.6.

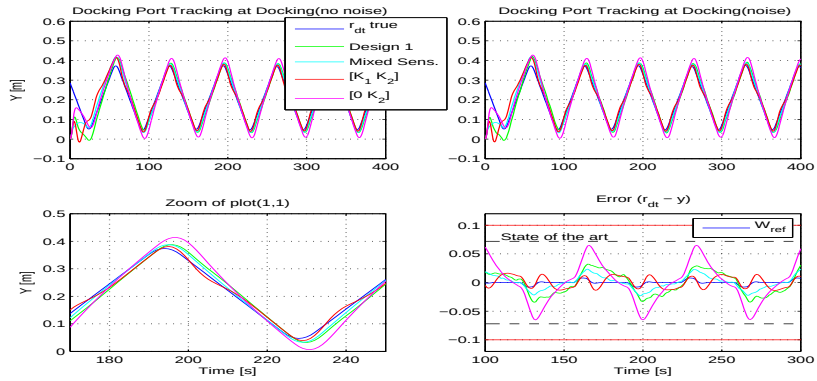

Figure 10.6: *Tracking of worst case target port motion, shortest reverse time and as defined in Figure 3.5, for the three controllers. Design* 1 *is the one degree of freedom model reference controller. The error plot compares the various errors with the error of* $\mathbf{W}_{ref}$*, which is considered the best possible. The requirement is marked in red horizontal and the state of the art as dashed.*

In Figure 10.6 it is observed that all controllers fulfill the requirements also for the velocity though not illustrated.

It is clear that the two degree of freedom controller tracks the reference significantly better than the other two. We also investigate the case of fault in the transmission of the target attitude motion used for the feed forward. This is the case, where we consider $\mathbf{K}_1 = \mathbf{0}$ and it is observed to become only slightly worse than the others remaining well inside specifications. It is therefore considered fault tolerant to such errors.

On the error plot in Figure 10.6 the error signals of the different controllers are compared as well as the error between the target motion and the $\mathbf{W}_{ref}$. The latter is considered the best we can obtain. It is also clear that the two degree of freedom controller out performs the others. The same relations are valid at s_4 as illustrated in Figure D.7.

As we seek a LTI controller to cover the whole range with varying measurement

σ Force	-20 m	0 m
Mixed sensitivity	135	52
One DOF model reference $[\mathbf{K}_2]$	114	36
Two DOF model reference $[\mathbf{K}_1\ \mathbf{K}_2]$	42	38
Two DOF model reference $[\mathbf{0}\ \mathbf{K}_2]$	36	29

Table 10.4: *Standard deviation of the control signal for the different controllers at the two locations* s_4 *and docking. They track the worst case target port motion, as defined in Figure 3.5, with the shortest reverse time as in Figure 10.6.*

	A_x	A_z	M_x	M_z	ω_x	ω_z	ζ
$\mathbf{W}_{0_{x,z}} = [0.03, 0.03]$							
$\mathbf{W}_{n_{x,z}} = [0.5, 0.5]$							
$W_{r_{x,z}} = \frac{\frac{1}{M}s+\omega}{s+A\omega}$	1	1	100	100	0.1	0.1	
$W_{e_{x,z}} = \frac{\frac{1}{M}s+\omega}{s+A\omega}$	0.01	0.01	2	2	0.05	$\frac{0.05}{4}$	
$W_{u_{x,z}} = \frac{\frac{1}{M}s+\omega}{s+A\omega}$	100	100	0.01	0.01	1	$\frac{1}{4}$	
$W_{ref_{x,z}} = \frac{\omega^2}{s^2+2\zeta\omega s+\omega^2}\frac{s+\omega}{\omega}$					0.05	0.05	0.5

Table 10.5: *Summary of all weights used for the x,z axes $\mathcal{H}_\infty$ two degree of freedom controller design.*

noise, one needs to assess the demand from the propulsion. In Table 10.4 the spread of the control signals is listed for the two extreme points. It varies linearly between them. They are all feasible though the first two track more noise than the rest.

From these investigations, it is clear that the two degree of freedom controller has the best performance with the least control effort and good stability margins. It will be chosen for further implementation despite the slightly increased complexity.

10.5 In Plane Position Control

For the in plane coupled control there will be used the same type of two degree of freedom controller as in Section 10.4. Scaling is as earlier for each axis for both feed forward and feedback part.

The first logical step is to use directly the out of plane weights from Table 10.3 for both the x and z-axis. It provides the same stability margins and γ value, but the control signal required on the x-axis is too large in demand of around 400 N. This is driven by the larger sensor noise along that axis. It is therefore necessary to re tune the controller, which we can do without performance loss as the x-axis target port motion is benign.

The obvious choice would be to either permit a larger error via $\mathbf{W}_e$ or change $\mathbf{W}_u$ to constrain the control signal. It turns out that it is difficult to re tune without affecting the z-axis controller, which we desire to keep. It appears that changing both $\mathbf{W}_e$ and $\mathbf{W}_u$ by the same ratios for the x-axis, the design on the z-axis remains unaffected. This is what has been performed and after some iterations the weights in Table 10.5 have been selected.

All the plots from the out of plane design in Figures 10.3 to 10.5 are rather representative for the in plane design and will not be repeated here. The only difference is that the closed loop transfer fro the x-axis has little gain increase at the bandwidth frequency and the phase decreases at a lower frequency, see Figure 10.5. The loop by loop stability

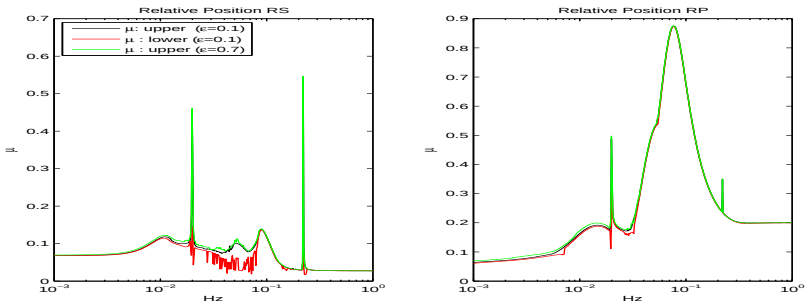

Figure 10.7: *Robust stability and performance for the relative position and orbital eccentricities* $\varepsilon = 0.1$ *and* $\varepsilon = 0.7$.

margins obtained are

$$\begin{array}{l} GM_x = 11.8 \text{ db (at } 0.08 \text{ Hz)} \text{ and } PM_x = 42.4 \deg \text{ (at } 0.03 \text{ Hz)} \\ GM_z = 12.7 \text{ db (at } 0.17 \text{ Hz)} \text{ and } PM_z = 51.1 \deg \text{ (at } 0.05 \text{ Hz)} \end{array} \tag{10.24}$$

and the suboptimal $\mathcal{H}_\infty$ optimization yields

$$\gamma_{min} = 0.65 \tag{10.25}$$

As usual a model order reduction is performed to eliminate the very fast and unnecessary poles in the controller. The controller is implemented in a discretized state space form and combined with the out of plane one.

At this stage we will find the RS and RP for the relative position decoupled from the relative attitude. It serves as an intermediate check of the design. The RS and RP are found satisfactory and shown in Figure 10.7. The same uncertainties are used as in Sections 9.12 and 9.13. For the RP the maximum reference is selected as $r_{max} = 0.4$ m and maximum $r_{max}(error) = 0.1$ m. For the performance weighting function in Equation (8.100) we select $\omega = 0.005$ Hz, $M = 4$ and $A = 0.25$. We see from Figure 10.7 that both RS and RP have a μ well below 1 for all uncertainties, as well as NP is fulfilled.

10.6 Relative Attitude Control

For the design of the relative attitude control it is recalled from Section 10.3 that the design can be done fully decoupled from the relative position. We only need to take into account the decoupling matrix $\mathbf{V}_d$ in Equation (10.8) when implementing the controller.

The relative attitude requirement is listed in Table 2.2 to 5 deg on all axes. Knowing that the target has a maximum amplitude of 0.7 deg one could fulfill the requirement by a slow non tracking controller. We will nevertheless try to track the relative attitude between the chaser and the target, as well as we can in order to obtain a design useful

	A	M	ω
$W_0 = 0.03$			
$W_1 = \frac{\frac{1}{M}s+\omega}{s+A\omega}$	0.2	2	0.063
$W_2 = \frac{s+A\omega}{\frac{1}{M}s+\omega}$	0.5	10	1.26
$W_3 = \frac{\frac{1}{M}s+\omega}{s+A\omega}$	100	0.01	1.26
$W_n = \frac{\frac{1}{M}s+\omega}{s+A\omega}$	14.3	5	0.063
$W_r = 1.0$			

Table 10.6: *Summary of all weights used for the mixed sensitivity $\mathcal{H}_\infty$ relative attitude design.*

for other missions than the one used here. We will only use the relative attitude angular measurements from the RVS, which is not measuring any rates. By using the chaser gyro measurements less latency in the feedback loop can be obtained as well as a faster tracking, but seen from the present requirements this complexity is not needed.

The natural choice for the controller type would be a similar 2 degree of freedom controller as chosen for the relative position in Section 10.4. This is encouraged by the availability of the target attitude motion. The RVS provides the relative attitude measurements. The noise level is specified in Table 3.3 to 1 deg at 3σ for the two lateral axes and 0.1 deg for the axial axis at 20 m relative port to port distance. This noise level is too large to obtain good target tracking, retain one controller for the entire final approach and keep the command signal within the available torque.

From the above reasons there is no need to retain a more complex controller and it is decided to continue with a $\mathcal{H}_\infty$ mixed sensitivity 1 degree of freedom controller. The problem formulation used is the same as for the relative position in Figure 9.4.

We select a cross over frequency of 0.01 Hz, which provides a good compromise between tracking error, noise and stability margins.

The weights are similar to those selected in Section 9.5. For the weight representing the noise $\mathbf{W}_n$ we have 7% noise at low frequencies and assume increasing to some 20% at higher frequencies. After some iterations on design and simulations the final weights are listed in Table 10.6.

The shape of the functions $\mathbf{S}$ and $\mathbf{T}$ is not too different from those in Section 9.5 and are not repeated here. We obtain from the optimization

$$\gamma_{min} = 0.93 \tag{10.26}$$

and the classical one loop open at the time stability margins become

$$\begin{array}{l} GM_x = 12.4 \text{ db (at } 0.063 \text{ Hz)} \text{ and } PM_x = 60\,\text{deg (at } 0.017 \text{ Hz)} \\ GM_y = 14.7 \text{ db (at } 0.059 \text{ Hz)} \text{ and } PM_y = 65\,\text{deg (at } 0.014 \text{ Hz)} \\ GM_z = 14.7 \text{ db (at } 0.059 \text{ Hz)} \text{ and } PM_z = 65\,\text{deg (at } 0.014 \text{ Hz)} \end{array} \tag{10.27}$$

In Figure 10.8 is shown the open loop worst case frequency response for the x-axis. This axis has the lowest inertia and therefore the largest effect from the flexible modes

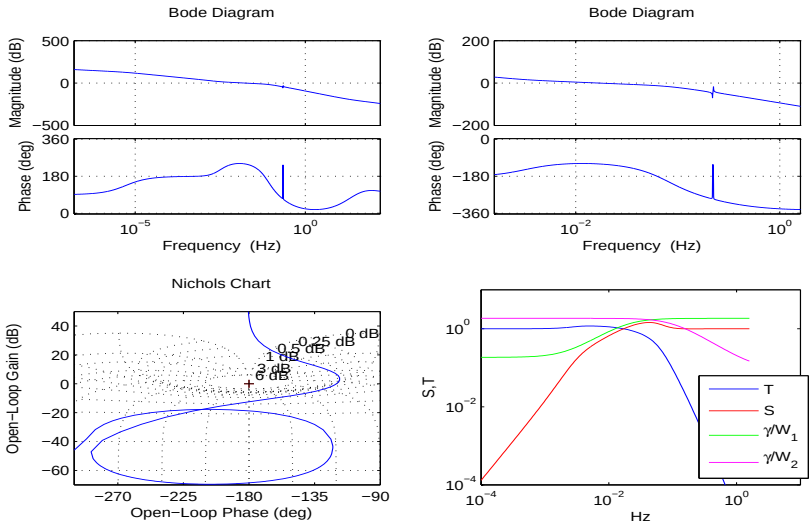

Figure 10.8: *The upper row illustrates the open loop frequency response for the x-axis with slosh and flexible modes. The solar panels are oriented for the worst case angle. The lower left plot illustrates better the flexible modes in a Nichols plot. The lower right plot shows the frequency response for the sensitivity and complementary sensitivity functions for the x-axis.*

clearly visible on the right hand zoomed figure. The flex mode will not have a destabilizing effect as the phase crosses -180 deg well before the mode. It is nevertheless desirable not to increase the gain too much in order to keep a distance of classically -6 db. If a larger loop gain should be required more loop shaping would be needed or the flex modes should be included in the synthesis. In the present design this has been avoided as we can obtain sufficient performance and margins without it and keep the order of $\mathbf{K}$ lower. The Nichols plot in Figure 10.8 illustrates better the flex mode and the sufficient distance from the critical point. If the solar panels are rotated by 90 deg the illustrated effect will be dominant on the z-axis, though less as the inertia is larger.

The lower right plot in Figure 10.8 shows the $\mathbf{S}$ and $\mathbf{T}$ functions for the design. The illustration is for the x-axis, but all axes are fairly similar.

The designed closed loops have a bandwidth of about 0.015 Hz, which is close to the design goal. The rise time for a step response is 15 s, the response has no oscillations and a slight 5% overshoot.

Finally the RS and RP have been evaluated at this decoupled level and found satisfactory and shown in Figure 10.9. The same uncertainties are used as in Sections 8.13 and 8.14. For the RP the maximum reference is selected as $r_{max} = 5$ deg and maximum $\theta_{max}(error) = 1$ deg. For the performance weighting function in Equation (8.100) we select $\omega = 0.01$ Hz, $M = 3$ and $A = 0.2$. We see from Figure 10.9 that both RS and RP have a μ well below 1 for all uncertainties, as well as NP is fulfilled.

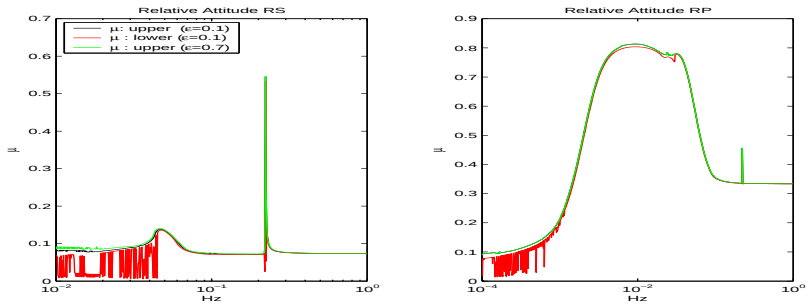

Figure 10.9: *Robust stability and performance for the relative attitude for the orbital eccentricities* $\varepsilon = 0.1$ *and* $\varepsilon = 0.7$.

10.7 Coupled 6 Degree of Freedom $\mathcal{H}_\infty$ Control

In this section we will combine the earlier designs into one overall coupled 6 DOF feedback system. As we decoupled the synthesis part theoretically in Section 10.3, we can combine the controllers for the relative port to port control and the relative attitude control directly. The decoupling matrix $\mathbf{V}_d$ in Equation (10.8) is taken into account in the nonlinear model of the measurement system.

The complete discretized controller is implemented in the full non linear simulator as used for all previous final results. It will simulate the complete GNC from s_4 until docking with an approach velocity of 0.05 m/s. The guidance profile selected is a constant acceleration followed by the constant approach velocity.

It is recalled that the target docking port oscillates in a worst case triangular type of motion due to the ISS attitude motion described in Figure 3.5.

Figure 10.10 shows the results of the complete final design from a full nonlinear simulation providing relative port to port position, velocities and the forces on the chaser spacecraft.

For the x-axis we observe that there is a station keeping at s_4 for 100 s, after which the final approach begins. The velocity moves from zero to the 0.05 m/s as expected. For the y and z-axes one sees that the relative position is controlled very well inside the specification of 0.1 m. The same is the case for the lateral relative velocities. It is observed that the COM is moving around in order to track the target port motion. It is recalled that the requirements are for the $\mathbf{s}_{pp}$ and not the COM motion. The demand for actuation force is inside the envelope and we observe less need for actuation along the axial than the lateral motion.

In Figure 10.11 we see illustrated the 2 docking ports lateral positions and velocities in the LVLH frame. They are very close to each other indicating that the controller is tracking the target very well. If we compare with Figure 9.16, we see that the box shape of the velocities in the y-z plane is no longer present, as we now track the target and not its mean value, as for the farther distances.

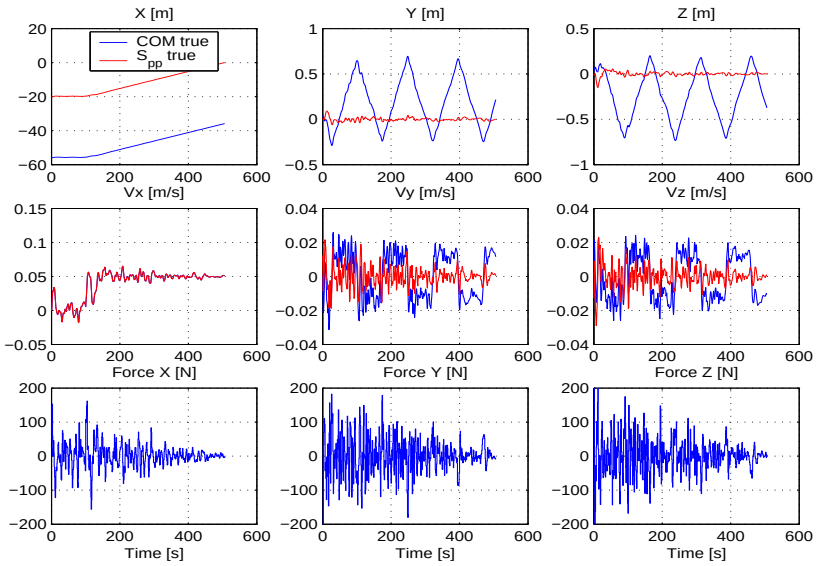

Figure 10.10: *The full nonlinear simulation showing the port to port $\mathbf{s}_{pp}$ motion, the chaser COM motion, the associated velocities and control forces. The initial condition is $\mathbf{s}_{pp}(0) = [-20, 0, 0]^T$ m and $\dot{\mathbf{s}}_{pp}(0) = \mathbf{0}$ m/s. The port to port is well controlled and the COM motion moves more to achieve that. The approach velocity of 0.05 m is kept and the lateral velocities controlled to zero.*

The cases where the worst case target docking port flexible modes are taken into account as specified in Table C.1 are illustrated in Section D.6.

The Figure D.8 corresponds to Figure 10.10. From Figure D.8 it is seen that the target port vibrations cause a moderate increase in the signal amplitude, but it has only very minor impact with no requirement violation. The Figure D.9 corresponds to Figure 10.11 and also shows no real practical deterioration of the performance of the control loops. It is recalled the simulation is for the worst case vibrations of the target port.

In Figure 10.12 is illustrated the results for the relative attitude, where we observe the performance to be better than 0.4 deg. This is well below the requirement of 5 deg. It is recalled that this result is obtained without using the angular rate information between the two spacecraft. The angular rate is more than 3 times better than required and the applied torque is rather low. It is observed that very little control action is required around the x-axis, which is due to the fact that there is no kinematic coupling to the position for the used operating point, see Equation (5.39), and no significant lever arm on the ISS for the docking port. The plots in Figure 10.12 are also fully representative for the target port flexible motion as no visible impact. Should faster and tighter tracking be needed it is recommended to include the added complexity of angular rate measurements.

It can be concluded from the Figures 10.10 to 10.12 that the overall 6 DOF GNC

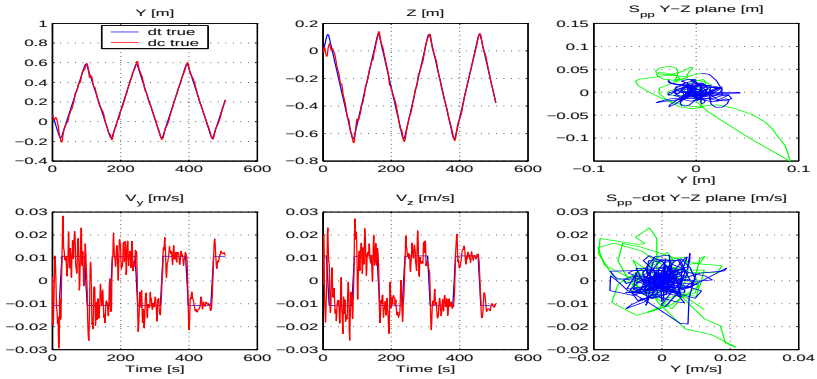

Figure 10.11: *The full nonlinear simulation showing the true LVLH lateral port motions as well as the relative motion in the cross section y-z plane. The green part of the curve is during the station keeping at s_4. It is recalled that the requirements are for the port to port motion.*

design is performing well and significantly better than required. Further results are provided in the connection of the MC analysis in Section 11.4.

10.8 Robust Stability

The background for the RS analysis is the same as in the previous section, explained in detail in Section 8.13, and not repeated here. All the LFT uncertainties models are the same as have been developed and used in the previous analysis.

Now it all has to be combined into a 6 DOF coupled system for analysis, where the coupled dynamics is expressed in Equation (10.4). The LFT formulations will be combined such that all the repeated δ will be combined together in order to reduce the conservatism. Attention needs to be paid to the uncertainties for forces and torques. The 5 % uncertainty applied earlier is now split evenly as the physical uncertainty is on the thrusters, which produce both forces and torques. For the delay uncertainty, we will replace the LFT with the maximum delay, which in practice is the worst case for stabilization. This is considered a reasonable approach in order to reduce the size of the Δ matrix to 43 for the real parameter uncertainties.

As evident from the past sections there are only real parametric uncertainties, which means we need to add some complex uncertainty in order to reliably find the lower bound of the structured singular value μ. The procedure and structure are the same as illustrated in Figure 8.23. In order to reliably find the lower bound and to have it close to the upper bound, we need to add about 40 % complex uncertainty. This is significant but it is a known difficulty with a large number of real parametric uncertainties.

It is recalled that the prime research is for the use of LTI controllers for the time varying elliptical orbital environment. The objectives are for eccentricities of $\varepsilon = 0.1$

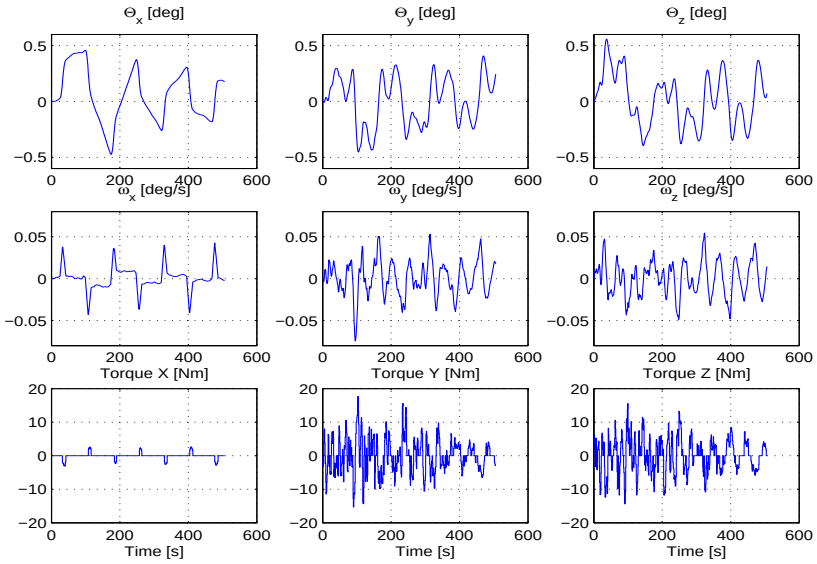

Figure 10.12: *The full nonlinear simulation showing the relative attitude $\boldsymbol{\theta}_{ra}$ between the two ports, the relative angular velocities and the control torques. All values are very well inside the requirements of* $5\,\mathrm{deg}$.

and the RS found is shown in Figure 10.13.

In Figure 10.13 we see that the upper and lower bounds for $\varepsilon = 0.1$ are fairly close in the areas where it is important, namely at the two peak values. For the other frequencies it is clear that the lower bound suffers from the large size of the Δ block with real parametric uncertainties, which is a well known problem. It is seen that both the sloshing and flexible mode peaks are well below 1 and we have RS with some margin.

The boundary with $\varepsilon = 0.7$ has also been investigated here. As seen in Figure 10.13 there is only a marginal increase in the μ value for this controller design. The fact that the peaks are larger than seen earlier is driven by the excitation by both position and attitude controllers simultaneously.

In conclusion it can be seen that a very robust controller design has been achieved, which is covering a wide range of uncertainties with a very comfortable margin.

10.9 Robust Performance

The background for the RP analysis is the same as earlier and detailed in Section 8.14. The 6 DOF RP setup is the same as illustrated in Figure 8.25. The only difference is that the matrices $\mathbf{D}_e$, $\mathbf{D}_d$, $\mathbf{W}_d$ and $\mathbf{W}_e$ are now block diagonal. All couplings are accommodated in the controller and plant.

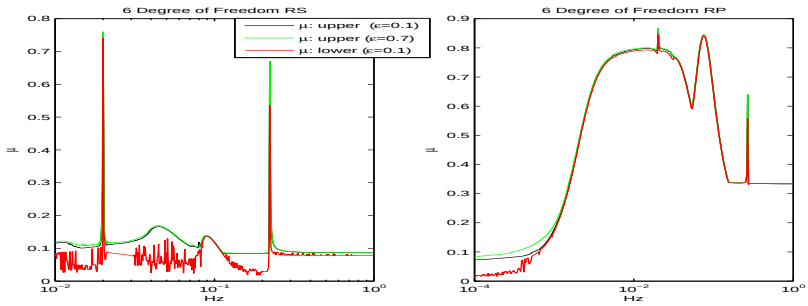

Figure 10.13: *Robust stability and performance for the* 6 *DOF design with coupled relative position and relative attitude. The left plot shows the RS, where the lower frequency peak is caused by the sloshing modes and the higher frequency one by the flexible modes. The right plot shows the RP, where it is seen that the peak is at the sloshing frequency and well below one. The orbital eccentricities are* $\varepsilon = 0.1$ *and* $\varepsilon = 0.7$.

The scaling of signals and the performance weighting functions used are the same as used for the RP relative attitude and position individually. For the relative attitude they are documented in Section 10.6 and for the relative position in Section 10.5.

When we look at the robustness it is important to consider only the driving performance variables. For the 6 DOF that is the relative position and attitude port to port. Δ_p in Equation (8.92) is a full complex matrix connecting the relevant part of $\mathbf{z}$ to $\mathbf{w}$ in Figure 8.20 for the RP analysis. With all the disturbances Δ_p is a 12×6 matrix and a 6×6 without. The influence of the disturbances is barely visible for which reason the latter Δ_p is chosen.

In Figure 10.13 we observe that $\mu_{max} = 0.86$ at frequencies around the sloshing modes. This means, we have RP with good margin at the sloshing resonance frequency. The design can tolerate about 116 % uncertainty at that frequency. Considering the results in Figures 10.10 and 10.12, we see that the maximum signal size, as used for RP analysis, is never reached, which leads to additional RP margin. It is confirmed by the MC analysis in Section 11.4, where the parameters from unwrapping the $\Delta(\mu_{max})$ have been included and no performance problems have been observed.

In conclusion a successful and robustly performing LTI $\mathcal{H}_\infty$ design has been achieved, which exhibits good RS and RP over a large LTV domain.

10.10 Conclusion

A 6 DOF relative position and attitude control has been developed for the docking port to port control. It is based on the $\mathcal{H}_\infty$ worst case approach with a 2 degree of freedom controller for the relative position and a standard mixed sensitivity design for the relative attitude.

A formal decoupling has been achieved for the synthesis, which is then reintroduced into the fully coupled analysis setup. This has resulted in a well performing 6 DOF closed loop design with excellent RS and RP properties for the application domain considered.

With the present LTI type of design it is possible to achieve boundaries of $0.01 - 0.02$ m docking accuracy with the worst case target port motion. For less extreme target motion, e.g. CMG controlled or having a short lever arm, sub centimeter accuracy can easily be achieved. The design is very robust to orbital eccentricity, see Figure 11.9. As sloshing and flexible modes have been treated as unmodeled dynamics in the design process, this can be included as modeled to achieve higher performance where needed. The type of design developed here would be applicable for most RVD missions irrespective of orbit, as well as formation flying missions.

This development and results correspond to the objectives of bullet 9 in Section 1.3.

Chapter 11

Verification and Evaluation

In the interest of forming a complementary to the worst case analysis as well as performing a commonly used practical verification a series of Monte Carlo analysis will be performed in the sequel.

11.1 Sample Size Computation

All stochastic processes involved are assumed to be Gaussian distributed, which will be verified graphically on the produced results.

We will only provide the main formulas to compute the approximate number of samples, which will be needed in order to reach a certain specified width of the confidence intervals of the mean μ and the variance σ. For the MC the largest number will be used. We will concentrate on the variance as experience has shown it is always requiring more runs than for the mean.

The computations are based on an approach of confidence interval for the variance with unknown mean and results from (Ankersen 2002).

$$M(n) = \left(1 + \frac{\delta_b}{3s}\right)^2 \quad \text{and} \quad N(n) = \left(1 - \frac{\delta_a}{3s}\right)^2 \tag{11.1}$$

where s^2 is the variance estimate and δ_a, δ_b being the interval width for 95 % confidence. Most often it is chosen symmetric such that $\delta_a = \delta_b$. This is under the assumption that the stochastic variables have a Gaussian distribution. This is mostly fulfilled though some are less, as can be seen in the following results, due to the oscillatory nature of the target motion. This have little practical importance though.

The functions $M(n)$ and $N(n)$ in Equation (11.1) are plotted against the sample size (Ankersen 2002). The procedure is therefore to compute Equation (11.1) and read off the number of runs needed to gain the confidence.

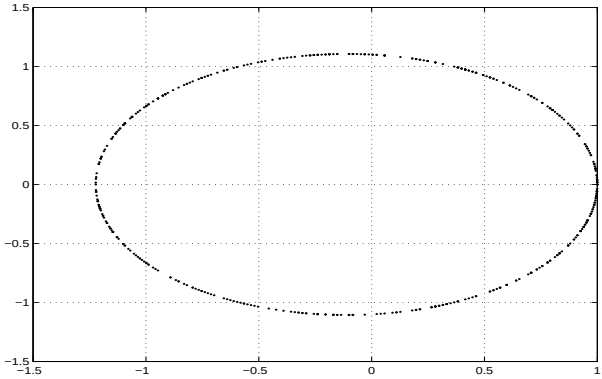

Figure 11.1: *Illustration of the initial orbital* $\varepsilon = 0.1$ *locations for the* 500 *simulations.*

11.2 Attitude Control

A conservative approach is taken, where the requirements are split symmetrically such that $\theta = 1.5$ deg and $\dot{\theta} = \pm 0.1$ deg/s. We assume that the estimated mean is zero, $\mu = 0$.

We select a 95 % confidence interval δ to be 0.1 deg and 0.01 deg/s. We can now evaluate the two functions for θ and $\dot{\theta}$.
For θ:

$$M(n) = \left(1 + \frac{0.1}{1.5}\right)^2 = 1.14 \quad \text{and} \quad N(n) = \left(1 - \frac{0.1}{1.5}\right)^2 = 0.87 \tag{11.2}$$

leading to $n = 480$.
For $\dot{\theta}$:

$$M(n) = \left(1 + \frac{0.01}{0.1}\right)^2 = 1.21 \quad \text{and} \quad N(n) = \left(1 - \frac{0.01}{0.1}\right)^2 = 0.81 \tag{11.3}$$

Results	Mean	σ
$\theta_x(\text{deg})$	$-8.6 \cdot 10^{-3}$	$8.4 \cdot 10^{-3}$
$\theta_y(\text{deg})$	$-1.0 \cdot 10^{-2}$	$5.7 \cdot 10^{-3}$
$\theta_z(\text{deg})$	$3.3 \cdot 10^{-3}$	$4.1 \cdot 10^{-3}$
$\omega_x(\text{deg}/s)$	$-4.2 \cdot 10^{-5}$	$1.3 \cdot 10^{-3}$
$\omega_y(\text{deg}/s)$	$3.4 \cdot 10^{-6}$	$6.2 \cdot 10^{-4}$
$\omega_z(\text{deg}/s)$	$1.3 \cdot 10^{-5}$	$4.0 \cdot 10^{-4}$

Table 11.1: *Statistical results of* 500 *simulations for each state variable.*

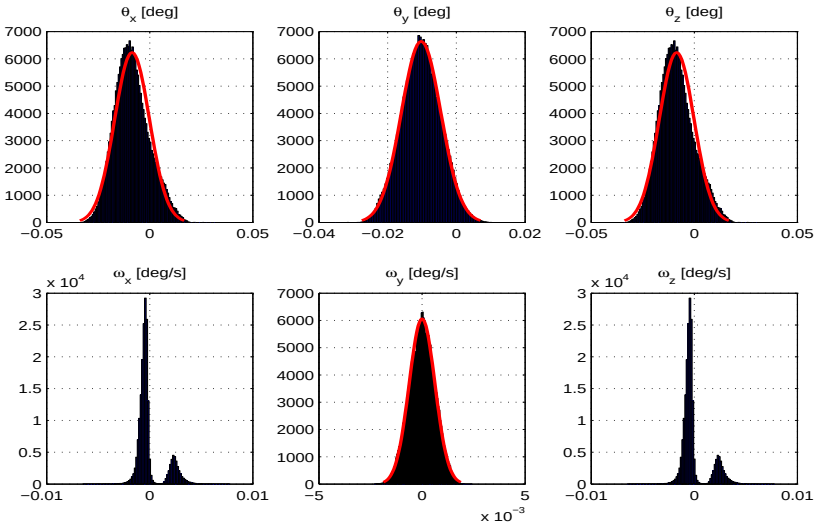

Figure 11.2: *Histograms illustrating the density functions of the variables in the attitude MC simulations. The larger variance on the y-axis is caused by a larger gravity gradient disturbance torque.*

leading to $n < 200$. We select to perform 500 runs.

We see from Figure 11.1 that the orbit is fairly evenly covered by 500 simulations. The statistical results are listed in Table 11.1 and can only be said to be very well inside

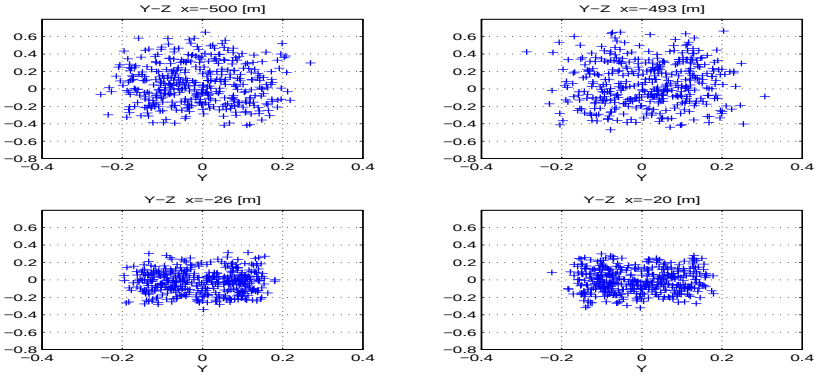

Figure 11.3: *Trajectory passage through the cross section y-z plane. Sampled at s_3 just before the pulse, at s_{31} just after the pulse, at s_{32} just before the pulse and at the s_4 end of SK*

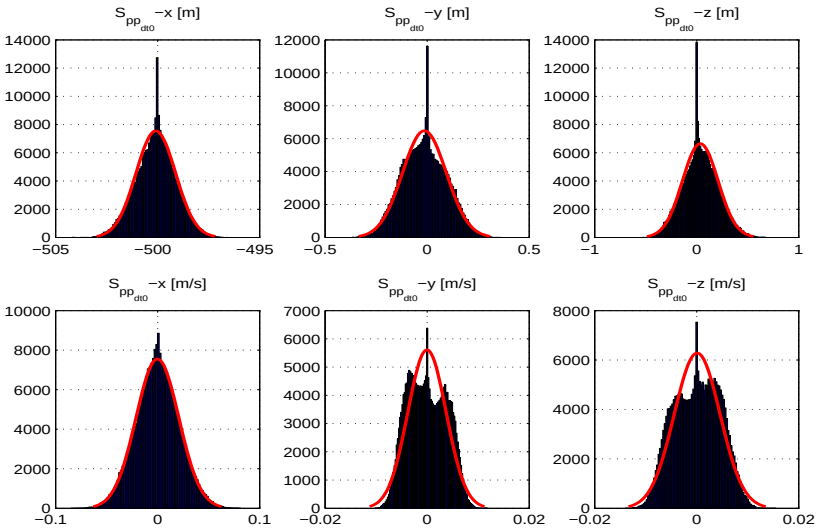

Figure 11.4: *Histograms illustrating the density functions of the variables in the position MC simulations at* s_3

the specifications.

In Figure 11.2 is shown the estimated density functions and the density histograms for the full state vector elements.

The attitude on the x and z-axis are a little skewed compared to the y-axis, which is more normal distributed.

The attitude rate shows the same pattern. The apparent two distributions for x and z-axis are due to the behavior visible in Figure 8.5 also, where the rates distribute around 2 different means. This is predominantly caused by the dead band of the PWM in the propulsion. The larger gravity gradient disturbance torque on the y-axis causes less operation close to the dead band, hence a single normal distribution.

Overall it can be concluded that the assumptions of normality are well respected and valid conclusion can be drawn from the set.

11.3 Position Control s_3 to s_4

The requirements change as a function of the distance so we select the more stringent one of the arrival at s_4 which is ± 1.0 m. The departure is less, so we choose in between a band of ± 0.5 m. The sample size computation is according to Section 11.1. This means that the estimated standard deviation is $3\text{ s} = 0.5$.

We select a 95 % confidence interval δ to be 0.05 m. This leads to $M(n) = 1.2$ and $N(n) = 0.8$ inserting into Equation (11.1) and gives $n = 310$, which means we

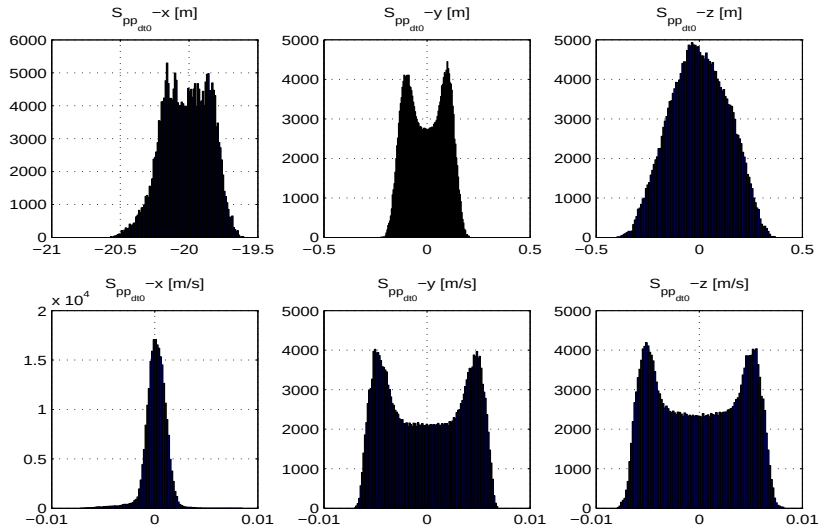

Figure 11.5: *Histograms illustrating the density functions of the variables in the position MC simulations at s_4*

select $n = 400$. As for the attitude the calculations for the rate lead to fewer runs so not detailed any further.

The computations will be based upon data as follows

- SK at s_3 during 600 s
- A sample right after s_{31} in Figure 7.10
- A sample right before s_{32} in Figure 7.10
- SK at s_4 during 600 s

All computations are performed with respect to the mean target motion $\mathbf{r}_r$, see also Figure 3.6. From Figure 5.1 we can write $\mathbf{r}_{dt} + \mathbf{s}_{pp} = \mathbf{r}_r + \mathbf{x}$ giving $\mathbf{x} = \mathbf{r}_{dt} + \mathbf{s}_{pp} - \mathbf{r}_r$, which is what we use here.

The random distribution is very similar to the one shown in Figure 11.1. In Figure 11.3 we see the penetration of the trajectory at the four locations in the y-z plane. They are slightly more spread at the far distances, but all very well inside the specifications.

In Figure 11.4 we see the histograms and their estimated normal distributions which fit very well for the positions and the x-axis velocity. The velocities for y and z have a tendency to grow on the sides. This is caused by the constant of the target velocity profile which also caused the box like appearance in Figure 9.16.

	s_3		s_{31}	
	Mean	σ	Mean	σ
x(m)	-500.1	$9.7 \cdot 10^{-1}$	-494.0	1.3
y(m)	$-1.3 \cdot 10^{-2}$	$1.1 \cdot 10^{-1}$	$1.6 \cdot 10^{-2}$	$1.1 \cdot 10^{-1}$
z(m)	$3.6 \cdot 10^{-2}$	$1.8 \cdot 10^{-1}$	$6.2 \cdot 10^{-2}$	$2.5 \cdot 10^{-1}$
$\dot{x}$(m/s)	$-1.6 \cdot 10^{-4}$	$2.1 \cdot 10^{-2}$	$1.8 \cdot 10^{-1}$	$1.5 \cdot 10^{-2}$
$\dot{y}$(m/s)	$-2.2 \cdot 10^{-5}$	$3.8 \cdot 10^{-3}$	$-3.2 \cdot 10^{-4}$	$3.9 \cdot 10^{-3}$
$\dot{z}$(m/s)	$9.7 \cdot 10^{-5}$	$4.5 \cdot 10^{-3}$	$1.9 \cdot 10^{-3}$	$4.7 \cdot 10^{-3}$
	s_{32}		s_4	
	Mean	σ	Mean	σ
x(m)	-26.2	$7.1 \cdot 10^{-2}$	-20.0	$1.7 \cdot 10^{-1}$
y(m)	$-3.4 \cdot 10^{-3}$	$9.6 \cdot 10^{-2}$	$-2.3 \cdot 10^{-3}$	$9.4 \cdot 10^{-2}$
z(m)	$-2.4 \cdot 10^{-2}$	$1.3 \cdot 10^{-1}$	$-6.8 \cdot 10^{-4}$	$1.4 \cdot 10^{-1}$
$\dot{x}$(m/s)	$2.0 \cdot 10^{-1}$	$6.0 \cdot 10^{-4}$	$1.1 \cdot 10^{-4}$	$1.7 \cdot 10^{-3}$
$\dot{y}$(m/s)	$-2.1 \cdot 10^{-5}$	$3.8 \cdot 10^{-3}$	$-1.7 \cdot 10^{-5}$	$3.8 \cdot 10^{-3}$
$\dot{z}$(m/s)	$-2.0 \cdot 10^{-5}$	$4.4 \cdot 10^{-3}$	$5.7 \cdot 10^{-6}$	$4.2 \cdot 10^{-3}$

Table 11.2: *Statistical results of* 400 *simulations for each state variable at the* 4 *locations.*

In Figure 11.5 we still see the nature of a normal distribution. The side lobes are more pronounced as the oscillatory signals dominate more as the sensor noise is much less at this short distance.

All results nevertheless show excellent performance with a very small spread and good performance all around the elliptical orbit. The means and standard deviations are summarized in Table 11.2 and they fit well expectations.

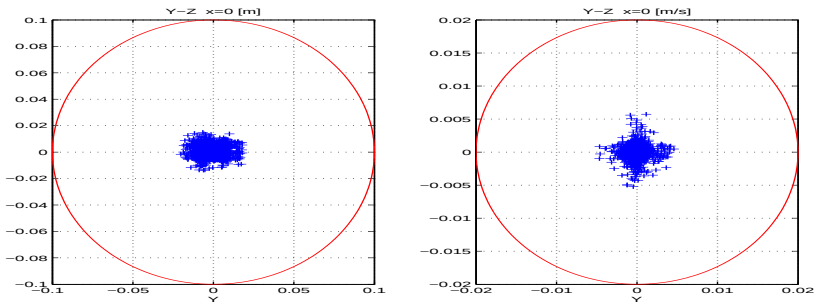

Figure 11.6: *The docking performance in the y-z plane for an axial distance of* $x = 0$ *m. It shows the relative positions and velocities, which have requirements of* ± 0.1 *m and* ± 0.02 *m/s respectively.*

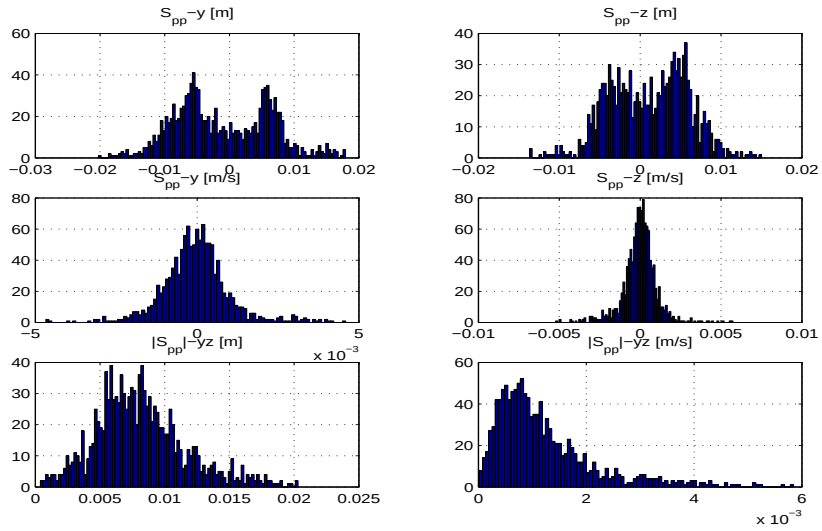

Figure 11.7: *Histograms illustrating the density functions at docking in the y-z plane and the velocities. The lower two plots show the radial densities from the center of the docking port, which are Rayleigh distributions.*

11.4 6 Degree of Freedom Control s_4 to Docking

The requirements from s_4 until docking are considered to vary in a linear manner between the two points as described in Section 2.4.2 and Tables 2.6 and 2.7. The number of simulations will, as earlier, be based upon Section 11.1 and the requirements at docking.

We select a 95% confidence interval δ to be 0.005 m for the 3σ requirement of 0.1 m. This leads to $M(n) = 1.1$ and $N(n) = 0.9$ inserting into Equation (11.1) and gives $n = 1100$. For the relative attitude with $\delta = 0.2$ deg and a 3σ requirement of 5 deg, we get $M(n) = 1.08$ and $N(n) = 0.92$ leading to $n = 1200$. The rates are all leading to less runs, so we will select $n = 1200$ for the MC analysis to follow. The computations will be based upon data as follow

- Station keeping at s_4 during 100 s
- Approach to docking with a velocity of 0.05 m/s
- Orbital eccentricity $\varepsilon = 0.1$ and sampled as illustrated in Figure 11.1 for 1200 samples

In Figure 11.6 we see illustrated the docking performance for the 1200 simulations. It exhibits very good performance below 0.02 m, which is some 5 times better than the requirement. The velocities are well below the requirement with a margin of a factor of $3 - 4$.

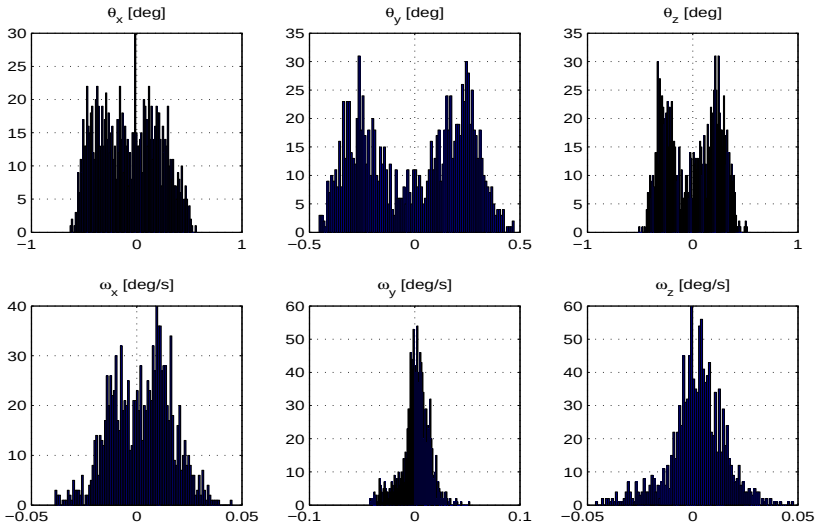

Figure 11.8: *Histograms illustrating the relative attitude and relative angular rate densities at docking.*

In Figure 11.7 is illustrated the histograms of the data in Figure 11.6. The tendency of the 2 maxima for the positions is driven by the triangular motion, as defined in Figure 3.5, of the target docking port. This naturally gives more samples at the amplitudes. The velocities are more clean normal distributed. The lower two plots in Figure 11.7 provide the radial distance and velocity from the port center line. They mostly have a

	Rigid Port		Flexible Port	
	Mean	σ	Mean	σ
y(m)	$-1.0 \cdot 10^{-3}$	$7.3 \cdot 10^{-3}$	$-1.3 \cdot 10^{-3}$	$1.3 \cdot 10^{-2}$
z(m)	$1.1 \cdot 10^{-3}$	$4.8 \cdot 10^{-3}$	$8.0 \cdot 10^{-4}$	$1.2 \cdot 10^{-2}$
$\dot{y}$(m/s)	$-2.7 \cdot 10^{-5}$	$1.1 \cdot 10^{-3}$	$1.9 \cdot 10^{-4}$	$9.9 \cdot 10^{-3}$
$\dot{z}$(m/s)	$-2.5 \cdot 10^{-5}$	$1.1 \cdot 10^{-3}$	$-4.4 \cdot 10^{-4}$	$9.8 \cdot 10^{-3}$
θ_x(deg)	$-7.3 \cdot 10^{-2}$	$2.9 \cdot 10^{-1}$	$-7.4 \cdot 10^{-2}$	$2.9 \cdot 10^{-1}$
θ_y(deg)	$-2.5 \cdot 10^{-3}$	$2.4 \cdot 10^{-1}$	$-2.9 \cdot 10^{-3}$	$2.4 \cdot 10^{-1}$
θ_z(deg)	$2.2 \cdot 10^{-3}$	$2.5 \cdot 10^{-1}$	$2.7 \cdot 10^{-3}$	$2.5 \cdot 10^{-1}$
ω_x(deg/s)	$2.3 \cdot 10^{-3}$	$1.4 \cdot 10^{-2}$	$2.2 \cdot 10^{-3}$	$1.4 \cdot 10^{-2}$
ω_y(deg/s)	$1.2 \cdot 10^{-3}$	$1.3 \cdot 10^{-2}$	$1.2 \cdot 10^{-3}$	$1.3 \cdot 10^{-2}$
ω_z(deg/s)	$2.1 \cdot 10^{-3}$	$1.3 \cdot 10^{-2}$	$2.1 \cdot 10^{-3}$	$1.3 \cdot 10^{-2}$

Table 11.3: *Statistical results of* 1200 *simulations for each relevant state variable at docking.*

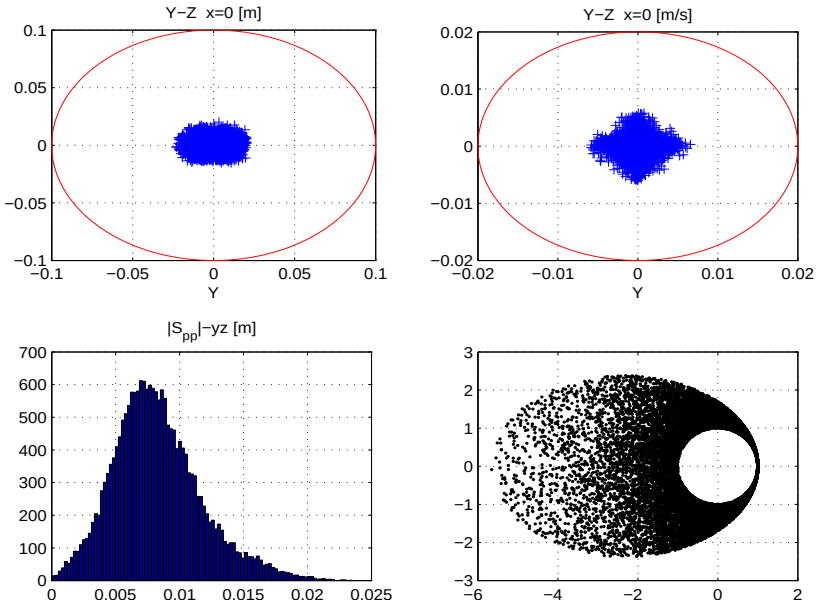

Figure 11.9: *The docking performance in the y-z plane. It shows the relative positions and velocities, which have requirements of* ± 0.1 *m and* ± 0.02 *m/s respectively, and the radial distance from the docking port axis. Orbital eccentricity is* $\varepsilon \leq 0.7$*. The lower right plot shows the* 20000 *samples on the plane of the orbits.*

Rayleigh [1] density function.

In Figure 11.8 is shown the densities for the relative attitude and the angular velocities. They are well behaved and inside the requirements by an order of magnitude. We see also here that the side lobes are more pronounced for the same reasons as earlier.

All the results show excellent performance with very small spread and good performance all around the elliptical orbit. The mean and standard deviations are summarized in Table 11.3. We observe that the presence of target port vibrations only slightly degrade the results.

11.5 6 Degree of Freedom Control s_4 to Docking for Large Eccentricities

This section presents the results from a set of simulations covering the range from a circular orbit to highly eccentric ones with an eccentricity up to $\varepsilon = 0.7$. This is coherent

[1] If a random variable $X = \sqrt{Y^2 + Z^2}$ and Y and Z are normally distributed and independent with similar variance, then X has a Rayleigh density (Papoulis 1984).

with the extreme case investigated in the previous robustness analysis for the RS and RP. The results are shown in Figure 11.9. In order to reasonably sample the space at the far out points 20000 simulations have been performed.

11.6 Conclusion

The number of simulations needed to reach a 95% confidence interval has been found for the different simulations. Full high fidelity non linear simulations have been performed successfully for the LVLH based attitude, the far and the close RVD phases. All have performed well and show a performance well inside the specification. The worst case parameters identified in the μ analysis have been included in the simulations and they have not shown any problems in the non linear simulations.

Chapter 12

Conclusion

This chapter provides the main conclusion of the research performed in the thesis as well as it identifies directions of future research for continuation and completion of areas not covered in this work.

12.1 Conclusion

A general 6 degree of freedom GNC system for relative motion between spacecraft on general elliptic orbits has been developed in this thesis. The focus is on the rendezvous and docking problem to the International Space Station imagined on a non circular orbit, but not restricted to that. The rendezvous problem has been explained and broken down into the individual maneuvers followed by the requirements and data used in this work.

Models for external disturbances have been developed for gravity gradient and differential air drag for elliptic orbits. Models for internal disturbances for flexible modes formulated in a scalable form and liquid sloshing have been developed in detail. Finally accurate models for all used sensors and actuators have been developed.

The general dynamics between spacecraft on elliptical orbits have been derived in the equivalent form of the Hill equations, the latter restricted to circular orbits. The system dynamics of coupled periodic time varying differential equations has been successfully solved in a closed form solution, which provides ΔV computations for maneuver and trajectory propagation in an unrestricted framework. This is a generalization in the form of a state transition matrix, equivalent to the well known circular Clohessy Wiltshire equations, and valid for any closed Keplerian orbit. The solution has been derived such that for orbital eccentricity $\varepsilon = 0$, it reduces to the well known solution for the circular case, leaving unrestricted validity. A set of equations has been developed for general ΔV maneuvers as well as the special cases for radial and tangential maneuvers with their special properties. Particular solutions have been found for constant forces in both local and inertial frames useful for drag and solar radiation pressure compensation during maneuvers.

These solutions have been successfully implemented and demonstrated in flight on the Swedish RendezVous and Formation Flying technology demonstration mission *Prisma*. They are operational on the mission, which is the best achievable validation possible.

In preparation of the control designs an analytical 6 degree of freedom coupled relative attitude and position model has been developed. This model was derived both as a large and small signal one. This makes the same model structure available for control design as well as for large signal simulations. The model is general in the sense of describing the relative dynamics and kinematics linearly between any two arbitrarily located points on the spacecraft.

The avionics equipment for rendezvous missions is described and a scaleable overall GNC architecture has been proposed. For on board implementation of the GNC system a functional software structure has been provided, including the functional interactions between the higher levels of mode management, measurement system, failure detection and the control system.

Linear periodic time varying systems have been analyzed for the relative dynamics. The periodic variations are efficiently analyzed representing them as uncertainties in a robust control analyses framework. This has been performed successfully by means of LFT models.

Detailed analytical LFT models have been derived for all relevant uncertainties in the flexible appendices, fuel sloshing, input gain, delays, mass, inertia and the periodic variation of the orbital rate in the relative dynamics. The latter gives as a side result a generic LFT formulation of matrices with arbitrary elements of linear quadratic nature.

Algorithms for the guidance for all maneuvers applicable to both position and attitude have been derived. The algorithms feature constant or exponential acceleration profiles, constant speed and hold points as well as combinations of those.

The control designs are based on worst case $\mathcal{H}_\infty$ multi variable robust control. Robustness is measured by means of the structured singular value μ. For distances far from the target the closed loop control tracks only the target docking port mean motion in order to save fuel. For short distances up to docking, which requires more precision, the docking port is tracked with respect to both relative position and relative attitude. The mode switching is considered in a classical manner with time to settle transients. All controllers have been designed for orbital locations close to the perigee, where the disturbances are larger and the relative dynamics the fastest, in order to perform well on the entire orbit with one controller. This ensures robustness elsewhere.

In the far distance parts the attitude control has been designed with respect to the local vertical local horizontal frame and designed by LQG achieving a robust performance better than 0.05 deg for all axes and eccentricities. The relative port to port mean motion position control has been performed as a $\mathcal{H}_\infty$ mixed sensitivity design and achieves a robust performance better than 0.5 m at 500 m distance and 0.3 m at 20 m for all axes and eccentricities.

For the final approach, the relative attitude and position control, a 6 degree of freedom design has been performed as a two degree of freedom $\mathcal{H}_\infty$ model reference controller. This provides a dynamic feed forward control with significant performance im-

provement for target port tracking. The design has been proven to be robustly fault tolerant to possible lack of the feed forward control. The achieved docking performance is better than 0.02 m and 0.5 deg for all eccentricities.

It has been demonstrated that it is possible by choice of robust control design to obtain a highly performing GNC LTI system for a LTV relative dynamics for all eccentricities. The designs all have RS and RP with μ values well below 1 over the whole frequency spectrum. This is an important conclusion as it provides a framework for simpler systems, than time varying controllers, for proximity maneuvers in elliptical orbits. The results obtained in this thesis will also be applicable and beneficial for planetary exploration sample return missions as well as to formation flying missions.

From the performed research it is recommended to utilize sensors for relative measurements which can provide also the relative velocities as it would further enhance the performance.

12.2 Future Research

During the course of this project several areas have been identified, which will require further research as it could not be accommodated within the time resources and the scope of this project.

Regarding control it would be interesting to establish the boundaries of position accuracy that can be achieved with the present approach, and establish when need be for the time varying nature to be included in the synthesis. It is recommended to quantify the performance increase, which can be achieved including uncertainties during the synthesis. It can be interesting to investigate, if there is any performance increase using Linear Parameter Varying control or Model Predictive Control considering the increased complexity. The former would feature a controller with bounded time varying matrices ensuring similar performance around the orbit as it would be function of the parameter variations. The latter would feature an optimization based controller with a receding horizon capturing the parameter variations. In addition it can perform constraint based optimization accounting for e.g. actuator saturation.

Regarding the relative dynamics it is recommended to develop expressions for ΔV maneuvers accounting for the particular solution contribution and functional approximations of the intractable integrals identified. A particular solution for a constant force in a frame attached to the tangential velocity vector would be beneficial for drag compensation. Expressions with no singularities for $\varepsilon \rightarrow 0$ would enhance one particular solution for both circular and elliptical orbits.

These are issues that will further the contributions of this project to space application GNC systems for relative control as well as enhance the developed solutions for relative dynamics between spacecraft.

Appendix A

Detailed Derivation of Relative Motion Dynamics

This chapter will contain all the details and intermediate calculations in order to derive the general equations of the relative motion, which are not covered in Chapter 4.

A.1 General Differential Equation System

This section deals with the details in connection with deriving the linear equations of relative motion.

A.1.1 Jacobian Matrix Elements

The elements of the Jacobian matrix in Equation (4.8) will be derived here. As vectors are defined as column vectors the Jacobian matrix becomes (Wie 1998):

$$\frac{d\mathbf{g}(\mathbf{x})}{d\mathbf{x}} = \begin{bmatrix} \frac{\partial g_1}{\partial x_1} & \cdots & \frac{\partial g_1}{\partial x_3} \\ \vdots & \ddots & \vdots \\ \frac{\partial g_3}{\partial x_1} & \cdots & \frac{\partial g_3}{\partial x_3} \end{bmatrix}$$

We will initially find the diagonal elements of the Jacobian, where we define $\mathbf{r} = [r_x, r_y, r_z]^{\mathrm{T}}$ and $r = |\mathbf{r}| = (r_x^2 + r_y^2 + r_z^2)^{\frac{1}{2}}$. For element (i, j), where $i = j$, and using Equation (4.2):

$$\begin{aligned} \frac{\partial f_g(r_i)}{\partial r_j} &= -\mu \left[r^{-3} + r_i(-\frac{3}{2})(r_x^2 + r_y^2 + r_z^2)^{-\frac{5}{2}} 2r_i \right] \\ &= -\mu \left[r^{-3} - 3r^{-5} r_i^2 \right] \\ &= -\frac{\mu}{r^3} \left[1 - 3\frac{r_i^2}{r^2} \right] \end{aligned} \tag{A.1}$$

For element (i,j) where $i \neq j$ and it shall be noticed that r_i is not a function of r_j:

$$\begin{aligned}\frac{\partial f_g(r_i)}{\partial r_j} &= -\mu\left[-\frac{3}{2}(r_x^2+r_y^2+r_z^2)^{-\frac{5}{2}}2r_jr_i\right] \\ &= -\mu\left[-3r^{-5}r_ir_j\right] \\ &= -3\frac{\mu}{r^3}\frac{r_ir_j}{r^2} \end{aligned} \tag{A.2}$$

We will now rewrite Equation (4.8) and insert Equations (4.6), (A.1) and (A.2) and that $\mathbf{r} = \mathbf{r}_t$.

$$\mathbf{f}_g(\mathbf{r}_c) - \mathbf{f}_g(\mathbf{r}_t) = -\frac{\mu}{r_t^3}\mathbf{M}\mathbf{s}$$

where part of the Jacobian $\mathbf{M}$ is

$$\mathbf{M} = \begin{bmatrix} 1-3\frac{r_x^2}{r_t^2} & 3\frac{r_xr_y}{r_t^2} & 3\frac{r_xr_z}{r_t^2} \\ 3\frac{r_yr_x}{r_t^2} & 1-3\frac{r_y^2}{r_t^2} & 3\frac{r_yr_z}{r_t^2} \\ 3\frac{r_zr_x}{r_t^2} & 3\frac{r_zr_y}{r_t^2} & 1-3\frac{r_z^2}{r_t^2} \end{bmatrix} \tag{A.3}$$

A.1.2 Rotating Frame Elements

Now we will compute the individual terms of Equation (4.12), which is repeated in Equation (A.4) for clarity.

$$\frac{d^{*2}\mathbf{s}^*}{dt^2} + \boldsymbol{\omega}\times(\boldsymbol{\omega}\times\mathbf{s}^*) + 2\boldsymbol{\omega}\times\frac{d^*\mathbf{s}^*}{dt} + \frac{d\boldsymbol{\omega}}{dt}\times\mathbf{s}^* + \frac{\mu}{r_t^3}\mathbf{M}\mathbf{s}^* = \frac{\mathbf{F}}{m_c} \tag{A.4}$$

Expressed in the target frame we get for $\mathbf{r}_t$ and $\boldsymbol{\omega}$

$$\mathbf{r}_t = \begin{bmatrix} 0 \\ 0 \\ -r \end{bmatrix} \text{ and } \boldsymbol{\omega} = \begin{bmatrix} 0 \\ -\omega \\ 0 \end{bmatrix}$$

The terms of Equation (A.4) become

$$\boldsymbol{\omega}\times\mathbf{s}^* = \begin{bmatrix} -\omega z \\ 0 \\ \omega x \end{bmatrix}$$

$$\boldsymbol{\omega}\times(\boldsymbol{\omega}\times\mathbf{s}^*) = \begin{bmatrix} -\omega^2 x \\ 0 \\ -\omega^2 z \end{bmatrix}$$

$$\boldsymbol{\omega}\times\frac{d^*\mathbf{s}^*}{dt} = \begin{bmatrix} -\omega\dot{z} \\ 0 \\ \omega\dot{x} \end{bmatrix}$$

$$\frac{d\boldsymbol{\omega}}{dt} \times \mathbf{s}^* = \begin{bmatrix} -\dot{\omega} z \\ 0 \\ \dot{\omega} x \end{bmatrix}$$

$$\mathbf{M}\mathbf{s}^* = \begin{bmatrix} 1 & 0 & 0 \\ 0 & 1 & 0 \\ 0 & 0 & -2 \end{bmatrix} \mathbf{s}^* = \begin{bmatrix} x \\ y \\ -2z \end{bmatrix}$$

A.2 Conic Sections

For the sake of completeness, we will derive and solve the polar coordinate equations for the motion under a central gravitational field for a planar motion. This solution will be needed to find the general solution of Equation (4.15) for arbitrary elliptic orbits.

We will present the 2 differential equations directly presented in polar coordinates (Symon 1979), where the first line in Equation (A.5) is for the central force acting along the radius vector, defined with Equation (4.1), and the second line in Equation (A.5) is in the direction of the increasing angle θ, where no force is acting.

$$\begin{aligned} m\ddot{r} - mr\dot{\theta}^2 &= F_r \\ r\ddot{\theta} + 2\dot{r}\dot{\theta} &= 0 \end{aligned} \tag{A.5}$$

and the second line of Equation (A.5) reformulates to

$$\frac{1}{r}\left(\frac{d}{dt}\left(r^2\dot{\theta}\right)\right) = 0$$

The differential is a constant, which is known from Equation (4.13)

$$\begin{aligned} r^2\dot{\theta} &= h \\ \dot{\theta} &= \frac{h}{r^2} \end{aligned} \tag{A.6}$$

We will now change the independent variable to become θ and inserting Equation (A.6)

$$\frac{dr}{dt} = \frac{dr}{d\theta}\frac{d\theta}{dt} = hr^{-2}\frac{dr}{d\theta} \tag{A.7}$$

and

$$\begin{aligned} \frac{d^2r}{dt^2} &= hr^{-2}\frac{d^2r}{d\theta^2}\frac{d\theta}{dt} - h2r^{-3}\frac{dr}{dt}\frac{dr}{d\theta} \\ &= h^2r^{-4}\frac{d^2r}{d\theta^2} - 2h^2r^{-5}\left(\frac{dr}{d\theta}\right)^2 \end{aligned} \tag{A.8}$$

Inserting Equations (A.7) and (A.8) into Equation (A.5) together with Equation (A.6) we get

$$\ddot{r} - r\dot{\theta}^2 = -\mu r^{-2}$$

$$h^2 r^{-4} \frac{d^2 r}{d\theta^2} - 2h^2 r^{-5} \left(\frac{dr}{d\theta}\right)^2 - r h^2 r^{-4} = -\mu r^{-2}$$

and multiplying through with $h^{-2} r^4$ we obtain

$$\frac{d^2 r}{d\theta^2} - 2r^{-1} \left(\frac{dr}{d\theta}\right)^2 - r = -\mu h^{-2} r^2 \tag{A.9}$$

To simplify further we will change variable to u, where $r = \frac{1}{u}$

$$\frac{dr}{du} = -u^{-2}$$

$$\frac{dr}{d\theta} = \frac{dr}{du}\frac{du}{d\theta} = -u^{-2}\frac{du}{d\theta}$$

$$\frac{d^2 r}{d\theta^2} = 2u^{-3} \left(\frac{du}{d\theta}\right)^2 - u^{-2}\frac{d^2 u}{d\theta^2}$$

Inserting into Equation (A.9) we now obtain

$$2u^{-3} \left(\frac{du}{d\theta}\right)^2 - u^{-2}\frac{d^2 u}{d\theta^2} - 2u \left(-u^{-2}\frac{du}{d\theta}\right)^2 - u^{-1} = -\mu h^{-2} u^{-2}$$

rearranging terms and multiplying through with $-u^2$ we get

$$\frac{d^2 u}{d\theta^2} + u = \mu h^{-2} \tag{A.10}$$

This is the well known oscillator and the solution to Equation (A.10) becomes

$$u(\theta) = \underbrace{A\cos(\theta - \theta_0)}_{homogeneous} + \underbrace{\mu h^{-2}}_{particular}$$

and back substituting $u(\theta) = r^{-1}(\theta)$ gives

$$\begin{aligned} r(\theta) &= \frac{1}{\mu h^{-2} + A\cos(\theta - \theta_0)} \\ &= \frac{h^2 \mu^{-1}}{1 + A h^2 \mu^{-1} \cos(\theta - \theta_0)} \end{aligned} \tag{A.11}$$

θ_0 is arbitrary as it only determines the orientation and not the shape of the orbit, so $\theta_0 = 0$

$$r(\theta) = \frac{p}{1 + \varepsilon\cos(\theta)} \tag{A.12}$$

where

$$\begin{aligned} p &= h^2\mu^{-1} \\ \varepsilon &= Ah^2\mu^{-1} \end{aligned}$$

See also (Ankersen 1999).

A.2.1 Conic Sections Elliptical Case

A few needed properties specific for elliptical orbits will be derived. For elliptical orbits we also have that $p = a(1-\varepsilon^2)$ (Symon 1979), where a is the major axis.

The true anomaly angular rate in Equation (A.6) can, by inserting Equation (A.12) and h, be expressed as a function of the true anomaly as

$$\dot{\theta}(\theta) = \sqrt{\frac{\mu}{p^3}}(1+\varepsilon\cos(\theta))^2 \tag{A.13}$$

and by direct differentiation of Equation (A.13) the true anomaly angular acceleration yields

$$\ddot{\theta}(\theta) = -2\varepsilon\frac{\mu}{p^3}\sin(\theta)(1+\varepsilon\cos(\theta))^3 \tag{A.14}$$

The speed at any point in the orbit can be found from the fact that the energy in the system is constant. The specific energy per mass $e = e_{pot} + e_{kin}$ is the sum of the potential and kinetic energies. The potential energy is $e_{pot} = -\frac{\mu}{r}$ and the kinetic energy is $e_{kin} = \frac{1}{2}v^2$

$$e = \frac{v^2}{2} - \frac{\mu}{r} \tag{A.15}$$

The total specific energy can be found from data at e.g. the perigee, where the true anomaly is zero, $r = \frac{p}{1+\varepsilon}$ and $h = \sqrt{\mu p} = vr$. Inserting into Equation (A.15)

$$e = \frac{\mu p(1+\varepsilon)^2}{2p^2} - \frac{\mu(1+\varepsilon)}{p}$$

and after some manipulations

$$e = -\frac{\mu}{2a} \tag{A.16}$$

Inserting Equation (A.16) into Equation (A.15) and solving for v, it gives the general expression for the elliptical orbital speed

$$\begin{aligned} \frac{v^2}{2} - \frac{\mu}{r} &= -\frac{\mu}{2a} \\ v &= \sqrt{\mu\left(\frac{2}{r} - \frac{1}{a}\right)} \end{aligned} \tag{A.17}$$

For $r = a$ Equation (A.17) gives the circular orbital speed and for $a \to \infty$ it gives the speed for a parabola and the escape velocity.

Finally the orbital period will be determined. The area of an ellipse is $S = \pi ab$, where $b = a\sqrt{1-\varepsilon^2}$ is the minor axis. The area swept for a small angle is $dS = \frac{1}{2}r^2 d\theta$ and per time it becomes

$$\frac{dS}{dt} = \frac{1}{2}r^2\frac{d\theta}{dt} = \frac{h}{2} \tag{A.18}$$

which is constant in Equation (A.6). Integrating over a full period T the area is $S = \frac{h}{2}T = \pi ab$. Inserting the expressions for the constants and rearranging, the period T becomes

$$T = 2\pi\frac{ab}{h} = 2\pi\frac{a^2\sqrt{1-\varepsilon^2}}{\sqrt{\mu a(1-\varepsilon^2)}} = 2\pi\sqrt{\frac{a^3}{\mu}} \tag{A.19}$$

A.3 General Solution

The intermediate calculations leading to the final solution are to be found in this chapter.

A.3.1 Differential Equations Domain Change

Equation (4.24) is found as follows

$$\begin{aligned}
\frac{d^2a}{dt^2} &= \frac{d^2a}{d\theta^2}\left(\frac{d\theta}{dt}\right)^2 + \frac{da}{d\theta}\frac{d^2\theta}{dt^2} \\
&= \omega^2\frac{d^2a}{d\theta^2} + \frac{da}{d\theta}\frac{d\omega}{dt} \\
&= \omega^2\frac{d^2a}{d\theta^2} + \omega\frac{d\omega}{d\theta}\frac{da}{d\theta} \\
&= \omega^2 a'' + \omega\omega' a'
\end{aligned} \tag{A.20}$$

The derivative of Equation (4.22) becomes

$$\begin{aligned}
\frac{d\omega}{d\theta} &= \omega' \\
&= \frac{d}{d\theta}\left(k^2(1+\varepsilon\cos(\theta))^2\right) \\
&= 2k^2(1+\varepsilon\cos(\theta))(-\varepsilon\sin(\theta)) \\
&= -2\varepsilon k^2\varrho\sin(\theta)
\end{aligned} \tag{A.21}$$

Finding Equation (4.26) from the second row of Equation (4.15) we obtain as follow

$$\ddot{y} + k\omega^{\frac{3}{2}}y = 0$$

$$\omega^2 y'' + \omega\omega' y' + k\omega^{\frac{3}{2}}y = 0$$

$$(k^2\varrho^2)^2 y'' - 2\varepsilon k^2 \varrho \sin(\theta)(k^2\varrho^2)y' + k(k^2\varrho^2)^{\frac{3}{2}} y = 0$$

and after some algebraic manipulations one obtains

$$\varrho y'' - 2\varepsilon \sin(\theta) y' + y = 0 \tag{A.22}$$

Finding Equation (4.27) from the first row of Equation (4.15) we get

$$\ddot{x} - \omega^2 x - 2\omega\dot{z} - \dot{\omega} z + k\omega^{\frac{3}{2}} x = 0$$

$$\omega^2 x'' + \omega\omega' x' - \omega^2 x - 2\omega^2 z' - \omega\omega' z + k\omega^{\frac{3}{2}} x = 0$$

$$\omega^2 x'' + \omega\omega'(x' - z) + (k\omega^{\frac{3}{2}} - \omega^2)x - 2\omega^2 z' = 0$$

$$(k^2\varrho^2)^2 x'' - 2\varepsilon k^2 \varrho \sin(\theta)(k^2\varrho^2)(x' - z) + [k(k^2\varrho^2)k\varrho - (k^2\varrho^2)^2]x - 2(k^2\varrho^2)^2 z' = 0$$

and after some rearrangement of terms one obtains

$$\varrho x'' - 2\varepsilon \sin(\theta) x' + 2\varepsilon \sin(\theta) z - \varepsilon \cos(\theta) x - 2\varrho z' = 0 \tag{A.23}$$

Finding Equation (4.28) from the third row of Equation (4.15) we get

$$\ddot{z} - \omega^2 z + 2\omega\dot{x} + \dot{\omega} x - 2k\omega^{\frac{3}{2}} z = 0$$

$$\omega^2 z'' + \omega\omega' z' - \omega^2 z + 2\omega^2 x' + \omega\omega' x - 2k\omega^{\frac{3}{2}} z = 0$$

$$(k^2\varrho^2)^2 z'' - 2\varepsilon k^2 \varrho \sin(\theta)(k^2\varrho^2)(z' + x) + (k^2\varrho^2)^2(2x' - z) - 2k(k^2\varrho^2)(k\varrho)z = 0$$

and dividing on both sides with $(k^2\varrho^2)$ and then by $(k^2\varrho)$ we obtain

$$\varrho z'' - 2\varepsilon \sin(\theta)(z' + x) + \varrho(2x' - z) - 2z = 0$$

Expanding the parenthesis and substituting for ϱ on the z term gives

$$\varrho z'' - 2\varepsilon \sin(\theta) z' - 2\varepsilon \sin(\theta) x + 2\varrho x' - (3 + \varepsilon \cos(\theta)) z = 0 \tag{A.24}$$

The general transformation for one component of Equation (4.30), e.g. α has the first derivative as

$$\alpha' = \varrho' x + \varrho x'$$

$$\alpha' = \frac{\varrho'}{\varrho}\alpha + \varrho x'$$

$$x' = \frac{1}{\varrho}\left(\alpha' - \frac{\varrho'}{\varrho}\alpha\right) \tag{A.25}$$

as in Equation (4.32) and the second derivative becomes

$$\alpha'' = \varrho'' x + \varrho' x' + \varrho' x' + \varrho x''$$

$$\varrho x'' = \alpha'' - \varrho'' x - 2\varrho' x'$$

$$\varrho x'' = \alpha'' - \frac{\varrho''}{\varrho}\alpha - 2\frac{\varrho'}{\varrho}\left(\alpha' - \frac{\varrho'}{\varrho}\alpha\right) \tag{A.26}$$

For the third row of Equation (4.34) we obtain as in Equation (4.37)

$$\varrho z'' = -2\varrho' z' - 2\varrho' x - 2\varrho x' + (2+\varrho)z$$

$$\begin{aligned}
\gamma'' - \frac{\varrho''}{\varrho}\gamma - 2\frac{\varrho'}{\varrho}\left(\gamma' - \frac{\varrho'}{\varrho}\gamma\right) = \\
- 2\frac{\varrho'}{\varrho}\left(\gamma' - \frac{\varrho'}{\varrho}\gamma\right) - 2\frac{\varrho'}{\varrho}\alpha - \frac{2\varrho}{\varrho}\left(\alpha' - \frac{\varrho'}{\varrho}\alpha\right) + (2+\varrho)\frac{\gamma}{\varrho} \\
\gamma'' = \frac{\varrho''}{\varrho}\gamma - 2\frac{\varrho'}{\varrho}\alpha - 2\alpha' + 2\frac{\varrho'}{\varrho}\alpha + (2+\varrho)\frac{\gamma}{\varrho} \\
\gamma'' = -2\alpha' + \frac{\varrho'' + \varrho + 2}{\varrho}\gamma \\
\gamma'' = \frac{3}{\varrho}\gamma - 2\alpha'
\end{aligned} \tag{A.27}$$

A.3.2 Elements of Homogeneous In Plane Solution

We will now find the result of the under brace in Equation (4.56)

$$\lambda' = \varrho' \cos - \varrho \sin$$

$$\lambda'' = \varrho'' \cos - \varrho' \sin - \varrho' \sin - \varrho \cos$$

and inserting as defined in Equation (4.31) we get, writing the θ argument only when double angle

$$\lambda'' = -\varepsilon \cos^2 + 2\varepsilon \sin^2 - \cos - \varepsilon \cos^2$$

$$\lambda'' = -2\varepsilon \cos(2\theta) - \cos$$

Back substituting we obtain

$$\begin{aligned}
\lambda'' + (4 - \tfrac{3}{\varrho})\lambda &= -2\varepsilon \cos(2\theta) - \cos + 4\varrho \cos - 3\cos \\
&= -2\varepsilon \cos(2\theta) - \cos + 4\cos + 4\varepsilon \cos^2 - 3\cos \\
&= 2\varepsilon(2\cos^2 - \cos^2 + \sin^2) \\
&= 2\varepsilon
\end{aligned} \tag{A.28}$$

We will here calculate Equation (4.58) by inserting into Equation (4.57) using also Equation (4.31)

$$k_1(2(\varrho \cos - \varepsilon \sin^2)\varrho^{-2} + 2\varrho \sin^2 \varrho^{-3}\varepsilon) + k_2 2\varepsilon + 4 - \frac{3}{\varrho} = 0$$

$$
\begin{gathered}
k_1(2\varrho^{-1}\cos -2\varepsilon\varrho^{-2}\sin^2 +2\varepsilon\varrho^{-2}\sin^2) + k_2 2\varepsilon + 4 - \frac{3}{\varrho} = 0 \\
2k_1\cos +2\varepsilon k_2\varrho + 4\varrho - 3 = 0 \\
2k_1\cos +2\varepsilon k_2 + 2k_2\varepsilon^2\cos +4 + 4\varepsilon\cos -3 = 0 \\
(2k_1 + 4\varepsilon + 2k_2\varepsilon^2)\cos +2\varepsilon k_2 + 1 = 0
\end{gathered} \tag{A.29}
$$

A.3.3 Wronskian

The Wronskian in Equation (4.60) becomes

$$
\begin{aligned}
W &= \varphi_1\varphi_2' - \varphi_1'\varphi_2 \\
&= \varrho\sin\{3\varepsilon^2(\varrho'\sin J + \varrho\cos J + \varrho\sin J') + \varrho'\cos -\varrho\sin\} \\
&\quad -(\varrho'\sin +\varrho\cos)(3\varepsilon^2\varrho\sin J + \varrho\cos -2\varepsilon) \\
&= 3\varepsilon^2\varrho^2\sin^2 J' + 2\varepsilon\varrho'\sin +2\varepsilon\varrho\cos -\varrho^2(\sin^2 +\cos^2) \\
&= 3\varepsilon^2\sin^2 -2\varepsilon^2\sin^2 +2\varepsilon\cos +2\varepsilon^2\cos^2 -1 - \varepsilon^2\cos^2 -2\varepsilon\cos \\
&= \varepsilon^2\sin^2 +\varepsilon^2\cos^2 -1 \\
&= \varepsilon^2 - 1
\end{aligned} \tag{A.30}
$$

A.3.4 Particular Solution Integrals

The solution to Equation (4.68) becomes

$$
\begin{aligned}
-3\varepsilon\int Jg'd\theta &= -3\varepsilon\left[Jg - \int J'g\right] \\
&= -3\varepsilon\left[Jg - \frac{1}{2}\int d\theta\right] \\
&= -3\varepsilon\left[Jg - \frac{1}{2}\theta\right] \\
&= -3\varepsilon\left[\frac{1}{2}\varrho^2 J - \frac{1}{2}\theta\right] \\
&= -\frac{3}{2}\varepsilon\varrho^2 J + \frac{3}{2}\varepsilon\theta
\end{aligned} \tag{A.31}
$$

The solution to Equation (4.69) becomes

$$
\begin{aligned}
\int(\varrho\cos -2\varepsilon)d\theta &= \int((1+\varepsilon\cos)\cos -2\varepsilon)\,d\theta \\
&= \int\left(\cos +\varepsilon\cos^2 -2\varepsilon\right)d\theta \\
&= \sin +\varepsilon\left(\frac{\theta}{2} + \frac{\sin(2\theta)}{4}\right) - 2\varepsilon\theta \\
&= \sin -\frac{3}{2}\varepsilon\theta + \frac{1}{2}\varepsilon\sin\cos
\end{aligned} \tag{A.32}
$$

We now add Equations (A.31) and (A.32) to get the integral yielding

$$\begin{aligned}\int \varphi_2 d\theta &= -\frac{3}{2}\varepsilon\varrho^2 J + \frac{3}{2}\varepsilon\theta + \sin - \frac{3}{2}\varepsilon\theta + \frac{1}{2}\varepsilon\sin\cos \\ &= -\frac{3}{2}\varepsilon\varrho^2 J + \sin(1 + \frac{1}{2}\varepsilon\cos) \\ &= -\frac{3}{2}\varepsilon\varrho^2 J + \frac{1}{2}(2 + \varepsilon\cos)\sin \\ &= -\frac{3}{2}\varepsilon\varrho^2 J + \frac{1}{2}(1 + \varrho)\sin \end{aligned} \tag{A.33}$$

To find the particular solution φ_p we insert Equations (4.45), (4.59), (4.66) and (4.70) into Equation (4.65) and obtain

$$\begin{aligned}\varphi_p &= \frac{2k_{\alpha_1}}{\varepsilon^2 - 1}\left[\varrho\sin\left(-\frac{3}{2}\varepsilon\varrho^2 J + \frac{1}{2}(1+\varrho)\sin\right)\right] \\ &\quad -\frac{2k_{\alpha_1}}{\varepsilon^2 - 1}\left[(3\varepsilon^2\varrho\sin J + \varrho\cos - 2\varepsilon)\left(-\frac{1}{2\varepsilon}\varrho^2\right)\right] \\ &= \frac{k_{\alpha_1}}{\varepsilon^2 - 1}\left[\varrho\sin((\varrho+1)\sin - 3\varepsilon\varrho^2 J) + (3\varepsilon^2\varrho\sin J + \varrho\cos - 2\varepsilon)\frac{\varrho^2}{\varepsilon}\right] \\ &= \frac{k_{\alpha_1}}{\varepsilon^2 - 1}\left[\varrho^2\sin^2 + \varrho\sin^2 + \frac{1}{\varepsilon}\varrho^3\cos - 2\varrho^2\right] \\ &= \frac{k_{\alpha_1}}{\varepsilon^2 - 1}\varrho\left[\varrho\sin^2 + \sin^2 + \frac{1}{\varepsilon}\varrho^2\cos - 2\varrho\right] \\ &= \frac{k_{\alpha_1}}{\varepsilon^2 - 1}\varrho\left[\varrho\sin^2 + \sin^2 + \frac{1}{\varepsilon}\varrho(1+\varepsilon\cos)\cos - 2\varrho\right]\end{aligned}$$

$$\begin{aligned}\varphi_p &= \frac{k_{\alpha_1}}{\varepsilon^2 - 1}\varrho\left[-\varrho + \sin^2 + \frac{1}{\varepsilon}(1+\varepsilon\cos)\cos\right] \\ &= \frac{k_{\alpha_1}}{\varepsilon^2 - 1}\varrho\left[-1 - \varepsilon\cos + 1 + \frac{1}{\varepsilon}\cos\right] \\ &= \frac{k_{\alpha_1}}{\varepsilon^2 - 1}\varrho\cos\frac{1-\varepsilon^2}{\varepsilon} \\ &= -\frac{k_{\alpha_1}}{\varepsilon}\varrho\cos\end{aligned} \tag{A.34}$$

A.3.5 Integration of α'

Computation of Equation (4.75)

$$\alpha' = 2k_{\gamma_1}\varrho\sin + \left(k_{\gamma_2} - \frac{k_{\alpha_1}}{\varepsilon}\right)2\varrho\cos + k_{\alpha_1} - 4k_{\gamma_2}\varepsilon + 6k_{\gamma_2}\varepsilon^2\varrho\sin J$$

$$\alpha' = 2k_{\gamma_1}\varrho\sin + \left(k_{\gamma_2} - \frac{k_{\alpha_1}}{\varepsilon}\right)2\varrho\cos + \frac{k_{\alpha_1}}{\varepsilon}\varepsilon - k_{\gamma_2}\varepsilon - 3k_{\gamma_2}\varepsilon + 6k_{\gamma_2}\varepsilon^2\varrho\sin J$$

$$\alpha' = 2k_{\gamma_1}\varrho\sin + \left(k_{\gamma_2} - \frac{k_{\alpha_1}}{\varepsilon}\right)(2\varrho\cos - \varepsilon) - 3k_{\gamma_2}\varepsilon(1 - 2\varepsilon\varrho\sin J) \tag{A.35}$$

Equation (4.76) becomes

$$\begin{aligned}
\int \varrho\sin d\theta &= \int (1+\varepsilon\cos)\sin d\theta \\
&= \int (\sin + \varepsilon\cos\sin)d\theta \\
&= \int \sin d\theta + \varepsilon\int \sin\cos d\theta \\
&= -\cos - \varepsilon\int -\sin\cos d\theta \\
&= -\cos - \varepsilon\frac{1}{2}\cos^2 \\
&= -\frac{1}{2}(2\cos + \varepsilon\cos^2) \\
&= -\frac{1}{2}(\varrho+1)\cos
\end{aligned} \tag{A.36}$$

Equation (4.77) becomes

$$\begin{aligned}
\int (2\varrho\cos - \varepsilon)d\theta &= \int (2(1+\varepsilon\cos)\cos - \varepsilon)d\theta \\
&= \int (2\cos + 2\varepsilon\cos^2 - \varepsilon)d\theta \\
&= \int (2\cos + 2\varepsilon\cos^2 - \varepsilon(\cos^2+\sin^2))d\theta \\
&= \int (2\cos + \varepsilon\cos^2 - \varepsilon\sin^2)d\theta \\
&= 2\sin + \varepsilon\left[\frac{1}{2}\theta + \frac{1}{4}\sin(2\theta) - \frac{1}{2}\theta + \frac{1}{4}\sin(2\theta)\right] \\
&= 2\sin + \frac{1}{2}\varepsilon\sin(2\theta) \\
&= 2\sin + \varepsilon\sin\cos \\
&= (1+\varrho)\sin
\end{aligned} \tag{A.37}$$

Equation (4.78) becomes

$$\begin{aligned}\int (1-2\varepsilon\varrho\sin J)d\theta &= \int d\theta - 2\int \varepsilon\varrho\sin J d\theta \\ &= \theta + 2\int \varrho\varrho' J d\theta \\ &= \theta + 2\int Jg' d\theta \\ &= \theta + 2\left[Jg - \int J'g d\theta\right] \\ &= \theta + 2\left[Jg - \frac{1}{2}\int d\theta\right] \\ &= \theta + 2Jg - \theta \\ &= \varrho^2 J \end{aligned} \tag{A.38}$$

A.3.6 Differentiation of γ

For $\gamma'(\theta)$ it is easier to differentiate Equation (4.82) to obtain Equation (4.84)

$$\begin{aligned}\gamma'(\theta) &= k_2(\varrho'\sin+\varrho\cos)+k_3(\varrho'\cos-\varrho\sin)-3k_4\varepsilon(\varrho'\sin J+\varrho\cos J+\varrho\sin J') \\ \gamma'(\theta) &= k_2[-\varepsilon\sin^2+(1+\varepsilon\cos)\cos]+k_3[-\varepsilon\sin\cos-(1+\varepsilon\cos)\sin] \\ &\quad -3k_4\varepsilon[(\varrho'\sin+\varrho\cos)J+\varrho\sin J'] \\ \gamma'(\theta) &= k_2[\cos(\theta)+\varepsilon\cos(2\theta)]-k_3[\sin(\theta)+\varepsilon\sin(2\theta)] \\ &\quad -3k_4\varepsilon\left[(\cos(\theta)+\varepsilon\cos(2\theta))J(\theta)+\frac{1}{\varrho(\theta)}\sin(\theta)\right] \end{aligned} \tag{A.39}$$

A.3.7 Transition Matrix Φ_0 Determinant

We will now find the determinant of Equation (4.88) using the first column for elimination and leave out the argument for convenience

$$\begin{aligned}\det\mathbf{\Phi}_0 &= \varrho\sin(2\varrho\cos-\varepsilon)(-3\varepsilon\frac{\sin}{\varrho})+3\varrho\cos(\cos+\varepsilon\cos(2\theta))-4\varrho\sin(\sin+\varepsilon\sin(2\theta)) \\ &\quad -2(2\varrho\cos-\varepsilon)(\cos+\varepsilon\cos(2\theta))+(\sin+\varepsilon\sin(2\theta))3\varrho\sin+3\varepsilon\frac{\sin}{\varrho}2\varrho\sin\varrho\cos \\ &= -\varrho\cos^2-\varrho\sin^2-\varrho\varepsilon\cos\cos(2\theta)-\varrho\varepsilon\sin\sin(2\theta) \\ &\quad +2\varepsilon\cos+2\varepsilon^2\cos(2\theta)+3\varepsilon^2\sin^2 \\ &= -\varrho-\varrho\varepsilon\cos^3+\varrho\varepsilon\cos\sin^2-2\varrho\varepsilon\cos\sin^2 \\ &\quad +2\varepsilon\cos+2\varepsilon^2\cos^2-2\varepsilon^2\sin^2+3\varepsilon^2\sin^2 \\ &= -\varrho-\varrho\varepsilon\cos+2\varepsilon\cos+\varepsilon^2(2\cos^2+\sin^2) \\ &= -1-\varepsilon\cos-\varepsilon\cos-\varepsilon^2\cos^2+2\varepsilon\cos+2\varepsilon^2\cos^2+\varepsilon^2\sin^2 \\ &= \varepsilon^2-1 \end{aligned} \tag{A.40}$$

A.3.8 Transition Matrix $\mathbf{\Phi}_0$ Inverse

We will now find the cofactors for all 16 elements of $\mathbf{\Phi}$ in order to determine the inverse matrix. We find the minors of $\mathbf{\Phi}_0$ and later transpose the adjoint matrix and divide by $\det \mathbf{\Phi}_0$ to obtain $\mathbf{\Phi}_0^{-1}$ (Ogata 1970). Here we will not write all the intermediate calculation for the minors M_{ij}, as they are fairly trivial trigonometric manipulations, but the first line followed by the result.

$$M_{11} = \varepsilon^2 - 1$$

$$\begin{aligned} M_{21} &= -(\varrho+1)\cos(2\varrho\cos - \varepsilon)\left(-3\varepsilon\frac{\sin}{\varrho}\right) + 3(\varrho+1)\sin(\cos + \varepsilon\cos(2\theta)) \\ &\quad + 3(\sin + \varepsilon\sin(2\theta))(-(\varrho+1)\cos) + 3\varepsilon\frac{\sin}{\varrho}2\varrho\sin(\varrho+1)\sin \\ M_{21} &= 3\varepsilon\frac{\varrho+1}{\varrho}\sin \end{aligned}$$

$$\begin{aligned} M_{31} &= -(\varrho+1)\cos\varrho\cos\left(-3\varepsilon\frac{\sin}{\varrho}\right) + 2(\varrho+1)\sin(\cos + \varepsilon\cos(2\theta)) \\ &\quad + (\sin + \varepsilon\sin(2\theta))2(-(\varrho+1)\cos) + 3\varepsilon\frac{\sin}{\varrho}\varrho\sin(\varrho+1)\sin \\ M_{31} &= (\varrho+1)\varepsilon\sin \end{aligned}$$

$$\begin{aligned} M_{41} &= -3(\varrho+1)\cos\varrho\cos + 4(\varrho+1)\sin\varrho\sin \\ &\quad + 2(2\varrho\cos - \varepsilon)(\varrho+1)\cos - 3(\varrho+1)\sin\varrho\sin \\ M_{41} &= 2 - \varrho\varepsilon\cos \end{aligned}$$

$$M_{12} = 0$$

$$\begin{aligned} M_{22} &= -3\varepsilon\frac{\sin}{\varrho}(2\varrho\cos - \varepsilon) + 3(\sin + \varepsilon\sin(2\theta)) \\ M_{22} &= 3\sin\left(\frac{\varepsilon^2}{\varrho} + 1\right) \end{aligned}$$

$$\begin{aligned} M_{32} &= -3\varepsilon\frac{\sin}{\varrho}\varrho\cos + 2(\sin + \varepsilon\sin(2\theta)) \\ M_{32} &= (\varrho+1)\sin \end{aligned}$$

$$M_{42} = 3\varrho\cos - 2(2\varrho\cos - \varepsilon)$$

$$M_{42} = 2\varepsilon - \varrho\cos$$

$$M_{13} = 0$$

$$M_{23} = -3\varepsilon\frac{\sin}{\varrho}2\varrho\sin -3(\cos +\varepsilon\cos(2\theta))$$
$$M_{23} = -3(\varepsilon + \cos)$$

$$M_{33} = -3\varepsilon\frac{\sin}{\varrho}\varrho\sin -2(\cos +\varepsilon\cos(2\theta))$$
$$M_{33} = -((\varrho + 1)\cos +\varepsilon)$$

$$M_{43} = 3\varrho\sin -4\varrho\sin$$
$$M_{43} = -\varrho\sin$$

$$M_{14} = 0$$

$$M_{24} = -2\varrho\sin(\sin +\varepsilon\sin(2\theta)) - (\cos +\varepsilon\cos(2\theta))(2\varrho\cos -\varepsilon)$$
$$M_{24} = 1 - 3\varrho - \varepsilon^2$$

$$M_{34} = -\varrho\sin(\sin +\varepsilon\sin(2\theta)) - \varrho\cos(\cos +\varepsilon\cos(2\theta))$$
$$M_{34} = -\varrho^2$$

$$M_{44} = \varrho\sin(2\varrho\cos -\varepsilon) - 2\varrho\sin\varrho\cos$$
$$M_{44} = -\varepsilon\varrho\sin$$

We now know that the elements of the inverse become

$$\tilde{a}_{ij} = \frac{A_{ji}}{\det\mathbf{A}} \qquad\qquad A_{ij} = (-1)^{i+j}M_{ij}$$

We will insert all the minors, transpose and find the adjoint matrix. For convenience the resulting inverse matrix will be multiplied through with (-1) in both numerator and denominator and $\varrho(\theta_0) = \varrho_0$.

$$\mathbf{\Phi}_0^{-1} = \frac{1}{1-\varepsilon^2}\begin{bmatrix} 1-\varepsilon^2 & 3\varepsilon\frac{\varrho_0+1}{\varrho_0}\sin(\theta_0) & -(\varrho_0+1)\varepsilon\sin(\theta_0) & 2-\varrho_0\varepsilon\cos(\theta_0) \\ 0 & -3\left(\frac{\varepsilon^2}{\varrho_0}+1\right)\sin(\theta_0) & (\varrho_0+1)\sin(\theta_0) & \varrho_0\cos(\theta_0)-2\varepsilon \\ 0 & -3(\varepsilon+\cos(\theta_0)) & \varepsilon+(\varrho_0+1)\cos(\theta_0) & -\varrho_0\sin(\theta_0) \\ 0 & \varepsilon^2+3\varrho_0-1 & -\varrho_0^2 & \varepsilon\varrho_0\sin(\theta_0) \end{bmatrix} \tag{A.41}$$

A.3.9 Transition Matrix Φ Determinant

We will now find the determinant of Equation (4.85) using the first column for elimination and leave out the argument for convenience. The second column is used for finding the sub determinants.

$$\begin{aligned}
\det \mathbf{\Phi} \;=\; & \varrho \sin \begin{vmatrix} 2\varrho\cos -\varepsilon & 3(1-2\varepsilon\varrho\sin J) \\ -(\sin +\varepsilon\sin(2\theta)) & -3\varepsilon\left[(\cos +\varepsilon\cos(2\theta))J+\frac{\sin}{\varrho}\right] \end{vmatrix} \\
& -2\varrho\sin \begin{vmatrix} \varrho\cos & 2-3\varepsilon\varrho\sin J \\ -(\sin +\varepsilon\sin(2\theta)) & -3\varepsilon\left[(\cos +\varepsilon\cos(2\theta))J+\frac{\sin}{\varrho}\right] \end{vmatrix} \\
& +(\cos +\varepsilon\cos(2\theta)) \begin{vmatrix} \varrho\cos & 2-3\varepsilon\varrho\sin J \\ 2\varrho\cos -\varepsilon & 3(1-2\varepsilon\varrho\sin J) \end{vmatrix}
\end{aligned} \tag{A.42}$$

All terms without J gives the earlier result $\varepsilon^2 - 1$ from Equation (4.89), so we will now continue only with the terms containing J. We will omit most of the trivial expansions and trigonometric manipulations.

$$\begin{aligned}
& \varrho\sin\left[3\varepsilon^2(\cos+\varepsilon\cos(2\theta))J-6\varepsilon\varrho\cos(\cos+\varepsilon\cos(2\theta))J-6\varepsilon\varrho\sin^2 J-6\varepsilon^2\varrho\sin\sin(2\theta)J\right] \\
& -2\varrho\sin\left[-3\varepsilon\varrho\cos(\cos+\varepsilon\cos(2\theta))J-3\varepsilon\varrho\sin^2 J-3\varepsilon^2\varrho\sin\sin(2\theta)J\right] \\
& +(\cos+\varepsilon\cos(2\theta))(-3\varepsilon^2\varrho\sin J) = \\
& J\left[3\varepsilon^2\varrho\sin\cos+3\varepsilon^3\varrho\sin\cos(2\theta)-3\varepsilon^2\varrho\sin\cos-3\varepsilon^3\varrho\sin\cos(2\theta)\right] = J\cdot 0 = 0
\end{aligned} \tag{A.43}$$

Hence there is no contribution to the determinant from the J terms in $\mathbf{\Phi}$.

A.3.10 Transition Matrix Φ Inverse for Particular Solution

We will now find the minors for all 6 elements of $\mathbf{\Phi}$ in order to determine the inverse matrix needed for the particular in plane solution. Again the minor is the result obtained in Section A.3.8 plus the terms holding J, which we will take advantage of to simplify computations. Here we will not write all the intermediate calculation for the minors M_{ij}, as they are fairly trivial trigonometric manipulations, but the first line followed by the result.

$$M_{31} = \det \begin{bmatrix} -(\varrho+1)\cos & (\varrho+1)\sin & 3\varrho^2 J \\ \varrho\sin & \varrho\cos & 2-3\varepsilon\varrho\sin J \\ \cos+\varepsilon\cos(2\theta) & -(\sin+\varepsilon\sin(2\theta)) & -3\varepsilon\left[(\cos+\varepsilon\cos(2\theta))J+\frac{\sin}{\varrho}\right] \end{bmatrix}$$

Now collecting only the terms with J we get

$$\begin{aligned}
M_{31}(J) = & -(\varrho+1)\cos\left[-3\varepsilon\varrho\cos(\cos+\varepsilon\cos(2\theta))J-3\varepsilon\varrho\sin^2 J-3\varepsilon^2\varrho\sin\sin(2\theta)J\right] \\
& -\varrho\sin\left[-3\varepsilon(\varrho+1)\sin(\cos+\varepsilon\cos(2\theta))J+3\varrho^2\sin J+3\varepsilon\varrho^2\sin(2\theta)J\right] \\
& +(\cos+\varepsilon\cos(2\theta))\left[-3\varepsilon\varrho(\varrho+1)\sin^2 J-3\varrho^3\cos J\right] \\
M_{31}(J) = & -3\varrho^2 J
\end{aligned}$$

Using the earlier result the complete minor yield

$$\underline{M_{31} = (\varrho+1)\varepsilon\sin - 3\varrho^2 J} \tag{A.44}$$

$$M_{41} = \det\begin{bmatrix} -(\varrho+1)\cos & (\varrho+1)\sin & 3\varrho^2 J \\ \varrho\sin & \varrho\cos & 2-3\varepsilon\varrho\sin J \\ 2\varrho\sin & 2\varrho\cos - \varepsilon & 3(1-2\varepsilon\varrho\sin J) \end{bmatrix}$$

Now collecting only the terms with J we get

$$\begin{aligned} M_{41}(J) &= 3\varepsilon^2\varrho(\varrho+1)\cos\sin J + 6\varepsilon\varrho^2(\varrho+1)\sin^3 J - 3\varepsilon\varrho^3\sin J \\ &\quad +6\varrho^4\cos\sin J - 6\varepsilon\varrho^2(\varrho+1)\sin^3 J - 6\varrho^4\cos\sin J \\ M_{41}(J) &= -3\varepsilon\varrho\sin J \end{aligned}$$

Using the earlier result the complete minor yield

$$\underline{M_{41} = 2 - \varepsilon\varrho(\cos + 3\sin J)} \tag{A.45}$$

Below arbitrary elements will be marked with a $\star$ as they have no contribution due to the structure.

$$M_{32} = \det\begin{bmatrix} 1 & \star & \star \\ 0 & \varrho\cos & 2-3\varepsilon\varrho\sin J \\ 0 & -(\sin + \varepsilon\sin(2\theta)) & -3\varepsilon\left[(\cos + \varepsilon\cos(2\theta))J + \frac{\sin}{\varrho}\right] \end{bmatrix}$$

Now collecting only the terms with J we get

$$\begin{aligned} M_{32}(J) &= -3\varepsilon\varrho\cos(\cos + \varepsilon\cos(2\theta))J - 3\varepsilon\varrho\sin^2 J - 3\varepsilon^2\varrho\sin\sin(2\theta)J \\ M_{32}(J) &= -3\varepsilon\varrho^2 J \end{aligned}$$

Using the earlier result the complete minor yield

$$\underline{M_{32} = (\varrho+1)\sin - 3\varepsilon\varrho^2 J} \tag{A.46}$$

$$M_{42} = \det\begin{bmatrix} 1 & \star & \star \\ 0 & \varrho\cos & 2-3\varepsilon\varrho\sin J \\ 0 & 2\varrho\cos - \varepsilon & 3(1-2\varepsilon\varrho\sin J) \end{bmatrix}$$

Now collecting only the terms with J we get

$$\begin{aligned} M_{42}(J) &= -6\varepsilon\varrho^2\cos\sin J - 3\varepsilon^2\varrho\sin J + 6\varepsilon\varrho^2\cos\sin J \\ M_{42}(J) &= -3\varepsilon^2\varrho\sin J \end{aligned}$$

Using the earlier result the complete minor yield

$$\underline{M_{42} = 2\varepsilon - \varrho\cos - 3\varepsilon^2\varrho\sin J} \tag{A.47}$$

$$M_{33} = \det\begin{bmatrix} 1 & \star & \star \\ 0 & \varrho\sin & 2-3\varepsilon\varrho\sin J \\ 0 & \cos + \varepsilon\cos(2\theta) & -3\varepsilon\left[(\cos + \varepsilon\cos(2\theta))J + \frac{\sin}{\varrho}\right] \end{bmatrix}$$

Now collecting only the terms with J we get

$$\begin{aligned} M_{33}(J) &= -3\varepsilon\varrho\sin(\cos+\varepsilon\cos(2\theta))J + 3\varepsilon\varrho\sin(\cos+\varepsilon\cos(2\theta))J \\ M_{33}(J) &= 0 \end{aligned}$$

Using the earlier result the complete minor yield

$$\underline{M_{33} = -((\varrho+1)\cos+\varepsilon)} \tag{A.48}$$

$$M_{43} = \det\begin{bmatrix} 1 & \star & \star \\ 0 & \varrho\sin & 2-3\varepsilon\varrho\sin J \\ 0 & 2\varrho\sin & 3(1-2\varepsilon\varrho\sin J) \end{bmatrix}$$

Now collecting only the terms with J we get

$$\begin{aligned} M_{43}(J) &= -6\varepsilon\varrho^2\sin^2 J + 6\varepsilon\varrho^2\sin^2 J \\ M_{43}(J) &= 0 \end{aligned}$$

Using the earlier result the complete minor yield

$$\underline{M_{43} = -\varrho\sin} \tag{A.49}$$

The last two minors are unchanged from earlier, but we will list them here for the sake of completeness.

$$\underline{M_{34} = -\varrho^2} \tag{A.50}$$

$$\underline{M_{44} = -\varepsilon\varrho\sin} \tag{A.51}$$

A.4 Coefficients for Transfer of Duration One Orbit

The denominator coefficients of Equation (4.138) for $t = T$, $\theta = \theta_0$, $\varrho = \varrho_0$ and $J = k^2T$ are found.

$$\begin{aligned} d_{13} &= \frac{1}{k^2\varrho_0^2}(\mathbf{\Phi}\mathbf{\Phi}_0^{-1})_{13} \\ d_{13} &= [-(\varrho_0+1)\varepsilon\sin(\theta_0) - (\varrho_0+1)(\varrho_0+1)\cos(\theta_0)\sin(\theta_0) + \\ &\quad (\varrho_0+1)(\varepsilon+(\varrho_0+1)\cos(\theta_0))\sin(\theta_0) - 3\varrho_0^2\varrho_0^2 J]\frac{1}{k^2\varrho_0^2(1-\varepsilon^2)} \\ d_{13} &= -\frac{3\varrho_0^2 T}{1-\varepsilon^2} \end{aligned} \tag{A.52}$$

$$\begin{aligned} d_{14} &= \frac{1}{k^2\varrho_0^2}(\mathbf{\Phi}\mathbf{\Phi}_0^{-1})_{14} \\ d_{14} &= [2-\varrho_0\varepsilon\cos(\theta_0) - (\varrho_0+1)\cos(\theta_0)(\varrho_0\cos(\theta_0)-2\varepsilon) - \\ &\quad \varrho_0\sin(\theta_0)(\varrho_0+1)\sin(\theta_0) + 3\varrho_0^3\varepsilon\sin(\theta_0)J]\frac{1}{k^2\varrho_0^2(1-\varepsilon^2)} \\ d_{14} &= \frac{3\varrho_0\varepsilon\sin(\theta_0)T}{1-\varepsilon^2} \end{aligned} \tag{A.53}$$

$$
\begin{aligned}
d_{23} &= \frac{1}{k^2\varrho_0^2}(\mathbf{\Phi}\mathbf{\Phi}_0^{-1})_{23} \\
d_{23} &= [(\varrho_0+1)\varrho_0\sin(\theta_0)^2 + \varrho_0(\varepsilon+(\varrho_0+1)\cos(\theta_0))\cos(\theta_0) - \\
&\quad (2-3\varepsilon\varrho_0\sin(\theta_0)J)\varrho_0^2]\frac{1}{k^2\varrho_0^2(1-\varepsilon^2)} \\
d_{23} &= \frac{3\varepsilon\varrho_0\sin(\theta_0)T}{1-\varepsilon^2}
\end{aligned} \tag{A.54}
$$

$$
\begin{aligned}
d_{24} &= \frac{1}{k^2\varrho_0^2}(\mathbf{\Phi}\mathbf{\Phi}_0^{-1})_{24} \\
d_{24} &= [\varrho_0\sin(\theta_0)(\varrho_0\cos(\theta_0)-2\varepsilon) - \varrho_0^2\cos(\theta_0)\sin(\theta_0) + \\
&\quad 2\varepsilon\varrho_0\sin(\theta_0) - 3\varepsilon^2\varrho_0^2\sin(\theta_0)^2 J]\frac{1}{k^2\varrho_0^2(1-\varepsilon^2)} \\
d_{24} &= -\frac{3(\varepsilon\sin(\theta_0))^2 T}{1-\varepsilon^2}
\end{aligned} \tag{A.55}
$$

A.5 Combined State Space Model

The Equations (4.16) and (4.18) will here be combined into one system by defining a state vector $\mathbf{x}_p = [x, y, z, \dot{x}, \dot{y}, \dot{z}]^{\mathrm{T}}$ and $\mathbf{F} = [F_x, F_y, F_z]^{\mathrm{T}}$.

$$
\dot{\mathbf{x}}_p = \begin{bmatrix}
0 & 0 & 0 & 1 & 0 & 0 \\
0 & 0 & 0 & 0 & 1 & 0 \\
0 & 0 & 0 & 0 & 0 & 1 \\
\omega^2 - k\omega^{\frac{3}{2}} & 0 & \dot{\omega} & 0 & 0 & 2\omega \\
0 & -k\omega^{\frac{3}{2}} & 0 & 0 & 0 & 0 \\
-\dot{\omega} & 0 & \omega^2 + 2k\omega^{\frac{3}{2}} & -2\omega & 0 & 0
\end{bmatrix} \mathbf{x}_p + \begin{bmatrix}
0 & 0 & 0 \\
0 & 0 & 0 \\
0 & 0 & 0 \\
\frac{1}{m_c} & 0 & 0 \\
0 & \frac{1}{m_c} & 0 \\
0 & 0 & \frac{1}{m_c}
\end{bmatrix} \mathbf{F} \tag{A.56}
$$

$$
\boxed{\dot{\mathbf{x}}_p = \mathbf{A}_p\mathbf{x}_p + \mathbf{B}_p\mathbf{F}} \tag{A.57}
$$

A.6 Integral Details of Section 4.8.1

This section contains the detailed solutions to selected integrals including the intermediate calculations.

Integral I_3 from Equation (4.189) becomes

$$\begin{aligned}
I_3(\theta) &= \int_{\theta_0}^{\theta} \frac{1}{\varrho(\theta)^3} d\theta = \int_{E_0}^{E} f(E) dE = (1-\varepsilon^2)^{-\frac{5}{2}} \int_{E_0}^{E} (1-\varepsilon\cos(E))^2 dE \\
I_3(E) &= (1-\varepsilon^2)^{-\frac{5}{2}} \int_{E_0}^{E} (1+\varepsilon^2\cos(E)^2 - 2\varepsilon\cos(E)) dE \\
I_3(E) &= (1-\varepsilon^2)^{-\frac{5}{2}} \left[E + \varepsilon^2 (\frac{1}{2}E + \frac{1}{4}\sin(2E)) - 2\varepsilon\sin(E) \right]_{E_0}^{E} \\
I_3(E) &= (1-\varepsilon^2)^{-\frac{5}{2}} \Big[(\frac{1}{2}\varepsilon^2 + 1)(E-E_0) + \frac{1}{2}\varepsilon^2(\sin(E)\cos(E) - \sin(E_0)\cos(E_0)) \\
&\quad -2\varepsilon(\sin(E) - \sin(E_0)) \Big] \qquad \text{(A.58)}
\end{aligned}$$

Integral $I_{s_{2J}}$ from Equation (4.192) becomes

$$\begin{aligned}
I_{s_{2J}}(\theta) &= \int_{\theta_0}^{\theta} \frac{\sin(\theta)}{\varrho(\theta)^2} J(\theta) d\theta = \int_{\theta_0}^{\theta} \frac{\sin(\theta)}{\varrho(\theta)^2} \left(\int_{\theta_0}^{\theta} \frac{1}{\varrho(\tau)^2} d\tau \right) d\theta \\
I_{s_{2J}}(E) &= (1-\varepsilon^2)^{-1} (1-\varepsilon^2)^{-\frac{3}{2}} \int_{E_0}^{E} \sin(E)(E - \varepsilon\sin(E) + C_1) dE \\
I_{s_{2J}}(E) &= (1-\varepsilon^2)^{-\frac{5}{2}} \int_{E_0}^{E} (E\sin(E) - \varepsilon\sin(E)^2 + C_1\sin(E)) dE \\
I_{s_{2J}}(E) &= (1-\varepsilon^2)^{-\frac{5}{2}} \Big[\sin(E) - E\cos(E) - \varepsilon(\frac{1}{2}E - \frac{1}{4}\sin(2E)) - C_1\cos(E) \Big]_{E_0}^{E} \\
I_{s_{2J}}(E) &= (1-\varepsilon^2)^{-\frac{5}{2}} \Big[\sin(E)(1+\frac{\varepsilon}{2}\cos(E)) - E(\frac{\varepsilon}{2}+\cos(E)) - \sin(E_0)(1+\frac{\varepsilon}{2}\cos(E_0)) \\
&\quad + E_0(\frac{\varepsilon}{2}+\cos(E_0)) - C_1(\cos(E)-\cos(E_0)) \Big] \qquad \text{(A.59)}
\end{aligned}$$

A.7 Integral Details of Section 4.8.2

This section contains the detailed solutions to selected integrals including the intermediate calculations.
Integral $I_{s_{32}}$ from Equation (4.202) becomes using the substitutions of Equations (4.173)

and (4.177)

$$
\begin{aligned}
I_{s_{32}}(\theta) &= \int_{\theta_0}^{\theta} \frac{\sin(\theta)^2}{\varrho(\theta)^3} d\theta = \int_{E_0}^{E} f(E) dE \\
I_{s_{32}}(E) &= \int_{E_0}^{E} \frac{\left(\frac{\sqrt{1-\varepsilon^2}\sin(E)}{1-\varepsilon\cos(E)}\right)^2}{\left(\frac{1-\varepsilon^2}{1-\varepsilon\cos(E)}\right)^3} (1-\varepsilon^2)^{\frac{1}{2}} (1-\varepsilon\cos(E))^{-1} dE \\
I_{s_{32}}(E) &= (1-\varepsilon^2)^{-\frac{3}{2}} \int_{E_0}^{E} \sin(E)^2 dE = (1-\varepsilon^2)^{-\frac{3}{2}} \left[\frac{1}{2}E - \frac{1}{4}\sin(2E)\right]_{E_0}^{E} \\
I_{s_{32}}(E) &= \frac{1}{2}(1-\varepsilon^2)^{-\frac{3}{2}} \left[E - E_0 - (\sin(E)\cos(E) - \sin(E_0)\cos(E_0))\right] \quad \text{(A.60)}
\end{aligned}
$$

Integral I_{sc_3} from Equation (4.204) becomes

$$
\begin{aligned}
I_{sc_3}(\theta) &= \int_{\theta_0}^{\theta} \frac{\sin(\theta)\cos(\theta)}{\varrho(\theta)^3} d\theta = \int_{E_0}^{E} f(E) dE \\
I_{sc_3}(E) &= (1-\varepsilon^2)^{-2} \int_{E_0}^{E} \sin(E)(\cos(E) - \varepsilon) dE \\
I_{sc_3}(E) &= (1-\varepsilon^2)^{-2} \int_{E_0}^{E} (\sin(E)\cos(E) - \varepsilon\sin(E)) dE \\
I_{sc_3}(E) &= (1-\varepsilon^2)^{-2} \left[\frac{1}{2}\sin(E)^2 + \varepsilon\cos(E)\right]_{E_0}^{E} \\
I_{sc_3}(E) &= (1-\varepsilon^2)^{-2} \left[\frac{1}{2}(\sin(E)^2 - \sin(E_0)^2) + \varepsilon(\cos(E) - \cos(E_0))\right] \quad \text{(A.61)}
\end{aligned}
$$

Integral I_{sc_2} from Equation (4.206) becomes adding and subtracting $\sin(\theta)$

$$
\begin{aligned}
I_{sc_2}(\theta) &= \int_{\theta_0}^{\theta} \frac{\sin(\theta)\cos(\theta)}{\varrho(\theta)^2} d\theta = -\frac{1}{\varepsilon} \int_{\theta_0}^{\theta} \frac{-\varepsilon\sin(\theta)\cos(\theta)}{\varrho(\theta)^2} d\theta \\
I_{sc_2}(\theta) &= -\frac{1}{\varepsilon} \int_{\theta_0}^{\theta} \frac{\sin(\theta) - \sin(\theta) - \varepsilon\sin(\theta)\cos(\theta)}{\varrho(\theta)^2} d\theta \\
I_{sc_2}(\theta) &= -\frac{1}{\varepsilon} \int_{\theta_0}^{\theta} \frac{\sin(\theta) - \sin(\theta)(1+\varepsilon\cos(\theta))}{(1+\varepsilon\cos(\theta))^2} d\theta \\
I_{sc_2}(\theta) &= -\frac{1}{\varepsilon^2} \int_{\theta_0}^{\theta} \left[\frac{\varepsilon\sin(\theta)}{(1+\varepsilon\cos(\theta))^2} - \frac{\varepsilon\sin(\theta)}{1+\varepsilon\cos(\theta)}\right] d\theta \\
I_{sc_2}(\theta) &= -\frac{1}{\varepsilon^2} \left[\frac{1}{1+\varepsilon\cos(\theta)} + \ln(1+\varepsilon\cos(\theta))\right]_{\theta_0}^{\theta} \\
I_{sc_2}(\theta) &= -\frac{1}{\varepsilon^2} \left[\frac{1}{\varrho} + \ln(\varrho) - \left(\frac{1}{\varrho_0} + \ln(\varrho_0)\right)\right] \quad \text{(A.62)}
\end{aligned}
$$

Integral $I_{c_{32}}$ from Equation (4.207) becomes

$$\begin{aligned}
I_{c_{32}}(\theta) &= \int_{\theta_0}^{\theta} \frac{\cos(\theta)^2}{\varrho(\theta)^3} d\theta = \int_{E_0}^{E} f(E) dE \\
I_{c_{32}}(E) &= \int_{E_0}^{E} (\cos(E) - \varepsilon)^2 (1 - \varepsilon\cos(E))^{-2} (1 - \varepsilon^2)^{-3} \\
&\quad (1 - \varepsilon\cos(E))^3 (1 - \varepsilon^2)^{\frac{1}{2}} (1 - \varepsilon\cos(E))^{-1} dE \\
I_{c_{32}}(E) &= (1 - \varepsilon^2)^{-\frac{5}{2}} \int_{E_0}^{E} (\cos(E) - \varepsilon)^2 dE \\
I_{c_{32}}(E) &= (1 - \varepsilon^2)^{-\frac{5}{2}} \int_{E_0}^{E} (\cos(E)^2 + \varepsilon^2 - 2\varepsilon\cos(E)) dE \\
I_{c_{32}}(E) &= (1 - \varepsilon^2)^{-\frac{5}{2}} \left[\frac{1}{2} E + \frac{1}{4} \sin(2E) + \varepsilon^2 E - 2\varepsilon \sin(E) \right]_{E_0}^{E} \\
I_{c_{32}}(E) &= (1 - \varepsilon^2)^{-\frac{5}{2}} \left[\left(\frac{1}{2} + \varepsilon^2 \right) (E - E_0) - 2\varepsilon(\sin(E) - \sin(E_0)) \right. \\
&\quad \left. + \frac{1}{4} (\sin(2E) - \sin(2E_0)) \right]
\end{aligned} \tag{A.63}$$

Integral I_{c_1} from Equation (4.208) becomes

$$\begin{aligned}
I_{c_1}(\theta) &= \int_{\theta_0}^{\theta} \frac{\cos(\theta)}{\varrho(\theta)} d\theta = \frac{1}{\varepsilon} \int_{\theta_0}^{\theta} \frac{\varepsilon\cos(\theta)}{\varrho(\theta)} d\theta = \frac{1}{\varepsilon} \int_{\theta_0}^{\theta} \frac{\varepsilon\cos(\theta)}{1 + \varepsilon\cos(\theta)} d\theta \\
I_{c_1}(\theta) &= \frac{1}{\varepsilon} \int_{\theta_0}^{\theta} \frac{1 + \varepsilon\cos(\theta) - 1}{1 + \varepsilon\cos(\theta)} d\theta = \frac{1}{\varepsilon} \int_{\theta_0}^{\theta} \left(1 - \frac{1}{1 + \varepsilon\cos(\theta)} \right) d\theta \\
I_{c_1}(\theta) &= \frac{1}{\varepsilon} \left[\theta - \frac{2}{\sqrt{1 - \varepsilon^2}} \arctan\left(\frac{1 - \varepsilon}{\sqrt{1 - \varepsilon^2}} \tan\left(\frac{\theta}{2} \right) \right) \right]_{\theta_0}^{\theta} \\
I_{c_1}(\theta) &= \frac{1}{\varepsilon} \left[\theta - \theta_0 - \frac{2}{\sqrt{1 - \varepsilon^2}} \left\{ \arctan\left(\frac{1 - \varepsilon}{\sqrt{1 - \varepsilon^2}} \tan\left(\frac{\theta}{2} \right) \right) \right. \right. \\
&\quad \left. \left. - \arctan\left(\frac{1 - \varepsilon}{\sqrt{1 - \varepsilon^2}} \tan\left(\frac{\theta_0}{2} \right) \right) \right\} \right]
\end{aligned} \tag{A.64}$$

Appendix B

Detailed Derivation of Attitude Kinematics, Dynamics and Environment

This chapter will contain all the details and intermediate calculations in order to derive the general equations of the attitude motion, which are not covered in Chapter 5.

B.1 Direction Cosine Matrix

This section will summarize the DCM for an Euler(3,2,1) rotation, as the individual matrices will be needed, recalling that 1 is x-axis, 2 is y-axis and 3 is z-axis. The rotation from a frame a to a frame b, such that

$$\mathbf{v}_b = \mathbf{R}_{ba}\mathbf{v}_a \tag{B.1}$$

where $\mathbf{v}_a$ is a vector projected on the axes of the a frame and $\mathbf{v}_b$ is the same vector projected on the axes of the b frame. The DCM is derived by a rotation around the third axis of a followed by rotations around the second and first axes of the resulting intermediate frames. We can therefore write the 3 individual matrices as follows.

$$\mathbf{R}_{ba}(\boldsymbol{\theta}) = \mathbf{R}_1(\theta_1)\mathbf{R}_2(\theta_2)\mathbf{R}_3(\theta_3) \tag{B.2}$$

$$\mathbf{R}_{ba}(\boldsymbol{\theta}) = \begin{bmatrix} 1 & 0 & 0 \\ 0 & \cos(\theta_1) & \sin(\theta_1) \\ 0 & -\sin(\theta_1) & \cos(\theta_1) \end{bmatrix} \begin{bmatrix} \cos(\theta_2) & 0 & -\sin(\theta_2) \\ 0 & 1 & 0 \\ \sin(\theta_2) & 0 & \cos(\theta_2) \end{bmatrix} \begin{bmatrix} \cos(\theta_3) & \sin(\theta_3) & 0 \\ -\sin(\theta_3) & \cos(\theta_3) & 0 \\ 0 & 0 & 1 \end{bmatrix} \tag{B.3}$$

We will use that $s_i = \sin(\theta_i)$ and $c_i = \cos(\theta_i)$ where $i = 1, 2, 3$.

$$\mathbf{R}_{ba}(\boldsymbol{\theta}) = \begin{bmatrix} c_3c_2 & c_2s_3 & -s_2 \\ s_1s_2c_3 - c_1s_3 & s_1s_2s_3 + c_1c_3 & s_1c_2 \\ c_1s_2c_3 + s_1s_3 & c_1s_2s_3 - s_1c_3 & c_1c_2 \end{bmatrix} \tag{B.4}$$

where $\boldsymbol{\theta} = [\theta_1, \theta_2, \theta_3]^{\mathrm{T}}$ is the rotation angle about the respective axis. The inverse rotation is found from the transpose of the orthonormal [1] matrix $\mathbf{R}_{ba}$ such that $\mathbf{R}_{ab} = \mathbf{R}_{ba}^{\mathrm{T}}$.

B.2 Attitude Dynamics Linearization

Here we will find the first Jacobian matrix of Equation (5.5), which is a linearization of Equation (5.2) in which only the cross product is a function of $\boldsymbol{\omega}$ and all other terms give zero in the differentiation. Let us define $\mathbf{p}(\boldsymbol{\omega})$ as

$$\mathbf{p}(\boldsymbol{\omega}) = \boldsymbol{\omega} \times \mathbf{I}\boldsymbol{\omega} \tag{B.5}$$

and the Jacobian from Equation (5.5) becomes

$$\begin{aligned} \frac{\partial \mathbf{I}\dot{\boldsymbol{\omega}}}{\partial \boldsymbol{\omega}} &= \frac{\partial \mathbf{N}}{\partial \boldsymbol{\omega}} - \frac{\partial(\boldsymbol{\omega} \times \mathbf{I}\boldsymbol{\omega})}{\partial \boldsymbol{\omega}} \\ &= \mathbf{0} - \frac{\partial \mathbf{p}(\boldsymbol{\omega})}{\partial \boldsymbol{\omega}} \end{aligned}$$

which expanding the last term gives

$$\mathbf{p}(\boldsymbol{\omega}) = \begin{bmatrix} \omega_y(I_{31}\omega_x + I_{32}\omega_y + I_{33}\omega_z) - \omega_z(I_{21}\omega_x + I_{22}\omega_y + I_{23}\omega_z) \\ \omega_z(I_{11}\omega_x + I_{12}\omega_y + I_{13}\omega_z) - \omega_x(I_{31}\omega_x + I_{32}\omega_y + I_{33}\omega_z) \\ \omega_x(I_{21}\omega_x + I_{22}\omega_y + I_{23}\omega_z) - \omega_y(I_{11}\omega_x + I_{12}\omega_y + I_{13}\omega_z) \end{bmatrix} \tag{B.6}$$

[1] A matrix $\mathbf{A}$ is called orthogonal if $\mathbf{A}\mathbf{A}^{\mathrm{T}}$ is a diagonal matrix, and is called orthonormal if $\mathbf{A}\mathbf{A}^{\mathrm{T}}$ is an identity matrix. For an orthonormal matrix $\mathbf{A}$, we have $\mathbf{A}^{-1} = \mathbf{A}^{\mathrm{T}}$.

We will now differentiate Equation (B.6)

$$\frac{\partial p_x}{\partial \omega_x} = I_{31}\omega_y - I_{21}\omega_z$$

$$\begin{aligned}\frac{\partial p_x}{\partial \omega_y} &= I_{31}\omega_x + 2I_{32}\omega_y + I_{33}\omega_z - I_{22}\omega_z \\ &= I_{31}\omega_x + 2I_{32}\omega_y + (I_{33} - I_{22})\omega_z\end{aligned}$$

$$\begin{aligned}\frac{\partial p_x}{\partial \omega_z} &= I_{33}\omega_y - I_{21}\omega_x - I_{22}\omega_y - 2I_{23}\omega_z \\ &= (I_{33} - I_{22})\omega_y - I_{21}\omega_x - 2I_{23}\omega_z\end{aligned}$$

$$\begin{aligned}\frac{\partial p_y}{\partial \omega_x} &= I_{11}\omega_z - 2I_{31}\omega_x - I_{32}\omega_y - I_{33}\omega_z \\ &= (I_{11} - I_{33})\omega_z - I_{32}\omega_y - 2I_{31}\omega_x\end{aligned}$$

$$\frac{\partial p_y}{\partial \omega_y} = I_{12}\omega_z - I_{32}\omega_x$$

$$\begin{aligned}\frac{\partial p_y}{\partial \omega_z} &= I_{11}\omega_x + I_{12}\omega_y + 2I_{13}\omega_z - I_{33}\omega_x \\ &= (I_{11} - I_{33})\omega_x + I_{12}\omega_y + 2I_{13}\omega_z\end{aligned}$$

$$\begin{aligned}\frac{\partial p_z}{\partial \omega_x} &= 2I_{21}\omega_x + I_{22}\omega_y + I_{23}\omega_z - I_{11}\omega_y \\ &= (I_{22} - I_{11})\omega_y + I_{23}\omega_z + 2I_{21}\omega_x\end{aligned}$$

$$\begin{aligned}\frac{\partial p_z}{\partial \omega_y} &= I_{22}\omega_x - I_{11}\omega_x - 2I_{12}\omega_y - I_{13}\omega_z \\ &= (I_{22} - I_{11})\omega_x - I_{13}\omega_z - 2I_{12}\omega_y\end{aligned}$$

$$\frac{\partial p_z}{\partial \omega_z} = I_{23}\omega_x - I_{13}\omega_y$$

Collecting terms we can now write the Jacobian matrix as

$$\frac{\partial \mathbf{I}\dot{\boldsymbol{\omega}}}{\partial \boldsymbol{\omega}} =$$

$$-\begin{bmatrix} I_{31}\omega_y - I_{21}\omega_z & I_{31}\omega_x + 2I_{32}\omega_y + (I_{33} - I_{22})\omega_z & -I_{21}\omega_x + (I_{33} - I_{22})\omega_y - 2I_{23}\omega_z \\ -2I_{31}\omega_x - I_{32}\omega_y + (I_{11} - I_{33})\omega_z & -I_{32}\omega_x + I_{12}\omega_z & (I_{11} - I_{33})\omega_x + I_{12}\omega_y + 2I_{13}\omega_z \\ 2I_{21}\omega_x + (I_{22} - I_{11})\omega_y + I_{23}\omega_z & (I_{22} - I_{11})\omega_x - 2I_{12}\omega_y - I_{13}\omega_z & I_{23}\omega_x - I_{13}\omega_y \end{bmatrix} \tag{B.7}$$

Inserting the vector for the operating point $\boldsymbol{\omega}_{oi} = [0, -\omega_0, 0]^{\mathrm{T}}$ we obtain the following

$$\frac{\partial \mathbf{I}\dot{\boldsymbol{\omega}}}{\partial \boldsymbol{\omega}} = \omega_0 \begin{bmatrix} I_{31} & 2I_{32} & I_{33} - I_{22} \\ -I_{32} & 0 & I_{12} \\ I_{22} - I_{11} & -2I_{12} & -I_{13} \end{bmatrix} \tag{B.8}$$

B.3 Target Port Linearization

We will derive the Jacobian of Equation (5.29), using that $s_i = \sin(\theta_i)$, $c_i = \cos(\theta_i)$ and $i = x, y, z$ and the DCM from Equation (B.4). It is observed that all terms containing s_x or s_z become zero and will not be written down. For simplicity we denote $\tilde{\mathbf{r}}_{dt} = \mathbf{g}$.

$$\begin{aligned}
\frac{\partial g_x}{\partial \theta_x} &= (c_x s_y c_z + s_x s_z) r_{dt_y} + (c_x s_z - s_x s_y c_z) r_{dt_z} = s_y r_{dt_y} \\
\frac{\partial g_x}{\partial \theta_y} &= -s_y c_z r_{dt_x} + s_x c_y c_z r_{dt_y} + c_x c_y c_z r_{dt_z} = c_y r_{dt_z} - s_y r_{dt_x} \\
\frac{\partial g_x}{\partial \theta_z} &= -s_z c_y r_{dt_x} - (s_x s_y s_z + c_x c_z) r_{dt_y} + (s_x c_z - c_x s_y s_z) r_{dt_z} = -r_{dt_y} \\
\frac{\partial g_y}{\partial \theta_x} &= (c_x s_y s_z - s_x c_z) r_{dt_y} - (s_x s_y s_z + c_x c_z) r_{dt_z} = -r_{dt_z} \\
\frac{\partial g_y}{\partial \theta_y} &= -s_y s_z r_{dt_x} + s_x c_y s_z r_{dt_y} + c_x c_y s_z r_{dt_z} = 0 \\
\frac{\partial g_y}{\partial \theta_z} &= c_y c_z r_{dt_x} + (s_x s_y c_z - c_x s_z) r_{dt_y} + (c_x s_y c_z + s_x s_z) r_{dt_z} = c_y r_{dt_x} + s_y r_{dt_z} \\
\frac{\partial g_z}{\partial \theta_x} &= c_x c_y r_{dt_y} - s_x c_y r_{dt_z} = c_y r_{dt_y} \\
\frac{\partial g_z}{\partial \theta_y} &= -c_y r_{dt_x} - s_x s_y r_{dt_y} - c_x s_y r_{dt_z} = -c_y r_{dt_x} - s_y r_{dt_z} \\
\frac{\partial g_z}{\partial \theta_z} &= 0
\end{aligned}$$

and the Jacobian becomes in matrix form

$$\frac{\partial \tilde{\mathbf{r}}_{dt}}{\partial \boldsymbol{\theta}_t} = \begin{bmatrix} s_y r_{dt_y} & c_y r_{dt_z} - s_y r_{dt_x} & -r_{dt_y} \\ -r_{dt_z} & 0 & c_y r_{dt_x} + s_y r_{dt_z} \\ c_y r_{dt_y} & -(c_y r_{dt_x} + s_y r_{dt_z}) & 0 \end{bmatrix} = \mathbf{B}_{dt_1} \tag{B.9}$$

For the velocity linearization we need to find the Jacobian of the last term in Equation (5.32) and for convenience we define $\dot{\tilde{\mathbf{r}}}_{dt} = \mathbf{g}(\boldsymbol{\theta}_t, \boldsymbol{\omega}_t)$. We will compute the cross product and the DCM as

$$\mathbf{g}(\boldsymbol{\theta}_t, \boldsymbol{\omega}_t) = \mathbf{R}^{\mathrm{T}} \begin{bmatrix} \omega_{t_y} r_{dt_z} - \omega_{t_z} r_{dt_y} \\ \omega_{t_z} r_{dt_x} - \omega_{t_x} r_{dt_z} \\ \omega_{t_x} r_{dt_y} - \omega_{t_y} r_{dt_x} \end{bmatrix} = \tag{B.10}$$

$$\begin{bmatrix} c_z c_y(\omega_{t_y} r_{dt_z} - \omega_{t_z} r_{dt_y}) + (s_x s_y c_z - c_x s_z)(\omega_{t_z} r_{dt_x} - \omega_{t_x} r_{dt_z}) + (c_x s_y c_z + s_x s_z)(\omega_{t_x} r_{dt_y} - \omega_{t_y} r_{dt_x}) \\ c_y s_z(\omega_{t_y} r_{dt_z} - \omega_{t_z} r_{dt_y}) + (s_x s_y s_z + c_x c_z)(\omega_{t_z} r_{dt_x} - \omega_{t_x} r_{dt_z}) + (c_x s_y s_z - s_x c_z)(\omega_{t_x} r_{dt_y} - \omega_{t_y} r_{dt_x}) \\ -s_y(\omega_{t_y} r_{dt_z} - \omega_{t_z} r_{dt_y}) + s_x c_y(\omega_{t_z} r_{dt_x} - \omega_{t_x} r_{dt_z}) + c_x c_y(\omega_{t_x} r_{dt_y} - \omega_{t_y} r_{dt_x}) \end{bmatrix}$$

The partial derivatives become

$$\begin{aligned} \frac{\partial g_x}{\partial \omega_x} &= s_y r_{dt_y} \\ \frac{\partial g_x}{\partial \omega_y} &= c_y r_{dt_z} - s_y r_{dt_x} \\ \frac{\partial g_x}{\partial \omega_z} &= -c_y r_{dt_y} \\ \frac{\partial g_y}{\partial \omega_x} &= -r_{dt_z} \\ \frac{\partial g_y}{\partial \omega_y} &= 0 \\ \frac{\partial g_y}{\partial \omega_z} &= r_{dt_x} \\ \frac{\partial g_z}{\partial \omega_x} &= c_y r_{dt_y} \\ \frac{\partial g_z}{\partial \omega_y} &= -s_y r_{dt_z} - c_y r_{dt_x} \\ \frac{\partial g_z}{\partial \omega_z} &= s_y r_{dt_y} \end{aligned}$$

and the Jacobian becomes in matrix form

$$\frac{\partial \dot{\tilde{\mathbf{r}}}_{dt}}{\partial \boldsymbol{\omega}_t} = \begin{bmatrix} s_y r_{dt_y} & c_y r_{dt_z} - s_y r_{dt_x} & -c_y r_{dt_y} \\ -r_{dt_z} & 0 & r_{dt_x} \\ c_y r_{dt_y} & -(s_y r_{dt_z} + c_y r_{dt_x}) & s_y r_{dt_y} \end{bmatrix} = \mathbf{B}_{dt_2} \tag{B.11}$$

B.4 Quaternions

This section will provide the basic equations and relations for quaternion operations and how they can be derived from the fundamental definitions. The definition of the quaternion can be found in Equation (5.10). All DCM and quaternions here describe the rotation from a frame A to a frame B, where B is rotated with respect to A.

B.4.1 Euler(3,2,1) to Quaternion

The direct transformation from Euler angles into a quaternion can be found by finding the quaternions for the intermediate Euler rotations. For a 3,2,1 rotation the first rotation is around the z-axis, and in that case the eigen axis for the rotation is directly the z-axis and that intermediate quaternion will be $\mathbf{q} = [\cos(\frac{\theta_z}{2}), 0, 0, \sin(\frac{\theta_z}{2})]^{\mathrm{T}}$. Subsequently we find the intermediate ones for the other two rotations. To find the final quaternion

they are multiplied together by means of the quaternion multiplication defined in Section B.4.4.

$$\begin{aligned}
q_0 &= \cos(\frac{\theta_x}{2})\cos(\frac{\theta_y}{2})\cos(\frac{\theta_z}{2}) + \sin(\frac{\theta_x}{2})\sin(\frac{\theta_y}{2})\sin(\frac{\theta_z}{2}) \\
q_1 &= \sin(\frac{\theta_x}{2})\cos(\frac{\theta_y}{2})\cos(\frac{\theta_z}{2}) - \cos(\frac{\theta_x}{2})\sin(\frac{\theta_y}{2})\sin(\frac{\theta_z}{2}) \\
q_2 &= \cos(\frac{\theta_x}{2})\sin(\frac{\theta_y}{2})\cos(\frac{\theta_z}{2}) + \sin(\frac{\theta_x}{2})\cos(\frac{\theta_y}{2})\sin(\frac{\theta_z}{2}) \\
q_3 &= \cos(\frac{\theta_x}{2})\cos(\frac{\theta_y}{2})\sin(\frac{\theta_z}{2}) - \sin(\frac{\theta_x}{2})\sin(\frac{\theta_y}{2})\cos(\frac{\theta_z}{2})
\end{aligned} \tag{B.12}$$

B.4.2 Quaternion to DCM

The DCM can be expressed by means of the Euler eigen axis and the rotation angle, (Junkins & Turner 1986). From that and the half angle identities and the constraint that the quaternion length is one, we can derived the equation for the DCM (Junkins & Turner 1986).

$$\mathbf{R} = \begin{bmatrix} 1-2(q_2^2+q_3^2) & 2(q_1q_2+q_0q_3) & 2(q_1q_3-q_0q_2) \\ 2(q_1q_2-q_0q_3) & 1-2(q_1^2+q_3^2) & 2(q_2q_3+q_0q_1) \\ 2(q_1q_3+q_0q_2) & 2(q_2q_3-q_0q_1) & 1-2(q_1^2+q_2^2) \end{bmatrix} \tag{B.13}$$

B.4.3 Quaternion to Euler(3,2,1)

The Euler angles can be found directly from the elements of the DCM in Equation (B.13) by the well knows relations

$$\begin{array}{rcccl}
\theta_x & = & \arctan(\frac{R_{23}}{R_{33}}) & = & \arctan(\frac{2(q_2q_3+q_0q_1)}{1-2(q_1^2+q_2^2)}) \\
\theta_y & = & \arcsin(-R_{13}) & = & \arcsin(-2(q_1q_3-q_0q_2)) \\
\theta_z & = & \arctan(\frac{R_{12}}{R_{11}}) & = & \arctan(\frac{2(q_1q_2+q_0q_3)}{1-2(q_2^2+q_3^2)})
\end{array} \tag{B.14}$$

B.4.4 Quaternion Multiplication

We can define a sequence of rotations by multiplication of the individual quaternions as e.g. a rotation from a frame a to a frame c via an intermediate frame $\mathbf{q}_{ca} = \mathbf{q}_{cb}\mathbf{q}_{ba} = \mathbf{q}''\mathbf{q}'$. By means of the quaternion product (Junkins & Turner 1986) we can write $\mathbf{q}_{ca}$ as

$$\mathbf{q}_{ca} = \begin{bmatrix} q_0'' & -q_1'' & -q_2'' & -q_3'' \\ q_1'' & q_0'' & q_3'' & -q_2'' \\ q_2'' & -q_3'' & q_0'' & q_1'' \\ q_3'' & q_2'' & -q_1'' & q_0'' \end{bmatrix} \begin{bmatrix} q_0' \\ q_1' \\ q_2' \\ q_3' \end{bmatrix} \tag{B.15}$$

B.4.5 Quaternion Conjugate

The conjugate of a quaternion means the rotation in the opposite direction, which can either be obtained by the opposite sign of the angle or the eigenvector is opposite. From the definition it follows directly as

$$\mathbf{q}^* = \begin{bmatrix} q_0 \\ -q_1 \\ -q_2 \\ -q_3 \end{bmatrix} \tag{B.16}$$

B.4.6 Vector Transformation

We can use the frame work of the quaternion to perform a vector transformation from one frame to another as described in Equation (B.1) using a DCM.

We want to perform $\mathbf{v}_b = \mathbf{R}_{ba}\mathbf{v}_a$ which we can do as $\mathbf{v}_b = \mathbf{q}_{ba}\mathbf{v}'_a\mathbf{q}^*_{ba}$, where $\mathbf{v}'_a = [0, \mathbf{v}_a^{\mathrm{T}}]^{\mathrm{T}}$ and it shall be noted that $\mathbf{v}'_a$ is not a quaternion, but only written in that notation. We first compute $\mathbf{b} = \mathbf{q}\mathbf{a} = \mathbf{q}_{ba}\mathbf{v}'_a$ as

$$\begin{array}{rcl} b_0 &=& -q_1a_1 - q_2a_2 - q_3a_3 \\ b_1 &=& q_0a_1 + q_3a_2 - q_2a_3 \\ b_2 &=& -q_3a_1 + q_0a_2 + q_1a_3 \\ b_3 &=& q_2a_1 - q_1a_2 + q_0a_3 \end{array} \tag{B.17}$$

and finally we compute $\mathbf{b}\mathbf{q}^*_{ba}$ for the vector part only

$$\begin{array}{rcl} v_{b_1} &=& b_1q_0^* + b_0q_1^* + b_3q_2^* - b_2q_3^* \\ v_{b_2} &=& b_2q_0^* - b_3q_1^* + b_0q_2^* + b_1q_3^* \\ v_{b_3} &=& b_3q_0^* + b_2q_1^* - b_1q_2^* + b_0q_3^* \end{array} \tag{B.18}$$

B.4.7 Quaternion Rate

We will now go through the principles leading to the quaternion differential equation for the kinematics, transforming a vector $\mathbf{a}$ to a vector $\mathbf{b}$ as $\mathbf{b} = \mathbf{R}\mathbf{a}$ and $\mathbf{a} = \mathbf{R}^{\mathrm{T}}\mathbf{b}$. Differentiating $\mathbf{a}$, which is time invariant gives $\dot{\mathbf{a}} = \mathbf{0} = \dot{\mathbf{R}}^{\mathrm{T}}\mathbf{b} + \mathbf{R}^{\mathrm{T}}\dot{\mathbf{b}}$ and we can write $\dot{\mathbf{b}}$ as $\dot{\mathbf{b}} = \boldsymbol{\omega} \times \mathbf{b}$. As we look from the rotating frame $\boldsymbol{\omega}$ changes sign and defining $\boldsymbol{\Omega}$ as a skew symmetric matrix the cross product can be formulated as a matrix multiplication as $(\dot{\mathbf{R}}^{\mathrm{T}} - \mathbf{R}\boldsymbol{\Omega})\mathbf{b} = \mathbf{0}$. Recalling that $\boldsymbol{\Omega}^{\mathrm{T}} = -\boldsymbol{\Omega}$ and after some manipulations we arrive at the kinematic differential equation for a DCM

$$\dot{\mathbf{R}} = -\boldsymbol{\Omega}\mathbf{R} \tag{B.19}$$

From Equation (B.19) we can write the individual differential equations for the elements of the $\boldsymbol{\omega}$ vector as a function of the DCM elements and their derivatives. Inserting the elements of the DCM in terms of quaternion elements from Equation (B.13) and using the differential of the relation $q_0^2 + q_1^2 + q_2^2 + q_3^2 = 1$ and combining rows we can write the result as shown in Equation (5.11).

B.5 Gravity Gradient Linearization

We will linearize Equation (3.5) around the nominal attitude of $\boldsymbol{\theta_0} = [0, \theta_0, 0]^{\mathrm{T}}$. Represented in the body frame we can write the gravity gradient torque as follows

$$\mathbf{N}_g = 3\frac{\mu}{r^3}\begin{bmatrix} -\sin(\theta_y) \\ \sin(\theta_x)\cos(\theta_y) \\ \cos(\theta_x)\cos(\theta_y) \end{bmatrix} \times \mathbf{I}\begin{bmatrix} -\sin(\theta_y) \\ \sin(\theta_x)\cos(\theta_y) \\ \cos(\theta_x)\cos(\theta_y) \end{bmatrix} \tag{B.20}$$

Using the notation of trigonometric functions as $s_i = \sin(\theta_i)$, $c_i = \cos(\theta_i)$, $t_i = \tan(\theta_i)$ and $i = x, y, z$, we can write Equation (B.20) as follows after some manipulations

$$\mathbf{N}_g = 3\frac{\mu}{r^3}\begin{bmatrix} I_{21}c_xc_ys_y - I_{22}c_xs_xc_y^2 - I_{23}c_x^2c_y^2 - I_{31}c_xs_yc_y + I_{32}s_x^2c_y^2 + I_{33}c_xs_xc_y^2 \\ -I_{11}c_xc_ys_y + I_{12}c_xs_xc_y^2 + I_{13}c_x^2c_y^2 - I_{31}s_y^2 + I_{32}s_xs_yc_y + I_{33}c_xc_ys_y \\ I_{11}s_xc_ys_y - I_{12}s_x^2c_y^2 - I_{13}s_xc_xc_y^2 + I_{21}s_y^2 - I_{22}s_xc_ys_y - I_{23}c_xc_ys_y \end{bmatrix} \tag{B.21}$$

The constant term in the Taylor series becomes

$$\mathbf{N}_g(\mathbf{0}) = 3\frac{\mu}{r^3}\begin{bmatrix} I_{21}s_yc_y - I_{23}c_y^2 \\ (I_{33} - I_{11})s_yc_y + I_{13}c_y^2 - I_{31}s_y^2 \\ I_{21}s_y^2 - I_{23}s_yc_y \end{bmatrix} \tag{B.22}$$

We will now find the Jacobian matrix for the operating point $\boldsymbol{\theta_0}$.

$$\begin{aligned}\frac{\partial N_x}{\partial \theta_x} &= I_{21}c_ys_ys_x - I_{22}c_y^2(c_x^2 - s_x^2) + 2I_{23}c_y^2c_xs_x \\ &\quad - I_{31}c_xs_yc_y + 2I_{32}c_y^2s_xc_x + I_{33}c_y^2(c_x^2 - s_x^2) \\ &= (I_{33} - I_{22})c_y^2 - I_{31}s_yc_y\end{aligned}$$

$$\begin{aligned}\frac{\partial N_x}{\partial \theta_y} &= I_{21}c_x(c_y^2 - s_y^2) + 2I_{22}c_xs_xc_ys_y - 2I_{23}c_x^2c_ys_y \\ &\quad - I_{31}s_x(c_y^2 - s_y^2) - 2I_{32}s_x^2c_ys_y - 2I_{33}c_xs_xc_ys_y \\ &= I_{21}(c_y^2 - s_y^2) - 2I_{23}s_yc_y\end{aligned}$$

$$\frac{\partial N_x}{\partial \theta_z} = 0$$

$$\begin{aligned}\frac{\partial N_y}{\partial \theta_x} &= I_{11}s_x c_y s_y + I_{12}c_y^2(c_x^2 - s_x^2) - 2I_{13}c_x s_x c_y^2 \\ &\quad + I_{32}c_x s_y c_y - I_{33}s_x c_y s_y \\ &= I_{12}c_y^2 + I_{32}s_y c_y\end{aligned}$$

$$\begin{aligned}\frac{\partial N_y}{\partial \theta_y} &= -I_{11}c_x(c_y^2 - s_y^2) - 2I_{12}c_x s_x c_y s_y - 2I_{13}c_x^2 c_y s_y \\ &\quad - 2I_{31}s_y c_y + I_{32}s_x(c_y^2 - s_y^2) + I_{33}c_x(c_y^2 - s_y^2) \\ &= (I_{33} - I_{11})c_y^2 + I_{11}s_y^2 - 2(I_{13} + I_{31})s_y c_y\end{aligned}$$

$$\frac{\partial N_y}{\partial \theta_z} = 0$$

$$\begin{aligned}\frac{\partial N_z}{\partial \theta_x} &= I_{11}c_x c_y s_y - 2I_{12}s_x c_x c_y^2 - I_{13}c_y^2(c_x^2 - s_x^2) \\ &\quad - I_{22}c_x c_y s_y + I_{23}s_x c_y s_y \\ &= (I_{11} - I_{22})s_y c_y - I_{13}c_y^2\end{aligned}$$

$$\begin{aligned}\frac{\partial N_z}{\partial \theta_y} &= I_{11}s_x(c_y^2 - s_y^2) + 2I_{12}s_x^2 c_y s_y + 2I_{13}s_x c_x s_y c_y \\ &\quad + 2I_{21}s_y c_y - I_{22}s_x(c_y^2 - s_y^2) - I_{23}c_x(c_y^2 - s_y^2) \\ &= 2I_{21}s_y c_y - I_{23}(c_y^2 - s_y^2)\end{aligned}$$

$$\frac{\partial N_z}{\partial \theta_z} = 0$$

The final linear equation is written in Equation (3.7).

Appendix C

Spacecraft Data

This chapter will contain all the specific data for the chaser and target spacecraft, as well as the data for avionics.

C.1 Target Data

The data for the ISS is valid for the configuration 16A. The mass is

$$m_t = 451310 \text{ kg} \tag{C.1}$$

and the inertia

$$\mathbf{I}_t = \begin{bmatrix} 127902 & 3047 & 7802 \\ 3047 & 98997 & 1343 \\ 7802 & 1343 & 192066 \end{bmatrix} 10^3 \text{ kg m}^2 \tag{C.2}$$

The numerical data for the ISS flexible modes for the attitude motion of the docking port is listed in Table C.1.
With respect to the geometrical frame $\mathcal{F}_{gt}$ the COM is located at

$$\mathbf{r}_{bt} = [-4.94, -0.21, 4.40]^{\mathrm{T}} \text{ m} \tag{C.3}$$

and the center of the docking port is located at

$$\mathbf{r}_{gdt} = [-35.84, 0, 4.14]^{\mathrm{T}} \text{ m} \tag{C.4}$$

The cross sectional profile of the spacecraft along the x,y,z body axes is 967, 776 and 3510 m^2 respectively.

C.2 Chaser Data

The data for the ATV spacecraft is as follows, where the mass is

$$m_c \in [14000; 20200] \text{ kg} \tag{C.5}$$

	$1^{st}mode$	$2^{nd}mode$	$3^{rd}mode$
Frequency Hz	$[0.12; 0.18]$	$[0.48; 0.72]$	$[1.0; 1.5]$
Angular			
α_z deg	0.023	0.02	0.004
α_y deg	0.023	0.02	0.004
α_x deg	0.02	0.02	0.0027
$\dot{\alpha}_z$ deg/s	0.022	0.075	0.03
$\dot{\alpha}_y$ deg/s	0.022	0.075	0.03
$\dot{\alpha}_x$ deg/s	0.02	0.075	0.02
Linear			
x m	0	0	0
y m	$1.0 \cdot 10^{-2}$	$3.8 \cdot 10^{-3}$	$7.0 \cdot 10^{-4}$
z m	$1.0 \cdot 10^{-2}$	$3.8 \cdot 10^{-3}$	$7.0 \cdot 10^{-4}$

Table C.1: *ISS flexible modes for the motion of $\mathcal{F}_{dt}$ with respect to $\mathcal{F}_{dt0}$ as Euler(3,2,1) angles and the linear motion. Frequencies are uniformly distributed including phase angles between the axes. The angular and linear data are uncorrelated.*

with uncertainty of ± 320 kg. The inertia matrix is

$$\mathbf{I}_c = \begin{bmatrix} [41000; 62000] & 1600 & 1600 \\ 1600 & [82000; 143000] & 1000 \\ 1600 & 1000 & [82000; 143000] \end{bmatrix} \text{ kg m}^2 \qquad \text{(C.6)}$$

with uncertainties of $I_{c_{xx}} = \pm 2500$ kg m^2 and $I_{c_{yy}} = I_{c_{zz}} = \pm 1300$ kg m^2. All uncertainties are uniformly distributed and are 3σ values.

With respect to the geometrical frame $\mathcal{F}_{gc}$ the COM location is defined in Section 3.2.2 and the center of the docking port is located at

$$\mathbf{r}_{gdc} = [8.5, 0, 0]^{\mathrm{T}} \text{ m} \qquad \text{(C.7)}$$

The cross sectional profile of the spacecraft along the x,y,z body axes is 51, 40 and 40 m^2 respectively.

Specification	Fine Mode	Coarse Mode
Max. rate	2 deg/s	30 deg/s
Max. drift after ground calibration	10 deg/h	10 deg/h
Global drift after in flight calibration (3σ)	0.3 deg over 1 hour	1 deg over 0.5 hour
Scale factor	10^{-3}	10^{-3}
Angular rate noise (3σ)	6 deg/h at 10 Hz	0.03 deg/s

Table C.2: *GNC relevant specifications for the gyro assembly unit DTG T100. Noise is Gaussian.*

Specification	Data
Max. angular rate	fine: 2 deg/s
	coarse: 5 deg/s
Stars	$3 - 10$
Bias (3σ)	lateral: $5.56 \cdot 10^{-3}$, axial: $1.11 \cdot 10^{-2}$ deg
Low freq. error (3σ)	lateral: $4.17 \cdot 10^{-3}$, axial: $1.61 \cdot 10^{-2}$ deg
Noise Equivalent Angle (3σ)	lateral: $1.00 \cdot 10^{-2}$, axial: $5.28 \cdot 10^{-2}$ deg
When 2 deg/s $< rate <$ 5 deg/s (3σ)	lateral: $2.78 \cdot 10^{-2}$, axial: $8.47 \cdot 10^{-2}$ deg
Sampling	5 Hz
Time tag	$< 400\mu$ s
Delay	1 s nominal
Dazzling recovery	10 s

Table C.3: *GNC relevant specifications for one unit of SED-16 star sensor. Noise is Gaussian.*

C.3 Gyro Data

The gyro performances along the spacecraft axes are shown in Table C.2.

C.4 Star Sensor Data

The numerical data for one star sensor unit is specified in Table C.3.

C.5 Chaser Flexible Modes Data

The flexible modes are expressed in terms of eigen frequencies, damping and the modal coupling factors. The modal data for one flexible solar panel is provided in Table C.4 and is valid for all four panels used.

C.6 Propulsion Data

The only propulsion system on the chaser spacecraft is a thruster assembly consisting of 28 thrusters, which provides the needed forces and torques. The uncertainties for the thrusters can be found in Table C.5. The location and orientation of the thrusters is listed in Table C.6.

Mode #	1	2	3	4	5	6
Description	out	in	out	in	out	in
f_k Hz	0.219	0.280	1.288	1.706	3.421	14.77
ζ_k	$0.001 - 0.005$					
L_{kmx} kgm	-4.472	0	2.594	0	-1.507	0
L_{kmy} kgm	0	0	0	0	0	0
L_{kmz} kgm	0	4.438	0	2.427	0	2.040
L_{kix} kgm^2	0	29.24	0	5.933	0	2.668
L_{kiy} kgm^2	0	0.0519	0	0	0	0
L_{kiz} kgm^2	29.22	0	-6.132	0	2.431	0

Table C.4: *Modal data and participation factors for one flexible solar panel presented in frame $\mathcal{F}_p$ and for being either in or out of the y-z plane. The data is valid for all four panels.*

	Data	Distribution
Nominal thrust	217 N	
MIB	0.025 s	
Rise/fall time (90 %)	20 ms	
Bias on thrust	$[-3\ \%; 2\ \%]$	3σ Uniform
Noise on thrust	± 3.1 %	3σ Gaussian
Repeatability	± 2.5 %	3σ Uniform
Thrust orientation	< 1 deg half cone	3σ Uniform

Table C.5: *Thruster specifications.*

		Location m			Thrust direction		
#	Type	x	y	z	x	y	z
1	acceleration	0.235	1.563	1.563	0.9659	−0.1830	−0.1830
2	roll	0.610	1.298	1.843	0.0	0.0	−1.0
3	brake	0.813	1.431	1.673	−0.5906	−0.2760	−0.7583
4	brake	0.856	1.601	1.577	−0.5906	−0.2760	−0.7583
5	roll	0.505	1.815	1.298	0.5	−0.8660	0.0
6	acceleration	0.235	−1.563	1.563	0.9659	0.1830	−0.1860
7	roll	0.505	−1.815	1.298	0.5	0.8660	0.0
8	brake	0.856	−1.601	1.577	−0.5906	0.2760	−0.7583
9	brake	0.813	−1.431	1.673	−0.5906	0.2760	−0.7583
10	roll	0.610	−1.298	1.843	0.0	0.0	−1.0
11	acceleration	0.235	−1.563	−1.563	0.9659	0.1830	0.1830
12	roll	0.610	−1.298	−1.843	0.0	0.0	1.0
13	brake	0.813	−1.431	−1.673	−0.5906	0.2760	0.7583
14	brake	0.856	−1.601	−1.577	−0.5906	0.2760	0.7583
15	roll	0.505	−1.815	−1.298	0.5	0.8660	0.0
16	acceleration	0.235	1.563	−1.563	0.9659	−0.1830	0.1830
17	roll	0.505	1.815	−1.298	0.5	−0.8660	0.0
18	brake	0.856	1.601	−1.577	−0.5906	−0.2760	0.7583
19	brake	0.813	1.431	−1.673	−0.5906	−0.2760	0.7583
20	roll	0.610	1.298	−1.843	0.0	0.0	1.0
21	rotation -z	7.025	2.185	0.522	0.0	−0.9726	−0.2325
22	rotation -z	7.025	2.130	0.715	0.0	−0.9480	−0.3183
23	rotation +y	7.025	0.1	2.2445	0.0	−0.0446	−0.9990
24	rotation +y	7.025	−0.1	2.2445	0.0	0.0446	−0.9990
25	rotation +z	7.025	−2.130	0.715	0.0	0.9480	−0.3183
26	rotation +z	7.025	−2.185	0.522	0.0	0.9726	−0.2325
27	rotation -y	7.025	−0.1	−2.2445	0.0	0.0446	0.9990
28	rotation -y	7.025	0.1	−2.2445	0.0	−0.0446	0.9990

Table C.6: *GNC relevant specifications for the propulsion system. The thrust direction is the direction of the produced force vector. All data is with respect to the geometrical frame* $\mathcal{F}_{gc}$.

Appendix D

GNC Details

This chapter will contain all the specific non central mathematical details needed for the GNC.

D.1 Simplex Optimization

The detailed functionalities of linear programming and a simplex algorithm will be based directly on the material from (Press, Flannery, Teukolsky & Vetterling 1986), but the basic structure is recalled here in order to be able to formulate and solve the present problem in a new manner. The general problem is for N independent variables $x_1, \ldots, x_N$ to maximize the function z and

$$z = a_{01}x_1 + a_{02}x_2 + \cdots + a_{0N}x_N \tag{D.1}$$

subject to the main constraints

$$x_1 \geq 0, x_2 \geq 0, \cdots, x_N \geq 0 \tag{D.2}$$

and simultaneous subject to $M = m_1 + m_2 + m_3$ additional constraints. m_1 of the form with $b_i \geq 0$

$$a_{i1}x_1 + a_{i2}x_2 + \cdots + a_{iN}x_N \leq b_i \tag{D.3}$$

and $i = 1, \cdots, m_1$. Now m_2 constraints of the form

$$a_{j1}x_1 + a_{j2}x_2 + \cdots + a_{jN}x_N \geq b_j \geq 0 \tag{D.4}$$

and $j = m_1 + 1, \cdots, m_1 + m_2$. Finally m_3 constraints of the form

$$a_{k1}x_1 + a_{k2}x_2 + \cdots + a_{kN}x_N = b_k \geq 0 \tag{D.5}$$

and $k = m_1 + m_2 + 1, \cdots, m_1 + m_2 + m_3$. The various coefficients can have either sign or be zero.

The fact that the b's are all nonnegative is by convention as one can always multiply through with -1. The number of constraints M as such can be smaller, equal or larger than the unknowns N.

	Time	Location	Position	Speed
VI	$t_3 = t_2 + \frac{\dot{s}_2 - \dot{s}_1}{a}$	s_4	$s = s_4 + \dot{s}_2(t - t_3)$	$\dot{s} = \dot{s}_2$

Table D.1: *Lists all equations needed to calculate the profile illustrated in Figure 7.10.*

	Time	Location	Position	Speed
III	$\delta t = t_3 - t_2 = \frac{\dot{s}_2 - \dot{s}_{31}}{d}$ $t_1 = \sqrt{\frac{1}{d}(s_4 - s_3 + \frac{\dot{s}_2^2}{2d})}$	$s_{31} = \frac{s_3 + s_4}{2} + \frac{\dot{s}_2^2}{4d}$	$x = t - t_1$ $s = s_{31} + \dot{s}_{31}x + \frac{1}{2}dx^2$	$\dot{s} = \dot{s}_{31} + dx$
VI	$t_3 = t_1 + \frac{\dot{s}_2 - \dot{s}_{31}}{a}$	s_4	$s = s_4 + \dot{s}_2(t - t_3)$	$\dot{s} = \dot{s}_2$

Table D.2: *Lists all equations, different from Table 7.5, needed to calculate the profile in Figure 7.10, when $\dot{s}_1$ is not reached. This means phase II is omitted and $t_1 = t_2$, $s_{31} = s_{32}$ and $\dot{s}_{31} = at_1$ from I. Observe in III that d is a deceleration and $d < 0$. Typically $d = -a$.*

D.2 Guidance

This section provides the guidance profile, when there is no SK at point s_4. Parts IV and V disappear. Only the parts different from those in tables 7.5 and 7.6 are presented here in Tables D.1 and D.2 respectively. Observe that $s_{41} = s_4$ and $t_3 = t_4 = t_{41}$.

D.3 Linear Fractional Transformations

This section will derive and present the LFTs which are used in the project. A more comprehensive treatment and properties can be found in (Zhou, Doyle & Glover 1995).

Let us first just consider the transfer matrix $\mathbf{M}$ in Figure D.1, where the input and output can be scalars or vectors.

$$\mathbf{v} = \mathbf{M}\mathbf{r}$$

and written as a 2-port system we get

$$\begin{bmatrix} \mathbf{v}_1 \\ \mathbf{v}_2 \end{bmatrix} = \begin{bmatrix} \mathbf{M}_{11} & \mathbf{M}_{12} \\ \mathbf{M}_{21} & \mathbf{M}_{22} \end{bmatrix} \begin{bmatrix} \mathbf{r}_1 \\ \mathbf{r}_2 \end{bmatrix} \tag{D.6}$$

D.3.1 Lower LFT

We want to find the relation from $\mathbf{r}_1$ to $\mathbf{v}_1$ closing the lower loop via $\mathbf{K}$. We can write the following set of equations

$$\begin{aligned} \mathbf{v}_1 &= \mathbf{M}_{11}\mathbf{r}_1 + \mathbf{M}_{12}\mathbf{K}\mathbf{v}_2 \\ \mathbf{v}_2 &= \mathbf{M}_{21}\mathbf{r}_1 + \mathbf{M}_{22}\mathbf{K}\mathbf{v}_2 \end{aligned} \tag{D.7}$$

and after some algebraic manipulation we obtain

$$\mathbf{v}_1 = \{\mathbf{M}_{11} + \mathbf{M}_{12}\mathbf{K}(\mathbf{I} - \mathbf{M}_{22}\mathbf{K})^{-1}\mathbf{M}_{21}\}\mathbf{r}_1 \tag{D.8}$$

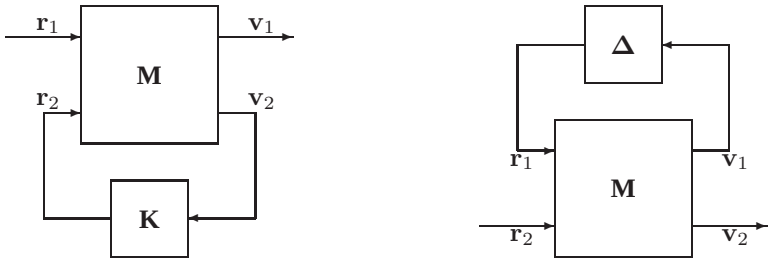

(a) Lower LFT (b) Upper LFT

Figure D.1: *The LFT for a lower respectively an upper interconnection.*

We now define the lower LFT as

$$F_l(\mathbf{M},\mathbf{K}) \triangleq \mathbf{M}_{11} + \mathbf{M}_{12}\mathbf{K}(\mathbf{I}-\mathbf{M}_{22}\mathbf{K})^{-1}\mathbf{M}_{21} \tag{D.9}$$

D.3.2 Upper LFT

The upper LFT can be derived in a similar manner as the lower one as

$$\begin{array}{rcl} \mathbf{v}_1 &=& \mathbf{M}_{11}\boldsymbol{\Delta}\mathbf{v}_1 + \mathbf{M}_{12}\mathbf{r}_2 \\ \mathbf{v}_2 &=& \mathbf{M}_{21}\boldsymbol{\Delta}\mathbf{v}_1 + \mathbf{M}_{22}\mathbf{r}_2 \end{array} \tag{D.10}$$

and after some algebraic manipulation we obtain

$$\mathbf{v}_2 = \{\mathbf{M}_{22} + \mathbf{M}_{21}\boldsymbol{\Delta}(\mathbf{I}-\mathbf{M}_{11}\boldsymbol{\Delta})^{-1}\mathbf{M}_{12}\}\mathbf{r}_2 \tag{D.11}$$

We now define the upper LFT as

$$F_u(\mathbf{M},\boldsymbol{\Delta}) \triangleq \mathbf{M}_{22} + \mathbf{M}_{21}\boldsymbol{\Delta}(\mathbf{I}-\mathbf{M}_{11}\boldsymbol{\Delta})^{-1}\mathbf{M}_{12} \tag{D.12}$$

D.3.3 Inverse of LFT

For deriving the inverse of the LFT, both upper and lower, we will need the matrix inversion lemma, stated in Lemma D.1.

Lemma D.1
The inverse of the following matrix expression can be formulated as

$$(\boldsymbol{A}_1 + \boldsymbol{A}_2\boldsymbol{A}_3\boldsymbol{A}_4)^{-1} = \boldsymbol{A}_1^{-1} - \boldsymbol{A}_1^{-1}\boldsymbol{A}_2(\boldsymbol{A}_4\boldsymbol{A}_1^{-1}\boldsymbol{A}_2 + \boldsymbol{A}_3^{-1})^{-1}\boldsymbol{A}_4\boldsymbol{A}_1^{-1} \tag{D.13}$$

where the proof is given in (Bernstein 2005).

Considering the following partitioned matrix

$$\mathbf{H} = \begin{bmatrix} \mathbf{H}_{11} & \mathbf{H}_{12} \\ \mathbf{H}_{21} & \mathbf{H}_{22} \end{bmatrix} \tag{D.14}$$

for which the inverse LFT will be developed in the following sections.

D.3.3.1 Inverse of Lower LFT

The lower inverse LFT is formulated in Lemma D.2.

Lemma D.2
Let $\boldsymbol{H}$ be a partitioned matrix as in Equation (D.14), then the inverse becomes

$$F_l(\boldsymbol{H}, \boldsymbol{K})^{-1} = F_l(\boldsymbol{H}_{li}, \boldsymbol{K}) \tag{D.15}$$

where

$$\boldsymbol{H}_{li} = \begin{bmatrix} \boldsymbol{H}_{11}^{-1} & -\boldsymbol{H}_{11}^{-1}\boldsymbol{H}_{12} \\ \boldsymbol{H}_{21}\boldsymbol{H}_{11}^{-1} & \boldsymbol{H}_{22} - \boldsymbol{H}_{21}\boldsymbol{H}_{11}^{-1}\boldsymbol{H}_{12} \end{bmatrix} \tag{D.16}$$

Proof: We take the inverse of Equation (D.9) and formulate it in terms of Equation (D.13), recognizing the associated elements.

$$[\underbrace{\mathbf{H}_{11}}_{\mathbf{A}_1} + \underbrace{\mathbf{H}_{12}\mathbf{K}}_{\mathbf{A}_2}\underbrace{(\mathbf{I} - \mathbf{H}_{22}\mathbf{K})^{-1}}_{\mathbf{A}_3}\underbrace{\mathbf{H}_{21}}_{\mathbf{A}_4}]^{-1} =$$

$$\mathbf{H}_{11}^{-1} - \mathbf{H}_{11}^{-1}\mathbf{H}_{12}\mathbf{K}(\mathbf{H}_{21}\mathbf{H}_{11}^{-1}\mathbf{H}_{12}\mathbf{K} + (\mathbf{I} - \mathbf{H}_{22}\mathbf{K}))^{-1}\mathbf{H}_{21}\mathbf{H}_{11}^{-1} =$$

$$\underbrace{\mathbf{H}_{11}^{-1}}_{11} \underbrace{-\mathbf{H}_{11}^{-1}\mathbf{H}_{12}}_{12}\mathbf{K}(\mathbf{I} - (\underbrace{\mathbf{H}_{22} - \mathbf{H}_{21}\mathbf{H}_{11}^{-1}\mathbf{H}_{12}}_{22})\mathbf{K})^{-1}\underbrace{\mathbf{H}_{21}\mathbf{H}_{11}^{-1}}_{21} \tag{D.17}$$

On the right side of Equation (D.17) we recognize the form of the LFT as in Equation (D.9) using the indices to map it to Equation (D.16), which completes the proof. ■

D.3.3.2 Inverse of Upper LFT

The upper inverse LFT is formulated in Lemma D.3.

Lemma D.3
Let $\boldsymbol{H}$ be a partitioned matrix as in Equation (D.14), then the inverse becomes

$$F_u(\boldsymbol{H}, \boldsymbol{\Delta})^{-1} = F_u(\boldsymbol{H}_{ui}, \boldsymbol{\Delta}) \tag{D.18}$$

where

$$\boldsymbol{H}_{ui} = \begin{bmatrix} \boldsymbol{H}_{11} - \boldsymbol{H}_{12}\boldsymbol{H}_{22}^{-1}\boldsymbol{H}_{21} & \boldsymbol{H}_{12}\boldsymbol{H}_{22}^{-1} \\ -\boldsymbol{H}_{22}^{-1}\boldsymbol{H}_{21} & \boldsymbol{H}_{22}^{-1} \end{bmatrix} \tag{D.19}$$

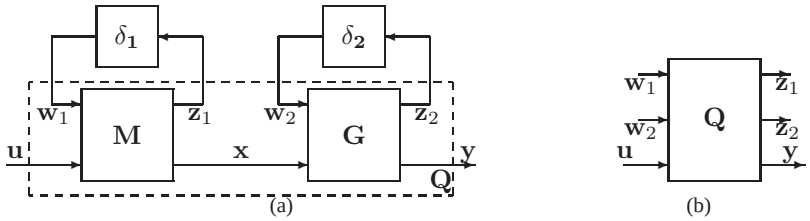

Figure D.2: *The (a) part of the figure illustrated the concatenation of two LFTs with the combined LFT shown in (b).*

Proof: We take the inverse of Equation (D.12) and formulate it in terms of Equation (D.13), recognizing the associated elements.

$$[\underbrace{\mathbf{H}_{22}}_{\mathbf{A}_1}+\underbrace{\mathbf{H}_{21}\boldsymbol{\Delta}}_{\mathbf{A}_2}\underbrace{(\mathbf{I}-\mathbf{H}_{11}\boldsymbol{\Delta})^{-1}}_{\mathbf{A}_3}\underbrace{\mathbf{H}_{12}}_{\mathbf{A}_4}]^{-1}=$$

$$\mathbf{H}_{22}^{-1}-\mathbf{H}_{22}^{-1}\mathbf{H}_{21}\boldsymbol{\Delta}(\mathbf{H}_{12}\mathbf{H}_{22}^{-1}\mathbf{H}_{21}\boldsymbol{\Delta}+(\mathbf{I}-\mathbf{H}_{11}\boldsymbol{\Delta}))^{-1}\mathbf{H}_{12}\mathbf{H}_{22}^{-1}=$$

$$\underbrace{\mathbf{H}_{22}^{-1}}_{22}\underbrace{-\mathbf{H}_{22}^{-1}\mathbf{H}_{21}}_{21}\boldsymbol{\Delta}(\mathbf{I}-(\underbrace{\mathbf{H}_{11}-\mathbf{H}_{12}\mathbf{H}_{22}^{-1}\mathbf{H}_{21}}_{11})\boldsymbol{\Delta})^{-1}\underbrace{\mathbf{H}_{12}\mathbf{H}_{22}^{-1}}_{12} \tag{D.20}$$

On the right side of Equation (D.20) we recognize the form of the LFT as in Equation (D.12) using the indices to map it to Equation (D.19), which completes the proof. ■

D.3.4 Concatenation of upper LFTs

The concatenation of two LFTs as illustrated in Figure D.2 is expressed in Lemma D.4.

Lemma D.4
Let $\boldsymbol{M}$ *and* $\boldsymbol{G}$ *be partitioned matrices as in Equation (D.6). Then the concatenated LFT is*

$$F_u(\boldsymbol{Q},\boldsymbol{\Delta})=F_u(\boldsymbol{G},\delta_2)F_u(\boldsymbol{M},\delta_1) \tag{D.21}$$

where

$$\boldsymbol{Q}=\left[\begin{array}{ll|l} \boldsymbol{M}_{11} & \boldsymbol{0} & \boldsymbol{M}_{12} \\ \boldsymbol{G}_{12}\boldsymbol{M}_{21} & \boldsymbol{G}_{11} & \boldsymbol{G}_{12}\boldsymbol{M}_{22} \\ \hline \boldsymbol{G}_{22}\boldsymbol{M}_{21} & \boldsymbol{G}_{21} & \boldsymbol{G}_{22}\boldsymbol{M}_{22} \end{array}\right] \tag{D.22}$$

and

$$\boldsymbol{\Delta} = \begin{bmatrix} \delta_1 & 0 \\ 0 & \delta_2 \end{bmatrix} \tag{D.23}$$

Proof: Using Equation (D.6) we can write the equations for $\mathbf{M}$ and $\mathbf{G}$ respectively as

$$\begin{bmatrix} \mathbf{z}_1 \\ \mathbf{x} \end{bmatrix} = \begin{bmatrix} \mathbf{M}_{11} & \mathbf{M}_{12} \\ \mathbf{M}_{21} & \mathbf{M}_{22} \end{bmatrix} \begin{bmatrix} \mathbf{w}_1 \\ \mathbf{u} \end{bmatrix} \text{ and } \begin{bmatrix} \mathbf{z}_2 \\ \mathbf{y} \end{bmatrix} = \begin{bmatrix} \mathbf{G}_{11} & \mathbf{G}_{12} \\ \mathbf{G}_{21} & \mathbf{G}_{22} \end{bmatrix} \begin{bmatrix} \mathbf{w}_2 \\ \mathbf{x} \end{bmatrix} \tag{D.24}$$

Eliminating the connecting variable $\mathbf{x}$ and after some algebraic manipulations one obtains Equation (D.22) with the input output relationship illustrated in Figure D.2. ■
The concatenation of three LFTs is expressed in Lemma D.5.

Lemma D.5
*Let **M**, **G** and **H** be partitioned matrices as in Equation (D.6). Then the concatenated LFT is*

$$F_u(\boldsymbol{Q}, \boldsymbol{\Delta}) = F_u(\boldsymbol{H}, \delta_3) F_u(\boldsymbol{G}, \delta_2) F_u(\boldsymbol{M}, \delta_1) \tag{D.25}$$

where

$$\boldsymbol{Q} = \left[\begin{array}{lll|l} \boldsymbol{M}_{11} & \boldsymbol{0} & \boldsymbol{0} & \boldsymbol{M}_{12} \\ \boldsymbol{G}_{12}\boldsymbol{M}_{21} & \boldsymbol{G}_{11} & \boldsymbol{0} & \boldsymbol{G}_{12}\boldsymbol{M}_{22} \\ \boldsymbol{H}_{12}\boldsymbol{G}_{22}\boldsymbol{M}_{21} & \boldsymbol{H}_{12}\boldsymbol{G}_{21} & \boldsymbol{H}_{11} & \boldsymbol{H}_{12}\boldsymbol{G}_{22}\boldsymbol{M}_{22} \\ \hline \boldsymbol{H}_{22}\boldsymbol{G}_{22}\boldsymbol{M}_{21} & \boldsymbol{H}_{22}\boldsymbol{G}_{21} & \boldsymbol{H}_{21} & \boldsymbol{H}_{22}\boldsymbol{G}_{22}\boldsymbol{M}_{22} \end{array}\right] \tag{D.26}$$

and

$$\boldsymbol{\Delta} = \begin{bmatrix} \delta_1 & 0 & 0 \\ 0 & \delta_2 & 0 \\ 0 & 0 & \delta_3 \end{bmatrix} \tag{D.27}$$

Proof: The proof is similar to the one for Lemma D.4 applied in two consecutive steps. ■

D.3.5 Star Product of LFTs

A generalization of the upper and lower LFT is presented in the Redheffer star product (Redheffer 1959) and used on LFTs in (Redheffer 1960). The interconnections are defined in Figure D.3.

Lemma D.6
*Let **Q**, **M** and **R** be partitioned matrices as in Equation (D.6), then the interconnection structure illustrated in Figure D.3 can be computed as*

$$\begin{bmatrix} \boldsymbol{v}_3 \\ \boldsymbol{v}_2 \end{bmatrix} = \begin{bmatrix} \boldsymbol{R}_{11} & \boldsymbol{R}_{12} \\ \boldsymbol{R}_{21} & \boldsymbol{R}_{22} \end{bmatrix} \begin{bmatrix} \boldsymbol{r}_3 \\ \boldsymbol{r}_2 \end{bmatrix} \tag{D.28}$$

where

$$\boldsymbol{R} = \mathcal{S}(\boldsymbol{Q}, \boldsymbol{M}) = \begin{bmatrix} F_l(\boldsymbol{Q}, \boldsymbol{M}_{11}) & \boldsymbol{Q}_{12}(\boldsymbol{I} - \boldsymbol{M}_{11}\boldsymbol{Q}_{22})^{-1}\boldsymbol{M}_{12} \\ \boldsymbol{M}_{21}(\boldsymbol{I} - \boldsymbol{Q}_{22}\boldsymbol{M}_{11})^{-1}\boldsymbol{Q}_{21} & F_u(\boldsymbol{M}, \boldsymbol{Q}_{22}) \end{bmatrix} \tag{D.29}$$

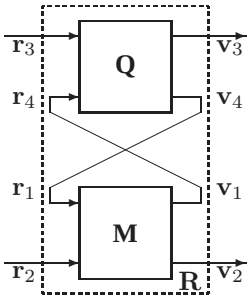

Figure D.3: *Star product of* $\mathbf{Q}$ *and* $\mathbf{M}$*, where* $\mathbf{R} = \mathcal{S}(\mathbf{Q}, \mathbf{M})$.

It shall be noted that $\mathcal{S}(\boldsymbol{Q}, \boldsymbol{M})$ *depends on the partitioning of the matrices* $\boldsymbol{Q}$ *and* $\boldsymbol{M}$*.* $\mathcal{S}(\boldsymbol{Q}, \boldsymbol{M})$ *is associative and if* $\boldsymbol{Q}$ *and* $\boldsymbol{M}$ *are dissipative* [1] *matrices then* $\mathcal{S}(\boldsymbol{Q}, \boldsymbol{M})$ *is also dissipative. (Redheffer 1959)*

Proof: Using the structure of Equation (D.6) and we have from Figure D.3 that $\mathbf{r}_4 = \mathbf{v}_1$ and $\mathbf{r}_1 = \mathbf{v}_4$ we can write

$$\mathbf{v}_2 = \mathbf{M}_{21}\mathbf{r}_1 + \mathbf{M}_{22}\mathbf{r}_2 = \mathbf{M}_{21}(\mathbf{Q}_{21}\mathbf{r}_3 + \mathbf{Q}_{22}\mathbf{r}_4) + \mathbf{M}_{22}\mathbf{r}_2 \tag{D.30}$$

and

$$\begin{aligned}
\mathbf{r}_4 &= \mathbf{M}_{11}\mathbf{r}_1 + \mathbf{M}_{12}\mathbf{r}_2 \\
\mathbf{r}_4 &= \mathbf{M}_{11}(\mathbf{Q}_{21}\mathbf{r}_3 + \mathbf{Q}_{22}\mathbf{r}_4) + \mathbf{M}_{12}\mathbf{r}_2 \\
\mathbf{r}_4 &= (\mathbf{I} - \mathbf{M}_{11}\mathbf{Q}_{22})^{-1}(\mathbf{M}_{11}\mathbf{Q}_{21}\mathbf{r}_3 + \mathbf{M}_{12}\mathbf{r}_2)
\end{aligned} \tag{D.31}$$

using the equality constraints of the interconnections above. Inserting Equation (D.31) into Equation (D.30) multiplying out and collecting terms we can write

$$\begin{aligned}
\mathbf{v}_2 \quad = \quad & (\mathbf{M}_{21}\mathbf{Q}_{21} + \mathbf{M}_{21}\mathbf{Q}_{22}(\mathbf{I} - \mathbf{M}_{11}\mathbf{Q}_{22})^{-1}\mathbf{M}_{11}\mathbf{Q}_{21})\mathbf{r}_3 + \\
& (\mathbf{M}_{21}\mathbf{Q}_{22}(\mathbf{I} - \mathbf{M}_{11}\mathbf{Q}_{22})^{-1}\mathbf{M}_{12} + \mathbf{M}_{22})\mathbf{r}_2
\end{aligned} \tag{D.32}$$

The last term in Equation (D.32) we recognize as the upper LFT $F_u(\mathbf{M}, \mathbf{Q}_{22})$. The first term we will rewrite as

$$\mathbf{M}_{21}(\mathbf{I} + \mathbf{Q}_{22}(\mathbf{I} - \mathbf{M}_{11}\mathbf{Q}_{22})^{-1}\mathbf{M}_{11})\mathbf{Q}_{21} \tag{D.33}$$

The outer parenthesis of Equation (D.33) can be recognized as the right hand side of the matrix inversion lemma in Equation (D.13) with a little rewriting. The numbers at the following under braces refer to the index numbers of Equation (D.13).

$$\underbrace{\mathbf{I}}_{1} + \mathbf{Q}_{22}(\underbrace{\mathbf{I}}_{3} \underbrace{-\mathbf{M}_{11}}_{4} \underbrace{\mathbf{Q}_{22}}_{2})^{-1}\mathbf{M}_{11} =$$

[1] A matrix $\mathbf{A}$ is dissipative if $\mathbf{A} + \mathbf{A}^*$ is negative definite. (Bernstein 2005)

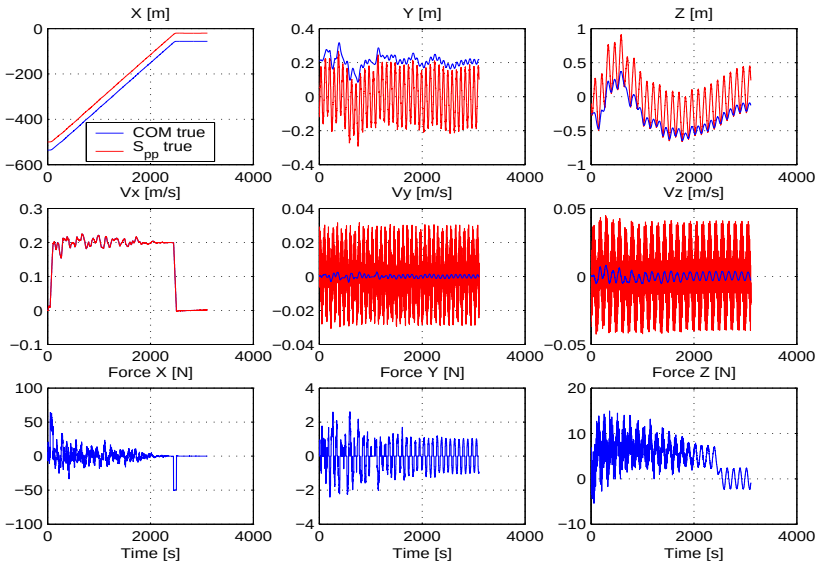

Figure D.4: *The full nonlinear simulation showing the port to port* $\mathbf{s}_{pp}$ *motion, the chaser COM motion, the associated velocities and the forces.* $\mathbf{x}(0) = [-500, 0, 0]^T$ *m and* $\dot{\mathbf{x}}(0) = \mathbf{0}$ *m/s.*

$$\mathbf{I}^{-1} - \mathbf{I}^{-1}\mathbf{Q}_{22}(-\mathbf{M}_{11}\mathbf{I}^{-1}\mathbf{Q}_{22} + \mathbf{I}^{-1})^{-1}(-\mathbf{M}_{11})\mathbf{I}^{-1} =$$

$$(\mathbf{I} - \mathbf{Q}_{22}\mathbf{M}_{11})^{-1} \tag{D.34}$$

Inserting Equation (D.34) back into Equation (D.33) then Equation (D.32) can be written as

$$\mathbf{v}_2 = \mathbf{M}_{21}(\mathbf{I} - \mathbf{Q}_{22}\mathbf{M}_{11})^{-1}\mathbf{Q}_{21}\mathbf{r}_3 + F_u(\mathbf{M}, \mathbf{Q}_{22})\mathbf{r}_2 \tag{D.35}$$

This completes the proof of the lower row of Equation (D.29). The upper row is verified by the same approach. ■

D.4 Simulation with Target Flexible Port Motion $\mathbf{s}_3$ to $\mathbf{s}_4$

The Figures 9.15 and 9.16 are repeated in this section in Figures D.4 and D.5 to show the difference when the flexible modes of the target docking port are used.

It is concluded that in terms of GNC performance there are no real differences. The velocities are clearly noisier as the RVS measures all the port vibrations.

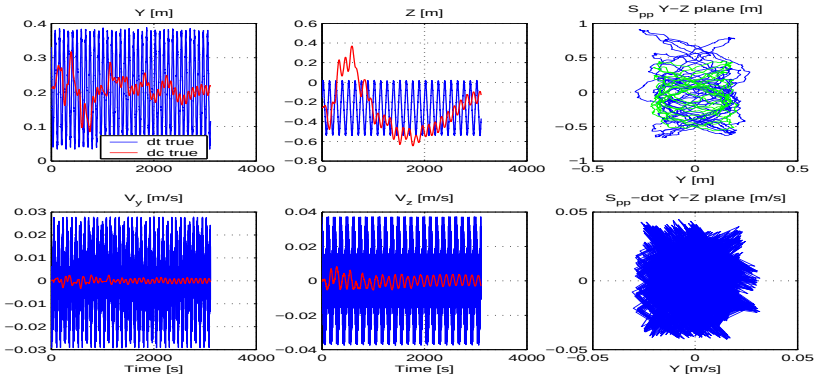

Figure D.5: *The full nonlinear simulation showing the true LVLH lateral port motions as well as the relative motion in the cross section y-z plane. The green part of the curve is for relative distance smaller than* 100 *m.*

D.5 Selection of Controller Type for the Final Approach

This section documents the design of the one degree of freedom model reference controller in Figure D.6. The weights used for this design are as listed in Table D.3.

In Figure D.7 is illustrated the tracking performance of the chaser port motion at worst case at the location s_4.

D.6 Simulation with Target Flexible Port Motion s_4 to Docking

The Figures D.8 and D.9 are repeated in this section to show the difference when the flexible modes of the target docking port are present for the worst case.

	A	M	ω	ω_1
$W_0 = 0.03$				
$W_n = 0.5$				
$W_e = \frac{\frac{1}{M}s+\omega}{s+A\omega}$	0.05	2	0.31	
$W_u = \frac{\frac{1}{M}s+\omega}{s+A\omega}$	100	0.01	9.42	
$W_{ref} = \frac{\omega^2}{s^2+2\zeta\omega s+\omega^2}\frac{s+\omega_1}{\omega_1}$			0.31	0.63

Table D.3: *Summary of all weights used for the one degree of freedom model reference $\mathcal{H}_\infty$ design.*

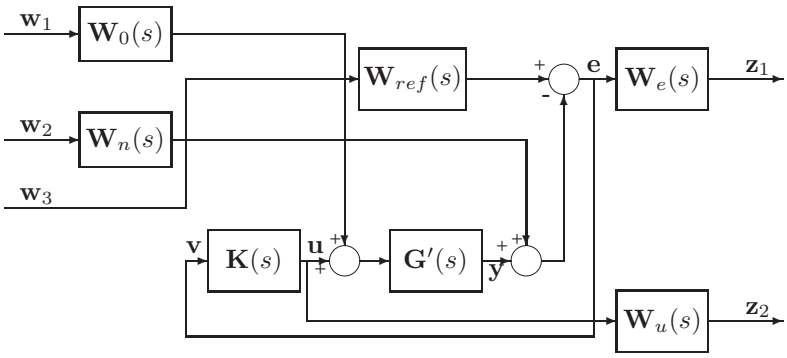

Figure D.6: *Signal based model reference configuration for the $\mathcal{H}_\infty$ design of a one degree of freedom controller.*

It is concluded that in terms of GNC performance there are no real practical differences. The velocities are clearly noisier as the RVS measures all the port vibrations.

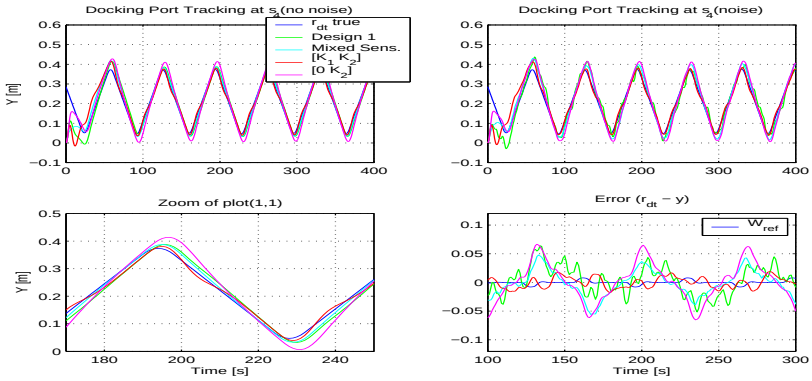

Figure D.7: *Tracking of worst case target port motion for the three controllers. Design* 1 *is the one degree of freedom model reference controller. The error plot compare the various errors with the error of* $\mathbf{W}_{ref}$*, which is considered the best possible.*

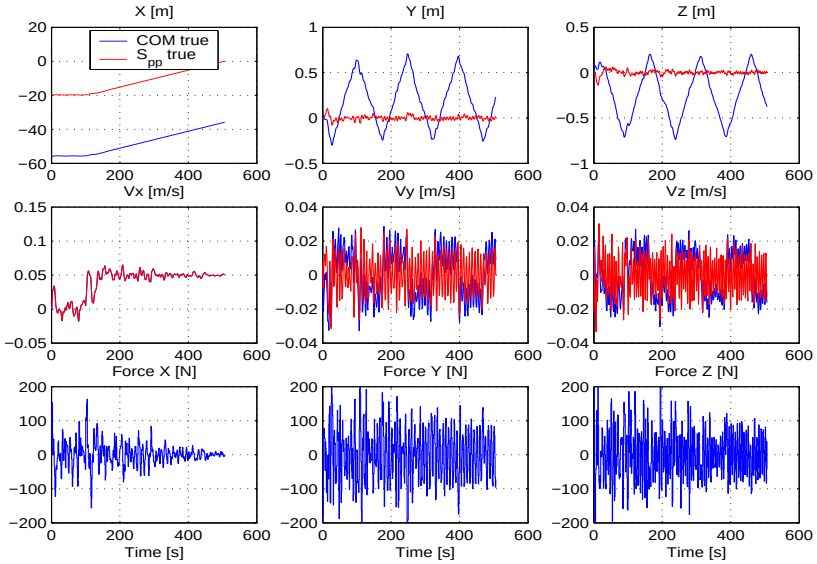

Figure D.8: *The full nonlinear simulation showing the port to port* $\mathbf{s}_{pp}$ *motion, the chaser COM motion, the associated velocities and control forces. The initial condition is* $\mathbf{s}_{pp}(0) = [-20, 0, 0]^T$ *m and* $\dot{\mathbf{s}}_{pp}(0) = \mathbf{0}$ *m/s.*

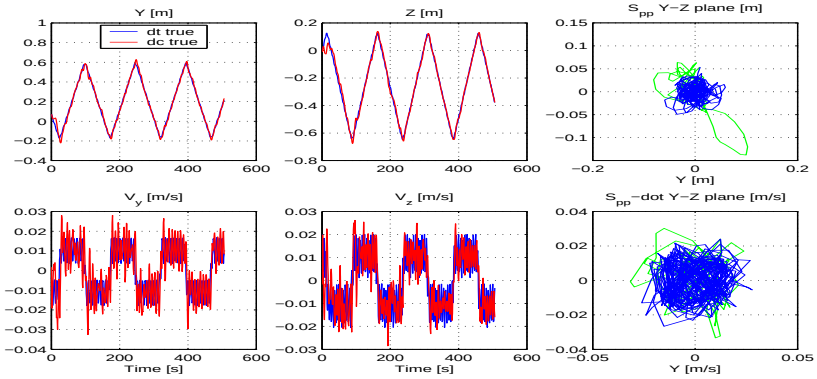

Figure D.9: *The full nonlinear simulation showing the true LVLH lateral port motions as well as the relative motion in the cross section y-z plane. The green part of the curve is during the station keeping at* s_4.

Bibliography

Ankersen, F. (1989), 'Thruster Modulation Techniques: Application to Eureca Attitude and Orbit Control System.', *ESA working paper.* p. EWP 1528.

Ankersen, F. (1990*a*), 'Assessment of Existing and Model Reference Control Systems for RVD.', *ESA working paper.* p. 900827FA.

Ankersen, F. (1990*b*), 'Derivation of Relative Motion Equations for RVD.', *ESA working paper.* pp. TN/FA–90/01 Issue 1.0.

Ankersen, F. (1990*c*), 'Thruster Failure Impact on Control Performance and Docking Kinematics.', *ESA working paper.* pp. TN/FA–90/02 Issue 2.1.

Ankersen, F. (1990*d*), 'Thruster Open Failure Simulation and Analysis.', *ESA working paper.* p. EWP 1601.

Ankersen, F. (1991), 'Accuracy of Finite Pulse Hohmann Orbit Transfer.', *ESA working paper.* p. EWP 1632.

Ankersen, F. (1993), 'Application of CAE methods for the On-Board Flight Control System on the ARC Mission.', *ESA working paper* pp. TN/FA–001 Issue 1.0.

Ankersen, F. (1998), 'Design of Realtime Onboard GNC Systems Using Integrated Design Tools.', *Proceedings of 14th IFAC Symposium on Automatic Control in Aerospace. August 24-28, Seoul, Korea*. .

Ankersen, F. (1999), 'Control Design for the Rosetta Comet Lander.', *Proceedings of 14th IFAC Symposium on Automatic Control in Aerospace. August 24-28, Seoul, Korea and in Space Technology* **19**(3-4), 179–189.

Ankersen, F. (2002), 'A Mathematical Approach to Monte Carlo Simulations and their Statistical Post Processing.', *ESA working paper.* p. EWP 2271.

Ankersen, F., Wu, S., Aleshin, A., Vankov, A. & Volochinov, V. (2004), 'On Optimization of Spacecraft Thruster Management Function', *Proceedings of AIAA Guidance, Navigation and Control Conference, August 16-19, Rhode Island, USA* .

Ankersen, F., Wu, S., Aleshin, A., Vankov, A. & Volochinov, V. (2005), 'Optimization of Spacecraft Thruster Management Function', *Journal of Guidance, Control and Dynamics*. **28**(6), 1283–1291.

Anthony, M. & Sasaki, F. (1965), 'Rendezvous Problem for Nearly Circular Orbits', *AIAA Journal* **3**(9), 1666–1673.

Anthony, T., Wie, B. & Carroll, S. (1989), 'Pulse-Modulated Control Synthesis for a Flexible Spacecraft', *Journal of Guidance* **13**(6), 1014–1022.

Arnold, W. & Laub, A. (1984), 'Generalized Eigenproblem Algorithms and Software for Algebraic Riccati Equations', *Proceedings of the IEEE* **72**(12), 1746–1754.

Åström, K. (1997), *Computer Controlled Systems, Theory and Design*, Prentice-Hall, Englewood Cliff, N.J.

Åström, K. & Wittenmark, B. (1989), *Adaptive Control*, Addison-Wesley Publishing Company.

Balas, G., Doyle, J., Glover, K., Packard, A. & Smith, R. (1998), *μ-Analysis and Synthesis Toolbox*, MUSYN Inc. and MathWorks, Inc.

Balas, G., Packard, A., Safonov, M. & Chiang, R. (2004), 'Next Generation of Tools for Robust Control', *Proceedings of the 2004 American Control Conference, Boston, Massachusetts June 30 - July 2* .

Belew, L. (1973), 'Skylab Systems Flight Performance - An Interim Report', *IAF, International Astronautical Congress, 24th, Baku, Azerbaidzhan SSR* .

Bernelli-Zazzera, F., Mantegazza, P. & Nurzia, V. (1998), 'Multi-Pulse-Width Modulated Control of Linear Systems', *Journal of Guidance, Control and Dynamics* **21**(1).

Bernstein, D. S. (2005), *Matrix Mathematics*, Princeton University Press.

Berreen, T. & Crisp, J. (1976), 'An Exact and a New First-Order Solution fot the Relative Trajectories of a Probe Ejected from a Space Station', *Celestial Mechanics* **13**(1), 75–88.

Berreen, T. & Sved, G. (1979), 'Relative Motion of Particles in Coplanar Elliptic Orbits', *Journal of Guidance and Control* **2**(5).

Bodineau, G., Boulade, S., Frapard, B., Chen, W., Salehi, S. & Ankersen, F. (2005), 'Robust Control of Large Flexible Appendages for Future Space Missions', *Proceedings Fifth ESA International Conference on Spacecraft Guidance, Navigation and Control Systems,Loutraki , Greece, Oct. 17-20* .

Bourdon, J., Delpy, P., Ganet, M., Quinquis, I. & Ankersen, F. (2003), 'Application of H_∞ Design on ATV Control Loop during the Rendezvous Phase', *Space Technology* **24**(00).

Bristol, E. (1966), 'On a new measure of interactions for multivariable process control', *IEEE Transactions on Automatic Control* **11**, 133–134.

Brondino, G. & Legenne, J. (1991), 'Hermes Guidance, Navigation, and Control System for Rendezvous Phases', *ESA, Spacecraft Guidance, Navigation and Control Systems Conference* pp. 245–255.

Bronstein, I. (1999), *Taschenbuch der Mathematik*, Verlag Harri Deutsch.

Broucke, R. (2002), 'A Solution of the Elliptic Rendezvous Problem with the Time as Independent Variable', *AAS paper 02-144* pp. 585–604.

Calhoun, P. & Dabney, R. (1995), 'A Solution to the Problem of Determining the Relative 6-DOF State for Spacecraft Automated Rendezvous and Docking', *Proceedings of the SPIE* **2466**, 175–184.

Campbell, M. (2003), 'Planning Algorithm for Multiple Satellite Clusters', *Journal of Guidance, Control and Dynamics* **26**(5), 770–780.

Cao, L. (1997), 'Mixed Sensitivity Optimization to Avoid Pole/Zero Cancellation', *Automatica* **33**(7), 1379–1385.

Carpenter, J. R. & Bishop, R. (1997), 'Navigation Filter Estimate Fusion for Enhanced Spacecraft Rendezvous', *Journal of Guidance, Control, and Dynamics* **20**(2), 338–345.

Carter, T. (1984), 'Fuel-Optimal Maneuvers of a Spacecraft Relative to a Point in Circular Orbit', *Journal of Guidance, Control and Dynamics* **7**(6), 710–716.

Carter, T. E. (1990), 'New Form for the Optimal Rendezvous Equations Near Keplerian Orbits', *Journal of Guidance, Control and Dynamics* **13**(1), 183–186.

Carter, T. E. (1998), 'State Transition Matrices for Terminal Rendezvous Studies: Brief Survey and New Example', *Journal of Guidance, Control and Dynamics* **21**(1).

Carter, T. & Humi, M. (2002), 'Clohessy-Wiltshire Equations Modified to Include Quadratic Drag', *Journal of Guidance, Control and Dynamics* **25**(6), 1058–1063.

Chang, J. & Yu, C. (1990), 'The relative gain for non-square multivariable systems', *Chemical Engineering Sciences* **45**, 1309–1323.

Cislaghi, M., Fehse, W., Paris, D. & Ankersen, F. (1999), 'The ATV Rendezvous Pre-Development Programme (ARP)', *Proceedings of the 22nd AAS Guidance and Control Conference, Feb. Breckenridge, Colorado* .

Clohessy, W. & Wiltshire, R. (1959), 'Terminal Guidance System for Satellite Rendezvous', *Inst. of the Aerospace Sciences Summer Meeting, Los Angeles* . 59-93.

Clohessy, W. & Wiltshire, R. (1960), 'Terminal Guidance System for Satellite Rendezvous', *Journal of the Aerospace Sciences* **27**(9), 653–658.

Copps, S. & Goode, J. (1971), 'Operations and Functions of the Minkey Rendezvous Computer Program in the Apollo Command Module Computer', *ION* .

Cruzen, C., Lomas, J. & Dabney, R. (2000), 'Test Results for the Automated Rendezvous and Capture System', *Guidance and Control 2000; Proceedings of the Annual AAS Rocky Mountain Conference, Breckenridge* **104**, 35–56.

Dahleh, M. & Kammash, M. (1993), 'Controller Design for Plants with Structured Uncertainty', *Automatica* **29**(1), 37–56.

Doyle, J. C. (1978), 'Guaranteed Margins for LQG Regulators', *IEEE Transactions on Automatic Control* **23**(4), 756–757.

Doyle, J. C., Glover, K., Khargonekar, P. P. & Francis, B. A. (1989), 'State-Space Solutions to Standard $\mathcal{H}_2$ and $\mathcal{H}_\infty$ Control Problems', *IEEE Transactions on Automatic Control* **34**(8), 831–847.

Doyle, J. C. & Stein, G. (1979), 'Robustness with Observers', *IEEE Transactions on Automatic Control* **24**(4), 607–611.

Doyle, J. C. & Stein, G. (1981), 'Multivariable Feedback Design: Concepts for a Classical/Modern Synthesis', *IEEE Transactions on Automatic Control* **26**(1), 4–16.

Duboshin, G. (1963), *Nebesnaya Mekhaniki. Osnovnyye zadachi i metody (Celestial Mechanics)*, Yizmatgiz.

Eckstein, M. (1987), 'Safe Rendezvous Approach to a Space Station by Impulsive Transfers and Continuous Thrust Arcs', *AAS Paper 87-540* pp. 1515–1535.

Eggleston, J. (1960), 'Optimum Time to Rendezvous', *ARS Journal* **30**, 1089–1091.

Euler, E. & Shulman, Y. (1967), 'Second-Order Solution to the Elliptical Rendezvous Problem', *AIAA Journal* **5**(5), 1033–1035.

Fabrega, J., Frezet, M. & Gonnaud, J. (1997), 'ATV GNC During Rendezvous', *ESA International Conference on Spacecraft Guidance, Navigation and Control Systems, 3rd, Noordwijk, Netherlands* pp. 85–93.

Fabrega, J., Godet, V., Pairot, J. & Perarnaud, D. (1998), 'ATV - Designing Avionics for Rendezvous Safety', *IAF Paper 98-T210, International Astronautical Congress, 49th, Melbourne,Australia* .

Fehse, W. (2003), *Automated Rendezvous and Docking of Spacecraft*, Cambridge University Press.

Fehse, W. & Ortega, G. (1998), 'Operator Monitoring and Support System for Rendezvous and Docking, Paper ID: 2a004', *SpaceOps98 Proceedings, Fifth International Symposium on Space Mission Operations and Ground Data Systems. National Space Development Agency of Japan, Tokyo, Japan* .

Fle (1994), *Docking Berthing Control Analysis, RVD_DBCA_II_TN_ERN_02*, Deutche Aerospace, Bremen.

Florac, W., Carleton, A. & Barnard, J. (2000), 'Statistical Process Control: Analyzing Space Shuttle Onboard Software Process', *IEEE Software* **17**(4), 97–106.

Franklin, G., Powell, J. & Workman, M. (1998), *Digital Control of Dynamic Systems*, Addison Wesley.

Friedlander, M. & Hare, J. (1987), 'Shuttle and ELV Flight Planning Using the Flight Design System', *AIAA Paper 871908* .

Garrison, J., Gardner, T. & Axelrad, P. (1995), 'Relative Motion in Highly Elliptical Orbits', *Advances in the Astronautical Sciences* **89**(1), 1359–1376.

Geller, D. (2006), 'Linear Covariance Techniques for Orbital Rendezvous Analysis and Autonomous Onboard Mission Planning', *Journal of Guidance, Control and Dynamics* **29**(6), 1404–1414.

Geller, D. (2007), 'Orbital Rendezvous: When Is Autonomy Required?', *Journal of Guidance, Control and Dynamics* **30**(4), 974–981.

Gim, D. & Alfriend, K. (2003), 'State Transition Matrix of Relative Motion for the Perturbed Noncircular Reference Orbit', *Journal of Guidance, Control and Dynamics* **26**(6), 956–971.

Glad., T. & Ljung, L. (1981), *Reglerteknik, Grundläggende teori*, 1 edn, Studentlitteratur.

Glover, K. & Doyle, J. C. (1988), 'State-space formulae for all stabilizing controllers that satisfy an $\mathcal{H}_\infty$-norm bound and relations to risk sensitivity', *Systems & Control Letters* **11**, 167–172.

Gonnaud, J., Tsang, M. & Sommer, J. (1997), 'ARPK GNC Design and Performances Evaluation for ATV Rendezvous', *ESA International Conference on Spacecraft Guidance, Navigation and Control Systems, 3rd, Noordwijk, Netherlands* pp. 95–101.

Goodwin, M. & Bochsler, D. (1987), 'Expert System Issues in Automated, Autonomous Space Vehicle Rendezvous', *SPIE Application of Artificial Intelligence* pp. 71–78.

Gradshteyn, I. & Ryzhik, I. (2007), *Table of Integrals, Series and Products*, 7 edn, Academic Press.

Green, M. & Limebeer, D. (1995), *Linear Robust Control*, Prentice Hall.

Guibout, V. & Scheeres, D. (2006), 'Spacecraft Formation Dynamics and Design', *Journal of Guidance, Control and Dynamics* **29**(1), 121–133.

Gurfil, P. (2005), 'Relative Motion Between Elliptic Orbits: Generalized Boundedness Conditions and Optimal Formationkeeping', *Journal of Guidance, Control and Dynamics* **28**(4), 761–767.

Gurfil, P. & Kasdin, N. (2004), 'Nonlinear Modeling of Spacecraft Relative Motion in the Configuration Space', *Journal of Guidance, Control and Dynamics* **27**(1), 154–157.

Gurfil, P. & Kholshevnikov, K. (2006), 'Manifolds and Metrics in the Relative Spacecraft Motion Problem', *Journal of Guidance, Control and Dynamics* **29**(4), 1004–1010.

Gustafson, D. & Kriegsman, B. (1973), 'A Guidance and Navigation System for Automatic Stationkeeping in Earth Orbit', *Journal of Spacecraft* **10**(6), 369–376.

Ha, J. & Mugellesi (1989), 'Analytical Models for Relative Motion Under Constant Thrust', *Journal of Guidance* **13**(4), 644–650.

Hablani, H. (2009), 'Autonomous Inertial Relative Navigation with Sight-Line-Stabilized Integrated Sensors for Spacecraft Rendezvous', *Journal of Guidance, Control and Dynamics* **32**(1), 172–183.

Hablani, H., Tapper, M. & Dana-Bashian, D. (2002), 'Guidance and Relative Navigation for Autonomous Rendezvous in a Circular Orbit', *Journal of Guidance, Control and Dynamics* **25**(3), 553–562.

Hartje, H. (1997), Guidance Performance Analysis, Technical Report ARPK-TN-RVC-2013-Dasa, ATV Pre Development Project, Daimler-Benz Aerospace.

Hechler, F. & Fertig, J. (1987), 'Minimum Delta-V Control of Relative Motion under Operational and Safety Constraints', *AAS paper 87-520* pp. 1279–1302.

Hechler, M. (1997), 'Rosetta Mission Design', *Advances in Space Research* **19**(1), 127–136.

Hedin, A. (1986), 'MSIS-86 Thermospheric Model', *Journal of Geophysics Research* **92**.

Heimbold, G. & Steward, N. (1988), 'Hardware Simulation of Spacecraft Motion with the European Proximity Operations Simulator (EPOS)', *Simulation Environments and Symbol and Number Processing on Multi and Array Processors. Proceedings of the European Simulation Multiconference, Nice, France* pp. 87–92.

Hill, G. (1874), 'A Method of Computing Absolute Perturbations', *Astronomische Nachrichten* **83**(1982), 209–224.

Hill, G. (1878), 'Researches in the Lunar Theory', *American Journal of Mathematics* **1**(1), 5–26.

Ho, C.-C. & McClamroch, N. (1993), 'Automatic Spacecraft Docking Using Computer Vision-Based Guidance and Control Techniques', *Journal of Guidance, Control and Dynamics* **16**(2), 281–288.

Hsiao, F. & Scheeres, D. (2005), 'Design of Spacecraft Formation Orbits Relative to a Stabilized Trajectory', *Journal of Guidance, Control and Dynamics* **28**(4), 782–794.

Hu, J., Unbehauen, H. & Bohn, C. (1996), 'A Practical Approach to Selecting Weighting Functions for $\mathcal{H}_\infty$ Control and its Applications to a Pilot Plant', *UKACC International Conference on CONTROL* . Conference Publication 427.

Hua, T., Kubiak, E., Lin, Y. & Kilby, M. (1993), 'Control/Structure Interaction during Space Station Freedom-Orbiter Berthing', *The Fifth NASA/DOD Controls-Structures Interaction Technology Conference* pp. 181–203.

Hughes, P. (1986), *Spacecraft Attitude Dynamics*, John Wiley & Sons.

Humi, M. (1993), 'Fuel-Optimal Rendezvous in a General Central Force Field', *Journal of Guidance, Control and Dynamics* **16**(1), 215–217.

Humi, M. (2005), 'Planar Three-Body Problem in Rendezvous Coordinates', *Journal of Guidance, Control and Dynamics* **28**(3), 553–557.

Humi, M. & Carter, T. (2002), 'Rendezvous Equations in a Central-Force Field with Linear Drag', *Journal of Guidance, Control and Dynamics* **25**(1), 74–79.

Ieko, T., Ochi, Y. & Kanai, K. (1997), 'A New Digital Redesign Method for Pulse-Width Modulation Control Systems', *AIAA proceedings AIAA-97-3700* .

Ignagni, M. (1990), 'Separate-Bias Kalman Estimator with Bias State Noise', *IEEE Transactions on Automatic Control* **35**(3), 338–341.

Inalhan, G., Tillerson, M. & How, J. (2002), 'Relative Dynamics and Control of Spacecraft Formations in Eccentric Orbits', *Journal of Guidance, Control and Dynamics* **25**(1), 48–59.

ISS (2006), *Reference Guide to the International Space Station, NASA SP-2006-557*, International Space Station Program.

Iwens, R. & Farrenkopf, R. (1971), 'Performance Evaluation of a Precision Attitude Determination System (PADS)', *AIAA Guidance, Navigation and Flight Mechanics Conference, Hempstead, NY, Paper 71-964* .

Jacchia, L. (1977), Thermospheric Temperature, Density and Composition: New Models, Technical Report 375, Smithsonian Astrophysical Observatory, .

Jones, R. (1992), 'An Autonomous Rendezvous, Docking and Landing System Using Cruise Missile Technologies', *SPIE Proceedings* **1694**, 102–107.

Jösson, U. & Rantzer, A. (1996), 'Systems with Uncertain Parameters; Time-Variations with Bounded Derivatives', *International Journal of Robust and Nonlinear Control* **6**(9-10), 969–982.

Junkins, J. & Turner, J. (1986), *Optimal Spacecraft Rotational Maneuvers*, Elsevier.

Karlgaard, C. (2006), 'Robust Rendezvous Navigation in Elliptical Orbit', *Journal of Guidance, Control and Dynamics* **29**(2), 495–499.

Karlgaard, C. & Lutze, F. (2003), 'Second-Order Relative Motion Equations', *Journal of Guidance, Control and Dynamics* **26**(1), 41–49.

Kawano, I., Mokuno, M., Kasai, T. & Suzuki, T. (2001), 'Result of Autonomous Rendezvous Docking Experiment of Engineering Test Satellite-VII', *Spacecraft Design, Testing and Performance* **38**(1), 105–111.

Kechichian, J. (1992), 'Techniques of Accurate Analytic Terminal Rendezvous in Near-Circular Orbit', *Acta Astronautica* **26**(6), 377–394.

Khalil, H. (1996), *Nonlinear Systems*, Prentice Hall.

Kida, T., Yamaguchi, I., Chida, Y. & Sekiguchi, T. (1997), 'On-Orbit Robust Control Experiment of Flexible Spacecraft ETS-VI', *Journal of Guidance, Control, and Dynamics* **20**(5), 865–872.

Kluever, C. (1999), 'Feedback Control for Spacecraft Rendezvous and Docking', *Journal of Guidance, Control and Dynamics* **22**(4), 609–611.

Kreyszig, E. (1979), *Advanced Engineering Mathematics*, 4 edn, Wiley.

Kruse, F. & Ankersen, F. (1992), 'The RendezVous Onboard System Simulator (Ross) - System Software Design Concepts.', *Proceedings of 2'nd Workshop on Simulators for European Space Programmes.* .

Kunugi, M., Koyama, H., Okanuma, T., Nakamura, T., Mokuno, M., Kawano, I., Horiguchi, H. & Kibe, K. (1994), 'Guidance, Navigation and Control System in Engineering Test Satellite VII Rendezvous and Docking Experiment', *IFAC, IEEE, Proceedings of 13th Symposium on Automatic Control in Aerospace, Palo Alto, CA* pp. 303–308.

Kwakernaak, H. & Sivan, R. (1972), *Linear Optimal Control Systems*, Wiley Interscience.

Lancaster, E. (1970), 'Relative Motion of Two Particles in Co-Planar Elliptical Orbits', *AIAA Journal* **8**(10).

Landshof, J., Harvey, R. & Marshall, M. (1994), 'Concurrent Engineering: Spacecraft and Mission Operations System Design', *NASA, Goddard Space Flight Center, Third International Symposium on Space Mission Operations and Ground Data Systems* .

Lane, C. & Axelrad, P. (2006), 'Formation Design in Eccentric Orbits Using Linearized Equations of Relative Motion', *Journal of Guidance, Control and Dynamics* **29**(1), 146–160.

Larson, W. & Wertz, J. (1991), *Space Mission Analysis and Design*, 1 edn, Kluwer Academic Publishers.

Lathi, B. (1974), *Signals, Systems, and Controls*, 1 edn, Thomas Y. Crowell Harper & Row, Publishers.

Lawden, D. (1954), 'Fundamentals of Space Navigation', *British Interplanetary Society Journal* **13**, 87–101.

Lawden, D. (1993), 'Time-Closed Optimal Transfer by Two Impulses Between Coplanar Elliptic Orbits', *Journal of Guidance, Control and Dynamics* **16**(3).

Limebeer, D., Kasenally, E. & Perkins, J. (1993), 'On the Design of Robust Two Degree of Freedom Controllers', *Automatica* **29**(1), 157–168.

Ljung, L. (1981), *Reglerteori, Moderna analys- och syntesmetoder*, 1 edn, Studentlitteratur.

London, H. (1963), 'Second Approximation to the Solution of the Rendezvous Equations', *AIAA Journal* **1**(7), 1691–1693.

Lopes, I. & McInnes, C. (1995), 'Autonomous Rendezvous Using Artificial Potential Function Guidance', *Journal of Guidance, Control and Dynamics* **18**(2), 237–241.

Luo, Y., Lei, Y. & Tang, G. (2007), 'Optimal Multi-Objective Nonlinear Impulsive Rendezvous', *Journal of Guidance, Control and Dynamics* **30**(4), 994–1002.

Luo, Y., Tang, G., Lei, Y. & Li, H. (2007), 'Optimization of Multiple-Impulse, Multiple-Revolution, Rendezvous-Phasing Maneuvers', *Journal of Guidance, Control and Dynamics* **30**(4), 946–952.

Malcom, H. & Utterback, H. (1999), 'Flight Software in the Space Department: a Look at the Past and a View Toward the Future', *Johns Hopkins APL Technical Digest* **20**(4), 522–532.

Manceaux-Cumer, C. & Chretien, J. (2001), 'Minimal LFT form of a spacecraft build up from two bodies', *AIAA Guidance, Navigation and Control Conference and Exhibit, Montreal, Canada* .

McAdams, J. V. (1997), 'Postlaunch Contingency Trajectories for the Near-Earth Asteroid Rendezvous Mission', *Journal of Guidance, Control and Dynamics* **20**(4), 819–823.

McGlathery, D. (1973), Space Shuttle Rendezous, Radiation and Reentry Analysis Code, Technical Report NASA-TM-X-64768, Nasa, Marshall Space Flight Center, Huntsville, AL.

Megretski, A. & Rantzer, A. (1997), 'System Analysis via Integral Quadratic Constraints', *IEEE Transactions on Automatic Control* **42**(6), 819–830.

Melton, R. (2000), 'Time-Explicit Representation of Relative Motion Between Elliptical Orbits', *Journal of Guidance, Control and Dynamics* **16**(4).

Melton, R. (2003), 'Comparison of Relative-Motion Models for Elliptical Orbits', *Satellite Constellation and Formation Flying Third International Workshop, Feb. 24-26, Pisa, Italy* .

Mohler, R. (1991), *Nonlinear Systems, Dynamics and Control*, Prentice Hall.

Mokuno, M., Kawano, I., Horiguchi, H. & Kibe, K. (1995), 'Development of ETS-VII RVD System - Preliminary Design and EM Development Phase', *AIAA Guidance, Navigation and Control Conference, Baltimore, MD* .

Montgomery, R. & Wu, S. (1993), 'Simulation of the Attitude Determination System for Space Station Berthing Dynamics Research', *NASA, Langley Research Center, Hampton, VA, ND210491* .

Mora, E., Ankersen, F. & Serrano, J. (1996), 'MIMO Control for 6DoF Relative Motion.', *Proceedings of 3'rd ESA International Conference on Spacecraft Guidance, Navigation and Control Systems. Nov.26-29* .

Moreau, G. & Marcille, H. (1998*a*), 'On-board Precise Relative Orbit Determination', *GNSS 98 - European Symposium on Global Navigation Satellite Systems, 2nd, Toulouse, France, A99-39551 10-32* .

Moreau, G. & Marcille, H. (1998*b*), 'RGPS Post-Flight Analysis of ARP-K Flight Demonstrations', *ION GPS-98; Proceedings of the 11th International Technical Meeting of the Satellite Division of the Institute of Navigation, Nashville, TN* .

Mukhopadhyad, V. & Newsom, J. (1984), 'A Multiloop System Stability Margin Study Using Matrix Singular Values', *Journal of Guidance* **7**(5), 582–587.

Mukundan, R. & Ramakrishnan, K. (1995), 'A Quaternion Solution to the Pose Determination Problem for Rendezvous and Docking Simulations', *Mathematics and Computers in Simulations* **39**(1), 143–153.

Neff, J. & Fowler, W. (1991), 'Minimum-Fuel Rescue Trajectories for the Extravehicular Excursion Unit', *Journal of the Astronautical Sciences* **31**(1), 21–45.

Newsom, J. R. & Mukhopadhyad, V. (1985), 'A Multiloop Robust Controller Design Study Using Singular Value Gradients', *Journal of Guidance* **8**(4), 514–519.

Newton, I. (1713), *Mathematical Principles of Natural Philosophy*, Royal Society.

Ogata, K. (1970), *Modern Control Engineering*, Prentice-Hall.

OMV (1985), *Automatic rendezvous and docking systems functional and performance requirements, NASA-CR-171866*, Scientific Systems, Inc., Cambridge, MA.

Packard, A. & Doyle, J. (1993), 'The Complex Structured Singular Value', *Automatica* **29**(1), 71–109.

Papoulis, A. (1984), *Probability, Random Variables, and Stochastic Processes*, McGraw-Hill.

Parry, P., Golub, A. & Southwood, D. (1989), 'Orbital Maneuvering Vehicle Attitude Control System', *AIAA Guidance, Navigation and Control Conference, Boston, MA* pp. 1465–1475.

Pauvert, C., Ankersen, F. & Soppa, U. (1991), 'Verification Tests for a Prototype RVD GNC on-board Software.', *Proceedings of ESA International Conference on Spacecraft GNC Systems, 4-7 June, ESTEC Noordwijk, Netherlands* .

Paw, Y. & Balas, G. (2008), 'Uncertainty Modeling, Analysis and Robust Flight Control Design for a Small UAV System', *AIAA Guidance, Navigation and Control Conference, Honolulu, Hawaii* .

Peiman, G., Maghami, D., Sparks, D. & Lim, K. (1998), 'Fault Accommodation in Control of Flexible Systems', *Journal of Guidance, Control, and Dynamics* **21**(3), 500–507.

Pery, V., Bouchery, J., Querrec, L., Maurel, E. & Ruffino, F. (2004), 'ATV "Jules Verne" Tests Campaign', *Proceedings of the 5th International Symposium on Environmental Testing for Space Programmes 15-17 June 2004, Noordwijk, The Netherlands* .

Philip, N. & Malik, N. (1993), 'Guidance and Control Aspect of Space Rendezvous and Docking', *Journal of Spacecraft Technology* **3**(1), 48–56.

Poolla, K. & Tikku, A. (1995), 'Robust Performance Against Time-Varying Structured Perturbations', *IEEE Transactions on Automatic Control* **40**(9), 1589–1602.

Press, W., Flannery, B., Teukolsky, S. & Vetterling, W. (1986), *Numerical Recipies, The Art of Scientific Computing*, Cambridge University Press.

Rabenstein, A. L. (1975), *Elementary Differential Equations with Linear Algebra*, second edn, Academic Press, Inc.

Redheffer, R. (1959), 'Inequalities for a Matrix Ricatti Equation', *Journal of Mathematics and Mechanics* **9**, 349–367.

Redheffer, R. (1960), 'On a Certain Linear Fractional Transformation', *Journal of Mathematics and Physics* **39**, 269–286.

Renner, U. (1983), *Satelliten-Technik*, Springer Verlag.

Roy, A. E. (1976), *Orbital Motion.*, Hilger.

Rugh, W. (1996), *Linear System Theory*, Prentice Hall.

Scheeres, D., Hsiao, F. & Vinh, N. (2003), 'Stabilizing Motion Relative to an Unstable Orbit: Applications to Spacecraft Formation Flight', *Journal of Guidance, Control and Dynamics* **26**(1), 62–73.

Schweighart, S. & Sedwick, R. (2002), 'High-Fidelety Linearized J_2 Model for Satellite Formation Flight', *Journal of Guidance, Control and Dynamics* **25**(6), 1073–1080.

Scott, M. A., Gilbert, M. & Demeo, M. (1993), 'Active Vibration Damping of the Space Shuttle Remote Manipulator Arm', *Journal of Guidance, Control and Dynamics* **16**(2), 275–280.

Seetharama-Bath, M., Sreenatha, A. & Shrivastava, S. (1991), 'Robust Low order Dynamic Controller for Flexible Spacecraft', *IEE Proceedings (Control Theory and Applications)* **138**(5), 460–468.

Sengupta, P. & Vadali, S. (2007), 'Relative Motion and the Geometry of Formations in Keplerian Elliptic Orbits', *Journal of Guidance, Control and Dynamics* **30**(4), 953–963.

Shamma, J. (1994), 'Robust Stability with Time-Varying Structured Uncertainty', *IEEE Transactions on Automatic Control* **39**(4), 714–724.

Shen, H. & Tsiotras, P. (2003), 'Optimal Two-Impulse Rendezvous Using Multiple-Revolution Lambert Solutions', *Journal of Guidance, Control and Dynamics* **26**(1), 50–61.

Shibata, M. & Ichikawa, A. (2007), 'Orbital Rendezvous and Flyaround Based on Null Controllability with Vanishing Energy', *Journal of Guidance, Control and Dynamics* **30**(4), 934–945.

Shulman, Y. & Scott, J. (1966), 'Terminal Rendezvous for Elliptical Orbits', *AIAA Paper* . 66-533.

Silva, N., Martel, F. & Delpy, P. (2005), 'Automated Transfer Vehicle Thrusters Selection and Management Function', *Proceedings of the* 6^{th} *International ESA conference on Guidance, Navigation and Control Systems, Loutraki, Greece* .

Singla, P., Subbarao, K. & Junkins, J. (2006), 'Adaptive Output Feedback Control for Spacecraft Rendezvous and Docking Under Measurement Uncertainty', *Journal of Guidance, Control and Dynamics* **29**(4), 892–902.

Skogestad, S. & Postlethwaite, I. (1996), *Multivariable Feedback Control*, Wiley.

Skogestad, S. & Postlethwaite, I. (2005), *Multivariable Feedback Control*, Wiley.

Sommer, J., Tobias, A., Ankersen, F. & Pauvert, C. (1992), 'On-Board Software for Automatic RVD and its Embedding in the System Simulator ROSS.', *Proceedings of Spacecraft Guidance, Navigation and Control Systems Software for Design and Implementation, Sept.29 - Oct.1, ESTEC Noordwijk, Netherlands.* .

Soppa, U., Ankersen, F. & Pauvert, C. (1992), 'RendezVous On-Board System Simulator Ross and Test Results from RVD Proof of Concept.', *Proceedings of Workshop on Spacecraft Automation and On-board Autonomous Mission Control. Sept.14-16, Darmstadt, Germany* .

Soppa, U., Sommer, J., Tobias, A., Panicucci, M. & Olivier-Martin, L. (1991), 'Mission and Vehicle Management and FDIR Functions for GNC Systems for Rendezvous Operations', *ESA, Spacecraft Guidance, Navigation and Control Systems Conf.* pp. 231–236.

Spradlin, E. (1960), 'The Long-Time Satellite Rendezvous Trajectory', *Aerospace Engineering* **19**.

Stoustrup, J. & Niemann, H. (1997), 'Multiobjective Control for Multivariable Systems with Mixed-Sensitivity Specifications', *International Journal on Control* **66**(2), 225–243.

Strauch, H., Görlach, T. & Ankersen, F. (1996), 'Controller Design for RVB with a HERA Type Manipulator.', *Proceedings of 3'rd ESA International Conference on Spacecraft Guidance, Navigation and Control Systems. Nov.26-29* .

Sund, A., Tailhades, J. & Linden, P. (1991), 'Advanced Fault Tolerant AOCS Computer for Rendezvous and Docking Missions', *ESA, Spacecraft Guidance, Navigation and Control Systems Conf.* pp. 447–454.

Suslennikov, V. (1992), Radio System for Automatic Rendezvous and Docking of Soyuz, Progress Spacecraft and Mir Space Station, Technical report, Scientific-Research Institute of Precision Instruments., Moscow, Russia.

Symon, K. R. (1979), *Mechanics*, Addison-Wesley.

Terraillon, J., Ankersen, F., Vardanega, T. & Carranza, J. (1999), 'Automatic Code Generation and Space On-board Software.', *Proceedings of Data Systems in Aerospace, Lisbon, Portugal, May 17-21.* .

Tobias, A., Ankersen, F., Fehse, W., Pauvert, C. & Pairot, J. (1992), 'Design and Ground Verification of Proximity Operations.', *Proceedings of AAS/AIAA Space Flight Mechanics conference in Colorado Springs, USA. Feb. 24-26* .

Tong, C., Shijie, X. & Songxia, W. (2007), 'Relative Motion Control for Autonomous Rendezvous Based on Classical Orbit Element Differences', *Journal of Guidance, Control and Dynamics* **30**(4), 1003–1014.

Tsai, M., Geddes, E. & Postlethwaite, I. (1990*a*), 'Pole-Zero Cancellations and Closed-Loop Properties of an $\mathcal{H}^\infty$ Mixed Sensitivity Design Problem', *Proceedings of the* 29^{th} *Conference on Decision and Control* pp. 1028–1029.

Tsai, M., Geddes, E. & Postlethwaite, I. (1990*b*), 'Pole-Zero Cancellations and Closed-Loop Properties of an $\mathcal{H}^\infty$ Mixed Sensitivity Design Problem. Part 1: The Multivariable Case', *University of Leicester, Dept. of Engineering, Report 90-6* .

Tsai, M., Geddes, E. & Postlethwaite, I. (1992), 'Pole-Zero Cancellations and Closed-Loop Properties of an $\mathcal{H}^\infty$ Mixed Sensitivity Design Problem', *Automatica* **28**(3), 519–530.

Tsai, M., Postlethwaite, I. & Geddes, E. (1990), 'Pole-Zero Cancellations and Closed-Loop Properties of an $\mathcal{H}^\infty$ Mixed Sensitivity Design Problem. Part 1: The Scalar Case', *University of Leicester, Dept. of Engineering, Report 90-3* .

Tschauner, J. (1965), 'Neue Darstellung des Rendezvous bei elliptischer Ziel-bahn', *Astronautica Acta* **11**(5), 312–321.

Tschauner, J. (1967), 'Elliptic Orbit Rendezvous', *AIAA Journal* **5**(6), 1110–1113.

Tschauner, J. & Hempel, P. (1964), 'Optimale Beschleunigungsprogramme fur das Rendezvous-Manover', *Astronautica Acta* **10**(2), 296–307.

Tschauner, J. & Hempel, P. (1965), 'Rendezvous zu einem in elliptischer Bahn umlaufenden Ziel', *Astronautica Acta* **11**(2), 104–109.

Vaissiere, A. & Griseri, G. (1990), 'Attitude and Relative Position Measurement Assembly and GNC Computer Assembly On Board the Columbus Free Flying Laboratory', *AIAA Guidance, Navigation and Control Conference, Portland, OR, AIAA paper 90-3391* pp. 686–689.

Vallado, D. A. (2004), *Fundamentals of Astrodynamics and Applications*, Microcosm Press and Kluwer Academic Publishers.

Vankov, A., Alyoshin, A., Chliaev, P., Fehse, W. & Ankersen, F. (1996), 'Remote Intervention in Automatic On-Board GNC Systems.', *Proceedings of 3'rd ESA International Conference on Spacecraft Guidance, Navigation and Control Systems. Nov.26-29* .

Vinti, J. P. (1998), *Orbital and Celestial Mechanics*, American Institute of Aeronautics and Astronautics.

Voloshinov, V. & Levitin, E. (1999), 'Approximate Search for a Global Minimum in Problems of Mathematical Programming that are Close to Convex', *Computational Mathematics and Mathematical Physics* **39**(3), 365–396.

Walls, J., Greene, M. & Teoh, W. (1987), 'A Mathematical Model of the Orbital Maneuvering Vehicle', *Simulation* **48**(3), 98–102.

Weiss, J. (1981), Solution of the Equations of Motion for High Elliptic Orbits, Technical Report TN PRV-5 No. 7/81, ERNO Raumfahrttechnik, Bremen, Germany.

Wheelon, A. (1959), 'Midcourse and Terminal Guidance', *Space Technology* pp. 26–32.

Wie, B. (1998), *Space Vehicle Dynamics and Control*, American Institute of Aeronautics and Astronautics.

Wiesel, W. (2003), 'Optimal Impulsive Control of Relative Satellite Motion', *Journal of Guidance, Control and Dynamics* **26**(1), 74–78.

Wisniewski, R. (1996), Satellite Attitude Control Using Only Electromagnetic Actuation, Technical Report ISSN 0908-1208, Aalborg University, Aalborg, Denmark.

Wolfram, S. (1999), *The Mathematica Book*, Cambridge University Press.

Xu, Y., Fitz-Coy, N., Lind, R. & Tatsch, A. (2007), 'μ Control for Satellites Formation Flying', *Journal of Aerospace Engineering* **20**(1), 10–21.

Yamamoto, T., Ishijima, Y., Mitani, S., Oda, M., Ueda, S., Kase, T. & Murata, S. (2006), 'Study on the Navigation Laser Sensor for Spacecraft Rendezvous Missions', *Uchu Kagaku Gijutsu Rengo Koenkai Koenshu (Japanese)* **50**.

Yamanaka, K. (1997), 'Rendezvous Strategy of the Japanese Logistics Support Vehicle to the International Space Station', *Proceedings Third International Conference on Spacecraft Guidance, Navigation and Control Systems, ESTEC, Noordwijk, Nov. 26-29* .

Yamanaka, K. & Ankersen, F. (2002), 'New State Transfer Matrix for Relative Motion on an Arbitrary Elliptical Orbit.', *Journal of Guidance, Control and Dynamics.* **25**(1), 60–66.

Zanon, D. & Campbell, M. (2006), 'Optimal Planner for Spacecraft Formations in Elliptical Orbits', *Journal of Guidance, Control and Dynamics* **29**(1), 161–171.

Zetocha, P., Self, L., Wainwright, R., Burns, R. & Surka, D. (2000), 'Commanding and Controlling Satellite Clusters', *IEEE Intelligent-Systems* **15**(6), 8–13.

Zhao, K. & Stoustrup, J. (1997), 'Computation of the Maximal Robust $\mathcal{H}_2$ Performance Radius for Uncertain Discrete Time Systems with Nonlinear Parametric Uncertainties', *International Journal of Control* **67**(1), 33–43.

Zhou, K. & Doyle, J. (1998), *Essentials of Robust Control*, Prentice Hall.

Zhou, K., Doyle, J. & Glover, K. (1995), *Robust and Optimal Control*, Prentice Hall.

Zhou, K., Khargonekar, P., Stoustrup, J. & Niemann, H. (1995), 'Robust Performance of Systems with Structured Uncertainties in State Space', *Automatica* **31**(2), 249–255.

Ziegler, J. & Nichols, N. (1942), 'Optimum Settings for Automatic Controllers', *Transactions of the American Society of Mechanical Engineers* **64**, 759–768.

Zimpfer, J., Shieh, S. & Sunkel, J. (1998), 'Digitally Redesigned Pulse-Width Modulation Spacecraft Control', *Journal of Guidance, Control, and Dynamics* **21**(4), 529–534.

Symbols and Variables

The symbols used are listed where they are used the first time or where the same symbol is used later with a different meaning.

Chapter 1:
None

Chapter 2:

ε	orbit eccentricity
s_1	station keeping point
s_2	station keeping point
s_3	station keeping point
s_{3a}	station keeping point
s_4	station keeping point

Chapter 3:

A	spacecraft cross sectional area
$\mathbf{A}_f$	flexible state space model matrix
$\mathbf{A}_s$	sloshing state space model matrix
α	ISS flexible modes Euler angles for docking port
α_{rvs}	Rendezvous sensor elevation angle
α_s	sloshing constant
$\mathbf{B}_f$	flexible state space model matrix
$\mathbf{B}_s$	sloshing state space model matrix
β	ISS rigid attitude angle for one axis
β_{rvs}	Rendezvous sensor azimuth angle
C_B	ballistic coefficient
C_d	drag coefficient
$\mathbf{C}_f$	flexible state space model matrix
$\mathbf{C}_s$	sloshing state space model matrix
c_s	sloshing damping constant
d	target attitude reversal time

$\mathbf{D}_f$	flexible state space model matrix
$\mathbf{d}_g$	gyro drift
η	flexible modes state
$\mathbf{F}$	force vector
$\mathcal{F}_b$	intermediate frame
$\mathcal{F}_{bc}$	chaser body frame
$\mathcal{F}_{bt}$	ISS body frame
$\mathbf{F}_d$	air drag force
$\mathbf{F}_{dc}$	chaser drag force
$\mathcal{F}_{dc}$	chaser docking frame
$\mathbf{F}_{dd}$	differential drag force on chaser spacecraft
$\mathbf{F}_{dt}$	target drag force
$\mathcal{F}_{dt}$	ISS docking frame
$\mathcal{F}_{dt0}$	ISS auxiliary docking frame
$\mathcal{F}_{gc}$	chaser geometrical frame
$\mathcal{F}_{gt}$	ISS geometrical frame
$\mathcal{F}_i$	inertial frame
$\mathbf{F}_L$	sloshing perturbation force, liquid part
$\mathbf{F}_P$	sloshing perturbation force
$\mathbf{F}_p$	force vector of the propulsion
$\mathcal{F}_o$	local orbital frame (LVLH)
$\mathcal{F}_{rc}$	Rendezvous sensor measurement frame on the chaser spacecraft
$\mathbf{F}_S$	sloshing perturbation force, solid part
$\mathbf{F}_{th}$	thruster force vector
f_k	eigen frequency of flexible mode k
γ_{index}	sloshing related accelerations
$\mathbf{I}$	general inertia matrix
$\mathbf{I}_c$	chaser inertia matrix
$\mathbf{I}_t$	ISS inertia matrix
k_g	gyro scale factor
k_s	sloshing spring constant
$\mathbf{L}_{index}$	flexible modes modal participation factors matrix
$\mathbf{l}_{index}$	flexible modes modal participation factors vector
λ	empirical function for sloshing
$\mathbf{M}_T$	mass/inertia matrix for flexible modes model
m_c	chaser mass
m_k	modal mass
m_L	fuel mass
m_t	target mass
m_0	solid sloshing fuel mass

m_1	liquid sloshing fuel mass
μ	Earth gravitational constant
$\mathbf{N}_g$	gravity gradient torque vector
$\mathbf{N}_p$	torque vector of the propulsion
$\mathbf{n}_g$	gyro noise vector
$\boldsymbol{\omega}$	spacecraft angular rate
$\boldsymbol{\omega}_g$	gyro measured angular rates
R	Rendezvous sensor range
$\mathbf{R}_p$	rotation matrix from nominal panel frame to panel frame
$\mathbf{R}_{pbc}$	rotation matrix from body frame to panel frame
$\mathbf{r}$	orbit radius
$\hat{\mathbf{r}}$	unit vector along orbit radius
$\mathbf{r}_{bc}$	location of $\mathcal{F}_{bc}$ given in $\mathcal{F}_{gc}$
$\mathbf{r}_{bt}$	location of $\mathcal{F}_{bt}$ given in $\mathcal{F}_{gt}$
$\mathbf{r}_{dc}$	chaser docking port with respect to COM
$\mathbf{r}_{dt}$	target docking port with respect to COM
$\mathbf{r}_f$	target docking port flexible displacement
$\mathbf{r}_{gdc}$	location of $\mathcal{F}_{dc}$ given in $\mathcal{F}_{gc}$
$\mathbf{r}_{gdt}$	location of $\mathcal{F}_{dt}$ given in $\mathcal{F}_{gt}$
$\mathbf{r}_r$	target docking port rigid displacement
$\mathbf{r}_{rc}$	location of $\mathcal{F}_{rc}$ given in $\mathcal{F}_{gc}$
$\mathbf{r}_{rt}$	location of the target pattern given in $\mathcal{F}_{dt}$
$\mathbf{r}_{th}$	location of a thruster given in $\mathcal{F}_{gc}$
$\mathbf{r}_1$	lever arm of sloshing mass m_1
ρ	atmospheric density
τ	tank filling ratio
τ	STR delay
$\boldsymbol{\theta}$	true attitude vector $[\theta_x, \theta_y, \theta_z]^{\mathrm{T}}$
$\boldsymbol{\theta}_{str}$	star tracker measured attitude
$\boldsymbol{\theta}_{str_b}$	star tracker attitude bias
$\boldsymbol{\theta}_{str_n}$	star tracker attitude noise
$\mathbf{u}$	input vector to flexible modes model
$\mathbf{v}$	velocity vector relative to atmosphere
$\mathbf{v_t}$	target attitude rate boundary
X,x	refers to first axis of a frame
$\mathbf{x}_f$	state vector for flexible modes
$\mathbf{x}_{rvs}$	Rendezvous sensor Cartesian position vector
$\mathbf{x}_s$	state vector for sloshing
$\mathbf{x}_1$	state vector one sloshing mass
Y,y	refers to second axis of a frame

$\mathbf{y}_f$	output vector for flexible modes
Z,z	refers to third axis of a frame
ζ_k	damping of flexible mode k

Chapter 4:

$\mathbf{A}(\theta)$	out of plane transition matrix
$\mathbf{A}_{CW}(\tau)$	out of plane state transition matrix for circular orbits
$\mathbf{A}_p$	state coefficient matrix
$\mathbf{A}_{pi}$	in plane coefficient matrix
$\mathbf{A}_{po}$	out of plane coefficient matrix
$[\alpha, \beta, \gamma]^{\mathrm{T}}$	transformed state vector variables of $[x, y, z]^{\mathrm{T}}$
$\mathbf{B}(\theta, \theta_0)$	out of plane state transition matrix
$\mathbf{B}_p$	state input matrix
$\mathbf{B}_{pi}$	in plane coefficient matrix
$\mathbf{B}_{po}$	out of plane coefficient matrix
C_1	integration constant of $J(\theta)$
c_{comp}	compensation between linear and curvilinear coordinate systems
c_i	i^{th} integration constant
D	matrix to derive equations for the general ΔV maneuvers
d_{ij}	elements of matrix D
ε	orbit eccentricity
E	eccentric anomaly
$\mathbf{F}$	force vector
$\mathbf{F}_g$	gravity field force vector
$\mathbf{F}_i$	in plane force vector
$\mathbf{F}_o$	out of plane force vector
$\mathbf{f}_g$	normalized gravity field force vector
$\mathbf{F}(\theta, E)$	integral matrix for elliptical out of plane solution
G	universal gravitational constant
h	normalized angular momentum
$I(\theta)$	earlier integral for obtaining second homogeneous in plane solution
I_{ijk}	integrals of the particular solutions
$J(\theta)$	new integral for obtaining second homogeneous in plane solution
k	constant for elliptical orbits
k_i	i^{th} integration constant
$\mathbf{L}$	angular momentum vector
$\mathbf{\Lambda}(\theta)$	transformation matrix from time domain to θ domain out of plane
$\mathbf{\Lambda}_i(\theta)$	transformation matrix from time domain to θ domain for in plane
$\lambda(\theta)$	intermediate variables
$\mathbf{M}$	Jacobian matrix

M	mass of the Earth
m	mass
m_c	chaser mass
m_t	target mass
μ	Earth gravitational constant
$\boldsymbol{\omega}$	angular velocity vector
ω	modulus of $\boldsymbol{\omega}$
p	$p = h^2\mu^{-1}$ conic section
$\mathbf{\Phi}$	in plane state transition matrix
$\mathbf{\Phi}_{CW}(\tau)$	in plane state transition matrix for circular orbits
$\phi(\theta)$	intermediate variables
φ_i	i^{th} differential equation solution for the in plane solutions
$\mathbf{r}$	general position vector
$\mathbf{r}_c$	chaser inertial position vector
$\mathbf{r}_t$	target inertial position vector
ϱ	function for conic section denominator
$\mathbf{s}$	relative inertial position vector
T	orbital period
t	time
τ	relative time interval
θ	true anomaly
$\mathbf{U}$	fundamental matrix of homogeneous solution
W	Wronskian
$\mathbf{x}$	state vector
$\mathbf{x}_p$	position state vector of linear dynamics state space system
$\mathbf{x}_{pi}$	in plane position state vector of linear dynamics system
$\mathbf{x}_{p_i}$	in plane particular solution
$\mathbf{x}_{po}$	out of plane position state vector of linear dynamics system
$\mathbf{x}_{p_o}$	out of plane particular solution

Chapter 5:

$\mathbf{A}_c$	attitude system matrix
$\mathbf{A}_d$	dynamics system matrix
$\mathbf{A}_k$	kinematics system matrix
$\mathbf{A}_{ra}$	relative attitude system matrix
$\mathbf{A}_t$	target attitude system matrix
$\mathbf{a}$	auxiliary variable
$\mathbf{B}_c$	attitude input matrix
$\mathbf{B}_d$	dynamics input matrix
$\mathbf{B}_k$	kinematics input matrix

$\mathbf{B}_{ra_1}$	relative attitude input matrix
$\mathbf{B}_{ra_2}$	relative attitude input matrix
$\mathbf{e}$	Euler eigen axis
$\mathbf{I}$	inertia matrix
k	target attitude frequency
$\mathbf{N}$	external torque vector
$\mathbf{\Omega}$	angular velocity skew matrix
$\boldsymbol{\omega}$	angular velocity
$\boldsymbol{\omega}_{bci}$	angular velocity body frame to inertial frame
$\boldsymbol{\omega}_{bco}$	angular velocity body frame to orbit frame
$\boldsymbol{\omega}_c$	chaser attitude angular rate
$\boldsymbol{\omega}_{oi}$	angular velocity orbit frame to inertial frame
$\boldsymbol{\omega}_{ra}$	relative attitude rate
$\boldsymbol{\omega}_t$	target attitude angular rate
$\boldsymbol{\omega}_0$	angular velocity of operating point
$\mathbf{q}$	quaternion
$\mathbf{R}$	rotation matrix
$\mathbf{r}_{dc}$	chaser docking port with respect to COM
$\mathbf{r}_{dt}$	target docking port with respect to COM
$\tilde{\mathbf{r}}_{dt}$	target docking port with respect to COM small signal
$\mathbf{r}_{pp}$	port to port distance
φ	phase angle for the ISS attitude motion
t_{start}	time of 1^{st} amplitude in ISS attitude
$\boldsymbol{\theta_c}$	chaser small signal attitude
$\boldsymbol{\theta}_{ra}$	relative attitude
$\boldsymbol{\theta_t}$	target small signal attitude
u	auxiliary variable
x	auxiliary variable
$\mathbf{x}_c$	attitude state vector
$\mathbf{x}_t$	target attitude state vector
$\mathbf{y}_{ra}$	relative attitude output vector

Chapter 6:
None

Chapter 7:

$\mathbf{A}$	a system matrix
a	acceleration
a	semi major axis
a	guidance acceleration

a	parameter in ellipse formulation
a_{ij}	simplex coefficients
α	arbitrary variable
$\mathbf{B}_{ra_1}$	relative attitude input matrix
$\mathbf{B}_{ra_2}$	relative attitude input matrix
b	parameter in ellipse formulation
b_{ij}	simplex coefficients
d	guidance deceleration, typically $d = -a$
ε	orbit eccentricity
$\mathbf{F}$	discrete time state space matrix
F_{th}	thrust size
γ	arbitrary constant
k	arbitrary constant
λ_i	i^{th} root
$\mathbf{M}$	monodromy matrix
M	total simplex constraints $M = m_1 + m_2 + m_3$
μ	Earth gravitational constant
ν	guidance exponential braking slope
$\mathbf{N}$	torque vector from propulsion
$\mathbf{n}_n$	the direction unit vector of the n^{th} thruster
p	$p = h^2\mu^{-1}$ conic section
$\mathbf{\Phi}(t, t_0)$	state transition matrix
r	orbital radius
$\mathbf{R}$	constant matrix
ρ	atmospheric density
s_3	station keeping point
s_{31}	point from acceleration to const. speed
s_{32}	point from const. speed to acceleration
s_4	station keeping point
s_{41}	point from acceleration to const. speed
T	sampling time or period time
T_{MIB}	Minimum Impulse Bit on time
t_0	start of guidance velocity profile
t_1	guidance velocity switching time
t_2	guidance velocity switching time
t_3	guidance velocity switching time
t_4	guidance velocity switching time
t_{41}	guidance velocity switching time
t_{sk}	guidance SK duration at s_4
t_{on}	thruster on time

θ	true anomaly
θ_0	attitude offset angles
v	orbital speed
$\mathbf{x}(t)$	state vector
x_n	simplex variable for n^{th} thruster
z, z_{th}	performance index

Chapter 8:

$\mathbf{A}$	a system matrix
$\mathbf{A}_c$	attitude system matrix
$\mathbf{B}$	a system matrix
β	solar panel rotation angle
$\mathbf{C}$	a system matrix
$\mathbf{D}$	a system matrix
$\mathbf{D}$	scaling matrix for RS and RP
$\mathbf{\Delta}$	uncertainty block diagonal matrix in LFT
δ_i	uncertainty parameter in LFT
$\delta_{\dot{\omega}}$	uncertainty parameter for $\dot{\omega}$
$\mathbf{e}$	output equation noise
e_{max}	maximum value of control error
ε	orbit eccentricity
$\mathbf{F}$	discrete time state space matrix
$\mathbf{F}_{max}$	maximum omni directional force
$\mathbf{G}$	discrete time state space matrix
$\mathbf{G}$	transfer function matrix
$\mathbf{I}$	identity matrix and inertia matrix
J	performance index function
$\mathbf{K}$	general controller
$\mathbf{K}$	Kalman filter gain matrix
k_f	scaling constant in LFT flexible model
k_i	scaling constant in LFT models
$k_{\dot{\omega}}$	scale factor for $\dot{\omega}$ uncertainty
$\mathbf{L}$	feedback gain matrix
$\mathbf{L}_i$	factorizing variable for LFT
λ_i	i^{th} root
$\mathbf{M}$	arbitrary transfer function matrix
M_P	maximum overshoot
m	matrix index variable
μ	structured singular value

$\mathbf{N}$	plant transfer matrix in robustness formulation
$\mathbf{N}_{max}$	maximum omni directional torque
n	matrix index variable
$\mathcal{O}$	observability matrix
$\dot{\omega}$	orbital angular acceleration
ω_l	orbital rate lower bound
ω_u	orbital rate upper bound
$\mathbf{\Phi}(t, t_0)$	state transition matrix
$\mathbf{Q}$	weighting matrix
$\mathbf{R}$	weighting matrix
$\mathbf{S}$	sensitivity function
$\mathbf{S}_i$	factorizing variable for LFT
$\mathbf{\Sigma}$	singular value matrix in SVD
$\bar{\sigma}$	maximum singular value
$\underline{\sigma}$	minimum singular value
$\mathbf{T}$	complementary sensitivity function
t_r	rise time
t_s	settling time
θ	true anomaly
$\mathbf{U}$	unitary matrix in SVD
$\mathbf{u}$	input vector
$\mathbf{V}$	unitary matrix in SVD
$\mathbf{v}$	state equation noise
$\mathbf{W}$	uncertainty weighting matrix
$\mathbf{w}$	exogenous inputs
$\mathbf{X}$	solution of ARE
$\mathbf{x}(t)$	state vector
$\hat{\mathbf{x}}(t)$	estimated state vector
$\mathbf{Y}$	solution of ARE
$\mathbf{z}$	exogenous outputs
ζ_k	damping of flexible mode k
ζ_l	damping lower bound
ζ_u	damping upper bound

Chapter 9:

$(\cdot)'$	a variable normalized wrt. its maximum value
$\mathbf{A}$	a system matrix
a	acceleration
$\mathbf{A}_d$	dynamics system matrix
$\mathbf{A}_k$	kinematics system matrix

$\mathbf{A}_{pi}$	in plane coefficient matrix
$\mathbf{A}_{po}$	out of plane coefficient matrix
$\mathbf{B}$	a system matrix
$\mathbf{B}_k$	kinematics input matrix
$\mathbf{B}_{pi}$	in plane coefficient matrix
$\mathbf{B}_{po}$	out of plane coefficient matrix
$\mathbf{C}$	a system matrix
$\mathbf{D}$	a system matrix
$\mathbf{D}$	scaling matrix for RS and RP
d	target attitude reversal time
$\mathbf{\Delta}$	uncertainty block diagonal matrix in LFT
δ_m	uncertainty parameter for m_c
δ_m	uncertainty parameter for m_c
$\delta_{\dot{\omega}}$	uncertainty parameter for $\dot{\omega}$
δ_s	uncertainty parameter in LFT sloshing model
$\mathbf{e}$	control error
e_{max}	maximum value of control error
ε	orbit eccentricity
$\mathbf{F}$	force vector from propulsion or system matrix
F_{acc}	guidance acceleration force
$\mathbf{F}_{max}$	maximum omni directional force
$\boldsymbol{F}_{\infty}$	central controller in $\mathcal{H}_{\infty}$ algorithm
γ	condition number
$\mathbf{G}_{fr}$	transfer function frequency response matrix
γ	arbitrary constant
$\mathbf{I}$	identity matrix and inertia matrix
$\mathbf{K}$	general controller
k_i	scaling constant in LFT models
k_m	scaling constant in LFT of m_c
$k_{\dot{\omega}}$	scale factor for $\dot{\omega}$ uncertainty
k_p	arbitrary constant
κ_s	scaling constant in LFT of sloshing model
$\mathbf{L}$	feedback gain matrix
$\mathbf{M}$	arbitrary transfer function matrix
M_P	maximum overshoot
ω_{cl}	closed loop cross over frequency
$\dot{\omega}$	orbital angular acceleration
ω_l	orbital rate lower bound
ω_u	orbital rate upper bound
$\mathbf{P}$	arbitrary transfer function matrix

$\mathbf{P}$	plant transfer matrix in robustness formulation
$\mathbf{Q}$	arbitrary transfer function matrix
$\mathbf{R}$	arbitrary transfer function matrix
$\mathbf{r}_{bt}$	target body frame location in $\mathcal{F}_{gt}$
$\mathbf{r}_{gdt}$	target docking port with respect to $\mathcal{F}_{gt}$
$\mathbf{r}_{dt}$	target docking port with respect to COM
ρ	spectral radius
r_{max}	maximum value of reference
$\mathbf{S}$	sensitivity function
s_3	station keeping point
s_4	station keeping point
$\mathbf{T}$	complementary sensitivity function
t_r	rise time
θ	true anomaly
$\mathbf{u}$	input vector
$\mathbf{v}$	robust controller input
$\mathbf{W}_i$	weighting functions for mixed sensitivity
$\mathbf{w}$	exogenous inputs
$\boldsymbol{X}_\infty$	Riccati equation solution in $\mathcal{H}_\infty$ algorithm
$\mathbf{Y}$	arbitrary transfer function matrix
$\boldsymbol{Y}_\infty$	Riccati equation solution in $\mathcal{H}_\infty$ algorithm
$\mathbf{z}$	exogenous outputs

Chapter 10:

$(\cdot)'$	a variable normalized wrt. its maximum value
$\mathbf{A}$	a system matrix
$\mathbf{B}$	a system matrix
$\mathbf{C}$	a system matrix
$\mathbf{\Delta}$	uncertainty block diagonal matrix in LFT
e_{max}	maximum value of control error
ε	orbit eccentricity
$\mathbf{G}$	transfer function matrix
γ	arbitrary constant
$\mathbf{K}$	general controller
$\mathbf{K}_1$	feedforward controller for two degree of freedom controller
$\mathbf{K}_2$	feedback controller for two degree of freedom controller
M_P	maximum overshoot
$\mathbf{P}$	arbitrary transfer function matrix
$\mathbf{P}$	plant transfer matrix in robustness formulation
r_{max}	maximum value of reference

$\mathbf{S}$	sensitivity function
$\mathbf{S}_2$	sensitivity function for two degree of freedom controller
$\mathbf{s}_{pp}$	port to port distance
$\dot{\mathbf{s}}_{pp}$	port to port velocity
$\mathbf{T}$	complementary sensitivity function
$\mathbf{T}_2$	equivalent to $\mathbf{T}$ for two degree of freedom controller
t_r	rise time
$\boldsymbol{\theta_c}$	chaser small signal attitude
$\boldsymbol{\theta}_{ra}$	relative attitude
$\mathbf{W}$	uncertainty weighting matrix
$\mathbf{W}_i$	weighting functions for mixed sensitivity
$\mathbf{x}(t)$	state vector
$\mathbf{V}_d$	decoupling matrix

Chapter 11:

δ_a, δ_b	interval width for 95% confidence
ε	orbit eccentricity
M, N	tabular values to determine sample size
n	number of Monte Carlo runs
s^2	variance estimate
σ	standard deviation
θ	attitude

Appendix A:	See chapter 4
$\mathbf{A}_p$	state coefficient matrix
a	semi major axis
$\mathbf{B}_p$	state input matrix
b	semi minor axis
e	total energy
e_{pot}	potential energy
e_{kin}	kinetic energy
$\mathbf{F}$	force vector
S	area of ellipse
T	orbital period
v	orbital speed
$\mathbf{x}_p$	position state vector of linear dynamics state space system

Appendix B:

$\mathbf{a}$	auxiliary variable
$\mathbf{b}$	auxiliary variable

$\mathbf{g}$	auxiliary variable
$\mathbf{p}$	auxiliary variable
$\mathbf{q}$	quaternion
$\mathbf{q}^*$	conjugate quaternion
$\mathbf{q}_{ba}$	quaternion from frame a to frame b
$\mathbf{q}_{ca}$	quaternion from frame a to frame c
$\mathbf{q}_{cb}$	quaternion from frame b to frame c
$\mathbf{q}'$	auxiliary variable
$\mathbf{q}''$	auxiliary variable
$\mathbf{R}$	DCM rotation matrix
$\mathbf{R}_{ba}$	DCM from frame a to frame b
$\mathbf{R}_1$	intermediate rotation matrix
$\mathbf{R}_2$	intermediate rotation matrix
$\mathbf{R}_3$	intermediate rotation matrix
$\mathbf{r}_{dt}$	target docking port with respect to COM
$\tilde{\mathbf{r}}_{dt}$	target docking port with respect to COM small signal
$\mathbf{v}_a$	arbitrary vector
$\mathbf{v}'_a$	vector in quaternion notation, auxiliary
$\mathbf{v}_b$	arbitrary vector

Appendix C:

α	ISS flexible modes Euler angles for docking port
$\mathbf{I}_t$	ISS inertia matrix
m_t	target mass
$\mathbf{r}_{bt}$	location of $\mathcal{F}_{bt}$ given in $\mathcal{F}_{gt}$
$\mathbf{r}_{gdt}$	location of $\mathcal{F}_{dt}$ given in $\mathcal{F}_{gt}$

Appendix D:

$\mathbf{A}$	arbitrary matrix
a, b	Simplex intermediate variables
Δ	arbitrary matrix
$\mathbf{H}$	partitioned arbitrary matrix
$\mathbf{K}$	arbitrary matrix
$\mathbf{M}$	partitioned arbitrary matrix
m_I	Simplex constraints
$\mathbf{Q}$	arbitrary matrix
$\mathbf{R}$	arbitrary matrix
$\mathbf{r}$	input for LFT computations
s_i, t_i	intermediate points and times for guidance
$\mathbf{v}$	output for LFT computations

x_i Simplex constraints
z Simplex function to maximize

Index